DEFORMATION PROCESSING APPLIED TO THE AL-MG ALLOY SYSTEM

by

MICHAEL GEORGE TUTCHER B.Sc.(ENG.), A.R.S.M.

A thesis presented for the Degree
of Doctor of Philosophy of the
University of London

September 1979

John Percy Research Group
Department of Metallurgy and
Materials Science
Imperial College of Science and
Technology
London SW7 2BP

DEFORMATION PROCESSING APPLIED TO THE AL-MG ALLOY SYSTEM

MICHAEL GEORGE TUTCHER B.Sc.(ENG.), A.R.S.M.

Abstract

The hot deformation of three commercial aluminium-magnesium alloys has been thoroughly investigated. Hot working theory has been successfully applied to both hot torsion tests and the direct extrusion process enabling flow stress to be related to both strain rate and temperature.

Two axi-symmetric upper bound solutions have been proposed to predict extrusion pressures and strain rates.

The effects of ram speed, billet temperature and reduction ratio upon the maximum extrusion pressure and excess pressure necessary to initiate extrusion have been investigated. New relationships relating pressure to extrusion ratio have been derived showing the considerable effect of temperature upon the quasi-static deformation zone geometry; a feature not revealed from theoretical considerations. The onset of unacceptable surface condition has been related to the extrusion process variables.

The development of structure during extrusion has been extensively investigated using a super-pure aluminium 5% magnesium alloy and a commercial equivalent. High temperature restoration via dynamic recovery was observed in the former case while dynamic recrystallization has been shown to be operative in the latter case at temperatures above 400°C.

Both metallographic and property studies, via tensile and hardness testing, have been made to relate structure and properties to the process variables. It has been concluded that the onset of dynamic recrystallization radically modifies both features and precludes their inclusion in limit diagrams. Limit diagrams are presented for limiting pressures and surface conditions.

A comparative study has been made between the process of hot torsion and hot extrusion.

The effect of billet heat treatment upon product structure has been investigated.

ACKNOWLEDGEMENTS

The author wishes to express his sincere thanks to Dr. T. Sheppard for his initiation of the project and his encouragement, supervision and guidance during the course of this work. Sincere thanks are also expressed to past and present members of the John Percy Research Group notably Dr. H. McShane, Dr. D. Wright, P. Tunnicliffe, T. Pitt and S. Patteson for their helpful discussions and suggestions. Also to R. Parkinson who helped with part of the practical work.

Thanks are also due to Mr. A. Neve and his colleagues in the John Percy Group Technical Staff for equipment design and manufacture and maintenance of the press. Thanks are also extended to the other technical staff in the department who assisted in specimen preparation and thesis production.

The author also wishes to express his appreciation to Alcan International Ltd. and the Aluminium Company of America Ltd. for their generous and prompt supplying of experimental materials and to the Science Research Council for their financial support.

Thanks are also expressed to Mrs. S. Greenwood for her prompt and accurate typing of this thesis.

Finally, thanks are expressed to the author's parents, Mr. and Mrs. L.G. Tutcher, his wife Jill, and all members of his family for their unending moral and financial support throughout the entire duration of the work.

CONTENTS

	Page
CHAPTER 1. LITERATURE REVIEW	18
1.1. Introduction	18
1.1.1. The Load-Displacement Locus	19
1.1.2. Metal Flow During Extrusion	23
1.1.3. General Structural Aspects of Aluminium Extrusion	24
1.2. The Aluminium-Magnesium Alloy System	25
1.3. The Analysis of Extrusion	28
1.3.1. Theoretical Approach to Extrusion Pressure	28
1.3.1.1. Slip Line Field Techniques	29
1.3.1.2. Plane Strain Upper Bound Solutions	30
1.3.1.3. Axi-symmetric Upper Bound Solutions	31
1.3.2. Empirical Approaches to Pressure Determination	33
1.3.3. Strain Rate During Extrusion	35
1.3.4. Temperature Changes During Extrusion	37
1.4. Hot Working	39
1.4.1. Methods of Testing	40
1.4.1.1. Tensile Tests	40
1.4.1.2. Compression Tests	40
1.4.1.3. Torsion Testing	41
1.4.2. Empirical Approach to Hot Working	42
1.4.3. Structural Aspects of Hot Working	44
1.4.3.1. Static Restoration Processes	46
1.4.3.2. Dynamic Restoration Processes	48
1.4.3.3. Deformation Mode	54
1.4.3.4. The Effect of High Temperature Deformation on the Room Temperature Mechanical Properties	56
1.5. Defects in Extrusion	57
1.6. Limit Diagrams	58
CHAPTER 2. THEORY	62
2.1. Introduction	62
2.2. Axisymmetric Upper Bound Analyses for Rod Extrusion	62
2.2.1. Single Triangle Deformation Field	63
2.2.2. Double Triangle Deformation Field	71
2.3. Strain Rate During Extrusion	75

	Page
2.4. General Hot Working Equation	76
2.4.1. Assessment of High Temperature Flow Stress	76
2.4.1.1. Calculation of the Flow Stress from Torsion Data	77
2.4.1.2. Temperature Changes During Torsion Testing	79
2.4.2. Determination of the Constants in the Hot Working Equation	80
2.4.2.1. Graphical Analyses	80
2.4.2.2. Mathematical Treatment	81
2.5. Temperature Changes During Extrusion	85
2.5.1. Temperature Rise at Peak Pressure	85
2.5.2. Temperature Rise During the Ram Stroke	86
2.6. Homogenization	86
CHAPTER 3. EXPERIMENTAL	89
3.1. Introduction	89
3.2. The Extrusion Press	89
3.2.1. The Container Heating	92
3.2.2. Billet Preheat	92
3.2.3. Ram Speed and Displacement	93
3.2.4. Load Measurement	93
3.2.5. Tooling	93
3.3. The Water Quench	94
3.4. Experimental Procedure	94
3.5. Heat Treatment	96
3.6. Torsion Tests	96
3.7. Tensile Tests	99
3.8. Optical Microscopy	100
3.9. Transmission Electron Microscopy	100
3.10. Hardness Tests	101
3.11. Impact Tests	101
3.12. Partially Extruded Billets	101
3.13. Material	102

	Page
CHAPTER 4. RESULTS AND DISCUSSION	105
4.1. The Analysis of the Torsion Data	105
4.1.1. Nature of the Torque-Twist Curve	105
4.1.2. Torsion Test Results	111
4.1.3. Derivation of the Constants in the Hot Working Equation	129
4.1.3.1. Evaluation of the Constants from Torque Minimization	131
4.1.3.2. Flow Stress Minimization	137
4.1.3.3. Alternative Minimization of the Torque Data	138
4.1.3.4. Graphical Determination of the Hot Working Constants	140
4.2. Axisymmetric Upper Bound Analysis	158
4.2.1. Variation of $^{P}/\sigma$ with Extrusion Ratio	158
4.2.2. Theoretical Pressure Predictions	164
4.2.3. Variation of Deformation Zone Angles	170
4.2.4. Strain Rate Determination from the Upper Bound Analyses	174
4.3. Deformation Processing via High Temperature Extrusion	182
4.3.1. Extrusion Parameter Measurements	185
4.3.1.1. Variation of Peak Pressure with Initial Temperature	185
4.3.1.2. Variation of Peak Pressure with Ram Speed	189
4.3.1.3. Variation of Peak Pressure with Extrusion Ratio	191
4.3.1.4. Variation of Peak Pressure with the Z Parameter	194
4.3.1.5. Variation of Δp with the Z Parameter	201
4.3.1.6. Variation of $^{P}/\sigma$ with Extrusion Ratio	205
4.3.1.7. Variation of $^{P}/\sigma$ with the Z Parameter	209
4.3.1.8. The Relationship between Pressure, Extrusion Ratio and the Z Parameter	215
4.3.1.9. The Dependence of Surface Conditions upon the Process Variables	221
4.4.1. Development of Structure During Plastic Flow	225
4.4.1.1. Structural Development in Super-pure Al-5% Mg.	227
4.4.1.2. Structural Investigations	235
4.4.1.3. Extrudate Structure	242
4.4.1.4. Sub-grain Misorientations	242

		Page
4.4.1.5.	Sub-grain Size	245
4.4.1.6.	Development of Dislocation Structure related to the Peak Pressure	247
4.4.1.7.	Sub-grain Banding	248
4.4.2.1.	Structural Development in the Commercial Alloy D222 (5456)	249
4.4.2.2.	Structural Investigations	254
4.4.2.3.	Extrudate Structure	265
4.4.2.4.	Development of Dislocation Structure in Commercial 5456 (D222)	267
4.4.2.5.	Sub-grain Size	268
4.4.2.6.	Misorientations in 5456 (D222)	270
4.4.2.7.	Comparison of Restoration Processes for Super-pure and Commercial Al-5% Mg	270
4.5.1.	Structure of the Extrude	271
4.5.1.1.	Surface Condition of the Extrude	272
4.5.1.2.	Initial Material Structure	274
4.5.1.3.	The Variation of Microstructure across and along the Extrude	276
4.5.1.4.	Variation of Structure with Temperature and Strain Rate	282
4.5.1.5.	Variation of Substructure with the Process Variables	286
4.6.	Room Temperature Properties Resulting from the High Temperature Deformation	293
4.6.1.	Tensile Tests	299
4.6.1.1.	Nature of the Stress-Strain Curves	299
4.6.1.2.	Tensile Test Results	301
4.6.1.3.	Hardness Measurements	312
4.6.1.4.	Fracture Toughness	315
4.6.1.5.	Heat Treatment of 5456	315
4.6.1.6.	Sub-grain Size Relationship to Process Variables	317
4.7.	Limit Diagrams	317
4.7.1.	The Pressure Line	320
4.7.2.	The Incipient Melting Line	320
4.8.	Validity of Torsion as a Model for Extrusion	323
4.9.	Effect of Billet Homogenization	327

	Page
CHAPTER 5. CONCLUSIONS	330
Recommendations for Further Work	334
Appendix A	335
Appendix B	345
Appendix C	351
Appendix D	353
Appendix E	358
Appendix F	363
Appendix G	366
Errors	384
Nomenclature	385
References	387

Back cover: Enclosed- 2 publications submitted in support of this work.

List of Plates

Plate 1 General layout of extrusion press.

Plate 2 Container and die assembly

Plate 3 Torsion specimen and geometry

Plate 4 General layout of torsion machine

List of Tables

Table 1.1. Al-Mg alloy properties

Table 1.2. Analysis and notations of Experimental Materials

Table 4.2. Torsion results for D222 (5456)

Table 4.3. Torsion results for 5052

Table 4.4. Torsion results for 5083 (h)

Table 4.5. Torsion results for 5083

Table 4.6. Results for power relationship, $\sigma = A\dot{\varepsilon}^{m}$

Table 4.7. Mathematical results for max. torque-twist rate plots.

Table 4.8. Torque data minimization output for D222 (5456).

Table 4.9. Hot working constants from torque minimization

Table 4.10. Values of n and ΔH from reported creep work

Table 4.11. Hot working constants from flow stress minimization

Table 4.12. Torque data minimization output for D222 (5456)

Table 4.13. Hot working constants from alternative torque minimization

Table 4.14. Results for power and exponential fits to torsion data

Table 4.15. Gradient and intercept results for activation energy calculation

Table 4.16. Predicted deformation zone angles

Table 4.17. Upper bound strain rates

Table 4.18. Results for pressure variation with temperature

Table 4.19. Results for pressure variation with extrusion ratio

Table 4.20. Results for pressure variation with $\mathrm{Ln}Z_i$

Table 4.21. Results for P/σ variation with extrusion ratio

Table 4.22. Results for P/σ variation with the Z parameter

Table 4.23. Sub-grain misorientations for super-pure material

Table 4.24. Sub-grain sizes of super-pure material

Table 4.25. Sub-grain sizes of commercial alloy D222 (5456)

Table 4.26. Sub-grain misorientations of commercial alloy D222 (5456)

Table 4.27. Hardness variation with location on product

Table 4.28. Tensile properties for room temperature tests

Table 4.29. Tensile properties for 200°C tests

Table 4.30. Tensile properties for variation in test conditions

Table 4.31. Hardness results

Table 4.32. Ageing results

List of Figures

Fig. 1	Idealised load-displacement locus
Fig. 2	Flow curves for restoration by dynamic recovery and both dynamic recovery and dynamic recrystallization
Fig. 3	Basic Limit Diagram
Fig. 4	Axi-symmetric upper bound velocity field and hodograph for single triangle arrangement
Fig. 5	Nomenclature of elemental single triangle upper bound analysis
Fig. 6	Axi-symmetric upper bound velocity field and hodograph for double triangle arrangement
Fig. 7	Aluminium corner of the Al-Mg binary phase diagram
Figs.8-10	Experimental torque-twist curves
Fig. 11	Torque calibration curves
Figs.12-22	Stress-Strain curves for alloy D222 (5456)
Figs.23-25	Power relationships for σ vs $\dot{\varepsilon}$, for alloy D222 (5456)
Fig. 26	Torque-twist rate curves for alloy D222 (5456)
Fig. 27	Torque-twist rate curves for alloy 5083 (h)
Fig. 28	Torque-twist rate curves for alloy 5083
Fig. 29	Torque-twist rate curves for alloy 5456
Fig. 30	Torque-twist rate curves for alloy 5052
Fig. 31	Hot ductility variation with temperature
Fig. 32	$\ln\dot{\varepsilon}$ vs $\ln\sigma$, alloy D222 (5456)
Fig. 33	$\ln\dot{\varepsilon}$ vs σ, alloy D222 (5456)
Fig. 34	α vs Temperature, alloy D222 (5456)
Figs 35&36	Activation energy determination, alloy D222 (5456)
Fig. 37	ΔH vs Temperature, alloy D222 (5456)
Fig. 38	Derivation of variation of A and n with temperature
Fig. 39	Variation of A with temperature, alloy D222 (5456)
Fig. 40	Variation of n with temperature, alloy D222 (5456)
Fig. 41	Hot working relationship for temperature dependent A, α, n and ΔH

Fig. 42	LnZ vs Ln Sinh ($\alpha\sigma$), alloy D222 (5456)
Fig. 43	LnZ vs Ln Sinh ($\alpha\sigma$) using substituted torque data, alloy D222 (5456)
Fig. 44	Stress predictions from constituitive equations
Fig. 45	Theoretical $^{P}/\sigma$ variation with LnR.
Fig. 46	Comparison of theoretical and experimental $^{P}/\sigma$ for 2 inch container
Fig. 47	Comparison of theoretical and experimental $^{P}/\sigma$ for 3 inch container
Fig. 48	Pressure prediction for 3 inch container, alloy D222 (5456)
Fig. 49	Low temperature pressure prediction for 2 inch container, alloy D222 (5456)
Fig. 50	High temperature pressure prediction for 2 inch container, alloy D222 (5456)
Fig. 51	Variation of predicted and experimental pressures with temperature
Fig. 52	Pressure variation with temperature using experimental deformation zone angles
Fig. 53	Alternative velocity fields for direct rod extrusion
Fig. 54	Deformation zone angle variation with extrusion ratio from single triangle analysis.
Fig. 55	Deformation zone angle variation with extrusion ratio for double triangle analysis.
Figs56-59	Strain rate variation with extrusion ratio for theoretical ane experimental calculations
Figs 60-61	Strain rate variation with ram speed for theoretical and experimental calculations
Fig. 62	Experimental load-displacement loci
Figs 63-66	Max. Pressure vs. Initial Temperature for alloy D222 (5456)
Figs 67-68	Max. Pressure vs. Initial Temperature for 5052, 5083 and 5456
Fig. 69	Max. Pressure vs. Ram Speed
Figs 70-71	Max. Pressure vs. LnR, alloy D222, (5456)
Fig. 72	Max. Pressure vs. LnR, alloy 5052, 5083 and 5456
Fig. 73	Redundant Work vs. Temperature, alloy D222 (5456)

Figs 74-75 Max. Pressure vs. LnZ_i, alloy D222 (5456)

Figs 76-77 Max. Pressure vs. LnZ_i alloys 5052, 5083 and 5456

Fig. 78 Tangential construction for Δp evaluation

Fig. 79 Δp vs. LnZ_i, alloys 5083 and 5456

Figs 80-81 Δp vs. LnZ_i, alloy D222 (5456)

Figs 82-85 P/σ vs. LnR, alloy D222 (5456)

Figs 86-87 P/σ vs. LnZ_i, alloy D222 (5456)

Figs 88-89 Deformation patterns for low and high reductions, change with temperature

Figs 90-91 LnZ_i vs. Ln Sinh $\frac{\alpha p}{(a+bLnR-cLnZ)}$

Fig. 92 LnZ_i vs. Initial Temperature for various final surface conditions

Fig. 93 Locations of sampling positions on load-displacement locus for structural development

Fig. 94 Location of electron microscopy samples for structural development

Figs 95-101 Macrostructural development in super-pure Al-5% Mg alloy

Fig. 102 Deformation zone appearance for experimental observation

Fig. 103 Dislocation structure at location 1.C-E

Fig. 104 Dislocation wall formation at location 1E

Fig. 105 Sub-grain at a high angle grain boundary

Fig. 106 Sub-grain banding at die mouth, location 1A

Fig. 107 Sub-grain banding in sample 2A

Figs 108-110 Selected area diffraction patterns for banding at location 2A

Fig. 111 Sub-grains at a higne angle grain boundary

Fig. 112 Sub-grains with internal dislocation activity

Fig. 113 Sub-grains at a high angle grain boundary

Fig. 114 Elongated sub-grains in die mouth region of location 5A

Figs 115-116 Sub-grain formation at various orientations of high angle grain boundary

Fig. 117 High dislocation density within sub-grains at location 6A

Fig. 118 Sub-grain banding at location 6A

Fig. 119 Sub-grain structure in steady state deformation zone

Fig. 120 Substructure in dead-metal-zone

Fig. 121 Extrude peripheral structure

Fig. 122 Extrude core microstructure

Fig. 123 Extrude peripheral microstructure

Figs 124-128 Macrostructural development in alloy D222 (5456)

Fig. 129 Microstructure of die mouth region during upsetting

Fig. 130 Sub-grain walls pinned by second phase particles

Fig. 131 Sub-grain bands at location 4A

Fig. 132 Sub-grain wall formation

Fig. 133 Sub-grain free region

Fig. 134 Sub-grain formation

Fig. 135 Microstructure away from deformation zone

Fig. 136 Sub-grain formation

Figs 137-138 Deformation zone at location corresponding to peak pressure

Fig. 139 Dynamically recrystallized grain at a second phase particle

Figs 140-141 Diffraction patterns for dynamically recrystallized grain in Fig. 139

Fig. 142 Dislocation activity within a dynamically recrystallized grain

Figs 143-144 Sub-grains in the deformation zone from location 6

Fig. 145 Equi-axed dynamically recrystallized grains at original grain boundaries

Fig. 146 Sub-grains at a high angle grain boundary from location D

Fig. 147 Lining up of precipitates

Fig. 148 Degradation of structure prior to deformation zone

Fig. 149 Equi-axed sub-grains at location 7-B

Fig. 150 Sub-grain banding in the die mouth region

Fig. 151 Sub-grains in the die mouth region

Fig. 152 Dynamically recrystallized grains at original grain boundaries

Fig. 153 Sub-structure within the deformation zone

Fig. 154 Dynamically recrystallized grains from location 7-A

Figs 155-156 Dynamically recrystallized grain and internal substructure

Figs 157-158 Dynamically recrystallized grain and internal substructure

Fig. 159 Commercial alloy extrudate structure

Figs 160-163 Surface conditions of extrude

Fig. 164 Initial microstructure of alloy D222 (5456)

Fig. 165 Initial microstructure of alloy 5052

Fig. 166 Initial microstructure of alloy 5083

Fig. 167 Initial microstructure of alloy 5456

Figs 168-169 Low temperature extrude structure for a reduction of 10:1

Figs 170-171 High temperature extrude structure for a reduction of 10:1

Figs 172-175 Growth of statically recrystallized peripheral grains

Figs 176-180 Variation of microstructure with temperature for a reduction of 30:1

Figs 181-182 Microstructure of alloy 5083 for a reduction of 30:1

Fig. 183 Microstructure of alloy 5052

Fig. 184 Recrystallized annulus depth vs. $\mathrm{Ln}Z_i$

Figs 185-187 Substructure for run D222141

Figs 188-189 Substructure for run D222113

Figs 190-193 Substructure for runs D222117 and D222118

Figs 194-196 Substructure for run 119

Fig. 197 Substructure for alloy 5052

Fig. 198 Substructure for alloy 5083

Fig. 199 Substructure for alloy D222 (5456)

Fig. 200 High temperature substructure for a 10:1 reduction, alloy D222 (5456)

Fig. 201 Low temperature substructure for a 10:1 reduction, alloy D222 (5456)

Fig. 202 Room Temperature stress-strain curve

Fig. 203 Variation of tensile properties with test temperature for alloy D222 (5456)

Fig. 204 Variation of tensile properties with Crosshead Speed during the test for alloy D222 (5456)

Figs 205-207 Variation of tensile properties with LnZ_i, room temperature test for alloy D222 (5456)

Figs 208-210 Variation of tensile properties with LnZ_i, 200°C test, for alloy D222 (5456)

Fig. 211 Tensile property variation with LnZ_i for a reduction of 30:1, room temperature tests for alloy D222 (5456) for a crosshead speed of 0.05 cms/min

Fig. 212 Tensile property variation with LnZ_i for a reduction of 30:1, room temperature tests, for alloy D222 (5456) for a crosshead speed of 0.5 cms/mm

Figs 213-214 Tensile property variation with LnZ_i for a reduction of 30:1 room temperature tests, alloys 5052, 5083 and 5456

Fig. 215 Hardness vs. LnZ_i for a reduction of 10:1, alloy D222 (5456)

Fig. 216 Hardness vs. LnZ_i for a reduction of 30:1, alloy D222 (5456)

Fig. 217 Hardness vs. LnZ_i for a reduction of 30:1 for alloys 5052, 5083 and 5456

Fig. 218 Microhardness vs. LnZ_i for a reduction of 30:1 for alloy D222 (5456)

Fig. 219 Variation of Impact energy with LnZ_i for all alloys

Fig. 220 $(\text{Subgrain diameter})^{-1}$ vs. LnZ_i for alloy D222 (5456)

Fig. 221 Hardness vs. $(\text{sub-grain diameter})^{-1}$ for alloy D222 (5456)

Figs. 222-223 Experimental limit diagrams for alloy D222 (5456)

Figs 224-225 Low temperature torsion specimen microstructure, alloy D222 (5456)

Figs 226-227 High temperature torsion specimen microstructure, alloy D222 (5456)

Figs 228-233 Substructures for torsion and extrusion carried out for equivalent Z_i values

Figs 234-235 Low temperature unhomogenized extrude structure for a reduction of 10:1 for alloy D222 (5456)

Figs 236-237 High temperature unhomogenized extrude structure for a reduction of 10:1 for alloy D222 (5456)

CHAPTER 1

LITERATURE REVIEW

1.1 Introduction

Ever since the first record of the extrusion[1] process, attributed to Joseph Bramah for lead pipe production in 1797, researchers have endeavoured to enhance their fundamental knowledge of the process. Although the success of the early method is unknown, by the end of the nineteenth century the lead extrusion industry was well established and many of the features of modern day presses had been developed, such as bridge dies, fixed and floating mandrels, heated containers and accumulator drive. Because of the difficulty in producing sufficiently rigid materials for presses, the method was initially confined to working lead, but in 1894 Alexander Dick designed a horizontal press for extruding brass and the door was then open for growth in the field of metal extrusion. Since then the only significant changes have been in increasing size and efficiency through design and research to reach the present day situation when it is possible to extrude almost all metals from the soft aluminium alloys to the high temperature nickel alloys.

The great advantage of the process lies in the relative ease in which complex sections, including hollows, can be manufactured in one operation. In fact in some cases it is virtually the only production route available.

Early investigative work[1] was centred around developing empirical relationships between the extrusion parameters of pressure, speed, extrusion ratio, temperature and material. Although these results proved useful for background understanding, the work was very limited by the experimental facilities available and the narrow range of conditions researched.

An important step forward was the application of plasticity theory.[2,3] Both slip-line fields and load bounding solutions were obtained, but were seriously limited by the assumptions implicit in their derivation. In the initial cases both methods were restricted to situations of plane strain and to rigid perfectly

plastic materials. Later work removed the former condition from the upper bound case and solutions for strain hardening materials[4,5] were developed.

The recognition of the importance of temperature changes throughout the process initiated both experimental and theoretical investigations.[6-18] The results have shown the importance of temperature rise especially when dealing with situations close to the melting point or close to a phase change boundary. In addition the temperature changes also have a serious effect upon material properties and structure.

The most recent development has been the application of hot working theory to the extrusion process[19-23,16] and this has shown the limitations in predicting meaningful values of temperature, strain rate and flow stress to be used in any calculations.

Although the research to date has gone a long way to improve the understanding of the process it is only in the last few years that the industrial extruder has seen the importance of trying to relate final structure and properties to the process and material. It is in this direction that future work will undoubtably move in an attempt to overcome the argument previously made by industrialists that the research was of little or no importance.

1.1.1. The Load-Displacement Locus

In general terms the process involves pushing a metal billet through a die of required cross-section to give the product. Most metals are processed at elevated temperature for two reasons:

(1) To prevent work hardening increasing the load and thus the energy used.

(2) An extrude with a "cold worked" structure (i.e. high dislocation density) is very brittle.

Fig. 1 depicts an idealised load-displacement locus for the direct extrusion process and shows how it may be conveniently divided into three distinct stages. In this case the ram moves in the same direction as the product and there is relative movement

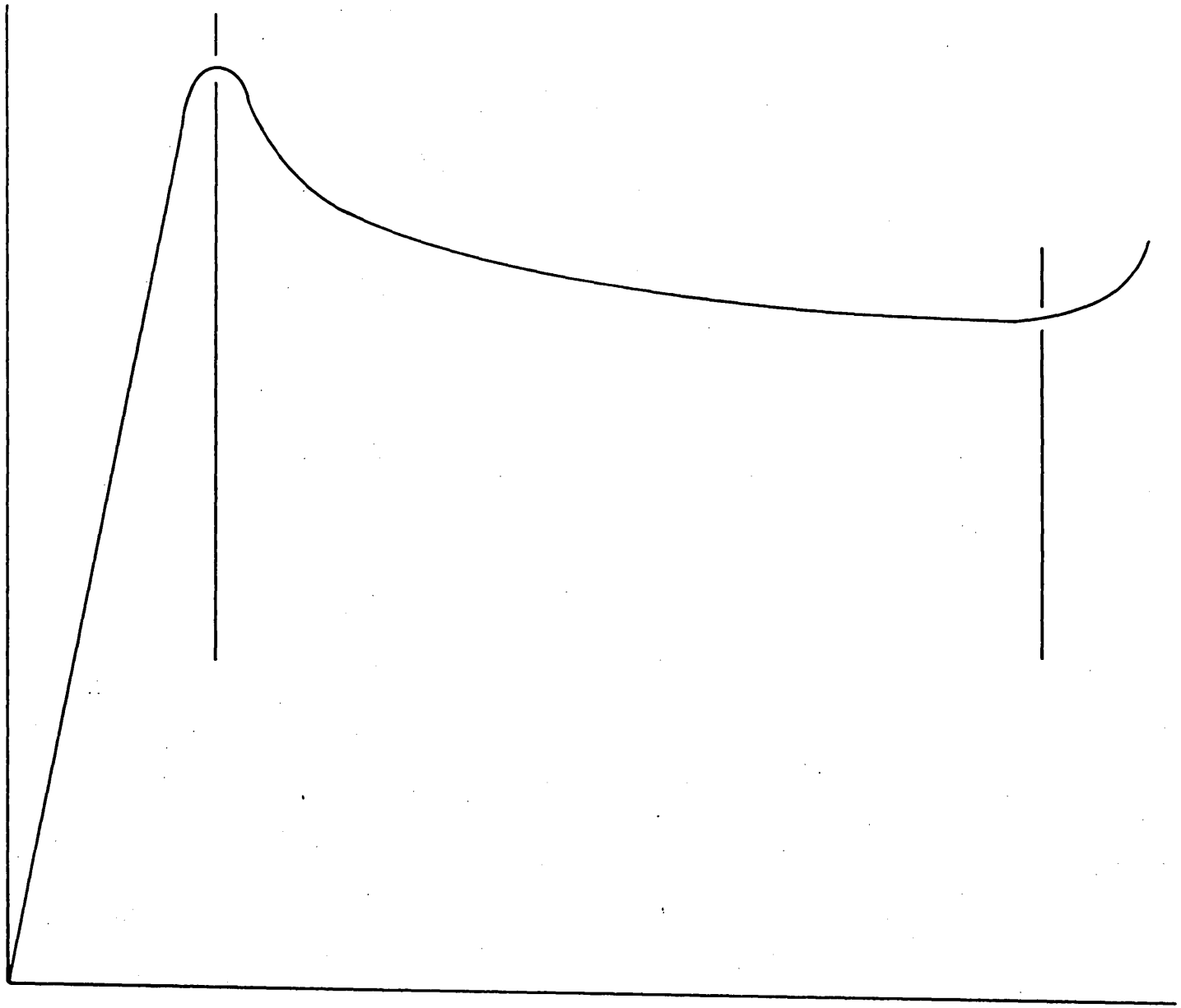


Fig. 1. Idealised load-displacement locus.

between the billet and the container. During the first stage (I) the billet is upset to fill the container and there is limited ram travel for a rapid increase in load. The second stage (II) is referred to as steady-state flow although for most complex alloys there is a rapid decrease in load between stages I and II usually accompanied in the industrial operation by an increase in ram velocity associated with the bulk modulus of the hydraulic fluid. The steady state shows a decrease in load with ram travel since the frictional force generated by the movement of billet relative to the container is reduced as the billet length decreases. The third stage (III) involves a rapid rise in load as the dummy block interferes with the deformation zone and for this reason a discard is left in the container and must be ejected prior to the repeat of the process. Immediately before this stage a piping defect[24] appears when the rear of the billet "caves" in and material from the sides of the billet flows laterally to occupy the newly created void. This often leads to a central core of undesirable material running through the latter stages of the extrude.

The controlling feature, which will determine whether extrusion proceeds or whether the billet sticks in the container is the maximum pressure which occurs at the boundary between stages (I) and (II). This pressure is referred to as the break-through pressure and must clearly lie within the capacity of the press. Hence the magnitude of this pressure imposes limitations upon the extrusion ratio, the initial billet temperature, the ram velocity and the billet length/diameter geometry, since each of these parameters affects the magnitude of the extrusion pressure. If it were possible to reduce this breakthrough pressure then larger reductions, longer billets, lower temperatures and higher ram speeds might be possible.

The existance of the peak between stages I and II has been recognised by many workers. Wilson[25] used mathematical techniques and suggested that it was caused by a transition from sticking to full-film lubrication. Since full-film lubrication is unlikely in the non-ferrous industrial situation no such transition could occur. Furthermore, Ziegler[26] has presented evidence that the peak exists in indirect extrusion where friction effects are virtually zero if

a flat faced die is utilised. Ashcroft and Lawson[27] associated the phenomenon with the temperature differential which exists between billet and die while Farag and Sellars[28] presented evidence supporting its connection with the die entrant angles. It has also been proposed[29] that this additional pressure represents the energy required to set up the dead metal zone, but since the peak has been observed[25,26,28] under conditions in which such a zone does not exist this explanation would appear to be invalid. Thus it would appear that mathematical explanations which ignore structural changes occurring in the material are unlikely to be fruitful.

Castle and Sheppard[23] indicated that it was much more likely that the additional pressure was associated with the energy required to establish the quasi-static deformation zone essential to all working processes. They proposed that the formation of the zone required an excess of dislocation sources leading to a greater than equilibrium dislocation density. This excess of dislocation production necessary to establish the steady state process would also imply a non-equilibrium flow stress resulting in the requirement of excess pressure.

A number of variations of Fig. 1 are commonly observed. Steel and Nimonic alloys[30] exhibit a 'steady state' region in which the load increases with ram displacement due to billet cooling from the high initial temperatures (1100-1200°C). This results in an increased flow stress and thus increased load. A derivative of the direct extrusion process is indirect extrusion.[26,31] In this case the ram is used to seal the open container end and the ram and container are then moved simultaneously at the same speed in the same direction. This process involves lower pressures since the relative movement of billet and container is removed and so the load/displacement locus therefore shows no reduction in load as the billet length is reduced. The only frictional forces which must be overcome are those due to the billet/die contact. On an industrial scale this involves a considerable reduction in load and offers a large energy saving route.

Recent developments in the extrusion field include the semi-continuous hydrostatic process suggested by Alexander and

Lengyel[32] and the continuous ("conform") extrusion process of Green.[33,34] In the past billet length has always been limited to minimize the amount of power wasted in overcoming friction effects, but both of these processes utilise this force to 'drag' the feedstock to the die.

The process of extrusion does have several disadvantages. One of the biggest is that variations in strain, strain rate and temperature throughout the deforming metal produce an extrude of varying structure. Thus the mechanical properties of the extrude vary with position. As the press capacity is dictated by the peak load in Fig. 1, the capacity is only utilised for a fraction of the duration of each cycle.

1.1.2. Metal Flow during Extrusion

Pearson and Parkin[1] categorised the metal flow observed during extrusion into three types:-

(1) No deformation is undergone before the material reaches the deformation zone, i.e. lubricated and inverted extrusion.

(2) As in type 1 but shear also occurs at the container/billet interface, i.e. unlubricated extrusion.

(3) A complex pattern where a rim of 'dead' material extends back from the die to the billet surface. This is the situation generally found in industry.

Smith[35] has described the shear region between the deforming billet and the dead-metal region in aluminium extrusion as being elliptical, although semi-circular approximations can also be made. A review of the flow patterns developed during extrusion has been published by Chadwick[36] who points out the differences for lubricated and unlubricated extrusion. In the former case the surface of the extruded product is produced by a shear at the die, whereas in the latter case the surface of the billet produces the surface of the product. Castle and Sheppard[16] have shown for circular rod extrusion that the flow pattern is not fully developed when extrusion commences, but is fairly well established when peak loading occurs. The flow patterns in multihole extrusion have been reviewed by Wood.[37]

The dependence of flow pattern with temperature and ram speed was studied by Hinesley and Conrad[38] using a conical die and low extrusion ratio. They found two types of flow were produced, one having a single maximum velocity while the other a double. They ascertained that the change was associated with a specific value of the Zener-Holloman parameter, Z. The double maximum was only produced in the high stress regions of a plot of LnZ vs σ, i.e. where there exists a strong dependence of σ upon Z. The variation was justified by consideration of incremental temperature changes in the deformation zone for both extremes of initial temperature.

Ikeda et al.[39] studied the inhomogenous flow in aluminium extrusion by using high purity gold wires as flow line markers to measure redundant strain from the centre to the surface layer of the extruded product. It was found that the redundant strain at the surface was almost ten times that at the centre.

1.1.3. General Structural Aspects of Extrusion

Aluminium and its alloys have cornered a large proportion of the extrusion industry, because of their ease of fabrication into both simple and complex shapes. In 1949, Smith[35] published a review of the aluminium extrusion industry, much of which is still relevant.

As stated in the latter part of the previous section (1.1.2.), the metal flow in the extrusion process is such that the material on the outer surface of the product is subjected to much greater shear than the inner regions. This can give rise to a large recrystallized grain size in these outer regions[1,35] even without subsequent heat treatment. The inhomogeneous nature of the flow during the deformation produces intense bands of shear at the dead-metal-zone boundary which are eventually fed to the outer regions of the product and generate the driving force for the recrystallization process. This appears analogous to the critical strain for recrystallization in cold worked materials, but as pointed out by Pearson[1] this is not the case in extrusion where the process is characterised by heavy deformation and high temperatures. An explanation put forward is that the degree of strain hardening may be the important factor and a critical value may be reached in the

outer region. Material is therefore of great importance and it is reported[1,40] that in Al-Mg-Mn-Cr alloys, coarse grain formation is restricted to cases where the combined percentage of Mn and Cr exceeds 0.65%. In alloys to be heat treated the possibility of a coarse grained peripheral region is a major problem because of its reduced properties.[35,41] It is reported that additions of zirconium and manganese[41] can retard its occurrence probably by increasing the nucleation rate and reducing the grain growth.

Apart from the heavily worked outer region, the structure can be fully recrystallized, fibrous, or a combination of the two depending upon the alloy, pre-extrusion heat treatment, the extrusion parameters and post extrusion heat treatment. The fibrous structure has the best mechanical properties, this being attributed[1,42] to the preferred orientation found in this structure.[43] The retention of the fibrous structure at high temperatures, called the extrusion effect, is aided by the presence of manganese[35,41] and to a lesser extent chromium.

The surface finish is of prime importance in many applications and defects can vary from visible blemishes such as cracks or die lines to invisible ones that appear after anodizing.[44] The control of these defects is a deciding factor in many problems. It is doubtful if lubrication is of any use in aluminium extrusion, a good surface finish being obtained by shear at the die face.[36] Surface blisters are caused by lubricant or other foreign matter on the billet exterior being dragged between the flowing metal and the dead metal zone.[36,35]

The reader is referred to the references given for a more complete and detailed description of the features of aluminium extrusion, but this brief review indicates the varied structures and quality of surface that can be achieved.

1.2. The Aluminium-Magnesium Alloy System

The commercial aluminium-magnesium alloys can contain from 0.5 to 13% magnesium together with additions of Si, Fe, Mn, Cr, Cu, Ni, Zn, Ti, B, Be, Li and Zr. The binary aluminium-magnesium system, to which these alloys may be approximated because of the overwhelming influence of the major addition, shows a good solubility

of magnesium in aluminium varying from around 1.5 wt.% at room temperature up to 17.4 wt.% at 450°C.[41] Although there is this substantial solid solubility in aluminium there is no appreciable precipitation hardening characteristics with concentrations below 7 wt.% magnesium.[45] Alloys below this composition are generally utilised as wrought alloys characterised by substantial substitutional solid solution strengthening[46] and high work hardening rates, whereas concentrations above are used primarily as casting alloys with an associated heat treatment to improve properties by precipitation of the β phase, Mg_2Al_3.[47] An added bonus is the weight reduction compared with pure aluminium due to the lower density of magnesium.

In the annealed condition the strength is proportional to the magnesium content and is the main factor that controls mechanical properties, but the remaining additions contribute to them. Additions of up to 0.75% manganese increases hardness and decreases ductility in the casting alloys while the ease of fabrication is reduced in the wrought alloys. It is also reported[45] to increase cracking during rolling while increasing the precipitation in the aluminium-magnesium system.

It is normal practice to produce the alloys in higher grade aluminium with reduced silicon and iron content to improve corrosion resistance and reflectivity. However in the amounts which may be present, silicon is reported[48] to slightly reduce ductility and notch toughness without a compensating strength increase. Iron and chromium have a strengthening effect,[48] but show reductions in ductility due to their presence as coarse particles. Zinc slightly increases the strength while titanium has no direct effect, but some hardening and increase in creep resistance can result from the grain refining and increase in recrystallization temperature that it produces.

The highest strength commercial wrought alloy is 5456 closely followed by 5083. The typical properties for the three alloys 5456, 5083 and 5052 are shown in Table 1.1.[45]

Material	Temper	Tensile Strength MN/m^2	Yield Strength MN/m^2	Elongation %
5052	0	193	89	24
	Strain Hardened and Stabilised	289	255	7
5083	0	289	144	22
	Strain Hardened Corrosion Resistant	358	282	8
5456	0	310	158	24
	Strain Hardened Corrosion Resistant	381	296	8

TABLE 1.1. Typical Properties for Al-Mg Alloys

In terms of application, the alloys are most useful in situations where moderate strength, good weldability and good corrosion resistance are essential. Major utilisation is in the marine environment[49,50] where reported applications are for 5456 plate and 5083 sheet in ship's superstructures,[51] hydrofoil craft for anti-submarine warfare[52] (where 5456 extrusions are employed), and in hovercraft.[53] In addition 5052 has been reported with reference to tubs for washing machines[54] and vehicles for rail transport[55] as well as all sorts of container applications. 5083 is reported with relation to cryogenic applications[56,57] and together with 5456 in armour plating.[58] The alloys are also used extensively for ornamental purposes,[48] automotive trim and architectural components: bright etching or electropolishing yielding highly reflective surfaces which after anodising retain most of their brightness and resist tarnishing.

Although these wrought alloys are classified as non-heat treatable the amount of magnesium soluble at the annealing temperature for alloys such as 5456 and 5083 is higher than that retained in solid solution at room temperature. This instability attains a critical state in the presence of severe strain hardening followed by long storage at room temperature or exposure to elevated temperatures, as precipitation occurs along grain

boundaries or along slip planes. This precipitation promotes intergranular attack and stress cracking in corrosive atmospheres, because it is anodic to the remainder and so preferentially attacked. This situation resulted in the development of specific tempers to eliminate or minimize this instability.[45]

The good welding response of the higher strength alloys, because of the limited amount of eutectic present and their relatively high strength to the annealled condition has meant their application in engineering structures, pressure vessels and chemical plant. Joint efficiencies of up to 80-90% of the annealed strength can be obtained using both the T.I.G. and M.I.G. processes.

1.3. The Analysis of Extrusion

The pressure developed during extrusion has received considerable attention and many attempts have been made to predict it. Both empirical and theoretical approaches are used and have been reviewed.[1,3,44,59] The analysis of extrusion experiments usually involves a knowledge of the mean flow stress and an accurate value is needed if a meaningful analysis is to be made.

1.3.1. Theoretical Approach to Extrusion Pressure

Bishop[44] has shown that for homogeneous deformation during axi-symmetric extrusion the following relationship is applicable:-

$$\delta w = aY\delta l$$

where δw = work increment

δl = length increment

a = cross-sectional area of extrude

Y = Tensile Yield Strength

Hence, $$w = \int_{l_o}^{l_f} \frac{Y.dl.v}{l}$$

but $W = P.v$

so $P = YLnR$ (1.1)

Inspection of flow during extrusion shows it to be far from homogeneous. Comparison of values predicted by equation (1.1) with experimental values determined by Pearson[1] shows that the error increases as the extrusion ratio is increased and becomes greater than 50% above ratios of 10:1.

An efficiency factor can then be introduced to compensate for this, producing:-

$$P = BY\,\mathrm{Ln}R \qquad (1.2)$$

In this form, the equation has some practical use when predicting loads for different metals under identical conditions,[60] although care must be taken when comparing metals of completely different characteristics.

Using the slab method of approach, it can be shown that the pressure, including a friction term may be expressed as:-

$$P = Y\,\mathrm{Ln}R + \frac{4\mu LY}{D} \qquad (1.3)$$

In view of the complex nature of the flow, it is desirable to have a theory that incorporates this feature.

1.3.1.1. Slip Line Field Techniques

This powerful method of solving complex plastic flow problems by establishing the maximum shear-line field is restricted in its application to conditions of plane strain and a rigid perfectly plastic material .[2,3] Solutions exist for a variety of conditions from perfectly lubricated to perfectly rough friction conditions and also for a series of die shapes.[61,62,63,64] The results are usually given as graphs of pressure against reduction and Johnson[1,62] has shown that these theoretical curves can be approximated over a limited range of reduction ratios by

$$\frac{P}{2K} = a + b\,\mathrm{Ln}R \qquad (1.4)$$

the constants a and b being determined by the frictional boundary conditions.

A problem in the application of these equations is the value of K, the shear yield stress to be used. A rigid perfectly plastic material assumed in the original theory has a constant value, but this is far from the case except in materials at high temperatures. Dodeja and Johnson[63] suggested that a mean value, $\bar{K}$, should be used for work hardening materials. This value is the mean value of K found from plane-strain compression tests to a strain of (a + bLnR). More recently solutions have been found for work hardening materials, although the reduction of 50% considered has a very limited application,[4,19] a criticism that can be made of most theoretical solutions.

However the theory is mathematically correct, but the solution is tedious to derive. The method to be used has been summarised by Johnson and Kudo.[3]

The tedious application, inapplicability to the axi-symmetric case and limitations imposed upon flow and material led to Johnson[65] developing the upper bound method of analysis.

1.3.1.2. Plane Strain Upper Bound Solutions

This method of analysis produces loads in excess of those predicted by slip-line fields, and in excess of the true values. By increasing the complexity of the upper bound solution (i.e. the number of velocity discontinuities in the field) the solution is brought closer and closer to that given by the slip line field method. (As the solution is an over-estimate on the load, it must be minimised to give the best solution). In view of the approximations of plane strain, mean yield stress and frictional boundary conditions common to both techniques, the saving in effort possible by this technique makes the less accurate answer acceptable in the majority of cases.

This technique is based on strain rather than stress equilibrium conditions. Elements of material are assumed to offer maximum resistance to deformation, i.e. they deform in such a way as to require the maximum amount of work to produce a given strain. The material is assumed to be incompressible and only velocity discontinuities and boundary conditions are considered. The material is assumed to deform as rigid plastic blocks.

The most difficult part of the procedure is the determination of the original field. Johnson and Kudo[3] suggested the following method:-

(1) Assume a velocity field for the body of the material, which is restricted only by the need to conform to the velocity boundary conditions and the law of incompressibility.
(2) Calculate the rate of work due to plastic deformation and due to slip of the material over the tool surface, using the assumed field.
(3) Calculate the extrusion load from the rate of working.

Step (1) may be simplified by basing the field on a known slip-line field, or on a knowledge of the flow pattern gained experimentally. Sheppard and Raybould[13] showed that a velocity field could be established by considering the sub-grain size at different positions in the deformation zone of a partial extrusion. Using a minimised plane strain upper bound solution, Johnson obtained solutions for extrusion through wedge and square shaped dies for conditions of zero and sticking friction.

Although simpler to use than the previous method, the plane strain upper bound methods suffer from serious drawbacks:-

(1) Strictly, they may be applied to plane strain conditions only (extrusion is an axi-symmetric process).
(2) They must be minimized by mathematical techniques.
(3) Intermediate friction conditions prove difficult to consider.
(4) The load predicted is always an overestimate.

1.3.1.3. Axisymmetric Upper Bound Solutions

As stated in the previous section extrusion is rarely, if ever, carried out under plane strain conditions. Therefore an axisymmetric solution is required. Thomsen[66] made the following observations:-

(1) Material flow is similar for geometrically similar shapes in axisymmetric and plane strain extrusion.
(2) The velocity during axisymmetric extrusion is the square of the velocity during plane strain extrusion.

Using this information Sheppard and Raybould[13] derived a simple axisymmetric solution by first finding a minimized plane strain solution. The areas of discontinuity surfaces were then obtained by revolving the plane strain field around the centre axis and the magnitude of the velocity discontinuities by squaring those given by the plane strain hodograph.

The first published upper bound solution for axisymmetric extrusion was derived by Alexander.[67] The calculation was later shown to be incorrect since the effect of a shear strain rate had been ignored.

Johnson and Kudo[68] used an axisymmetric technique for determining temperature distribution during extrusion through square and conical dies in 1960, while Kudo[69] applied the concept of unit deforming regions to axisymmetric limit analysis. Kobayashi[70] extended Kudo's approach by introducing curved velocity discontinuities into the deforming region as well as deriving a solution for drawing and extrusion through conical dies using triangular deforming regions.

Kobayashi and Thomsen[71] obtained both lower and upper bounds for frictionless extrusion through square and conical dies and their result showed a slight improvement over Kudo's.[69] Halling and Mitchell[72,73] used a double triangle arrangement of velocity discontinuities similar to previous workers[67,70] but allowed a dead metal zone to form if this gave a lower upper bound. Their solution agreed well with that of Kobayashi and Thomsen[71] for reductions up to 70% but deteriorated at higher values. Essentially their solution allowed the material within the triangles to accelerate along the flow lines, producing circumferential straining, and modified the hodograph accordingly. The method of representing the velocity field in the form of a hodograph offers a very convenient means of solving axisymmetric problems using solid billets and Halling and Mitchell's[72,73] method was extended by Adie and Alexander[74] and Adie[75] to utilise three triangle arrangement of velocity discontinuities for greater accuracy.

Recent advances in computer technology have enabled steady state plastic deformation processes to be treated by numerical

techniques. Zienkiewicz[76,77] applied a finite element method to extrusion and produced results which agree well with slip line field solutions. Greater accuracy could be obtained by increasing the number of elements in the mesh while any frictional condition could theoretically be accommodated.

With the increasing availability of large modern computers possessing large storage capabilities, the finite element approach to analysing metal working processes will undoubtably become more important.

1.3.2. Empirical Approaches to Pressure Determination

As indicated in section 1.3.1., the theoretical calculation due to Bishop[44] can be 50% in error at extrusion ratios greater than 10:1. Johnson,[78,79] working with aluminium and lead, showed that under plane strain conditions the discrepancy was due to not allowing for work hardening or the friction conditions. Alexander[80] stated the general form which empirical relationships take:-

$$\frac{P}{2K} = a + b\,\mathrm{Ln}R + Cl_B \qquad (1.5)$$

where a represents redundant work
b represents the efficiency
and Cl_B accounts for friction.

Dodeja and Johnson[63] suggested that it was possible to compensate for work hardening during extrusion by using a mean flow stress value taken from a plane strain compression test up to a strain of (a + bLnR). The constants a and b were found by extruding lead at room temperature where self-annealing takes place.

Subsequent work by Purchase and Tupper[81] showed that equations of the above forms were invalid for axisymmetric extrusion and that the pressure required approximates to that required for the equivalent plane strain reduction. This was confirmed[63] and the following equations were proposed:-[79]

$$\frac{P}{Y} = 0.8 + 1.5\,\mathrm{Ln}R \quad \text{for lubricated extrusion} \qquad (1.6)$$

$$2{:}1 \leqslant R \leqslant 16{:}1$$

$$\frac{P}{\bar{Y}} = 0.6 + 1.8 \ln R \text{ for dry extrusion} \qquad (1.7)$$
$$4:1 \leqslant R \leqslant 16:1$$

These results are strictly limited in scope since they consider only very low extrusion ratios and then only predict the pressure required to pass the material through the deformation zone adjacent to the die face.

Wilcox and Whitton[82] assumed the values of a and b were dependent on the frictional forces on the die face resolved in the direction of the applied force. I.e. on the die semi angle ω. They found that:-

$$\frac{P}{\bar{Y}} = (0.9 - 1.6 \cot\omega) + (1.5 + 0.8 \cot\omega) \ln R \qquad (1.8)$$

where $30^{\circ} \leqslant \omega \leqslant 90^{\circ}$ and $5:1 \leqslant R \leqslant 150:1$
Claims for this relationship are that it is accurate to within 6% although the difficulty still remains of predicting the mean yield stress.

Hirst and Ursell[83] modified Johnson's equation,[84] for the extrusion of short lubricated billets, to allow for frictional effects in the extrusion of tubes. They found that:-

$$P = \bar{Y} (0.47 + 1.2 \ln R) \exp \frac{4\mu L}{D_B - D_M} \qquad (1.9)$$

where μ = coefficient of friction
D_M = diameter of the mandrel

The value of μ was found by extruding billets of different lengths. Sheppard[85] analysed the situation as the total pressure being made of three components. The first, regarded as the base pressure, P_B corresponding to the homogeneous deformation pressure was calculated from (a + bLnR) while the second, the friction pressure, P_F was found from:-

$$P_f = P_B \exp \frac{4\mu L}{D_B} \qquad (1.10)$$

The final increment was the value Δp which is dependent upon dislocation dynamics and relates to the energy required to set up the quasi-static deformation zone. Values of flow stress were evaluated from hot torsion tests.

The applicability of any empirical equation over a wide range of conditions is limited by:-

(1) Selection of the correct flow stress as the true extrusion temperature and strain rate cannot be simulated during laboratory tests. Moreover these parameters vary widely in the deformation zone during the course of extrusion.

(2) Though frictional forces can be estimated when billet and tooling temperatures are similar, it is difficult with large differences. Small changes in pressure lead to large changes in μ; the extrusion pressure itself being highly dependent upon both billet temperature and container temperature.

1.3.3. Strain Rate During Extrusion

The strain rate during extrusion is a difficult parameter to define. It is obviously a function of the ram speed and extrusion ratio, but its value varies throughout the deformation zone. Sheppard and Raybould[13] applied the upper bound technique to the problem and calculated the strain rate along a series of streamlines by means of the following method:-

$$\varepsilon = \frac{u}{v}$$

ε = strain
v = velocity of material perpendicular to discontinuity
u = magnitude of discontinuity

The time to extrude a unit volume of material of unit area past the discontinuity $= \frac{1}{v}$.

Therefore the strain rate is given by:-

$$\dot{\varepsilon} = \frac{u}{v} \div \frac{1}{v} = u \qquad (1.11)$$

An average strain rate along each streamline is found by considering the number of velocity discontinuities intersected. The method permitted an indication of the variation across the section. There are however two main disadvantages:-

(1) The deformation is assumed to occur instantaneously at a number of discontinuities

(2) A mean overall strain rate has to be calculated from a knowledge of the strain rate along each stream line.

Feltham[86] proposed a mean strain rate calculated assuming that the deformation occurred within a cone of semi-angle 45°. He also assumed that the total strain was quantitatively equal to Ln (Extrusion ratio). By dividing the volume of metal extruded per unit time into the volume of the cone, he obtained a mean strain rate given by:-

$$\bar{\dot{\varepsilon}} = \frac{6.v.LnR}{D_B} \qquad (1.12)$$

v = Ram Speed

D_B = Billet diameter

However an error is incurred immediately in that, as previously stated, the value of Ln (Extrusion Ratio) is a value of homogeneous strain whereas the deformation during the process is considerably inhomogeneous. In an attempt to improve this feature Alexander[59] suggested that this value be replaced by (a + bLnR) giving:-

$$\bar{\dot{\varepsilon}} = \frac{6v(a + bLnR)}{D_B} \qquad (1.13)$$

Further sources of error are that the deformation zone is rarely a cone of semi-angle 45° and the relationship assumes the extrusion ratio is large, making D_E, the extrudate diameter, negligible compared to D_B. Wilcox and Whitton[87] proposed a more general expression of:-

$$\bar{\dot{\varepsilon}} = \frac{6vD\ LnRTan\omega}{(D_B^3 - D_E^3)} \qquad (1.14)$$

where ω is the deformation zone cone semi-angle. Incorporating the improved strain relationship Castle[88] proposed:

$$\bar{\dot{\varepsilon}} = \frac{6(a + b\mathrm{Ln}R).\mathrm{Tan}\omega.v.\ D_B^2}{(D_B^3 - D_E^3)} \qquad (1.15)$$

Chandra and Jonas[89-91] calculated strain rates averaged over accumulated strain, distance travelled through the die and the elapsed time. They also dealt with the case for a strain rate sensitive material and derived relationships for mean strain rate during extrusion containing a term for the strain rate sensitivity of the flow stress. Comparison of their results with those of Wilcox and Whitton[87] gave a difference of 24% at a reduction ratio of 4:1 and nearly 1000% at 169:1.

Although these various methods for strain rate calculation are available, the value must be applicable to both simple rod and more complex extrusion and the only simple measurement that can be made for all shapes is the deformation zone volume. This would tend to support the original work of Feltham and the modified result of Castle. It must be remembered, however, that these mean values do not give any indication of the changes occurring within the deformation zone. As will be shown in subsequent sections, these changes can be of an order of magnitude between beginning and end of the deformation zone.

1.3.4. Temperature Changes during Extrusion

The complex interaction between press mechanics, extrusion conditions, metal properties and deformation characteristics makes the prediction of temperature changes during extrusion very difficult.

Bishop[92] proposed a rigorous mathematical analysis, but this assumed plane strain conditions and no heat loss to the container. The method of solution using a slip line field method is also admitted to be laborious. Tanner and Johnson[7] simplified this by using an upper bound approach and showed that back conduction could be ignored when speeds normal to the velocity discontinuities exceeded 5 cms/sec. Johnson and Kudo[68] extended the solution for axi-symmetric conditions.

Watkins et al.,[93] Ashcroft and Lawson[94] and Singer et al.[10] carried out work in which the billet and container were initially at the same temperature. Thermocouples inserted into the billet showed that the temperature of the deformation zone and the emergent product rose quickly at first and then increased more slowly. During the latter stages of the cycle, the increasingly complex metal flow and diminishing heat losses to the tooling result in a final rapid rise in temperature. Singer and Coakham[95] measured the temperature rise in the extrusion of aluminium, lead and tin by means of a two pronged thermocouple situated just below the die. Their work was later extended to include a simple theory to explain the results. They considered all the deformation to take place in the plane of the die and then calculated the temperature distribution in the billet, assuming axial heat conduction from the deformation zone and a billet of infinite length. By assuming perfect contact between the billet and container an approximation to the heat losses was made.

Akeret[12] developed a technique which worked by dividing the billet into cells and calculating the heat flow between them. He also allowed a temperature gradient between the billet and container. The results gave temperature rises of 100°C in excess of those actually recorded because heat losses during upsetting were not considered and also the flow stress remained constant even though the temperature varied. Hughes and Sellars[96] improved this model by including for the heat losses to the container during upsetting.

Altan and Kobayashi[97] used a visioplastic method to analyse the nature of metal flow and then calculated the temperature rise from this data. Thermocouples were then placed in the billets to confirm the solutions. The lower extrusion ratios used, 2 and 4:1, enabled this to be carried out fairly easily.

Sheppard and Raybound[13] developed an integral profile method similar to that of Tanner and Johnson[7] by equating the amount of work put into the system to the amount of heat lost through the surrounding tooling and hence estimating the temperature rise. The failing was that differences in initial billet temperature and tooling were not accounted for. Sheppard recognised this and

proposed that additional losses could be considered by taking the billet as a thick cylinder. The temperature of this cylinder was taken as the initial temperature plus the temperature rise calculated by the method of Sheppard and Raybould. This method is unsatisfactory as it assumes the temperature of the deformation zone is in fact that of the whole billet, which contravenes one of the basic assumptions that there is virtually no back conduction between the deformation zone and the rest of the billet.

In practical terms it is very difficult to insert thermocouples into billets and other methods of temperature measurement must be found. Raybould and Sheppard[13] report the findings of placing thermocouples in the dead-metal-zone during extrusion which showed their theoretical to be consistently low, although the agreement was good enough to confirm the validity of their model. Woolvet[98] and Reynolds[15] describe how the surface temperature of extruded aluminium may be measured using an optical pyrometer.

1.4. Hot Working

Almost all metals, excluding some castings and sintered parts, are hot worked during processing into the final product. At low temperatures the stress to deform a metal increases as the strain increases due to work hardening caused by the complex interaction and formation of dislocations within the material. At higher temperatures the stress to deform the material for a given strain decreases due to the increased ease of dislocation motion[99] and also the rate of work hardening decreases as the high temperature restoration processes get under way. It is these restoration processes which have been studied in investigations into hot working.[100,101] An examination of the stress-strain curves at different temperatures and strain rates[101-107] shows the rate of deformation to be very important; the higher the strain rate, at a given temperature, the higher the flow stress. This observation is of great importance in the metal working industries where high strain rates are used to deform materials to large strains at high temperatures. In aluminium extrusion the reduction ratio can be up to 200:1. The practical importance of the subject has led to hot working becoming one of the most important subjects of modern metallurgical research.

Essentially there is a requirement to establish empirical relationships between flow stress, strain rates and temperature by using standard testing techniques adapted for high temperature and high strain rate work. In addition the use of these relationships can be somewhat extended if a knowledge of the accompanying structural changes, which affect final properties, is available.

1.4.1. Methods of Testing

Before discussing the approaches to hot working outlined in the previous section, it is useful to have a knowledge of the advantages and disadvantages of the various methods of testing and their applicability to industrial processes. These methods have been discussed by several authors.[108-110]

1.4.1.1. Tensile Tests

Tension testing at or below room temperature has given very useful results with respect to applications at these temperatures. It is unfortunate that the method is not entirely suitable for hot working studies.[111] This is because the strain rates produced are often too low and decrease during a test as the specimen elongates. Secondly necking and fracture prevent sufficiently large strains from being attained. The plastic instability known as necking is peculiar to tensile deformation and occurs when the incremental increase in strength due to strain hardening in a local region is insufficient to offset the incremental decrease in cross-section. This limits the uniform deformation to strains of less than 0.3 which is much less than that obtained in hot forming operations and is frequently less than that required for the inception of the steady state regions.

1.4.1.2. Compression Tests

Hot compression, which can be performed on the same equipment as tension tests, is more suitable to hot working studies since the stress system is closer to those found in deformation processing and no basic instabilities such as necking arise.[112] True strains of more than 0.7 can be obtained and strain rates

varying from 5×10^{-3} to 2×10^{3} sec^{-1}, using a modified Hopkinson pressure bar technique.[113] Constant strain rate tests can be carried out using a cam-plastometer.[105,106,114]

In axisymmetric compression, friction between the platens and the specimen leads to greater deformation in the midsection of the specimen than in the constrained ends. In severe cases there are cones of negligible flow at the ends and the bulging of the specimen causes the cylindrical surface to roll over into contact with the platens. The friction can be reduced by using suitable lubricants and improving its efficiency by machining grooves in the specimen ends to aid its retention. We must, however, conclude that the variability and quantification of friction conditions imposes severe limitations on this test.

1.4.1.3. Torsion Testing

The hot torsion test,[102,104,114-121] which consists of twisting a specimen with a heated gauge section, is capable of producing strains of the order of 20.[111] Since the dimensions remain constant, the strain rate remains constant throughout the test. With solid gauge specimens the strain rate varies from zero at the centre to a maximum at the edge. Likewise the strain varies in a similar manner and that quoted is normally that at the surface. Testing is normally carried out with axial constraint on the specimen, to maintain geometry at the expense of axial load.[119] It is reported that by modifying equipment it is possible to do programmed experiments, simulating rolling or forging schedules.[116] The method is also open to both variable strain rate and temperature testing.

The methods outlined above are all laboratory techniques that can provide valuable data on the behaviour of metals under different combinations of strain rate and temperature. However, they have the disadvantage of not being industrial processes. Compression comes close to rolling and forging, but there are still large differences. Some attention to industrial processes has been made,[19,20] but the complex deformations involved entails many assumptions in the analysis. Nevertheless, experiments of this kind are the only ones that can be used if the limits of a

particular process are to be found or structural changes during fabrication are to be examined. This is especially true in extrusion where true strains greater than 5 can be produced in one operation at strain rates of up to 100 sec^{-1}. By the very nature of the process it involves the shearing of metal over a tool under the influence of a high pressure. It is this interaction between the material and the tool that laboratory tests cannot reproduce.

1.4.2. Empirical Approach to Hot Working

Examination of the data from many workers has shown that two relationships can be applied to hot working data.[23,100,103-106,114] For low stresses at a constant temperature:-

$$\dot{\varepsilon} = A_1 \sigma^{n_1} \tag{1.16}$$

where n_1 and A_1 are temperature independent constants.
For high stresses and at a constant temperature:-

$$\dot{\varepsilon} = A_2 \exp(\beta\sigma) \tag{1.17}$$

where β and A_2 are temperature independent constants.

These relationships are very similar to those found to describe creep experiments, supporting the idea that creep and hot working are two extremes of the same phenomena. Working on the creep case, Garafalo[122] showed how these two equations could be combined into the form:-

$$\dot{\varepsilon} = A_3 \left[\sinh(\alpha\sigma)\right]^n \tag{1.18}$$

where A_3 is a temperature dependent constant. For values of $\alpha\sigma < 0.8$, the expression reduces to a power form, while values above 1.2 cause it to reduce to an exponential form. The value of α can be shown to equal β/n_1. Garafalo showed the applicability of equation (18) to the creep results for copper, austenitic stainless steel and an aluminium-3.1% magnesium alloy.

The similarity between steady state creep and steady state hot working led Sellars and Tegart[123] to propose the relationship:-

$$\dot{\varepsilon} = A\left[\mathrm{Sinh}(\alpha\sigma)\right]^{n} \quad \exp\frac{-\Delta H}{RT} \qquad (1.19)$$

where A, α and n were described as temperature independent constants and ΔH was referred to as the activation energy of the hot working process. This can be re-written in the form:-

$$Z = \varepsilon \exp\frac{\Delta H}{RT} = A\left[\mathrm{Sinh}(\alpha\sigma)\right]^{n} \qquad (1.20)$$

Z, the Zener-Holloman parameter,[124] was originally proposed for low temperature tests, but was shown to apply to hot working data.[123] The presence of the Arrhenius term in equation (20) implies that hot working is a thermally activated process[13] and ΔH is the activation energy of the rate controlling process. The activation energy has been evaluated for many metals and alloys[13,23,100,102,104,109,113,125] and it was found that values fell into two classes,[100,109] the classes being characterised by their stacking fault energy.

In the first class it was found that the activation energy for hot working and bulk self diffusion were similar. This was found to apply to alloys of high stacking fault energy.[13,100,104] This group has, in general, included aluminium and its alloys, zinc and α-iron. The similarity being a result of the ease of dislocation climb in this type of material.[126] The second class of materials which includes copper, nickel and austenitic steels were reported to have higher activation energies for hot working than for self diffusion and this was attributed to the difficulty of dislocation climb.

The critical factor would appear to be the stacking fault energy of the material since this governs the separation of partial dislocations and thereby controls the ease of dislocation movement. For dislocation climb the partials must come together, under the action of the applied energy, before climb can occur, and so dislocation climb is easier in high stacking fault energy metals.[126]

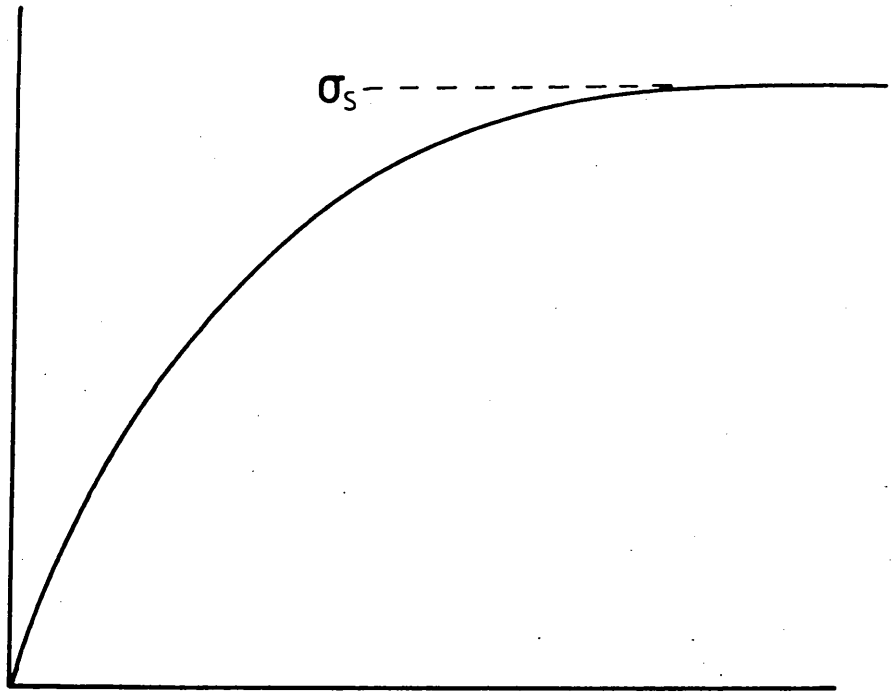
The values of A, α and n, in equation (20), are described as temperature independent constants,[88] but are functions of

structure and alloy content, although the literature is unclear on how they vary with complexity of structure. Their evaluation has traditionally followed a graphical technique whereby first α, by finding β and n_1, and then ΔH are found. This then enables A and n to be calculated from a logarithmic plot of Z versus $(\mathrm{Sinh}\alpha\sigma)$.

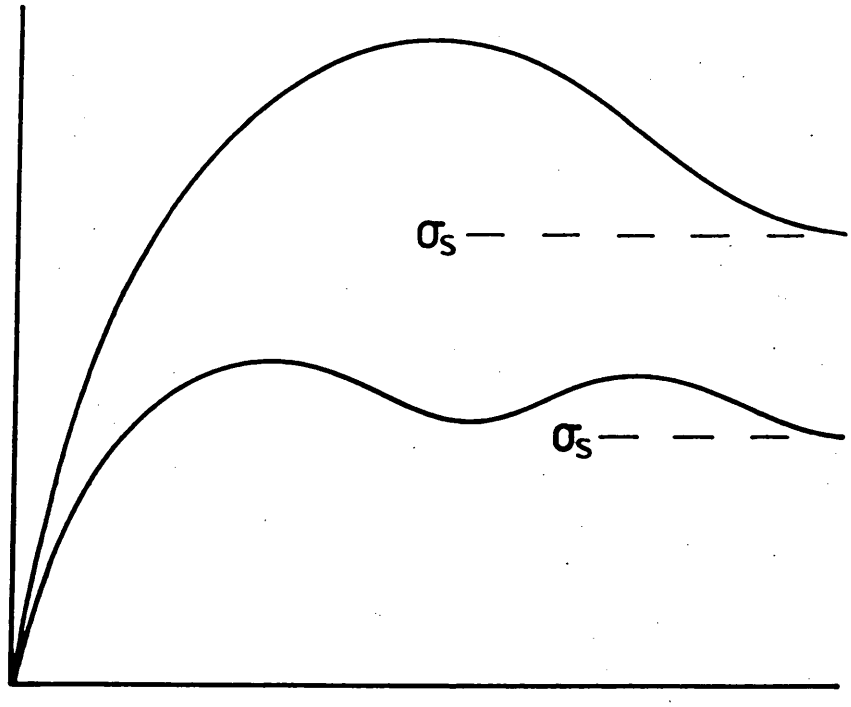
1.4.3. Structural Aspects of Hot Working

To account for the independence of flow stress upon strain, as implied from the empirical relationships, some high temperature restoration process or processes must be operating to overcome the effect of work hardening.[127,128] By analysing the results of many workers, Jonas et al.[100] have shown that there is a qualitative agreement between the structural changes observed in hot working. In terms of the high temperature stress-strain curve, the effect of a non-strain dependence is revealed by a steady state region following an initial rapid rise from zero. Depending upon the mechanism operating in the system, the curve can take any one of three basic shapes as shown in Fig. 2. In one case the curve can show a gentle rise to the steady state regime and is attributed to restoration by dynamic recovery. The two other cases are variations of the same mechanism namely dynamic recrystallization and dynamic recovery acting together. This mechanism is characterised by a rise to some peak followed by a gentle fall to the steady state region at higher strain rates. For lower strain rates the rise to peak is followed by a sinusoidal trace around a mean steady state value.

The production of these curves is, therefore, a reflection of the restoration processes in operation and these are a reflection of a material characteristic, namely stacking fault energy. Aluminium and its alloys, as stated previously, are reported to fall into the high stacking fault energy category and their hot worked structure is characterised by small equiaxed subgrains of low misorientation. These subgrains can either be found within the deformed original grains, at low deformations, or they can form a continuous structure when the original grain boundaries have been destroyed by large deformations.[13,113,129-132] A similar



(a)



(b)

Fig. 2. Flow curves for restoration by dynamic recovery and both dynamic recovery and dynamic recrystallization

structure has been observed in iron and ferritic alloys.[100,133] There is a marked similarity between these structures and those developed during the creep of metals.[100]

In the low stacking fault energy class of metals substructures are reported at low strains but deforming further produces equiaxed recrystallized grains[131] due to the increased difficulty of dislocation mobility. The result is an increase in stored energy which produces the driving force for the new process. This is in contrast to the structure produced in creep and suggests that a different mechanism is operating.

To examine the hot worked structure it is necessary to prevent any changes occurring during cooling. The exception to this is hot stage microscopy. These changes can be prevented by rapid cooling immediately after deformation, the more rapid the quench the better the chances of retaining the structure. The finite time involved before quenching may give the possibility of static restoration processes being initiated and thus a transition structure may be observed rather than the true deformation one. These static restoration processes will be looked at first.

1.4.3.1. Static Restoration Processes

These processes can be conveniently divided into two distinct categories.[134,135]

(a) the recovery processes, which involve the annihilation of disclocations in individual events.

(b) the recrystallization processes, in which dislocations are simultaneously eliminated in large numbers as a result of the motion of high angle boundaries.

The driving force for these two processes in the stored energy resulting from the prior deformation.

Recovery is brought about by changes in the number and distributions of point defects and dislocations. Byrne[136] has listed the processes according to the relative temperature ranges with which they are associated.

At low temperatures, like point defects pair off, defect clustering occurs and they migrate to dislocations, subgrain

boundaries and other surfaces. (The cold worked metal usually consists of a cell network of dislocation free regions surrounded by ragged dislocation tangles. The dislocation free regions are known as subgrains to distinguish them from the matrix grains).[126]

At intermediate temperatures, dislocation rearrangements within piled up groups occurs, dislocations of opposite signs annihilate each other and subgrain growth can occur.

At high temperatures dislocation climb occurs leading to polygonization, the rearrangement of dislocations into low energy configurations by the formation of cells. This is a different process to subgrain formation, which occurs by dislocation interaction during working.

Recrystallization involves the replacement of the worked structure by a new dislocation free one.[137-141] This is achieved by high angle boundaries sweeping through the structure. It is known that recrystallization is a nucleation and growth process,[136] but there are still arguments over the process of nucleation,[143,144] although recent work by Humphries[145,146] has shed considerable light on the subject.

As stated earlier the driving force for these restoration processes is the stored energy in the worked metal. If the metal can lower its energy by recovery there is a reduced driving force for recrystallization which has a nucleation time and below a critical value of this stored energy recrystallization cannot occur. Therefore in materials where dislocation climb and polygonization is relatively easy the possibility of recrystallization is reduced.[147]

It has been shown that the time for static recrystallization to occur decreases with an increase in the holding and working temperature.[116,130,148] Rossard and Blain[148] have also demonstrated that the time for recrystallization to occur depends upon the strain rate which is related to the flow stress or the stored energy. The amount of strain can also have an effect[130] when the flow stress is dependent upon strain. The time for recrystallization to be initiated decreased with strain in aluminium, deformed in torsion at a strain rate of 2 sec^{-1} and a temperature of 400°C.

Static recrystallization can occur in both classes of metals, but results obtained show that for low stacking fault metals structural changes are more rapid than that for aluminium.[100]

1.4.3.2. Dynamic Restoration Processes

Dynamic Recovery

Luton and Jonas[149] have described how the flow curve may be divided into three stages. The first stage is that of microstrain during which the strain rate in the sample increases from zero to the test value. The state of stress in the material rises rapidly and evidence[150] indicates some dislocation multiplication takes place. The end of the microstrain interval is signified by a decreasing in the slope of the loading curve. The increasing stress is caused by dislocation generation, but the thermal activation assists the dislocations to cross-slip and climb and either annihilate or find equilibrium positions. The increasing influence of the dislocation annihilation and movement causes a reduction in the rate of loading until the final stage is reached when the steady state regime prevails, the flow stress does not vary with strain and the rate of hardening by dislocation generation is balanced by the rate of annihilation.[151-157] The result of the dislocation activity is an equiaxed subgrain structure whose perfection, dimensions and misorientations depend upon the metal, the strain rate and the temperature of deformation. Jonas et al.[129] reported that the dislocation density between dislocation walls, the average spacing between them and the misorientation across them do not change during the course of steady state deformation.

The higher the temperature of deformation and the lower the strain rate, the larger are the subgrains that are formed during high temperature deformation.[129,158] As they increase in size the subgrains contain fewer dislocations and have boundaries in which there are less dislocations arranged in more orderly arrays. These substructural variations reflect the diminution in the equilibrium dislocation density arising from the increase in temperature and strain rate decrease through their effects on the generation and annihilation rates. The generation rate decreases because the effective stress decreases

with strain rate and with temperature increase. The annihilation rate on the other hand does not decrease as much because it is not so sensitive to a stress decrease.

In aluminium and its alloys it is reported that the subgrains consist of very sharp boundaries with equilibrium dislocation networks within the subgrains. The misorientation between them is small with reported values ranging from 1° to 7°. This can be attributed to the insensitive techniques used to measure the misorientation.[13,129,132,158,159] Smaller cell structures have been observed within these subgrains[13,158,160] and Raybould and Sheppard associated them with both the remnants of subgrains that have annealed out by rotation and the formation of the subgrains during deformation. The former mechanism occurring at the end of the deformation, the latter at the start. There is also the possibility that they occurred by subgrain coalescence[152] in the time between deformation and quenching. These microcells are very similar to those observed by Hu[161] which he associated with subgrain coalescence.

Solute elements increase the flow stress and decrease creep rate. The increase in flow stress of solid solution alloys is sufficiently great that considerably more force and energy is required to deform these materials in hot working operations.[109] The effect of solid solution alloying on the microstructures produced by working are diverse and require the individual discussion of each alloy system. In general, solute addition lowers the stacking fault energy which makes dynamic recovery more difficult. It is reported[162] that the addition of 5% tin in Zr-Sn alloys reduces the stacking fault energy from 240 to 60 mJ/m^2. The consequence is a reduction in equilibrium subgrain size, for similar temperature and strain rate conditions, from 3.5 to 0.7 μm as the tin concentration is increased.

In the case of the Al-Mg system, McQueen and Jonas[150] report that while strength increases with greater concentration of magnesium, the size of the subgrains also increases for tests at the same temperature and strain rate. They attributed this to the increased amount of work hardening in the alloys if the internal stress does not depend directly upon sub-boundary density,

as has been suggested previously, but increases with the square root of dislocation density instead. An alternative suggestion is that the internal stress contribution of the sub-boundaries is strongly dependent on the dislocation structure of the boundary itself and that this changes with alloying. Further reports of solute addition affecting stacking fault energy have been made by other workers.[163-165] Tensi et al.[165] report that an addition of 0.12% magnesium reduces the stacking fault energy from 168 mJm^{-2} to 108 mJm^{-2} while a 0.39% addition reduces it still further to 65 mJm^{-2}. Truszkowski et al.[167] also suggests a reduction from around 200 mJm^{-2} to 50 mJm^{-2} with an addition of 1%. Any excess additions causing a slower decrease. Comparing these values with those of the high stacking fault energy aluminium,[168,169] (value $\sim$ 238 mJ/m^{-2}) would tend to suggest that the Al-Mg system with magnesium in excess of 1% falls into the low stacking fault energy category of materials such as copper (value $\sim$ 25 mJm^{-2} [170,171] - 160 mJm^{-2} [168,169]). Thus the anticipated high temperature restoration process of dynamic recovery may not be operative in isolation in this system.

The presence of second phase particles causes further complication. In the case where the particles are not deformed by dislocation movement and are relatively stable, they serve as obstacles which help initially to build up the substructure and finally to stabilize it. Under these conditions the subgrain diameter may be reduced to the order of the interparticle spacing, which leads to an increase in flow stress. The presence of particles can prevent the formation of a subgrain structure altogether if the spacing is small enough or if, as a result of their shearing, they induce the formation of matrix superdislocations, which cannot leave their slip planes. These then are the basic structural features of dynamic recovery and we shall now turn our attention to the alternative mechanism of dynamic recrystallization.

Dynamic Recrystallization

The occurrence of dynamic recrystallization modifies the appearance of the flow curve produced at constant strain as shown in Fig. 2. At high strain rates in the hot working range the flow stress rises to a maximum at the peak strain. Thereupon, as a

result of dynamic recrystallization, it diminishes to a value intermediate between the yield stress and the maximum or peak stress. At lower strain rates the softening produced by dynamic recrystallization is followed by renewed hardening and a cyclic flow curve of approximately constant period, but declining amplitude is traced out.

In metals which undergo dynamic recrystallization a dislocation substructure develops in the initial stages of deformation which is poorly recovered; i.e. the cells have a relatively smaller size and more tangled walls compared to metals described previously which undergo a high degree of recovery. At lower strain rates, the evidence[172] indicates that nucleation occurs by bulging of an existing grain boundary. Although scalloped boundaries are also observed in high dynamic recovery metals, nucleation does not occur. The structural features peculiar to low recovery metals that account for the nucleation of dynamic recrystallization are:-

(1) The greater effectiveness with which a grain boundary is pinned by the highly tangled cell walls.
(2) The greater difference in strain energy within the bulge and that in front of it.

There is also a report[173] that nuclei formed in slip bands, presumably by a mechanism similar to that described below for high strain rates.

At high strain rates a fine tangled cellular structure is developed throughout all the grains, which does not leave grain boundary segments long enough to bulge. There is evidence that, with increasing strain, some tangles build up to high misorientations giving rise to nuclei throughout each grain.[174] The density of nuclei is probably greater near grain boundaries because the strain is higher there as a result of accommodation of plastic anisotropy.

Since straining of the material continues during nucleation and growth the new grains deform as they grow. When the strain rate is low, the gradient of strain energy from the centre of the recrystallized grain to the rapidly advancing boundary is low and

the region behind the boundary is relatively free of dislocations. As a result the driving force due to the difference in dislocation density on opposite sides of the boundary and hence the rate of migration, is not appreciably reduced by the continuing deformation. In this way recrystallization proceeds to completion. Once complete, the dislocation density builds up again raising the flow stress until recrystallization is again nucleated.

In the case of high strain rate deformation the gradient of deformation from centre to boundary of a recrystallized grain is high and so there is considerable dislocation density just behind the advancing boundary. By diminishing the driving force the rate of migration is reduced. Before recrystallization is complete, the dislocation densities at the centres of the recrystallized grains have increased sufficiently such that another cycle of nucleation occurs and new grains begin to grow again.

The start of recrystallization is quite marked on the stress-strain curve. The critical strain for the start is actually slightly less than the peak strain because while the first nuclei are softening the material locally, the remaining material continues to get stronger. The difference between the two strains is even greater at higher strain rates.

The critical strain may not be achieved for a variety of reasons. For instance, fracture may occur prior to the critical strain being attained, but this would suggest hot working conditions have not been reached. Dynamic recovery processes alone may lead to high enough dislocation annihilation and the nucleation avoided.[175]

In general the critical strain for recrystallization increases with increasing strain rate and decreasing temperature.[172] The increase with decreasing temperature is attributable to the decreased rate of recovery, and therefore of nucleation at lower temperatures. When the strain rate is increased at constant temperature there is actually a decrease in the time required for recrystallization to begin, although the decrease is insufficient to offset the increase in strain rate, leading to the net increase

in critical strain.[176,177] The strain for completion of the process also varies in the same way.

The periodicity arises at low strain rates because the strain for completion is much less than the strain for nucleation. At high strain rates the opposite applies and the periodicity disappears.

The size of dynamically recrystallized grains is reported[150] to decrease as the temperature compensated strain rate increases, because the associated increase in subgrain density gives rise to a higher density of nuclei. The grain structure affects the high temperature flow stress in two ways. In the first place, the volume fraction that has recently recrystallized determines the degree to which the flow stress approaches that of statically recrystallized material on the one hand or work hardened on the other. Secondly the grain size will influence the high temperature flow stress when grain boundaries act so as to impede the propagation of slip throughout the material.

Previous investigations on dynamic recrystallization have covered the traditionally low stacking fault energy materials,[172,177-180] while other workers have looked at more general aspects of the mechanism.[181,182] In a recent article, Gardner and Grimes[183] presented some evidence for dynamic recrystallization in an aluminium-magnesium alloy. Although the photographic evidence shows the presence of small equiaxed recrystallized grains at the original grain boundaries, which they attribute to dynamic recrystallization, during axisymmetric compression, they present no firm electron microscopical evidence. The single piece of indisputable evidence would be the presence of a recrystallized grain structure containing a dislocation substructure, this being produced by the deformation taking place during the recrystallization.

A further high temperature softening process may be invoked following dynamic recrystallization, which has no parallel in the static case. Halting high temperature deformation during dynamic recrystallization, many nuclei are already present within the material and some grain boundaries are migrating and sweeping regions free of dislocations. These boundaries can continue to

migrate and nuclei to grow without any classical incubation period being required. This softening has been referred to as metadynamic recrystallization.[150] As no nucleation interval is required, it proceeds very rapidly upon termination of deformation, but static recrystallization can still take place in regions which do not contain dynamic nuclei.

1.4.3.3. Deformation Mode

In the previous section the processes occurring during hot working, namely recovery and recrystallization, were discussed. Various theories[184] have been put forward to explain the mechanisms by which these processes occur. Most of the theories have been proposed for creep deformation.

Three basic models have been suggested to explain the mechanism operating during dynamic recovery. These are based upon:-

(1) The motion of jogged screw dislocations.
(2) The climb of edge dislocations.
(3) The existance of a network of dislocations inside the subgrains.

All three models assume the activation enthalpy is the same as that for self-diffusion. The differences arise in the terms comprising the structure factor and activation volume.

Barrett and Nix[185] proposed the first model for steady state creep. A jog is part of a screw dislocation which does not lie in the slip plane. Under the influence of a shear stress the screw dislocation glides and the jog is "pulled" with it leaving a trail of vacancies. The stress required to move the dislocation depends upon the vacancy concentration and its effect on the jog. Unfortunately this model does not permit the effect of alloying to be considered. Jonas[129] showed qualitatively, the applicability of this theory to high strain rate deformation.

Weertman[186,187] proposed the second model, based on the climb of edge dislocations. Dislocation sources are assumed to be distributed throughout the material. Under the effects of the applied shear stress they emit loops. These loops expand until they are blocked by the stress fields of loops on parallel planes.

The climb of piled up dislocations out of the slip plane then becomes the rate controlling process. Once again, this model was proposed for steady state creep and does not allow for alloying additions. Objections to this model have been raised[188] because the predicted substructure is not usually found in specimens deformed in creep tests.

The third model, based on a three dimensional dislocation network within the grains, was suggested by McLean.[189] Moving dislocations intersect this network and, under the influence of the applied shear stress, the unpinned segments bow out, decreasing the size of the network. Jogs migrate along the dislocations causing edge dislocations to climb. As a result, the network grows. The rate of recovery depends upon the diffusion coefficient. McLean[190] considered the effects of alloying additions and concluded that the dispersed phase particles anchored the network.

Unfortunately, to date, the validity of all three models remains in some doubt. As all were proposed for creep deformation their applicability to high strain rate hot working processes must also be doubtful.

Stuwe and Ortner[191] proposed a model for the mechanism by which dynamic recrystallization occurs. They based the model on the nucleation of recrystallized grains followed by deformation within the grains, but experimental verification of the model has yet to be produced.

Roberts and Ahlblom[192] proposed a nucleation criterion for dynamic recrystallization based on the contention that the reduced driving force due to concurrent deformation modifies the normal energy balance which defines the nucleation of new grains. The principal conclusion from the analysis is that the mechanism requires a critical dislocation density irrespective of whether dynamic recovery is occurring simultaneously or not. Their results showed quantitative agreement with experimental observations, but several reservations were made concerning the validity of the analysis:-

(1) They were not specific regarding the nucleation mechanism.
(2) They neglected an inhomogeneity of driving force distribution such as the presence of subgrains.
(3) They assumed the migration rate of a grain boundary during dynamic recrystallization was determined purely by the local stored energy difference across it.

1.4.3.4. The Effect of High Temperature Deformation on the Room Temperature Mechanical Properties

The room temperature mechanical properties will reflect the internal material structure and this in turn will depend upon the degree of retention of the hot worked structure. In order to have an effect, the dynamic recovery substructures must be retained after deformation which will require a suitable, rapid rate of cooling.

It has been found experimentally[150] that there is a relationship between room temperature yield stress and the subgrain size (i.e. diameter) of the form:-

$$\sigma_Y = \sigma_A + Kd^{-m} \qquad (1.21)$$

where d is the subgrain density, σ_A is the yield strength of a coarse grained material in the absence of sub boundaries, K is a purity factor and reflects the addition of any alloying elements[100] and the exponent m has values in the range 1 - 2.[135,156,193-195]

Alternative relationships have also been suggested by Jonas et al.[100]:-

$$d^{-1} = a + b \ln (\mathrm{Sinh}\ (\alpha\sigma)) \qquad (1.22)$$

and $$d^{-1} = p(\mathrm{Sinh}\ (\alpha\sigma))^q \qquad (1.23)$$

As the temperature compensated strain rate is also a function of the hyperbolic stress, it should prove possible to relate the subgrain size to this parameter as shown by Sheppard and Raybould.[13]

The strengthening due to a hot worked substructure has been reported[150] to be of industrial importance in the production

of non-heat-treatable aluminium and Al-Mg alloy sheet and extruded shapes.

If a hot worked material which undergoes dynamic recrystallization is rapidly quenched it is possible to retain the dislocation substructure and the fine dynamic grain size. McQueen and Jonas[150] report that the room temperature hardness increases with an increase in the temperature compensated strain rate of the hot forming process. This structure has a greater hardness than the equivalent statically recrystallized one. The structures are noted to be unstable at elevated service temperatures. They also report the room temperature hardness in copper-aluminium alloys to vary inversely with the square root of the dynamically recrystallized grain size.

The dependence of both subgrain and dynamically recrystallized grain size on the temperature compensated strain rate and their individual relationships with room temperature strength should enable the final properties to be related to the process variables of temperature and strain rate.

1.5. Defects in Extrusion

Johnson and Mamalis[24] classified extrusion defects under three headings:-

(1) Cracking defects.
(2) Contraction defects.
(3) Skin-inclusion defects.

Peripheral cracking is an example of the first type caused by hot or cold shortness accompanied by secondary tensile stresses generated in the region of the die, it leads to the so-called "fir-tree" defect. Central burst of chevrons are also occasionally encountered. Piping at the back end of the billet is an example of a contraction defect. During the final stages of extrusion, when the billet length is very small, the centre sometimes "caves in". This produces a central core of material containing voids at the rear of the extrude. Consequently in industry, the final length of extrude is discarded. A common example of a skin-inclusion defect involves foreign matter or lubricant on the side of the

billet, being dragged between the flowing metal and the dead metal zone. This produces blisters on the extrude. The familiar 'extrusion defect' is a combined contraction-skin-inclusion defect. In the final stages of extrusion, after the billet centre has caved in, oxidised material from the surface of the billet flows laterally to occupy this vacant space. This produces a final length of extrude with a core of oxide and inclusions.

These defects have also been reported by Bryant[196] who classified them according to appearance and origin.

In the particular case of aluminium extrusion, another problem is caused by the tendency of the aluminium to stick to the die land surface. This accumulation can lead to heavy scoring of the extrude surface as well as dimension reduction. Williams[197] reported that this could be prevented by two methods:-

(1) Starting and stopping the press which, unfortunately, leaves stop marks on the extrude.

(2) Using a die with a conical lead in.

In industry the achievement of a good surface finish is an art rather than a science. Much work remains to be done on the correlation of extrusion conditions with extrude surface finish.

1.6. Limit Diagrams

In 1958, Hirst and Ursell[83] first proposed the formation of so-called limit diagrams which defined the operating region for satisfactory extrusion. These were essentially graphical representations of the complex interaction of structure, strain rate and temperature, and enabled the onset of hot shortness and insufficient press capacity to be predicted. Unfortunately, to obtain these solutions a model for temperature rise and a good estimate of the strain rate are required, both of which are unlikely to conform to reality.

The diagrams of Hirst and Ursell, as shown in Fig. 3, were very simple. They used a line to define the maximum possible extrusion ratio that could be achieved with a given billet pre-heat

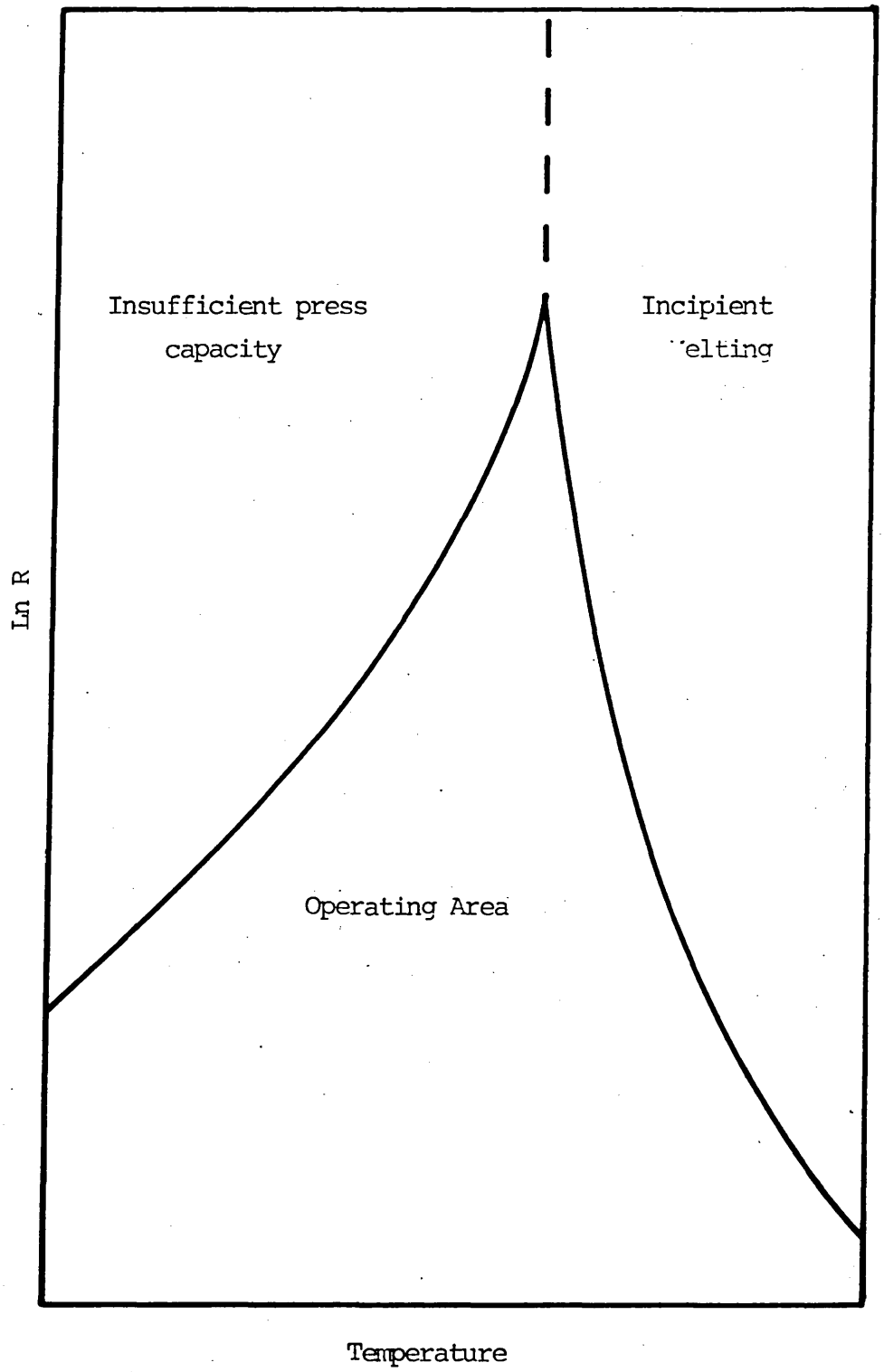


Fig. 3. Basic Limit Diagram

temperature at an arbitrary strain rate of 30 sec^{-1}. This was done using their equation for tube extrusion (equation 1.9).

To allow for temperature rises, adiabatic conditions were assumed and the following relationship was found:-

$$\text{LnR} = \frac{(T_m - T)\ S_g\ S_h}{4.43\ Y_m \dfrac{1 + 2\mu L}{D_B - D_E}} \qquad (1.24)$$

where S_g and S_h = specific gravity and heat of metal.
T = initial billet temperature.
T_m = maximum billet temperature permissable
and Y_m = mean yield stress.

Ashcroft and Lawson[9] produced a similar diagram for a Al-Zn-Mg-Cu alloy from experimental results by an iterative technique, while Meadows and Cutler[198] improved the original model by using the temperature rise prediction of Singer and Al-Sammarai[10] but retained the pressure limiting line.

Sheppard and Raybould[13] have further improved these diagrams for direct aluminium alloy extrusion. An integral profile method was used to estimate the temperature rise during deformation while the mean yield stress was determined from an upper bound solution. They considered not only the effect of ram speed, but also strain rate upon the pressure limiting line.

The diagram also incorporated the limiting conditions needed in the production of various structures. It was reported that water quenching the material caused the onset of recrystallization to be related to the temperature compensated strain rate. In a similar fashion they were able to plot lines for limiting subgrain sizes and material properties.

It was later recognised by Sheppard and Castle[199] that the pressure limiting line should be defined by the load required to initiate extrusion and not by the steady state load. The former invariably being equal or greater than the latter.

Wood[37] expanded the field by including both rod and shaped extrusion. He calculated the pressure line from an upper

bound solution incorporating a constituitive equation for flow stress, found from high temperature torsion tests, to predict the steady state pressure. He then added an experimental increment equal to the excess peak pressure, Δp.

In 1977, Sheppard[85] produced a diagram for an Al-Cu alloy by considering the pressure for homogeneous deformation, a friction contribution and an increment for the peak, Δp. The melting line was found from considering the temperature rise for the given conditions using an integral profile technique.

It should be remembered that any diagrams established on a theoretical basis must be carefully checked against experimental results.

CHAPTER 2

THEORY

2.1. Introduction

In this chapter the various analyses used in the work are presented in detail. The derivation of two upper bound solutions for axi-symmetric extrusion are described. A general hot working theory is also presented enabling flow stress, strain rate and temperature to be inter-related for a wide range of the last two variables. The evaluation of data from hot torsion tests is also discussed.

2.2. Axi-symmetric Upper Bound Analysis of Rod Extrusion

2.2.1. Single Triangle Deformation Field

A kinematically admissable velocity field for axi-symmetric extrusion, satisfying incompressibility, continuity and velocity boundary conditions was produced graphically by Halling and Mitchell.[73] They assumed a mode of deformation and determined the velocity components needed to produce the required hodograph by considering stream-line geometry. Their solution was for axi-symmetric extrusion through conical dies, but this can also be applied to unlubricated extrusion through square dies, as in this case the dead metal zone/deformation zone boundary effectively forms a conical lead in. A simple deformation field and hodograph for a single triangle arrangement of velocity discontinuities is shown in Fig. 4. The geometry divides the deformation into four regions. Region 1 is the undeformed original billet, region 2 the zone in which the deformation takes place, region 3 the material after the final velocity discontinuity and region 4 the dead metal zone. The boundary 24 constitutes the conical lead in used by Halling and Mitchell.[73] Assuming all metal flow in region 2 to be parallel to the boundary 24, then points on radial lines through O_2 have the same velocity vector. In the axi-symmetric case the boundaries 12, 24 and 23 are surfaces while region 2 is a volume. The total rate of energy dissipation can be found from summing the energies dissipated by shearing at the velocity discontinuities 12, 23 and 24

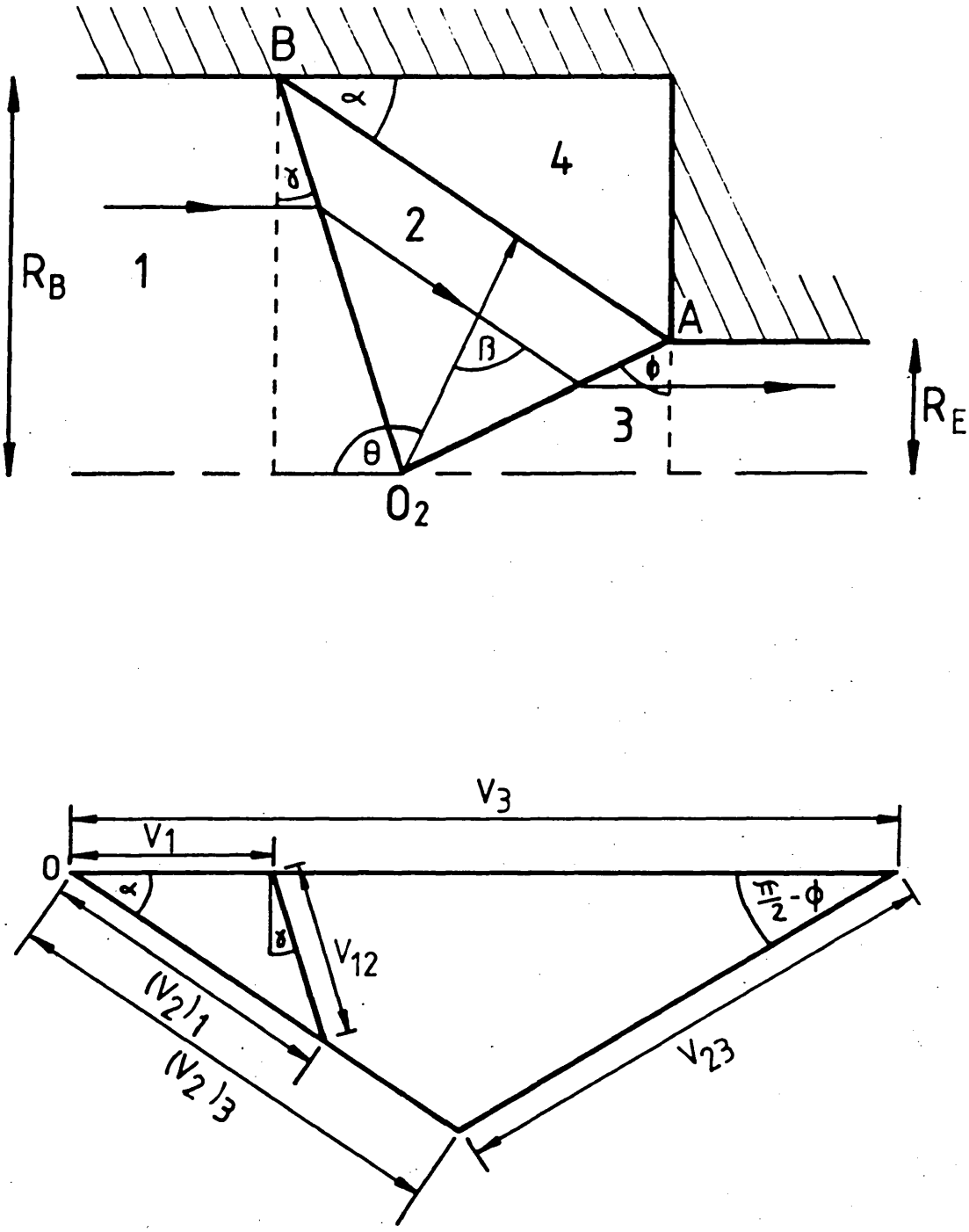


Fig. 4. Axi-symmetric upper bound velocity field and hodograph for single triangle arrangement.

and also that due to circumferential straining, manifested as an acceleration along the streamlines, in region 2:-

$$\dot{E} = \sum_{i,j=1}^{n} \left(\iiint_{v} \bar{\sigma}\, \bar{\dot{\varepsilon}}_i \, dv + \iint_{s} \tau_{ij} V_{ij} \, ds \right) \qquad (25)$$

where n = number of regions into which the problem is divided.

As the approach is towards an upper bound, the expression predicts a value that is equal to or greater than that actually encountered and so minimizing the value will give the best solution. As Fig. 4 shows, the geometry may be defined by the lengths R_B and R_E plus the angles α and ϕ. It is the variation of the latter two angles which permits the expression to be minimized. The terms involved in equation (25) must now be calculated. The rate of energy input on the left hand side can be simply expressed:-

$$\dot{E} = p\, v\, A_B$$

where p = extrusion pressure, v = ram velocity and A_B = cross-sectional area of the ram.

The first term on the right hand side represents the rate of energy dissipation within region 2. Alexander[74] demonstrated that the effective strain rate might be written:-

$$\dot{\bar{\varepsilon}}_1 = \frac{2}{\sqrt{3}} \left[\dot{\varepsilon}_{\theta\theta}^2 + \dot{\varepsilon}_{\psi\psi}^2 + \tfrac{1}{2} \dot{\varepsilon}_{r\theta}^2 \right]^{\frac{1}{2}} \qquad (26)$$

where:-

$$\dot{\varepsilon}_{\theta\theta} = \frac{1}{r}\left[v\cos\beta \left(1 + \frac{d\beta}{d\theta} \right) + \sin\beta \frac{dv}{d\theta} \right]$$

$$\dot{\varepsilon}_{\psi\psi} = \frac{v}{r}\left[\cos\beta + \cot\theta \sin\beta \right] \qquad (27)$$

$$\dot{\varepsilon}_{r\theta} = \frac{1}{r}\left[-v\sin\beta \left(1 + \frac{d\beta}{d\theta} \right) + \cos\beta \frac{dv}{d\theta} \right]$$

where $\beta = \theta - \alpha$ and v = velocity in region 2. N.B. dv/dr and $d\beta/dr = 0$.

In the case in question, the distance from 0_2 to any point on AB may be expressed in terms of θ thus:-

$$r = \frac{R_B \cos(\alpha + \gamma)}{\cos\gamma \sin(\theta - \alpha)} \tag{28}$$

Using a mass balance the velocity in region 2 may be expressed by:-

$$v = \frac{(V_2)_1 \, R_B}{r\sin\theta} \tag{29}$$

Using equations (26) and (27) we may write:-

$$\dot{\bar{\epsilon}} = \sqrt{\tfrac{2}{3}} \, {}^1/r \, \epsilon_i(\theta) \tag{30}$$

where $\epsilon_i(\theta)$ is a function of θ alone. Thus the expression for the energy dissipated in region 2 due to circumferential straining becomes:-

$$\dot{E}_2 = \Pi \, \bar{\sigma}_2 \sqrt{\tfrac{2}{3}} \int_{\theta_1}^{\theta_2} \left[r^2 \right]_{r_1(\theta)}^{r_2(\theta)} \epsilon_i(\theta) \sin\theta \, d\theta \tag{31}$$

The limits $r_1(\theta)$, $r_2(\theta)$, θ_1 and θ_2 define the boundaries of region 2, the deformation zone. At this stage it must be noted that for the geometry indicated in Fig. 4 there are two possibilities. The point 0_2 may lie behind or forward of B depending upon the magnitude of the angles α and ϕ. This will have an effect upon the mathematical expressions for the energy dissipations as well as some of the defining parameters. For instance the expression for r, equation (28) is correct for the situation illustrated in Fig. 4, but for 0_2 to the rear of B will be modified to:-

$$r = \frac{R_B \cos(\alpha - \gamma)}{\cos\gamma \sin(\theta - \alpha)} \tag{32}$$

The analysis will be developed for the case illustrated with the alternative expressions indicated where appropriate.

The second term on the right hand side of equation (25) must now be evaluated. The material deforming in region 2 is assumed to obey Von Mises yield criterion. Therefore at all the discontinuities within the material:-

$$K_{ij} = \bar{\sigma}_{yield}/\sqrt{3} \tag{33}$$

This also applies along boundary AB, as the dead metal zone, region 4, also consists of the extruding material. All the velocity discontinuities are either constants or functions of r. Therefore:-

$$\dot{E}_{ij} = \int_S \tau_{ij}\, v_{ij}\, ds \tag{33}$$

can be evaluated exactly.

The velocity discontinuities are given below:-

$$V_3 = v_1 \frac{R_B^2}{R_E^2} \tag{34}$$

$$V_{12} = \frac{v_1 \sin\alpha}{\sin(\Pi/2-(\gamma+\alpha))} \tag{35}$$

$$(V_2)_1 = \frac{v_1 \cos\gamma}{\sin(\Pi/2-(\gamma+\alpha))} \tag{36}$$

$$(V_2)_3 = \frac{v_1 R_B^2 \cos\phi}{R_E^2 \sin(\Pi/2-(\alpha-\phi))} \tag{37}$$

$$V_{23} = \frac{v_1 R_B^2 \sin\alpha}{R_E^2 \sin(\Pi/2-(\alpha-\phi))} \tag{38}$$

$$V_{24} = \frac{V_1 \cos\gamma R_B}{r \sin\theta \cos(\gamma+\alpha)} \tag{39}$$

For the alternative geometry, the term $(\gamma+\alpha)$ in equations (35), (36) and (37) must be replaced by $(\alpha - \gamma)$.

Substituting equations (34) - (39) into equation (33) we obtain:-

$$\dot{E}_{12} = \frac{\Pi R_B^2 \sigma_{12} v_1 \sin\alpha}{\sqrt{3}\cos\gamma\cos(\gamma+\alpha)} \tag{40}$$

$$\dot{E}_{23} = \frac{\Pi R_B^2 \sigma_{23} v_1 \sin\alpha}{\sqrt{3}\cos\phi\cos(\alpha-\phi)} \tag{41}$$

$$\dot{E}_{24} = \frac{2\Pi\sigma_{24}}{\sqrt{3}} \int_{\theta_1}^{\theta_2} \frac{v_1 \cos\gamma R_B r\, d\theta}{\cos(\gamma+\alpha)\cos\alpha} \tag{42}$$

For the alternative geometry, as before, the expression $(\gamma+\alpha)$ in equations (40) - (42) must be replaced by $(\alpha-\gamma)$.

Therefore, the total energy dissipated may be evaluated by summing $\dot{E}_{12}$, $\dot{E}_{23}$, $\dot{E}_{24}$ and $\dot{E}_2$ from equations (40), (41), (42) and (31). This may then be equated to the rate of energy input. By varying the angles α and ϕ, the value of the energy dissipated may be minimized and an optimim solution obtained.

By dividing the deformation zone into a mesh of elements, the problems of integration can be removed from equations (31) and (42) thus speeding up the calculation and offering the possibility of extracting values of strain rate from the elements throughout the deformation zone. Furthermore, the technique permits the flow stress to be evaluated from instantaneous values of strain rate as well as for varying degress of strain in the case of powder extrusion. The calculations performed on the element will depend upon its relative position in the deformation zone since elements within region 2 will only require circumferential straining to be considered, whereas an element with a velocity discontinuity as one or more boundaries will require this additional consideration.

The problem is set up with the deformation zone triangle divided into a matrix of (n x m) elements as shown in Fig. 5. The outer (n - 1) elements are of trapezoidal toroidal nature while the inner ones are of a revolved triangular nature, because of the imposed boundary conditions. The division of the dead metal zone

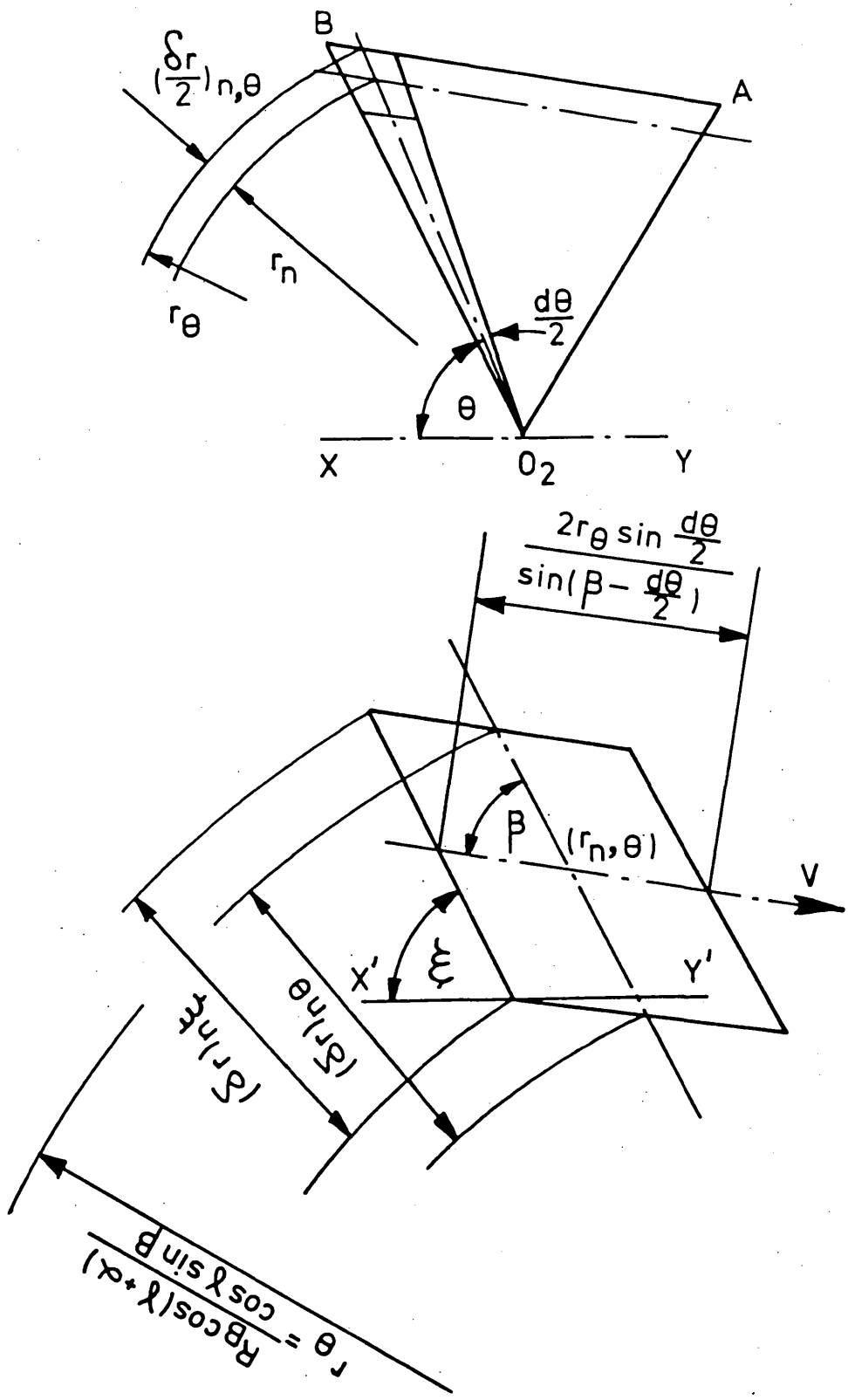


Fig. 5. Nomenclature of elemental single triangle upper bound analysis.

boundary, BA, into M elements will correspondingly divide the angle BO_2A into M equal parts, $d\theta$. A specific element can therefore be referenced through the two variables r_n and θ where r_n is the radius of the centroid of the element from O_2 and θ is the clockwise angular rotation from the horizontal.

As a general case we may take element M as shown in Fig. 5, where we must consider the following energy dissipations; that due to circumferential straining, and to the velocity discontinuities O_2B and BA. The geometry of the element is also shown in Fig. 5.

The plastic energy dissipation due to velocity discontinuity O_2B may be written:-

$$\dot{E}_{12} = K_{12}\ (\delta S)_{12}\ \bar{V}_{12} \tag{43}$$

$$= 2\Pi\ K_{12}\ (\delta r)_{n\xi}\ (r)_{n\xi}\ \bar{V}_{12} \tag{944}$$

In this case K_{12} is a function of strain rate as well as temperature. Ignoring temperature effects in the first instance, the strain rate at the discontinuity is infinite and as such cannot be evaluated. It can, however, be evaluated at the centre of the element M and it is this value which is assumed to be effective at the boundary.

Energy is also dissipated at the dead metal zone boundary, BA:-

$$\dot{E}_{24} = K_{r\theta}\ (\delta S)_2\ V_{2(1)} \tag{45}$$

$$= 4\Pi r_\theta\ K_{r\theta}\ V_{2(1)}\ R_B\ \frac{\sin\frac{d\theta}{2}}{\sin\beta\ \sin\left(\beta - \frac{d\theta}{2}\right)} \tag{46}$$

A similar method may again be used to determine $K_{r\theta}$; calculating $\dot{\bar{\epsilon}}_{r\theta}$ at the boundary (r,θ).

The internal energy dissipation due to circumferential straining is written:-

$$\dot{E}_2 = \sigma_{r,\theta}\ \dot{\bar{\varepsilon}}_{r,\theta}\ (dv)_{r,\theta} \tag{47}$$

$$= \frac{\sigma_{r\theta}\ \dot{\bar{\varepsilon}}_{r\theta}\ 4\Pi r_{n\theta}\ (\delta r)_{n\theta}}{\sin(\beta - \frac{d\theta}{2})} \quad \sin\frac{d\theta}{2} \tag{48}$$

Therefore the total energy dissipated for this element is given by:-

$$\dot{E}_{12} + \dot{E}_{24} + \dot{E}_2 \tag{49}$$

Hence, the total energy dissipated for the deformation zone is found by summing all the contributions from the (n x m) elements and this may then be equated to the total external energy input, once again given by:-

$$\dot{E} = p\ A_B\ V$$

A further energy dissipation term may also be included for the work done against friction as the billet moves relative to the container. This is most conveniently done by considering a shear stress, mK, where m lies in the range 0-1. Thus, with the value 0, a situation of zero friction is modelled, whereas a value of 1 will simulate full sticking friction. This stress is applied over the cylindrical length of billet remaining after the resolved length due to the dead metal zone is removed, since no relative movement is assumed in this region. The energy dissipated through this mechanism is given by:-

$$\dot{E}_f = 2\ \Pi\ R_B\ V\ l_{frict}\ M\ K \tag{50}$$

where l_{frict} = the length over which the stress acts and K is the shear stress of the material. The total energy dissipated must therefore include this term as well as those indicated previously.

Using this method a computer programme was developed and is documented in Appendix A.

The mesh was chosen to consist of five elements along the boundary O_2B and ten down the dead metal zone boundary BA.

A coarser mesh was found to produce a result in error to that generated with a considerably refined mesh while the size indicated mixed good accuracy with reasonable compilation and execution times. The programme described required an input of temperature and this, in conjunction with the internally calculated strain rates, enabled a quantitative evaluation of flow stress using hot working equation constants derived in subsequent sections. This then, enabled an extrusion pressure to be predicted for given values of temperature, ram speed and billet length/diameter geometry. A similar programme was used to predict values of P/σ. In this case the flow stress was not evaluated and values of shear stress were converted to true stress through Von Mises yield criterion.

Both computer programmes minimized the total energy dissipated through variation of the angles α and ϕ using a standard minimization routine specifically written for constrained optimisation situations,[200] and using a penalty function technique.[201] The constraints are imposed since the problem becomes indeterminant if either angle α or angle ϕ exceed 90° or go below 0°.

2.2.2. Double Triangle Deformation Field

An extension of the previously described solution was also proposed by Halling and Mitchell[73] involving representation of the deformation zone by two triangles. The deformation field and associated hodograph for this situation are shown in Fig. 6.

In this case the flow can be considered in two parts. Flow in region 4 takes place as if velocity discontinuities formed the triangle HFY, while in region 2 as if they formed triangle HBX. The streamlines are parallel to HF and HX in regions 4 and 2 respectively, while velocity vectors in the former case are constant on lines drawn through Y and constant on lines drawn through B in the latter case. N.B. $V_3 = V_5$.

The problem is formulated in a similar manner to the previous case. Internal energy dissipation is considered in regions 2 and 4 while the terms for the velocity discontinuities are summed, those for boundaries 24 and 46 being dependent upon

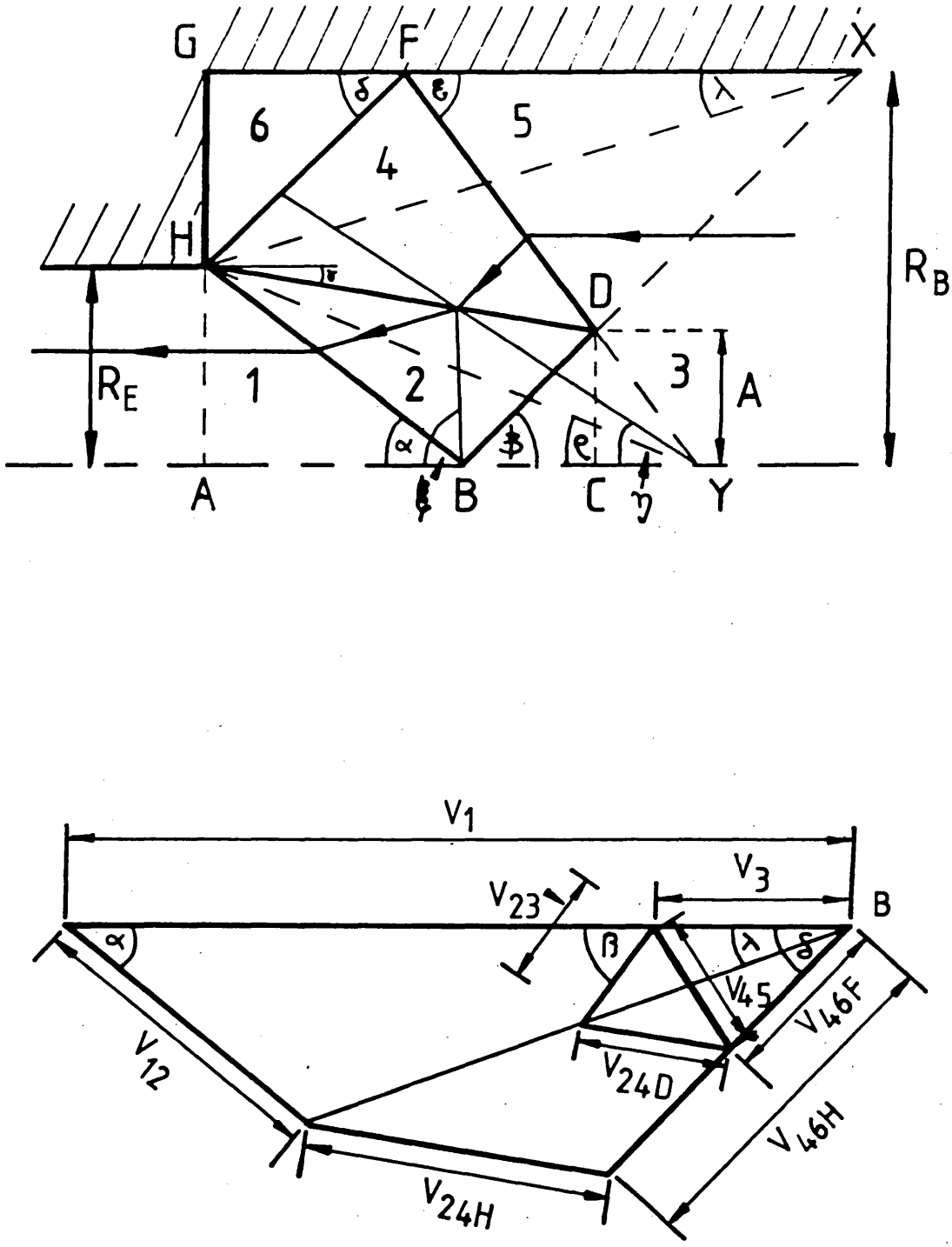


Fig. 6. Axi-symmetric upper bound velocity field and hodograph for double triangle arrangement.

radius and therefore requiring integration. The velocity discontinuities are given below:-

$$V_{45} = \frac{V_3 \, \mathrm{Sin}\delta}{\mathrm{Sin}(\varepsilon+\delta)} \tag{51}$$

$$V_{23} = \frac{V_{45} \, \mathrm{Sin}(\varepsilon-\gamma)}{\mathrm{Sin}(\beta+\gamma)} \tag{52}$$

$$V_{46F} = \frac{V_{45} \, \mathrm{Sin}\varepsilon}{\mathrm{Sin}\delta} \tag{53}$$

$$V_{46H} = \frac{V_1 \, \mathrm{Sin}\alpha \, \mathrm{Sin}(\lambda+\gamma)}{\mathrm{Sin}(\lambda+\alpha) \, \mathrm{Sin}(\gamma+\delta)} \tag{54}$$

$$V_{24D} = \frac{V_{23} \, \mathrm{Sin}(\beta+\varepsilon)}{\mathrm{Sin}(\varepsilon-\gamma)} \tag{55}$$

$$V_{24H} = \frac{V_1 \, \mathrm{Sin}\alpha \, \mathrm{Sin}(\lambda+\gamma) \, \mathrm{Sin}\,(\delta-\lambda)}{\mathrm{Sin}(\alpha+\gamma) \, \mathrm{Sin}\,(\lambda+\alpha)} \tag{56}$$

Applying equation (33) to the velocity discontinuities gives:-

$$\dot{E}_{12} = \frac{K_{12} \, V_{12} \, \Pi \, R_E^2}{\mathrm{Sin}\alpha} \tag{57}$$

$$\dot{E}_{23} = \frac{K_{23} \, V_{23} \, \Pi \, A^2}{\mathrm{Sin}\beta} \tag{58}$$

$$\dot{E}_{45} = \frac{K_{45} \, V_{45} \, \Pi \, (R_E^2 - A^2)}{\mathrm{Sin}\varepsilon} \tag{59}$$

For the discontinuity 46 the radius may be given as:-

$$R_{46} = \frac{R_B \, (\mathrm{cot}\delta + \mathrm{cot}\varepsilon)}{\mathrm{Sin}\delta \, (\mathrm{cot}\delta + \mathrm{cot}\eta)} \tag{60}$$

giving:-

$$\dot{E}_{46} = 2 \, \Pi \, K_{46} \, \mathrm{Sin}\delta \int_{\rho}^{\varepsilon} \frac{R_B^2 \, \mathrm{cosec}^2\eta \, (-(\mathrm{cot}\delta + \mathrm{cot}\varepsilon)) \, V_{46F} \, d\eta}{\mathrm{Sin}^2\delta \, (\mathrm{cot}\delta + \mathrm{cot}\eta)^2} \tag{61}$$

For the discontinuity 24, the radius may be given by:-

$$R_{24} = \frac{A(\mathrm{cot}\,\gamma - \mathrm{cot}\varepsilon)}{\mathrm{Sin}\gamma \, (\mathrm{cot}\gamma - \mathrm{cot}\eta)} \tag{62}$$

giving:-

$$\dot{E}_{24} = 2\,\Pi\,K_{24}\,\mathrm{Sin}\gamma \int_{\rho}^{\varepsilon} \frac{A^2(\cot\gamma - \cot\varepsilon)^2\,(\cot\delta + \cot\eta)\,\mathrm{cosec}^2\eta\,V_{24D}\,d\eta}{\mathrm{Sin}^2\gamma\,(\cot\gamma - \cot\eta)^3\,(\cot\gamma + \cot\varepsilon)} \quad (63)$$

The energy dissipated within regions 2 and 4 can be found using equation (31). The deforming region 2 (BDH) has boundaries:-

$$r_1 = 0$$

$$r_2 = {}^{R_E}\frac{(\cot\gamma - \cot\alpha)}{(\cot\gamma - \cot\xi)} \quad \mathrm{cosec}\xi$$

$$\xi_1 = \alpha \quad (64)$$

$$\xi_2 = \Pi - \beta$$

Using these and equation (31) gives:-

$$\dot{E}_2 = \Pi\,\sigma_2 \int_{\alpha}^{\Pi-\beta} \left[{}^{R_e}\frac{(\cot\gamma - \cot\alpha)}{(\cot\gamma - \cot\xi)} \quad \mathrm{cosec}\xi\right]^2 \varepsilon_i(\xi)\,\sin\xi\,d\xi \quad (65)$$

The deforming region 4 (DFH) has boundaries:-

$$r_1 = \frac{R_{E-A}}{\tan\gamma} \quad \frac{(\cot\gamma - \cot\varepsilon)}{(\cot\gamma - \cot\eta)} \quad \mathrm{cosec}\eta$$

$$r_2 = {}^{R_B}\frac{(\cot\delta + \cot\varepsilon)\,\mathrm{cosec}\eta}{(\cot\delta + \cot\eta)} \quad (66)$$

$$\eta_1 = \rho$$

$$\eta_2 = \varepsilon$$

giving:-

$$\dot{E}_4 = \Pi\,\sigma_4 \int_{\rho}^{\varepsilon} \left[{}^{R_B}\frac{(\cot\delta + \cot\varepsilon)\,\mathrm{cosec}\eta}{(\cot\delta + \cot\eta)}\right]^2 \cdot \left[\frac{(R_E - A)\,(\cot\gamma - \cot\varepsilon)\,\mathrm{cosec}\eta}{\tan\gamma\,(\cot\gamma - \cot\eta)}\right] \cdot \varepsilon_i(\eta)\,\sin\eta\,d\eta \quad (67)$$

Summing these various terms will give the total energy dissipation which can then be equated to the total external input as before.

Once again the solutions were found using the computer programme shown in Appendix B. The same minimization technique was employed as in the previous case with the four angles α, β, δ and ε being constrained to lie between 0° and 90°. Integration was performed by using Simpson's Rule with the range divided into 50 steps. Output is in the form of $^{P}/\sigma$ for the given conditions.

2.3. Strain Rate during Extrusion

Because of the differences in strain rate throughout the deformation zone, it is very difficult to define a mean strain rate. As outlined in the literature review, the original proposal by Feltham[86] defined the mean strain rate as:-

$$\dot{\bar{\varepsilon}} = \frac{\text{total strain}}{\text{time for strain to occur}} \qquad (68)$$

The time was calculated by assuming the deformation to occur in a cone of semi-angle 45°, but recent workers have evolved this early relationship to consider the cone angle as ω, in many cases 60°, and the total strain as not LnR but the value of $^{P}/\sigma$ gained from theory for each reduction ratio. This gives:-

$$\dot{\bar{\varepsilon}} = \frac{6\, D_B^{\,2}\, v\, c\, \tan\omega}{(D_B^{\,3} - D_E^{\,3})} \qquad (69)$$

where $c = {}^{P}/\sigma$ from theoretical predictions.

In this work the value of c was obtained from the single triangle upper bound solution, a straight line relationship being used to relate $^{P}/\sigma$ to LnR at the lower ratios. Furthermore, the upper bound solutions enable an angular prediction of ω to be made for varying extrusion ratio and this refinement has also been included giving a final relationship of:-

$$\dot{\bar{\varepsilon}} = \frac{6\, D_B^{\,2}\, v\, (a + b\text{LnR})\, (c + d\, \text{Tan}\omega)}{D_B^{\,3} - D_E^{\,3}} \qquad (70)$$

The single triangle upper bound solution outlined in section 2.2.1. also permits strain rate calculation at the centroid of each element. The problem is then one of finding the mean strain rate over the entire deformation area. Four methods are available for this; mathematical, volume, distance and time averaged. The first involves taking a straight forward average value while the second compensates for the individual element volume before dividing the sum of these by the total volume. The third method compensates each strain rate for the distance of flow line over which it acts, while the final method divides the total strain for each flow line by the time taken to achieve that strain. In the latter two cases adjustment must be made for the proportion of cross-sectional area over which the effect of each flow line is assumed to act.

2.4. General Hot Working Equation

A relationship between strain rate, flow stress and temperature during the hot deformation of metals (i.e. creep testing) was first proposed by Garofalo.[122] It was later applied to conventional hot working processes (i.e. extrusion) by Sellars and McG. Tegart.[123] The relationship involved a Sinh term and had the form:-

$$\dot{\varepsilon} = A\left[\text{Sinh } (\alpha\sigma)\right]^{n} \cdot \exp\left(\frac{-\Delta H}{RT}\right) \qquad (71)$$

Here A, α and n are temperature and stress independent constants and ΔH is the activation energy which is also assumed to be independent of temperature and stress. To make use of equation (71) the four constants must be evaluated.

2.4.1. Assessment of High Temperature Flow Stress

Prior to the four constants in the hot working equation (71) being evaluated a method must be found for assessing the flow stress-strain rate behaviour of the material at high temperatures. As mentioned in the previous chapter, the stress strain behaviour may be analysed using either tension, compression or torsion testing.

The method chosen was that of high temperature torsion testing since the ability to achieve high strains at high constant surface strain rates is of prime importance. Torsion tests introduce a stress condition of pure shear and theoretically there should be no change in the dimensions of the specimen, together with the absence of any frictional constraints. However it has been found that if specimens are not axially constrained, a dimension change appears,[118] lengthening for aluminium and contracting for most other materials. When constrained, these changes will cause the system to contain axial stresses and therefore the deformation will no longer be one of pure shear. The cause of the stresses is unclear, although they have been claimed to be due to anisotropy and texture development in the specimen.[202] However the axial stress is preferred to a specimen geometry change and is normally ignored.[109]

The conversion of shear stresses and strains from torsion into equivalent tensile stresses and strains is undertaken using Von Mises criterion:-

$$\sigma = \sqrt{3}\,\tau$$

$$\varepsilon = \gamma/\sqrt{3} \qquad (72)$$

$$\dot{\varepsilon} = \dot{\gamma}/\sqrt{3}$$

2.4.1.1. Calculation of the Flow Stress from Torsion Data

The strain and strain rate in the torsion of a solid cylindrical bar vary linearly from zero at the centre to a maximum at the surface. An analysis for the shear stress for a strain hardening material has been obtained by the method of Nadai.[203]

However if the flow stress is highly dependent on the strain rate, as is the case with aluminium alloys at hot working temperatures, then this method is no longer valid. A more rigorous approach is that due to Fields and Backofen[204] who showed that:-

$$\tau = \frac{1}{2\Pi r^3}\left[3M + \theta \frac{dM}{d\theta}\right] \qquad (73)$$

providing that $dM/d\theta$ is obtained from a torque-twist curve which satisfied $\dot{\theta} = \theta(\dot{\theta}_a/\theta_a)$ where $\dot{\theta}_a$ is the twist rate at some reference value of twist, θ_a. This means that the twist rate must vary in proportion to the twist. This can be simplified by the observation that plots of LnM against Lnθ at constant $\dot{\theta}$, and of LnM against Ln$\dot{\theta}$ at constant θ are often nearly straight lines. It can then be shown that:-

$$\frac{dM}{d\theta} = \frac{M}{\theta}\left[\frac{dLnM}{dLn\theta}\right]_{\dot{\theta}} + \frac{M}{\dot{\theta}}\left[\frac{dLnM}{dLn\dot{\theta}}\right]_{\theta}\left[\frac{\dot{\theta}}{\theta}\right] \qquad (74)$$

or $$\frac{dM}{d\theta} = \frac{M}{\theta}(n + m) \qquad (75)$$

where n = slope of $\frac{dLnM}{dLn\theta}$ at constant $\dot{\theta}$

m = slope of $\frac{dLnM}{dLn\dot{\theta}}$ at constant θ

Hence from equation (73) we get:-

$$\tau = \frac{M}{2\Pi r^3}(3 + n + m) \qquad (76)$$

which is no longer limited by the strain rate effects on the flow stress. Shear stress data can now be calculated from a series of torque-twist curves each at a different constant twist rate.

Calculations were performed using the computer programme shown in Appendix C. Torque readings were taken from torque-twist records every eighth of a revolution of the specimen thereby providing a matrix of torque, surface twist and surface twist rate for each initial temperature. By analysing the data as indicated previously (i.e. internally calculating the values of n and m) the computer programme produced an output of shear stress, surface shear strain and surface shear strain rate.

2.4.1.2. Temperature Changes During Torsion Testing

Before torsion results can be applied directly, it is necessary to make some allowance for the energy input causing a temperature rise within the specimen. It is known that a high percentage of the work done on the specimen is generated as heat and this can be substantial at high strain rates or with materials of large flow stress.

The method adopted was that proposed by Wright.[205] The adiabatic temperature rise can be expressed:-

$$\Delta T = \frac{\eta}{\rho C} \int_{0}^{\varepsilon_{max}} \sigma \, d\varepsilon$$

where ρ = density

C = Specific heat

σ = stress at any strain, ε

η = fraction of work turned into heat.

The specimen is divided into 20 radial and 40 axial elements, giving them equal length and width for the specimen geometry employed (see section 3.6.). Using a finite difference technique, radial and axial heat conductions are allowed for together with convective losses from surface elements. The calculation is carried out by a computer programme[205] which relates flow stress to strain rate through a relation of the form $\sigma = A \dot{\varepsilon}^{n}$ where A and n are temperature dependent constants; the equation being solved at several constant values of strain where necessary. Output is in the form of temperature profiles at various points up to the desired strain and, more usefully, a volume average temperature given by:-

$$T_{vol\ av} = \frac{1}{\Pi r_2^2 \, l} \int_{r_1=0}^{r_2} T_r \, V_r \, dr$$

where T_r is the temperature of an element of volume V_r at radius r.

A more complete description of the technique together with the mathematical relationships may be found in reference 205.

2.4.2. Determination of the Constants in the Hot Working Equation

2.4.2.1. Graphical Analysis

At high stress levels the relationship between strain rate and stress may be written:-

$$\dot{\varepsilon} = A_1 \exp(\beta\sigma) \tag{77}$$

where β is a temperature independent function. Also at high stress levels (i.e. $\alpha\sigma > 1.2$) and constant temperature equation (71) can be rewritten:-

$$\dot{\varepsilon} = A \operatorname{Sinh}(\alpha\sigma)^n \tag{78}$$

On expanding the Sinh term this approximates to:-

$$\dot{\varepsilon} = \frac{A}{2^n} \exp(n\alpha\sigma) \tag{79}$$

At low stress levels:-

$$\dot{\varepsilon} = A_2\sigma^{n_2} \qquad \text{i.e. } (\alpha\sigma < 0.8) \tag{80}$$

where n_2 is also assumed temperature independent.
Comparing equation (77) and equation (79) gives:-

$$\beta = n\alpha \tag{81}$$

Now $n \wedge n_2$

Therefore $\alpha = \frac{\beta}{n_2}$

β is evaluated by plotting $\operatorname{Ln}\dot{\varepsilon} \vee \sigma$ and n_2 by plotting $\operatorname{Ln}\dot{\varepsilon} \vee \operatorname{Ln}\sigma$ and hence α can be evaluated.

To find the activation energy we must reconsider equation (71). By taking natural logarithms we obtain:

$$\text{Ln}\,\varepsilon = n\text{Ln}\left[A \sinh (\alpha\sigma)\right] - \frac{\Delta H}{RT} \qquad (82)$$

Now at constant flow stress:-

$$-R \cdot \frac{\partial \text{Ln}\dot{\varepsilon}}{\delta 1/T} = \Delta H \qquad (83)$$

This may then be expanded[22] to give:-

$$-R\left[\frac{\partial \text{Ln}\dot{\varepsilon}}{\partial \text{Ln sinh}(\alpha\sigma)}\right]_T \cdot \left[\frac{\text{Ln Sinh }(\alpha\sigma)}{\delta 1/T}\right]_{\dot{\varepsilon}} = \Delta H \qquad (84)$$

Hence from plots of Ln$\dot{\varepsilon}$ vs LnSinh $(\alpha\sigma)$ at constant temperature and Ln Sinh$(\alpha\sigma)$ vs $1/T$ at constant strain rate the activation energy may be evaluated.

2.4.2.2. Mathematical Treatment

As previously stated in section 1.4.2. the general hot working equation may be written as:-

$$Z = \dot{\varepsilon} \cdot \exp \frac{\Delta H}{RT} = A\left[\text{Sinh}(\alpha\sigma)\right]^n \qquad (85)$$

This may simply be re-arranged to give:-

$$\alpha\sigma = \text{Sinh}^{-1}\left[Z/A\right]^{1/n} \qquad (86)$$

Now:-

$$\text{Sinh}^{-1} x = \text{Ln}\left[x + (1 + x^2)^{\frac{1}{2}}\right]$$

giving:-

$$\sigma = \frac{1}{\alpha} \text{Ln}\left[\left(Z/A\right)^{1/n} + \left[\left(Z/A\right)^{2/n} + 1\right]^{\frac{1}{2}}\right] \qquad (87)$$

Substituting for Z from equation (85) gives:-

$$\sigma = \frac{1}{\alpha} \cdot \mathrm{Ln}\left[\left(\frac{\dot{\varepsilon}\exp\frac{\Delta H}{RT}}{A}\right)^{1/n} + \left[\left(\frac{\dot{\varepsilon}\exp\frac{\Delta H}{Rt}}{A}\right)^{2/n} + 1\right]^{\frac{1}{2}}\right] \qquad (88)$$

The shear surface strain rate during a torsion test may be expressed as:-[206]

$$\dot{\gamma} = \frac{2\,\Pi\,r\,\dot{\theta}}{l} \qquad (89)$$

where r is the specimen gauge radius, $\dot{\theta}$ is the twist rate in revolutions per second and l is the specimen gauge length.

Using Von Mises Yield Criterion this may be re-expressed in terms of surface strain rate as:-

$$\dot{\varepsilon} = \frac{2\,\Pi\,r\,\dot{\theta}}{\sqrt{3}\,l} \qquad (90)$$

Thus equation (90) may be substituted into equation (88) to relate flow stress to surface twist rate during a torsion test.

The torque generated during a torsion test may be related to flow stress in a simple manner through:-[120]

$$M = \frac{2\,\Pi\,\sigma}{\sqrt{3}} \cdot \int_{r_1}^{r_2} r^2\,dr \qquad (91)$$

where M is the torque and r_1 and r_2 are the inner and outer radii of the gauge length respectively. For a solid specimen $r_1 = 0$.

Finally by substituting equations (90) and (91) into (88) we obtain:-

$$M = \frac{1}{\alpha}\,\frac{2\Pi}{\sqrt{3}} \int_{r_1}^{r_2} \mathrm{Ln}\left[\left(\frac{2\,\Pi\,r\,\dot{\theta}\exp\frac{\Delta H}{RT}}{\sqrt{3}\;l\;A}\right)^{1/n} + \left[\left(\frac{2\,\Pi\,r\,\dot{\theta}\exp\frac{\Delta H}{RT}}{\sqrt{3}\;l\;A}\right)^{2/n} + 1\right]^{\frac{1}{2}}\right] r^2\,dr \qquad (92)$$

This then relates torque, twist rate and temperature through the four constants A, α, n and ΔH.

The method of evaluation of the constants initially involves the production of a matrix of torque, twist rate and temperature data from hot torsion testing. Solution can then be obtained using the computer programme shown in Appendix D. Initial guesses of the four constants are used together with the experimental twist rate and temperature to predict a torque, M_p, which should be the same as the experimental torque, M_E. The computer programme minimizes the value of $(M_p - M_E)^2$ by internally changing the initial guesses of A, α, n and ΔH, over the whole data range using a constrained minimization routine[200] from the computer library. The constraints were necessary to prevent absurd values being produced, i.e. less than zero.

The method has the advantage of assessing all the values at once without incurring any errors from converting torque values to stress as well as removing the tedious task of evaluation using graphical means. However, should stress values be available equation (88) can be optimized in a similar manner.

2.4.2.3.

An alternative evaluation technique may be obtained by treating equation (92) in a slightly different way. We may define a parameter C such that:-

$$C = \left[\frac{2\,\Pi\,\dot{\theta}}{A\,1\,3}\ \exp\frac{\Delta H}{RT}\ \right]^{1/n} \qquad (93)$$

which enables equation (92) to be re-written:-

$$M = \frac{2\Pi}{\alpha\sqrt{3}} \int_{r_1}^{r_2} \left[\ \mathrm{Ln}(Cr^{1/n}) + \mathrm{Ln}(1 + (1 + (Cr^{1/n})^{-2})^{\frac{1}{2}}\ \right] r^2\,dr \qquad (94)$$

since $\sinh^{-1} x = \mathrm{Ln}\left[x + (1 + x)^{\frac{1}{2}}\ \right] = \mathrm{Ln}x + \mathrm{Ln}\ \ (1 + (1 + x^{-2})^{\frac{1}{2}})$

This may be rewritten as the sum of three integrals:-

$$M = \frac{2\Pi}{\alpha\sqrt{3}}\ (J_1 + J_2 + J_3) \qquad (95)$$

where $J_1 = LnC \int_{r_1}^{r_2} r^2\,dr$

$$J_2 = \frac{1}{n} \int_{r_1}^{r_2} r^2 Lnr\,dr \qquad (96)$$

$$J_3 = \int_{r_1}^{r_2} r^2 Ln\left[1 + (1 + (Cr^{1/n})^{-2})^{\frac{1}{2}}\right] dr$$

The integrals J_1 and J_2 may be evaluated exactly to obtain:-

$$J_1 = \frac{1}{3}(r_2^3 - r_1^3)\,LnC \qquad (97)$$

$$J_2 = \frac{1}{3n}\left[r_2^3\,(Ln\,r_2 - \tfrac{1}{3}) - r_1^3\,(Lnr_1 - \tfrac{1}{3})\right] \qquad (98)$$

Integration by parts provides a means of simplifying J_3. Let

$$u = Ln\left[1 + (1 + (Cr^{1/n})^{-2})^{\frac{1}{2}}\right] \quad \text{and}$$

$$dv = r^2\,dr$$

Then:-

$$du = \frac{-1}{nC^{\frac{1}{n}}}\, r^{-(1+2/n)}\left[1 + (Cr^{1/n})^{-2}\right]^{-\frac{1}{2}}\left[1 + (1 + (Cr^{1/n})^{-2})^{\frac{1}{2}}\right]^{-1} dr$$

and $v = \frac{1}{3}\,r^3$

Thus: $J_3 = uv\Big|_{r_1}^{r_2} - \int_{r_1}^{r_2} v\,du$

This second integral term may be further simplifed by the substitution:-

$w^2 = 1 + (Cr^{1/n})^{-2}$, so that

$dw = -nC^{-n}\ w\ (w^2-1)^{-(1+n/2)}\ dw$ and

$w_i = (1 + (Cr_i^{1/n})^{-2})^{\frac{1}{2}}, \quad i = 1,2$

Since $w_1 > w_2$ it follows that:-

$$J_4 = \int_{r_1}^{r_2} v\ du = -\frac{C}{3}^{-3n} \int_{w_2}^{w_1} \frac{w-1}{(w^2-1)^{1+3n/2}}\ dw \qquad (99)$$

The computer programme laid out in Appendix E performed the calculation.[207] Evaluation of the final integral in equation (99) was carried out by Simpson's Rule using 10 steps. The solution is found by iterating the values of A, α, ΔH and n to obtain a least squares regression for the torque value.

2.5. Temperature Changes During Extrusion

As mentioned previously, a considerable proportion of the energy input required to achieve some deformation may be returned as a temperature rise. A figure of 90% is commonly assumed.[208] The great dependence of flow stress and in numerical terms, the Zener-Holloman parameter, Z, upon temperature necessitates that some account be made for any changes during the process.

The majority of calculations associated with the extrusion process, in this work, have been related to the 'breakthrough' or peak pressure since it is felt that this is the critical stage which must be attained before any other features become of importance.

2.5.1. Temperature Rise at the Peak Pressure

Under normal metal extrusion conditions, the load rises in an almost linear fashion to the peak load. The ram displacement is small to this stage as the majority of the work is associated with upsetting the billet to completely fill the container.

The work done may be found from the area under the load-displacement curve:-

$$\text{Work done} = \frac{L_p \times d_p}{2}$$

where L_p is the peak load and d_p the ram travel to that situation. The temperature rise is found from:-

$$\eta.\left[\frac{L_p \cdot d_p}{2}\right] = V_B \rho C \Delta T$$

where η is the fraction of the work done converted to a temperature rise, V_B is the billet volume, and ρ and C are the density and specific heat of the material. With a 0.01 m length billet, 0.0375 m radius, a displacement of 10 mm at full load, i.e. 5 MN, this rise will be unlikely to exceed 25°C. Considering the short time involved and the small magnitude of the rise, any heat losses may be neglected.

2.5.2. Temperature Changes During the Ram Stroke

Although very little quantitative work has been carried out on the minimum load, where it has, the analysis of Sheppard and Raybould[13] and refined by Castle [88] has been adopted. The method involves an integral profile approach with a control volume being placed around the deformation zone, assumed conical. A full description of the technique may be found in Castle's thesis[88] and in Castle and Sheppard's publication[16] and need not be listed here.

2.6. Homogenisation

Under equilibrium cooling conditions the alloy of composition x (approx. 5% Mg) shown in Fig. 7 will initially begin solidification at temperature T_1 producing solid of composition α_1, and finish solidification at temperature T_3 with the final solid composition α_3. This will necessitate the solid composition changing from α_1 to α_3 in the limited time available during which the cooling takes place. This means that diffusion takes place in both the

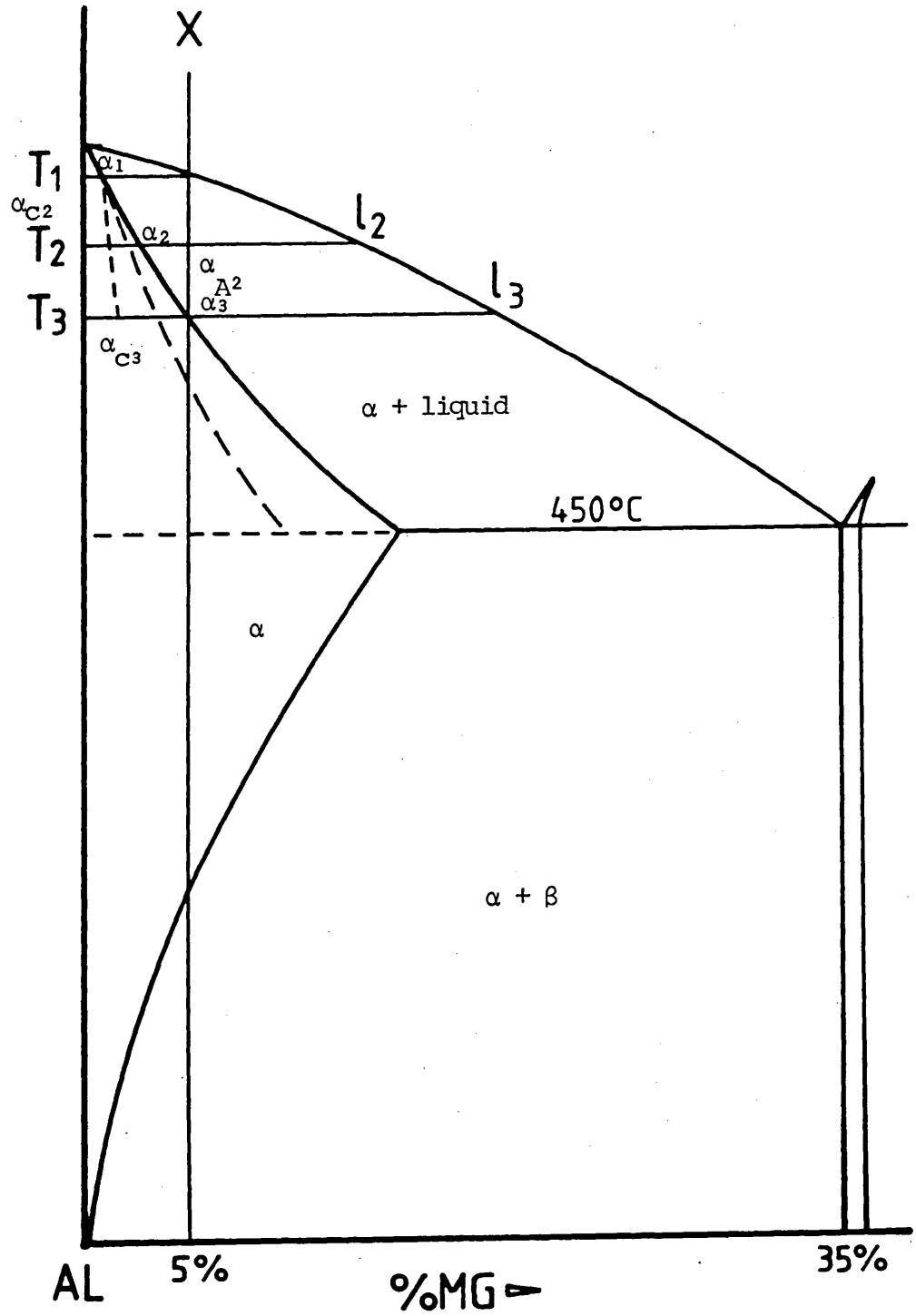


Fig. 7. Aluminium corner of the Al-Mg binary phase diagram.

solid and liquid phases as well as across the solid-liquid interface. However diffusion in the liquid occurs much faster than in the solid and with the rapid rates of cooling involved in industrial continuous casting techniques it is very unlikely that equilibrium conditions can be obtained.

Under non-equilibrium conditions it can be assumed that diffusion in the liquid and across the solid-liquid interface keep pace with the fall in temperature while that in the solid does not. As before, solidification commences at temperature T_1 rejecting solid of composition α_1. At temperature T_2 the liquid composition has reached l_2 while solid at the solid-liquid interface has composition α_2. Within the solid the restricted amount of diffusion means the composition has remained virtually unchanged from α_1 and is designated α_{C_2}. Thus the core composition has followed the line $\alpha_1\alpha_{C_2}$ meaning the average composition throughout the solid is α_{A_2}. At temperature T_3 the liquid now has a composition l_3 while the inner region of solid material has a composition α_{C_3} giving an average solid composition α_{A_3}. The line joining the average compositions $\alpha_1\alpha_{A_3}$ is called the Effective Solidus and it can be seen that in this case there is retained liquid at temperature T_3 indicating that solidification is incomplete.

Further cooling would cause complete solidification at some temperature above the eutectic temperature in this case. With a higher magnesium content it would be possible to produce retained liquid at 451°C and solidification to finish with the eutectic reaction. This reaction being completely unexpected from equilibrium considerations.

The solidification described shows that composition gradients exist in the material, solute concentration increasing from dendrite centre to edge. In addition an interdendritic distribution of second phase particles is produced. Because of the relatively low ductility of the intergranular and interdendritic networks of these second-phase particles, as-cast structures generally have inferior workability. It is the aim of the "ingot preheating" or "homogenisation" to remove these and minimize coring. This is achieved by maintaining the material at some high temperature for a time determined by empirical means.

CHAPTER 3

EXPERIMENTAL

3.1. Introduction

The following chapter describes the techniques and equipment employed during the research programme to:-

(i) determine the parameters defining the extrusion process;
(ii) determine the high temperature material properties;
(iii) evaluate the room temperature material properties resulting from the high temperature deformation process;
(iv) determine both the macro and microstructures resulting from high temperature deformation process.

3.2. The Extrusion Press

The extrusion press used was a 5 MN vertically mounted, fast action ENEFCO press. It was sited above a run out pit which enabled direct extrusion to be carried out through a die positioned above the pit and retained by a backing plate. The press layout is shown in Plate 1 which shows the positions of the controls, load indicating dial and oil pressure gauges.

Two containers of diameters 0.075 m and 0.057 m were available and were retained in a cast housing mounted on two hydraulic rams as shown in Plate 2. Billet length was variable up to 0.158 m, but for a 0.075 m diameter, a length of 0.1 m was used, while for 0.057 m a length of 0.076 m was employed to maintain a similar length to diameter ratio in each case.

An auxilliary pump enabled the ram approach speed prior to the commencement of extrusion to be greatly increased. This reduced the time for the hot billet to lose heat while the ram was being lowered to touch the pressure pad. Upon the load exceeding 0.2 MN the pump automatically 'cut out' and the ram proceeded to travel at the pre-set speed throughout the extrusion.

Plate 1. General layout of the extrusion press

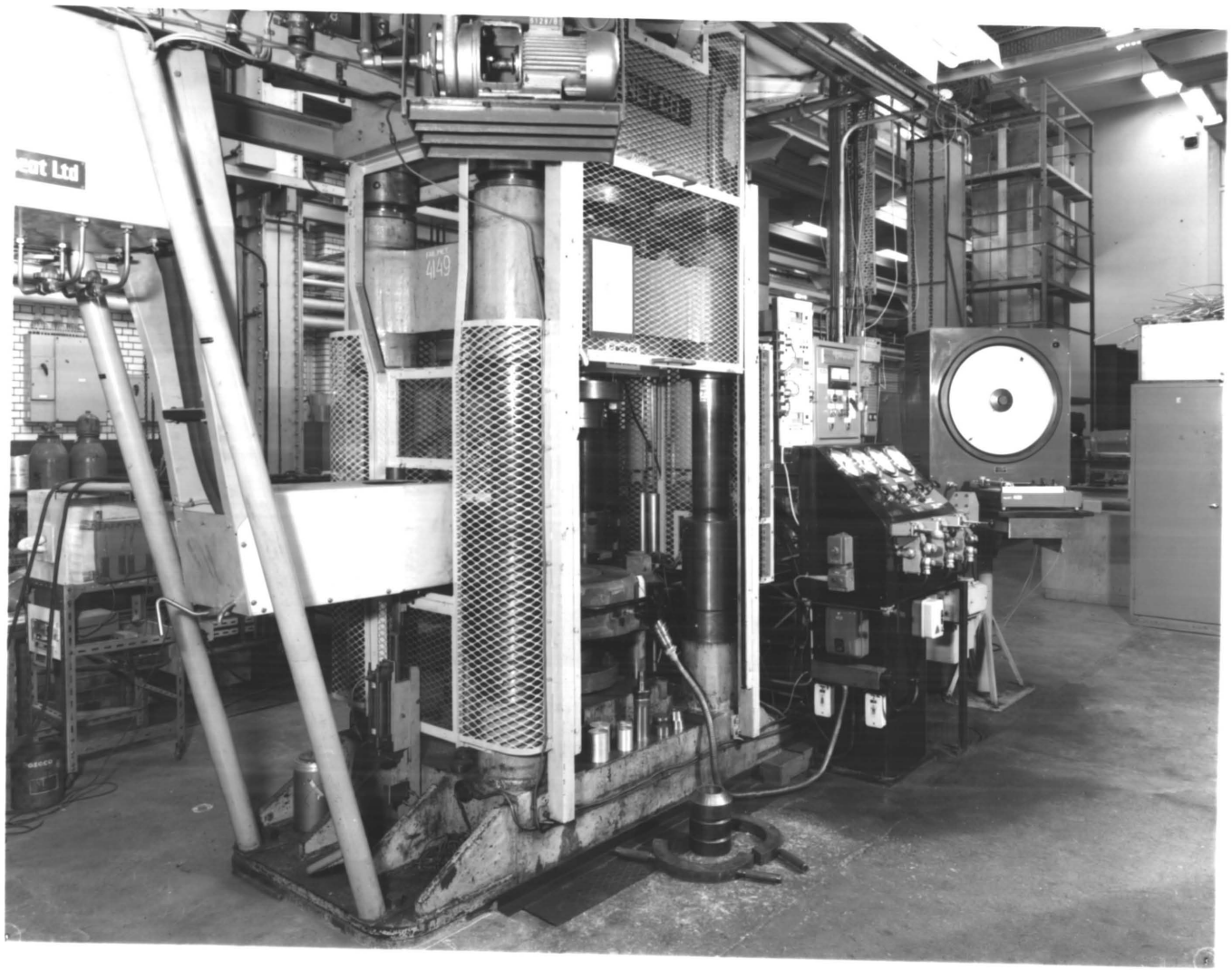

4149

Plate 2. Container, ram and die on extrusion press

3.2.1. The Container Heating

The container liner was maintained at 300°C by eight inconel heating elements placed around it and held in position inside the container holder casting. The heaters, with a total rating of 12 kilo-watts, had a maximum operational temperature of 700°C. To prevent their overheating, thermocouples, attached to Eurotherm temperature controllers, were braised to each element. With the heaters wired in a three phase system, two phases were maintained at maximum temperature while the third was varied by the Eurotherm to enable a consistent 300°C to be attained.

3.2.2. Billet Preheat

For the 0.075 m diameter billets, heating was via a Banyard Metalheat induction furnace which operated at mains frequency. Temperature measurement was through a Eurotherm Controller and a thermocouple inserted 0.01 m into the rear of the billet. The apparatus was calibrated initially and cooling curves produced for the billet for the various temperatures to be employed.

By means of a pneumatic system, the induction heater could be moved over the container. This enabled the hot billet to be transferred directly into the container by manually removing the rod supporting it within the heater. When the heater had returned to its original position, the extrusion cycle could be initiated.

In the case of the smaller 0.057 m diameter billets, preheat was facilitated by means of an air circulating furnace situated adjacent to the press. Temperature measurement was via a thermocouple positioned in a hole drilled 0.01 m into the top of the billet and connected to a digital thermometer. The billets were soaked at temperature for 40 minutes prior to transferring to the container manually using tongs. As before, it was necessary to determine the heat losses during the transfer to the container and this was carried out in a similar manner by constructing cooling curves for the various temperatures to be used. The cooling curves for both billet sizes are shown in Appendix F.

3.2.3. Ram Speed and Displacement

The ram speed was varied by adjustment of the pumps to give a range of speeds from 0.002 m/sec to 0.013 m/sec. Higher speeds, up to 0.6 m/sec could be achieved by accumulator drive, i.e. by discharging nitrogen filled bottles to increase the rate of delivery of oil to the main ram. Ram displacement was measured by a rectilinear potentiometer with a 0.6 m stroke which was fitted between the main ram and the base of the press. The output voltage, which varied with displacement was fed to a Hewlett Packard 136A X-Y recorder and plotted with time as the X-axis. Thus the slope of the plot gave the average ram speed. For the cases where high ram speeds were employed, the X-Y recorder proved insensitive to the rapid speed and the output voltage was connected to a high speed Ultra Violet recorder which enabled the time axis to be expanded considerably.

3.2.4. Load Measurement

The extrusion load was measured through a Mayes load cell situated directly above the ram stem. The output voltage was then fed to the Hewlett Packard 136A X-Y recorder and plotted against time and also to the dial gauge shown in Plate 1. Since the X-Y recorder pen speed was fixed, a Load-Displacement curve could be drawn.

3.2.5. Tooling

The ram, container, liner, dies, pressure pads and scraper pads were machined from KEA 145 5% Cr-V steel.

The dies used permitted extrusion ratios of 5,10,20,30,40, 50,60,70,80 and 100:1 to be investigated and were held in the die holder shown in Plate 2.

Changing the die involved removal of the retaining ring, which was held in position by 6 bolts, followed by removal of the die holder leaving die and backing ring exposed. The new die was then exchanged for the old one on top of the backing ring and the retaining ring replaced.

3.3. The Water Quench

In order that the structure of the material should reflect that due to the working process and not that due to static restoration the extruded product was passed into a water quench immediately upon exiting the die assembly.

The quench consisted essentially of two cylinders, the inner one containing 0.0012 m diameter radially drilled holes. Water was delivered to the system at approximately 60 gallons per minute via a centrifugal pump. The initial 0.26 m of quench tube contained 532 drilled holes while the remainder of the 1.37 m length contained 28 holes placed at 10 cm intervals. Regular cleaning was carried out because of the tendency for dirt particles to collect in the holes.

3.4. Experimental Procedure

Due to the large number of variables that must be considered during an investigation of this nature, a standard experimental procedure was adopted in order to minimise the sources of error.

The container was normally maintained at a constant 300°C, but in cases where the power was disconnected a period of 24 hours was allowed for the steady state to be attained. In the event of a die change, the die was placed in the bolster and left for at least one hour to attain thermal equilibrium before an extrusion was carried out. The pressure pads were also preheated to 300°C by leaving on the surface of the container.

In the case of a 0.075 m diameter billet, this was placed into the induction heater with a thermocouple inserted into a 0.01 m depth hole on the top surface. The billet was then heated to the preset temperature and allowed to remain for several minutes for equilibrium conditions to be achieved prior to the load cycle. At this stage the power was switched off, the thermocouple removed, the quench switched on and the timing begun. The induction heater was pneumatically inserted over the container, the billet charged into the container and the heater assembly withdrawn. The preheated pressure pad was then dropped onto the rear of the billet, two steel half rings placed on the top of the

container, the safety guards were lowered and the fast ram approach activated. Upon contact of the ram with the pad, the timing was stopped and the load and displacement measurement initiated. Upon a load being sensed in the hydraulics the fast ram approach was automatically cut out and the ram proceeded at the preset speed for the remainder of the cycle. The extrusion was continued until the main ram met the two steel rings when the pumps were deactivated and reversed to withdraw the ram. The steel rings were placed upon the container surface to prevent its damage by the ram and also, in the smaller diameter billet case, to prevent the tapered ram rear end being wedged into the inner container diameter.

The container was then lifted and the extrude sawn with a hacksaw, before being punched through to the pit below. The container was then fully raised and three rings placed on the die assembly before the container was lowered onto them. A tightly fitting scraper pad was then placed into the container and this and the discard forced through into the space created between the container and the die by the three rings, using the main ram. The use of the scraper pad ensured similar starting conditions for each run. The rings and discard were removed, the quench switched off, the extrude collected and labelled and the equipment was then ready for the procedure to be restarted.

In the case of the smaller, 0.057 m diameter, billet heating was via an air circulating furnace where they were left to soak at the required temperature for one hour. The furnace was then switched off, the timing sequence started, and the billet then transferred to the container manually using tongs. The procedure then continued as previously described.

Since the flow stress of a material is critically dependent upon the temperature, an accurate value is essential if a realistic analysis of the data is to be made. In both cases of billet loading a finite time exists between the heating and initiation of extrusion and this gives rise to billet cooling. The measured time from 'power off' to ram impact enabled the billet temperature to be predicted from the predetermined cooling curves shown in the Appendix F.

A sample length was removed from the middle region of the extrude and samples for tensile testing and both optical and transmission electron microscopy were removed from this sample.

3.5. Heat Treatment

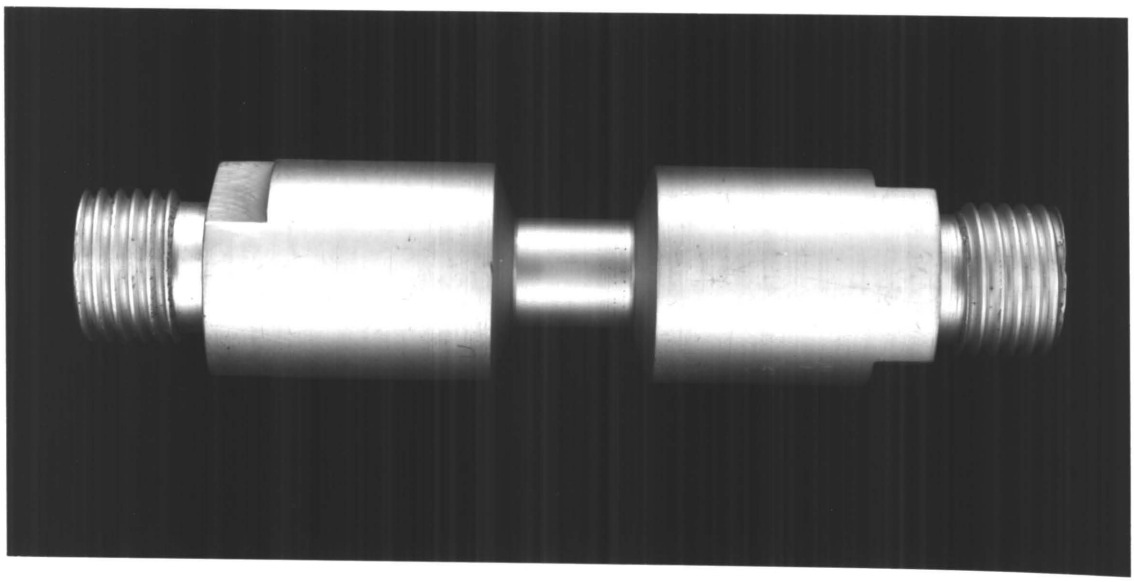
Although it is generally accepted that alloy compositions of less than 7% Magnesium do not show significant property improvement with heat treatment, it was decided to check the validity of the assumption for alloy A5456. The analysis was carried out on product from extrusion number 116 in an air circulating furnace. Twenty-four samples were cut transversely from the sample, 12 were soaked for 1½ hours at 350°C and water quenched while the remainder were soaked at 500°C for 1½ hours prior to water quenching. Six samples from each category were aged at room temperature while the remainder were treated at 120°C for periods of time from one hour to 1 month. Property evaluation being carried out at the appropriate times using hardness tests.

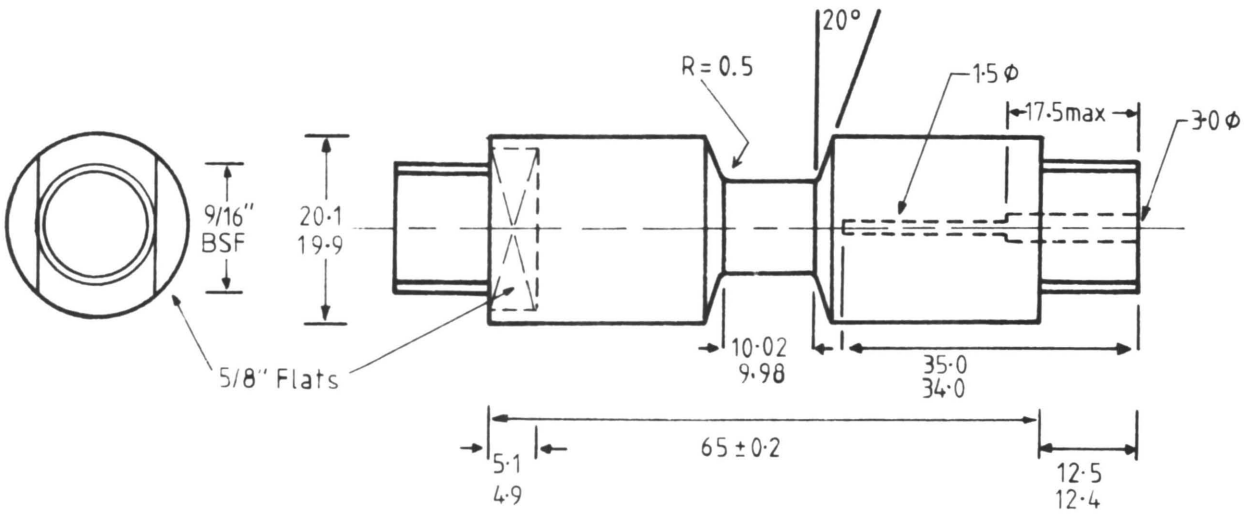
3.6. Torsion Tests

Solid torsion specimens were machined from extruded rods for all the alloys. The material was heat treated at 500°C for 24 hours in an air circulating furnace prior to machining, to produce a structure similar to that in the original cast material. Plate 3 shows a typical specimen and the specimen geometry. Testing was carried out on a machine built[209] in the Metallurgy Department, the general layout of which is shown in Plate 4.

Tests were performed over the temperature range 225°C to 525°C. The machine twist rate variation from 0 to 1000 revs per minute permitted a maximum surface shear strain rate of 50 sec^{-1} to be obtained with the specimen geometry employed. During the tests, the stationary end was restrained from moving axially by clamping. Specimen heating was facilitated by an in situ induction coil and temperature regulation was via a Eurotherm Controller driven by a thermocouple placed in the stationary end of the specimen to a depth of the gauge length shoulder. Uniformity of heating was produced by initially measuring the temperature at the centre and both ends of the gauge length using a digital

Plate 3. Torsion specimen and geometry





Torsion Specimen

Plate 4. General layout of the Torsion machine



thermometer and moving the induction coil to minimize temperature gradients throughout the gauge length. The situation was further aided by using a coil which enclosed the specimen shoulders as well, thus reducing heat flow away from the gauge length. The Eurotherm temperature settings were also calibrated in this way. The torque generated was measured by a lever arm and load cell arrangement operating on the stationary side of the specimen. Twist data was produced by a light source and photoelectric cell separated by a wheel containing sawn radial gaps positioned evenly around the circumference. A gap passing between the light source and photo cell produced a voltage drop which was fed to an Ultra Violet high speed recorder and produced a transverse line across the recording surface. The known speed of the recording paper permitted the twist rates to be established. The load cell output voltage resulting from the application of the torque, was also recorded on the same Ultra Violet recorder. Calibration of the load cell for conversion to torque was by application of known moments about the shaft. This was carried out before and after each series of tests.

Twisting was stopped either at failure or at some point after the maximum torque was obtained. Once the power to the induction coils has been switched off the entire system, enclosed in a sealed container, was flooded with water to achieve a rapid quench. This ensured that the high temperature structure was retained at room temperature and permitted both optical and transmission electron microscopical examination.

3.7. Tensile Tests

Tensile testing was carried out on an Instron universal testing machine using No. 12 Hounsefield specimens prepared from the as extruded rods. The diameter of the rods at higher extrusion ratios precluded any tests being made on them. Tests were carried out at cross head speeds from 0.001 m/min to 0.05 m/min and temperatures ranging from room temperature to 400°C using a Haddow's split furnace. The temperature was controlled using a contact thermocouple.

3.8. Optical Microscopy

Because of the variation of microstructure along the extrude length, specimens were always taken from positions corresponding to the mid point of the billet. Samples were cut both longitudinally and transversely and mounted in Metaserv type SW, slow hardening resin. The specimens were then polished first with silicon carbide papers and then diamond paste down to 1 μm. Final polishing was by a Buehler vibrating polisher using a slurry of 0.3 μm Alumina. Etching for grain size and distribution was carried out electrolytically using Barkers Reagent having the following composition:-

46 mls Tetra Fluoroboric Acid (HBF_4)
7 grms Boric Acid
970 mls Water

With the specimen as anode and using a stainless steel cathode, a potential of 20 volts was applied with a maximum current density of 0.2 amps/cm^2. Any unrequired area was masked off using a Lacomit sealing medium. The potential was applied for a minimum of two minutes, with no maximum, at which time the specimen was rapidly removed and washed in water and dried in a stream of warm air. The specimen was then viewed under crossed polarizers.

Optical microscopical examination of the original materials followed a similar preparation technique except etching was by an aqueous solution of 0.5% HF for around 25 seconds.

3.9. Transmission Electron Microscopy

Both transverse and longitudinal samples of about 2 mm thickness were carefully cut from the samples using a fine toothed piercing saw. These sections were then ground to the required thickness on silicon carbide papers. Two thinning techniques were employed. For a standard window technique, the final ground thickness was around 0.15 mm, at which stage electropolishing was carried out with the specimen as anode and a stainless steel cathode. A potential of 13 volts was applied at a bath temperature of between $-20^{o}C$ and $-30^{o}C$ using a 30% Nitric Acid in Methanol

electrolyte. For a disc polishing technique the final ground size was 0.3 mm from which 3 mm diameter discs were punched. These were then electropolished under the same conditions in a Struers automatic polisher. Because of the smaller sample size the second technique was preferred where possible since there was a more accurate knowledge of the location being investigated. Specimens were then observed in either a Siemens Elmiskop I or a Phillips 100 Kv electron microscope.

3.10. Hardness Tests

These were carried out on the specimens mounted for optical microscopy. In each case a 10 Kgrm weight was used on a standard Vickers Hardness machine, and values were collected at the edge, mid-radius and centre of each extrusion.

Micro-hardness results were obtained using 25 and 50 grm weights on a Reichart microhardness indenter attached to a Reichart Optical microscope.

3.11. Impact Tests

Impact tests on notched specimens were carried out using a Hounsfield balancing impact machine. The notch cross-section method of supporting the specimen and direction of delivery of the blow were the same as in the standard Izod impact test, but specimen size and shape were different. (0.008 m diameter bar 0.0445 m long compared with 0.01 m squared bar 0.075 m long for the Izod specimen). The energy reading given by this machine was multiplied by a factor of 2.4 to obtain the corresponding Izod value.

3.12. Partially Extruded Billets

Grided billets were prepared by splitting down the longitudinal axis, grinding one face and then machining a square grid onto it. Immediately prior to extrusion the two halves were coated with Molyslip to ensure easy separation after being partially extruded. The extrusion was then conducted at the required strain rate and temperature, as previously described,

except the cycle was interrupted midway through and the billet removed and allowed to cool, before being cleaned.

In the case of partially extruded billets for structural investigation, the billet was heated and the extrusion cycle carried out until a predetermined position on the load-displacement locus was reached. The billet was then removed as quickly as possible and quenched in water to retain the high temperature structure. The billets were then split down the longitudinal axis and one half polished on silicon carbide papers and diamond paste down to 3 μm for macrostructural investigation. Etching was by swabbing with a mixture of:-

160 mls HCl
14 mls HNO_3
20 mls HF
80 mls H_2O

which revealed both grain structure and deformation pattern.

The remaining half had a slice 2 mm thick removed parallel to the sectioned face and specimens were taken from the desired positions by using a fine toothed piercing saw and continuing as described in section 3.9.

Subsequent to macrostructural investigation, specimens for optical microscopy were removed and prepared in the fashion described in section 3.8.

3.13. Material

The materials were supplied by Alcan International Laboratories, Banbury, England in the form of 86 mm diameter continuously cast logs and from the Alcoa Technical Centre, Pittsburgh, Pennsylvania 15069, U.S.A., in the form of machined billets of diameter 0.0735 m and length 0.1 m.

The material supplied by Alcan was given an homogenising heat treatment of 24 hours at 500°C, prior to machining the billets to diameter 0.0735 m and length 0.1 m, and diameter 0.055m and length 0.076 m.

The material from ALCOA was received as commercially heat treated. This treatment consisted of a soak at 525°C for 6 hours followed by air cooling. Part of the 5083 material was additionally treated at 450°C for 24 hours and in the text is denoted by 5083(h).

The compositions and experimental notations used in this work are shown in Table 1.2.

Supplier	Experimental Notation	Aluminium Association Alloy	Mg	Mn	Fe	Cr	Si	Ti	Zn	Cu	B p.p.m.	Al
ALCAN	D222	5456	5.1	0.7	0.18	0.12	0.06	-	0.005	0.001	12	Balance
ALCAN	D331	5456	5.35	0.87	0.23	0.1	0.08	0.015	0.01	0.001	9	"
ALCOA	5456	5456	4.88	0.72	0.23	0.08	0.11	0.03	0.14	0.08		"
ALCOA	5083	5083	4.25	0.73	0.25	0.09	0.10	0.02	0.04	0.04		"
ALCOA	5052	5052	2.40	0.01	0.09	0.18	0.08	0.01	0.00	0.00		"
ALCAN	D75	-	4.9	0.001	0.001	0.001	0.003	0.001	-	-	-	"

Table 1.2. Compositions and notations for experimental materials.

CHAPTER 4
RESULTS AND DISCUSSION

4.1. The Analysis of the Torsion Data

The experimental programme was developed to produce torque-twist curves covering the range of temperatures and strain rates to be used in the extrusion work. The specimen geometry, section 3.6., permitted a maximum surface shear strain rate of 50 sec^{-1} (surface equivalent strain rate of 28.9 sec^{-1}) to be obtained. To cover this range the chosen values were 0.05, 0.5, 5, 15 and 50 sec^{-1} (0.0289, 0.289, 2.89, 8.67 and 28.9 sec^{-1} equivalent values) while the temperatures were chosen to fill the 250-500°C range.

The resulting matrices of torque, temperature and twist rate permitted the analyses set out below to be carried out.

4.1.1. Nature of the Torque-Twist Curves

The torque-twist data from the high temperature torsion test programme produced three general types of curve. Fig. 8 shows the curve applicable to most slow twist rate runs for all the alloys tested. The plot is analagous to a stress-strain curve at constant temperature and strain rate and is of the form shown in Fig. 2, section 1.4.3., indicating high temperature restoration by dynamic recovery processes. The initial rapid rise in torque corresponds to the interval of microstrain deformation. During this period the strain rate rises from zero to that applicable to the test. The decrease in the slope of the loading curve indicates this stage has been left and work hardening commences. As the rate of work hardening decreases, so the slope of the load curve decreases until the steady state is attained during which the rates of dislocation production and annihilation cancel out.

The second type of curve is shown in Fig. 9 and would compare with the curve shown in Fig. 2 (section 1.4.3.) for combined dynamic recovery and recrystallization at higher strain rates. The curve is typical for materials D222, 5083 and 5456 at temperatures between 350°C and 450°C and strain rates between

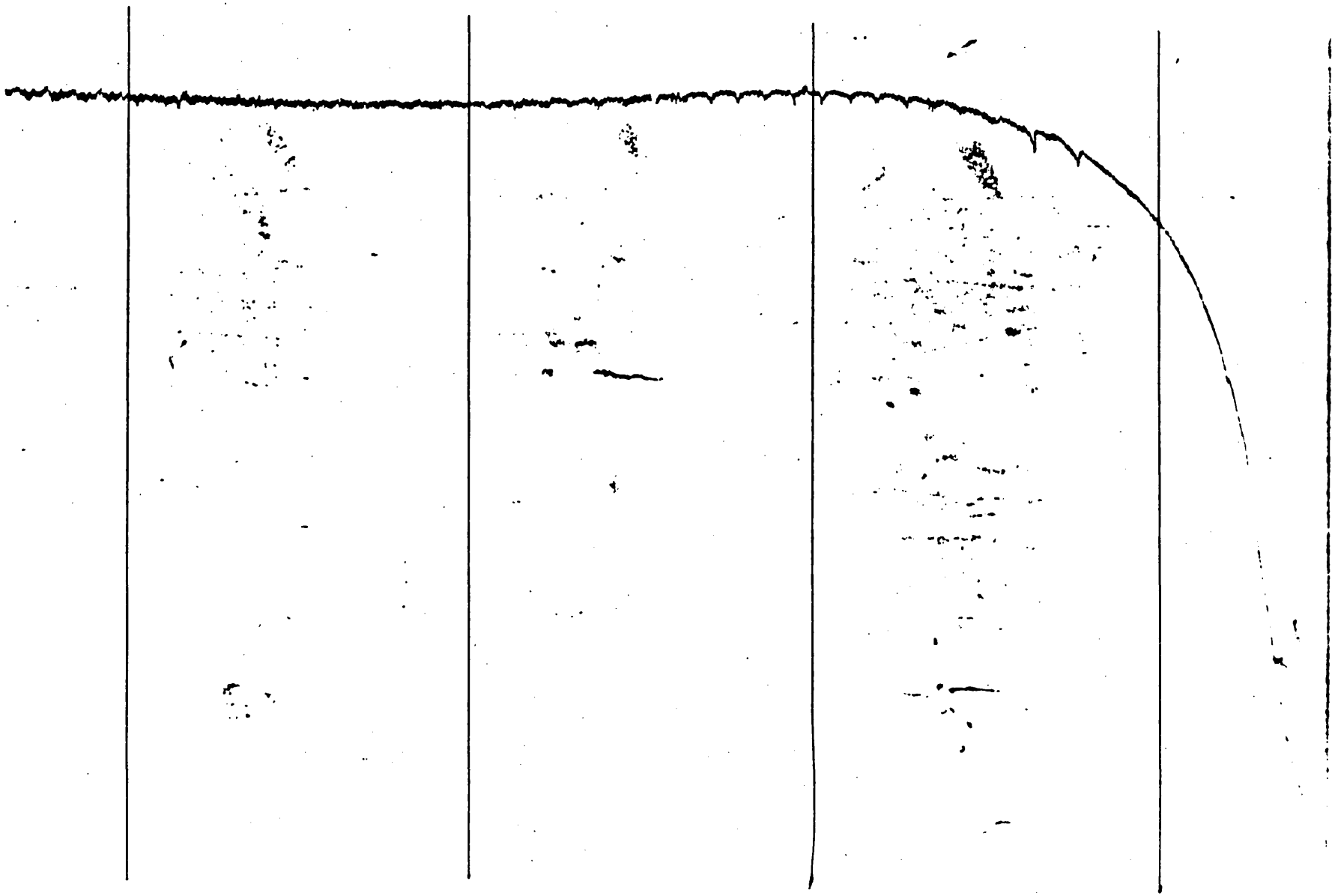


Fig. 8. Experimental Torque-Twist Curve

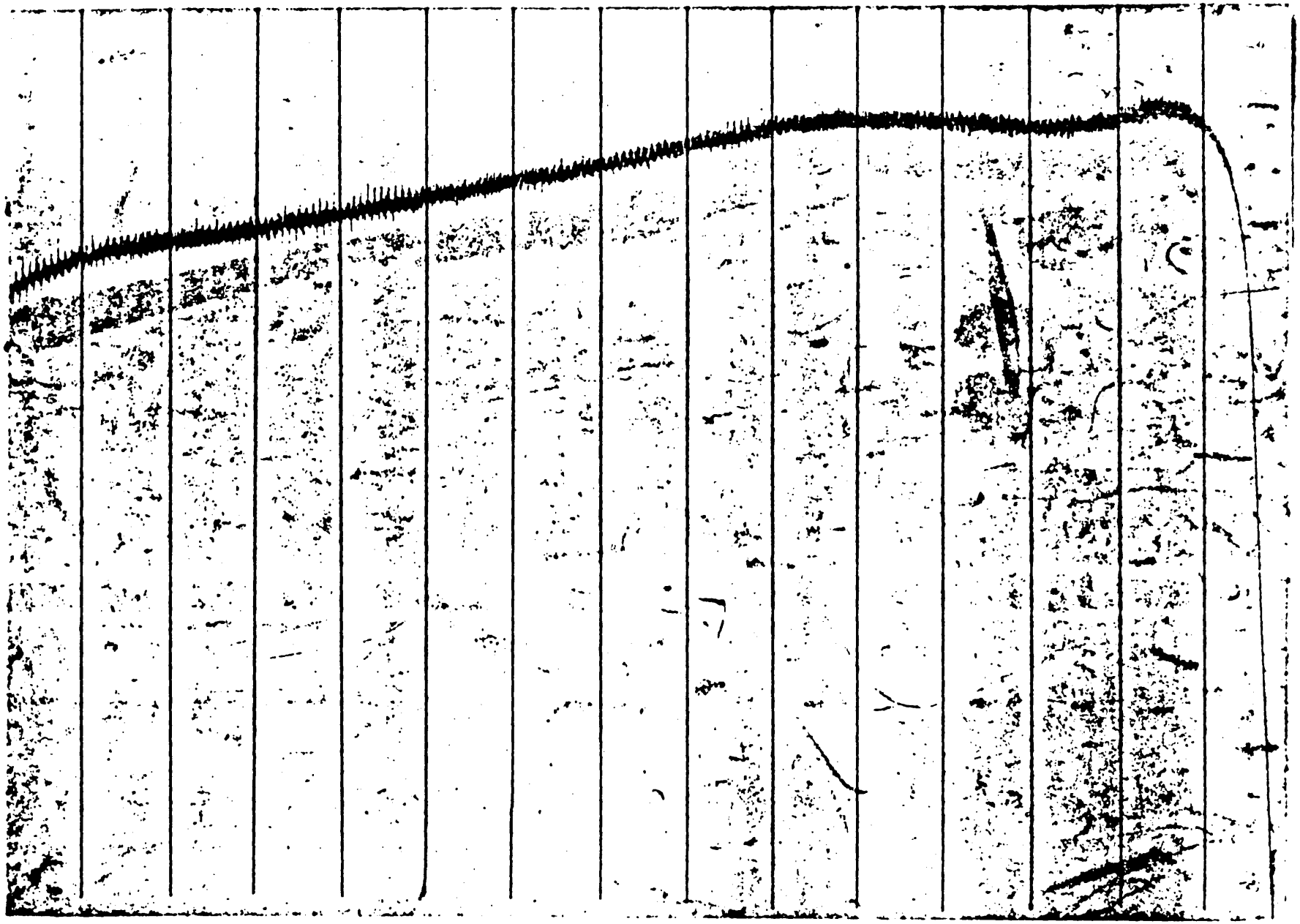


Fig. 9. Experimental Torque-twist Curve

5 → 15 sec^{-1}. The initial region of microstrain is followed by attainment of the critical strain for nucleation of dynamic recrystallization and an associated softening is found and indicated on the curve by the decrease in torque. As pointed out by Luton and Sellars,[172] in the case of high strain rate deformation, the strain for completion of recrystallization is much greater than the strain for its initiation and thus nucleation commences in the recrystallized regions prior to the original wave being completed. Thus the average flow stress of the material remains fairly constant and the consequence of this is that the deformation curve shows a steady state region during which there is very little change in the torque. The slight rise in Fig. 9 after attainment of the peak, and initial drop, may well be due to the associated dynamic recovery process, acting simultaneously with the dynamic recrystallization, coming into operation. The final steady decrease in torque is due to specimen heating, resulting from the deformation, causing a decrease in flow stress and an associated decrease in torque.

The final type of torque-twist curve encountered is shown in Fig. 10. This is typical for all materials at high temperatures and high strain rates. The initial period of microstrain deformation is followed by one of a decreasing work hardening rate prior to a fall in torque and failure. The steady, rapid decrease in torque after the peak value is due to the conversion of input energy to heat resulting in a reduced flow stress term.

Calculations from the traces are relatively easy to derive. The known speed of the chart paper and frequency of the event marks facilitate simple calculation of the surface twist rate while calibration of the load cell enables easy conversion of displacement to torque. A sample calibration is shown in Fig. 11.

In the case of torsion tests carried out on the more dendritic material, the only real difference was a greater strain to attainment of the steady state or peak value. This must be the result of some chemical and structural gradients delaying the equilibrium of dislocation generation and annihilation.

The torque twist curves produced from the 164 torsion tests carried out would indicate that for all the materials, excepting

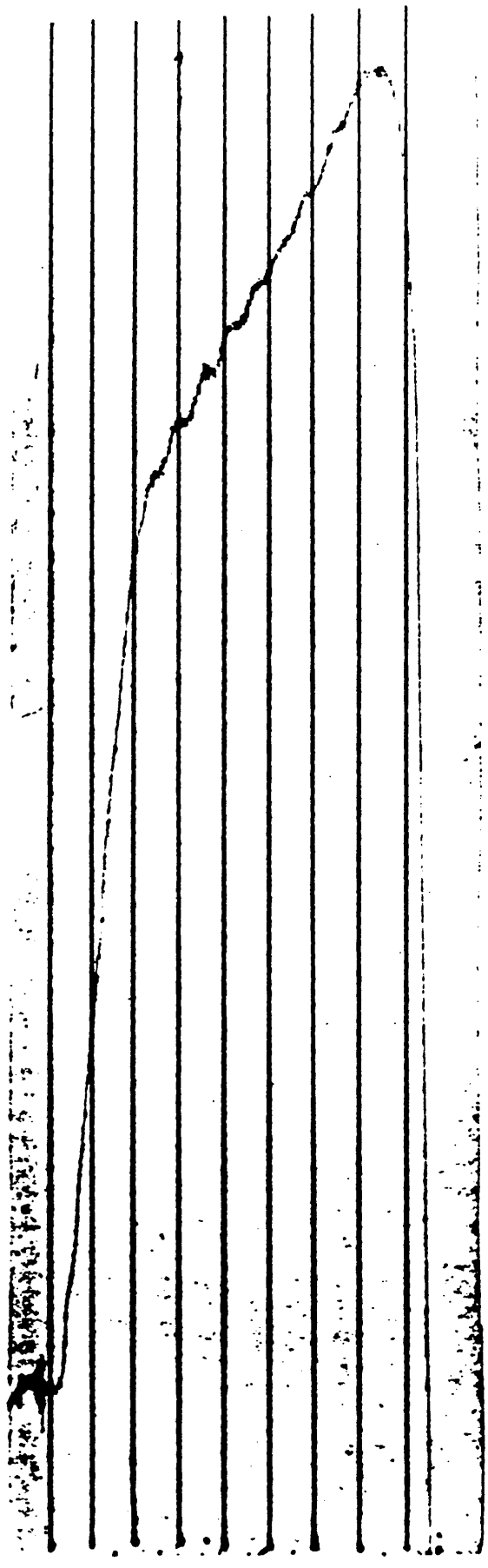


Fig. 10. Experimental Torque-twist curve.

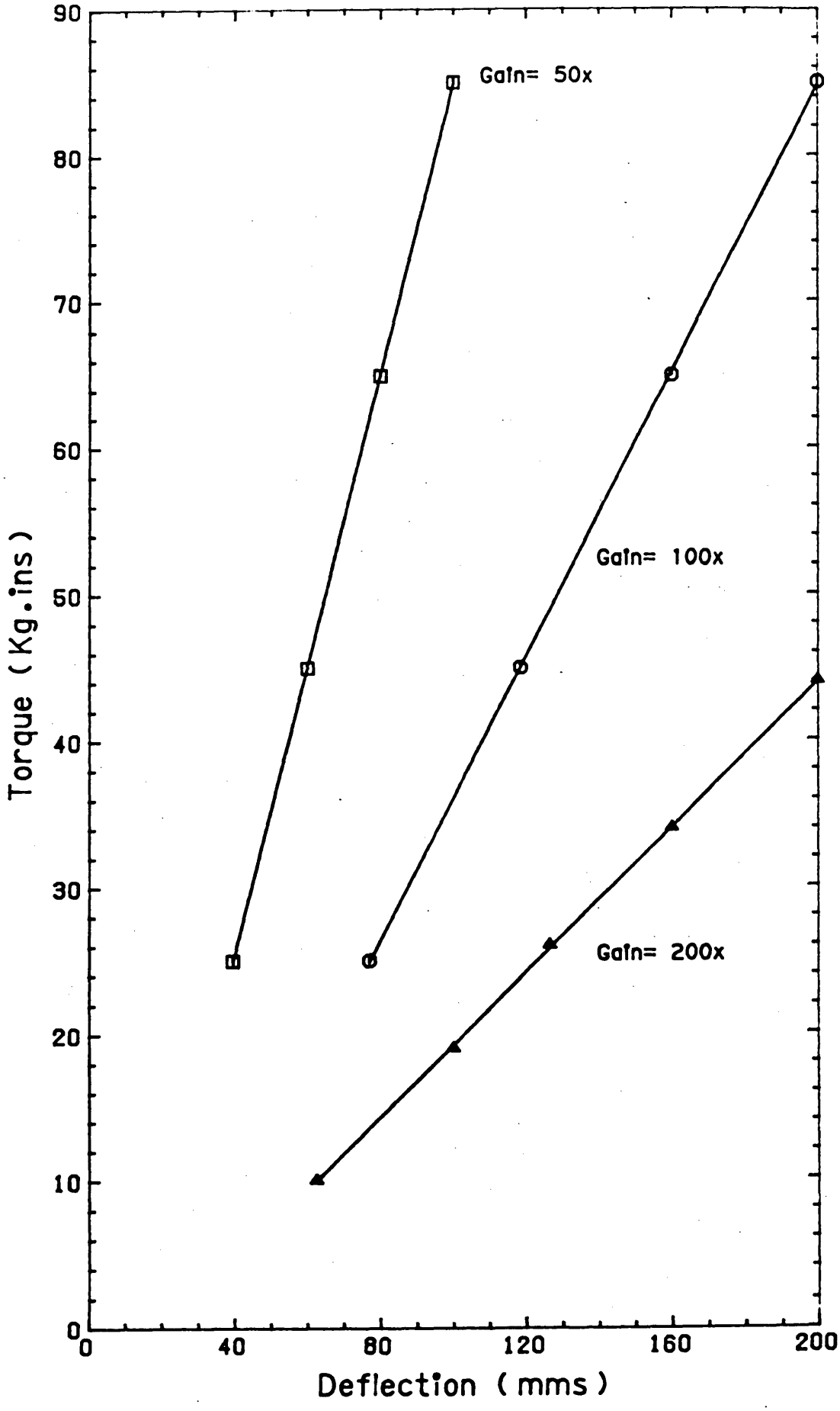


Fig. 11. Torque Calibration Curves

alloy 5052, some high temperature restoration process other than dynamic recovery is in operation under certain conditions. Cotner and McG.Tegart[130] have reported that torque-twist curves for aluminium-magnesium alloys, ranging in magnesium content from 0.3-5 wt%, were similar to curves found for pure aluminium. It should however be noted that their work involved super-purity materials and, as will be shown later, this may have a considerable effect upon the internal behaviour under high temperature deformation. A structural investigation of the torsion tests may be found in section 4.8.

4.1.2. Torsion Test Results

The results from the high temperature torsion tests on the various materials can be seen in Tables (4.1-4.5). The equivalent stress values were obtained by applying the technique of Fields and Backofen,[204] described in section 2.4.1.1., using the computer programme shown in Appendix C. For the alloy D222 this enabled stress-strain curves to be produced as shown in Figs. 12-22. These show the expected trend of increasing stress with both decreasing temperature at constant strain rate and increasing strain rate at constant temperature. Since the computer programme uses curve fitting techniques to approximate lines to the experimental points the results for the high strain rate tests show some irregularities due to the rapid changes in curvature of the line. Nevertheless the stress values produced show good agreement with the original torque data when evaluating the material constants as shown in section 4.1.3.2.

It is virtually impossible to relate stress to strain over a large range of temperature and strain rate with a single equation, but Wright[205] found a satisfactory correlation for stress-strain rate data at constant strain using a simple power relationship of the form:-

$$\sigma = A\dot{\varepsilon}^{m}$$

The results of these plots can be seen in Figs. 23-25 and are drawn for a true strain of 0.6. These plots are used to calculate the

RUN CODE	INITIAL TEMP	ACTUAL TEMP	MAX TORQUE	MAX STRESS	TWIST RATE	STRAIN RATE	STRAIN TO PEAK	TWIST TO FAIL
	DEG.C	DEG.C	NM	MN/M^2	REV/SEC	SEC^{-1}		
1	250	255	25.670	180.72	.019	.034	.46	4.00
2	310	315	17.980	125.21	.019	.034	.23	
3	370	371	11.830	80.83	.018	.033	.23	
4	430	431	6.040	42.86	.018	.033	.23	
5	500	501	3.200	22.89	.018	.033	.23	
6	250	261	28.980	212.27	.171	.310	.46	3.25
7	310	318	22.595	158.14	.169	.307	.46	3.75
8	370	374	16.266	116.55	.170	.308	.23	9.00
9	430	432	10.590	75.68	.171	.312	.23	9.00
10	500	502	5.980	42.54	.172	.312	.23	5.50
11	250	270	33.220	239.11	1.250	2.270	.46	1.75
12	310	318	26.470	184.54	1.378	2.500	.23	3.75
13	370	378	21.230	151.98	1.380	2.500	.23	4.75
14	430	434	15.370	109.11	1.493	2.710	.23	7.00
15	500	503	9.330	68.43	1.517	2.750	.23	1.50
16	250	274	34.860	243.35	4.616	8.370	.46	1.25
17	310	320	27.830	191.72	4.664	8.460	.23	1.25
18	370	378	21.290	150.89	4.746	8.610	.23	4.25
19	430	436	16.840	119.23	4.780	8.670	.23	4.00
20	500	508	11.240	75.32	4.616	8.370	.23	1.50
21	250	282	36.105	256.17	12.920	23.430	.46	.75
22	310	341	29.524	214.55	12.370	22.440	.69	1.00
23	370	387	23.668	172.57	13.690	24.830	.46	1.25
24	430	444	18.668	136.66	14.160	25.680	.46	1.25
25	500	505	13.786	100.01	14.460	26.230	.23	1.00
26	430	431	6.325	44.38	.015	.027	.23	
27	430	432	10.500	73.32	.168	.305	.23	6.00
28	310	334	28.842	203.35	6.540	11.860	.58	1.25
29	370	378	23.276	165.88	6.723	12.190	.23	2.00
30	430	436	17.710	125.62	6.782	12.300	.23	2 75
31	500	504	13.410	97.14	6.882	12.490	.23	1.00
32	250	297	35.450	242.39	6.523	11.832	.45	1.00
33	250	292	35.636	242.86	2.879	5.223	.24	1.50
34	310	344	28.890	196.71	2.993	5.428	.45	1.75
35	370	384	22.272	154.41	3.036	5.508	.63	6.50
36	430	440	18.136	128.60	3.059	5.547	.66	4.60
37	500	507	12.727	91.77	3.151	5.715	.45	2.00
38	250	255	29.527	198.08	.090	.164	.90	6.00
39	310	316	22.654	152.16	.091	.164	.80	9.00
40	370	377	16.036	110.29	.090	.163	.50	6.00
41	430	438	10.563	74.06	.091	.165	.80	5.00
42	500	509	6.491	46.69	.090	.164	.90	4.75
43	250	258	29.972	203.94	.045	.082	.45	4.25
44	310	322	21.636	147.55	.045	.081	.70	6.50
45	370	380	14.509	99.50	.045	.082	.70	5.50
46	430	440	7.931	60.35	.045	.082	.90	5.50
47	500	501	5.282	37.20	.045	.082	.70	4.00
48	250	275	30.961	206.46	.358	.649	.90	4.00
49	310	322	24.526	165.26	.420	.762	.45	4.75
50	370	379	19.091	131.94	.464	.842	.23	9.00
51	430	434	13.999	94.41	.485	.879	.23	6.00
52	500	502	9.163	65.43	.538	.976	.30	3.50
53	250	298	36.910	252.72	8.483	15.387	.45	1.00
54	310	330	29.868	199.67	8.612	15.621	.23	1.30
55	370	387	24.283	167.17	8.882	16.110	.50	1.75
56	430	453	19.184	133.79	8.917	16.175	.40	2.00
57	500	510	15.055	107.46	8.882	16.111	.25	1.25

Table 4.1. Torsion results for alloy D222 (5456)

RUN CODE	INITIAL TEMP DEG.C	ACTUAL TEMP DEG.C	MAX TORQUE NM	TWIST RATE REV/SEC	STRAIN RATE SEC^{-1}	STRAIN TO PEAK
1	450	451	3.605	.014	.023	1.82
2	500	500	3.03[illegible]	.014	.025	1.30
3	525	531	2.074	.014	.025	.76
4	225	230	37.510	.164	.298	3.23
5	300	304	26.349	.166	.301	2.39
6	350	353	19.140	.164	.298	1.44
7	400	401	12.058	.160	.290	.52
8	450	451	8.304	.166	.301	1.63
9	525	526	4.698	.166	.301	1.81
10	225	253	40.293	1.355	2.457	3.51
11	300	320	28.193	1.448	2.627	.69
12	350	383	23.287	1.474	2.673	1.91
13	400	422	18.311	1.500	2.721	1.49
14	450	463	13.526	1.527	2.770	.99
15	525	533	7.062	1.555	2.822	.94
16	225	330	40.05[illegible]	4.420	8.017	2.50
17	300	379	29.887	4.534	8.225	2.56
18	350	402	25.520	4.534	8.225	1.89
19	400	435	20.161	4.574	8.296	1.51
20	450	472	15.886	4.614	8.369	1.15
21	525	533	12.568	4.739	8.595	.49
22	225	344	41.832	13.387	24.282	2.22
23	300	380	31.944	13.833	25.091	1.93
24	350	416	25.652	14.068	25.516	1.84

Table 4.2. Torsion results for alloy 5456

RUN CODE	INITIAL TEMP DEG.C	ACTUAL TEMP DEG.C	MAX TORQUE NM	TWIST RATE REV/SEC	STRAIN RATE SEC^{-1}	STRAIN TO PEAK
1	250	252	21.798	.014	.025	2.08
2	310	312	15.759	.014	.025	.71
3	370	371	7.949	.014	.025	.88
4	430	430	[illegible].289	.014	.024	.50
5	500	501	2.571	.014	.025	1.77
6	250	253	22.022	.165	.299	1.62
7	310	312	17.992	.166	.301	1.27
8	370	380	12.760	.166	.301	1.09
9	430	437	8.156	.166	.301	1.09
10	500	502	4.876	.166	.301	.29
11	250	298	23.350	1.474	2.673	2.10
12	310	340	20.160	1.500	2.721	2.58
13	370	390	14.929	1.500	2.721	1.30
14	430	438	10.756	1.536	2.790	1.00
15	500	503	7.535	1.576	2.859	.37
16	250	317	24.320	4.574	8.296	2.21
17	310	355	21.182	4.534	8.225	1.69
18	370	397	16.843	4.534	8.225	1.25
19	430	446	13.079	4.614	8.369	1.02
20	500	506	8.924	4.680	8.488	.52
21	250	324	24.200	14.066	25.516	2.15
22	310	384	20.933	14.310	25.956	2.44
23	370	423	17.964	14.310	25.956	1.75
24	430	457	14.164	14.310	25.956	1.31
25	500	513	10.[illegible]	14.564	26.538	.77

Table 4.3. Torsion results for alloy 5052

Table 4.4.

Torsion results for alloy 5083(h)

RUN CODE	INITIAL TEMP DEG.C	ACTUAL TEMP DEG.C	MAX TORQUE NM	TWIST RATE REV/SEC	STRAIN RATE -1 SEC	STRAIN TO PEAK
1	250	252	25.149	.025	.046	.54
2	250	252	25.024	.025	.045	.54
3	310	311	18.135	.025	.046	.36
4	370	271	11.440	.025	.045	.18
5	430	431	6.630	.025	.046	.73
6	490	491	3.146	.025	.046	.76
7	490	491	3.864	.025	.046	.81
8	550	550	1.872	.025	.046	.73
9	250	255	29.382	.171	.310	.58
10	310	314	22.161	.171	.310	.45
11	310	314	21.539	.171	.310	.60
12	370	373	16.380	.171	.310	.36
13	430	432	10.790	.171	.310	.45
14	430	432	10.725	.171	.310	.42
15	490	492	6.323	.171	.310	.63
16	550	551	3.600	.171	.310	.54
17	250	268	30.627	1.422	2.576	.45
18	310	325	24.703	1.412	2.561	.54
19	370	381	19.350	1.467	2.660	.45
20	370	381	19.350	1.467	2.660	.45
21	430	435	14.706	1.482	2.688	.27
22	490	493	10.298	1.520	2.757	.36
23	550	553	6.792	1.560	2.830	.39
24	250	272	32.121	5.056	9.171	.45
25	310	331	25.896	4.982	9.036	.60
26	310	328	25.772	4.982	9.036	.54
27	370	384	21.414	4.909	8.904	.45
28	430	441	17.673	4.945	8.969	.45
29	490	496	11.268	5.094	9.240	.36
30	490	496	11.863	5.056	9.171	.45
31	550	554	8.921	5.133	9.310	.36
32	250	273	32.495	12.294	22.300	.54
33	250	274	33.117	13.660	24.780	.41
34	310	334	28.476	14.718	26.700	.54
35	370	393	23.140	13.397	24.300	.54
36	430	447	18.525	1[illegible].928	27.080	.54
37	490	501	14.040	15.539	28.180	.45
38	550	558	9.555	15.890	28.820	.45
39	550	556	11.180	14.169	25.700	.54

Table 4.5.

Torsion results for alloy 5083

RUN CODE	INITIAL TEMP DEG.C	ACTUAL TEMP DEG.C	MAX TORQUE NM	TWIST RATE REV/SEC	STRAIN RATE -1 SEC	STRAIN TO PEAK
1	300	301	19.140	.014	.025	1.40
2	350	351	13.016	.014	.025	1.35
3	400	401	8.224	.014	.025	1.47
4	450	451	4.550	.014	.025	1.35
5	500	501	2.420	.014	.025	1.29
6	250	255	31.200	.164	.298	3.59
7	300	303	23.900	.164	.298	1.33
8	350	352	17.400	.166	.301	2.47
9	400	402	12.120	.166	.301	2.18
10	450	451	9.442	.166	.301	1.96
11	500	500	4.730	.166	.301	1.63
12	300	345	25.652	1.474	2.673	2.10
13	350	382	21.561	1.474	2.673	1.65
14	400	419	17.220	1.489	2.701	1.09
15	450	463	13.207	1.511	2.740	1.04
16	500	503	8.270	1.531	2.780	1.72
17	300	376	27.346	4.534	8.225	2.35
18	350	404	23.350	4.534	8.225	1.88
19	400	426	19.012	4.534	8.225	1.09
20	450	471	14.030	4.656	8.443	1.06
21	500	514	11.100	4.614	8.369	.95
22	300	379	29.280	13.833	25.091	1.87
23	350	419	24.880	14.068	25.516	1.84
24	450	483	16.460	14.212	25.778	1.24
25	500	520	12.410	14.561	26.412	.95

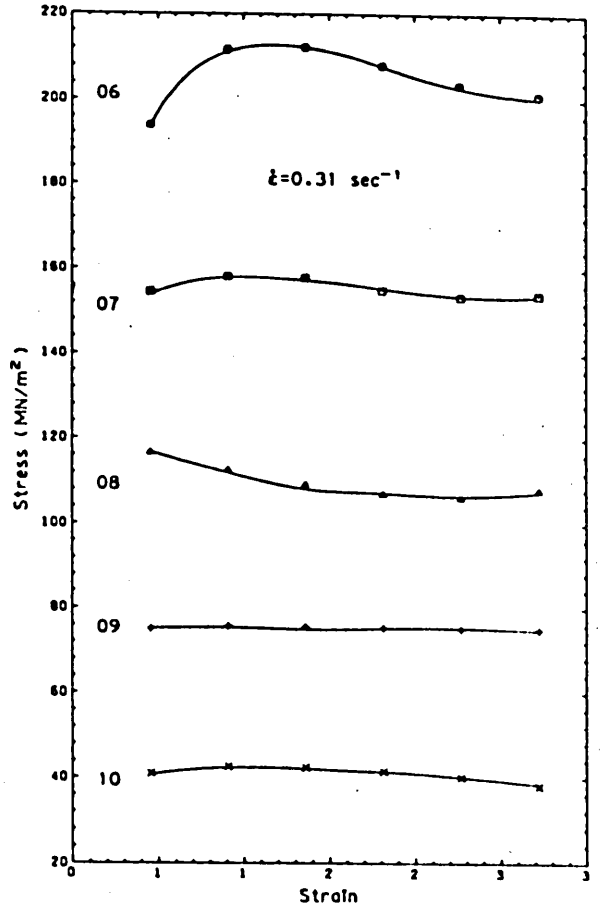


Fig. 13. Stress-strain data alloy D222

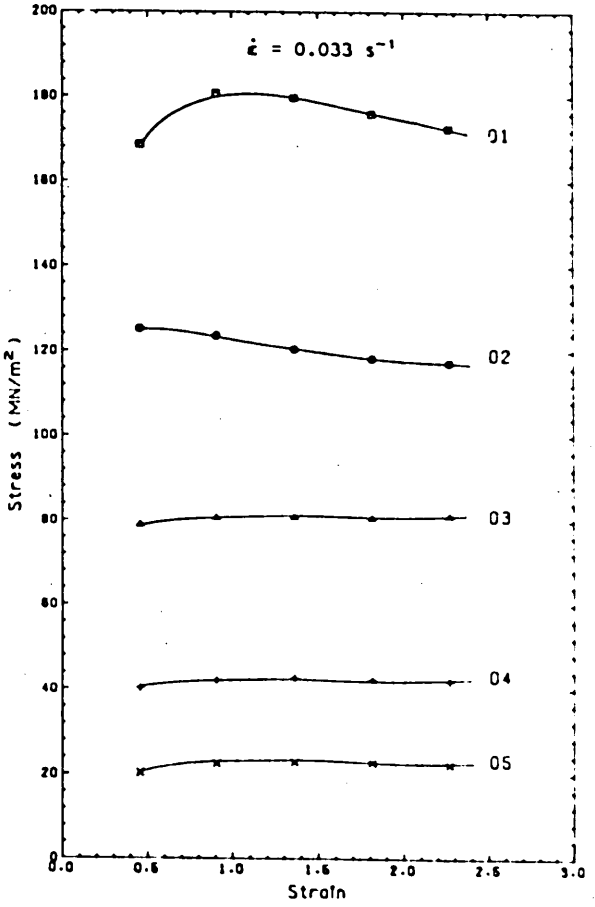


Fig. 12. Stress-strain data alloy D222

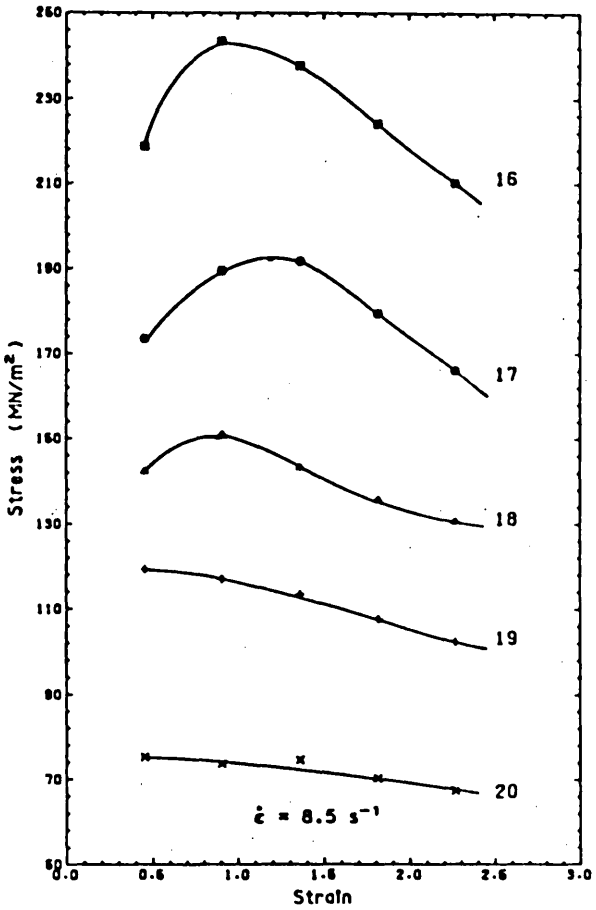


Fig. 15. Stress-strain data alloy D222

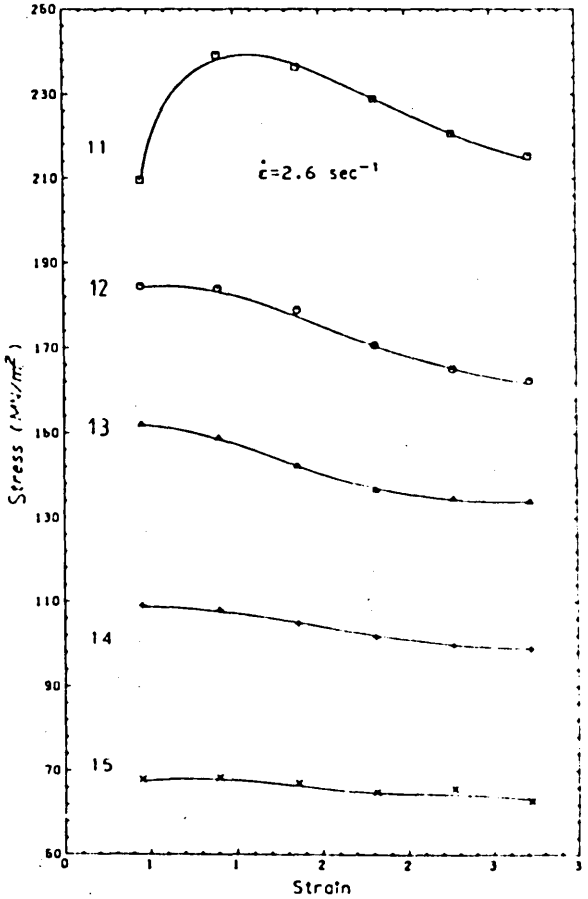


Fig. 14. Stress-strain data alloy D222

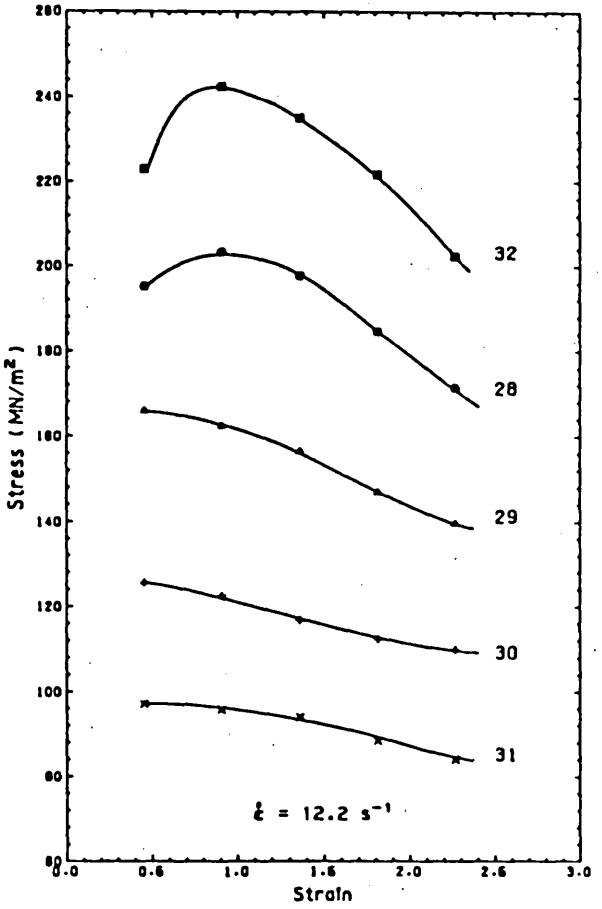


Fig. 17. Stress-strain data alloy D222

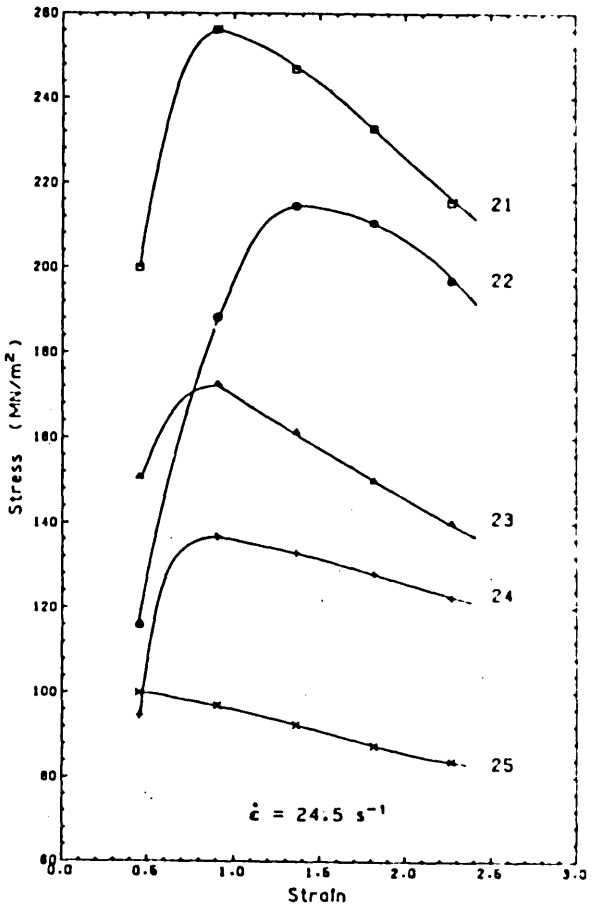


Fig. 16. Stress-strain data alloy D222

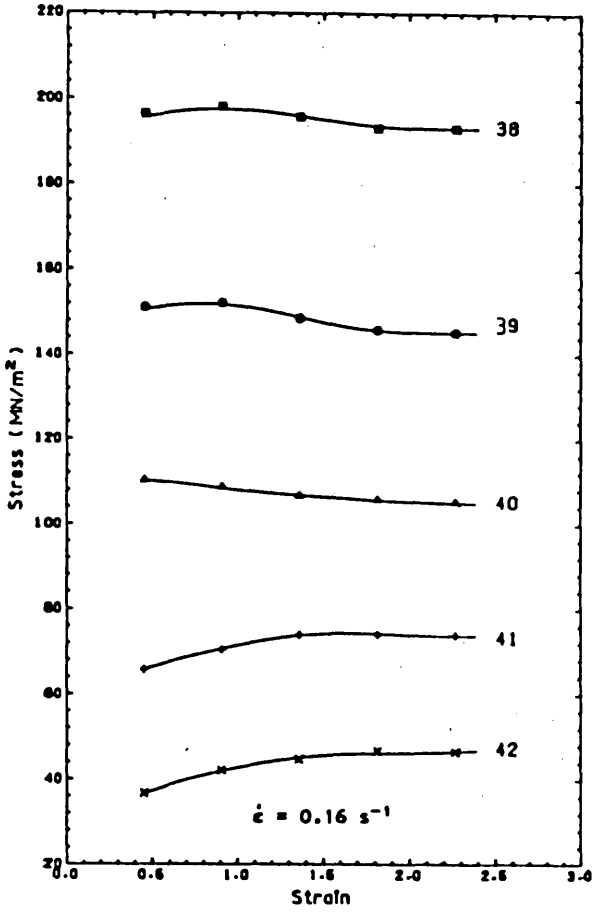


Fig. 19. Stress-strain data alloy D222

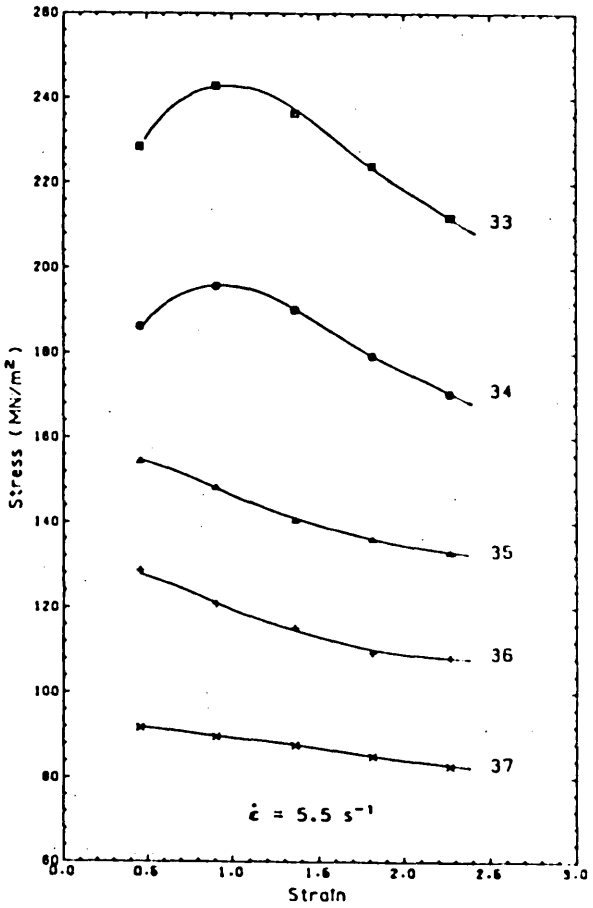


Fig. 18. Stress-strain data alloy D222

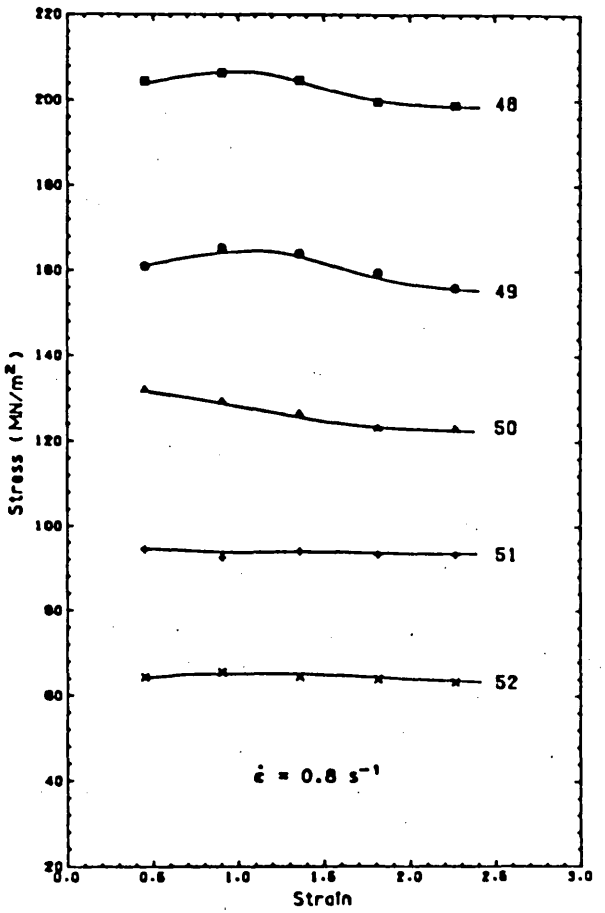


Fig. 21 Stress-strain data alloy D222

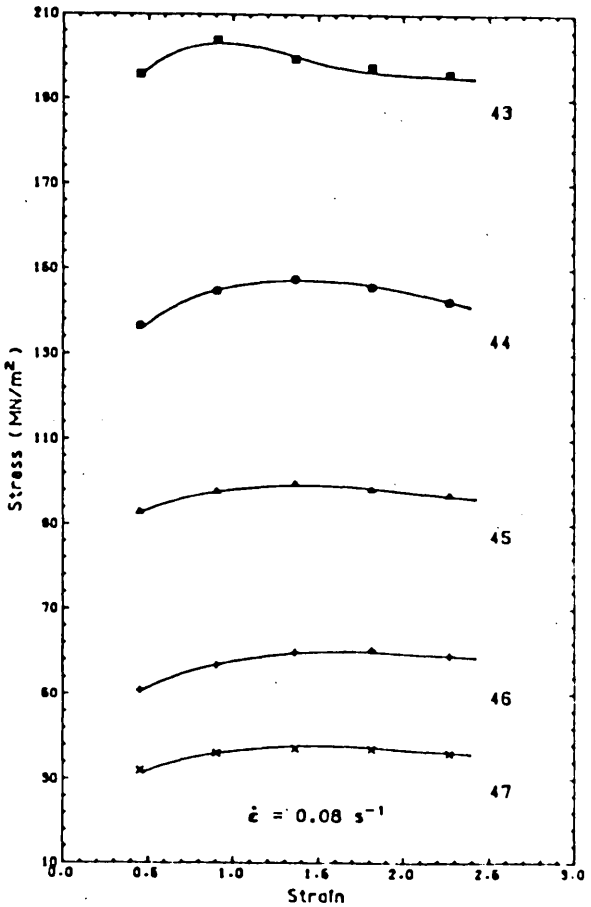


Fig. 20. Stress-strain data alloy D222

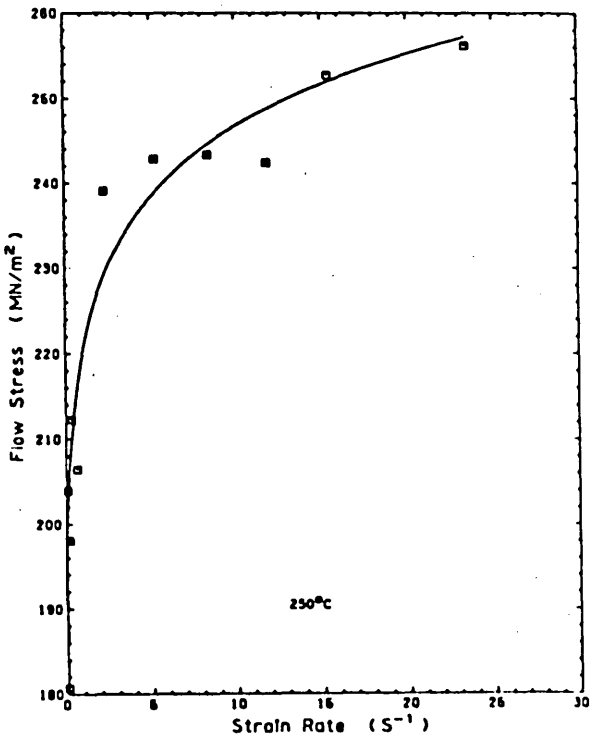


Fig. 23. Power relationships for σ vs $\dot{\varepsilon}$, alloy D222

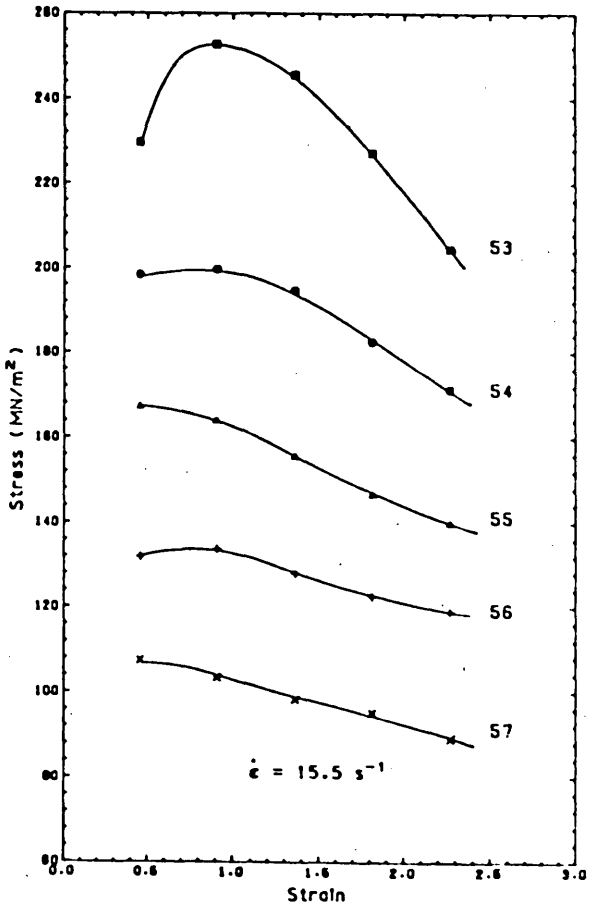
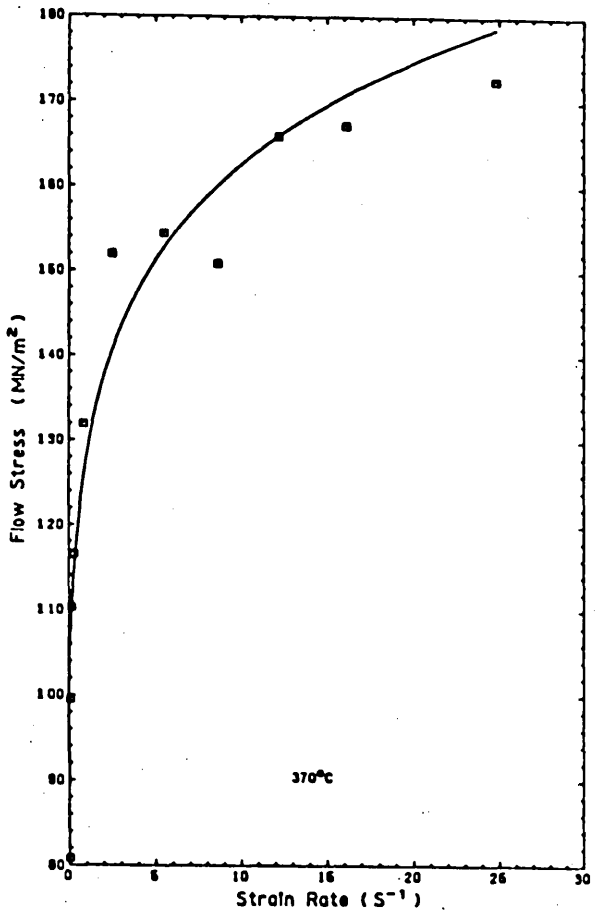


Fig. 22. Stress-strain data alloy D222



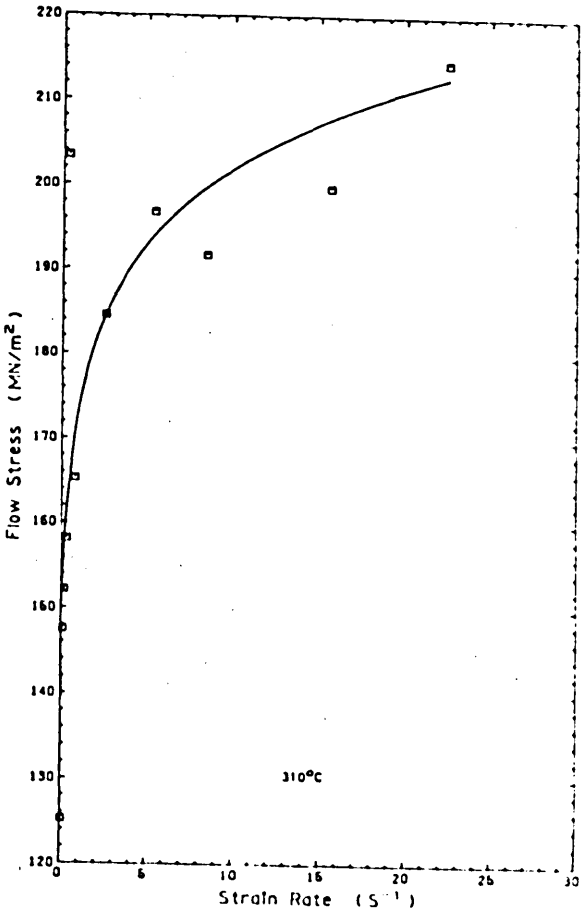
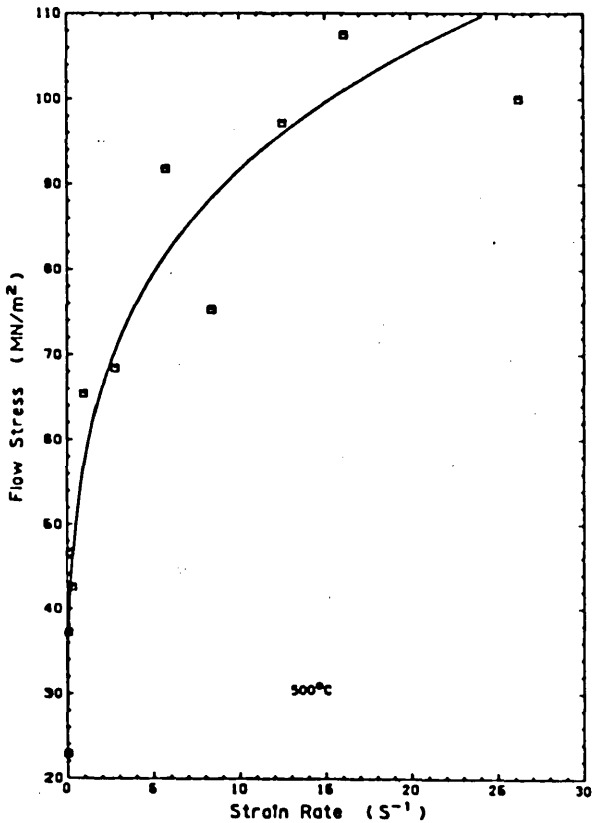


Fig. 24. Power relationships for σ vs $\dot{\varepsilon}$ alloy D222



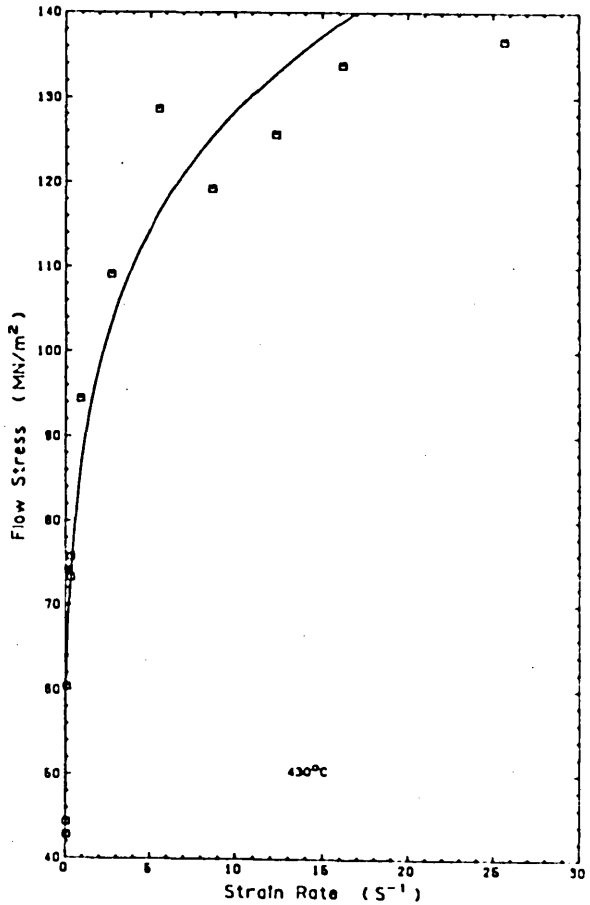


Fig. 25. Power relationships for σ vs $\dot{\epsilon}$
alloy D222

temperature rise during the torsion tests, the values of A and m being both temperature and strain dependent. These values can be seen in Table 4.6. The general trend here is one of A decreasing and m increasing with a temperature increase for each alloy. For constant temperature, the value of A increases with alloy content while the value of m follows the same trend, the difference being much less, i.e. the rate of change of flow stress with change in strain rate is virtually the same for the higher concentration magnesium alloys. The difference in flow stress arises from the differences in A. This would indicate that A is composition and structurally dependent, to a greater degree than m, and associated with the density of activatable sites.

The values of m can be compared with those found by Alder and Phillips[106] and Bailey and Singer[103] for pure aluminium and aluminium alloys under compression testing. Their values for m lay between 0.013 and 0.2 which would agree with the order of magnitude of the present results. The values of A were found to be considerably lower than the high magnesium alloy results, but more comparable for the 2.5% Mg, 5052 alloy. This would support the observation made above regarding the structural dependence of A.

The calculated temperatures, including temperature rise, in Tables 4.1-4.5 are those calculated using the method outlined in section 2.4.1.2. The strain at which the temperature rise was calculated was found from considering the torque twist curves and taking the value at which the steady state commenced.

The temperature rise was found to be larger at lower initial temperatures, when the flow stress is higher and the work done is therefore greater. The rises for D222 are in the range 0-30°C while those for the other alloys are greater because of the greater strains involved to the steady state regime. These latter strains were found to be of the order of an equivalent strain of 1.7 and the associated temperature rise should be considered less accurate than in the case of smaller strains. This arises due to the greater possibility of inaccuracies from applying the power fit. Nonetheless, adiabatic temperature rise calculations showed the computed rises to lie within this range and therefore reasonable. The use of the temperature rise calculations will be seen in the following section.

D222 (5456)				5083			
TEMP DEG.C	A	B	CORREL	TEMP DEG.C	A	B	CORREL
250	32.88	1.54	.96	300	25.50	1.38	.99
310	25.93	1.67	.98	350	20.58	1.74	.99
370	20.15	1.97	.92	400	16.14	2.12	.99
430	14.45	1.96	.99	450	11.82	1.72	.99
500	9.71	1.63	.96	500	8.22	1.49	.98
5456				5083 (H)			
225	39.37	.90	.95	250	30.05	1.20	.97
300	28.25	1.24	.98	310	24.10	1.50	.98
350	22.33	1.55	.97	370	18.66	1.79	.99
400	16.77	2.47	.99	430	13.97	1.90	.99
450	12.53	2.14	.99	490	9.25	1.58	.99
525	7.96	2.16	.91	550	6.52	1.37	.98
5052							
250	23.26	.41	.95				
310	19.45	.81	.98				
370	14.50	1.41	.99				
430	10.71	1.31	.99				
500	7.13	1.10	.99				

Table 4.7. Gradients and intercept for $M \rangle = A + B\mathrm{Ln}\theta$

D222 (5456)			5083 (H)			5052		
TEMP DEG.C	A	M	TEMP DEG.C	A	M	TEMP DEG.C	A	M
250	250	.04	250	201	.05	250	156	.02
310	173	.07	310	159	.07	310	128	.05
370	128	.10	370	117	.11	370	90	.12
430	88	.16	430	84	.16	430	63	.15
500	57	.20	490	51	.22	500	41	.20
			550	33	.26			
5456			5083					
225	250	.04	300	185	.06			
300	178	.06	350	147	.09			
350	140	.09	400	112	.12			
400	106	.13	450	81	.17			
450	77	.19	500	54	.23			
525	50	.27						

Table 4.6. Results for $\sigma = A\dot{\varepsilon}^{m}$

The results tabled from the torsion tests enable plots to be constructed of Maximum Torque vs. Twist Rate as shown in Figs. 26-30. The twist rate calculated from the test is plotted as the natural logarithm in each case. As the figures show, a linear relationship exists between maximum torque and twist rate when plotted in this manner. The lower temperature tests generate a greater torque value, for a given twist rate, because of the increase in flow stress associated with temperature decrease. Similarly an increase in twist rate generates a greater torque reading, for a given initial temperature, due to the flow stress dependence upon strain rate, i.e. stress increase with strain rate increase. Fig. 26 shows the results for the homogenised 5% magnesium alloy, D222. The dependence of maximum torque upon twist rate can be seen to be approximately constant throughout the temperature range investigated. This would tend to suggest that the rate controlling mechanism during deformation is the same from 250°C to 500°C. Taking the relationship to be of the form $M = a + b \text{ Ln } \dot{\theta}$, the results for a and b for the alloys are shown in Table 4.7. It should be remembered that 5456 differs from D222 (5456) through not having been heat treated for as long a time and has a smaller initial grain size (200 μm cf. 300 μm); the same applies for 5083; the (h) signifying an additional heat treatment had been applied. The results show that for both of the higher magnesium content alloys, the presence of the additional heat treatment, prior to working, decreases the dependence of torque upon twist rate (i.e. the value of b in Table 4.7 is lower in each case). The effect upon the value of a would appear to be less obvious. The reasons for this variation in the value of b must lie within the structural differences between the alloys and will be discussed in more detail in subsequent sections.

In the case of the weaker alloy, 5052, the lower magnesium content causes the values of both a and b to be reduced compared with those for the 5% Mg alloys. Fig. 30 also indicates that the dependence of torque upon twist rate is greater at higher temperatures. For given similar conditions of twist rate and temperature, the torque generated is greatest for the alloy D222 and least for the 5052. It can be concluded that the resistance to deformation is very dependent upon alloy content, more especially the magnesium content.

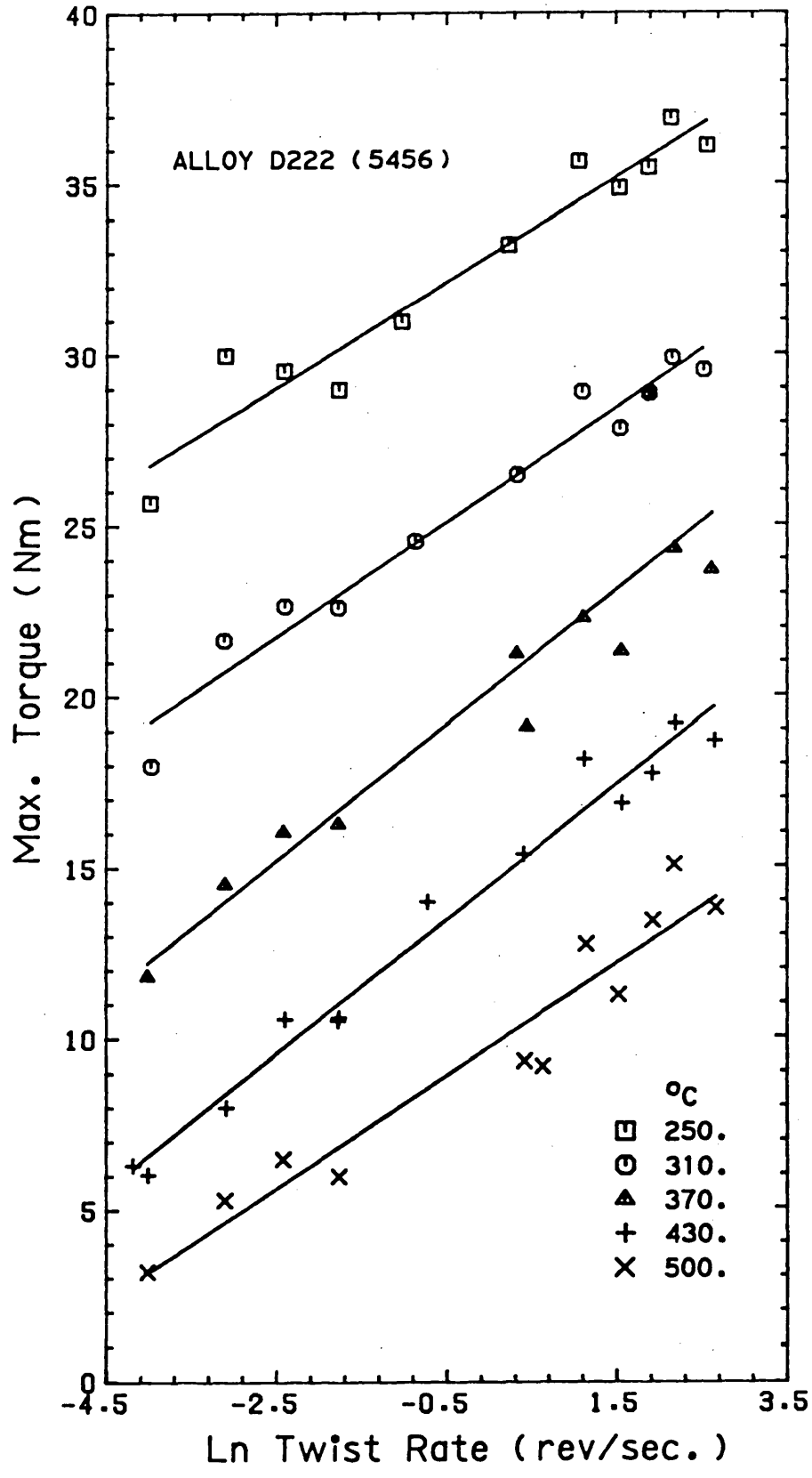


Fig. 26. Torque-twist rate curves for alloy D222 (5456)

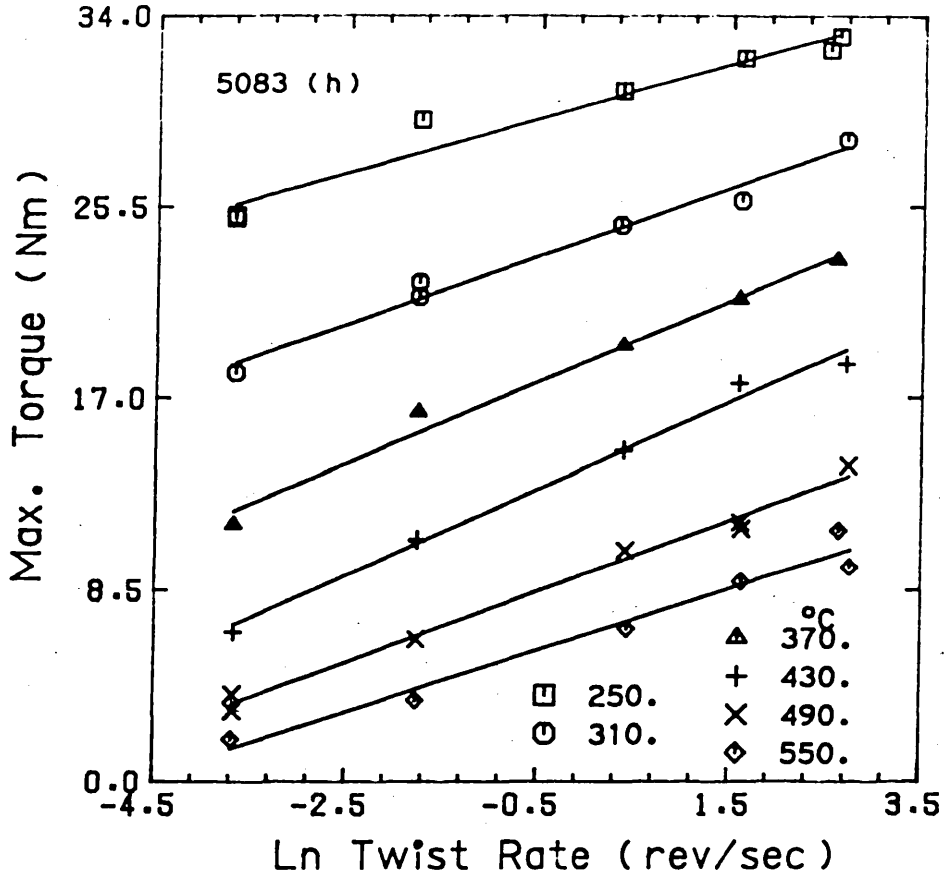
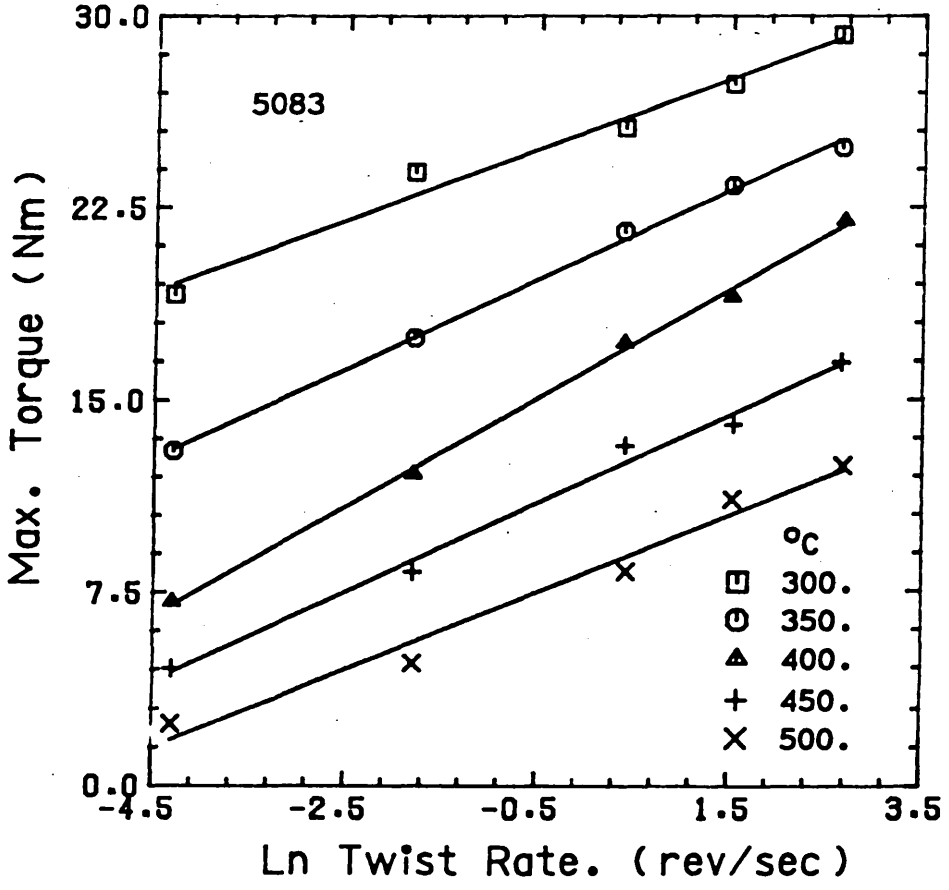


Fig. 27. Torque-twist rate curves for alloy 5083(h)

Fig. 28. Torque-twist rate curves for alloy 5083



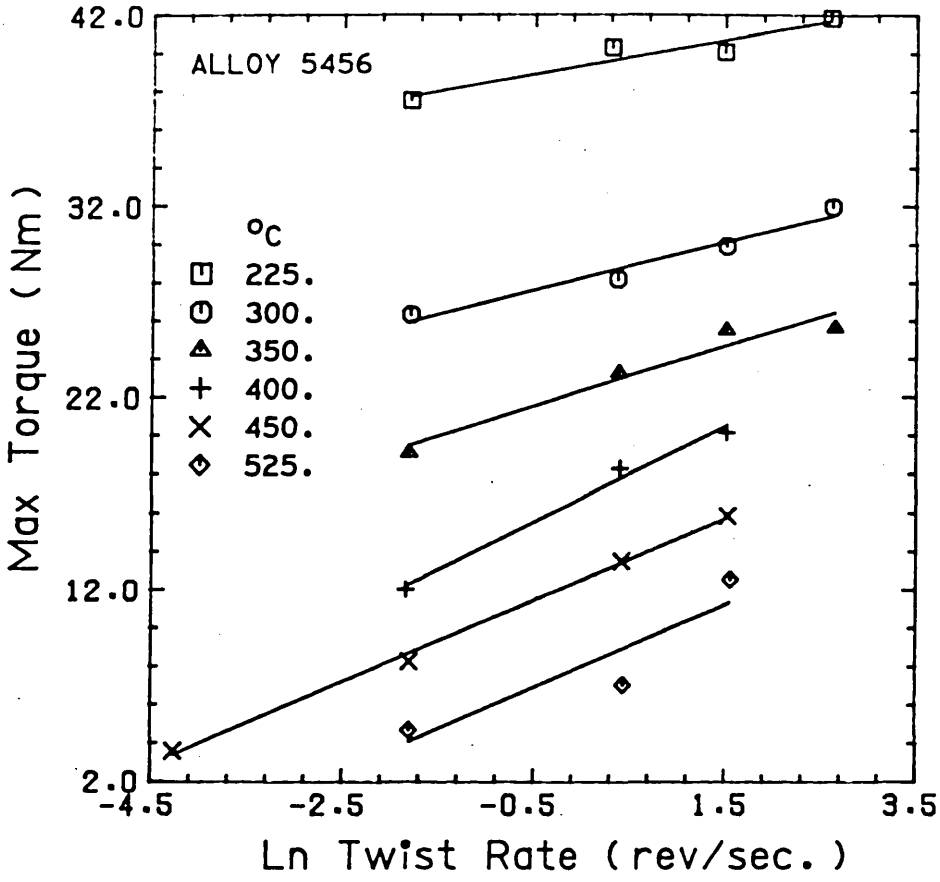
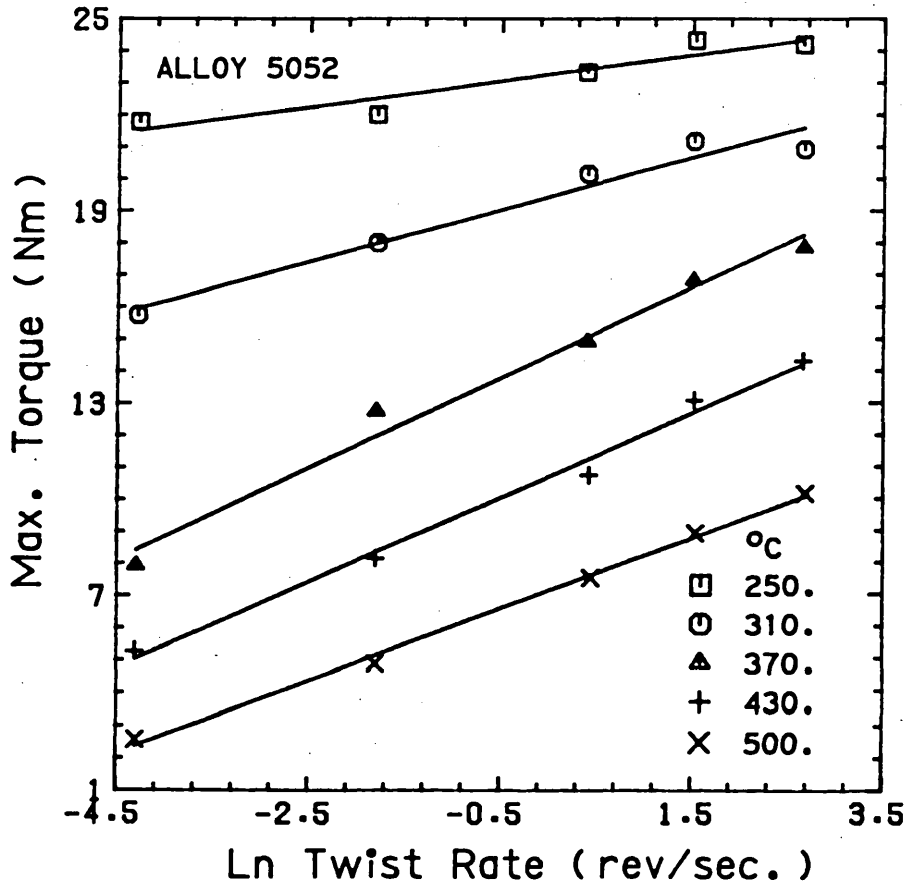


Fig. 29. Torque-twist rate curves for alloy 5456

Fig. 30. Torque-twist rate curves for alloy 5052



It was previously stated that the gradients in Figs. 26-30 were equal for a given alloy and starting condition. It is interesting to note, however, that when discrepancies do appear they do so at the temperatures around 400°C. In fact closer inspection reveals this to be the case for all the materials investigated and would appear to be more than a case of experimental inaccuracy. The evidence would suggest the possibility of some change in deformation mode at those temperatures where the effect is observed.

Where tests were carried out to failure, as shown in Tables 4.1-4.5, the hot ductility, as measured by twists to failure, showed an increase with increasing temperature. This increase attained a peak value at intermediate temperatures prior to a reduction at higher temperatures probably due to the onset of grain boundary sliding (Fig. 31). This would support in part, the work of Cotner and Tegart[130] who also found an increase in hot ductility with temperature increase. Their work, however, revealed no reduction at higher temperatures, ductility steadily increasing as the temperature was increased. In this case, the reduction in high temperature ductility is coincident with the temperature range at which dynamic recrystallization is initiated. It would therefore seem a reasonable assumption that the presence of the small equiaxed grain structure is permitting enhanced grain boundary cracking. In addition the fact that this alloy contains a large proportion of second phase, compared to the negligible amount in the super-pure material, may indicate that the soft matrix is deforming around the hard second phase particles generating voids and enhancing crack nucleation.

4.1.3. Derivation of the Constants in the Hot Working Equation

The analysis formulated in section 2.4 described the evolution of the general hot working equation from considering high and low stress relationships. The inclusion of an arrhenius term was made after recognition of the deformation processes being thermally activated. The relationship is generally expressed:-

$$Z = \dot{\varepsilon} \exp \frac{\Delta H}{RT} = [A \sinh (\alpha\sigma)]^{n}$$

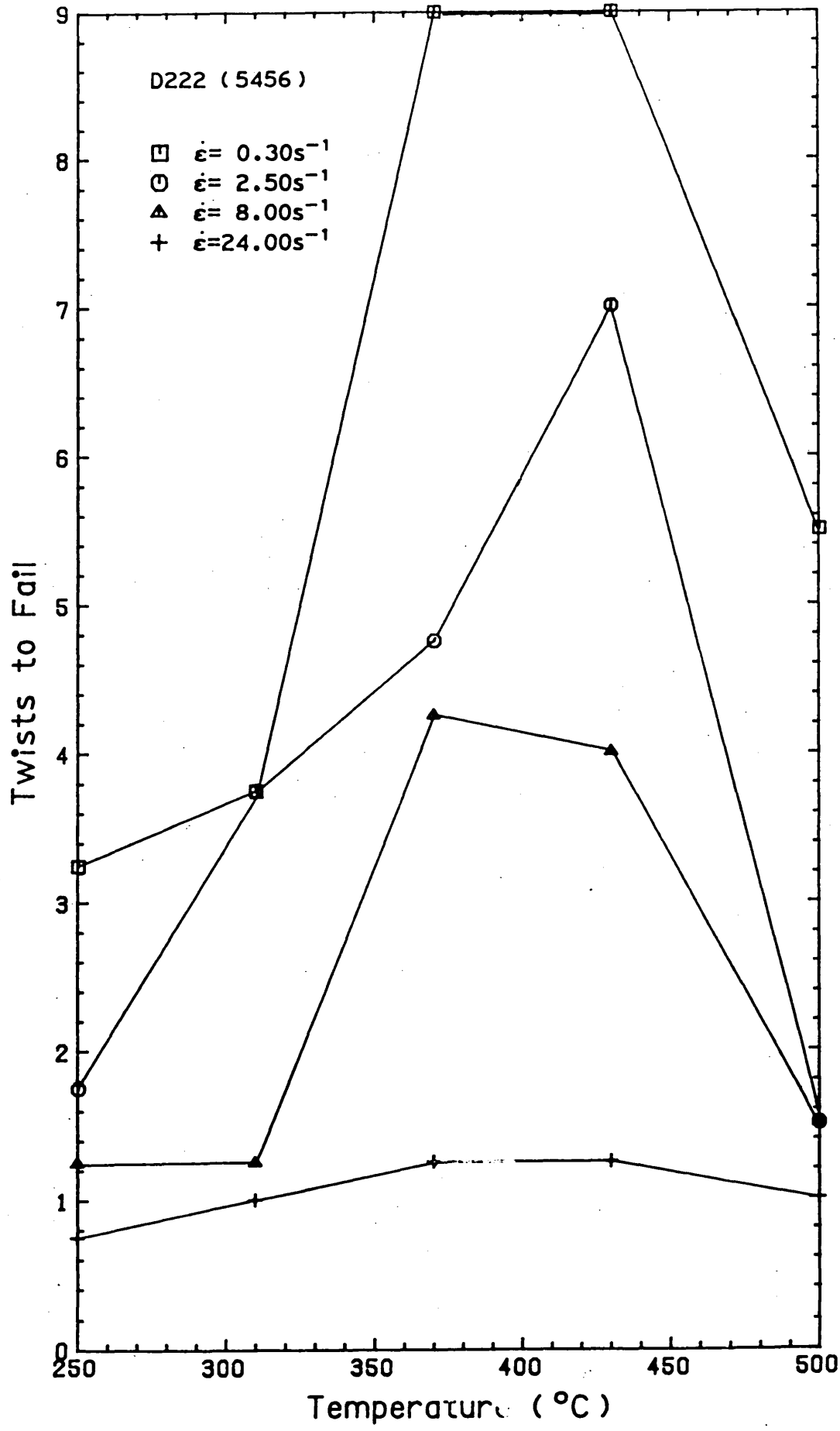


Fig. 31. Hot ductility variation with temperature

In order for this expression to be utilised, the four constants A, α, n and ΔH must be evaluated for each alloy system. The following sections describe their derivation from the techniques described in section 2.4.2.2.

4.1.3.1. Evaluation of the Constants from Torque Minimization

Following the method shown in section 2.4.2.2., the separation of the hot working equation and introduction of torque and twist rate terms permitted a relationship to be established suitable for computer optimization. Following the method described and using the computer programme documented in Appendix D, the values of A, α, n and ΔH were found for the three alloys in their various initial conditions. The type of output generated by the programme is shown in Table 4.8 for the D222 (5456) alloy. The table shows the maximum and minimum values of the four constants within which the result is constrained to lie. Initial runs of the programme used wider limits, but these were later reduced to avoid undue searching in regions where the result was unlikely to be found. The biggest problem of the technique is to avoid local minima and to derive the global minimum. It was found that initial different guesses for A, α, n and ΔH could produce different final results due to local minima being located. This was overcome by changing the increment steps for internal variation of the four to avoid too small an area being scanned. The low values of the differences, shown in Table 4.8, between the experimental and theoretical torques would indicate that the Sinh relationship gives a good fit to the data. The results for all the materials can be seen in Table 4.9 for conditions of no temperature rise and temperature rise inclusion. From the table for results without temperature rise inclusion, the results for ΔH can be seen to be high when compared with published data for aluminium alloys. Jonas et al.[100] report the value for aluminium as 155 KJ/mole while Farag and Sellars[28] used a value of 150 KJ/mole. Bailey et al.[120] found values of around 160 KJ/mole for commercial purity aluminium, an aluminium-magnesium-silicon alloy and an aluminium copper alloy. Sheppard and Raybould[210] reported a value of 156 KJ/mole for commercial purity aluminium and a similar value for a single phase Al-7% Mn -3% Mg alloy.

D222 (5456) WITH TEMPERATURE RISE.

MINIMISATION LIMITS ARE

	MAX	MIN
A	.10000E+18	.10000E+03
ALPHA	1.000	.001
N	10.00	1.00
D.H	400000.0	90000.0

VALUES OF CONSTANTS CALCULATED BY MINIMIZATION

A (PER SEC)	ALPHA (M2/MN)
.16141E+11	.0191
N	DELTA(H) (J/MOLE)
3.20	161177.4

VALUES OF THEORETICAL AND EXPERIMENTAL TORQUE (N.M)

EXPERIMENTAL	THEORETICAL	DIFFERENCE
25.670	26.741	-1.07058
17.980	18.503	.52260
11.830	12.212	-.38210
6.040	7.141	-1.10096
3.200	3.520	-.31975
28.980	30.684	-1.70428
22.595	22.908	-.31295
16.266	16.683	-.41699
10.590	11.346	-.75612
5.980	6.591	-.61140
33.220	33.634	-.41429
26.470	27.392	-.92222
21.230	20.779	.45120
15.370	15.702	-.33160
9.330	10.593	-1.26343
34.860	35.900	-1.03989
27.820	29.860	-2.04040
21.290	23.462	-2.17214
16.840	18.086	-1.24635
11.240	12.554	-1.31413
36.105	36.969	-.86400
29.524	29.458	.06560
23.668	24.793	-1.12502
18.668	19.728	-1.06028
13.786	15.125	-1.33850
6.325	6.829	-.50403
10.500	11.310	-.81043
28.842	28.871	-.02897
23.276	24.177	-.90121
17.710	18.804	-1.09372
13.310	13.615	-.30549
35.450	33.473	1.97715
35.636	32.348	3.28799
28.890	26.041	2.84942
22.272	21.862	.41018
18.136	16.745	1.39109
12.727	11.799	.92798
29.527	33.359	-3.83213
22.654	21.775	.87916
16.036	14.990	1.04555
10.563	9.625	.93845
6.491	5.224	1.26696
29.972	28.199	1.77309
21.636	19.511	2.12536
14.509	13.236	1.27254
7.991	8.145	-.15445
5.282	4.619	.66221
30.961	30.185	.77632
24.526	24.360	.16606
19.091	18.329	.76192
13.999	13.362	.63706
9.163	8.597	.56639
36.910	33.874	3.03647
29.863	29.914	-.04590
24.283	23.893	.38980
19.184	18.020	1.16375
15.055	13.793	1.26163

Table 4.8. Torque data minimization output for alloy D222 (5456)

The critical involvement of temperature in the Sinh relationship, through the exponential term, means an accurate value of temperature is essential if a meaningful solution is required. The temperature rise calculations for the torsion test have shown that large differences may be found between initial and actual temperatures at the required strain. In the event of the low temperature runs (225°C) for 5456, this rise can be as great as 110°C. It is essential that the instantaneous temperature at the maximum torque or onset of steady state should be applied in the analysis. The effect of its inclusion can be seen in Table 4.9. The value of ΔH falls to a figure between 160-170 KJ/mole for the three homogenized materials while the commercially heat treated ones fall even farther. The activation energies drop into the range of previous results and justify the inclusion of the temperature rise. The effect on the remaining three parameters is to reduce α, increase n and reduce A. We must now look at the meanings and implications of these results.

Results for creep in the aluminium magnesium system may be seen in Table 4.10 for a power relationship between strain rate and stress. These results show that the activation energy derived from the experimental work is of the same order of magnitude, although a little higher. Wright[205] found activation energies for pure aluminium and an aluminium 2% magnesium alloy of 157 and 155 KJ/mole respectively which would also appear to be greater than the activation energy for self-diffusion in aluminium. The reason for this could be that the temperature rise calculated is not great enough, causing the evaluated activation energy to be too great. (The inclusion of the temperature rise caused a decrease in this term). Nevertheless the results tend to support the hypothesis that hot deformation is a thermally activated process with an activation energy comparable to that for self-diffusion of aluminium.

In the case of the commercially heat treated materials, the activation energy is significantly lower, especially in the case of 5456, and it would seem that some alternative process is involved. The value of 145 KJ/mole for 5083 would tend to agree with the self-diffusion results although it should be remembered

that a similar process for temperature rise was utilised and so any error involved should also be apparent in this case. The lowest value, that for 5456 of 106.5 KJ/mole, corresponds to the activation energy for magnesium diffusion in aluminium.[215] This would seem a reasonable conclusion since the limited heat treatment means the concentration gradients of magnesium introduced by coring are not completely removed (as found in section 4.5.1.2.). The mid-range result for 5083 may well be the result of both processes being involved giving an 'average' result.

Reported work by Borch, Shepard and Dorn[216] on the creep of an aluminium 3 wt.% magnesium alloy showed a peak in the activation energy at a temperature of 330°C. At temperatures above 300°C they found the value coincided with that for self-diffusion in aluminium. The high temperature value was rationalized in terms of the climb mechanism for high temperature creep. Climb occurs by the migration of vacancies to or from jogs on dislocations. Since most of the migrating atoms are those of the host element, it is not surprising that the activation energy does not differ from that of self-diffusion in aluminium, especially in dilute solutions. The activation energy peak was explained in terms of Cottrell locking in which magnesium atoms diffuse to the expanded half cylinder of edge dislocations. The energy increase was described by changes in terms of the time involved for thermal activation. As dislocations approach a barrier, they stop and remain at the barrier for a period of time necessary for a local fluctuation in energy to cause their activation past the barrier. Consequently, solute atoms preferentially form atmospheres about dislocations over a period of time, t_a, during which the dislocations are arrested at barriers. The activation energy peak was attributed to this time, t_a, being greater than the time taken for the solute atoms to move this distance, t_b. At higher temperatures where this locking appeared to vanish, t_b must be greater than t_a. Since the activation energy found from the analysis carried out here is an average one, over the temperature range involved, it is possible that a low temperature activation energy rise is causing the average value to exceed that for self-diffusion in aluminium. Alternatively there may be an activation energy change at higher temperatures associated with the anticipated

onset of dynamic recrystallization. Luton and Sellars[172] report that the activation energy for dynamic recrystallization in nickel is lower than that for recovery creep and self-diffusion (56 Kcal/mole compared to 71 Kcal/mole) and so this would suggest this reasoning to be a possibility.

Analysis of the data in restricted temperature groups has shown the average activation energy to drop to 153.6 KJ/mole for an average temperature of 465°C. This would suggest that the value at the other end of the temperature scale must increase to produce the mean value of 161.2 KJ/mole. The observation agrees with the findings of Luton and Sellars, above, and would increase the evidence for dynamic recrystallization in this range. The values of A, α and n were found to remain unaltered in this temperature range from the values originally computed.

The value of n calculated for the alloys, of approximately 3, is lower than the reported value[100] for pure metals, of 4-5. Comparison with the values in Table 4.10 and Garafalo's[122] result for Al-3% Mg, of 2.4, shows that it compares well with that found in creep. This assumes the power exponent in creep compares with the Sinh exponent; an assumption made in section 2.4.2.1. The value of 3 has been attributed to solute atmosphere drag[211,217] and to viscous glide[212] being the rate controlling processes during creep of these alloys. The value of α computed for the higher magnesium content alloys is lower than that found by Garafalo[122] of 0.03 m^2/MN. This may be explained in terms of the commonly made definition of α as the reciprocal stress at which the temperature compensated strain rate changes from power to exponential stress dependence. This implies that α is dependent upon material and the additional magnesium, over the material used by Garafalo, has caused this variation. The result for 5052, which has a similar composition, is in good agreement. The result for A for 5052 compares well with the result of Wright[205] for an Al-2% Mg alloy of 3.25×10^{10} sec^{-1}. Jonas et al.[47] considered A to be a structure factor at high stress levels (i.e. proportional to the density of activatable sites) and as such dependent upon alloying additions and material purity. The present results would not appear to bear this idea out since the increased magnesium in two

	WITHOUT TEMPERATURE RISE				WITH TEMPERATURE RISE			
MATERIAL	A	ALPHA	N	DELTAH	A	ALPHA	N	DELTAH
	/SEC	M2/MN		J/MOLE	/SEC	M2/MN		J/MOLE
0222 (5456)	.29E+11	.043	2.00	179921	.16E+11	.019	3.20	161177
5456	.86E+12	.040	2.17	198365	.23E+08	.014	2.61	106428
5083 (H)	.47E+11	.057	1.50	186812	.23E+11	.027	2.46	168804
5083	.34E+12	.032	2.93	204192	.10E+11	.014	3.65	145101
5052	.32E+13	.134	1.13	224739	.17E+11	.033	2.74	165449

Table 4.9. A α, n and ΔH from Torque analysis

MATERIAL	REF	N	H
AT			KJ/MOLE
AL	211	4.2	148
AL-0.5 MG	211	4.2	138
AL-1.0 MG	211	3.3	135
AL-2.0 MG	211	3.0	142
AL-3.0 MG	211	3.0	147
AL-5.0 MG	211	3.0	139
AL-7.0 MG	211	3.0	143
AL-3.0 MG	212	3.0	142
AL-5.1 MG	213	2.9	143
AL-6.9 MG	213	2.9	143
AL-5.0 MG	214	3.1	140

Table 4.10. Values of n and ΔH from reported creep work

	WITHOUT TEMPERATURE RISE				WITH TEMPERATURE RISE			
MATERIAL	A	ALPHA	N	DELTAH	A	ALPHA	N	DELTAH
	/SEC	M2/MN		J/MOLE	/SEC	M2/SEC		J/MOLE
0222 (5456)	.87E+10	.041	1.92	170484	.15E+11	.024	2.96	164437
5083 (H)	.11E+11	.051	1.69	172720	.08E+10	.018	3.41	149927

Table 4.11. A, α, n and ΔH from Stress analysis

of the alloys appears to have no effect upon the magnitude of A. The only discrepancy would appear in the more dendritic 5456 alloy and may be caused by the inhomogeneity of the magnesium.

4.1.3.2. Flow Stress Minimization

As pointed out in section 2.4.2.2., an analysis similar to that carried out above may be undertaken if data is available in the form of stress, strain rate and temperature. The technique proves somewhat better from the computing viewpoint since calculation time is considerably reduced. This is achieved by the elimination of the time-consuming integration by Simpson's Rule when equation (88) is used compared to (92). The disadvantage, however, lies in the requirement of the tedious application of the Fields and Backofen analysis to generate the data in the first place. Data was only available for the alloys D222 (5456) and further heat treated 5083, the results for which are shown below in Table 4.11. Once again the trend, when introducing the temperature rise calculation, is one of reducing the α value, increasing n and reducing ΔH. The results, when compared with those found from torque minimization, show a fairly good agreement. The discrepancies arise from the increased possibility for error introduction through manipulation of the raw data with the Fields and Backofen analysis.

The major disadvantage with the two analytical methods described so far is the large amount of computational time involved. This is due, for the first case, to the application of Simpson's Rule, but in both cases to the slow convergence of the technique to the final result. This would appear to be an inherent problem of the constrained minimization technique and one which should be overcome if at all possible. The other problem has been previously mentioned, production of local minima instead of the global minimum. Thus although both of the methods generate results in good agreement with one another, a more direct, reliable technique would be of considerable advantage.

4.1.3.3. Alternative Minimization of Torque Data

The analysis shown in section 2.4.2.3. demonstrated that the general hot working equation, defined in terms of torque and twist rate, could be separated in a different manner from that utilised in the analyses above. The computer programme shown in Appendix E carried out the calculations from input data of torque, twist rate and test temperature. An example of the computed output is shown in Table 4.12 while the overall results are shown in Table 4.13. Comparing these values with those found from the original torque minimization, found in Table 4.9., it can be seen that the agreement is very good. This is not unexpected since the two analyses are only variations of the same basic concept.

The great advantage of this technique over those described previously is its rapid convergence to the final solution. In addition it suffers from no problems of local minima and can operate with a very limited volume of data.

In conclusion we may observe that the three techniques described, permit simple calculation of the four constants in the hot working equation. The results are in good agreement with one another as well as with values reported by other workers for similar alloys. Further evidence for the validity and applicability of the results was gained from analysis of hot compression and creep data,[218] using the flow stress minimization technique. The values produced were in good agreement and confirm the observations previously made.

An inherent assumption of the methods is initially that the hot working equation is mathematically correct and secondly that the four values are temperature independent. As already mentioned, results of previous[216] workers have demonstrated a variation of ΔH with temperature and should this be true then the assumptions regarding A, α and n must be seriously questioned. This variation in ΔH would undoubtably cause the resultant plot of Ln Z vs Ln sinh $(\alpha\sigma)$ to deviate from linearity, but while this may in itself not be incorrect, a change in any one of the remaining three with temperature could reinstate this linearity. Although further

FLOW STRESS DATA ANALYSIS FOR THE TORSION TEST
TABLE OF RESIDUALS FOR D222(5456) WITH TEMP RISE
THE SPECIMEN DIMENSIONS ARE:
OUTER RADIUS = 5.00MMS
LENGTH = 10.00MMS
THE PARAMETER VALUES ARE:
ALPHA = .02281 (M2/MN)
DELTA H = 163957. (J/MOLE)
N = 3.05
LN A = 23.47

POINT NUMBER	TWIST RATE (RPS)	TEMPERATURE (C)	OBSRVD TORQUE (N-MM)	ESTIM. TORQUE (N-MM)	RESIDUAL
1	.117	255.	25670.	26717.	-1047.
2	.118	315.	17980.	18468.	-488.
3	.114	371.	11830.	12187.	-357.
4	.114	431.	6040.	7159.	-1119.
5	.114	501.	3200.	3587.	-387.
6	1.074	261.	28980.	30678.	-1698.
7	1.064	318.	22595.	22889.	-294.
8	1.068	374.	16266.	16660.	-394.
9	1.075	432.	10590.	11336.	-746.
10	1.081	502.	5980.	6626.	-646.
11	7.854	270.	33220.	33644.	-424.
12	8.658	318.	26470.	27391.	-921.
13	8.671	378.	21230.	20768.	462.
14	9.381	435.	15370.	15690.	-320.
15	9.532	503.	9330.	10598.	-1268.
16	29.003	274.	34860.	35921.	-1061.
17	29.305	320.	27820.	29870.	-2050.
18	29.820	378.	21290.	23461.	-2171.
19	30.034	436.	16840.	18080.	-1240.
20	29.003	508.	11240.	12555.	-1315.
21	81.179	282.	36105.	36997.	-892.
22	77.723	341.	29524.	29473.	51.
23	86.017	387.	23668.	24800.	-1132.
24	88.970	444.	18668.	19729.	-1061.
25	90.855	505.	13786.	15125.	-1339.
26	.095	431.	6325.	6851.	-526.
27	1.056	432.	10500.	11300.	-800.
28	41.092	334.	28842.	28881.	-39.
29	42.242	378.	23276.	24179.	-903.
30	42.613	436.	17710.	18800.	-1090.
31	43.241	504.	13310.	13615.	-305.
32	40.985	297.	35450.	33491.	1959.
33	18.091	292.	35636.	32360.	3276.
34	18.804	344.	28890.	26042.	2848.
35	19.078	384.	22272.	21857.	415.
36	19.218	440.	18136.	16736.	1400.
37	19.798	507.	12727.	11801.	926.
38	.567	235.	29527.	33355.	-3828.
39	.569	316.	22654.	21751.	903.
40	.566	377.	16036.	14965.	1071.
41	.571	438.	10563.	9623.	940.
42	.567	509.	6491.	5275.	1216.
43	.263	258.	29972.	28182.	1790.
44	.280	322.	21636.	19481.	2155.
45	.284	380.	14509.	13212.	1297.
46	.284	440.	7991.	8156.	-165.
47	.283	501.	5282.	4676.	605.
48	2.247	275.	30961.	30182.	779.
49	2.639	322.	24526.	24348.	178.
50	2.917	379.	19091.	18311.	780.
51	3.045	434.	13999.	13349.	650.
52	3.325	502.	9163.	8613.	550.
53	53.301	298.	36910.	33894.	3016.
54	54.112	330.	29868.	29927.	-59.
55	55.810	387.	24283.	23896.	387.
56	56.029	453.	19184.	18017.	1167.
57	55.809	510.	15055.	13794.	1261.

PPROXIMATE VALUES
RESIDUAL SUM OF SQUARES = 99990041.
R-SQUARED = .9789

Table 4.12. Torque Data minimization output for alloy D222

mention will be made with respect to this feature in the next section, some simple changes were made to the previous analysis to investigate this finding.

Using the flow stress minimization technique, described in section 4.1.3.2., allowance was initially made for α to vary linearly with temperature such as $\alpha = a + bT$. This increased the number of variables to be minimized to 5. The trial was carried out on alloy D222(5456) and produced similar values for A, n and ΔH while the constant a had a value very close to 0.0191 m^2/MN and the value b was found to be negligible. This, it would seem, tends to imply that α is not temperature dependent. Following a similar method, ΔH was given a power relationship with temperature of the form $\Delta H = c\ (T_m - T)^d$ where T_m is the melting temperature and T the test temperature. Once again the results showed that a dependence upon temperature was not present. The investigation was stopped at this point, but some further discussion is required since it is not felt that the entire problem has been examined. Close observation of the inter-itteration values of the constants during computation, for any of the techniques, shows some definite relationships between the variables. For example, in all cases a reduction of α during the itterative cycle was inevitably associated with a rise in the n value and vice versa. A similar interplay was found for A and ΔH, but to a much smaller extent. This inter-dependence means that the lack of temperature dependence of α was caused by the constraint of n being kept to a constant, temperature independent value. This is a consequence which may be seen from their relationship in section 2.4.2. It is felt that further valuable work could well be carried out into this feature and perhaps expanded to include temperature variation for all four constants.

4.1.3.4. Graphical Derivation of the Hot Working Constants

Section 2.4.2.1. described how the four constants A, α, n and ΔH could be evaluated from graphical means. This analysis was carried out for alloy D222 (5456) to check the accuracy of the method compared with those already described.

At low stresses it was shown that the general hot working relationship could be replaced by a power expression of the form:-

$$\dot{\varepsilon} = A_2\sigma^{n2}$$

while at high stresses an exponential relationship was applicable:-

$$\dot{\varepsilon} = A_3 \exp(\beta\sigma)$$

The values of A_2, n_2 and A_3 and β can be derived from plots of $\mathrm{Ln}\dot{\varepsilon}$ vs $\mathrm{Ln}\sigma$ and $\mathrm{Ln}\dot{\varepsilon}$ vs σ respectively. These graphs are shown in Figs. 32 and 33. The plots show good linear relationships in both cases. For the low stress case, Fig. 32, the slopes are approximately constant at low temperatures and decrease as the temperature is raised, while for the high stress case, Fig. 33, all the slopes are virtually the same. The results are shown in Table 4.14. As was described in section 2.4.2.1., α may be evaluated by finding β/n_2. For the low stress fit, the highest temperature, 500°C, result for n_2 will be most applicable while the 250°C result will be for a high stress fit. Using this data the value for α is given as:-

$$\frac{0.0874}{4.57} = 0.019 \ m^2/MN$$

It may immediately be seen that this value corresponds remarkably well with that found in Tables 4.9, 4.11 and 4.13. The fact that the value approaches that of the solutions including temperature rise calculation may be explained from the fact that temperature effects are minimized in this case by using a logarithmic axis for σ and $\dot{\varepsilon}$. Nonetheless it would seem very fortuitous that the result corresponds so well.

The temperature dependence of α may be illustrated by calculating its value from the various temperature groupings in Table 4.14. These results are plotted against temperature and can be seen in Fig. 34. As the result shows, there would appear to be a linear relationship between the two, and it was this feature which initiated the investigation described in the previous section.

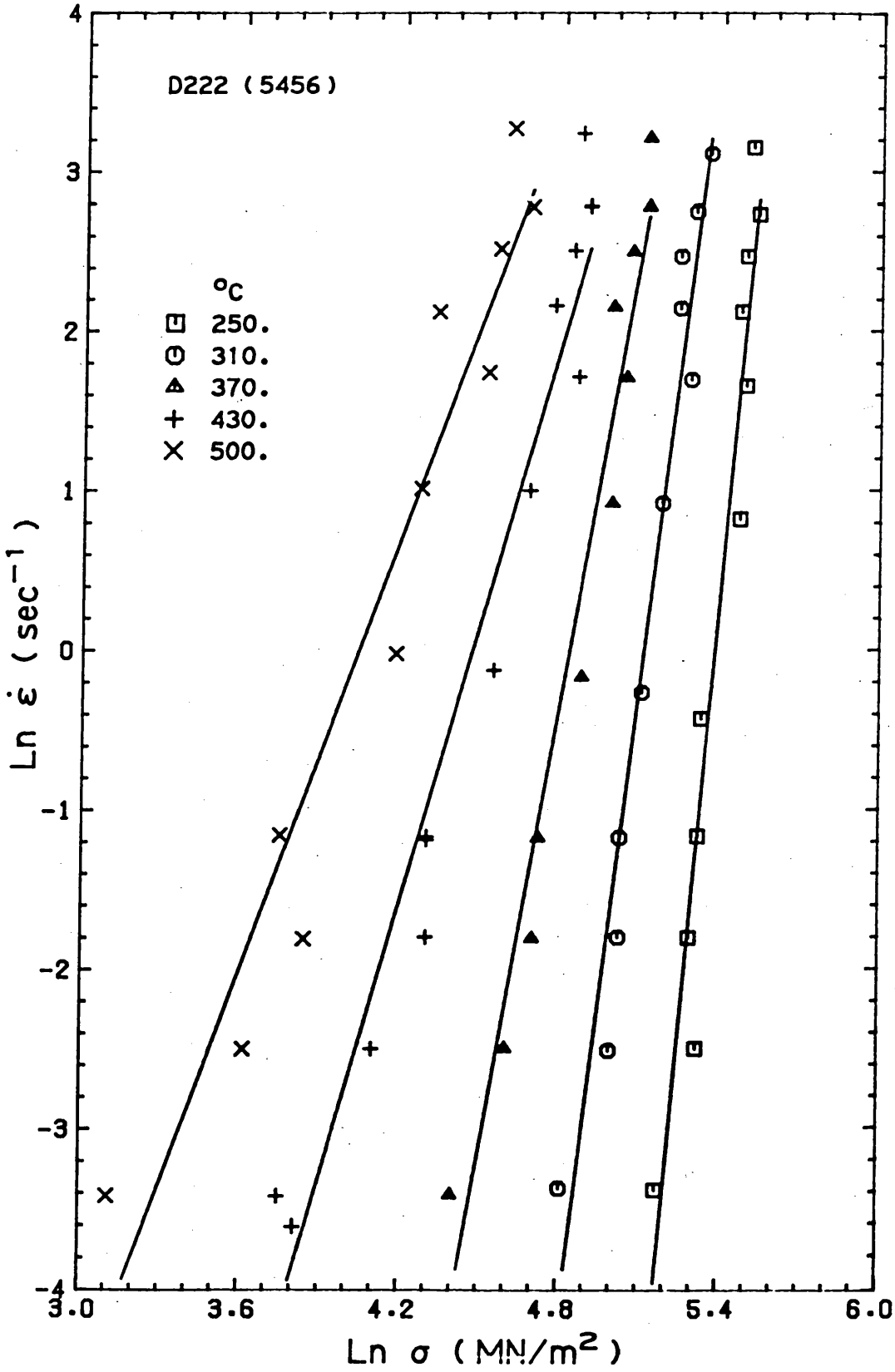


Fig. 32. Lnε̇ vs Lnσ, alloy D222 (5456)

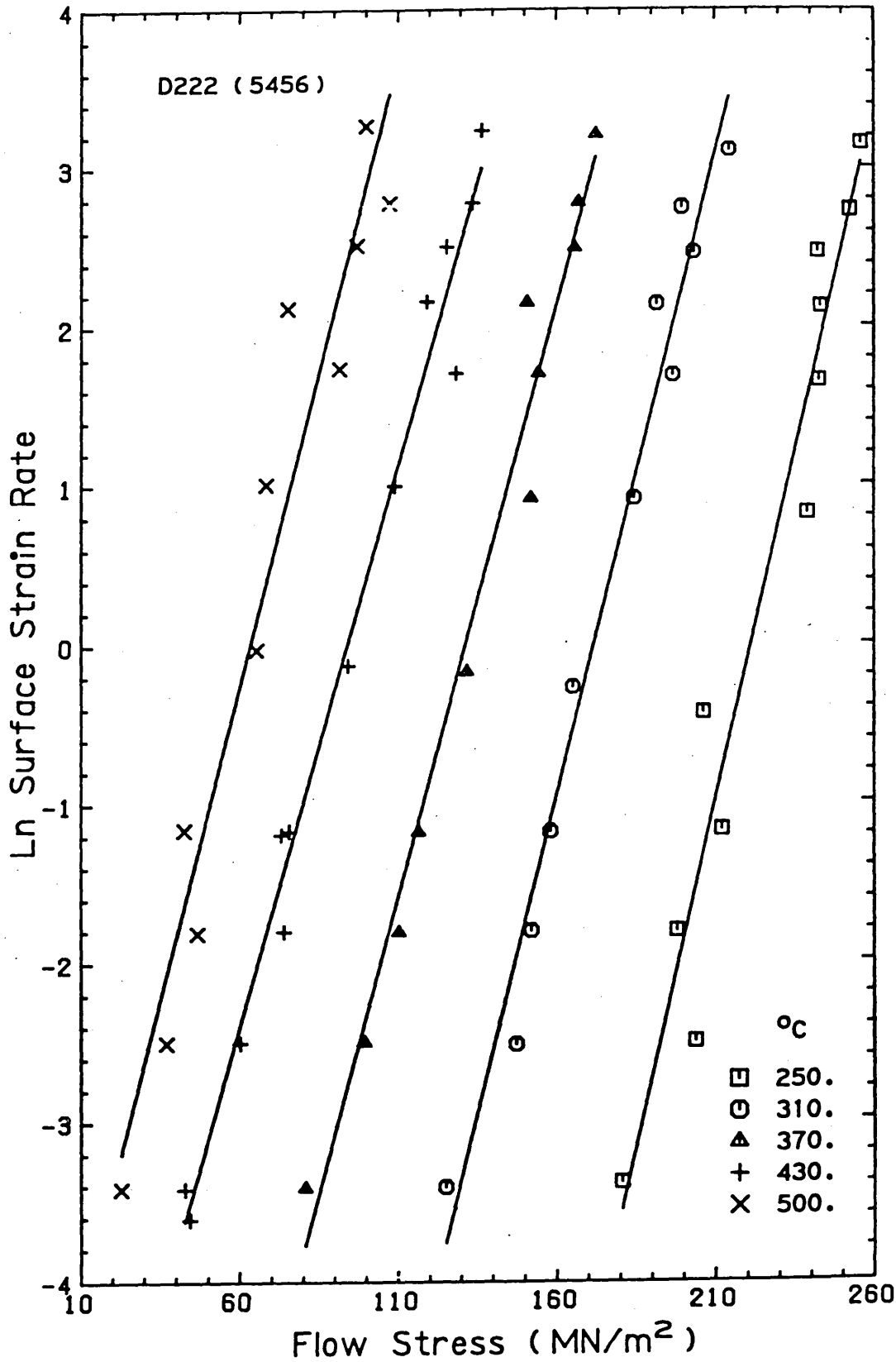


Fig. 33. Lnε̇ vs σ, alloy D222 (5456)

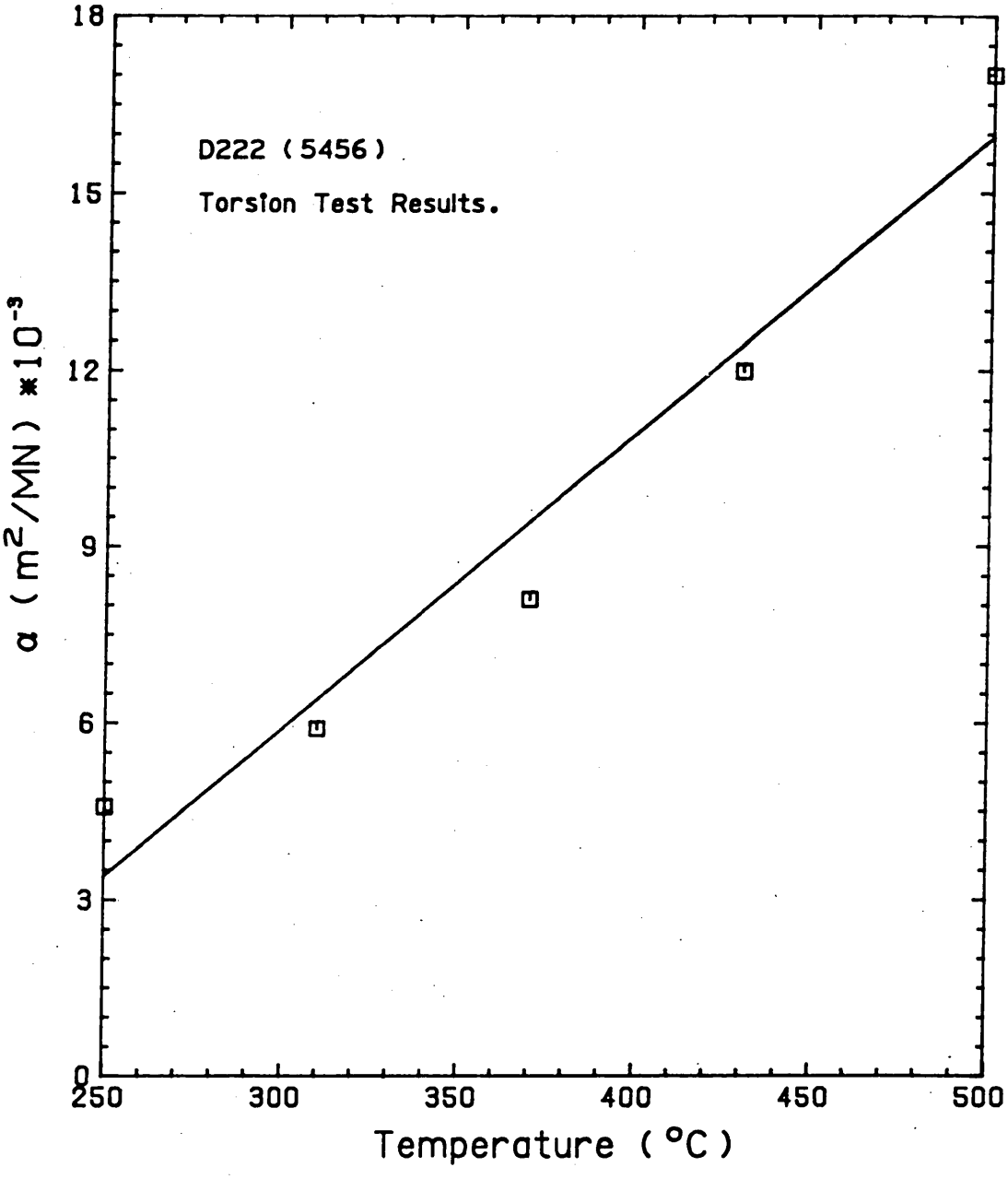


Fig. 34. α vs Temperature, alloy D222 (5456)

The observation agrees well with that found by McShane,[219] but no conclusion was drawn regarding the feature. Analysis of the data of Wong and Jonas[22] in the same way revealed a similar trend, but they chose a value calculated by the method used here to produce the value of 0.0191 m^2/MN. The description of α being the reciprocal stress at which the power law breaks down is inconsistent with the observation that α increases with temperature since we would expect this stress to increase with a temperature increase i.e. α to fall. The observation of Sheppard and Raybould[210] that α was proportional to the product of the burgers vector squared and the interjog spacing, is also inconsistent with this finding since the equilibrium number of jogs is related to temperature through an Arrhenius term. This implies that as the temperature increases the number of jogs increases and so the interjog spacing should decrease. Assuming that α is the reciprocal stress at which the power law relationship breaks down, as shown in Table 4.14, and back calculating the appropriate strain rate relevant to this, shows that for each temperature the strain rate is approximately equal to 0.7 $sec.^{-1}$ This means the powerlaw breakdown occurs at a regular value of strain rate for any test temperature. However this value of strain rate is just about the mean value of the experimental ones and may mean that α is calculated with reference to this value.

To calculate the activation energy from graphical means we must remember from section 2.4.2.1. that the product of the following two will give its value:-

$$\Delta H = R\left[\frac{d \operatorname{Ln} \dot{\varepsilon}}{d \operatorname{Ln} \sinh(\alpha\sigma)}\right]_T \left[\frac{d \operatorname{Ln} \sinh(\alpha\sigma)}{d\, 1/T}\right]_{\dot{\varepsilon}}$$

Thus plots of $\operatorname{Ln}\dot{\varepsilon}$ vs $\operatorname{Ln} \sinh(\alpha\sigma)$ at constant temperature and $\operatorname{Ln} \sinh(\alpha\sigma)$ vs $1/T$ at constant strain rate will serve to obtain the value. These plots may be seen in Figs. 35 and 36. As Fig. 35 shows, the data produces regular, constant gradient lines. As would be expected, increasing temperature decreases the flow stress and thus the magnitude of the sinh term, while increasing strain rate increases the flow stress with its corresponding effect upon the sinh value. Fig. 36 shows a linear relationship between

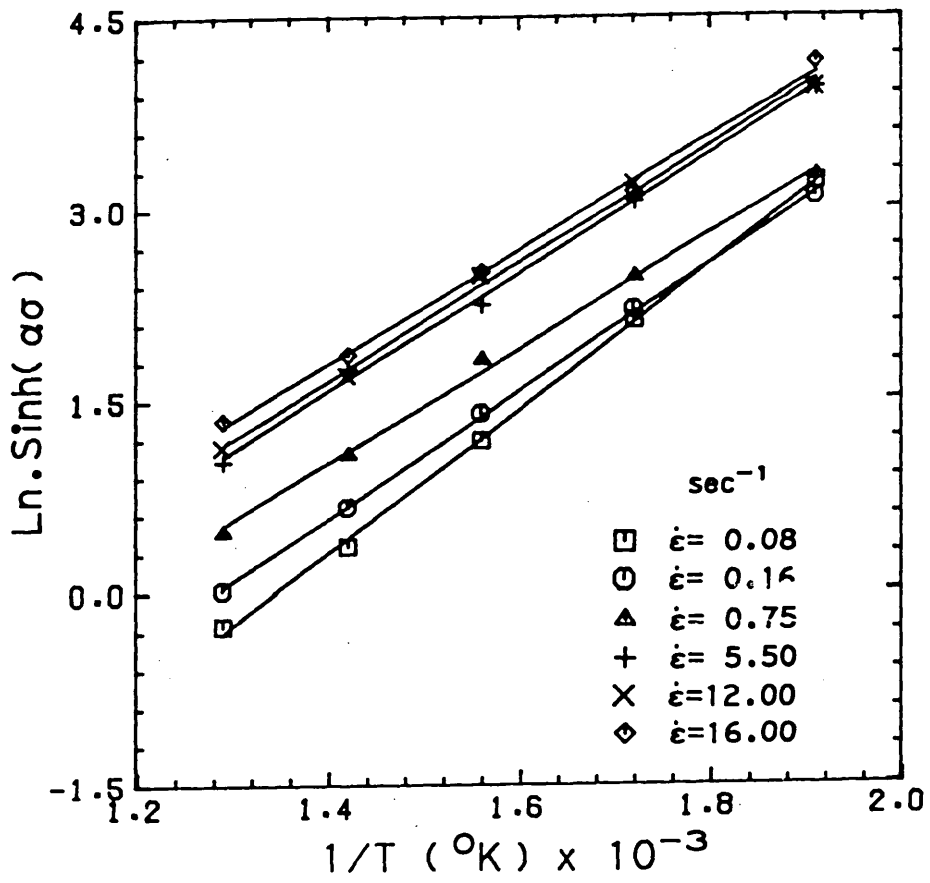


Fig. 35(a) Ln Sinh (ασ) vs 1/T

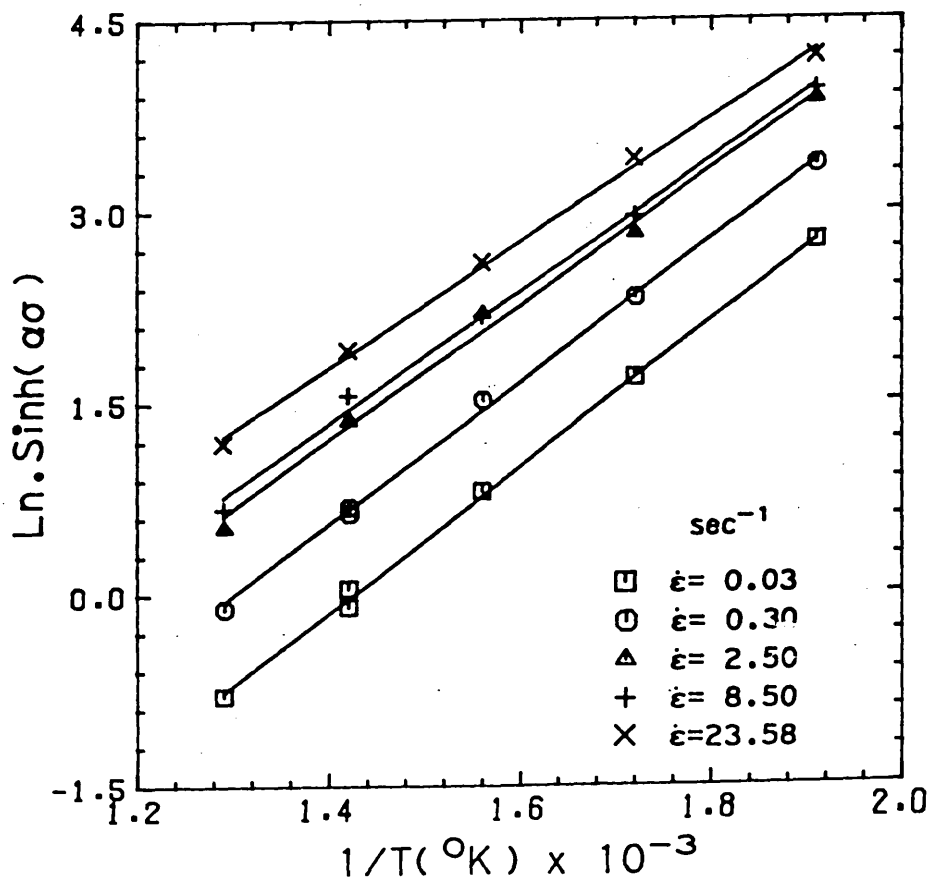


Fig. 35(b) Ln Sinh (ασ) vs 1/T

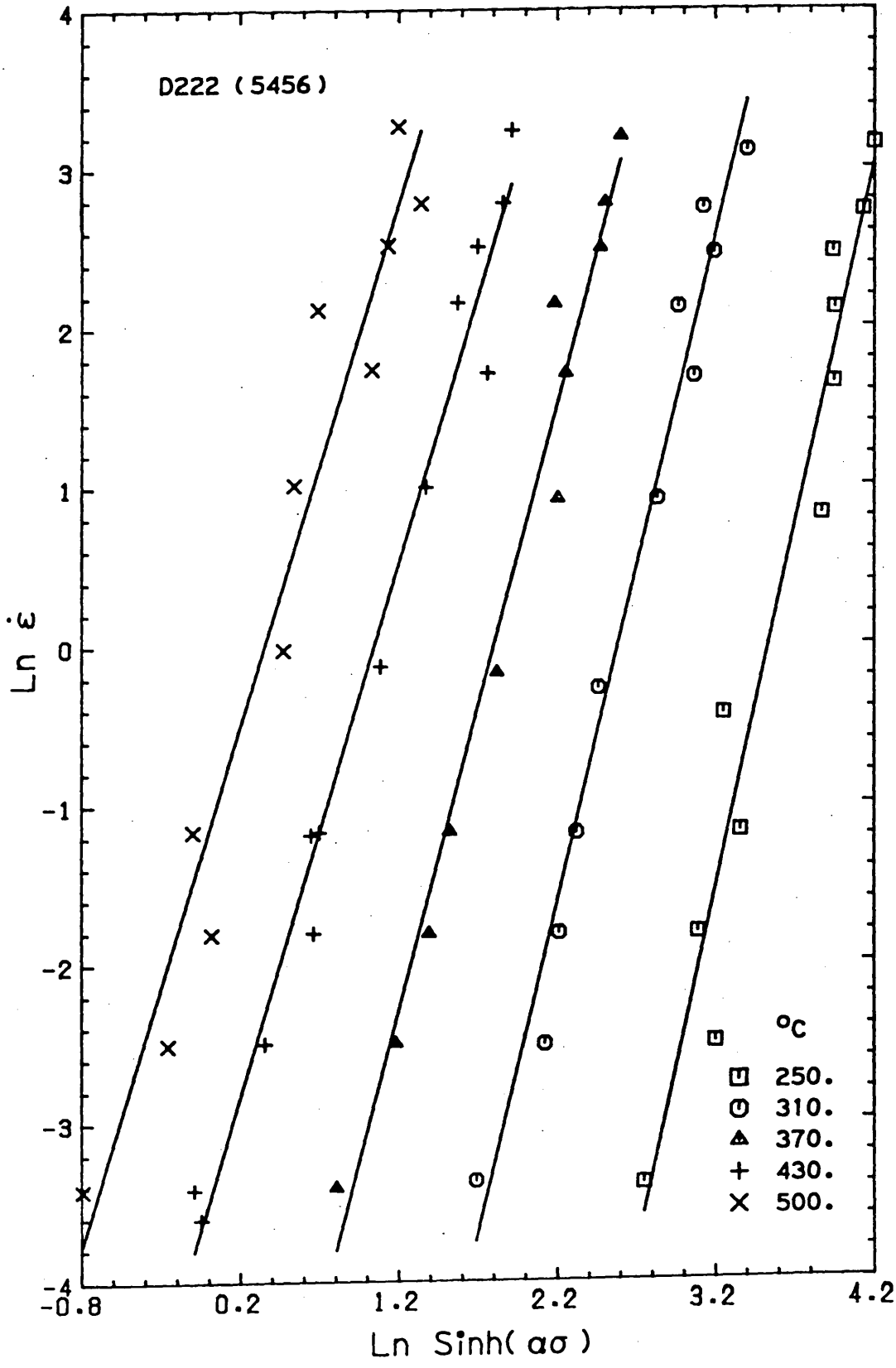


Fig. 36. Ln $\dot{\varepsilon}$ vs Ln Sinh (ασ)

MATERIAL	WITHOUT TEMPERATURE RISE				WITH TEMPERATURE RISE			
	A	ALPHA	N	DELTAH	A	ALPHA	N	DELTAH
	/SEC	M2/MN		J/MOLE	/SEC	M2/MN		J/MOLE
D222 (5456)	.27E+11	.031	2.08	178966	.15E+11	.022	3.05	163957
5456	.76E+12	.030	2.52	195053	.41E+08	.011	2.92	106818
5083 (H)	.54E+11	.047	1.77	186060	.94E+10	.031	2.22	166306
5083	.41E+13	.029	3.18	199136	.35E+11	.018	3.52	141094
5052	.29E+12	.127	1.23	222127	.17E+11	.027	3.21	165967

Table 4.13. A, α, n and ΔH from alternative torque minimization

$\dot{\varepsilon} = A_2 \sigma^{n_2}$			$\dot{\varepsilon} = A_3 \exp(\beta\sigma)$			
TEMP	A2	N2	TEMP	A3	BETA	ALPHA
250	.19E-44	19.08	250	.39E-8	.087	.0046
310	.26E-31	13.64	310	.94E-8	.081	.0059
370	.47E-19	9.17	370	.55E-4	.075	.0081
430	.54E-11	5.79	430	.13E-2	.071	.0120
500	.94E-08	4.57	500	.67E-2	.079	.0171

Table 4.14. Results for power and exponential fits to torsion data for alloy D222 (5456)

Ln Sinh($\alpha\sigma$) vs. $^1/T$			Ln$\dot{\varepsilon}$ vs Ln Sinh($\alpha\sigma$)			
	INTERCEPT	GRADIENT	TEMP	INTERCEPT	GRADIENT	DELTAH
/SEC			DEG.C			J/MOLE
0.03	.29E-5	5.716	250	.97E-8	4.572	191164
0.08	.49E-5	5.556	310	.19E-5	4.436	185477
0.16	.16E-4	4.257	370	.10E-3	3.822	159804
0.30	.73E-5	5.137	430	.30E-1	3.352	140153
0.75	.52E-4	4.850	500	.32E+0	3.273	136850
2.50	.21E-4	4.587				
5.50	.73E-4	4.637				
8.50	.29E-4	4.990				
12.00	.86E-4	5.650				
16.00	.12E-1	4.481				
23.50	.67E-4	4.462				

Table 4.15. Gradient and intercepts for ΔH evaluation for alloy D222 (5456)

Ln sinh ($\alpha\sigma$) and reciprocal temperature with the lines having virtually constant gradient, excepting one strain rate which is presumably due to erroneous data. The values for the gradients and intercepts are shown in Table 4.15 together with the calculated average ΔH for each temperature. The calculated values for ΔH show a steady decrease with temperature as is shown in Fig. 37. The average value over the temperature range is found to be 162689 J/mole which agrees well with the value established from the data minimization techniques. It would tend to confirm that the techniques derive a mean value after considering the ranges of data supplied. The drop in activation energy would support the hypothesis that an alternative high temperature restoration process is operative, namely dynamic recrystallization, following the observations of Luton and Sellars.[172] Had this duplex softening mechanism, dynamic recovery and recrystallization, not been operative, the material flow stress would have been increased for the given conditions. Thus the probability of thermal activation must be increased which necessitates a reduction in activation energy for a given temperature. This quantitative variation in ΔH initiated the introduction of a variable value in the minimization procedure described in the previous section. As reported then, no variation was produced, but this may be due to the restrictions of no temperature dependence placed on the remaining three constants. Thus the evidence presented for a variation in α and ΔH with temperature seriously questions the validity of the sinh relationship as it now stands. The method of deriving the values of A and n is to plot LnZ vs Ln sinh ($\alpha\sigma$) using the calculated values of α and ΔH, i.e. 0.019 m^2/MN and 162689 J/mole. However if this graph is constructed for the five values of α and ΔH already produced at their applicable temperatures, then an indication of the variance of A and n may be gained. This treatment is shown in Fig. 38. As this figure indicates, the value of n decreases while A increases as the temperature is increased. These results are shown in Figs. 39 and 40. The basic problem with this type of analysis is that we have assumed both power law and exponential fits apply at all the temperatures considered. Although this is undoubtably a rash assumption to make, it can be seen from Figs. 32 and 33 that neither

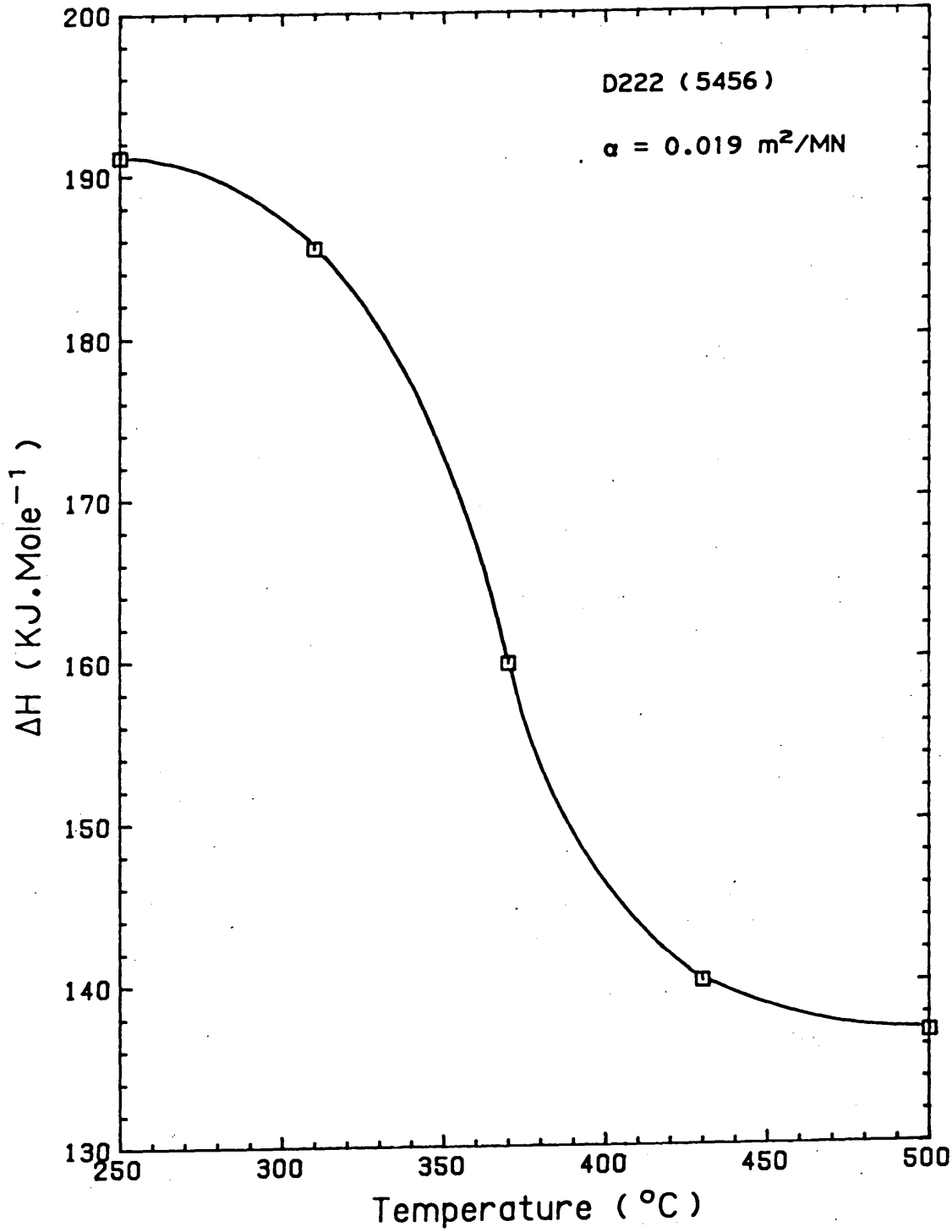


Fig. 37. ΔH vs temperature, alloy D222 (5456)

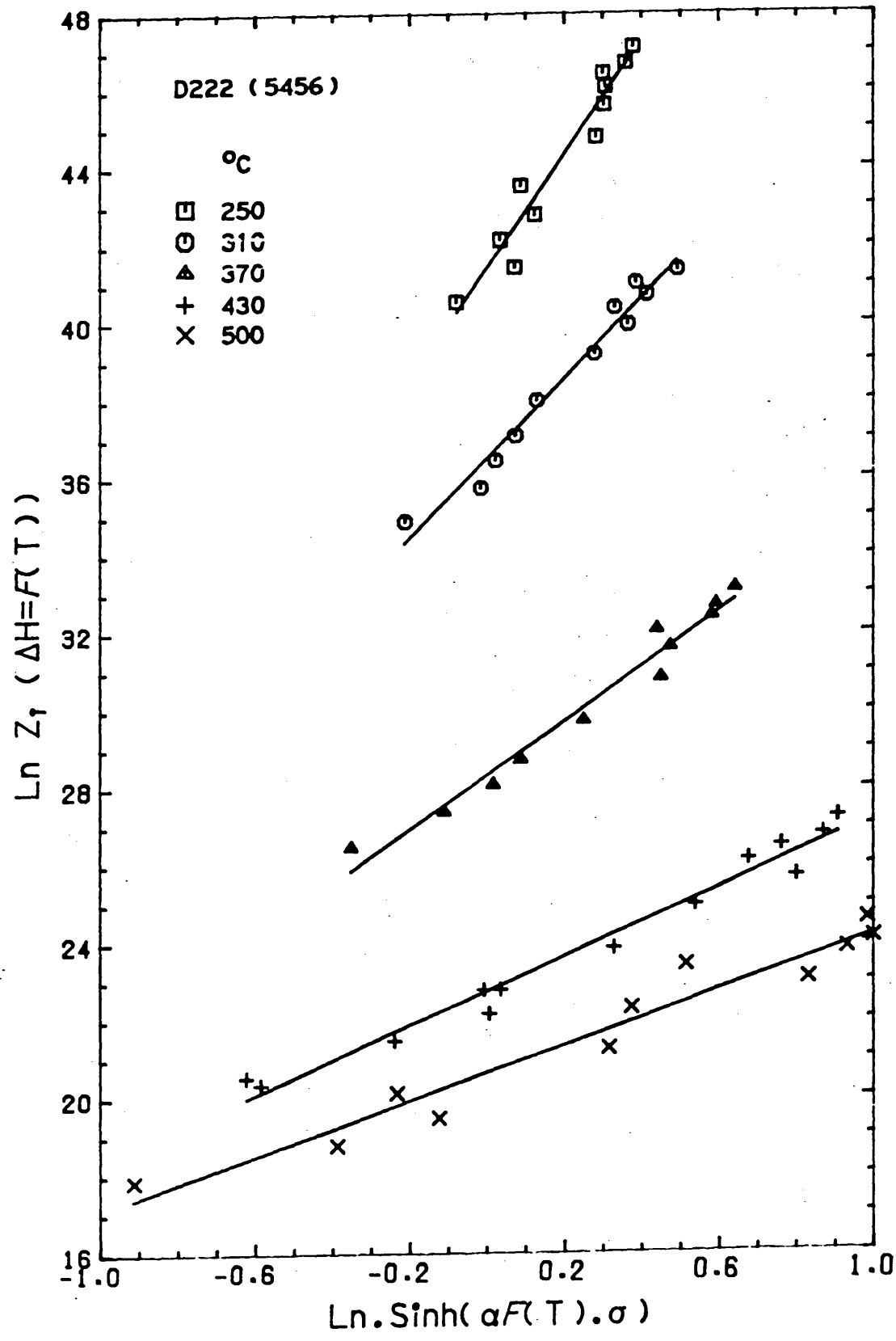


Fig. 38. Derivation of variation of A and n with temperature

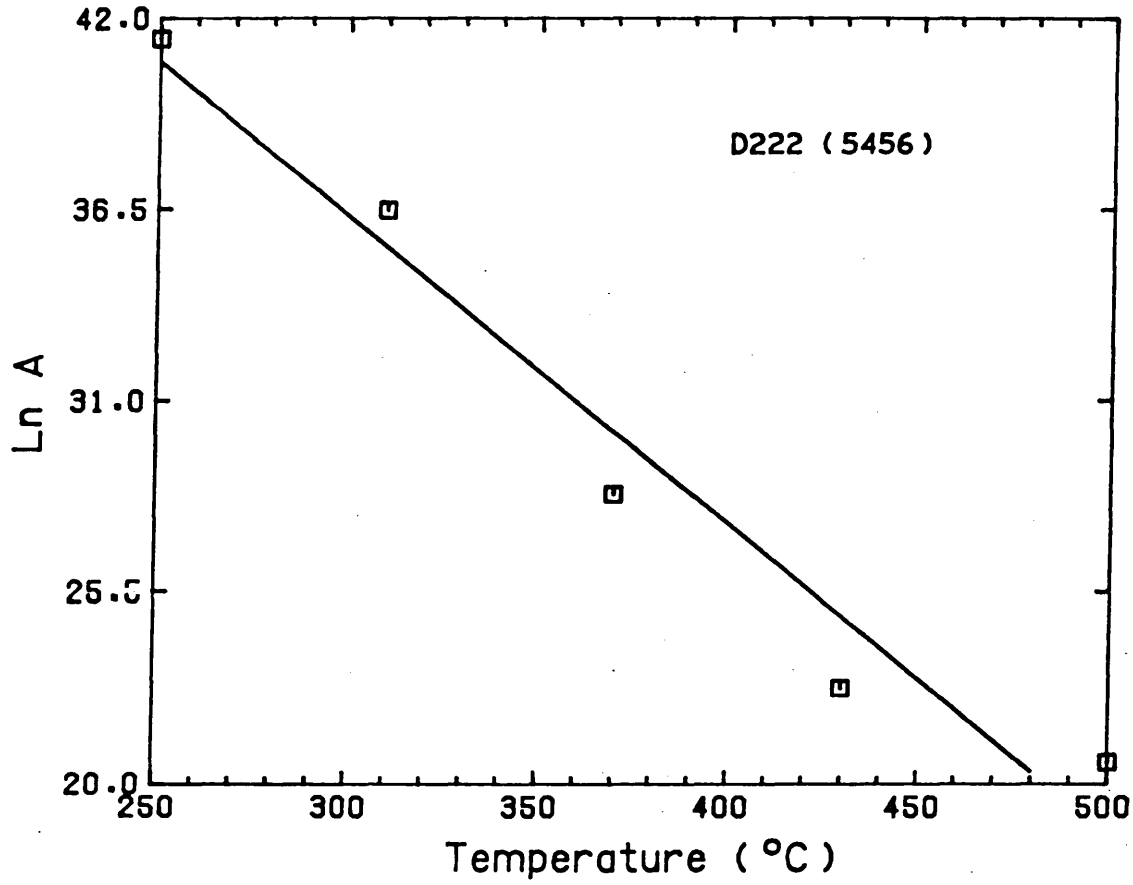


Fig. 39. Variation of A with Temperature, alloy D222 (5456)

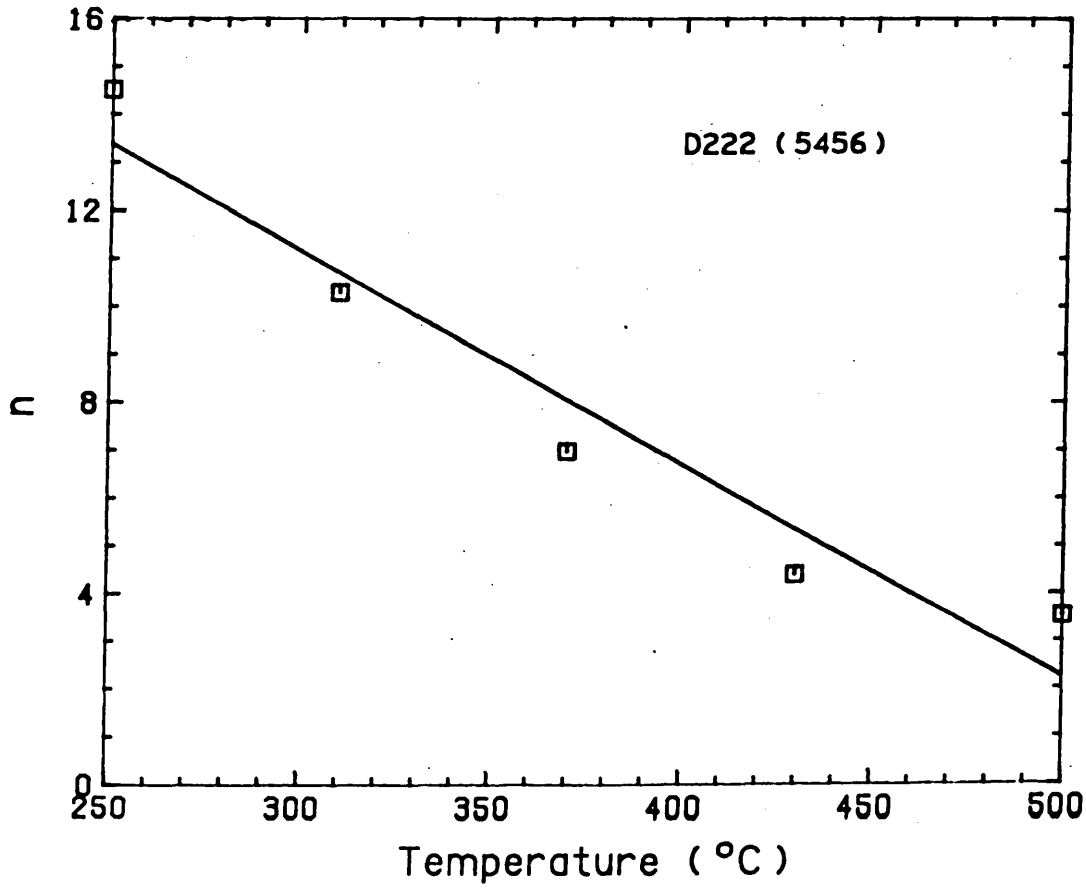


Fig. 40. Variation of n with Temperature, alloy D222 (5456)

relationship appears to fit the data in an obviously improved manner and the transition point is virtually impossible to detect. Thus the trends indicated for A, α, n and ΔH are probably justified and would suggest that the sinh relationship should be adjusted to something of the form:-

$$\dot{\varepsilon} . \exp \frac{\Delta Hf(T)}{RT} = Af(T) . \text{Sinh } (\alpha f(T)\ \sigma)^{nf(T)}$$

where the actual variations of A, α, n and ΔH with temperature need to be evaluated. Assuming linear relationships with temperature for LnA, α and n and fitting a 3rd order polynomial for ΔH permits the above relationship to be quantified for the torsion data. Thus plotting LnZ vs LnA + nLn sinh($\alpha\sigma$) using the temperature dependencies indicated above generates the graph shown in Fig. 41. An ideal fit would give a slope of 1 and an intercept of 0. The results give a gradient of 0.92 and intercept of 2.51. This indicates that the relationship does not apply as well as might have been hoped, but inaccuracies have been introduced through the temperature relationships assumed. Fig. 40 shows that n does not vary in a linear fashion with temperature while that for LnA, Fig. 39, does not give a good fit. The most important error is introduced via the third order polynomial fitted to the ΔH data which under predicts the value at low temperature and over predicts at high temperature. Taking these features into account, the resultant plot, Fig. 41, is not as unacceptable as might first have been thought. Further work with more test temperatures within the range would enable better mathematical relationships to be established and a greater degree of accuracy to be obtained. The result would also justify some work on the data minimization techniques to include variation of all four 'constants' with temperature.

Previously we had concluded that the best results for α and ΔH, from graphical means, were 0.019 m^2/MN and 162689 J/mole respectively. Using these values to establish those for A and n, generates the plot shown in Fig. 42. As the figure shows, the data fits a very good straight line and justifies the sinh relationship for a general hot working equation. The values of A and n generated,

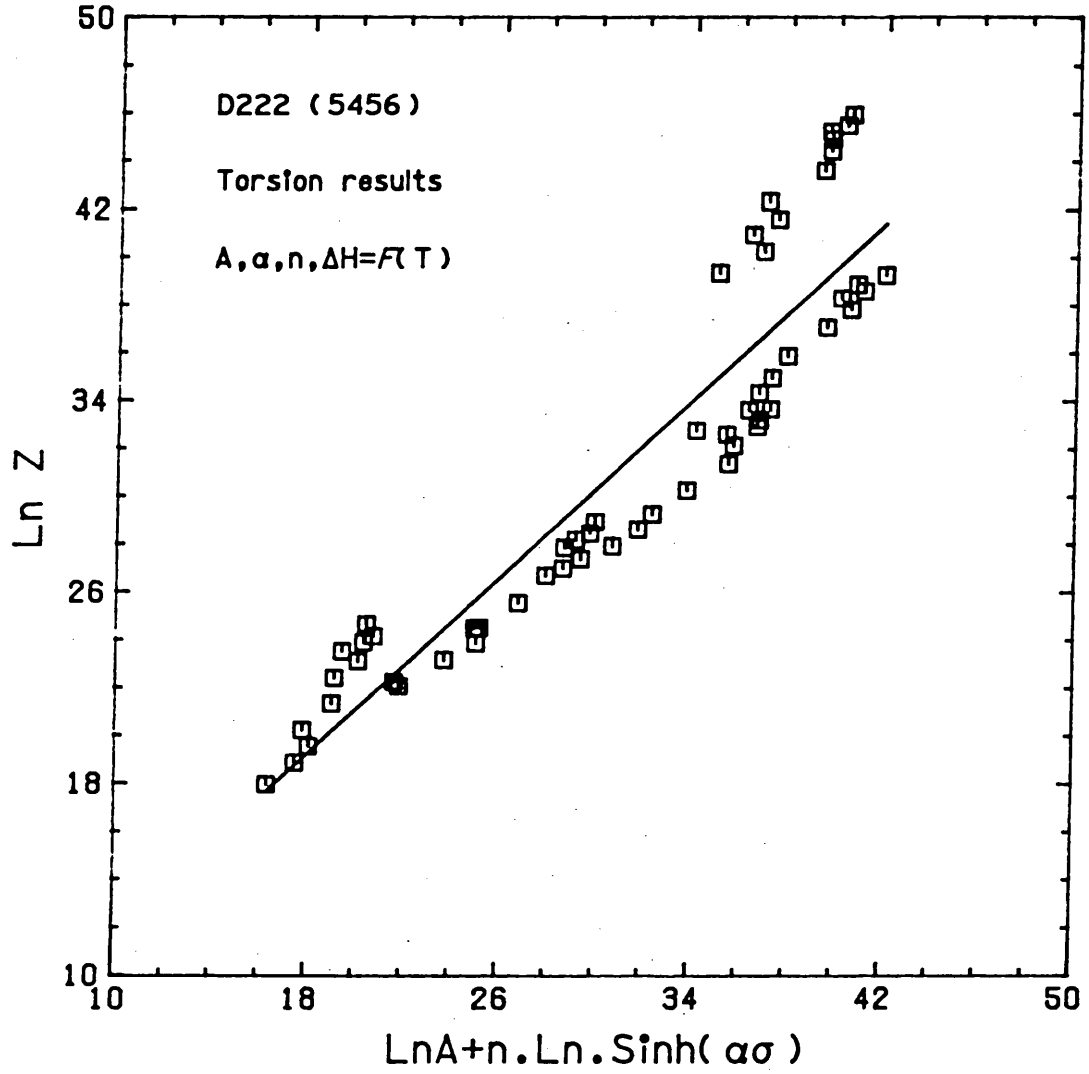


Fig. 41. Hot working relationship for temperature dependent A, α, n and ΔH

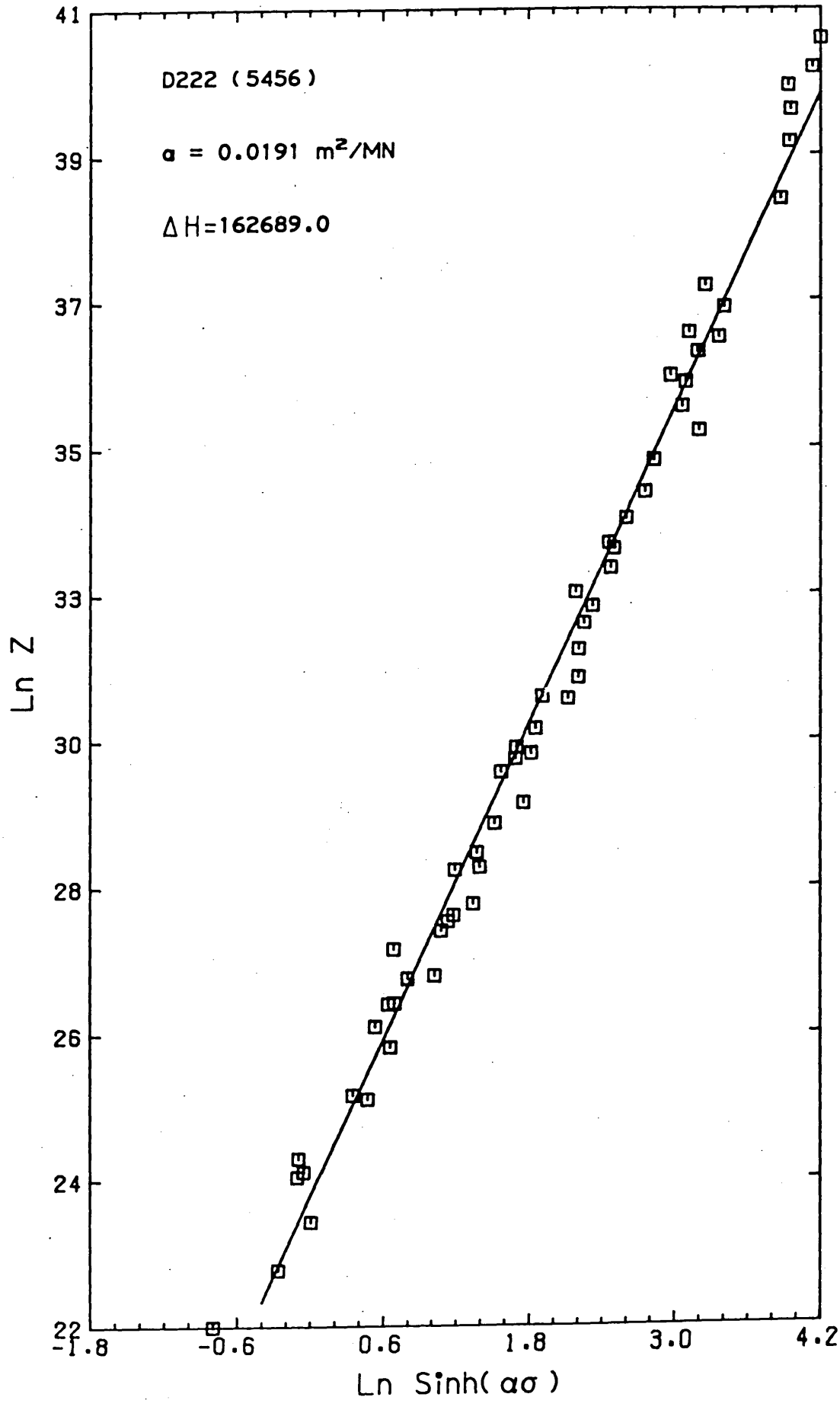


Fig. 42. LnZ vs Ln Sinh (ασ), alloy D222 (5456)

from intercept and slope, are 3.79 and 2.279 x 10^{10} sec^{-1} respectively. These values are in good agreement with those found by the minimization methods for the alloy. From an overall point of view, the values of A, α, n and ΔH from this method agree well with the values established previously and their correlation justifies the use of either technique for their evaluation.

An alternative method for calculating A and n, comparable with that shown above is to directly apply the torsion results by replacing the values of $\dot{\varepsilon}$ and σ with expressions for twist rate and torque. Thus:

$$\text{LnZ may be replaced by Ln } [\frac{2r\dot{\theta}}{3\sqrt{3}l}] \exp(\frac{\Delta H}{GT})$$

and Ln Sinh $(\alpha\sigma)$ by Ln Sinh $[\frac{\alpha\ 3\sqrt{3}\ M}{2\Pi r^3}]$

The second relationship involves direct replacement of stress with a torque relationship while in the first case an area averaged strain rate is derived thus:

$$\dot{\varepsilon} = \int_0^r \frac{\frac{\Pi r\dot{\theta}}{\sqrt{3}l}\ 2\Pi r\ dr}{\Pi r^2}$$

The result of this plot is seen in Fig. 43 producing values for A and n of 1.08 x 10^{10} sec^{-1} and 3.91 respectively. These are in greater error to those calculated above and in the preceding sections. This is due to direct application of a simple stress-torque relationship that does not account for strain rate effects and the assumption regarding strain rate-twist rate above, but it does illustrate agreement with theory and experiment.

The analyses described in this section of work have derived values of A, α, n and ΔH for inclusion in the general hot working equation. The work has shown the possibility of variation of these 'constants' with temperature and a test relationship was shown to describe the data in a reasonable way. However, taking the accepted route of temperature independence, the values of the

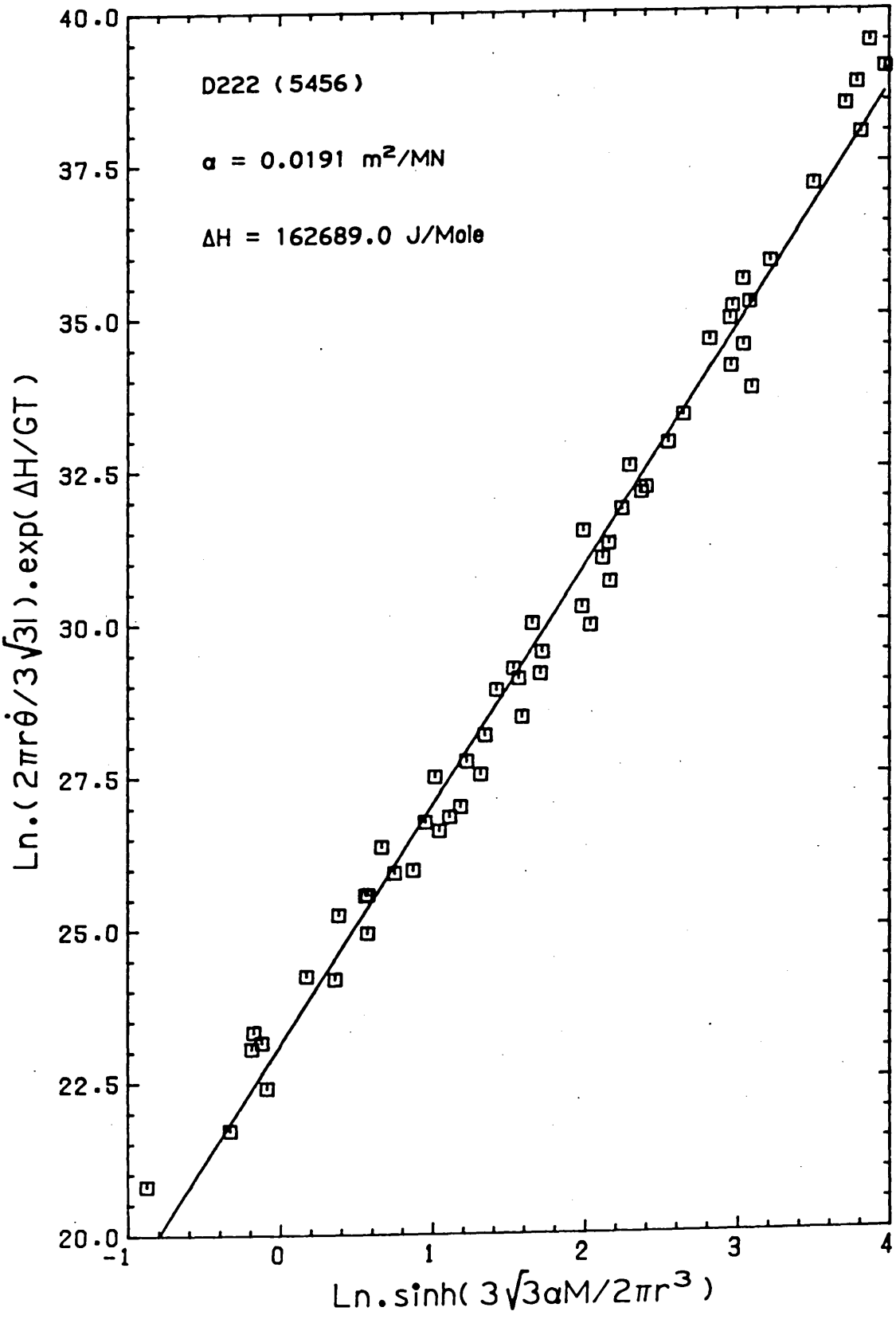


Fig. 43. LnZ vs Ln Sinh (ασ) using substituted torque data, alloy D222 (5456)

constants used in the remainder of the work are those shown in Table 4.9. As a final check, the results of the constituitive equations developed for each material must be looked at to inspect for obvious mistakes i.e. a prediction of a higher stress for 5052 against 5456 under similar conditions would seem unreasonable assuming resistance to deformation is dependent primarily upon magnesium content. Fig. 44 shows the stress predicted for each material for variation of Ln $^{Z}/A$.

As the results show, the strength as indicated by the deformation stress is dependent upon both magnesium content and prior heat treatment. The lower magnesium alloy, 5052, shows a marked reduction in stress notably at low temperatures for given deformation conditions, the reduction becoming less significant at higher temperatures as the solution strengthening effect is diminished. The materials given the extra heat treatment time, 5083(h), and D222 (5456) show reduced resistance to deformation compared with their commercially heat treated equivalents. Once again this difference is greater at lower temperatures.

4.2. Axi-symmetric Upper Bound Analyses

The theoretical descriptions laid out in sections 2.2.1. and 2.2.2. have shown that the upper bound technique may be applied to the axi-symmetric direct extrusion of rod. This section will discuss and present the results obtained by these methods.

4.2.1. Variation of $^{P}/\sigma$ with Extrusion Ratio

Application of Von Mises Yield Criterion within the computer programmes enables values of the group $^{P}/\sigma$ to be obtained for various values of extrusion ratio, R. These results, shown in Fig. 45, indicate that single line plots are produced independent of the ram speed and temperature conditions. For both solutions a non-linear relationship exists between $^{P}/\sigma$ and LnR which agrees with the findings of Halling and Mitchell,[73] Adie and Alexander,[74] and Adie[75] although they only considered low extrusion ratios.

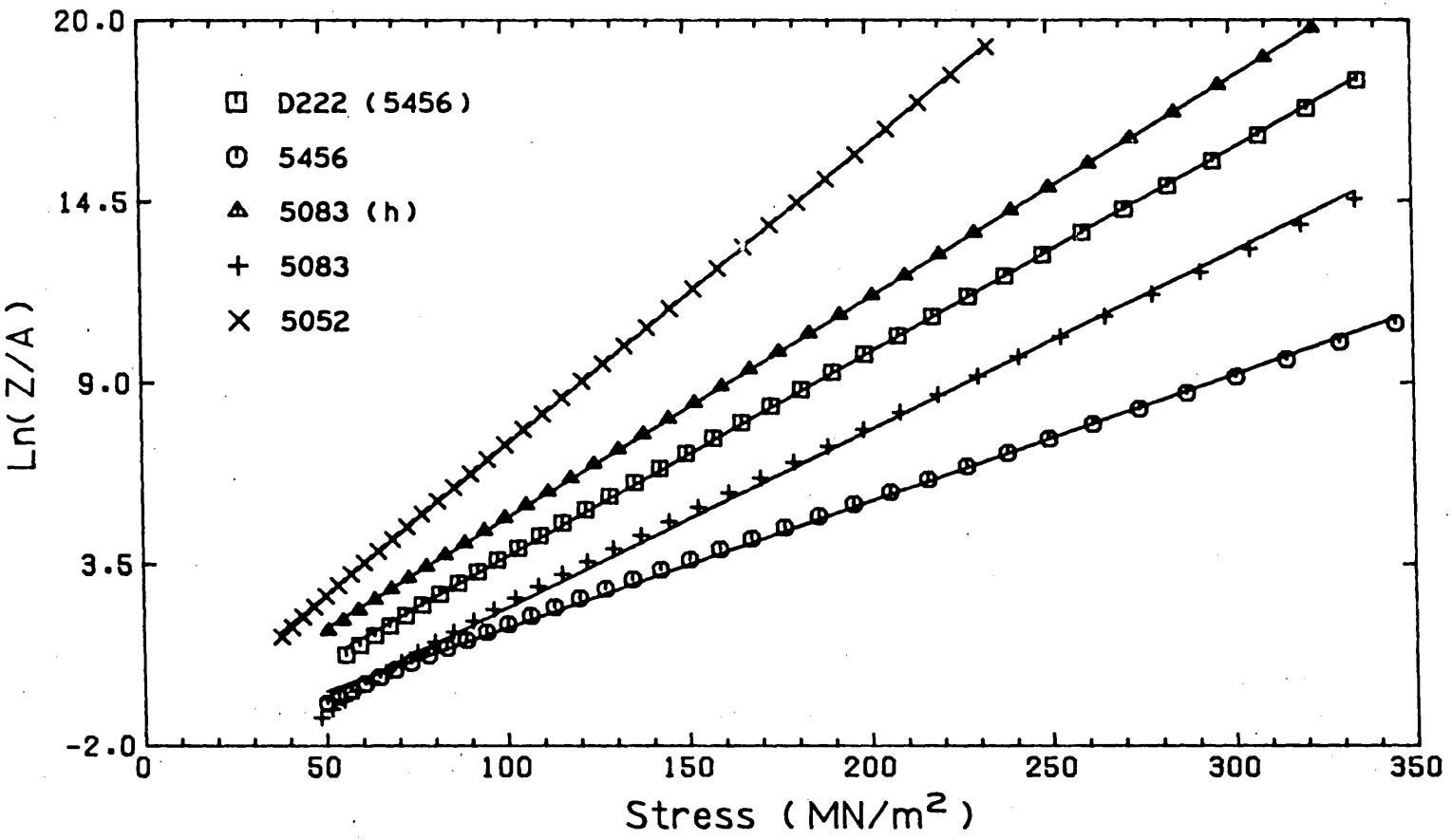


Fig. 44. Stress predictions from constituitive equations

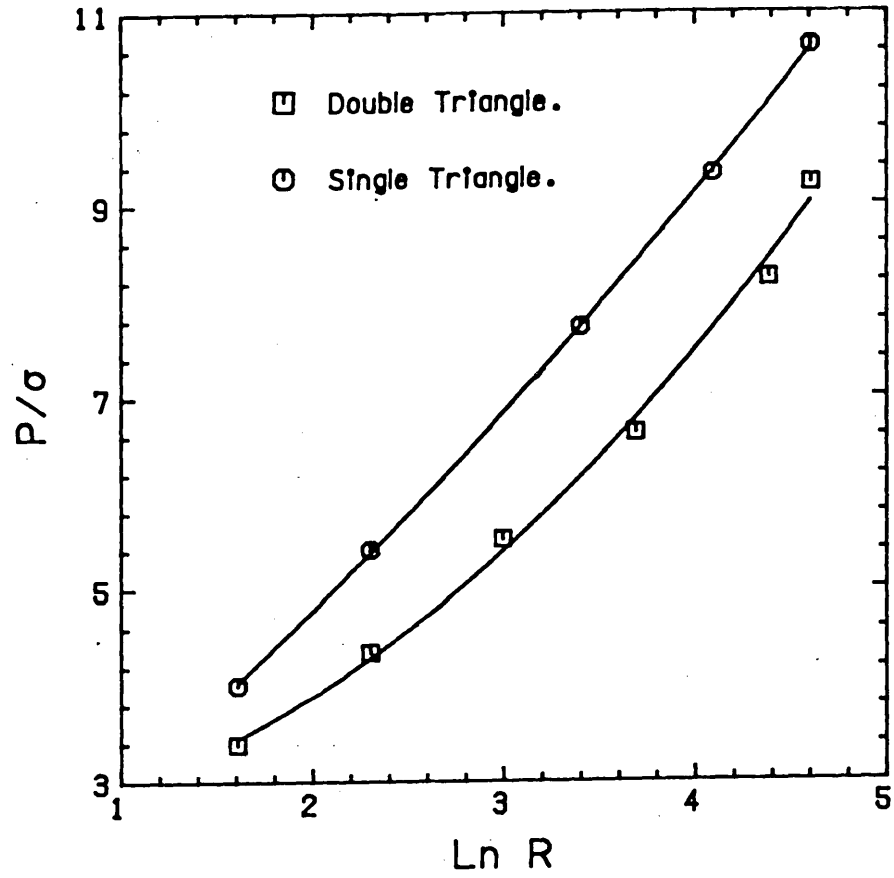


Fig. 45. Theoretical P/σ variation with LnR

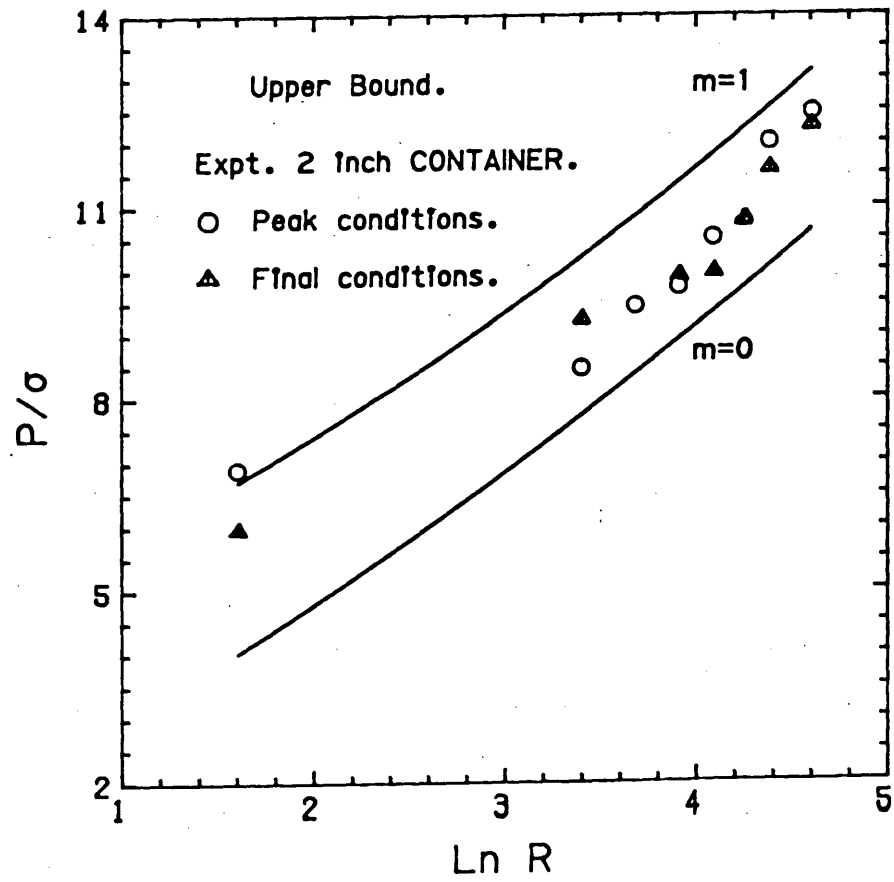


Fig. 46. Comparison of theoretical and experimental P/σ for 2 inch container

This conclusion is hardly surprising since their solutions were the foundation for the present ones. The results show that the single triangle solution predicts a higher value for $^{P}/\sigma$ in every case, indicating that the double triangle arrangement more closely approximates to the deformation zone characteristics in the real world case. At lower values of extrusion ratio the difference between the two solutions is reduced as the effectiveness of the single triangle field is improved. Adie[75] gives results from Halling and Mitchell[73] and Kobayashi and Thomsen,[71] but only for ratios between 1·1 and 10:1. The present results for both 5 and 10:1 agree well with those of Halling and Mitchell and Adie, any discrepancies arising from the use of differing minimization techniques. Kobayashi and Thomsen's results are marginally lower in both cases.

The production of a result from either method involves computer optimization via the itterative method outlined in sections 2.2.1. and 2.2.2. This means that both methods require quite considerable compilation and execution times and are therefore expensive in terms of cost and time. This is found to be even more relevant to the double triangle case where application of Simpson's Rule for integration and optimization of four variables led to the solution being submitted as a batch job to be run overnight. After producing the values shown in Fig. 45 it was decided to abandon the double triangle field technique because of the increased accuracy not outweighing the increased cost and time factors involved.

The single triangle technique was then concentrated upon to produce the theoretical loads and relationships described in the following sections. At lower extrusion ratios the single triangle predictions of $^{P}/\sigma$ may be related to LnR by a linear equation for simplicity. This takes the form

$$C = 0.6 + 2.15\ \mathrm{LnR}$$

where C is the load constant. It is this expression that will be used in strain rate calculations (section 2.3) for the strain during extrusion. Incorporation of a term to account for the energy dissipation due to container/billet friction permitted the calculation of a maximum and minimum

value depending upon whether sticking friction or perfect lubrication conditions applied. The introduction of this feature is shown in Fig. 46 where $^{P}/\sigma$ is plotted against LnR as before. The different friction conditions, illustrated by the plots for m = 0 and m = 1, (i.e. the shear stress in the material = mK) introduce a possible spread in the results of approximately 3 units in $^{P}/\sigma$. Also included in this figure are average experimental results for the 2 inch container while Fig. 47 is drawn for the larger 3 inch diameter container. From the aspect of the theoretical predictions both containers show identical results while the experimental results for the smaller container show consistently larger values of $^{P}/\sigma$ than those applicable to the larger one. In each case results are presented for experimental conditions applying to both maximum; i.e. peak, and minimum pressure. The values of flow stress were calculated from temperatures predicted for each condition by the methods shown in sections 2.5.1. and 2.5.2. and using the constants shown in Table 4.9 in the constituitive equation. In both cases the result for minimum pressure has a higher value for $^{P}/\sigma$ since the higher temperature, compared with peak conditions, results in a lower flow stress and thus increased value. Had the temperature rise calculations been accurate, we might have expected the peak and minimum values to have coincided since the pressure applicable to the pertaining conditions also reflects the status of the flow stress. It would be wrong to draw too many conclusions from these experimental points since, as will be seen in subsequent sections, the single line relationship between $^{P}/\sigma$ and LnR does not hold and average values must be used in this case. This average value will reflect the spread of conditions applied to each ratio and will therefore not be consistent across the range of ratios illustrated; i.e. at low ratios, lower temperatures may be employed where this would prove impossible at the higher ratios. The results for the two inch container show a much better correlation with the theoretical predictions than do the larger diameter results. This is a consequence of the 2 inch container results being incorrect. As was mentioned in the experimental procedure, two steel half rings were placed upon the container surface to protect it from damage by the ram. This leads to a constant

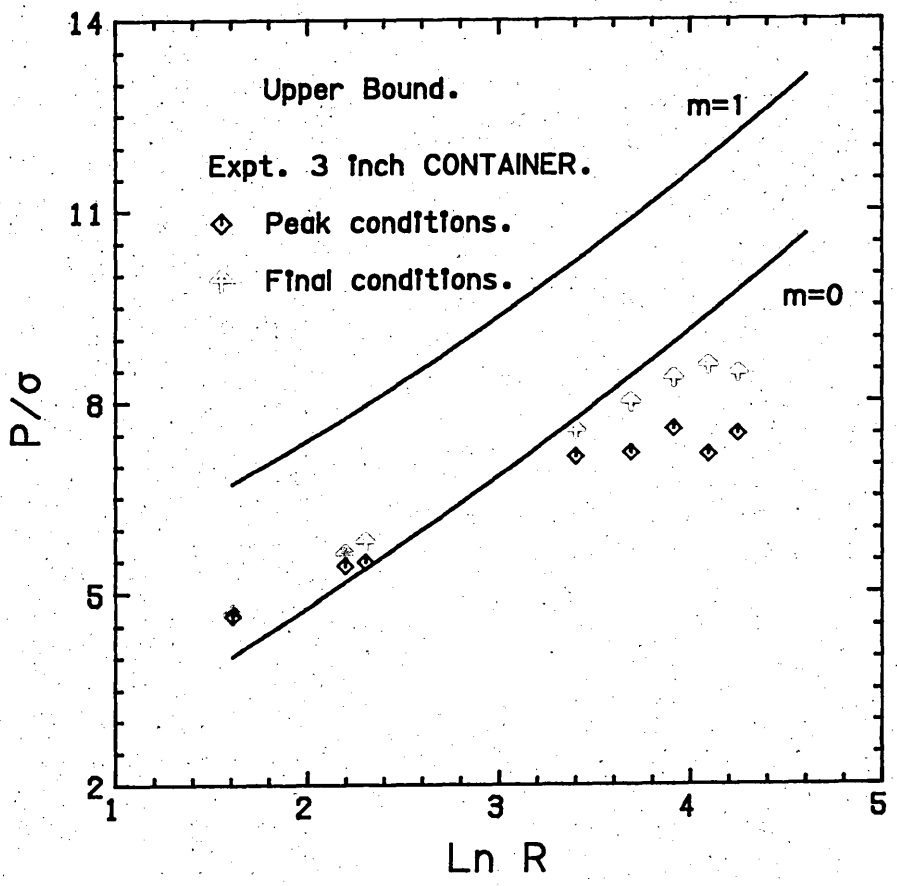


Fig. 47 Comparison of theoretical and experimental P/σ for 3 inch container

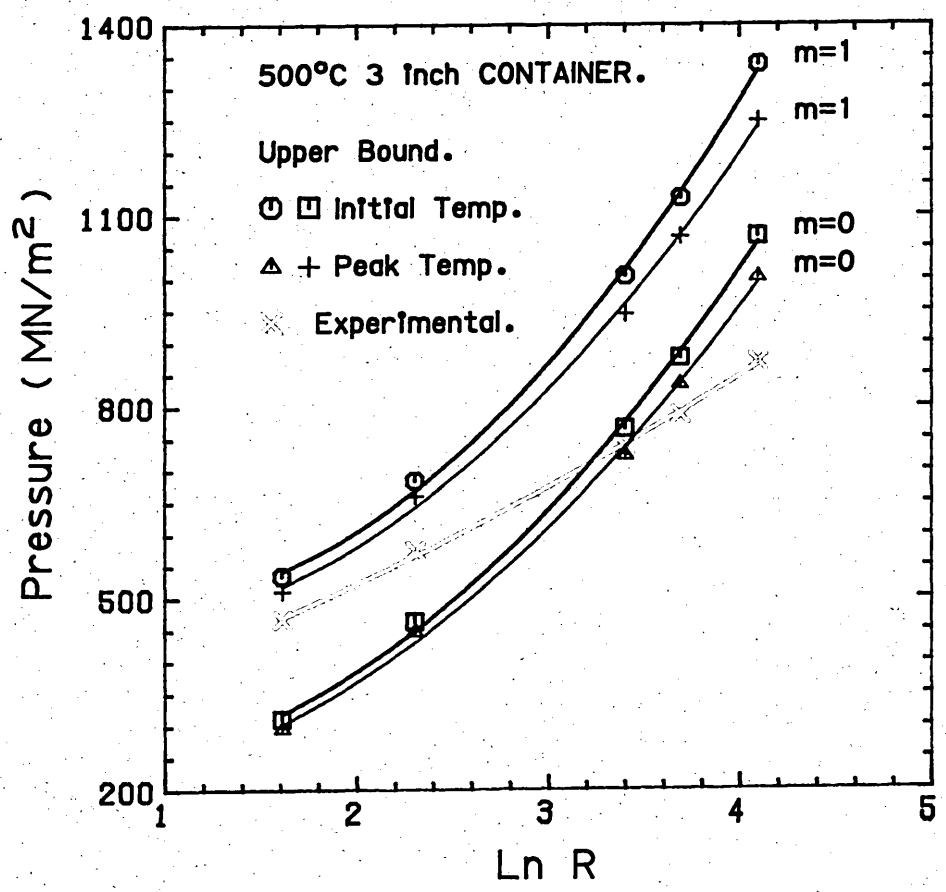


Fig. 48. Pressure prediction for 3 inch container

length of billet being left in the container, equal to the ring thickness, for all extrusions carried out. Thus a greater proportion of billet remains for the smaller diameter than the larger one and the minimum pressures for each are therefore not comparable. The 3 inch results are more correct and show that the theoretical prediction is a true upper bound since the predicted values are above those found experimentally.

4.2.2. Theoretical Pressure Predictions

Inclusion of stress calculation from the constituitive equations developed earlier, using the theoretical strain rate and various input temperatures, permits a theoretical pressure to be predicted from the upper bound solutions. Theoretical pressures were predicted for input temperatures corresponding to the initial and peak temperature and for both extremes of frictional conditions, denoted by $m = 0$ and $m = 1$, are shown in Figs. 48, 49 and 50. Calculation using the peak temperature reduces the pressure, in all cases, from that found using the initial temperature since the lower flow stress which results, reduces the energy dissipations. At high ratios the difference between peak and initial temperatures is greater, the difference in predicted pressures also increases. The experimental results, for the 3 inch container, show that the range of predictions include those for ratios below 25:1 while the experimental results fall below at higher ratios. This may be due to the single triangle deformation field being inappropriate at these higher ratios, or due to an incorrect theoretical temperature at the peak. The 2 inch container results, for lower temperature runs shown in Fig. 49, show a similar trend except in this case the smaller billet volume and lower initial temperature result in a more significant temperature rise at the peak pressure and therefore a greater decrease in theoretical pressure for this condition. The inclusion of the friction dissipation term is also somewhat erroneous since it takes only a superficial account of the situation. It takes no account of the shear zone depth associated with sticking friction which means an underestimation of the energy dissipated. This may be more important at higher extrusion ratios. Fig. 50 shows the comparison for 500°C runs using the 2 inch container. In this case

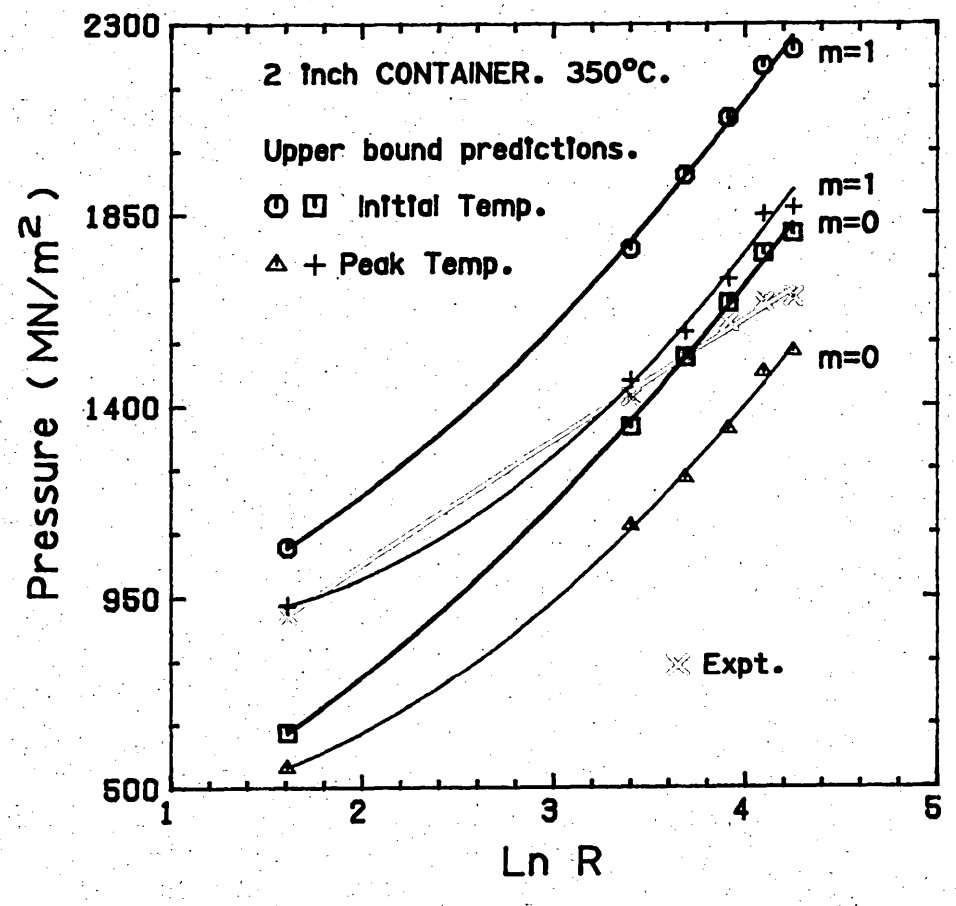


Fig. 49. Low temperature pressure predictions for 2 inch container

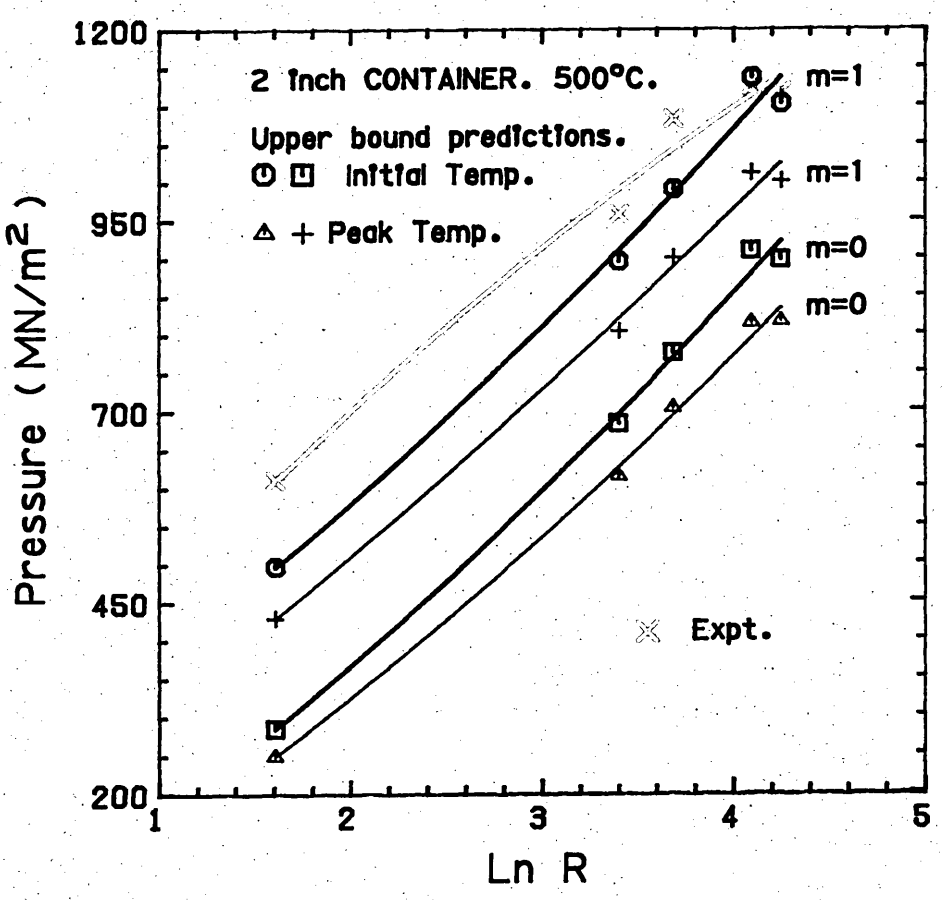


Fig. 50. High temperature pressure predictions for 2 inch container

the theoretical predictions are consistently lower than the experimental values and indicate that the upper bound model is incorrect under these conditions. The cause of this discrepancy, as will be seen later, is an incorrect deformation field prediction. The theoretical model does not predict a deformation zone shape change with temperature since it does not include any temperature-property relationships to generate this. The apparent inconsistency between Figs. 48 and 50 may be explained by considering the actual temperatures used. Although the specified temperature in each case is 500°C, this is the initial temperature and not that actually employed in the calculation. The data for the 3 inch container contained temperatures of about 460°C while for the smaller diameter work, the temperature approximates to 480°C. Thus, as will be seen in Fig. 51 the predicted value of pressure reduces to and becomes less than the experimental value as the temperature is increased. Therefore the under-estimation in Fig. 50 compared with the over-estimation in Fig. 48 is due to the operating temperature difference.

Fig. 51 shows the variation of pressure with temperature for a reduction ratio of 30:1 and a ram speed of 4 mms/sec. The results show that at 440°C and below the theoretical predictions over-estimate the pressure found necessary to extrude the material. The reasons for this may be found from looking at the deformation zone angles across this range.

Temp	α	ϕ
°C	m = 0	
346	49.86	75.16
394	49.92	75.14
443	49.98	75.10
480	50.05	75.07

As these figures show, the model predicts virtually no change in deformation zone shape or dimensions as the temperature is varied. More specifically the predictions for extrusion runs 171 and 172 have shown identical results while the gridded sections for these conditions, shown in Figs. 88 and 89, illustrate the dramatic

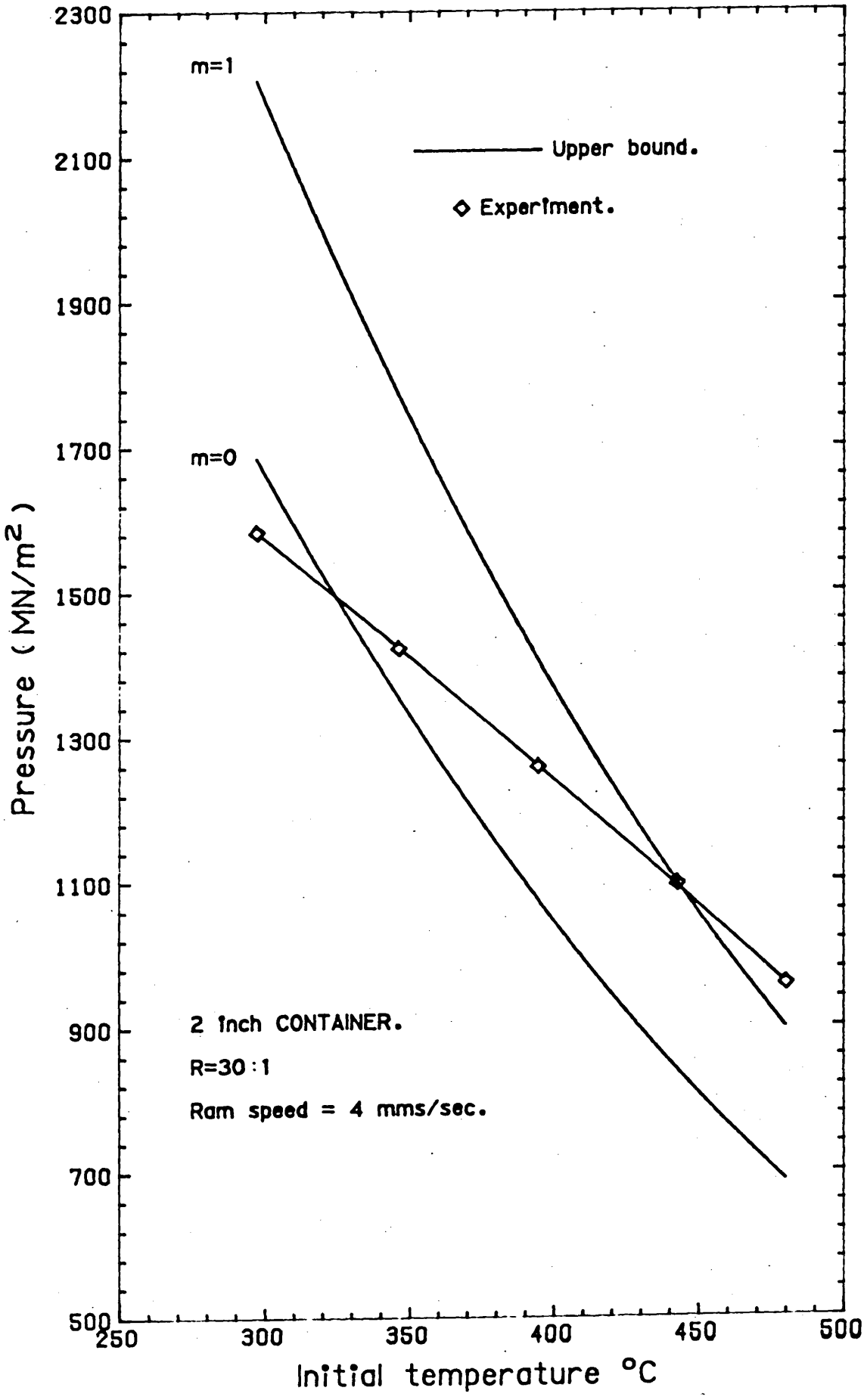


Fig. 51. Variation of predicted and experimental pressures with temperature.

variation in deformation conditions found in the experimental case. Inspection of these gridded sections indicates that the approximate deformation zone angles are $\alpha = 55^{o}$, $\phi = 70^{o}$ for the $335^{o}C$ case and $\alpha = 45^{o}$, $\phi = 73^{o}$ for the $465^{o}C$ case. Thus the low temperature angles are in reasonable agreement with the theoretical ones while the high temperature values show a greater deviation. The solution using the experimental values raises the predicted pressure to 481 MN/m^2 for m = 0 and 693 MN/m^2 for m = 1. This is seen in Fig. 52. Although this only raises the pressure by up to 10% it may be seen how the over rapid fall in predicted pressure is caused by an inadequate modelling of the deformation at high temperatures. This change in deformation zone with temperature is not entirely unexpected. Although this type of change has not been reported by previous workers, it would seem a reasonable consequence of the reduced flow stress since at low temperatures the material can withstand greater stress gradients and thus resist any deformation zone shape change. At high temperatures this ability to withstand any stress gradients is reduced by the material softening and the effects of deformation are consequentially found farther back into the billet. It would appear, therefore, that the model needs further development for high temperature prediction to include a deformation field capable of imposing the shear found farther back into the billet at the container/billet interface.

To sum up, it seems that the single triangle axi-symmetric upper bound solution results, when applied to pressure prediction, fails to reproduce the experimental situation under conditions of high extrusion ratio or high temperature. It would be reasonable to assume that the double triangle field would overcome most of the problems associated with the former case, but doubtful if it could enhance the situation with respect to the latter. To improve the analysis it would be beneficial to remodel the deformation in a more accurate manner. Inspection of partially extruded billets shows that the dead-metal-zone boundary is rarely a straight line while temperature increases cause deformation to be spread farther back into the billet. From these observations it is possible to put forward suggestions for the types of fields that could more accurately describe the flow.

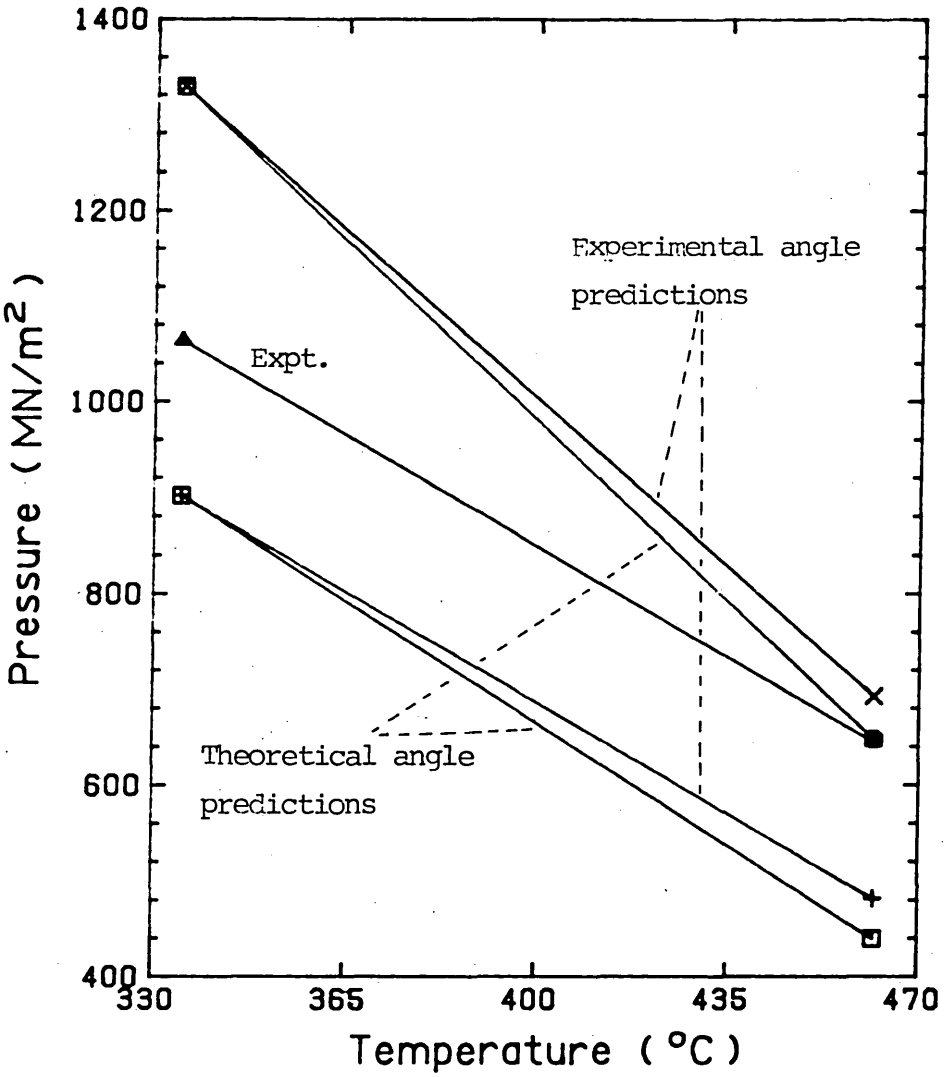


Fig. 52. Pressure variation with temperature using experimental deformation zone angles

Ideas, along these lines are shown in Fig. 53. The upper suggestion uses a simple double triangle arrangement to model the curved dead-metal-zone boundary while the lower diagram uses a more complex 4 triangle arrangement. This has the advantage of achieving the same as the diagram above while, in addition, also permitting the deformation to spread back into the billet at the edge. The problems would arise in deriving a hodograph to fit these fields.

The comparison of predicted pressures for 2 and 3 inch diameter containers shows that for identical input conditions, the smaller case requires a greater pressure. For a reduction of 30:1 at a ram speed of 4 mms/sec and temperature of 346°C the results are:-

	3 inch		2 inch	
	m = 0	m = 1	m = 0	m = 1
Pressure MN/m^2	1317	1730	1351	1768

The resulting angles are equal for all cases and so the pressure variation is due to some other feature. In this case the strain rate variation between the two causes the difference and it is this feature which will be discussed further, in section 4.2.4.

4.2.3. Variation of Deformation Zone Angles

A direct result of the predictions found, from both single and double triangle upper bound solutions, in section 4.2.1. is the variation of the angles describing the deformation field geometry with extrusion ratio. The results for both techniques can be seen in Table 4.16. These results are plotted against extrusion ratio in logarithmic form in Figs. 54 and 55. For the single triangle case, Fig. 54, the angle ϕ steadily increases with extrusion ratio indicating that the effect of the deformation is being felt farther back into the billet in the central portion. This is not unexpected since the higher the reduction, the greater is the imposed strain producing increased strain gradients within the material. Thus the likelihood of material being affected

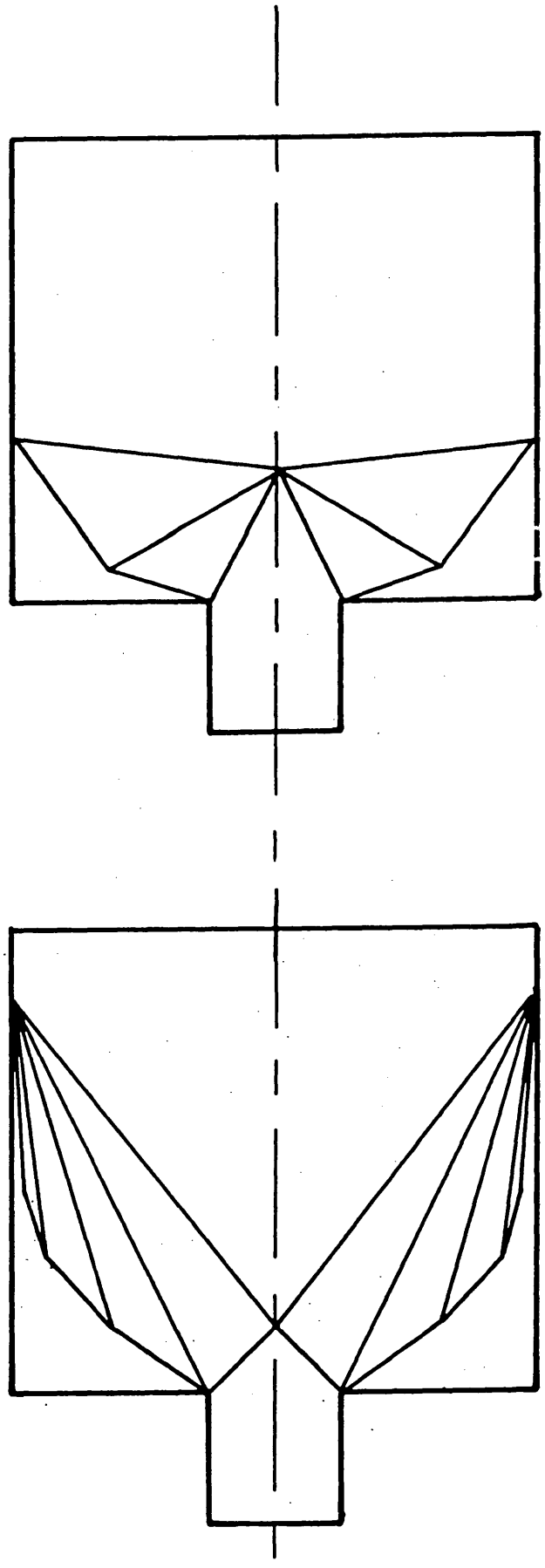


Fig. 53. Alternative velocity fields for direct rod extrusion

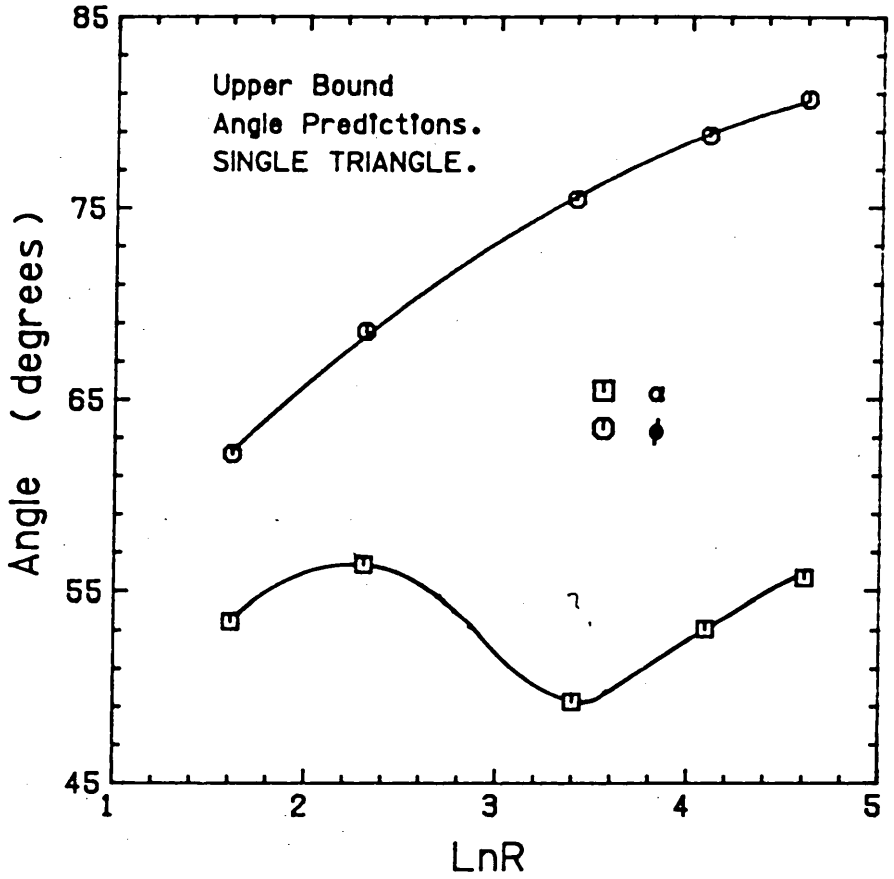


Fig. 54. Deformation zone angle variation with extrusion ratio from single triangle analysis

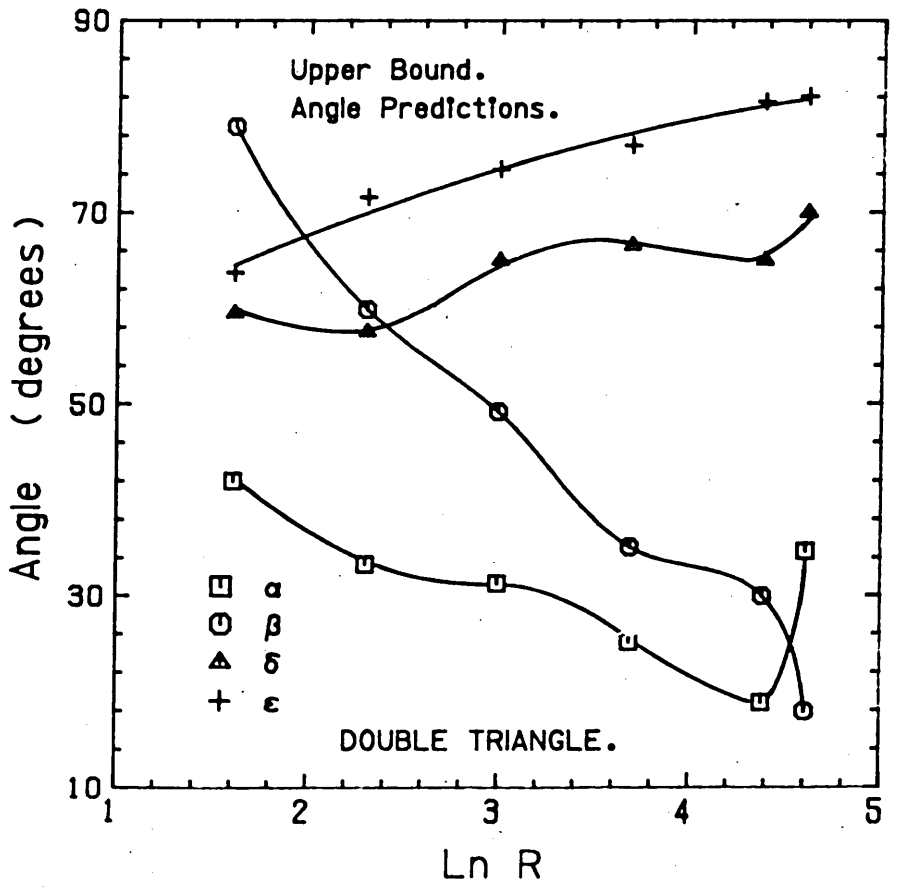


Fig. 55. Deformation zone angle variation with extrusion ratio for double triangle analysis

Double Triangle					
R	P/σ	α	β	δ	ε
5	3.39	42.0	78.9	59.5	63.7
10	4.35	33.3	59.9	57.5	71.6
20	5.52	31.3	49.2	64.9	74.5
40	6.63	25.2	35.1	66.6	76.9
80	8.23	18.8	29.9	65.0	81.5
100	9.22	34.7	17.9	69.9	82.1

Single Triangle			
R	P/σ	α	ϕ
5	6.96	53.5	62.2
10	9.37	56.4	68.6
30	13.39	49.3	75.5
60	16.15	53.1	78.8
100	18.44	55.7	80.8

Table 4.16. Deformation Zone Angles from Upper Bound Predictions.

towards the rear of the billet is increased. The results of an increased reduction on angle α is more complex. The trend above a ratio of 30:1 is one of a generally increasing α while below this minimum value the angle rises at 10:1 before falling once again. This inflection is the direct result of the geometry change discussed in section 2.2.1. At low ratios location 0_2 is to the rear of B, (Fig. 4), while at 30:1 this situation changes to 0_2 being forward of B. This trend is therefore a result of the mathematical optimization producing a reduced value of P/σ in these situations. It does not reflect how the quasi-static deformation zone geometry will change in the practical case. In Fig. 55 a similar feature is observed. All four angles contain some irregularities at ratios around 10:1, 40:1 and 80:1. This is due to the relative magnitudes of A and R_E (Fig. 6) changing as the optimum solution is computed. Although the results may not reflect the true activity within the material, general trends may be found and some rough quantitative use made of the results. From Fig. 55, the general overall trend of δ is one of an increase with increasing extrusion ratio. In section 2.3 the derivation of a mean strain rate during extrusion was set out in which, originally, the deformation was assumed to occur in a cone of semi-angle 45°. These results show how this cone angle, δ in this case, varies with extrusion ratio. Thus inclusion of this variation in the strain rate expression should improve its accuracy. Approximating the relationship to a straight line gives the result:

$$\omega = 54.1 + 3.45 \, \mathrm{Ln}R. \qquad (100)$$

where ω is the deformation cone semi angle.

4.2.4. Strain Rate Determination from the Upper Bound Analysis

As was pointed out in section 2.2.1., the single triangle upper bound analysis permits strain rates to be computed at the centroid of each element. The values are calculated using equations 26 and 27 and the 5 x 10 element mesh generates 50 values. The strain rate at a velocity discontinuity is infinite so calculation at these points is impossible. Sample results for reductions of

30:1 at a ram speed of 4 mms/sec and for both 2 and 3 inch diameter containers can be seen in Table 4.17. As these results show, the elemental strain rate increases towards the billet centre and on passing farther into the deformation zone. In the latter case the cause is the increased strain as the reduction is increased. In the former case, as equations 27 show, the polar co-ordinate strain rates are dependent upon $^1/r$ which means the reduced value of r in the central regions, n = 5, generates a correspondingly increased result. The results also indicate the cause of the discrepancy in pressure predicted for 2 and 3 inch containers for identical input conditions. Comparing the results for both temperatures shows that in all cases the strain rate calculated for the 2 inch container is greater than in the larger case. As the pressure is calculated from a knowledge of flow stress, calculated from the constituitive equation, this necessarily implies a greater pressure prediction. The greater strain rate calculated for 2 inch conditions is a result of the $^1/r$ dependence, since this value will always be greater in this case compared to the larger diameter for similar geometrical conditions. The marginal variation between strain rates, calculated for different temperature conditions, is a result of slight variations in the minimized final result giving marginally different values of α and ϕ. In the practical case, a strain rate variation might be anticipated due to the change in deformation zone shape. This would result in an alteration to the time taken for the strain to be accomplished producing a new strain rate value.

In order to compare these elemental values of strain rate with that used for the experimental work, it is necessary to calculate some mean value over the entire deformation zone. As was pointed out in section 2.3., there would appear to be four methods of achieving this:-

(1) Taking a mathematical mean of the 50 values generated. This, unfortunately, takes no account of the volumes or areas to which each value pertains.

(2) A volume averaged strain rate can be calculated which weighs the values with respect to the individual element volumes to which they apply. The value is generated by taking the product of elemental strain rate and elemental volume, summing the 50 cases and then dividing by the total deformation zone volume.

M	1	2	3	4	5	6	7	8	9	10
N										
1	.41	.49	.57	.66	.77	.93	1.18	1.60	2.36	3.98
2	.52	.63	.73	.85	.99	1.20	1.52	2.06	3.03	5.12
3	.73	.88	1.03	1.19	1.39	1.67	2.13	2.89	4.24	7.17
4	1.22	1.47	1.72	1.98	2.31	2.79	3.55	4.81	7.07	11.94
5	2.75	3.32	3.86	4.45	5.20	6.28	7.99	10.83	15.91	26.87
1	.41	.50	.58	.67	.78	.94	1.20	1.62	2.38	4.01
2	.53	.64	.74	.86	1.00	1.21	1.54	2.08	3.06	5.16
3	.74	.89	1.04	1.20	1.40	1.69	2.15	2.92	4.28	7.22
4	1.23	1.49	1.74	2.00	2.33	2.82	3.59	4.86	7.14	12.04
5	2.78	3.36	3.90	4.50	5.25	6.35	8.08	10.94	16.07	27.09
1	.54	.65	.75	.87	1.01	1.23	1.56	2.11	3.10	5.24
2	.69	.83	.97	1.12	1.30	1.58	2.00	2.72	3.99	6.74
3	.97	1.16	1.36	1.56	1.82	2.20	2.81	3.80	5.59	9.43
4	1.61	1.94	2.26	2.61	3.04	3.67	4.68	6.34	9.31	16.72
5	3.63	4.37	5.09	5.86	6.84	8.27	10.52	14.26	20.95	35.38
1	.54	.65	.76	.88	1.02	1.24	1.58	2.13	3.13	5.28
2	.70	.84	.98	1.13	1.32	1.59	2.03	2.74	4.03	6.79
3	.97	1.17	1.37	1.58	1.84	2.23	2.83	3.84	5.64	9.51
4	1.62	1.96	2.28	2.63	3.07	3.71	4.72	6.40	9.40	15.85
5	3.65	4.40	5.14	5.92	6.91	8.36	10.63	14.40	21.15	35.65

Table 4.17. Elemental values of strain rate from single triangle upper bound analysis. Mesh of n radial element and m down the dead-metal-zone boundary.

(3) A distance averaged strain rate may be defined by considering the lengths of flow line over which each individual strain rate applies. Thus for each row of elements the individual strain rates are multiplied by the lengths of flow line over which they act, summed, and divided by the total length. These five values are then compensated for area of application by multiplying by the area pertaining to each, prior to dividing by the cross sectional area of the billet.

(4) A time averaged strain rate may be evaluated by calculating the final strain that has been undergone at the final boundary and dividing by the time taken for this to be achieved. For each row, a procedure for area compensation similar to that described above is applied.

The four values of mean strain rate may then be compared to the experimental value calculated following the method described in section 2.3., using equation 70. The expressions for angular and strain variation with extrusion ratio are those found from the upper bound analyses described previously. The results are presented graphically in Figs. 56-59.

As the results show, in all cases an increase in strain rate is predicted for an increased reduction ratio. This is to be expected since an increasing value of extrusion ration gives an increased value of strain. For both container sizes and both low and high ram speeds the volume and distance averaged values give considerably lower results than for the other methods, notably at higher reductions. Thus it would appear that the values are over compensated for the lower strain rate outer regions of the deformation zone. In all cases, the best comparison with the experimental value is found for the time averaged calculation. This is comforting since the basic calculation for the experimental value comes from Felthams[86] analysis which was itself a time based strain rate. The figures show that the experimental value lies above that predicted from theory for all ratios below about 70:1 while above, the time averaged value exceeds it. Comparison of the results for the two container sizes shows that both experimental and theoretical values for the 2 inch case exceed

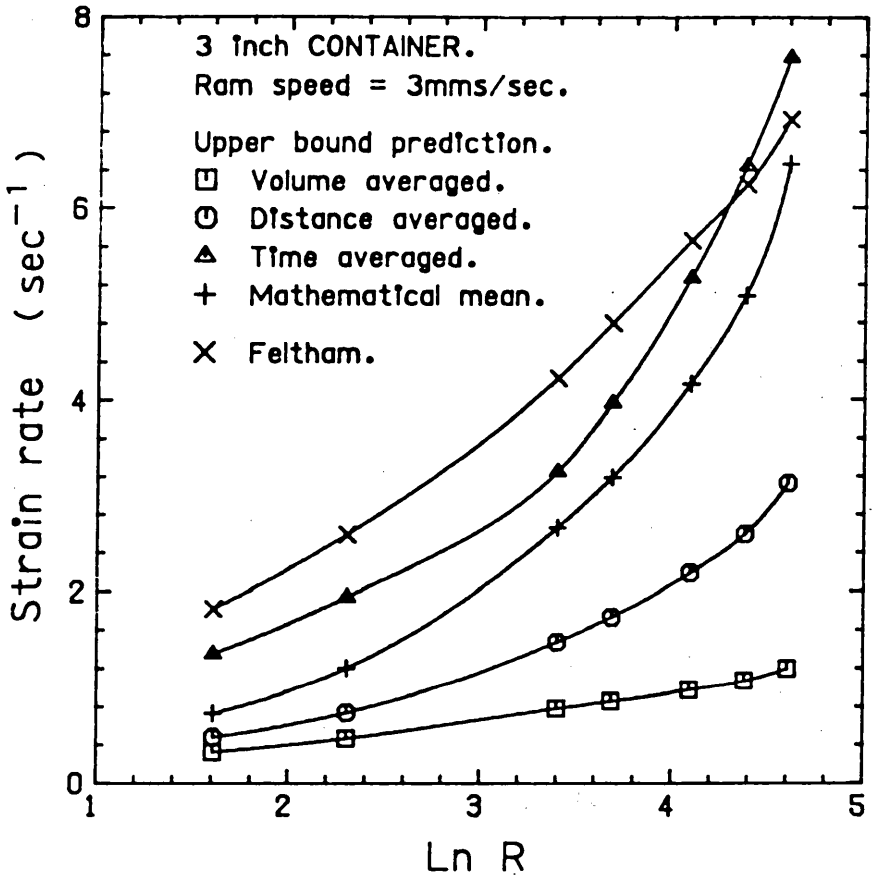


Fig. 56. Upper bound and Feltham's Strain rate variation with LnR

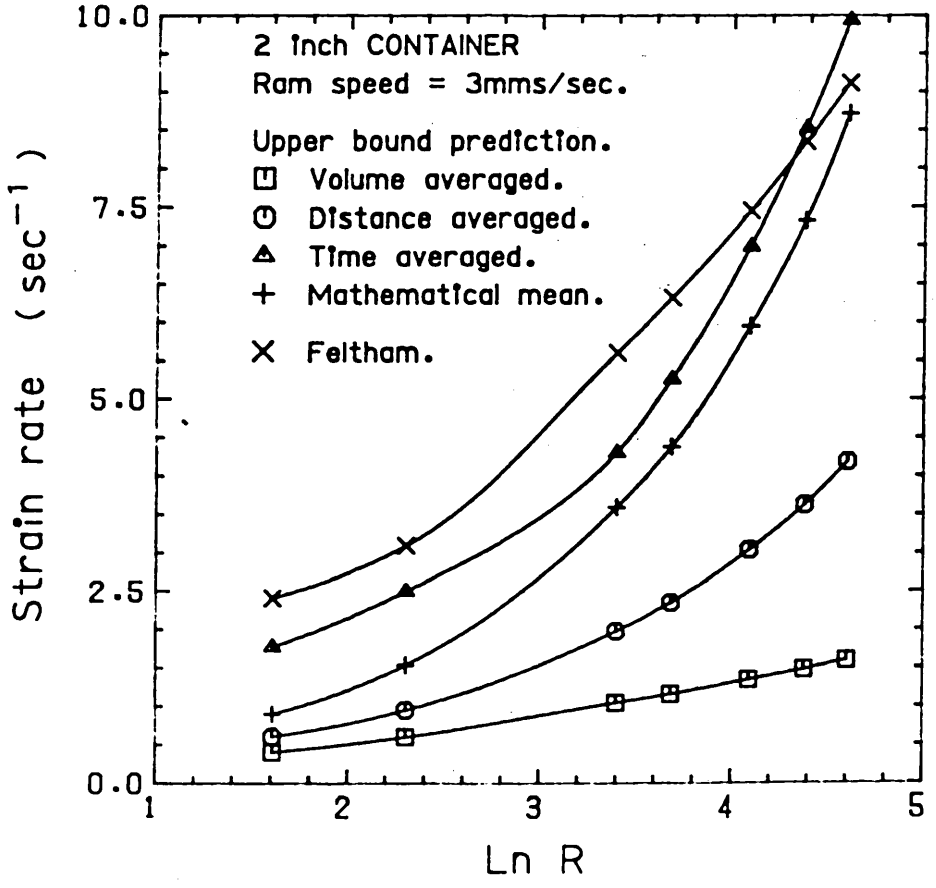


Fig. 57. Upper bound and Feltham's Strain rate variation with LnR

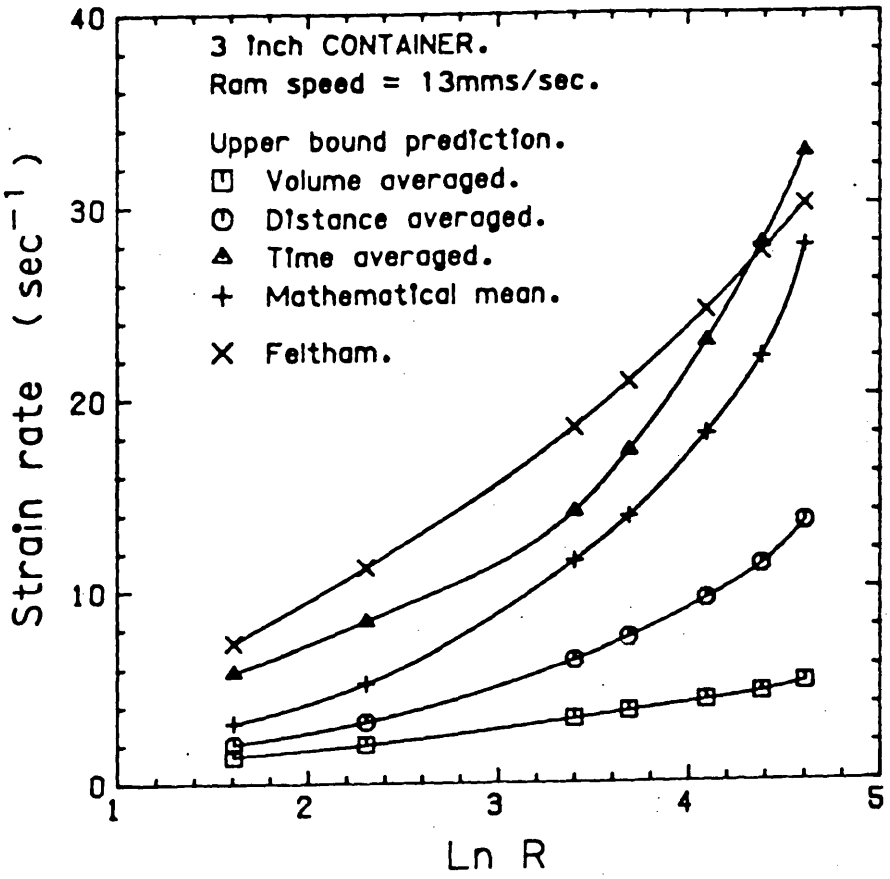


Fig. 58. Upper bound and Feltham's strain rate variation with LnR

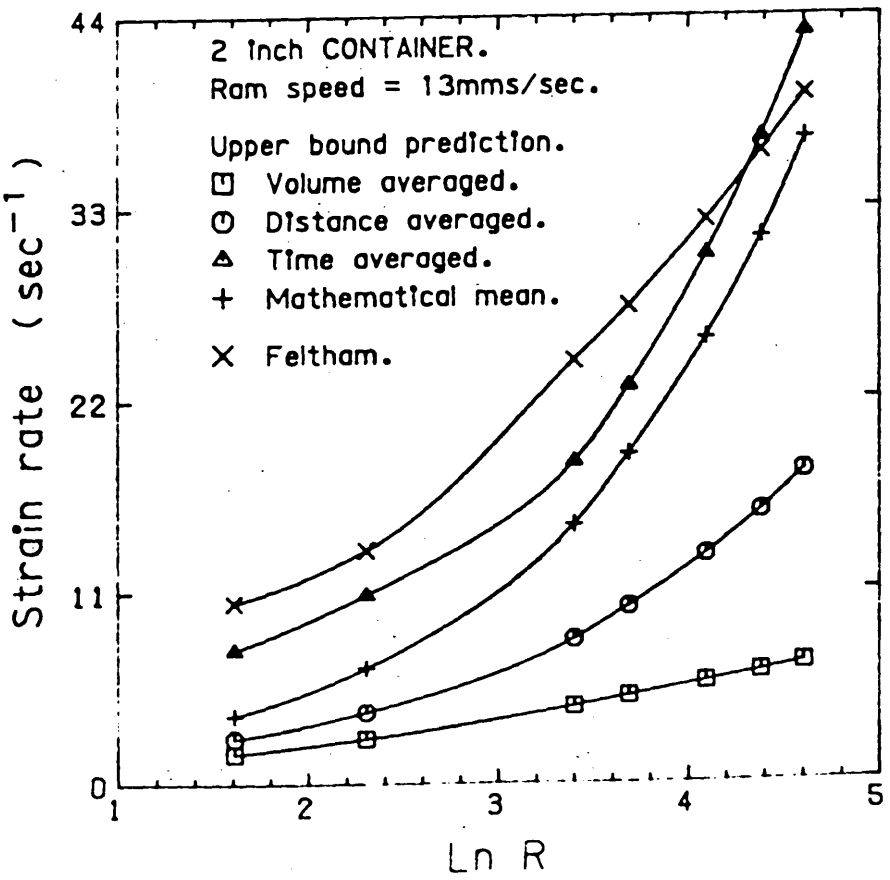


Fig. 59. Upper Bound and Feltham's strain rate variation with LnR

those for the larger diameter. This confirms the reason given in section 4.2.2. for pressure prediction variation between the two billet diameters. Figs. 60 and 61 show the strain rate comparisons for constant reductions of 30:1 with varying ram speed for both container sizes. All lines show a linear relationship between strain rate and ram speed. As would have been expected from Figs. 56-59, the experimental strain rate exceeds the predicted values across the entire range of ram speeds. The difference increasing at higher speeds.

Following the discovery that the average time based strain rate exceeds the experimental one for ratios above 70:1, further investigation of Figs. 48 and 49 may indicate why the experimental line falls below the theoretical one. Besides the reason that the single triangle model is inaccurate at high ratios we can see that a further discrepancy is introduced by this strain rate inconsistency. Thus at high ratios the experimental strain rate is less than that used in the theoretical prediction and accounts, in part, for the over-estimation by the theory. The situation would have been improved by an accurate calculation of the load constant in the experimental value. Instead of a linear relationship for P/σ vs LnR the true representation would have been a curved type which would have served to increase the strain rate term at higher ratios.

In conclusion it would appear that a theoretically predicted time averaged strain rate correlates well with the value used in experiment. The theoretical value is an under-estimate at low extrusion ratios while exceeding the experimental one at large reductions. This finding may explain some of the observations made earlier regarding pressure prediction and its comparison with experimentally determined values. The model predicts a change in strain rate for different diameter billets agreeing with the experimental case, but does not predict a variation with temperature. This would be expected because the model contains no features relating material properties to flow.

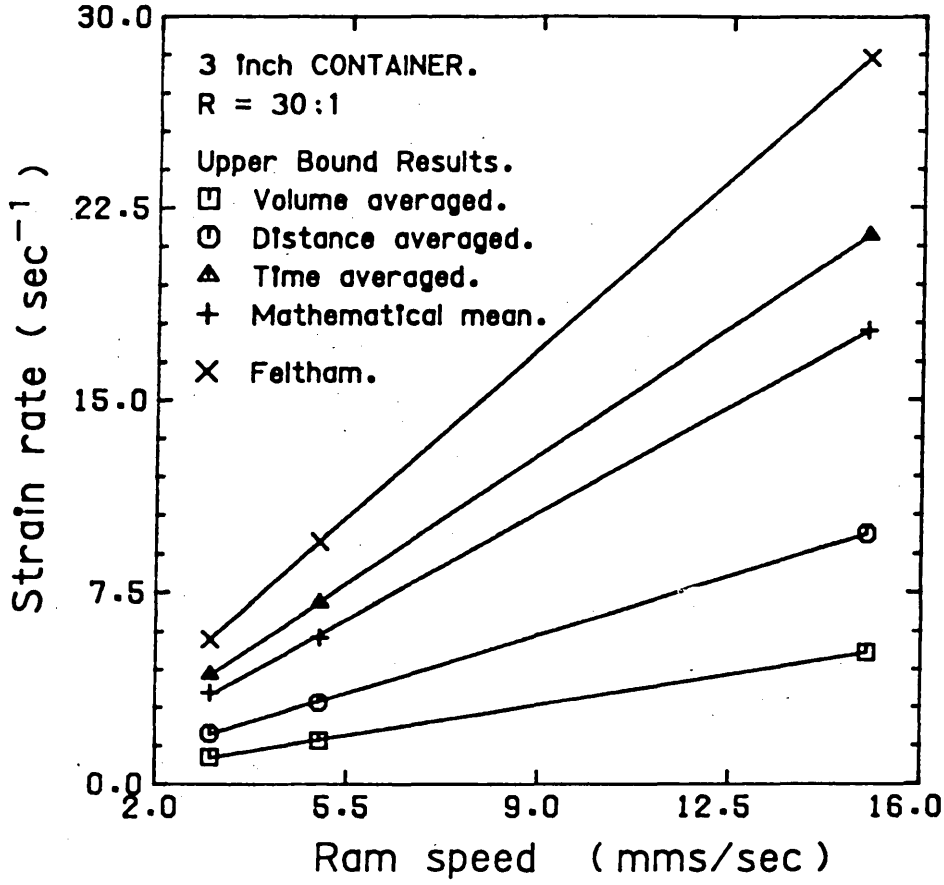


Fig. 60. Upper bound and Feltham's strain rate variation with ram speed

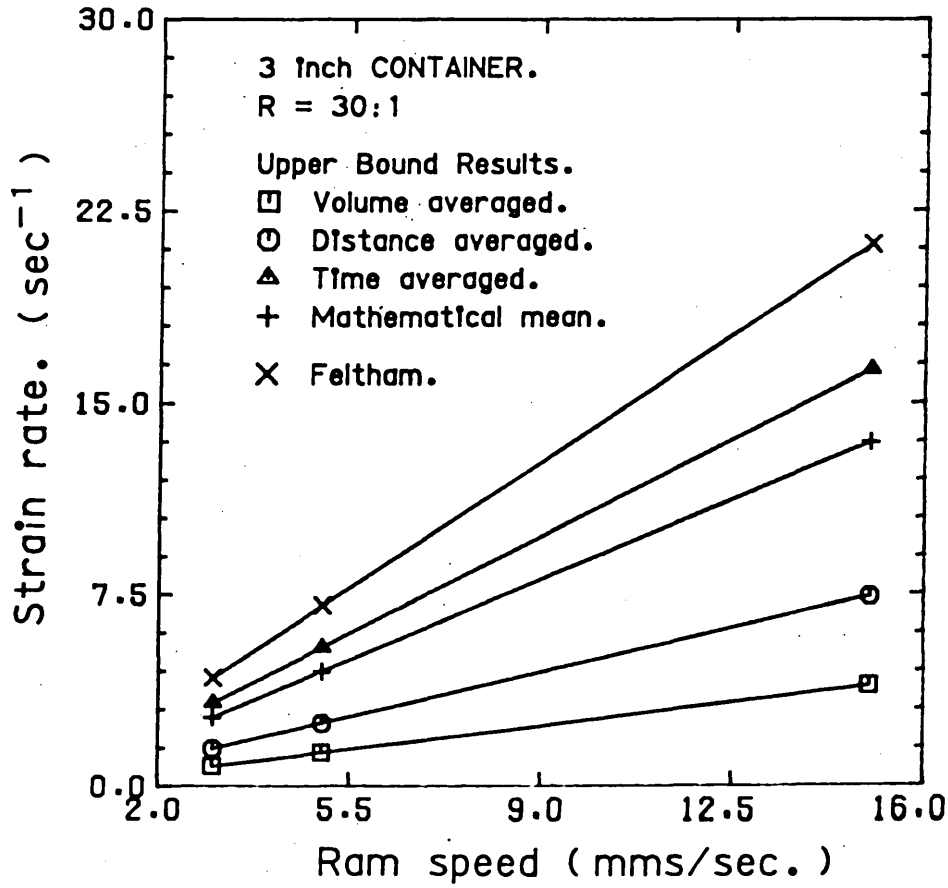


Fig. 61. Upper bound and Feltham's strain rate variation with ram speed

4.3. Deformation Processing via High Temperature Extrusion

In the following sections the high temperature extrusion of the aluminium-magnesium alloys will be discussed. The discussion will be based around three fundamental topics.

(a) Parameter Measurement

(b) Structural Development during the process comparing super-pure and commercial purity materials

(c) Property evaluation and structural correlation resulting from the deformation.

The load-displacement data generated by the extrusion process was recorded on a two pen X-Y recorder in the manner discussed in sections 3.2.3. and 3.2.4. Examples of the output are shown in Fig. 57.62 The idealised locus was discussed in section 1.1.1. and illustrated in Fig. 1. As the results in Fig. 62 indicate, this idealised case is only approximate. Result (a) shows the general nature of output from mid-temperature range runs, 350°C up to 450°C. The initial rapid rise in load to peak is associated with limited ram travel and the billet being upset to fill the container. After the peak the ram speed has attained its preset value and the 'steady state' regime is entered. The general trend of decreasing load with ram travel in this region is associated with reduced friction between billet and container as the contact length is reduced. However, this is not the only factor which causes this decrease. As mentioned in previous sections, some 90% of the input energy can be expected to be returned as some heat generation. Under suitable conditions this can be manifested as a temperature rise within the deforming material. The decrease in flow stress associated with this temperature increase will necessarily reduce the pressure required for the continued deformation and this feature must also be considered when discussing load fall in the steady state region. In the case under review, it would seem as if some temperature rise is present. Following the integral profile analysis of Castle and Sheppard[16] a final temperature of 537°C is predicted from an initial temperature of 440°C.

It should be noted that in none of the three curves does the load line enter the stage 3 (section 1.1.1.) regime where the

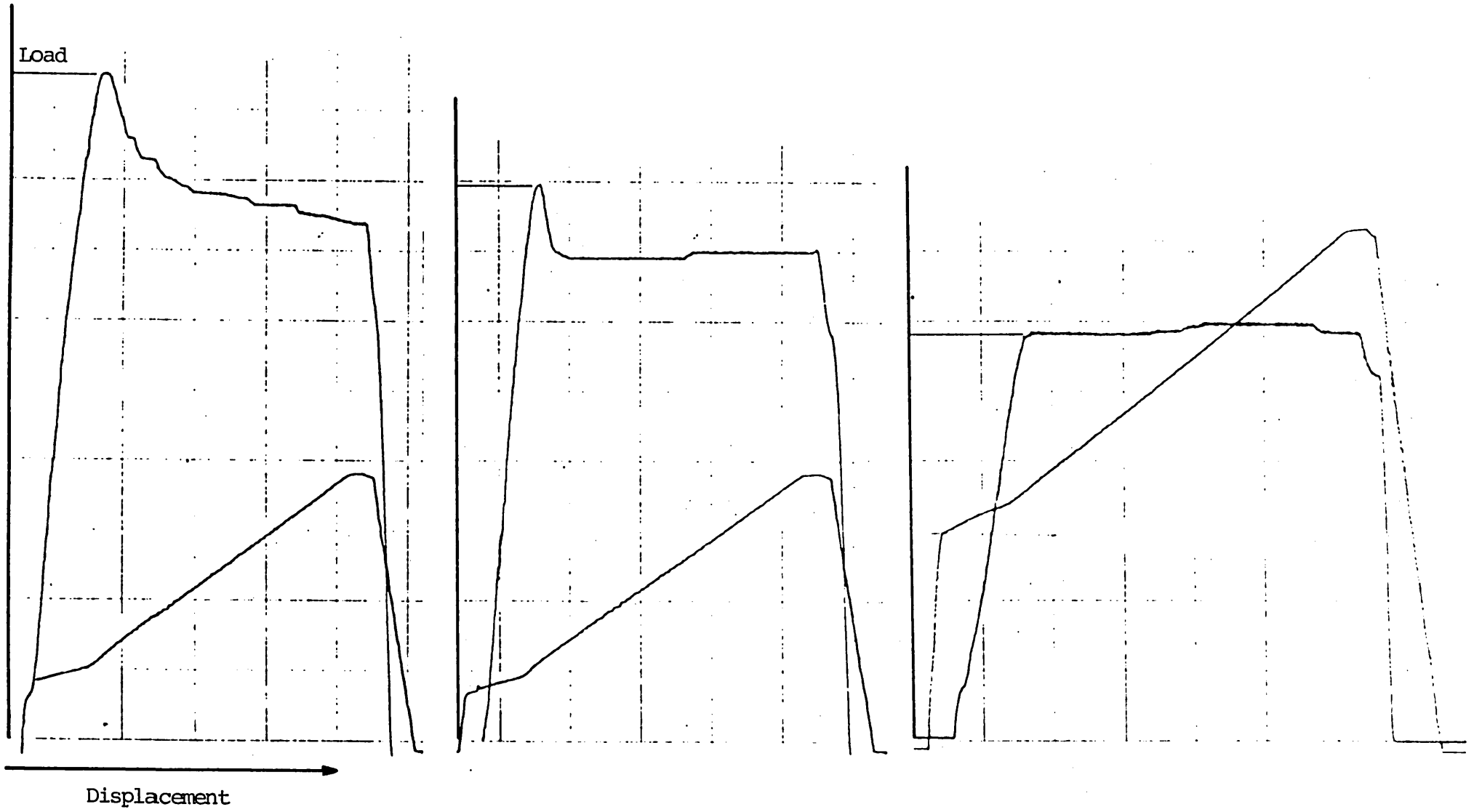


Fig. 62. Experimental load-displacement loci

dummy block interferes with the deformation zone. This is due to the steel rings, placed on the container surface to prevent its damage by the ram, restricting the ram travel and causing the cycle to be stopped prior to its inception.

Curve (b) shows the case for a high temperature extrusion at a comparable extrusion ratio. Once again the initial rapid rise in load is followed by a rapid decrease from the peak to the 'steady state'. Under conditions of lower extrusion ratio and slower ram speed the magnitude of the peak would have been much less and may even have disappeared completely. The steady state, in this case, shows no fall in load with ram travel as before, but rather a marginal increase. The reason for this feature is that the reduction due to frictional force decrease is outweighed by a temperature fall causing an increase in flow stress and an associated increase in resistance to deformation. The initial temperature of 500°C generates a steep temperature gradient when in contact with the container at 300°C and the heat losses would appear to outweight the heat generation. The integral profile analysis predicts a final temperature of 559°C which, when considering the curve shape, would seem to be in error.

Curve (c) shows the case for the alloy 5052 at an extrusion ratio of 70:1 and initial temperature of 481°C. This type of output was general for this alloy, a peak in the locus only being produced under conditions of low temperature and high ram speed even at these high reductions. The trace also shows no fall in load with ram travel in the steady state implying that heat losses are sufficient to prevent this. The reduced alloying additions in this material means its resistance to deformation is seriously impaired and the work done term used in the temperature rise calculation is reduced. The seemingly increased amount of ram travel in this case is caused by an expansion of the scale to twice that in the previous two cases.

4.3.1. Extrusion Parameter Measurements

The measurements taken from the extrusion data were:

initial temperature
ram speed
extrusion ratio
maximum pressure
minimum pressure
excess pressure due to peak

These results are tabulated in Appendix G together with the following calculated values and observations:-

run code
peak temperature
final temperature
billet length and diameter
calculated strain rate
Z from initial temperature
Z from peak temperature
Z from final temperature
flow stress calculated from initial temperature
flow stress calculated from peak temperature
flow stress calculated from final temperature
extrude quality

4.3.1.1. Variation of Peak Pressure with Initial Temperature

The result of variation of initial billet temperature upon the maximum extrusion pressure may be seen in Figs. 63-66. The former two compare results for the 3 inch container at low and high ram speeds while the latter two compare the same for the smaller diameter. The results show that a linear relationship exists between the two for all cases. Increasing the initial temperature results in a decreased flow stress in the material causing a reduced pressure to be required for deformation. The quantitative results for these figures together with those for the other materials, shown in Figs. 67 and 68 may be found in Table 4.18. This trend is apparent for all materials, extrusion ratios and ram speeds shown. At the higher ram speeds the rate of reduction of pressure with temperature exceeds that at low

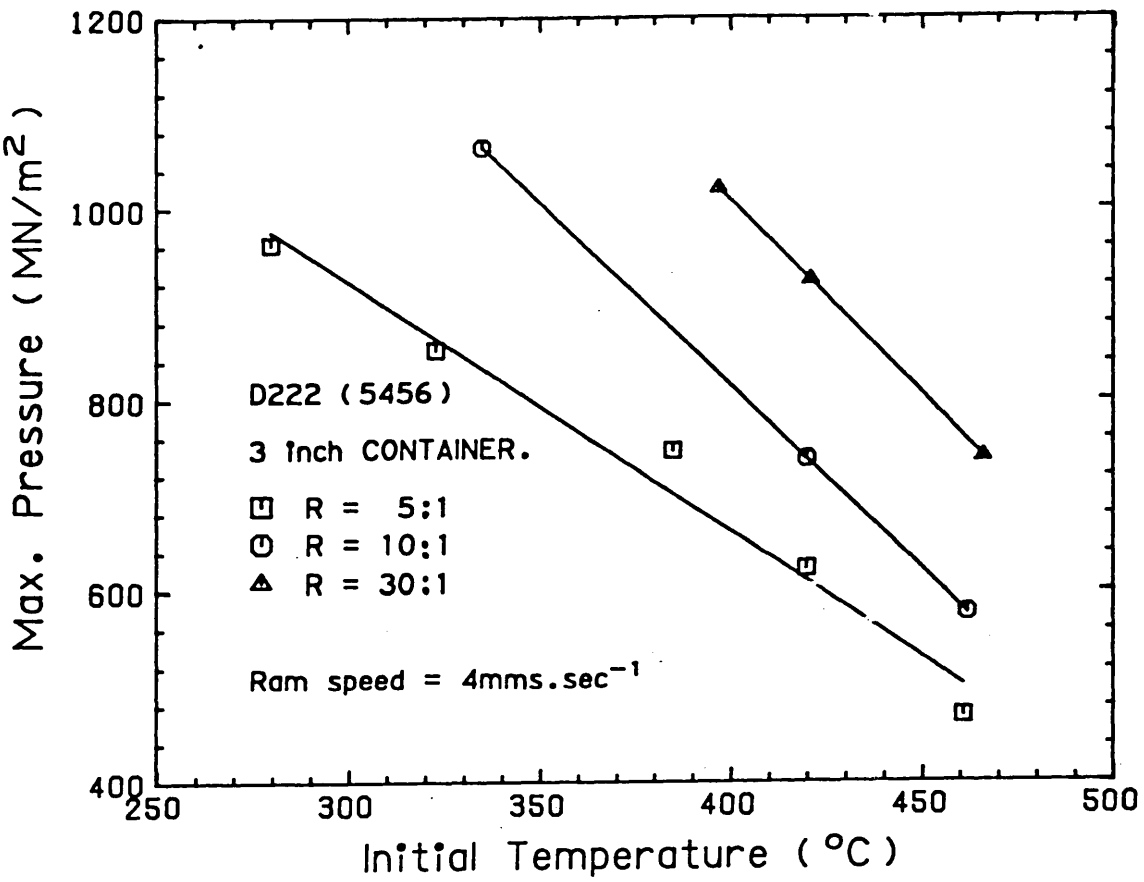


Fig. 63. Max. Pressure vs Temperature

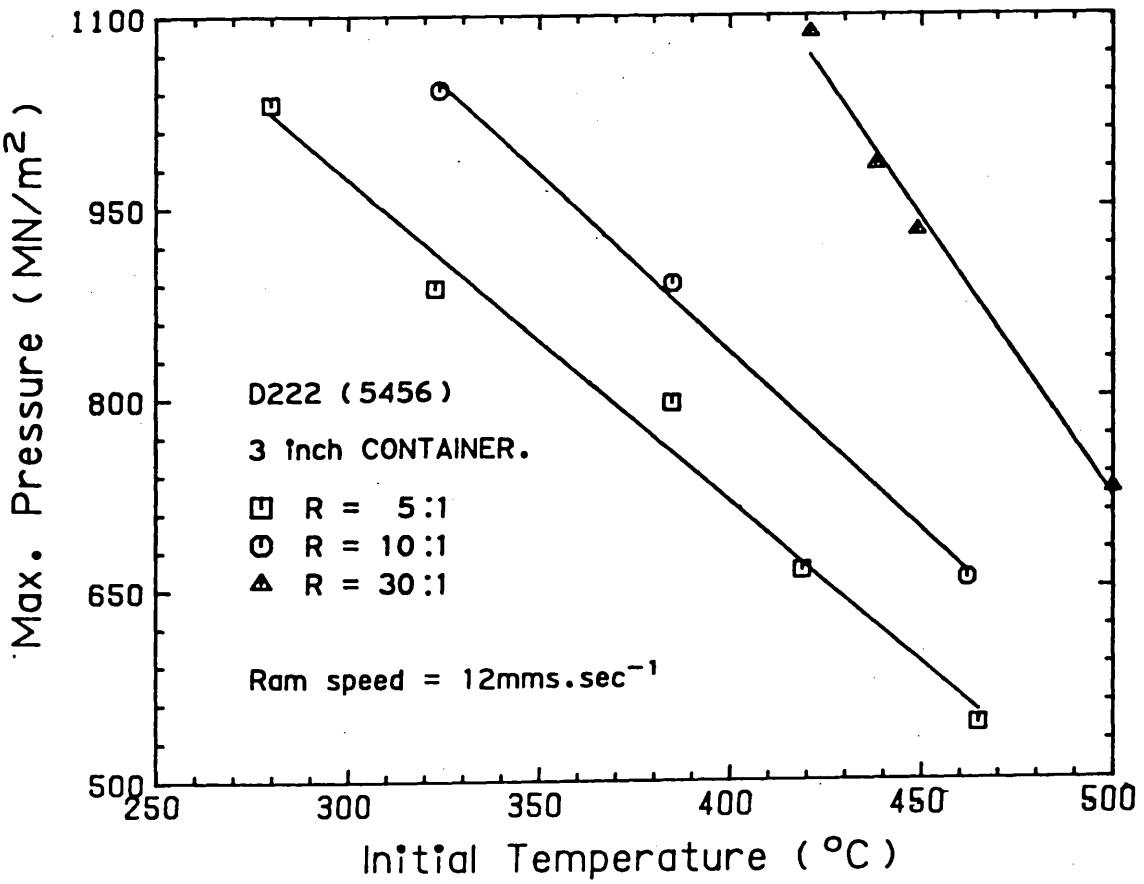


Fig. 64. Max. Pressure vs. Temperature

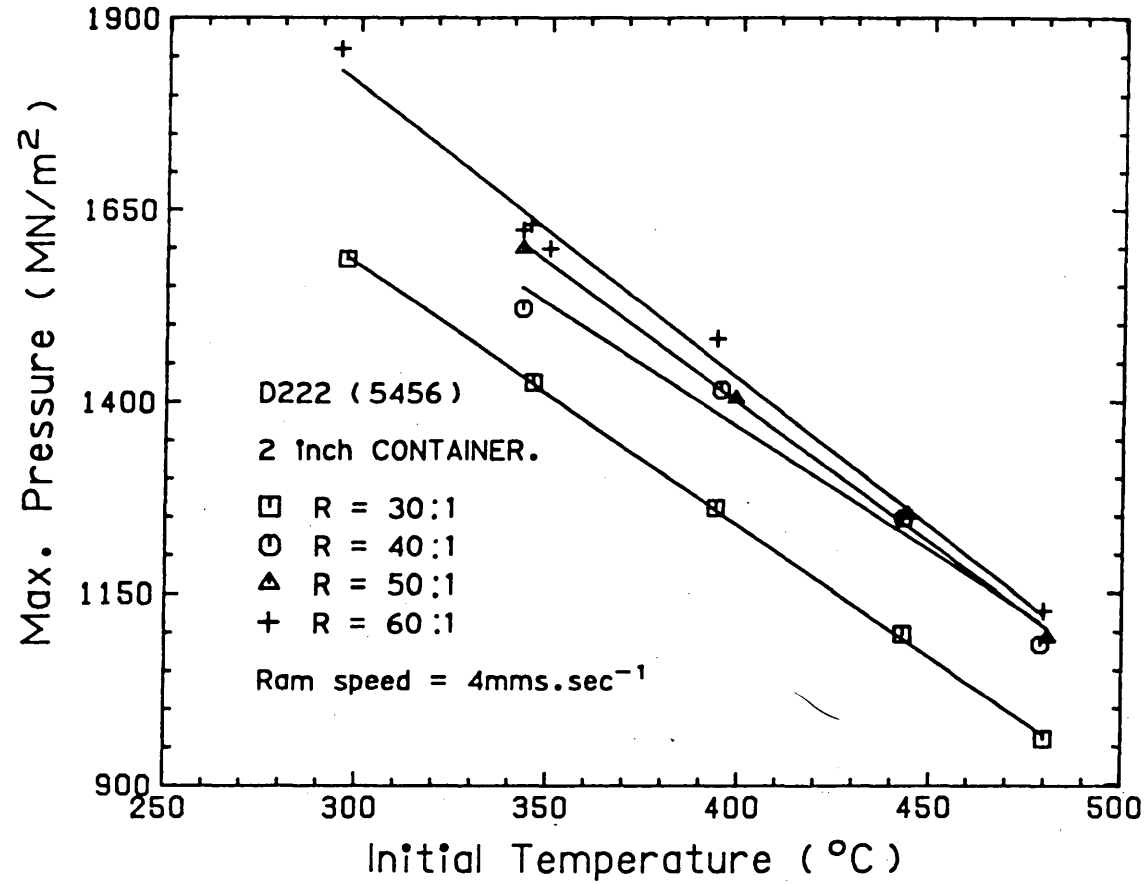


Fig. 65. Max. Pressure vs. Temperature

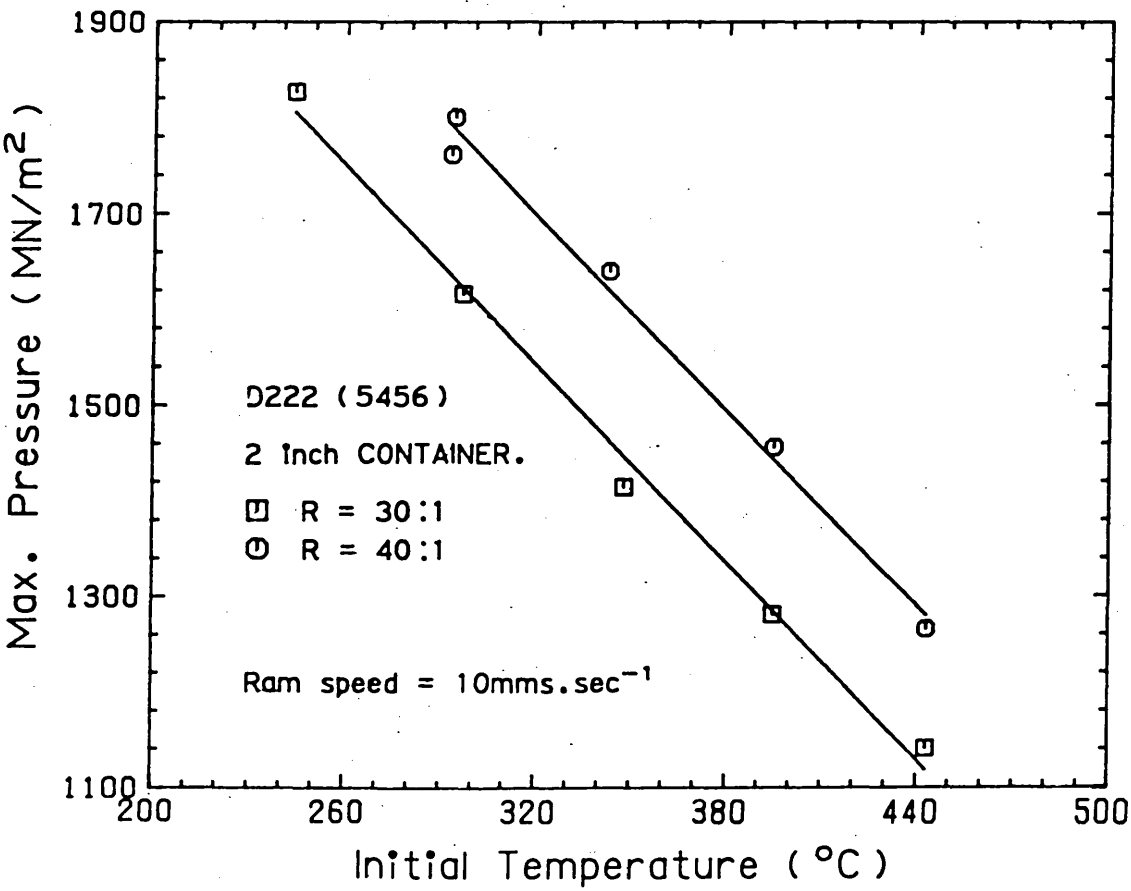


Fig. 66. Max. Pressure vs. Temperature

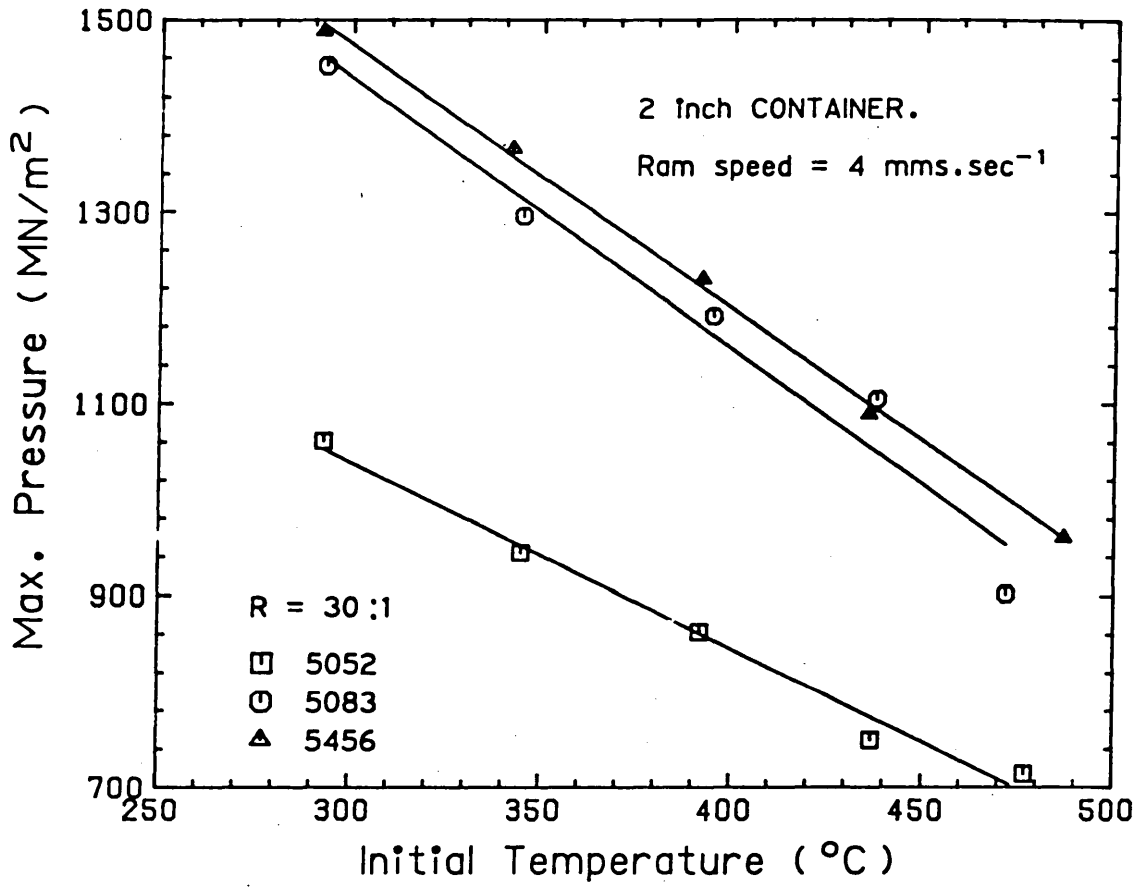


Fig. 67. Max. Pressure vs. Temperature

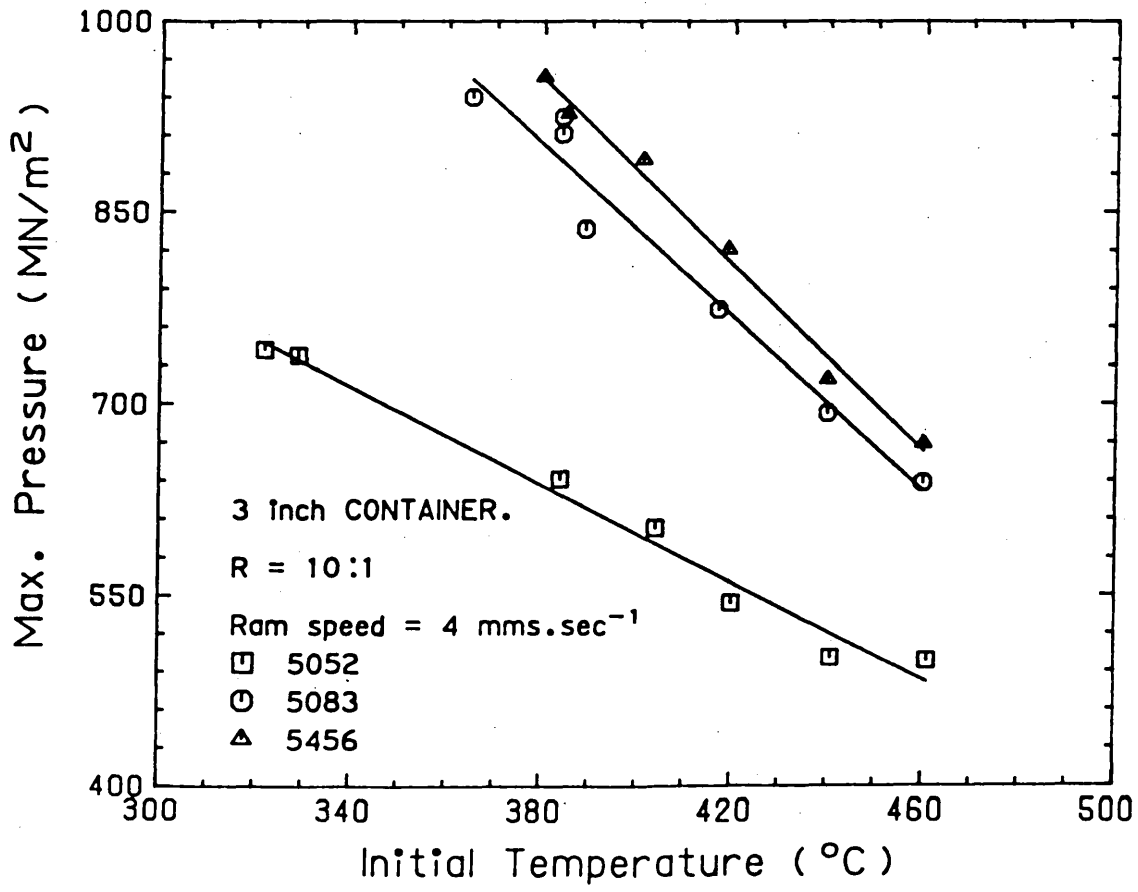


Fig. 68. Max. Pressure vs. Temperature

speeds due to the extra heat generated by the process causing an excess decrease in flow stress and therefore pressure. The same feature may be found upon comparing low and high extrusion ratios; higher reductions causing a more rapid decrease in pressure with temperature. Figs. 67 and 68 compare the variation for different magnesium content alloys. As might be expected, the pressure is highly dependent upon alloy content. Lower magnesium decreases the resistance to deformation at all temperatures. An increase of less than 0.5% magnesium causes an increase in pressure of something around 6% at the higher temperatures.

Since the maximum pressures attainable for the small and large diameter containers are 1959 and 1131 MN/m^2 respectively, it is possible to estimate the minimum temperature at which an extrusion can proceed for a given reduction from these plots. For example, Fig. 63 shows that at a reduction of 30:1 the lowest temperature at which extrusion will be possible is around 385°C while for the small diameter container, Fig. 65, it would be possible down to somewhere around 200°C for the ram speed indicated.

4.3.1.2. Variation of Peak Pressure with Ram Speed

As was shown in the previous section an increase in ram speed from 4 to 12 mms/sec resulted in an increase in pressure of up to 10%. The increase is due to the increased value of flow stress resulting from the strain rate increase. For a reduction of 5:1 at 400°C this increase is from 144 MN/m^2 to 158 MN/m^2. However, there are two competing features, the most prevalent of which will determine the magnitude of the pressure. On the one hand is the strain rate increase mentioned above while working against this is the magnitude of the temperature rise resulting from the energy input. Assuming the general hot working relationship to hold for extrusion, the flow stress is more highly dependent upon temperature than strain rate and so a small temperature increase will outweigh a larger strain rate change. In the situations described so far this balance has been weighted towards the strain rate, but Fig. 69 demonstrates the increasing effect of temperature rise. The diagram is drawn for a reduction of 20:1

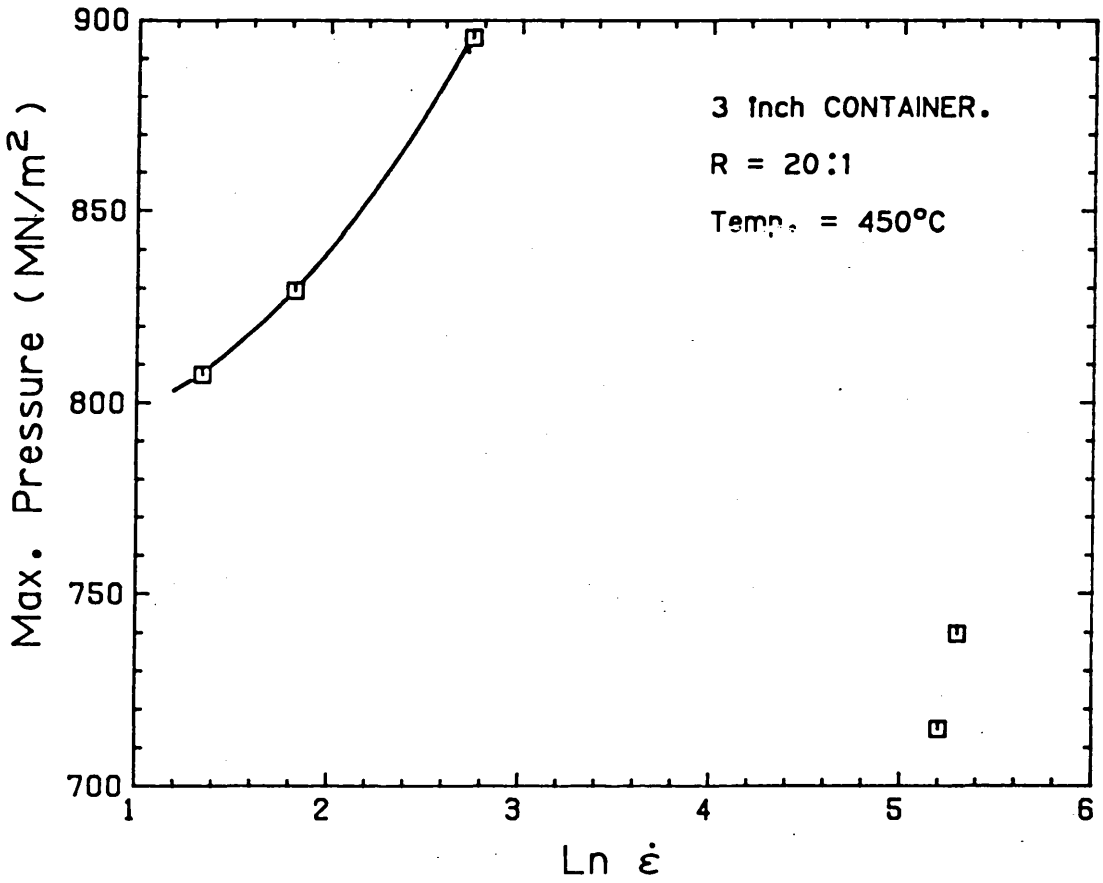


Fig. 69. Max. Pressure vs. Ram Speed

and a temperature of 450°C. At strain rates up to 15.5 sec^{-1}, ram speeds up to 13 mms/sec, the pressure shows a steady increase from 800 MN/m^2 at 4 mms/sec to 900 MN/m^2 at 13 mms/sec. However under similar conditions, but at ram speeds of 180 and 200 mms/sec the resultant pressure required to initiate extrusion has fallen to 730 and 780 MN/m^2 respectively. This is due to the heat generated by the deformation causing an internal temperature rise and an associated flow stress decrease.

Under the conditions in which most of the experimental work was carried out, i.e. ram speeds below 15 mms/sec, there was an increase in pressure associated with a ram speed increase.

4.3.1.3. Variation of Peak Pressure with Extrusion Ratio

The third process variable which will change the magnitude of the pressure necessary to initiate extrusion is the extrusion ratio, R. Most mathematical relationships have related these through the flow stress applicable to the imposed conditions and this situation will be dealt with in section 4.3.1.6. The problem associated with generating this type of data is to keep the two other variables of ram speed and temperature constant. This is not a difficult task with the former, but the latter introduces greater inaccuracies since the heat loss during transfer of the billet from the heating stage to the deformation stage will unlikely to be the same in every case. The results obtained for both container sizes and all materials are presented in Figs. 70-72. As the results indicate, in all cases an increase in reduction ratio produces a corresponding increase in pressure for a given temperature and ram speed. A linear relationship obviously exists between the two for the range of data indicated and these values are shown in Table 4.19. Because of the limited pressure available in each case, it is not possible to achieve higher reductions at lower temperatures. The same conclusions relating maximum reduction and temperature may be gained from these results as were drawn in section 4.3.1.1.

Figs. 71 and 72 show that an incremental decrease in temperature results in an increased pressure for all reductions, the relationships having very similar gradients. Fig. 72 compares

MATERIAL	CONTAINER DIAMETER	EXTRUSION RATIO	RAM SPEED	P=A-B.T A	B
	INS.		MMS/SEC		
D222	3	5	12	1735	2.5
D222	3	10	12	1954	2.8
D222	3	30	12	2926	4.4
D222	3	5	4	1709	2.6
D222	3	10	4	2348	3.8
D222	3	30	4	2645	4.1
D222	2	30	10	2648	3.5
D222	2	40	10	2787	3.4
D222	2	30	4	2600	3.4
D222	2	40	4	2647	3.2
D222	2	50	4	2850	3.6
D222	2	60	4	2965	3.8
5052	3	10	4	1364	1.9
5083	3	10	4	2193	3.4
5456	3	10	4	2345	3.7
5052	2	30	4	1622	1.9
5083	2	30	4	2289	2.8
5456	2	30	4	2298	2.7

Table 4.18. Results for Max. Pressure variation with the initial billet temperature

MATERIAL	CONT DIAM	TEMP	P=A+B.LNR A	B
	INS.	DEG.C		
D222	2	500	295.7	201.8
D222	2	450	360.4	230.6
D222	2	400	481.4	237.8
D222	2	350	472.7	283.8
D222	3	500	201.5	162.5
D222	3	450	363.9	161.6
5052	2	500	309.0	122.5
5083	2	500	295.9	190.0
5456	2	500	310.8	194.6

Table 4.19. Results for Max. Pressure variation with extrusion ratio

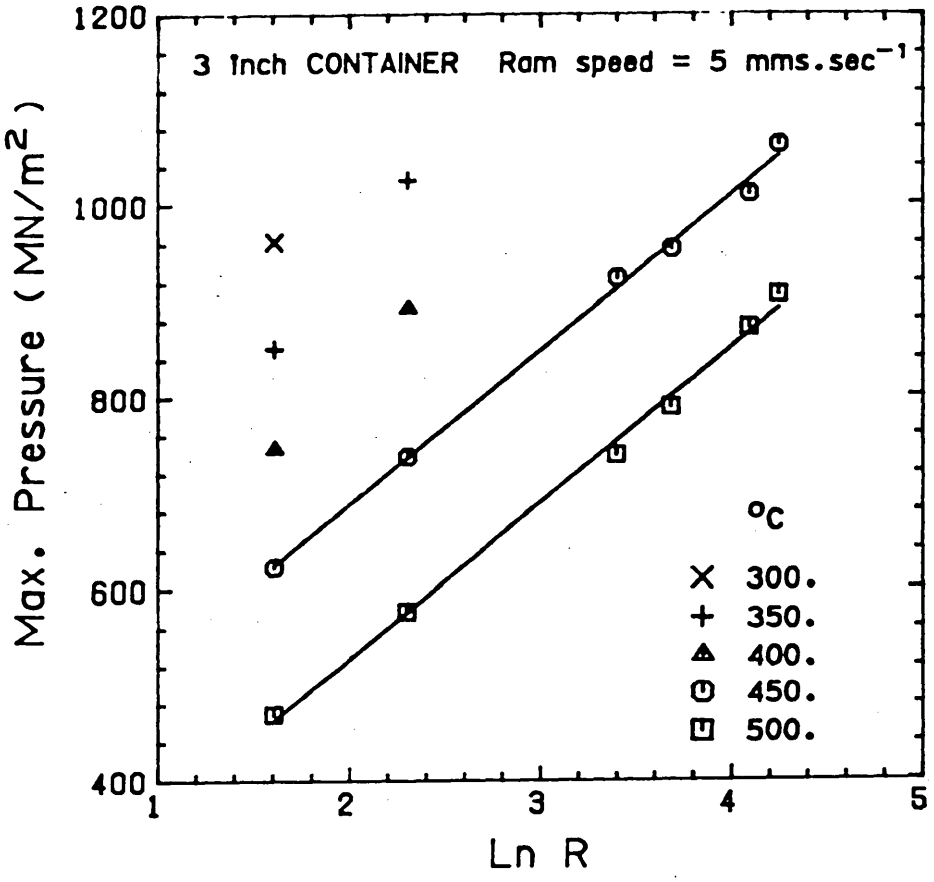


Fig. 70. Max. Pressure vs. LnR, alloy D222 (5456)

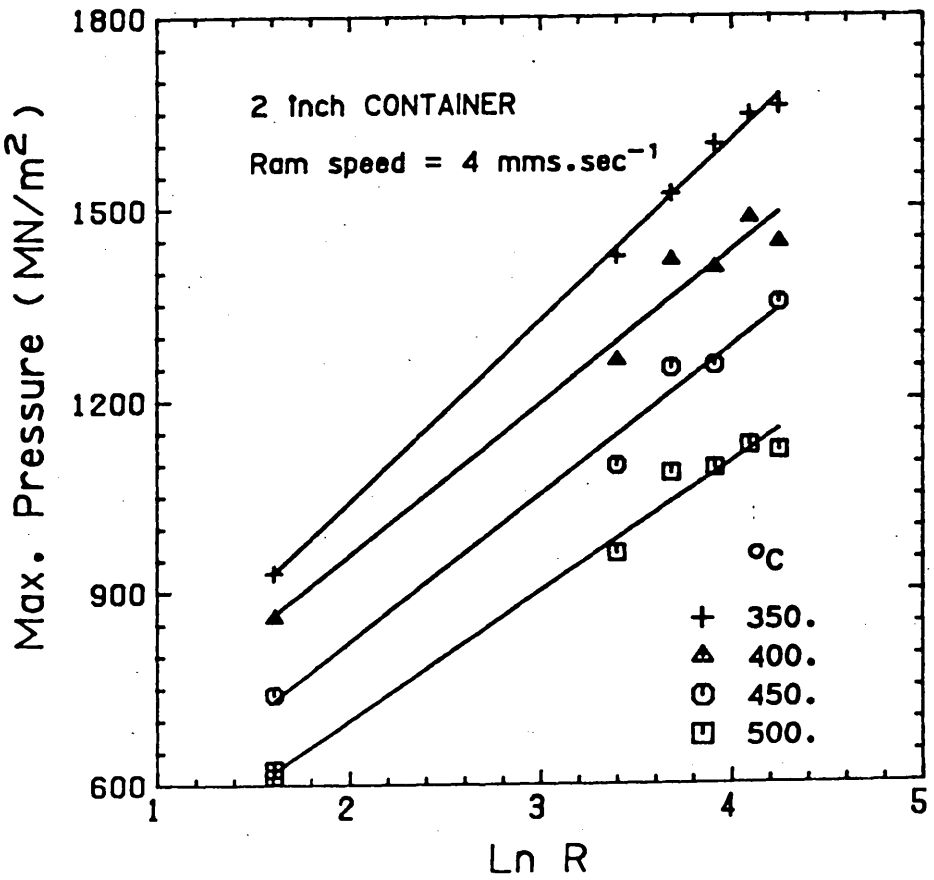


Fig. 71. Max. Pressure vs. LnR, D222 (5456)

the variation for the 2 inch container at an initial temperature of 500°C and ram speed of 4 mms/sec for alloys of various magnesium content. The resistance to deformation is increased with the higher alloy content materials for all reductions. The smaller gradient for the 5052 alloy compared with the other two is consistent with stress predictions from the constituitive equations.

The results for the variation of pressure with extrusion ratio agree in principle with the trends observed by Ashcroft and Lawson,[9] and McShane.[219] The latter evaluated the redundant work from this data by plotting P/σ against LnR for each temperature. By reducing the coefficient of LnR in the resulting equation to unity, the intercept term gives an indication of the redundant work or the work not directly contributing to the shape change. McShane,[219] working with powders illustrated that this redundant work term was reduced as the temperature of extrusion was increased indicating an increase in efficiency. Ashcroft and Lawson's[9] results showed a similar trend for commercially pure aluminium, but for an Al-Mg-Zn-Cu alloy no correlation was found. This would imply that the result is dependent upon alloy content and Fig. 73 tends to support this. The redundant energy, calculated in the manner described above is shown to increase to some degree as the temperature is increased indicating that the efficiency of the process is reduced. Some justification may be seen for this from considering Figs. 88 and 89 in which the higher temperature deformation structure contains a greater proportion of internal disorder resulting in the increased redundant deformation. In addition, the onset of dynamic recrystallization at the higher temperature may contribute to this increased redundant work.

4.3.1.4. Variation of the Peak Pressure with the Z Parameter

In an effort to overcome the separate relationships generated for plots of peak pressure against temperature by ram speed variation, the Z parameter was utilised. The parameter, defined as $\dot{\varepsilon}\exp^{\Delta H}/RT$, contains elements of both ram speed and temperature and might be expected to remove the variance. Figures 74-77 show graphically the results obtained and indicate the likelihood of a linear relationship between the two. In these

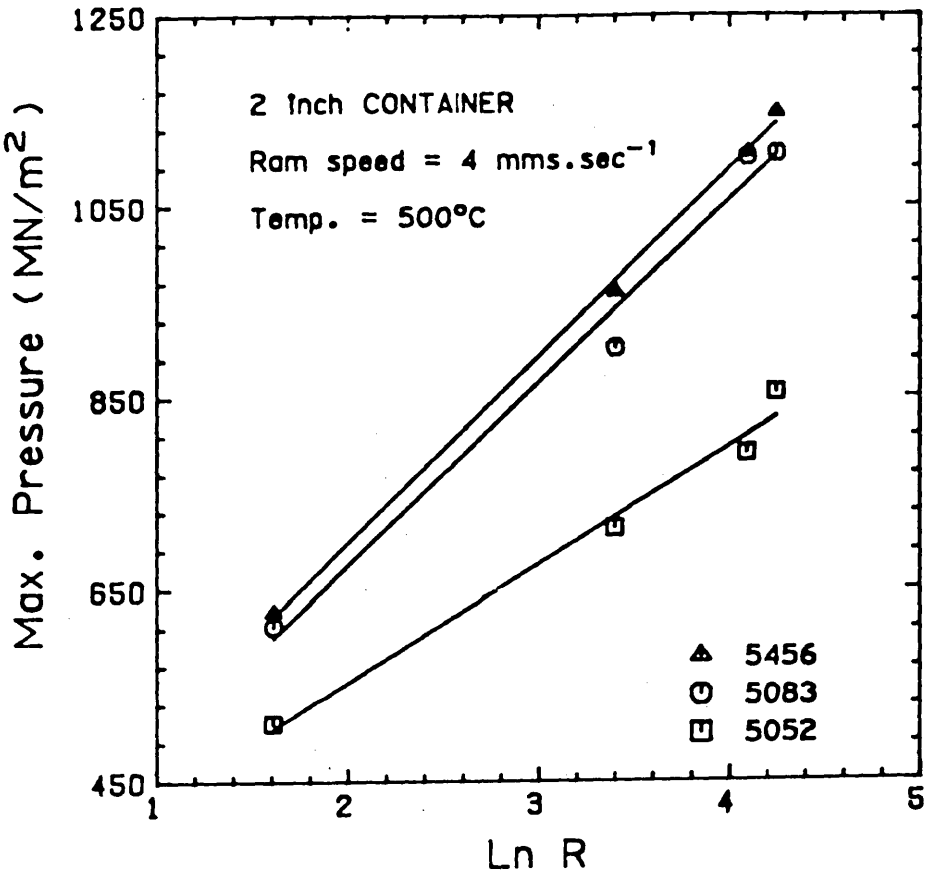


Fig. Max. Pressure vs. LnR, alloy 5052, 5083 and 5456.

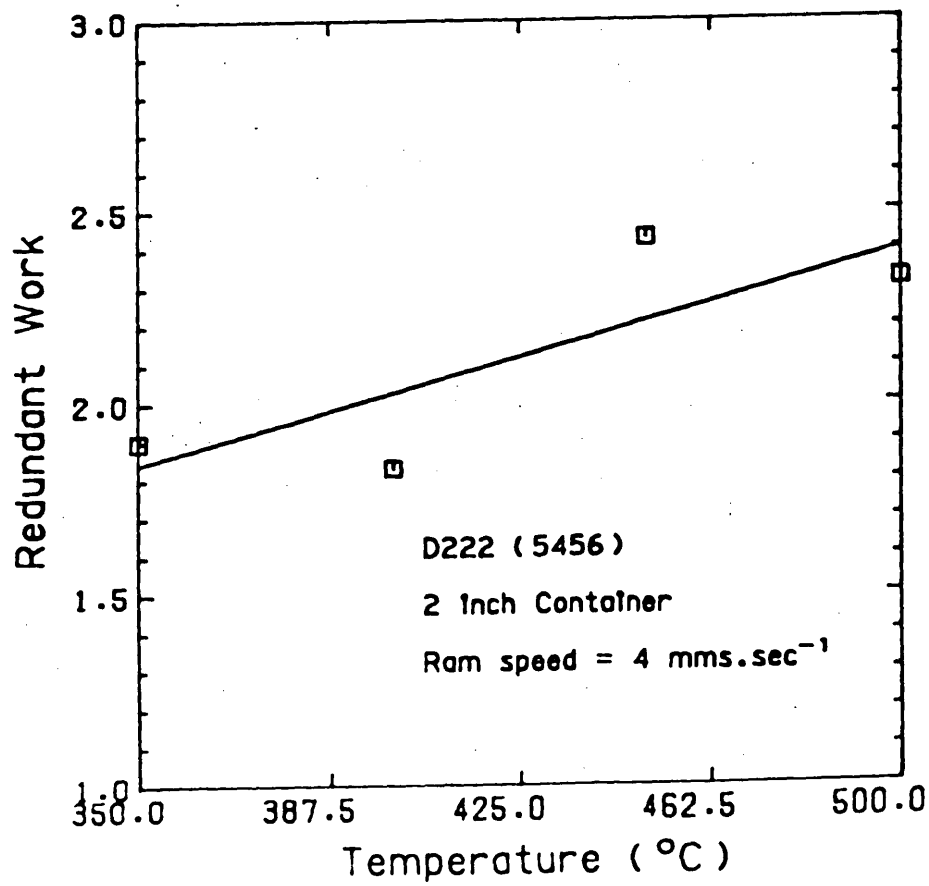


Fig. 73. Redundant work vs. Temperature, alloy D222 (5456)

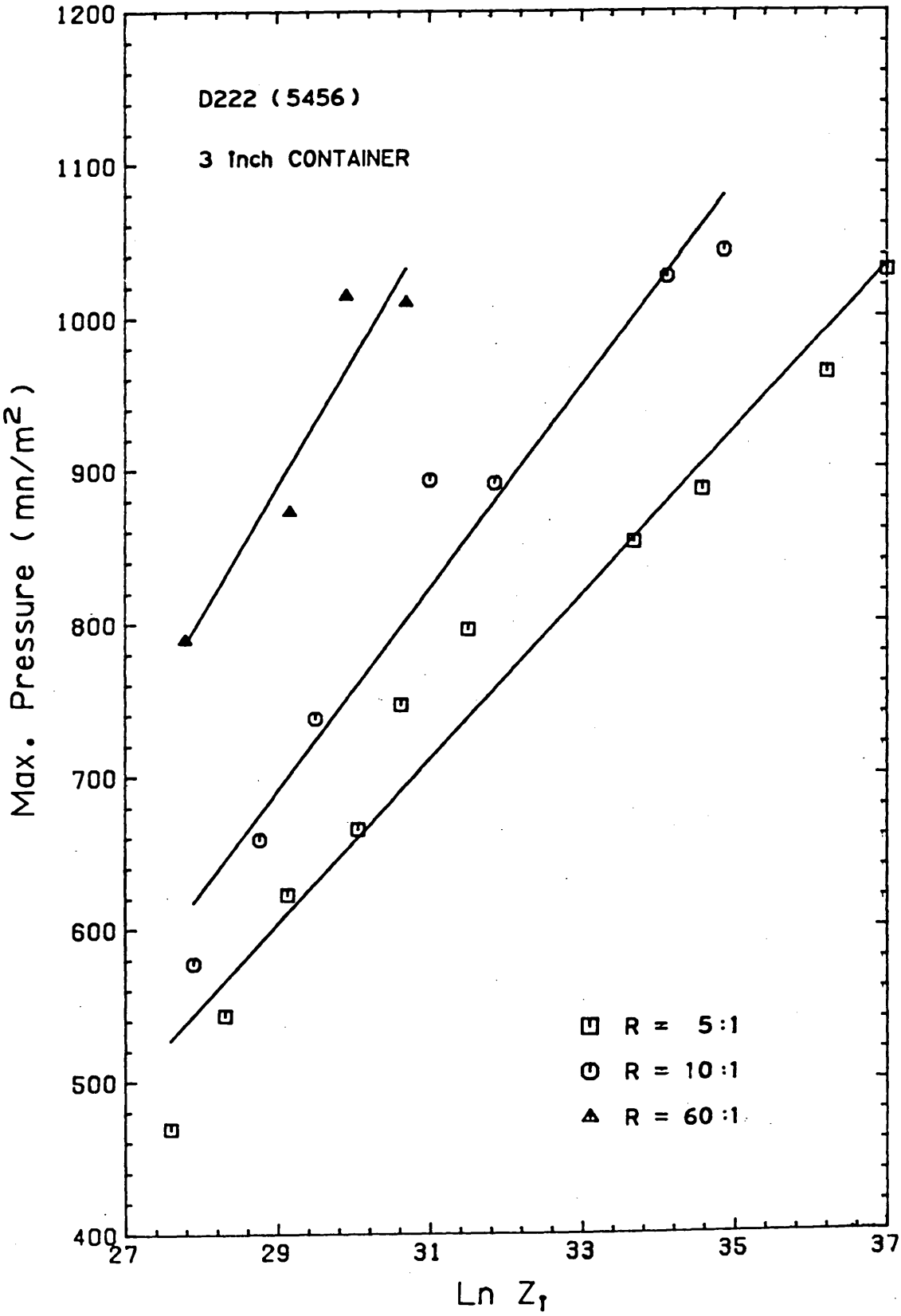


Fig. 74. Max. Pressure vs. LnZ_i, alloy D222 (5456)

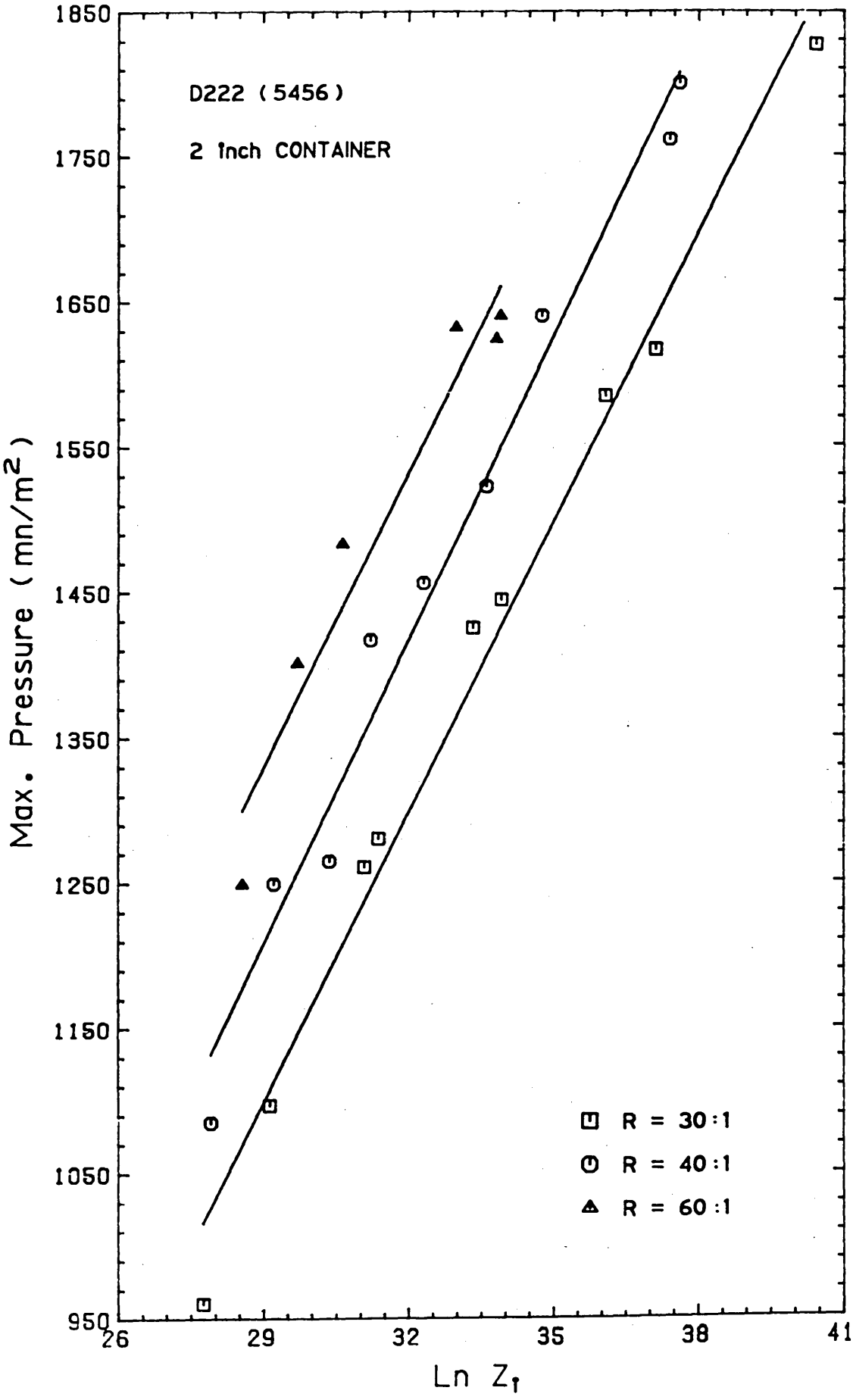


Fig. 75. Max. Pressure vs. LnZ_i, alloy D222 (5456)

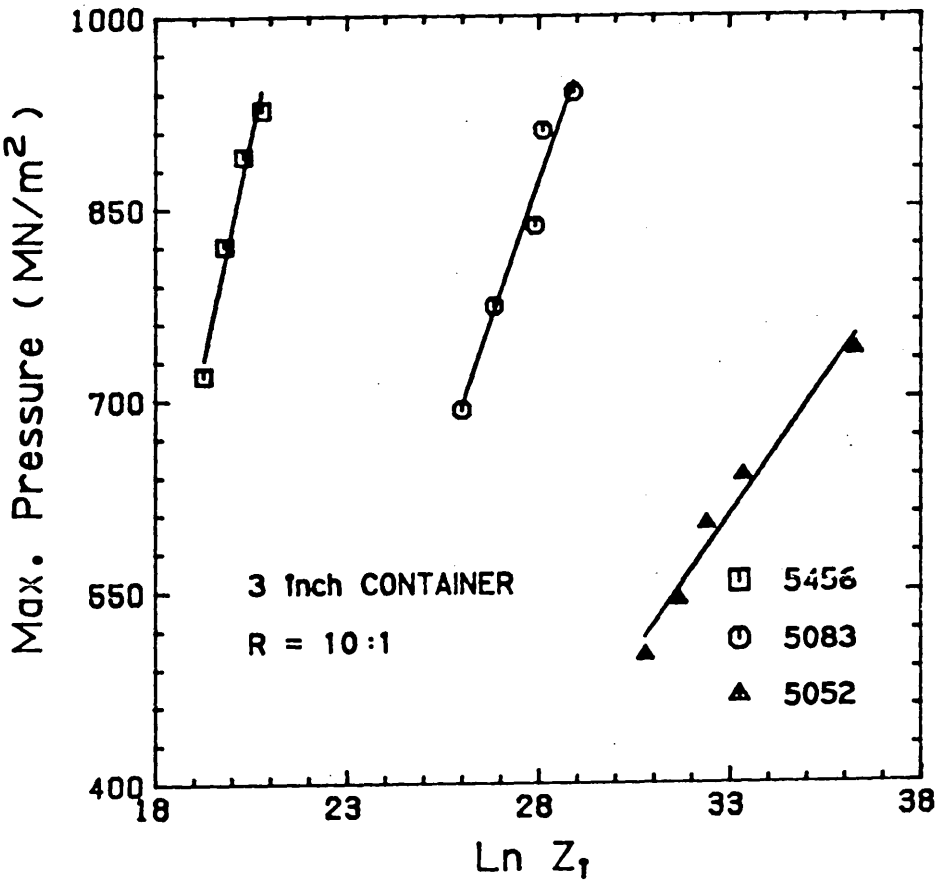


Fig. 76. Max. Pressure vs. LnZ_i alloys 5052, 5083 and 5456.

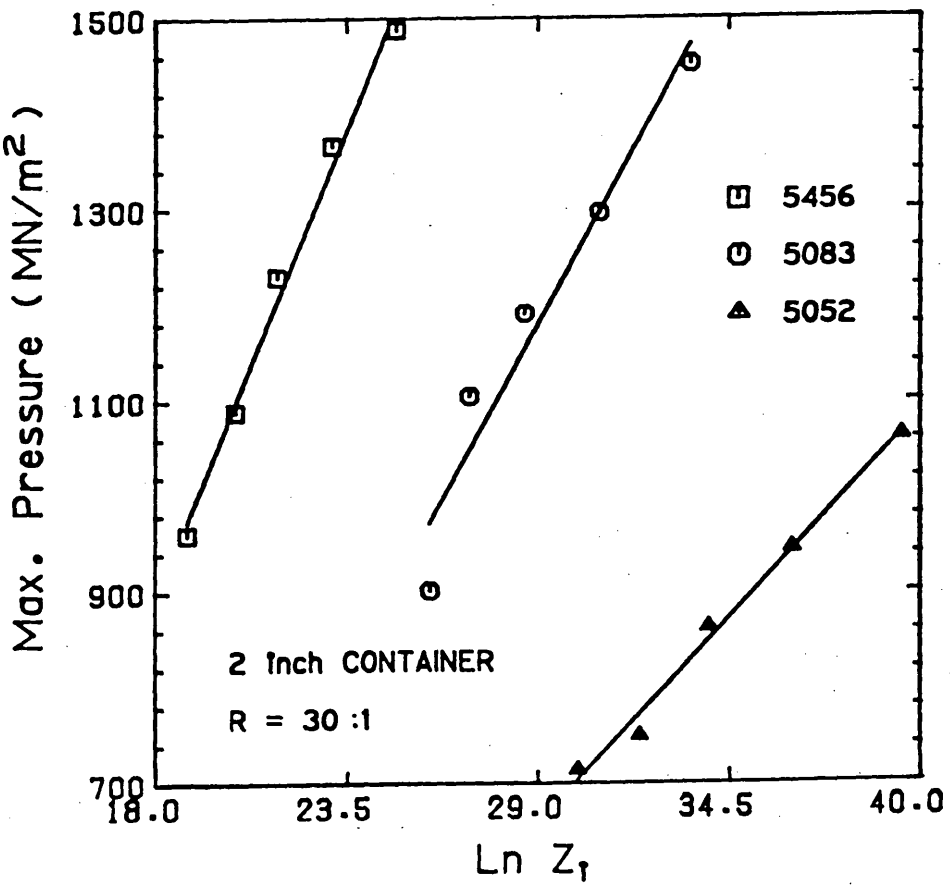


Fig. 77. Max, Pressure vs. LnZ_i alloys 5052, 5083 and 5456.

cases the high temperature values correspond to low Z values while an increase in ram speed increases the value of Z for the given temperature. The results show that the use of the Z parameter is justified since the various ram speeds employed are brought together for a given extrusion ratio. For a given value of Z, the pressure necessary to carry out extrusion increases with a reduction ratio increase as predicted in the previous section. Fig. 74 suggests that for the smaller diameter container the rate of increase of pressure with LnZ is similar for all extrusion ratios while Fig. 75 suggests an increase in the dependency at higher ratios for the larger container. The cause of this latter variation is probably due to the fewer number of experimental points available for the plot. The numerical results for the graphs may be found in Table 4.20.

In an attempt to generate a single line relationship for all extrusion ratios, the pressure data was compensated for the ratio change by dividing by its logarithmic value, but no success was found. A unique relationship, applicable for all ratios, between peak pressure and Z would enable limits of extrudability to be predicted for all temperatures and ram speeds. It is towards this goal that the latter sections of this part of the discussion will aim.

Figures 76 and 77 show the relationships found for the various magnesium content alloys. As before, single line relationships are found, but the vastly different activation energies derived for the alloys cause large differences to be generated between them. For both container sizes illustrated, the decrease in resistance to deformation with decrease in Z is greater with the higher magnesium content alloys 5456 and 5083. This is due to the reduced effect of the solute at higher temperatures.

MATERIAL	CONT DIAM	EXTRUSION RATIO	P=A.LNZ-B A	B
	INS.			
D222	3	5	53.8	958.9
D222	3	10	66.3	1230.8
D222	3	60	84.5	1562.8
D222	2	30	66.5	829.6
D222	2	40	69.6	809.1
D222	2	60	67.4	623.9
5456	2	30	89.3	715.7
5083	2	30	66.7	754.3
5052	2	30	38.6	458.4
5456	3	10	138.8	1940.4
5083	3	10	86.8	1560.8
5052	3	10	42.7	798.6

Table 4.20. Results for Max. Pressure variation with LnZ.

4.3.1.5. Variation of Δp with the Z Parameter

As was discussed in section 1.1.1, under many conditions a peak appears in the load-displacement locus at the bounding between Stages I and II, (Fig. 1). Many reasons for its existence have been postulated including changes in frictional conditions,[25] temperature differentials,[27] dead-metal-zone formation[29] and die entrant angles.[28] However each of these has been repudiated by substantial experimental evidence. It was Castle and Sheppard[23] who first considered that the excess pressure was associated with the energy required to establish the quasi-static deformation zone. They proposed that the formation of the zone required an excess of dislocation sources which in turn led to a greater than equilibrium dislocation density. Thus the pressure is associated with problems concerned with dislocation dynamics, since considerable dislocation movement will be required to produce the quasi-static deformation zone. Therefore we would anticipate this extra pressure value, Δp, to vary with temperature, strain rate, reduction ratio and alloy content if this hypothesis is correct. Fig. 78 shows the tangential method used for evaluating the magnitude of Δp. Fig. 79 shows the variation of this increment of pressure with the Z parameter for two alloys of differing magnesium content. The third alloy, 5052, showed no peak value at any reductions or temperatures. This may be due to the extreme ease with which dislocation activity occurs or alternatively it may be masked by the temperature loss causing an increase in flow stress and resultant general increase in pressure during the cycle. However, as Fig. 79 displays, the value of Δp increases as the value of LnZ is increased, in a linear fashion. Thus a reduction in temperature or a rise in strain rate increase Δp. This observation would tend to support the hypothesis since dislocation mobility, being a thermally activated process, is aided by higher temperatures. Once again the vast difference in calculated activation energy for each material has tended to separate the results. For a given temperature and strain rate, the value of Δp is higher for 5456 than for 5083. The increased magnesium content of the former alloy means that this pressure is dependent upon alloy content which is also consistent with the hypothesis that its value is related to dislocation mobility.

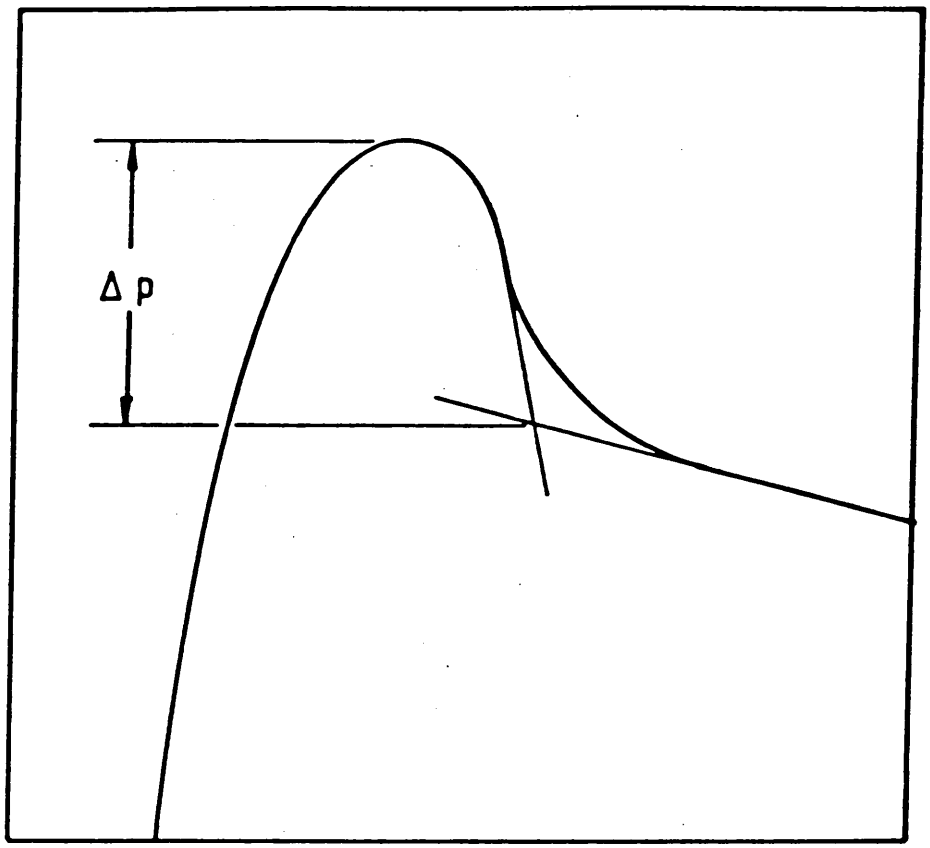


Fig. 78. Tangential construction for Δp evaluation

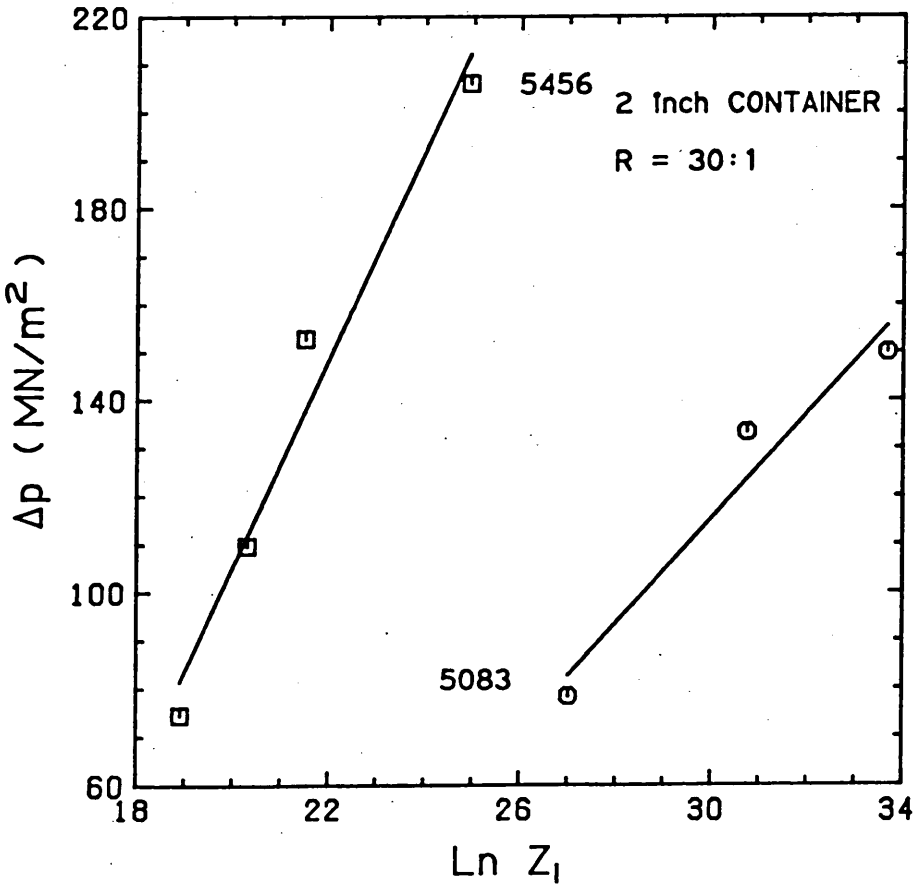


Fig. 79. Δp vs. LnZ_i, alloys 5083 and 5456.

Figs. 80 and 81 show the variation with LnZ for differing reduction ratios for both container sizes. In the former case, the 3 inch container, the results show that for all reduction ratios a linear relationship exists between the two. Similar features may be observed for the smaller container diameter. Thus the evidence confirms that a lower temperature increases the resistance to dislocation mobility. Therefore the peak increment, Δp, is associated with the thermally activated events pertaining. The linear relationship illustrated means the incorporation of Δp with upper bound results is applicable to this alloy system as shown by Sheppard.[85]

In conclusion it would appear that the information gained from this experimental programme agrees with the thesis of Castle and Sheppard[23] that the excess pressure, Δp, is associated with the energy required to set up the quasi-static deformation zone. Further reference will be made to this point in the section discussing structural development during extrusion.

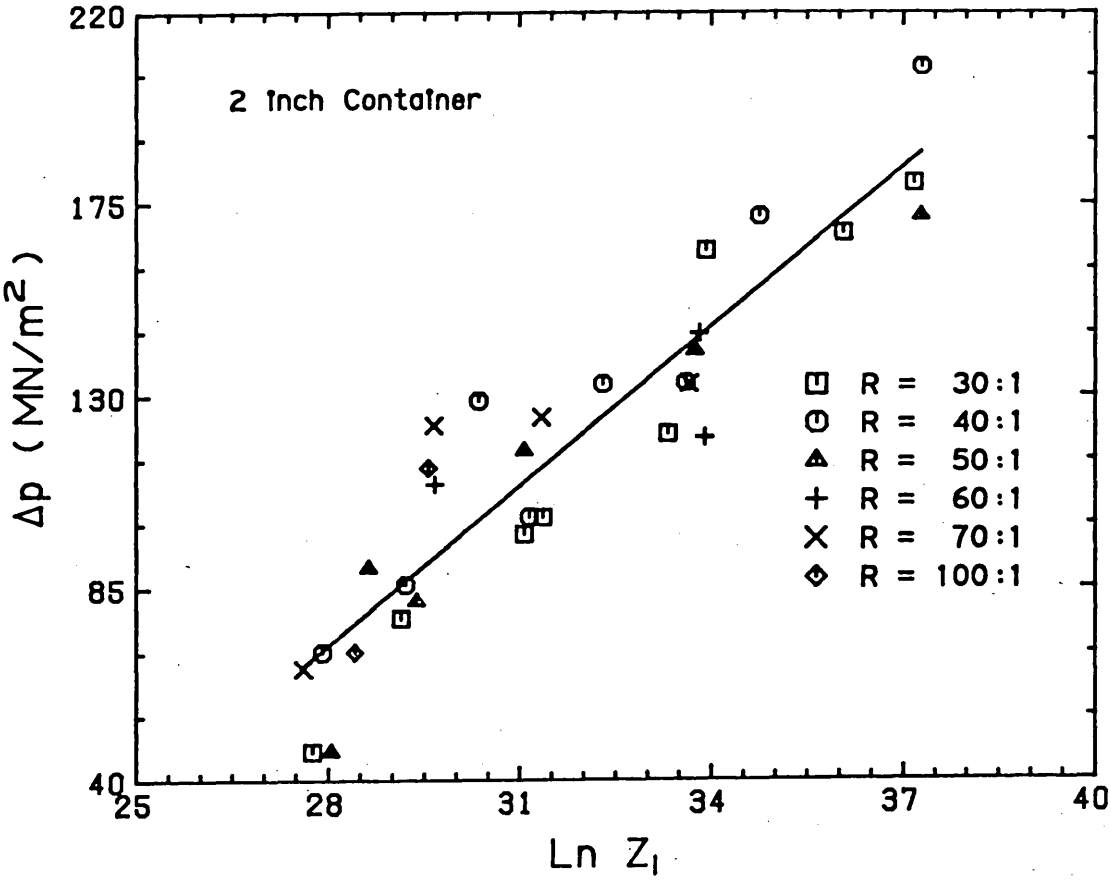


Fig. 80. Δp vs. LnZ_i, alloy D222 (5456)

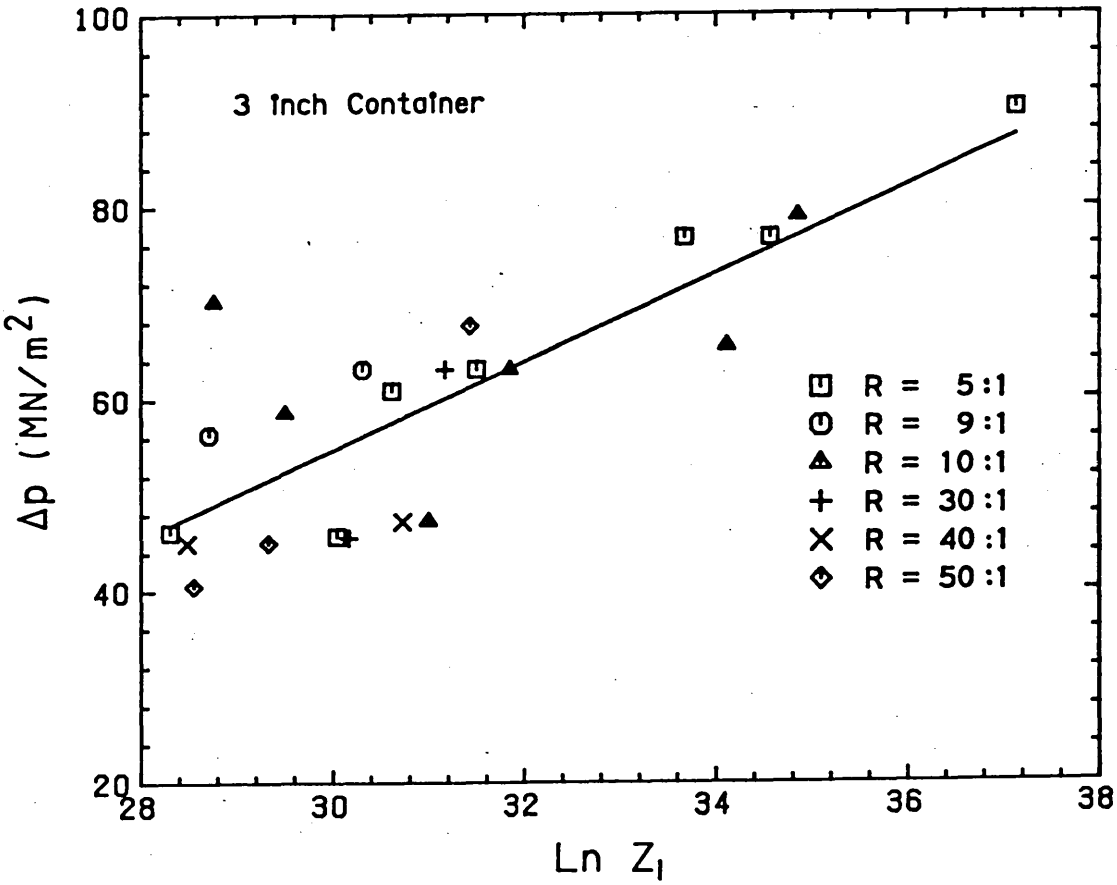


Fig. 81. Δp vs. LnZ_i, alloy D222 (5456)

4.3.1.6. Variation of P/σ with Extrusion Ratio

In section 4.2.1. it was shown from theoretical considerations that the dimensionless term P/σ varied with LnR in a smooth, continuous manner. A single line relationship was predicted, for all input values, and would appear to offer a neat method of correlating both pressure and flow stress. The value of flow stress applicable to the prevailing conditions may be evaluated through the constituitive equations developed earlier and using equation (88). This necessitates an accurate knowledge of both instantaneous strain rate and temperature for the analysis to be meaningful. Although the applicability of the strain rate expression developed in section 2.3 is not certain, its evaluation is simple and is probably the best approximation available. The temperature at each point is a much more complex value to ascertain. The method for its calculation at the peak pressure contains no allowance for heat losses while the analysis used for its determination at the minimum pressure is very difficult to check experimentally. Raybould[220] used an earlier developed temperature rise model which calculated a mean temperature value and could only be applied to conditions when the tooling and billet were initially at the same temperature. In an attempt to check his results, he extruded soft aluminium alloys at low ratios employing thermocouples inserted into the dead-metal-zone during extrusion at low ratios. His results indicated that the theoretical predictions were too low, but Wood[37] recalculated the results using the method indicated in section 2.5.2. and found a good correlation. Thus the method will predict a result of fair accuracy and can be used for the temperature calculation at the minimum pressure.

Using the experimentally derived pressure and flow stress values using these temperature models and peak and minimum load produces the results shown in Figs. 82-85. In the first two the results are shown for peak load for both container diameters while the final two consider the case for the minimum conditions. In all four cases it is immediately obvious that the results do not correspond to a single line relationship. Thus either the theoretical prediction is incorrect or the experimental strain rate and temperature calculations are in error. Further reference will be made to this in the next section.

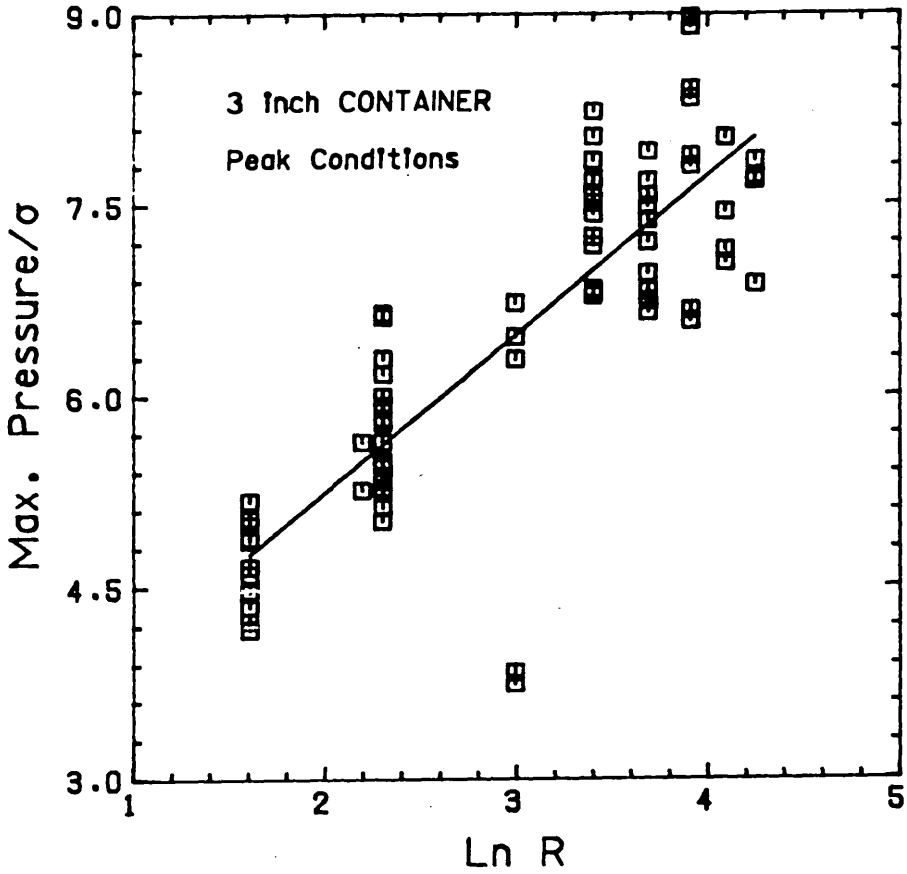


Fig. 82. P/σ vs. LnR, alloy D222 (5456)

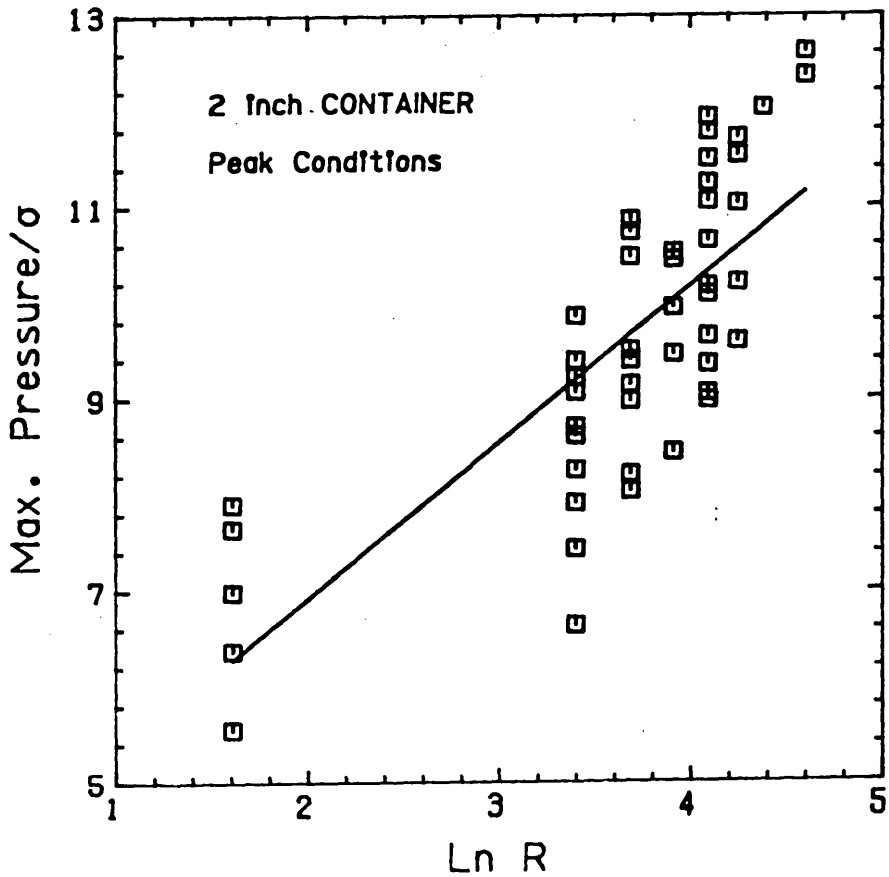


Fig. 83. P/σ vs. LnR., alloy D222 (5456)

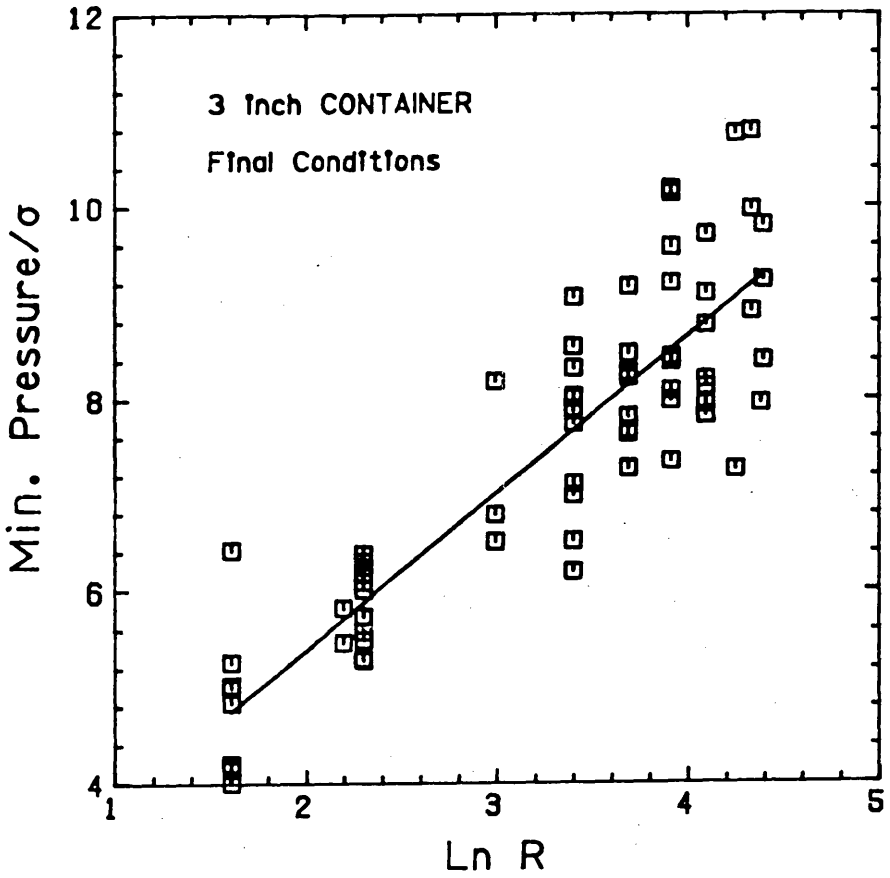


Fig. 84. P/σ vs. LnR, alloy D222 (5456)

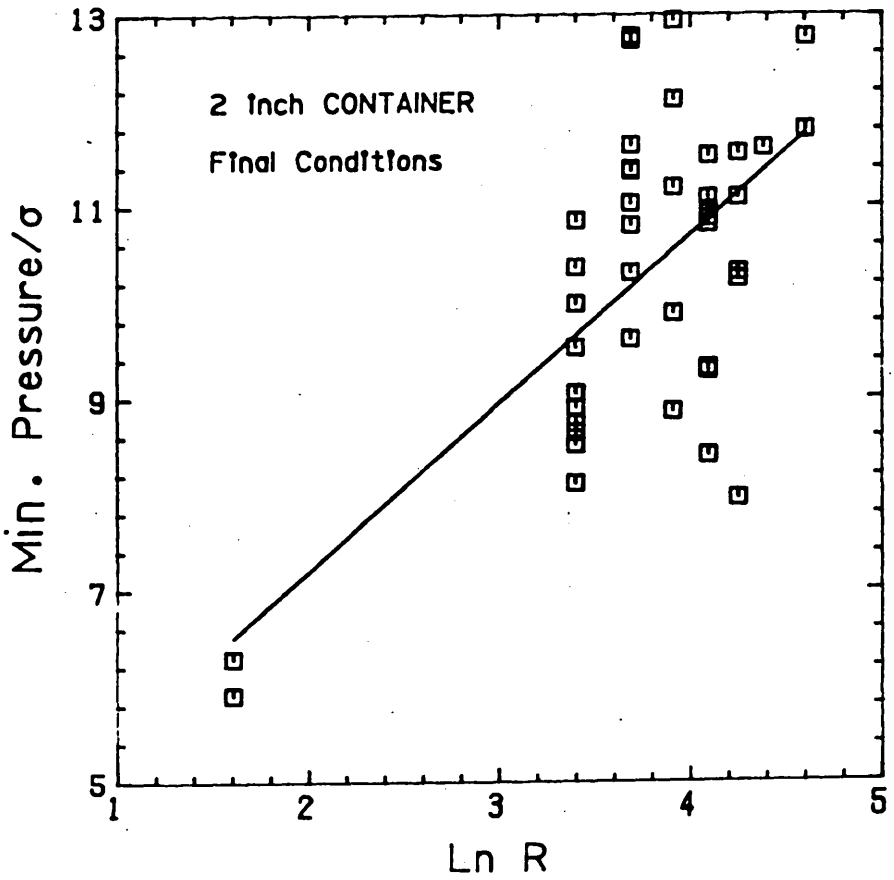


Fig. 85. P/σ vs. LnR, alloy D222 (5456)

The best straight lines calculated from these points are shown in each case, and the results for this are shown below:-

Description	$P/\sigma = a + b\text{LnR}$	
	a	b
Max.Pressure - 2 inch	3.67	1.63
Max.Pressure - 3 inch	2.76	1.24
Min.Pressure - 2 inch	3.69	1.75
Min.Pressure - 3 inch	2.13	1.63

Table 4.21. Relationships for P/σ vs LnR.

Although the gradients are similar for all cases the intercepts are larger for the 2 inch diameter container case. The reason for this was given in section 4.2.1. where it was pointed out that the practice of leaving the steel half rings on the container surface to prevent its damage causes the discard length remaining at the end of extrusion to be proportionally greater in the two inch container case. Thus the minimum pressure measured is not the true value, but rather the observed one. The mathematical relationships shown in Table 4.21 are those used in Figs. 46 and 47. The values of a and b, above, may be compared with those of previous workers. Johnson,[79] using results from lubricated experiments upon pure lead found values of 0.8 and 1.5 while Hurst and Ursell[83] used values of 0.47 and 1.2. Sheppard and Raybould[13] found the values 0.52 and 1.32 for reductions less than 100:1 from a minimized upper bound solution, (c.f. 0.6 and 2.15 for the single triangle solution presented here). The gradient, b, for all of these solutions agrees well with those obtained in this work while the intercept values, a, are significantly lower. This may well be due to the fact that their work incorporated lubricated conditions which will affect the magnitude of both a and b since these include contributions from redundant work. A further consideration must be that because of the spread in the results found here, the best straight line fit is weighted towards the position of the maximum numbers of points. Since, as will be shown in the next section, the greatest P/σ values are associated with the higher extrusion temperatures, the line will be biased towards these as more runs were conducted at the higher temperatures.

In conclusion it can be seen that a single line relationship does not appear to exist between P/σ and LnR, as predicted by the theory, although the best straight line fit agrees well with previous workers.

4.3.1.7. Variation of P/σ with the Z Parameter

As was pointed out in the previous section, considerable spread was found when plotting P/σ vs LnR. We shall now take a closer look at this variation in terms of the remaining process variables. These are conveniently contained within the Z parameter. The situation will only be considered for the maximum pressure since it is this which is of prime importance to the commercial extruder. In addition this minimizes the errors as the maximum pressure may be accurately measured while the temperature rise is both smaller and simpler to evaluate from the computational aspect. Figs. 86 and 87 illustrate the results of plotting P/σ against LnZ. In all cases a remarkably good straight line relationship was found, the results for which can be found in Table 4.22.

2 inch Container		
Reduction	$P/\sigma = a-bLnZ$	
Ratio	a	b
30:1	17.45	0.254
40:1	18.09	0.306
50:1	18.51	0.279
60:1	20.45	0.314
3 inch container		
5:1	7.59	0.092
10:1	8.87	0.108

Table 4.22. Results for P/σ vs LnZ_i

A decrease in Z, or increasing temperature, results in an increase in P/σ in all cases. Thus it would appear that the calculation for σ is seriously in error or the redundant deformation increases with a temperature rise.

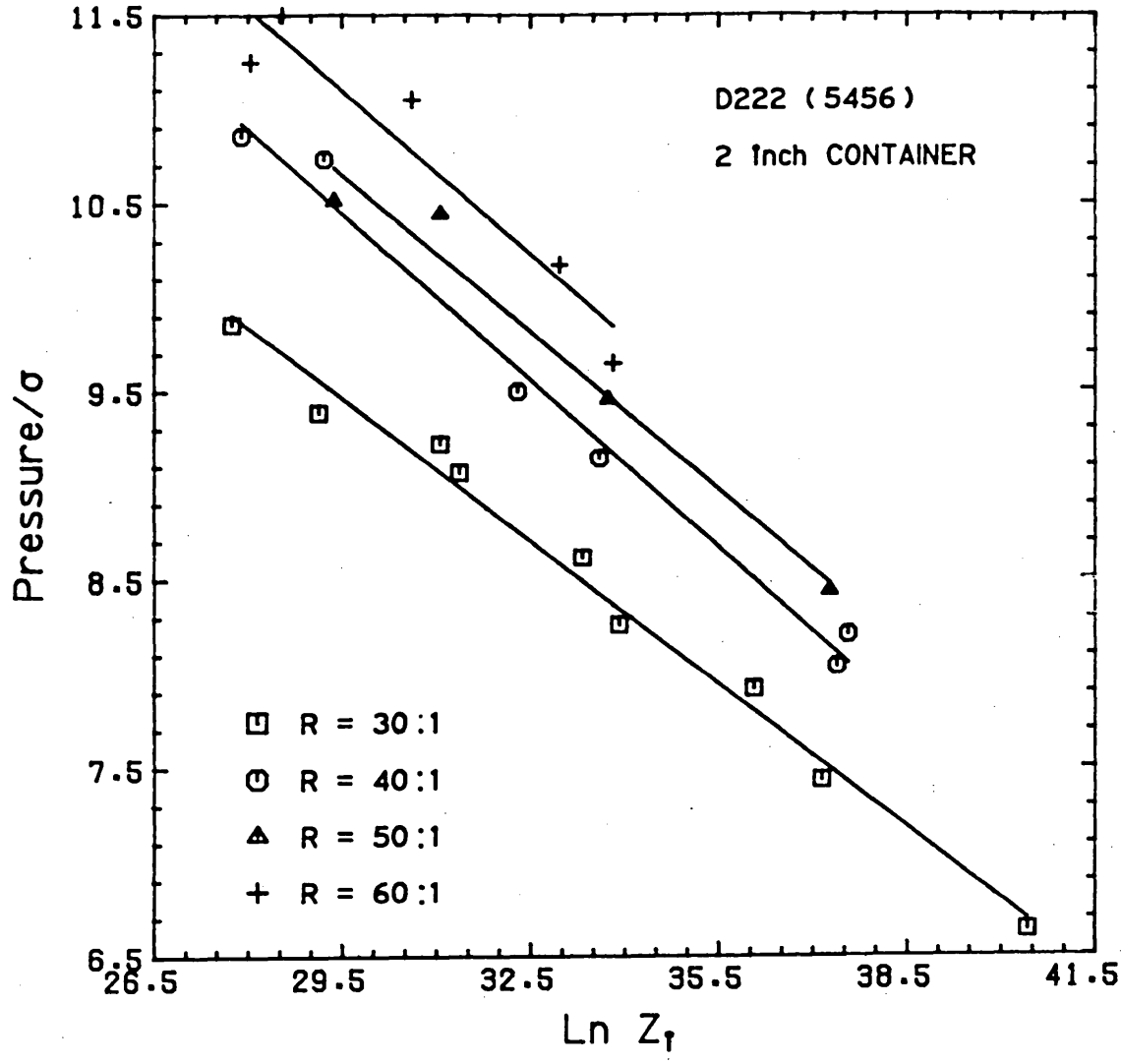


Fig. 86. P/σvs. LnZ_i, alloy D222 (5456)

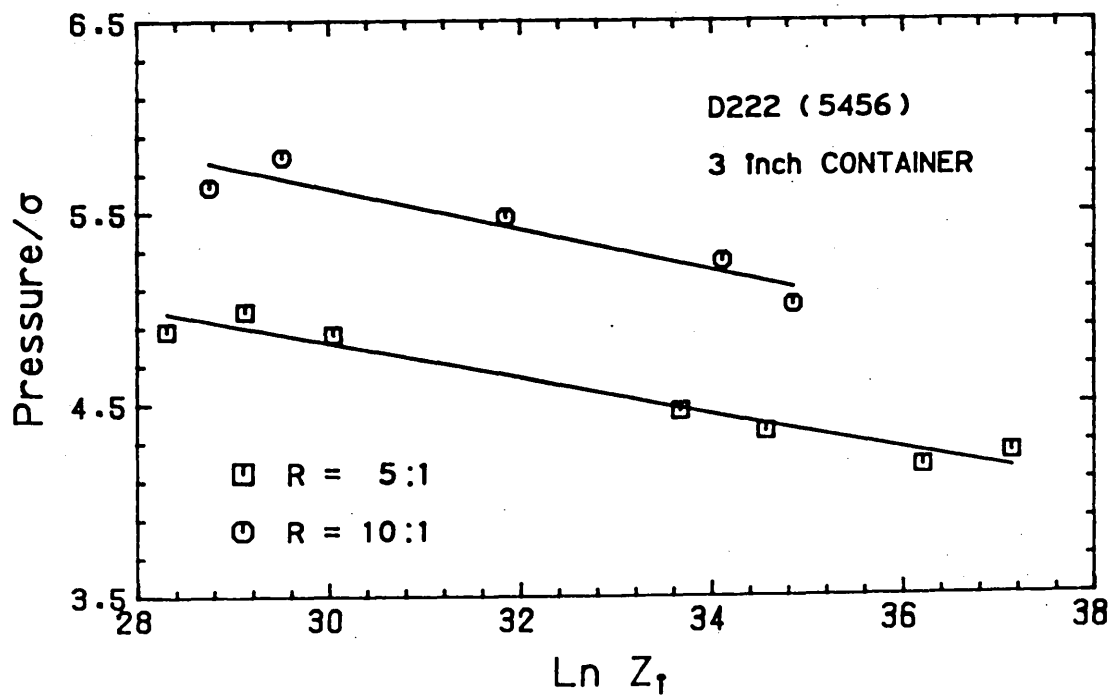


Fig. 87. P/σ vs. LnZ_i, alloy D222 (5456)

Considering the former possibility, permits the following observations to be made. For the 2 inch container and a reduction ratio of 30:1, for the high temperature value to drop to the low temperature value of 6.635 would require a temperature drop of 114°C to the peak while, vice versa, a rise of 90°C would be necessary. Even for an alteration of both to their mean value would require a rise of 55°C and a fall of 45°C respectively. It would seem highly unlikely that these temperature changes could possibly take place from consideration of both time available and work done. The changes in flow stress necessary to bring these results to a horizontal level, i.e. constant P/σ value for all temperatures, cannot be achieved by a strain rate change even if one were possible. The idea that the excess pressure, Δp, may be masking the true relationship is impossible since removal of Δp will further worsen the gradient of the lines. This is due to Δp being greater at low temperature, i.e. high Z. Therefore there must be some change occurring within the deformation zone to account for these findings.

Hinesley and Conrad[18] have reported the effects of both temperature and ram speed upon the flow pattern in axi-symmetric extrusion of an aluminium copper alloy (2024). Their results illustrated that the commonly observed flow pattern containing a single maximum at the vertical axis was only found at low Z values. At high values of Z this pattern was replaced by one containing a double maximum. They noted that previous workers[221,222] had found similar results and had related them to changes in lubrication at the die-billet interface. Working with conical dies of reduction 6:1 they concluded that the pattern change was not due to a change in friction conditions but rather due to changes in the material plastic flow behaviour. By simply relating the stress-strain curves for various temperatures to the deformation zone shape and anticipated temperature distributions within, they were able to justify their hypothesis and model the flow.

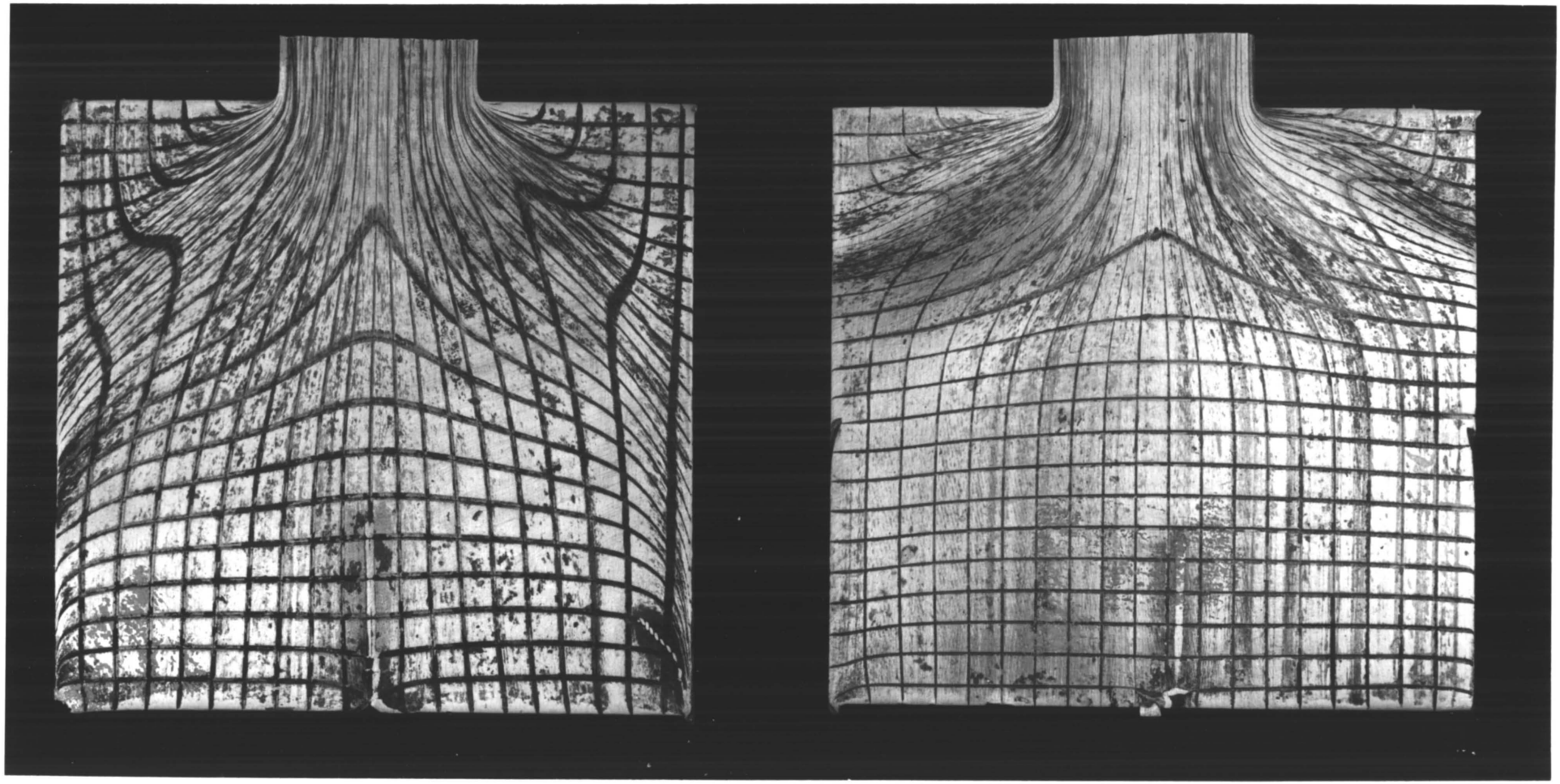
Following this lead, it was decided to carry out similar experimental work to ascertain whether any changes in deformation zone structure were likely in the case of the aluminium-magnesium alloys. In order to be able to conduct the work at both high and low temperatures with the 3 inch container, a low extrusion ratio

was chosen, 10:1. Two billets were sectioned along a meridian plane and on one section in each case, a square grid of lines 4 mms apart was machined. The surfaces were then treated with a graphite lubricant, to prevent sticking during extrusion, and rematched. Partial extrusion was then carried out at temperatures of 335°C and 500°C. The results may be seen in Figs. 88(a) and 88(b). As these figures illustrate, although no double maximum appears at either temperature, the single maximum is clearly evident in both cases, there is a significant change in deformation zone shape. In the case of the low temperature run, the effect of the deformation is strictly limited to a small volume close to the die mouth.. Over at least 50% of the surface shown there is no evidence of deformation, the grid is regular across the entire width. The formation of the dead-metal-zones is evident and the boundary reaches back from the die mouth at an angle of approximately 28°. The acceleration of the central regions appears slight since the maximum in the grid line has not projected a significant amount below the outer sections. Comparing this with the result of the high temperature run shows a considerable difference. In this case the effects of the deformation can be found over all the surface shown. Considerable amounts of cylinder wall shear may be seen stretching from the rear of the billet up to the dead-metal-zone boundary. In this case these boundaries have moved farther back into the billet, leaving the die mouth at an angle of 48°. In the central regions of the deformation zone, the central acceleration is greater, the maximum in the pattern showing a considerable displacement from its outer sections. Thus, in this case the deformation zone appears considerably larger than in the low temperature case. This would tend to imply a greater degree of internal energy dissipation, as found from the theoretical model when forcing a solution using the experimental values shown in section 4.2.2. Another factor which must be considered is the strain rate. Although the strain is the same for each case, i.e. in terms of the reduction, the time in which it is achieved is different. Since the deformation is initiated nearer the rear of the billet in the high temperature case, there will be an associated greater time available for the deformation to be completed and so a slower strain rate should be applicable.

(a) High temperature pattern

Fig. 88 Deformation patterns for a reduction of 5:1

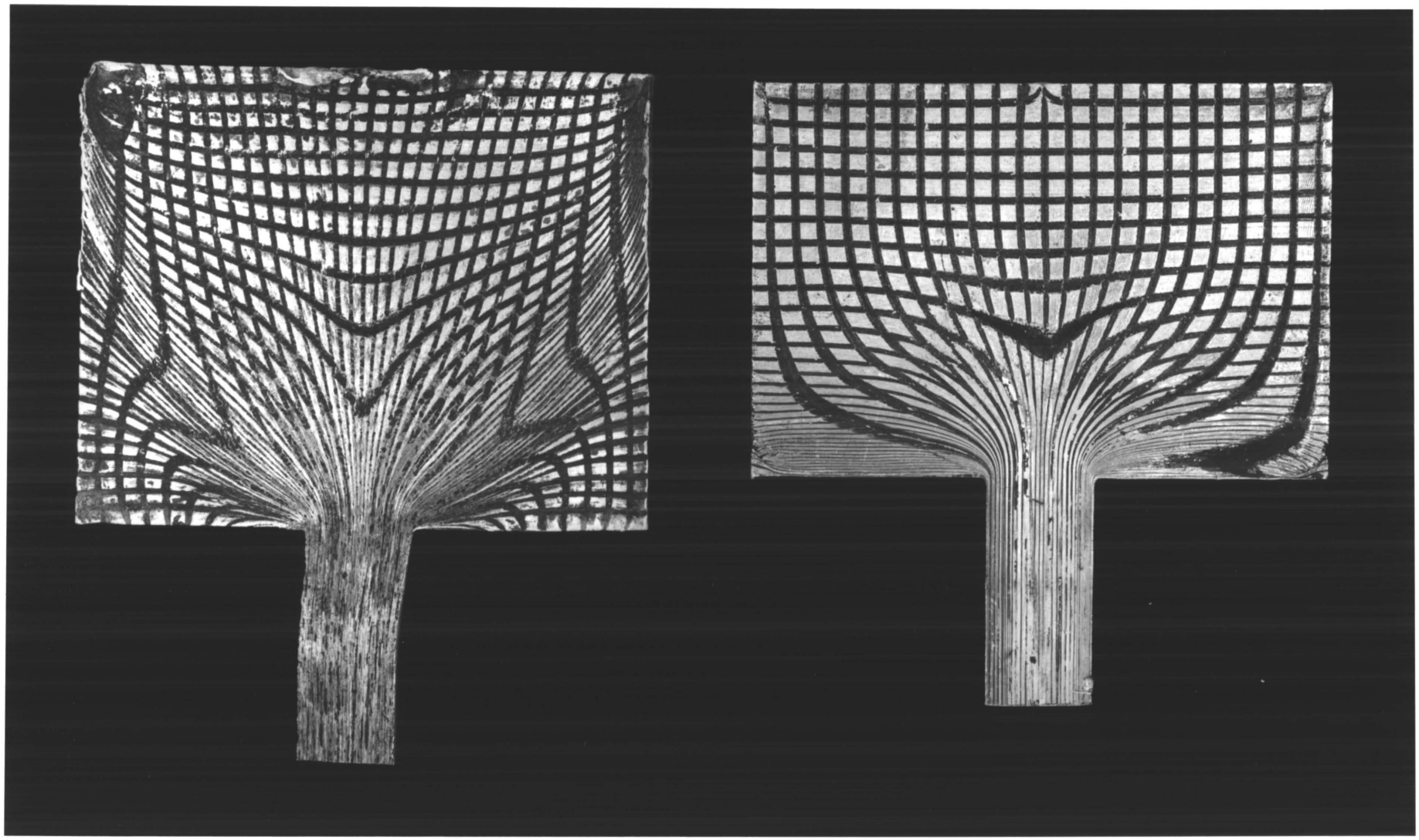
b) Low temperature pattern



a) high temperature

b) low temperature

Fig. 89. Deformation patterns for a reduction of 30:1



The consequence of this would be to reduce the flow stress value and thus increase the P/σ value. However this change would be incapable of producing the types of variation in σ necessary to generate horizontal plots in Figs. 86 and 87.

In terms of the material plastic flow behaviour the observations are not unrealistic. For the high temperature case, the material is much less able to withstand the strain gradients imposed by the deformation in elastic terms and some plastic strain will undoubtably result. At lower temperatures the increased resistance of the material to plastic flow permits more of the gradients to be contained in elastic strain.

The observations are also applicable at ratios above 10:1, work with softer aluminium alloys showing this to be true, Figs. 89(a) and 89(b). The results found in Figs. 86 and 87 of a decreasing P/σ with increasing Z term are therefore due to a change in deformation zone geometry caused by a variation in the plastic flow behaviour of the material.

4.3.1.8. The Relationship between Pressure, Extrusion Ratio and the Z Parameter

The results illustrated in Figs. 82-85 show that the dimensionless group P/σ is dependent upon the magnitude of both the Z parameter and the extrusion ratio. It would be desirable to relate pressure to flow stress through a relationship applicable for all the extrusion variables and then incorporate this feature in the sinh relationship to relate pressure to these variables. The results of the previous two sections permit this to be achieved.

In the previous section linear relationships were found between P/σ and LnZ as shown in Table 4.22. The equations were generated for the specific extrusion ratios stated. If we assume a relationship of the form:-

$$P/\sigma = a + bLnR + cLnZ \qquad (101)$$

then the data will permit the evaluation of the constants a, b and c.

For the 2 inch diameter container it was found that:-

For R = 30:1 $P/\sigma = 17.45 - 0.254\ LnZ$ (102)

For R = 50:1 $P/\sigma = 18.51 - 0.279\ LnZ$ (103)

comparing equations (102) and (103) with (101) gives:-

$$17.45 = a + b\ Ln(30) \quad (104)$$

$$18.51 = a + b\ Ln(50) \quad (105)$$

or $$17.45 = a + 3.401b \quad (106)$$

$$18.51 = a + 3.912b \quad (107)$$

Subtracting equation (106) from (107) gives:-

$$1.06 = 0.511b$$

or $$b = 2.074$$

Substituting this value back into equation (107) gives:-

$$a = 10.4$$

Thus we have evaluated that for the 2 inch diameter container:-

$$P/\sigma = 10.4 + 2.07\ LnR - 0.28\ LnZ \quad (108)$$

Following a similar analysis for the 3 inch diameter container, using the results for reduction ratios of 5 and 10:1 produces:-

$$P/\sigma = 6.37 + 1.08\ LnR - 0.11\ LnZ \quad (109)$$

It should be remembered that these relationships are derived from experimental results and cannot, therefore, be taken as the exact solution. From the results it would appear that the multiplying factor for the LnR term corresponds well with those published for a simple $P/\sigma = a + bLnR$ relationship while the LnZ term adjusts the

overall value for changes in deformation zone shape. The differences in multiplying factors for the LnZ term for each container size may come from accumulated inaccuracies in the experimental work. However, there is no reason why these two should be equal. In section 4.2.4. it was shown that for equivalent conditions of extrusion ratio and ram speed, the 2 inch container produced greater values for strain rate than the larger diameter one. Thus, assuming similar deformation zone changes for both 2 and 3 inch containers, for given changes in ram speed, the smaller multiplying factor appears because of the greater Z value. Restating these equations for load would give:-

$$\text{Load}_2 = \sigma\ (0.026 + 0.00528\text{LnR} - 0.00714\text{LnZ}) \qquad (110)$$

$$\text{Load}_3 = \sigma\ (0.028 + 0.00477\text{LnR} - 0.00485\text{LnZ}) \qquad (111)$$

i.e. excepting the Z term the equations are very similar and would appear to confirm their validity.

The expressions for P/σ in equations 108 and 109 may now be used to predict the pressure line for a limit diagram. Substituting the expressions for P/σ into the general hot working equation gives:-

For the 2 inch container:-

$$Z = A \cdot \sinh \left[\frac{\alpha P}{10.4 + 2.07\text{LnR} - 0.28\text{LnZ}} \right]^n \qquad (112)$$

For the 3 inch container:-

$$Z = A \cdot \sinh \left[\frac{\alpha P}{6.37 + 1.08\text{LnR} - 0.11\text{LnZ}} \right]^n \qquad (113)$$

A test of the validity of the result will be to plot:

$$\text{LnZ vs Ln sinh} \left[\frac{\alpha P}{a + b\text{LnR} - c\text{LnZ}} \right]$$

for each case using the previously calculated values of α and ΔH.

Should the relationships hold and extrusion be a thermally activated process then the experimental results should produce a linear relationship of slope n and intercept A. These values should coincide with those already evaluated from torsion testing of 3.2 and 1.614×10^{10} sec^{-1} respectively.

The results of the plots may be seen in Figs. 90 and 91. As the graphs show, the developed relationships produce very good straight line fits for the experimental extrusion data. The results for the gradients and intercepts from linear regression are:-

3 inch container $n = 3.18$ $A = 2.6 \times 10^{10}$ sec^{-1}

2 inch container $n = 3.34$ $A = 2.6 \times 10^{10}$ sec^{-1}

The remarkable correlation between these results and those evaluated from high temperature torsion tests confirms the supposition that hot working is a thermally activated process. For the 5% magnesium alloy being considered it would appear that the rate controlling process is the viscous glide of dislocations.[212] Murty et al.[212] quote the work of Weertman[187] who established from theoretical considerations that a stress exponent of around 3 was consistent with this type of rate controlling process. These observations are consistent with those of Wong and Jonas[22] for commercial purity aluminium, Castle and Sheppard[23] for aluminium copper alloys and Sheppard and Raybould[210] for commercial purity aluminium and an Al-7% Mn-3% Mg alloy.

The good straight line plots found in Figs. 90 and 91 permit their use for calculating the pressure line for a limit diagram. Since the relationships have been generated for ram speed, initial temperature and extrusion ratio, input of selected values of these will output the required minimum pressure necessary to initiate the process. Their use will be illustrated in subsequent sections.

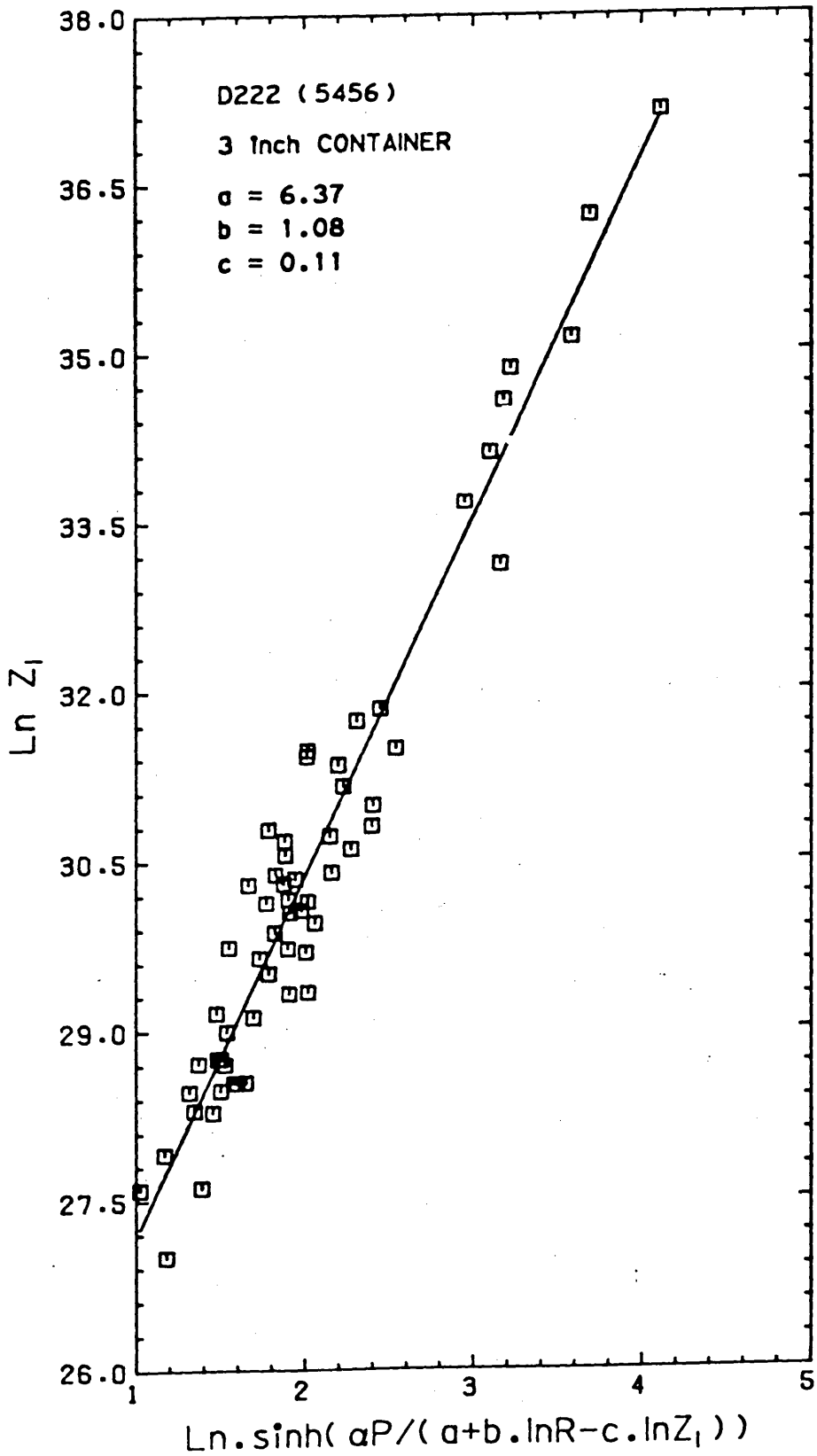


Fig. 90. LnZ_i vs Ln Sinh $\frac{\alpha p}{(a+bLnP-cLnZ)}$

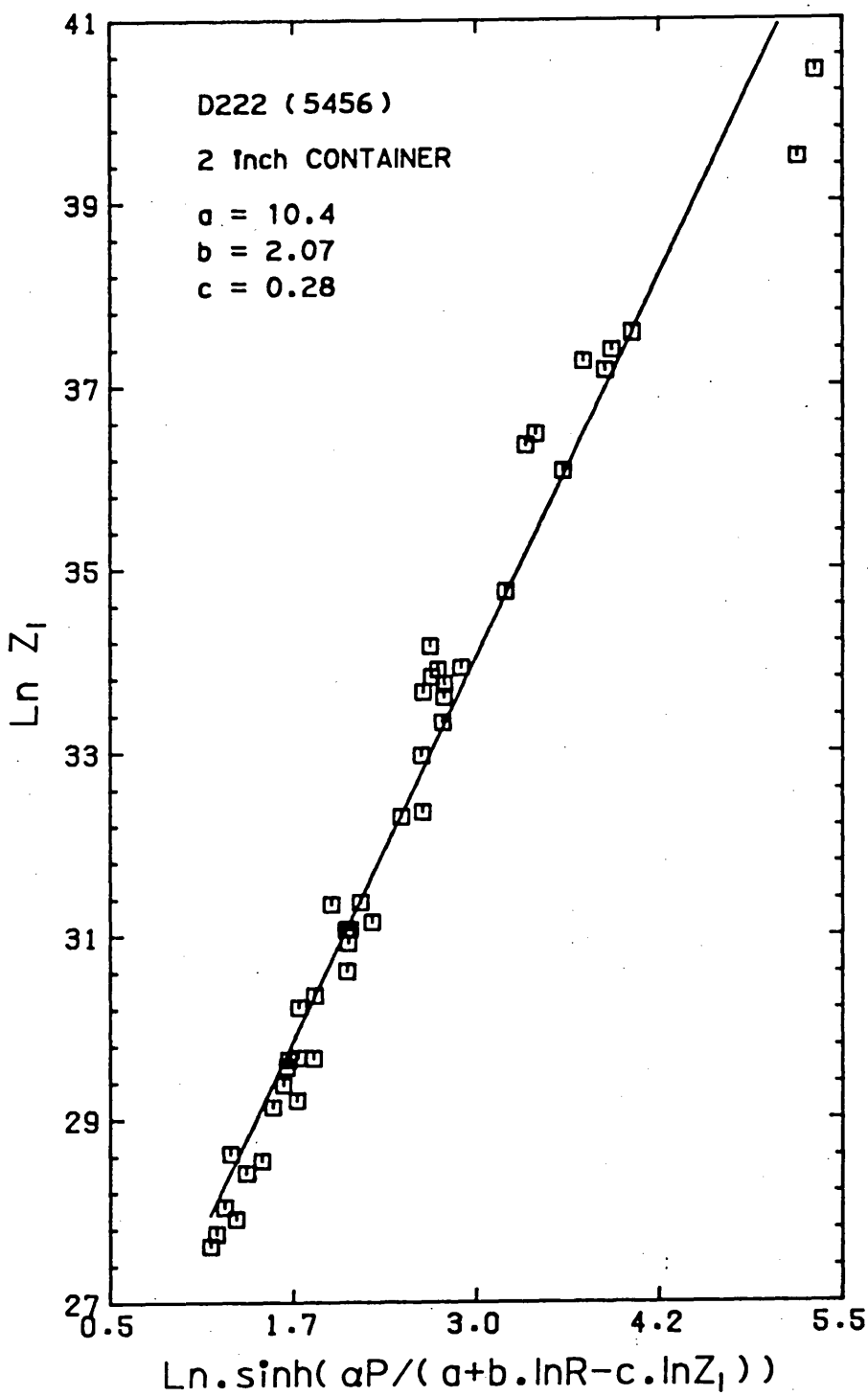


Fig. 91. LnZ_i vs. Ln Sinh $\frac{\alpha p}{(a+bLnR-cLnZ)}$

4.3.1.9. The Dependence of Surface Conditions upon the Process Variables

As was discussed in section 1.5, various alternatives of unacceptable surface finish may be manifested during the extrusion process. Of prime importance among these is the onset of incipient melting resulting, in the extreme case, with 'the fir tree effect'. The approach taken by previous workers has been to assume that the melting was caused by the extrude emergent temperature exceeding its solidus temperature. Thus, by calculating a temperature rise for the operation the onset of incipient melting can be predicted.

Hirst and Ursell[83] derived a solution for adiabatic extrusion. They started with a relationship for the work done during the process, considered a mean value of deformation stress, between initial and final temperatures, and concluded that for the onset of melting:-

$$\text{LnR} = \frac{(T_s - T_\theta)\ S_g\ S_h}{4.43\ Y_m\ [1+2\mu L/(D_B-D_E)]} - 0.39 \qquad (114)$$

where T_s = minimum solidus temperature
T_θ = preheat temperature
Y_m = mean deformation stress
μ = coefficient of friction between billet and container.

The analysis assumed that 100% of the work done was converted to heat and zero heat losses.

Ashcroft and Lawson[9] applied a more practical approach through extruding thermocouples close to the rear of the billet. They ascertained that for the Al-Zn-Mg-Cu alloy under investigation, melting occurred if the temperature exceeded 480°C.

Meadows and Cutler[198] improved the method of Hirst and Ursell by using the calculation of Singer and Al-Samarrai,[10] for the temperature rise calculation. Their method considered heat conduction to the die and container while assuming all the deformation occurred in the die plane. They found that:-

$$T_A = T_M \left[1 + \frac{\alpha_1 K_1}{(\rho_1 c_1 S)^2 A_B} + \frac{\alpha_2}{(\rho_1 c_1 S)} \right]^{-1} \qquad (115)$$

or $T_A = T_M\ (F)^{-1}$

where:

T_A = actual temperature rise
T_M = maximum theoretical temperature rise
K_1 = thermal conductivity of the billet
c_1 = specific heat of billet
S = ram speed
α_1 = rate of heat loss to container
α_2 = rate of heat loss to die
ρ_1 = specific gravity of the billet.

Thus a temperature correction factor, F, is produced which Meadows and Cutler used in equation (114). They did point out, however, that apart from any basic errors in the calculation, there was the problem of ascertaining accurate values of Y_m and μ.

Sheppard and Raybould[13] used their integral profile method to calculate the emergent temperature.

In all of these approaches, the basic concept of melting being caused by the die emergent temperature exceeding the solidus is maintained. The use of theoretical models for calculation of temperature rises during extrusion remains a very complex problem. In addition, no allowance is made for the internal condition of the material which may contain residual stresses sufficient to introduce sizeable tensile stresses in the outer regions enhancing the likelihood of cracking. Work with contact thermocouples on emergent material,[218] has shown cracking to appear at temperatures below that of the solidus. Indeed, inspection of tables in Appendix G, shows that for many of the cases where incipient melting was observed, the final temperature has not exceeded the solidus temperature of 570°C.

In an effort to overcome these problems it was decided to attempt to find a relationship between the emergent surface condition and the process variables from a purely experimental standpoint.

Of prime importance, in this respect, is the initial billet temperature. An increase in ram speed or extrusion ratio must serve to worsen the situation because of their effect in increasing the work done. For limit diagram production, it would be beneficial

to utilise the initial billet temperature since this is accurately known at the commencement of the process. Once again the Z parameter encompasses each of these variables and this was chosen to plot against initial billet temperature. The diagram was constructed for each extrusion carried out, plotting melted product with a red pen and sound product with a black pen. The results are found in Fig. 92.

As this plot shows, for a given value of temperature there would appear to be a specific value of LnZ above which unacceptable surface is produced. The line serves to indicate the approximate location of these values. The mathematical relationship describing this line will generate an equality predicting the surface condition of the product.
Thus for acceptable surface quality:-

$$\text{LnZ} < \frac{19766.3}{T_{(abs)}^{.989}} \qquad (116)$$

and for unacceptable surface quality:-

$$\text{LnZ} > \frac{19766.3}{T_{(abs)}^{.989}} \qquad (117)$$

It is interesting to note that whereas the pressure limiting line required two expressions for the different container sizes, one is applicable to the melting line. This is somewhat unexpected since for given ram speed and temperature conditions, the 2 inch diameter container gives an increased strain rate and an increase temperature rise, due to its reduced volume, compared with the larger diameter. Both of these would have been expected to enhance melting.

A satisfactory method has therefore been obtained for predicting bad surface from the experimental runs. Its use in drawing limit diagrams for the alloy will be described in later sections.

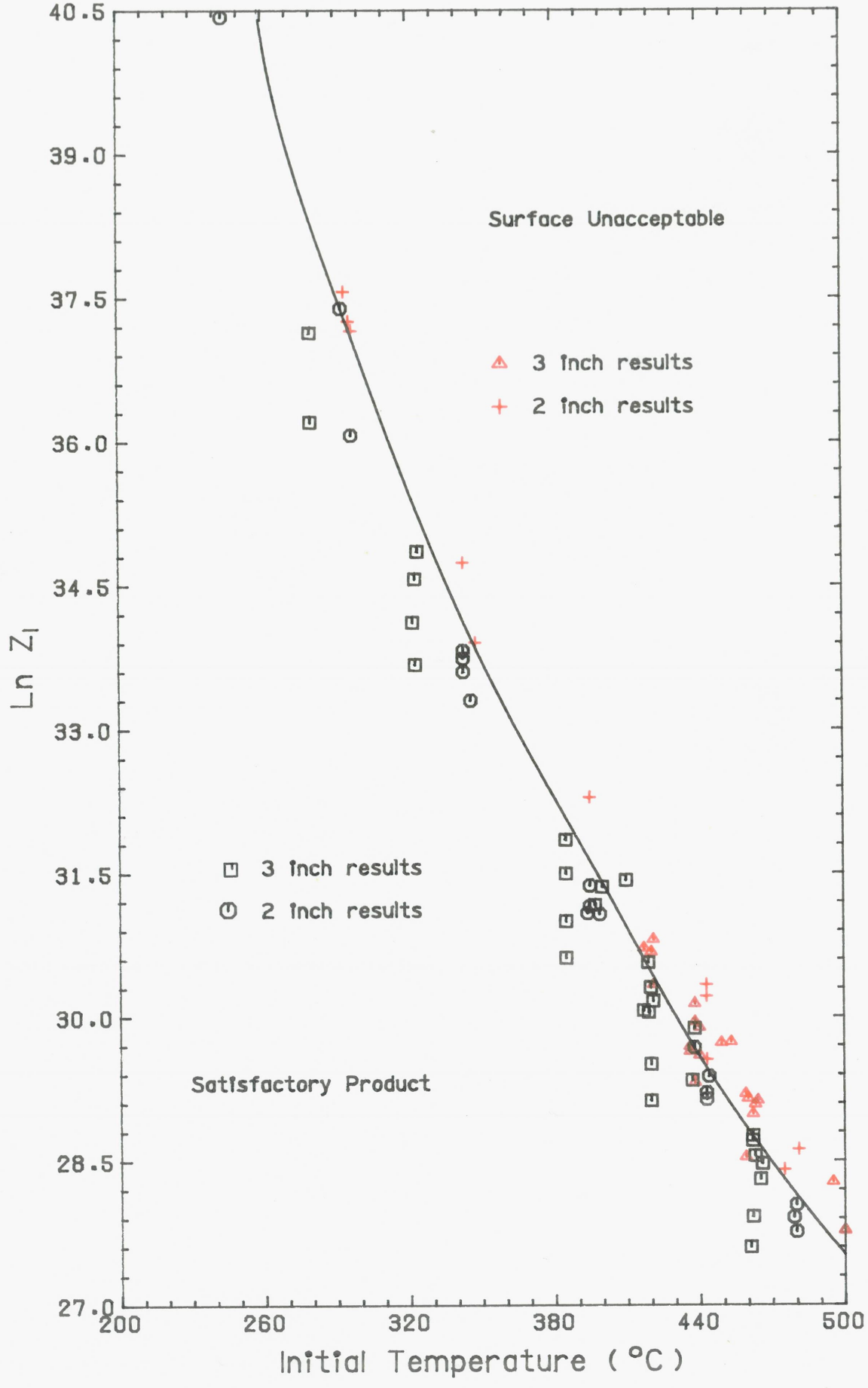


Fig. 92. LnZ_i vs. Initial Temperature for various final surface conditions

4.4.1. Development of Structure During Plastic Flow

Having seen how the process variables affect the magnitude of the pressure etc., we now turn our attention to the structural aspects of extrusion. Prior to investigation the final extrude structure it is of considerable interest to describe the development of structure during plastic flow. In the first case this will be discussed with reference to a super-pure aluminium 5% magnesium alloy, D75. This system offers a much simpler situation to analyse due to the lack of second phase particles. Following this a comparison will be made for the commercial alloy D222 (5456).

During all mechanical processing operations it is necessary to establish a deformation zone which is quasi-static. The material must thus be transformed from a state of as-cast dislocation density to one consistent with the thermally activated events obtaining during deformation. The establishment of this steady state density produces a non-linear external energy against time relation which varies with the process. Of the major processing routes rolling is limited by friction conditions at roll entry, but extrusion is very much governed by the pressure necessary to initiate the process. This section considers the development of the quasi-static deformation zone during the extrusion process.

The direct extrusion pressure-displacement locus is shown in Fig. 1 and the description of the three stages together with previous theories regarding the presence of the peak is made in section 1.1.1. Of all the theories put forward, Castle and Sheppard's[23] would appear the most pertinent. They indicated that the additional pressure, Δp, was associated with the energy required to establish the quasi-static deformation zone. They proposed that the formation of the zone required an excess of dislocation sources leading to a greater than equlibrium dislocation density. This excess of dislocation production would also imply a non-equilibrium flow stress resulting in the requirement of excess pressure. It is this basis which is used in this investigation.

Microstructural investigations[100,155] of aluminium alloys have shown that dynamic recovery is the major softening process.

Recent work by Gardner and Grimes[183] has reported evidence for dynamic recrystallization in an aluminium-5% magnesium alloy. Their lack of conclusive electron microscopical evidence in this case means that for the time being, the original mode of deformation will be assumed unless results to the contrary are found. In terms of dynamic recovery, therefore, the dislocation substructure produced is a direct result of temperature and stress induced mobility due to plastic deformation. This rapid increase in dislocation density produces a corresponding increase in the elastic strain energy (stored energy) which is released when dislocations meet and annihilate or rearrange themselves into lower energy configurations. It is this rearrangement which typically produces regular low angle boundaries forming sub-grains. The mechanism of boundary formation is by cross-slip and climb which, being thermally activated, is aided by high homologous temperatures. The distribution and mobility of dislocations is also affected by stacking fault energy, crystal structure, strain rate, grain boundaries and precipitates. Dislocation movement is relatively easy in the majority of aluminium alloys because of their high stacking fault energy which suppresses the formation of dissociated dislocations and extended nodes which would inhibit cross-slip and climb. Magnesium is reported[168] to modify the stacking fault energy to some degree and this reduction will accordingly be reflected in the ease of dislocation movement. Magnesium exhibits limited solid solubility in aluminium, but in the super-pure alloy being considered there is very little second phase present which could modify the dislocation substructure.

The development of substructure during deformation has been extensively studied and many theories have been proposed to account for observed work hardening characteristics.

The most detailed models for work hardening apply to cold deformation processes where climb is not involved. However, the build up in dislocation density to a level where either dynamic recovery or recrystallization takes place in hot working, presumably involves similar work hardening mechanisms to those taking place at lower temperatures. These mechanisms have been critically reviewed recently by Hirsch[223] and therefore no discussion of them is included here.

Experimentally the procedure followed that described in Chapter 3. Extrusion was performed at a reduction of 40:1 and a ram speed of 13 mms/sec. The temperature utilised was 450°C. The extrusion cycle was stopped at the positions shown in Fig. 93. Specimens for electron microscopical examination were taken from the locations shown in Fig. 94. This flow line was found from observation and substantiated by a combination of upper bound[222] and spherical velocity fields.[224] Investigation by macro and micro optical microscopy and transmission electron microscopy of these samples permitted the development of dislocation structure during the extrusion process to be observed.

4.4.1.1. Structural Development in Super-pure Al-5% Mg

Fig. 95 depicts the billet during the upsetting stage, location 1. The macrostructure does not vary from that of the original billet with the exception of the region adjacent to the die entry where some deformation may be detected. There is no evidence of deformation elsewhere in the billet although container/billet shear is suggested by the grain structure at the periphery. Fig. 96, illustrating the structure at a later stage in the upsetting process, location 2, does not exhibit radical changes but an extension of the main deformation zone has occurred and the grains in this die entry region have become elongated. It is interesting to note that a small quantity of material has been forced through the orifice and that the extreme front end reveals quite clearly the original undeformed structure. Even at this stage, however, there is a variation in structure from front to rear of the extrude pip. Fig. 97 is at a location of further increase in pressure with little ram travel and shows the deformation zone extending back into the billet, (location 3). There is still little change in bulk structure and no identifiable dead-metal-zone, but cylinder wall shear appears to have extended over the complete billet surface periphery. Fig. 98 corresponding to location 4 shows an almost identical macrostructure but the fibrous nature of the extrude structure suggests an increase in total deformation. The structure in Fig. 99 is located approximately at the point of peak pressure and shows very pronounced changes in morphology. The extrudate exhibits

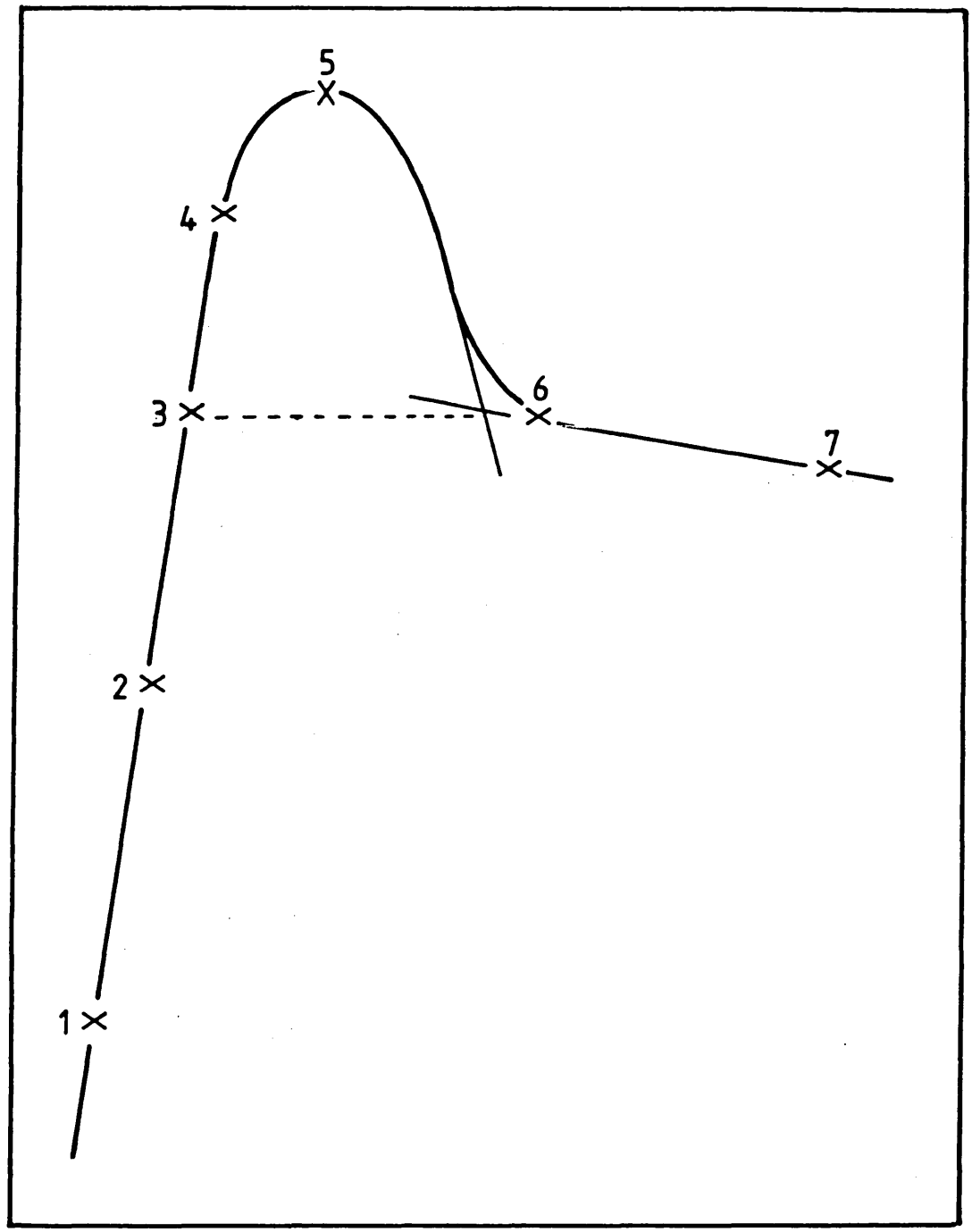


Fig. 93. Locations of sampling positions on load-displacement locus for structural development.

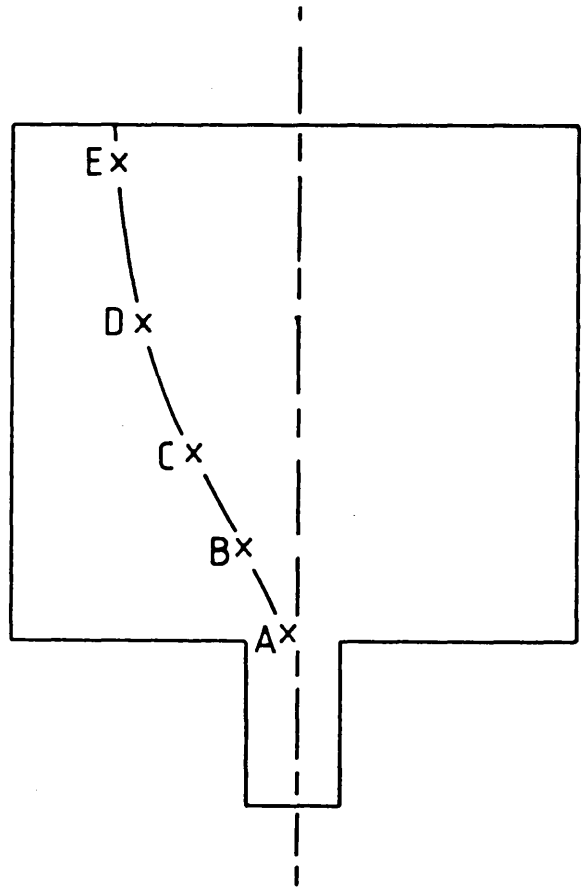


Fig. 94. Location of electron microscopy samples for structural development.

Fig. 95. Macrostructures from location 1

Fig. 96. Macrostructure from location 2.



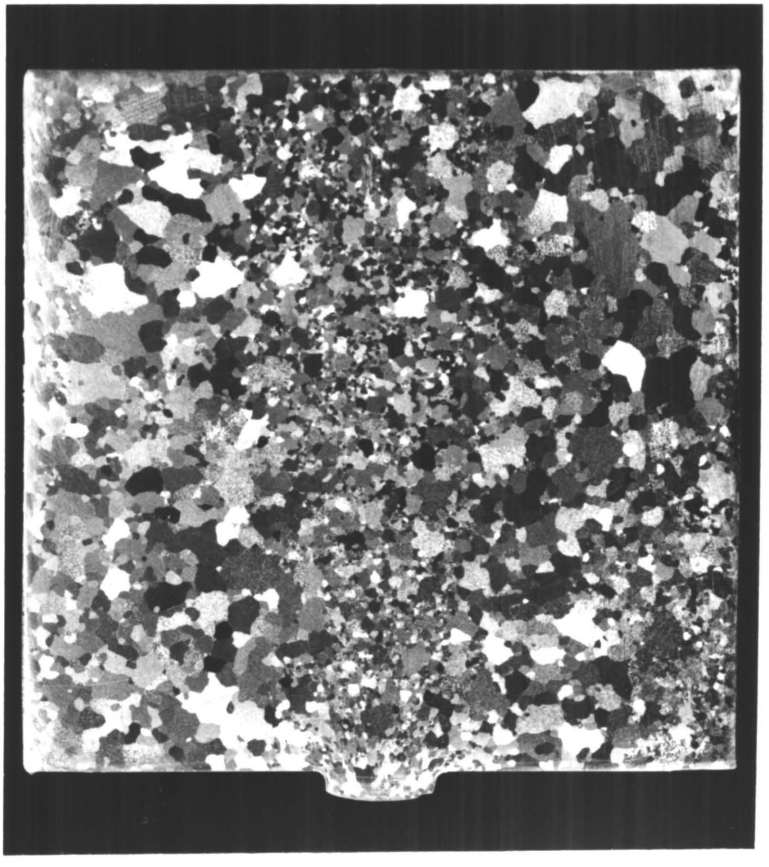
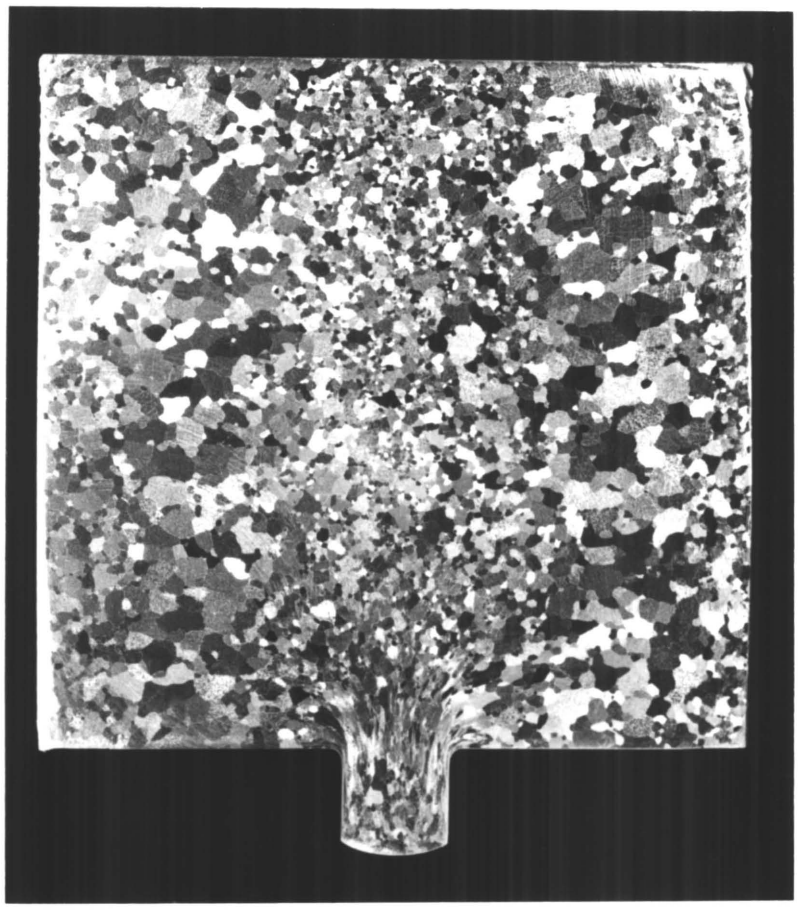
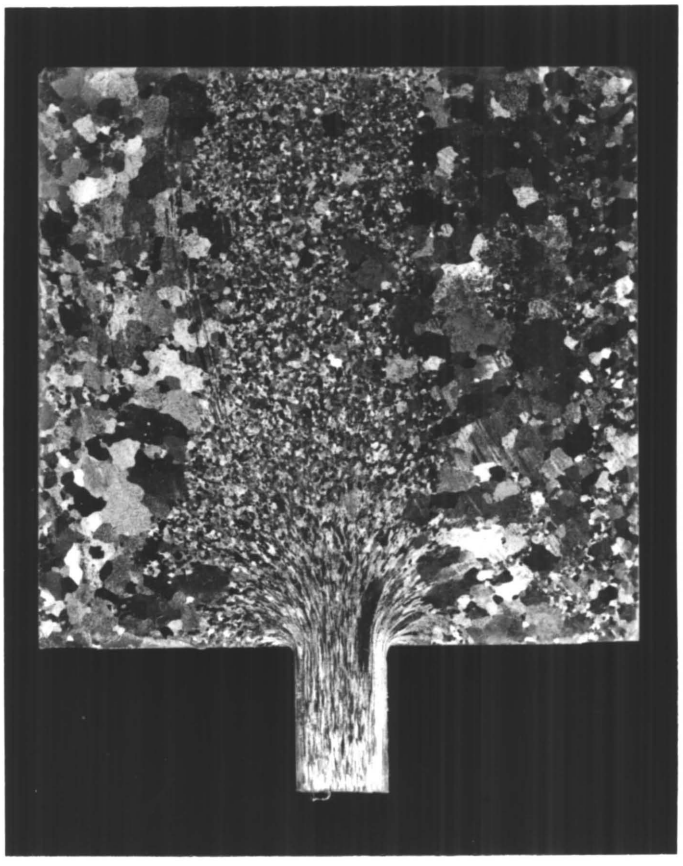


Fig. 97. Macrostructure from location 3

Fig. 98. Macrostructure from location 4





the typical fibrous or 'cold worked' structure and it should be noted that at this stage a considerable length of material has been extruded. Clearly the 'break through' pressure does not correspond to the commencement of extrusion. The deformation zone has again been extended backwards into the billet and the dead-metal-zones are beginning to be identified. Considerable cylinder wall shear is apparent and the billet peripheral layers are quite heavily deformed. This latter feature is less predominant in the surfaces adjacent to the die plane supporting the observation that the dead-metal-zone will be established in this area. In fact the deformation zone extends well back into the billet and grains can quite easily be identified which have been elongated within the central deformation zone. Fig. 100 shows the structure when the pressure has fallen by an amount Δp after the peak pressure and considerable ram travel has occurred. The central deformation zone has now fully developed and intense shear is occurring at this location; cylinder wall shear also appears to be more intense but it should be recalled that it is a deformation history which is being observed since quasi-static conditions do not obtain at this location. It should also be noted that although the dead-metal-zones can clearly be identified it is the lessening of surface shear and gradation of grain deformation which allows this observation; there is definite evidence that the quasi-static deformation zone is about to be established. Figure 101 illustrates the macrostructure during the steady state region, location 7, the quasi-static deformation zone is fully developed and the dead-metal-zone can be very easily identified. Regions of significant shear can be seen extending from die entry and along the central axis and from die entry to the periphery of the billet bounded by the dead-metal-zone and the container/billet interface. The large initial grain size allows the recognition of grains passing through three regions of intense deformation. The identification of two regions of lesser deformation on either side of the central zone and sandwiched by it and the 'peripheral' zone suggests a buffer zone which serves primarily to supply material to the regions of high deformation in the billet. Material flowing from the peripheral region of the billet can be seen to occupy about 35% of the extrudate cross-section whilst material from the axial deformation zone occupies approximately 55%. This implies that the

Fig. 99. Macrostructure from location 5

Fig. 100. Macrostructure from location 6



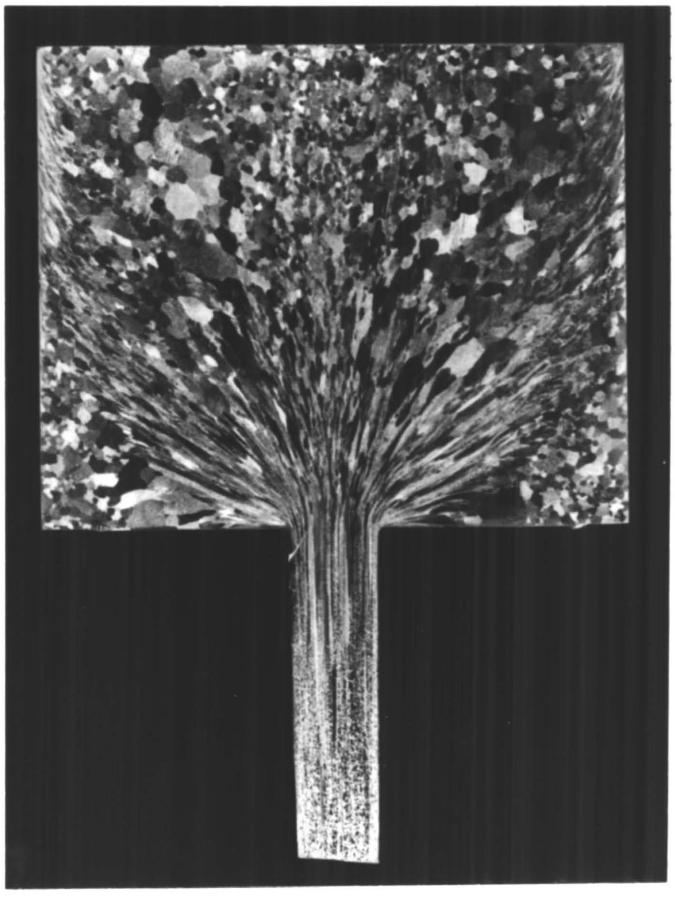
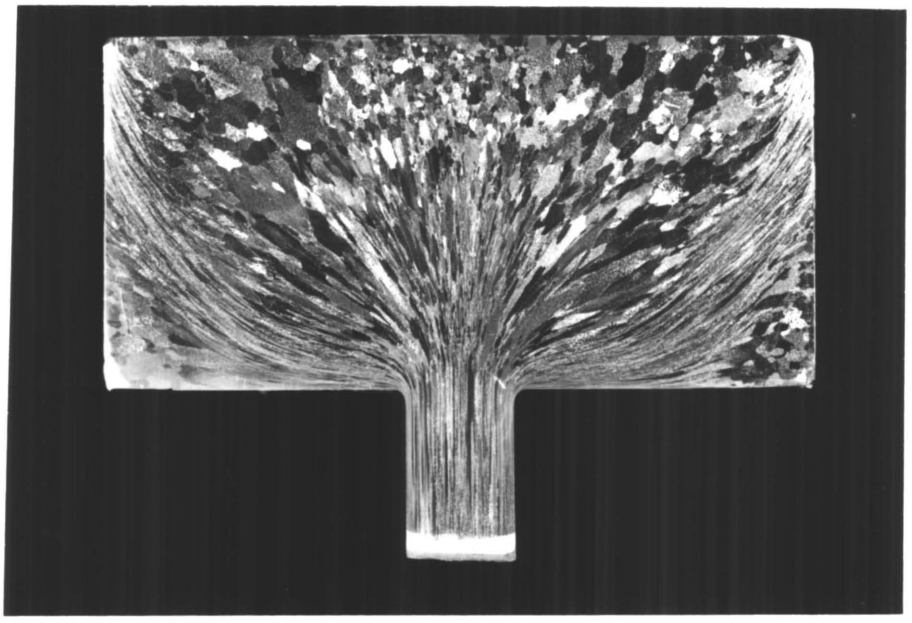
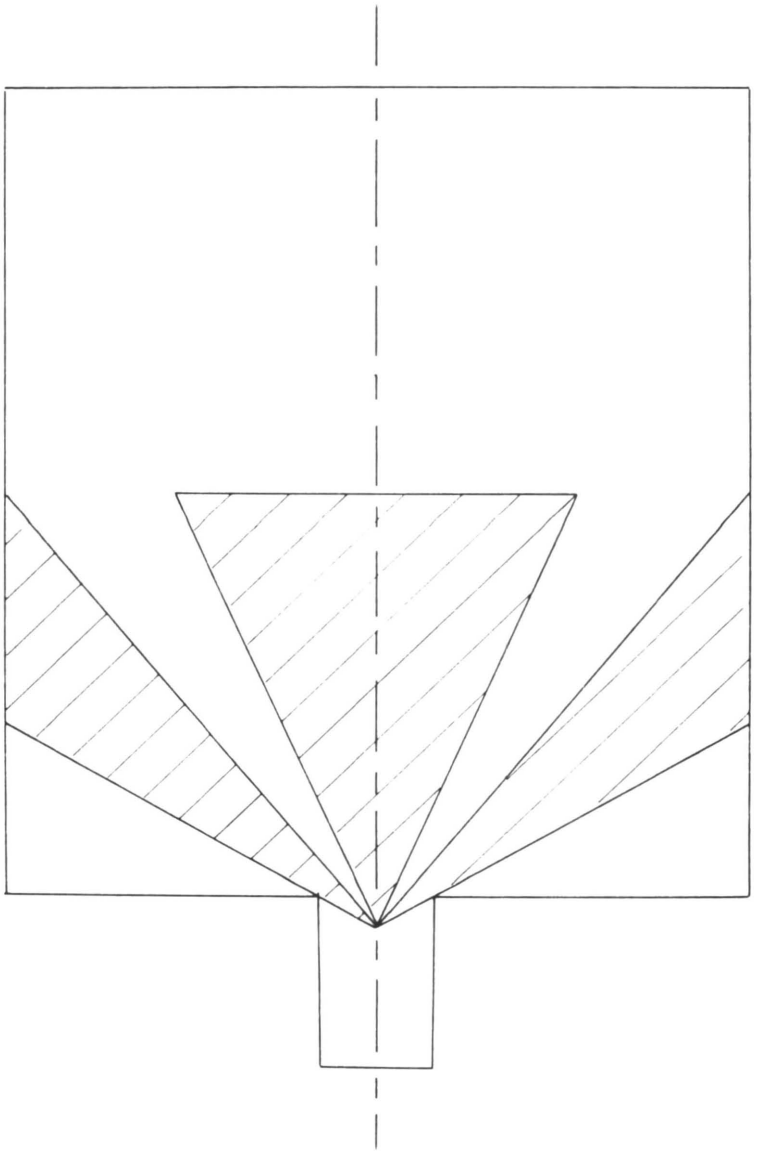


Fig. 101. Macrostructure from location 7

Fig. 102. Appearance of deformation zone from experimental observations.





two zones of lesser deformation are feeding only about 10% in total of the material section shown in Fig. 101. Clearly if these zones were not primarily feeding the intense shear zones, vortices would form within the deformation zone. This can occur when the dummy block destroys the mass balance of the various deformation zones. The deformation observed would support an upper bound deformation field as shown in Fig. 102 which, although more complex than presently described fields defines the deformation field in a more precise manner. The shape of the deforming region also correlates rather better with observed macroscopy and with grid deformation studies.[220]

In summary, it would appear that significant macrostructural changes occur only after the peak pressure. During upsetting the deformation zone extends backwards from the die mouth and along the cylinder wall and dead-metal-zone. At the peak pressure deformation is well developed but steady-state macro-conditions develop between the instant of peak pressure and a time corresponding to a decrease of Δp from this point. The steady-state region is characterised by much greater intensity of shear at the axis and periphery of the billet.

4.4.1.2. Structural Investigations

The dislocation structure within the billet arrested at location 1 in Fig. 93 was heterogeneous. Specimens extracted from the rear of the billet (positions C, D and E) had similar structures having a uniform density typified by Fig. 103. In isolated areas however, walls of dislocations were beginning to form and this feature is shown in Fig. 104. This micrograph is from position C, but similar walls were observed in the other rear positions indicating that the upsetting operation causes deformation throughout the billet. There did not appear to be any special deformation associated with possible ram/billet interaction. Further forward in position B dislocation wall formation was more pronounced and outcrops of sub-grains were observed at high angle boundaries. In general subgrains were not consistently observed at any position in this billet which is consistent with the thesis that strains imposed on the material during the upsetting process are absorbed by shear stress at the grain boundaries. This will involve the production of

dislocations to produce the strain and additional dislocation generation for storage within grains to maintain the strain gradients imposed by grain boundary shear. Thus the dislocation density is necessarily increased and a driving force for subgrain formation created. Fig. 105 clearly illustrates this feature. Although most grains were devoid of sub-grains the specimen extracted from the die mouth (position A) showed a subgrain banding phenomenon. Bands of sub-grains were observed bi-secting the grains and being quite severely elongated in the potential extrusion direction (at this stage extrusion has not commenced). Misorientations were higher between these bands than between the sub-grains along them which can be seen in Fig. 106 by noting the small contrast between the individual sub-grains and large contrast difference between these and the remainder of the grain. This was confirmed by measurement of misorientation from selected area diffraction patterns. The banding would seem to be the result of strains exerted upon abnormally large grains as they pass the velocity discontinuity associated with entry to the die mouth. These grains are preferentially elongated and the resulting localised regions of high strain require that areas of higher dislocation density also exist. Hence in this area there is sufficient dislocation mobility and density to effect the formation of subgrains. This observation may be even more significant in the industrial context where we would expect greater heterogeneity in the 'homogenised' billet by larger grain sizes, more diverse dendritic morphology and the presence of dissociated soluble constituents.

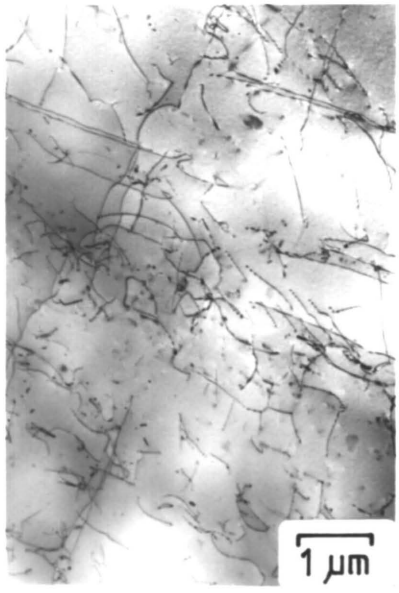
Specimens extracted from locations 2 and 3 in the billet exhibited similar structures. Banding was once more observed in the die entry region; in this case producing more equi-axed sub-grains as shown in Fig. 107. It should also be noted that in these sub-grains there is considerable internal dislocation density and in general walls are more clearly defined than those observed earlier in the extrusion cycle. The selected area diffraction patterns (Figs. 108, 109 and 110) show that the misorientation between the bands consists of a lattice rotation of 33° which reverses in sign across alternate bands. This was generally the case for all such bands investigated. At locations towards the rear of the billet dislocation wall build up is more pronounced and isolated outcrops

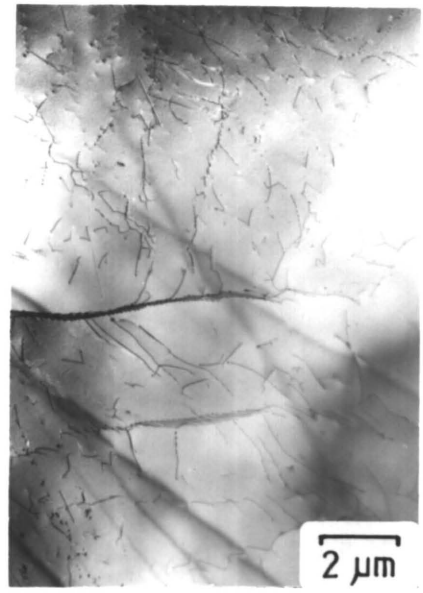
Fig. 103. Dislocation structure from location 1.C-E

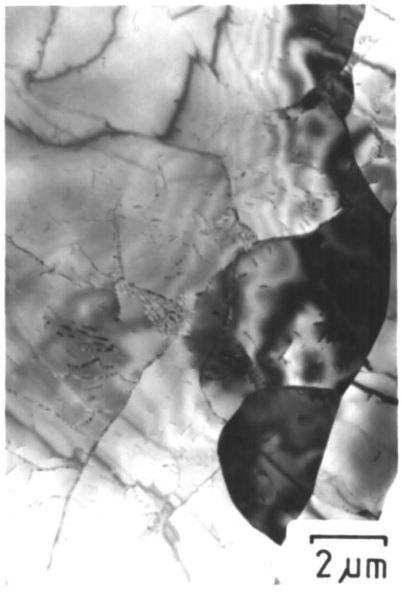
Fig. 104. Dislocation wall formation from location 1E

Fig. 105 Sub-grain at high angle grain boundary

Fig. 106. Sub-grain banding at the die mouth, location 1A


1 µm


2 µm


2 µm


4 µm



Fig. 107 Subgrain banding in sample 2A

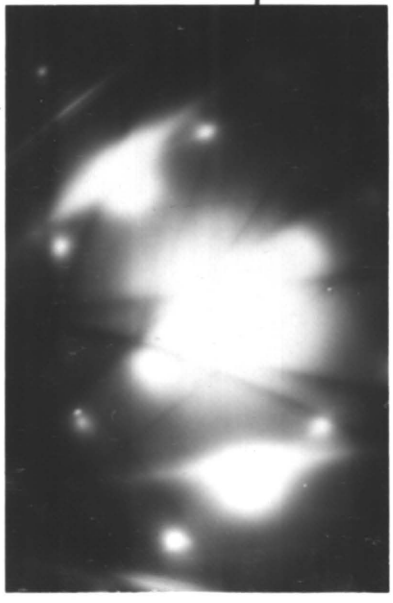


Fig. 108

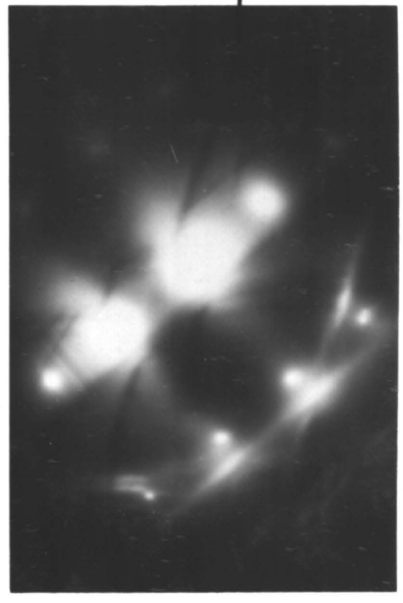


Fig. 109

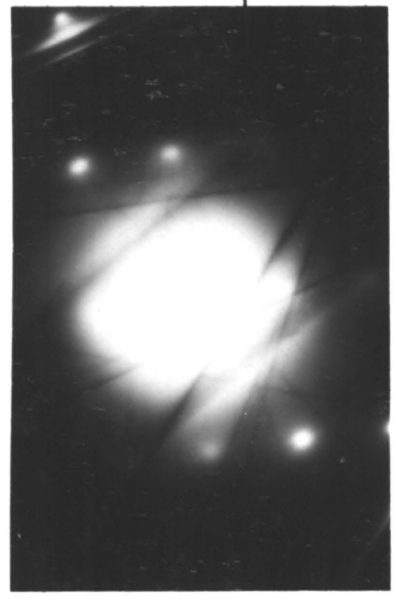


Fig. 110

Selected area diffraction patterns from regions above

of small subgrains emanating from high angle boundaries can be identified. Fig. 111 also shows that dislocation wall formation is aided by precipitates; these sites clearly act as locking points and extended walls with their extremities at precipitates can be observed. Humphreys[145] has recently shown that very large lattice rotations may occur at second phase particles and this will require high dislocation densities. The probability that sub-grain wall formation will develop is thus enhanced at these sites. This also could be an important feature in the industrial alloy in which a greater volume fraction of precipitate will be present.

Dislocation density within sub-grains indicates incomplete recovery and within completely unrecovered regions the dislocation density is much greater than earlier in the ram stroke as shown in Fig. 112.

Specimens taken from location 3 showed a similar structure. Once again banding was observed in the die mouth region while in locations D and E outcrops of sub-grains were found at high angle grain boundaries as shown in Fig. 113.

Specimens taken from billet location 5 which corresponds to the point of peak pressure shows an equi-axed sub-grain structure in positions A, B and C. The sub-grains are slightly elongated in the die mouth (Fig. 114) and are heterogeneous in size being smaller at high angle boundaries. It is interesting to note that dislocation density within subgrains is lower in specimens B and C (i.e. as we proceed backwards into the deformation zone) which is consistent with lower strains and lower strain gradients in these regions than those which occur around the theoretical exit velocity discontinuity. Nevertheless it is clear that at this stage the deformation zone is not quasi-static and the dead-metal-zone has not been fully developed since areas can be identified within the deformation zone in which sub-grain formation is incomplete and the macrographs indicate that the dead-metal-zone is not well defined.

When the ram had advanced such that location 6 had been reached an equi-axed subgrain structure can be observed in positions A, B, C and D. Specimens from the back end of the billet contain only small outcrops of sub-grains located at high angle grain

Fig. 111. Sub-grains at a high angle grain boundary

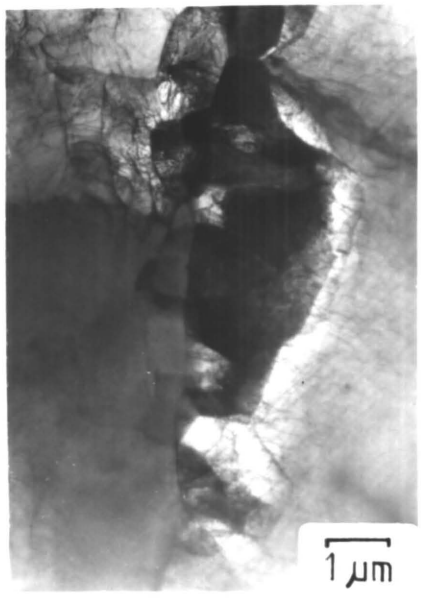
Fig. 112. Sub-grains with internal dislocation activity

Fig. 113. Sub-grains at a high angle boundary

Fig. 114. Elongated sub-grains in die mouth region, location 5A


·5 µm


2 µm


1 µm


4 µm

boundaries and intergranular dislocation walls. These sub-grains and dislocation wall formations are most probably remnants from compression during the upsetting stage. Although this deformation is not detectable in the macro-sections it is clear that compressive flow must occur throughout the billet during the initial ram contact. Proof that large strain gradients are associated with high angle grain boundaries is shown in Figs. 115 and 116. These depict a section of high angle grain boundary involving a bend through 90°. Sub-grains can be seen to be much better defined along the boundary aligned parallel to the billet axis (Fig. 115) and at the grain extremity than along the segment at right angles to it (Figs. 115 and 116). The latter is a region of much smaller strain gradient. At position A the sub-grains are locally smaller at high angle grain boundaries and have a high internal dislocation density as seen in Fig. 117. Some banding can still be detected (Fig. 118).

Samples inspected from the steady-state position (location 7) revealed equi-axed sub-grain structures. In locations A and B the sub-grains were of uniform size but location C included smaller sub-grains at high angle grain boundaries. Presumably this phenomenon is associated with a less acute breakdown of original structure than has occurred at later stages in the deformation zone i.e. locations A and B. Original high angle grain boundaries were impossible to find in the deformation zone-exit region because of the intense deformation history of the material in that location. Typical structures are illustrated by Fig. 119. The dislocation density within sub-grains is higher at the deformation zone exit than at position C which is consistent with the rapid increase in strain rate (and hence strain) which occurs in that region (section 4.2.4.).

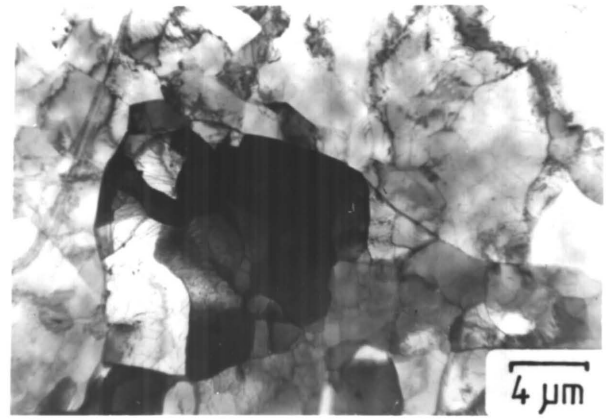
Specimens taken from the dead-metal-zone showed structures typified by Fig. 120. The appearance of a sub-grain structure could indicate that the specimen was not extracted accurately enough and included a portion of material from the band of intense shear. An alternative cause could be that the sub-grains are remnants from the compression stage of upsetting.

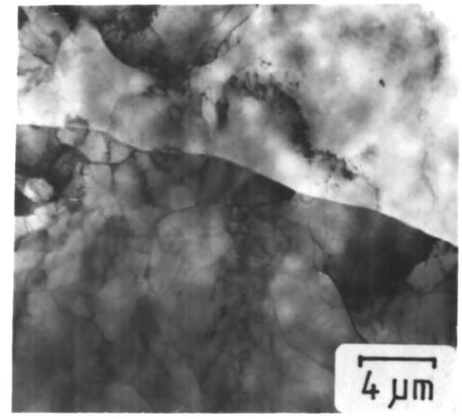
Fig. 115. Sub-grains at a high angle grain boundary

Fig. 116. Sub-grain development at a continuation of the high angle grain boundary above

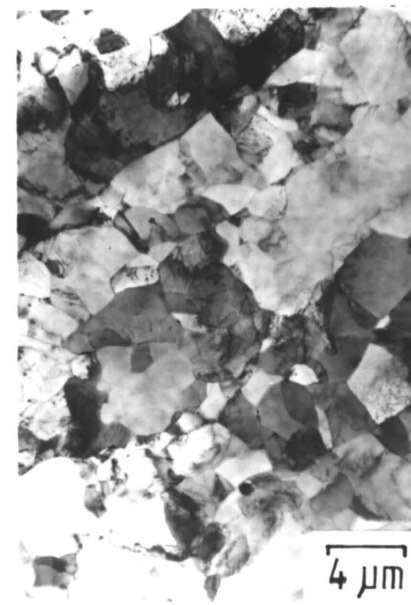
Fig. 117. High dislocation density within sub-grains at location 6A

Fig. 118. Sub-grain banding at location 6A


4 µm


4 µm


3 µm


4 µm

4.4.1.3. Extrudate Structure

The extrude structure exhibited a fibrous core consisting of equi-axed sub-grains surrounded by an annulus of recrystallized grains containing no substructure (Fig. 121). The recrystallized grain boundaries can be seen to be pinned at some locations by precipitates at triple points. This duplex structure is produced because much higher strains are imposed upon material fed to the surface layers providing a driving force for recrystallization which is not present in the central regions of the extrudate. Nucleation probably originates at sub-grain boundaries and must involve rapid sub-grain coalescence and sub-grain boundary migration. Fig. 122 illustrates this feature. The elongated original grains may be seen running vertically up the figure. At original grain boundaries where we have said the strains are greatest, nucleation of the statically recrystallized grains may be observed. In the commercial alloy this process would be aided by additional sites available at second phase particles. Fig. 123 illustrates the duplex structure with the equi-axed recrystallized grains and a fibrous, original grain running through them.

4.4.1.4. Subgrain Misorientation

Misorientation between sub-grains was established by analysis of selected area diffraction patterns and associated Kikuchi lines using standard techniques. The sub-grain misorientation depends not only upon the extent of deformation at the selected site and the position of that site but also upon the presence of heterogeneities such as grain boundaries, shear bands and second phase particles. Misorientations measured are shown in Table 4.23. which also provides information on the type of site at which the observation was made. Clearly for really detailed analysis a substantially greater number of measurements would be required. There is, however, clearly an increase in misorientation with increased deformation at any given position in a billet and misorientation also increases from entry to exit of the deformation zone. The maximum misorientation observed was about 4° which is greater than that observed by Raybould and Sheppard[210] but supports their thesis that the idea of some constant misorientation is erroneous.

Fig. 119. Sub-grain structure in steady state deformation zone

Fig. 120. Substructure in the dead-metal-zone

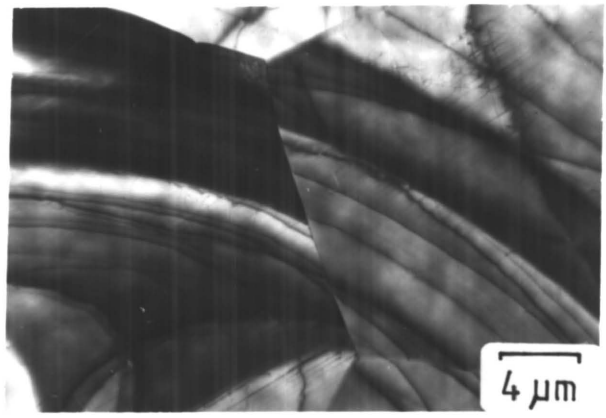
Fig. 121. Extrude peripheral structure

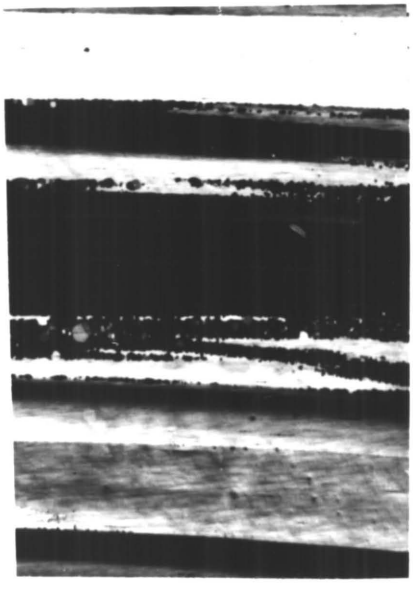
Fig. 122. Extrude core microstructure x 200

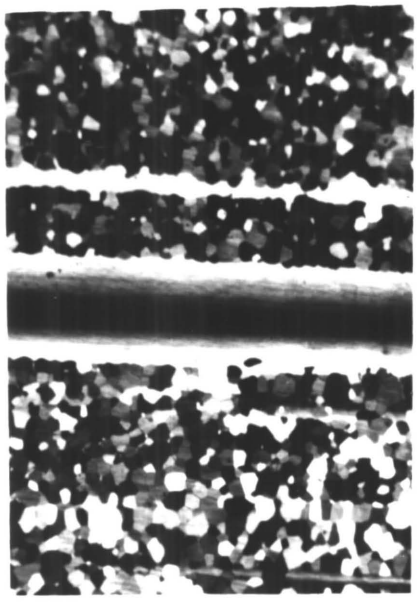
Fig. 123. Extrude peripheral microstructure x 25


4 µm


3 µm


4 µm





SPECIMEN CODE	MISORIENTATION DEGREES	REMARKS
1E	0.26	GENERAL
1B	0.12	GENERAL
	0.26	GENERAL
2C	0.50	GENERAL
	0.32	GENERAL
2B	1.66	NEAR A HIGH ANGLE GRAIN BOUNDARY
	2.20	AWAY FROM A HIGH ANGLE GRAIN BOUNDARY
2A	3.26	ACROSS A SUBGRAIN BAND
	3.96	ACROSS A SUBGRAIN BAND
	1.58	ALONG A SUBGRAIN BAND
	1.38	ALONG A SUBGRAIN BAND
3E	1.38	GENERAL
5B	0.74	GENERAL
	0.82	GENERAL
	0.88	GENERAL
6D	0.58	GENERAL
6A	3.72	ACROSS A SUBGRAIN BAND
	1.98	ALONG A SUBGRAIN BAND

Table 4.23. Sub-grain misorientations for super-pure material, D75

SPECIMEN CODE	SUBGRAIN SIZE MICRONS	REMARKS
1D	2.77	AT A HIGH ANGLE GRAIN BOUNDARY
1A	3.60	WITHIN A SUBGRAIN BAND
	0.85	ACROSS A SUBGRAIN BAND
2A	1.41	ACROSS A SUBGRAIN BAND
3E	1.53	AT A HIGH ANGLE GRAIN BOUNDARY
3B	2.69	GENERAL
3A	2.90	GENERAL
5C	2.30	GENERAL
5B	2.24	GENERAL
5A	2.60	GENERAL
6E	11.50	NOT TYPICAL
6D	2.60	ALONG A SUBGRAIN BAND
	1.37	ACROSS A SUBGRAIN BAND
6C	2.98	GENERAL
6B	2.80	GENERAL
6A	2.35	GENERAL
7A	2.35	GENERAL
	2.54	GENERAL
	2.40	GENERAL

Table 4.24. Sub-grain sizes for super-pure material, D75

4.4.1.5. Sub-grain Size

Sub-grain sizes were measured by an intercept method and the values listed are the mean of at least five readings. Table 4.24., notes those cases where sub-grains were found only at grain boundaries. In general the sub-grain size decreases from rear to front of the billet and decreases as the steady state condition is approached. Since average strain rates must greatly increase throughout the ram stroke and in addition must be very low (due to compression only) at the rear of the billet, these observations are consistent with the concept that sub-grain size is dependent upon the temperature compensated strain rate, Z. There is, however, not a noticeable change in size when moving from position C to A in any of the billets. This is somewhat surprising since we would expect the strain rate to vary by a factor of about two during that period. There is, however, also a temperature rise to be considered and the general trend in Z should be a decrease. Some change in sub-grain size should, therefore, be detected providing the opposing actions of strain rate and temperature do not cancel out. If this is not so, then the equation of state relating Z to sub-grain size must be violated in this region and perhaps explains why so many workers have obtained excellent substructural correlations using initial temperature conditions[225] or models based upon bulk temperature rise and average strain rates.[226] It is clear that the substructure cannot change as rapidly as any equation of state would dictate and it is not sufficient to propose a model which does not include time as a variable. Moreover, there must therefore be a critical rate of change of Z or LnZ beyond which the equation of state cannot be observed. If, for example, at entry to the deformation zone the material contains larger sub-grains with low density walls (as has been observed) and at exit contains smaller sub-grains with high density walls and some internal dislocation density then rearrangement is necessary as an element passes through the deformation zone. The final sub-grains were in general equi-axed and the number of sub-grains at exit is unlikely to be a number which would integrally fit the sub-grain size pertaining at entry to the deformation zone. Therefore, at each step during continuous deformation considerable adjustment must be required. This clearly implies that any equation of state must be sensitive to the rate of change of strain and must include at least a limiting time factor.

SAMPLE	REMARKS	SUBGRAIN SIZE (MI)
D331D-A	ACROSS A BAND	1.900
	ALONG A BAND	2.700
	ACROSS A BAND	0.200
	ACROSS A BAND	2.700
	ALONG A BAND	3.300
D331C-B	SMALL SUBGRAIN BAND AT A HIGH ANGLE GRAIN BOUNDARY	1.200
D331B-B	SMALL SUBGRAIN AT A HIGH ANGLE GRAIN BOUNDARY	1.700
	LARGE SUBGRAIN AT A HIGH ANGLE GRAIN BOUNDARY	6.100
D331B-A	GENERAL	2.100
D331A-C	AT A HIGH ANGLE BOUNDARY	0.035
D331A-B	AT A HIGH ANGLE BOUNDARY	1.250
	AT A PRECIPITATE	1.000
D331A-A	ACROSS A DEFORMATION BAND	3.100
D331A-B	DYNAMICALLY RECRYST GRAIN	3.000
		2.500
D331A-A	DYNAMICALLY RECRYST GRAIN	5.000
		3.000

Table 4.25. Sub-grain sizes for alloy D222 (5456)

DYNAMICALLY RECRYST GRAIN BOUNDARY	SUB-BOUNDARY WITHIN
DEGREES	DEGREES
19.1	0.9
35.2	0.3
30.0	0.4
19.1	
45.0	
54.7	
45.0	
26.6	
39.2	
35.3	
48.2	0.2
45.0	
16.8	

Table 4.26. Misorientations for alloy D222 (5456)

4.4.1.6. Development of Dislocation Structure Related to Peak Pressure

The general reduction of pressure during the extrusion process has always been attributed to the reduction in friction as the billet length decreases. The pressure curves for this alloy indicate that the reduction in pressure is so non-linear that this explanation cannot be justified. Castle and Sheppard[23] showed that the peak increased as extrusion rates increased and was reduced by increasing the initial temperature, features that this work has also confirmed. Their work showed the relationship between peak pressure and temperature to be of the Arrhenius type with an activation energy of about 160 KJ/mole which is close to the activation energy for bulk self-diffusion in aluminium. The results strongly indicate that the peak is controlled by thermally activated events involving the production, interaction and annihilation of dislocations.

The results reported here indicate that dislocation generation and motion commences and spreads from the die entry as the pressure is applied. Dislocation density increases rapidly as a consequence of the interaction of mobile dislocations with each other and with dislocations stored within grains. These latter dislocations are a necessary consequence of the strain gradients which exist both on a macroscopic scale (e.g. between the deformation zone and regions of undeformed material) and on a microscopic scale (i.e. across grain boundaries at which multiple slip is required from the start of deformation in order for the grains to remain continuous). Dislocation density increases most rapidly in these regions in which strain and strain gradients are highest. Grain boundaries, at which dislocations are generated are necessarily such sites. Eventually the stored dislocation density achieves a magnitude such that recovery by cross-slip and climb occurs resulting in the formation of sub-grains. This mechanism is consistent with the observation that sub-grains are first observed at grain boundaries and at high strain regions near the die entry. As extrusion proceeds the deformation extends rearwards to form the deformation zone and isolated sub-grain outcrops are observed progressively further back in the billet. In the later stages of extrusion when steady state conditions obtain, generation and annihilation of dislocations balance and hence recovery and sub-

grain formation ensure zero work-hardening effects. At this stage sub-grains are equi-axed and constant in size and misorientation. It should be recalled that in the earlier stages of deformation sub-grain walls are ragged and elongated in the extrusion direction and the cells contain a high internal dislocation density.

At peak pressure the steady state deformation zone is not fully established but this condition is achieved by the time the pressure has diminished by an amount equal to the additional increment required. The sub-grains diminish in size during this time interval. Considering the necessary fact that changes in substructure require finite time intervals it is clear that the peak pressure is required to effect the establishment of the quasi-static deformation zone. A side-effect is quite obviously that a quasi-static deformation zone is also formed. Hence it is not surprising that the peak pressure is associated with an activation energy similar to that for bulk self-diffusion and for creep since the controlling process in each case is the climb of dislocations.

4.4.1.7. Sub-grain Banding

Banding of sub-grains was observed in specimens taken before the peak pressure in regions where deformation was greatest. Misorientation was greater across the bands than along them while sub-grain size was greater along it than across it. Studies of diffraction patterns shows very large rotations across the bands. Starting within one band with a set diffraction pattern, this changed on moving into the next band but then returned to the original pattern in the following band and so on, e.g. Figs. 107-110, a rotation of 33° about a <122> direction was observed between bands.

Similar banding has been observed previously by a number of workers. For example, Rhines[227] has shown qualitatively similar bands in aluminium deformed in creep and suggested that they form when deformation of a pair of grains is possible in only one direction. To accommodate the shape change, one grain must deform by the alternative tilting of bands running across the crystal. Such a situation can readily be envisaged in the early stages of extrusion of a large grained material. Dilamore et al.[228] also considered the possibility that local differences in stress state

produce varying strains within a crystal causing a relative rotation between segments of the grain. This would be true in the extrusion case because of the inhomogeneous stress states at the die mouth region during upsetting. The situation is further worsened by the large original grain size and variation in grain size in the billets which tend to permit greater strain gradients. The banding observed in this material is almost certainly due to the necessity to accommodate grain sizes of widely varying magnitude in the die entry region. The large misorientations between the bands is similar to those encountered across high angle grain boundaries and thus dislocation activity is enhanced in these regions leading to the early formation of sub-grains and propagation of the sub-grain structure into the grain interiors.

The most important conclusion which may be drawn from this investigation is that for the material and imposed deformation conditions the high temperature softening mode is dynamic recovery producing an equi-axed sub-grain structure. We shall now turn our attention to the equivalent commercial alloy processed under identical conditions.

4.4.2.1. Structural Development in the Commercial Alloy 5456 (D222)

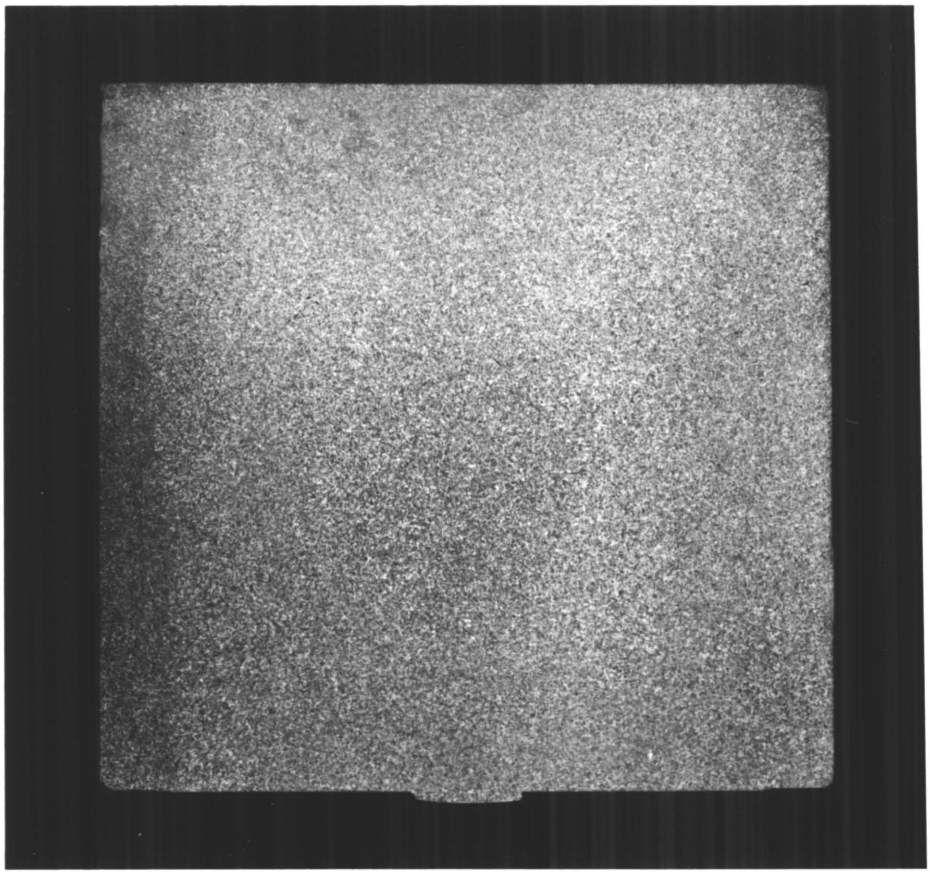
In this case the investigation was carried out in a manner similar to that described above. Specimens were extracted from positions corresponding to locations 1, 4, 5, 6 and 7 in Fig. 93.

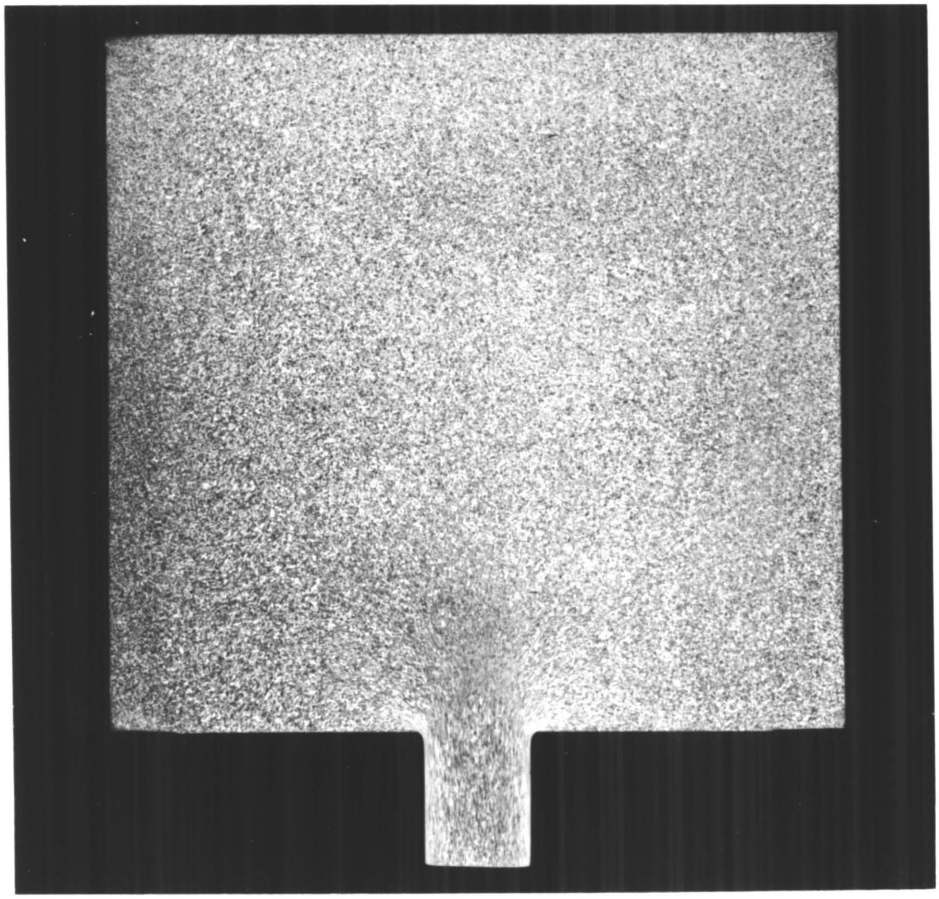
The macrographs obtained from these may be found in Figs. 124-128. The most obvious difference between this and the previous case is the considerable reduction in original grain size. (20 μm diameter as opposed to up to 3000 μm). This is caused by the additions of manganese and chromium which act as grain growth inhibitors. This smaller grain size makes macroscopial observations more difficult to make.

Fig. 124 shows the structure relevant to location 1. Apart from the small extrude pip it is very difficult to observe any form of deformation within the billet. Fig. 125 illustrates the structure corresponding to location 4. In this case there has been a considerable rise in pressure for limited ram travel, but a significant amount of material has passed through the die. The

Fig. 124. Macrostructure from location 1

Fig. 125. Macrostructure from location 3

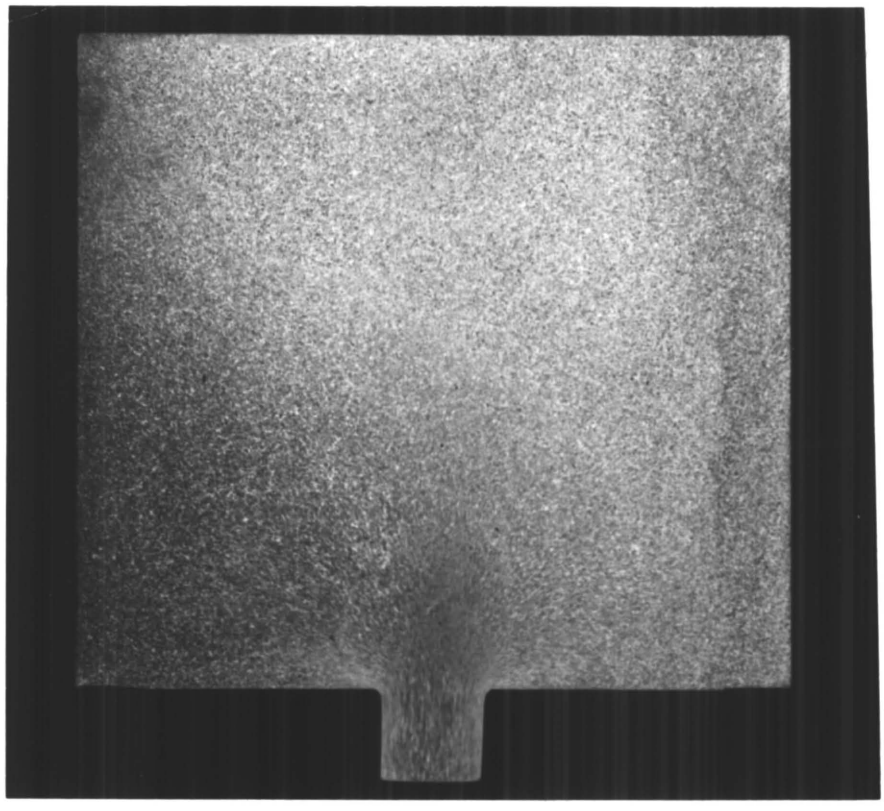




fibrous nature of the extrude may be observed while the deformation zone has extended farther back into the billet. The billet peripheral grain structure implies container/billet shear. There is still no evidence of deformation in the inner rear 80% of the billet. Fig. 126 corresponds to the peak pressure. Once again the deformation zone has moved farther back into the billet and is beginning to spread in a lateral direction. Compared with Fig. 99, the equivalent structure for the super-pure material, the deformation zone appears to be less well-defined although this may be a result of the vast differences in grain size. Once again the grain structure implies container/billet shear notably over the rear portions of the billet. Fig. 127 illustrates the structure corresponding to location 6, at which stage the pressure has fallen by an increment Δp and a considerable amount of ram travel has occurred. A significant change in macrostructure is apparent. As well as evidence of container/billet shear and the production of a fibrous extrude, the deformation zone volume has increased considerably. The regions of high shear are beginning to become apparent connecting the die mouth and the billet surface which would suggest the dead-metal-zone is about to be formed. Deformation is also reaching farther back into the billet and a region of increased shear is developing along the billet axis. Fig. 128 shows the structure pertaining to the steady state region at location 7. The macrograph compares well with that found in Fig. 101. The dead-metal-zone is now fully developed and the bands of intense shear may be easily observed. Once again three regions of increased shear may be observed confirming the thesis of the presence of buffer zones supplying material in the deformation region. Comparing the macrographs for the commercial and super-pure materials shows that in the former case a larger dead-metal-zone is generated. The bands of intense shear do not connect with the die face in this case and would tend to indicate that deformation zone geometry is dependent upon material properties. This confirms the observations made in section 4.3.1.7. regarding the variance of $^{P}/\sigma$ with LnZ. The value of the upper bound angle α (section 4.2.3.) appears to have decreased in the commercial alloy as well as the dead-metal-zone taking a more parabolic shape.

Fig. 126. Macrostructure from location 5

Fig. 127. Macrostructure from location 6



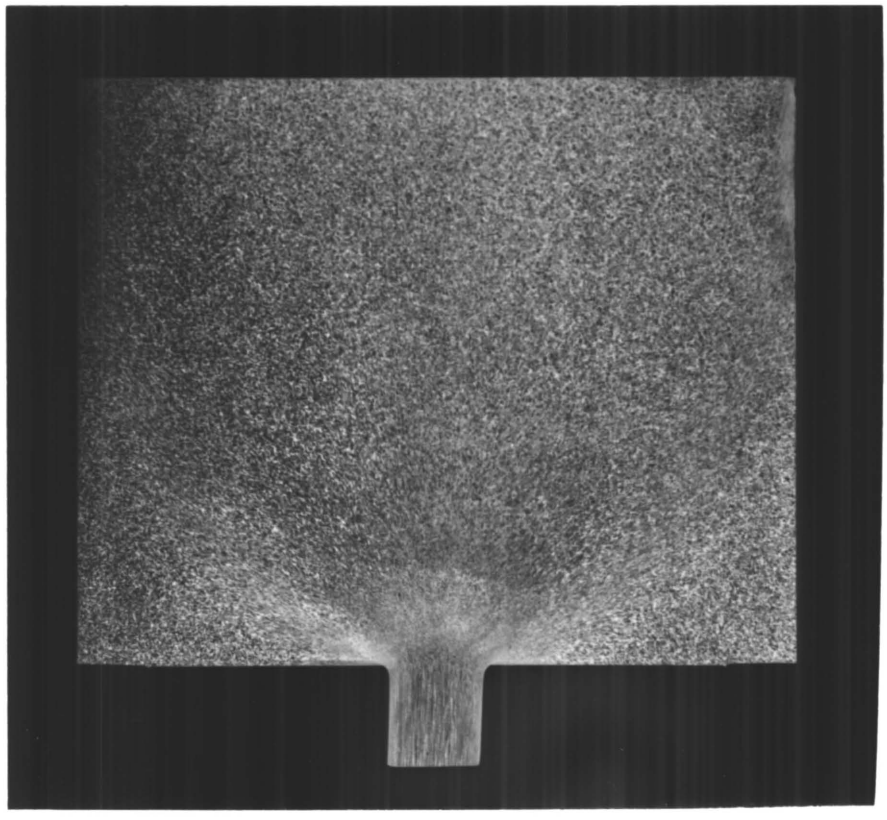
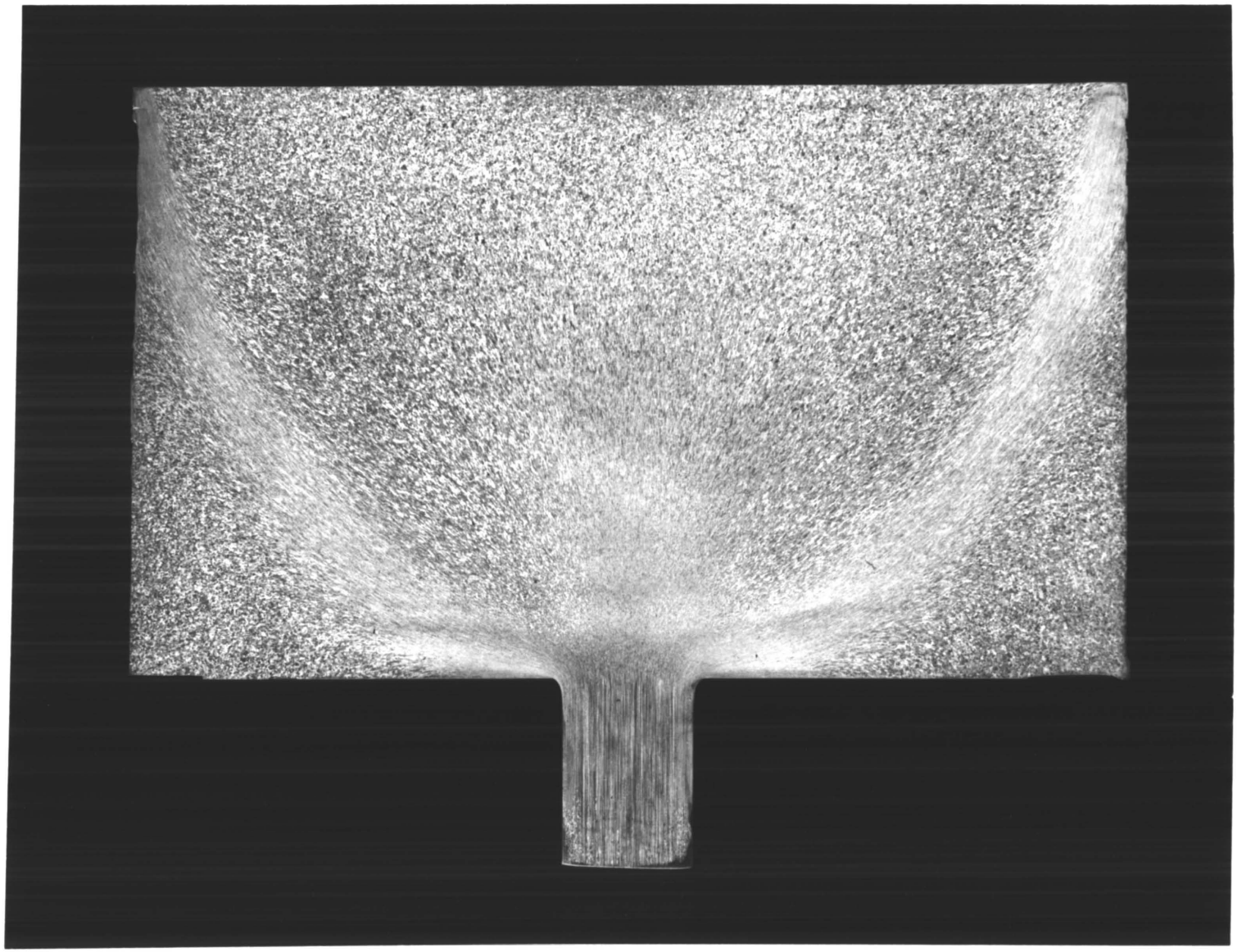


Fig. 128. Macrostructure from location 7



In conclusion it would appear that similar features are produced in the commercial alloy although they appear to be retarded prior to the steady state being reached. This may be due to the reduced grain size offering a more difficult macro-structure to observe or due to the increased resistance to deformation resulting from the additional elements present and the smaller grain size. The deformation zone shape appears to be dependent upon material properties.

4.4.2.2. Structural Investigations

In general terms, similar trends of deformation were observed in the commercial alloy, i.e. general increase in dislocation activity upon moving forward in the billet or progressively farther into the stroke.

Specimens from the billet arrested at location 1 showed very little deformation structure. Isolated outcrops of dislocation walls were observed in the front regions but otherwise little activity was encountered. The dislocation walls were associated with original high angle grain boundaries and second phase particles in all cases.

Specimens taken from location 4 showed a more highly deformed structure. Fig. 129 shows a micrograph of the region adjacent to the die mouth. The degree of deformation is sufficient to begin elongating and breaking down the original grain structure as some material is forced through the die. The gradient of strain can be observed via the changes in grain shape as they progress closer to the die. To the rear of the billet isolated outcrops of sub-grain activity were found, similar to the case with the super-pure material. The presence of the second phase particles modified the dislocation structure at positions where activity was greater. Fig. 130 shows a sub-grain formed in location B of the billet arrested at position 4. The triangular sub-grain may be seen pinned at each corner by second phase particles. Even with this small sub-grain, some dislocation activity may be seen within. Farther forward at location A,the strain gradients have increased and dislocation production is enhanced. This means that the likelihood of sub-grain formation is enhanced. Fig. 131 shows the

Fig. 129. Microstructure of die mouth region during upsetting x 100

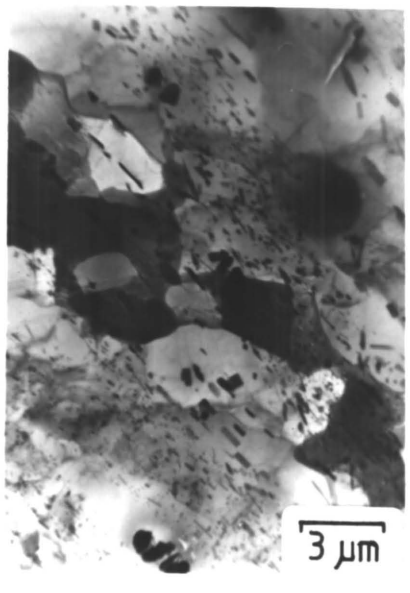
Fig. 130 Sub-grain walls pinned by second phase particles

Fig. 131. Sub-grain bands at location 4A

Fig. 132. Sub-grain wall formation




·5 µm


3 µm


·25 µm

presence of bands of sub-grains at this position. As in the super-pure case, the contrast differences infer a greater misorientation across than along but in this case the sub-grains appear reasonably equi-axed in morphology. The presence of banding is also enhanced by the lining up of precipitates resulting from the deformation. These may be seen running diagonally across the figure. It is interesting to note that the more well defined sub-grains are associated with the larger particles which could well be due to the larger lattice rotations they can cause. Even in these more advanced regions the dislocation structure is not complete. Areas could still be observed in which dislocation wall formation was taking place as shown in Fig. 132.

In specimens taken from the billet arrested at location 5, corresponding to the peak pressure, sub-grains were apparent at locations A, B and C. In the rear of the billet high angle grain boundaries could still be found at which there was no dislocation activity, Fig. 133, although in general there was some sub-grain wall formation as seen in Fig. 134. Once again the association of the dislocation walls with second phase particles may be seen.

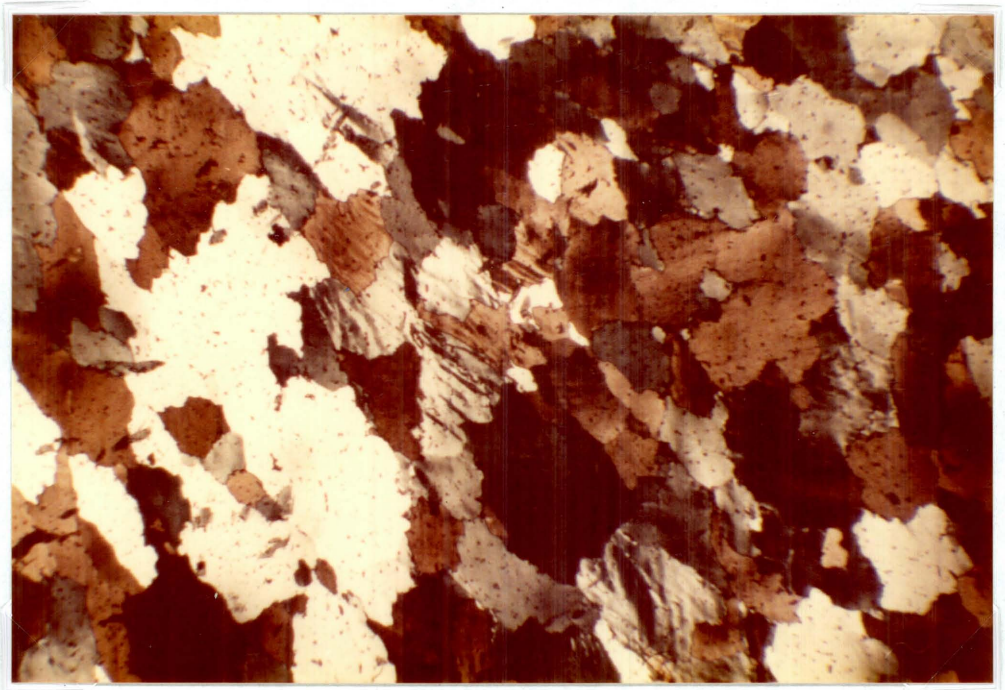


Fig. 135. Micrographs of lesser deformed regions x 60

Fig. 135 shows an optical micrograph of these regions in which little alteration in grain shape is observed. The only result of the deformation so far encountered is the appearance of deformation or transition bands within the grains. These bands are the result of inhomogeneities in the strain during compression and the early stages of deformation. These cause localized lattice rotations resulting in the contrast shown in Fig. 135 and also necessitate an enhanced dislocation generation to accommodate the strain gradients. Thus the driving force for sub-grain formation is greater in these regions.

Farther forward at locations A, B and C sub-grains are observed as shown in Fig. 136. The varied sizes apparent are due to the precipitate distributions present in those regions. So far the structures have closely followed those found in the previous sections, the only modifications being due to precipitate distributions. However at locations A and B new features were found which lead to considerable discrepancies between the commercial and super-pure deformation characteristics.

Figs. 137 and 138 show optical micrographs of the deformation regions associated with location 5 in Fig. 93.

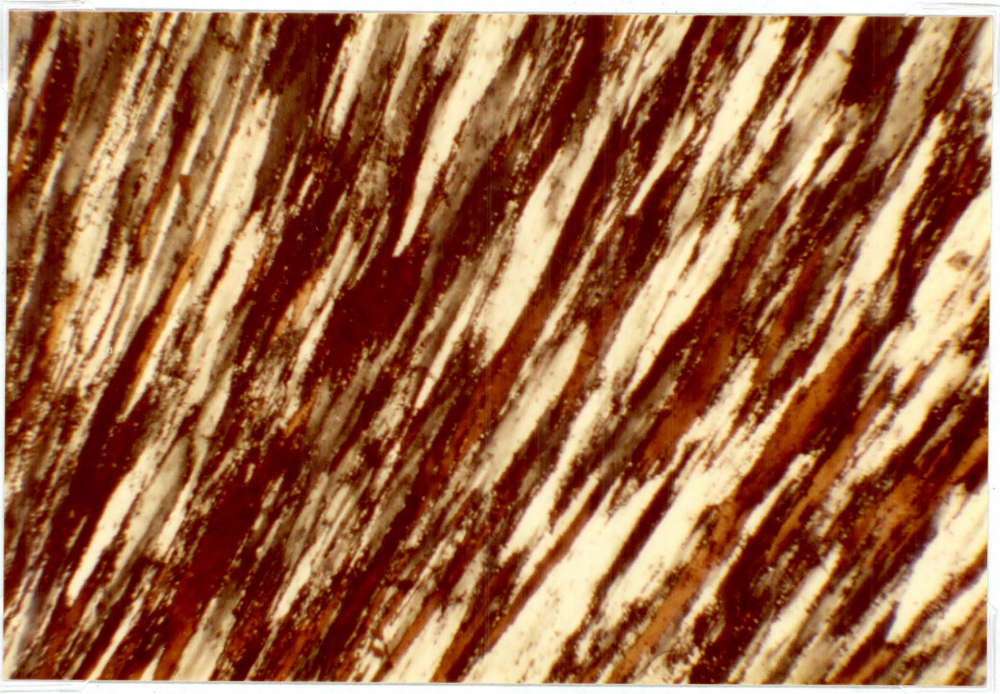


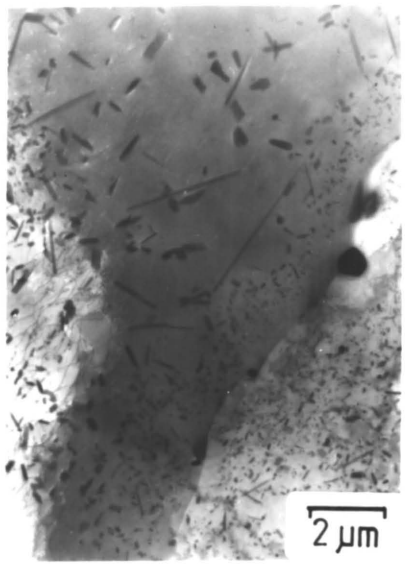
Fig. 138. Deformation zone - from location 5

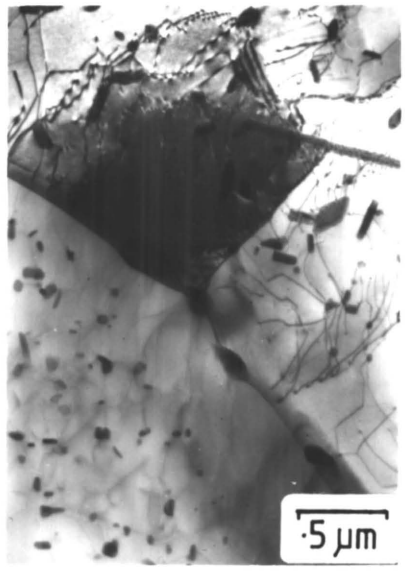
Fig. 133. Sub-grain free region

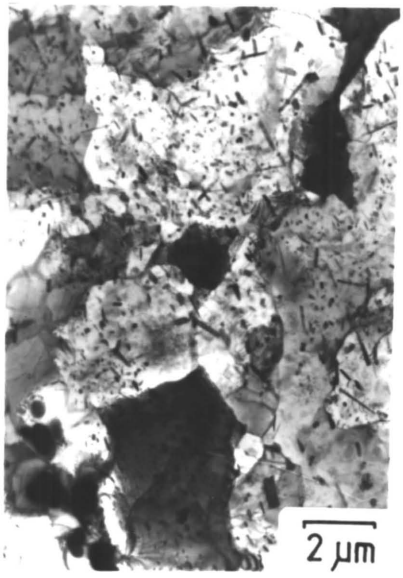
Fig. 134. Sub-grain formation

Fig. 136. Sub-grain formation

Fig.137. Deformation zone at a location corresponding to the peak pressure x 200


2 µm


·5 µm


2 µm



In both cases the original grain structure has been modified by the deformation to show elongation of grains towards the die mouth. However, at these grain boundaries small equi-axed grains are apparent which have not been observed in the super-pure alloy. The work described in the previous sections showed how the local strain gradients were greater in these regions and for this reason it was initially guessed that these grains were sub-grains of higher mis-orientation, their size and shape being consistent with this hypothesis. Alternatively they could be small statically recrystallized grains nucleated during removal of the billet prior to quenching.

Electron microscopical examination of samples from locations A and B showed neither of these to be the explanation. Fig. 139 shows a 'sub-grain' found at location B associated with a precipitate particle. However the selected area diffraction patterns shown in Figs. 140 and 141, taken within the dark region and across the boundary to the left respectively, show a mis-orientation of 45° exists indicating the presence of a high angle boundary. The dark grain is therefore not a sub-grain but rather a recrystallized one. The grain size of approximately 1.5 μm precludes it being an original grain. Fig. 142 shows a higher magnification electron micrograph of the dark grain in Fig. 139. This shows a dislocation structure which immediately removes the possibility of the grain being produced by static recrystallization. (The sweeping through of high angle grain boundaries during static recrystallization would remove dislocation structures). The grain is therefore the result of dynamic recrystallization. Although other such examples were observed the majority of the structure contained sub-grains.

Specimens taken from location 6, corresponding to a pressure decrease of Δp showed a sub-grain structure in positions A, B and C. Towards the rear of the billet, dislocation activity had increased from that found previously. Sub-grains were identifiable at most high angle grain boundaries and at regions where the proportion of second phase was increased. In the forward positions a continuous structure of sub-grains was observed, their size being locally smaller at high angle grain boundaries. The sub-grains

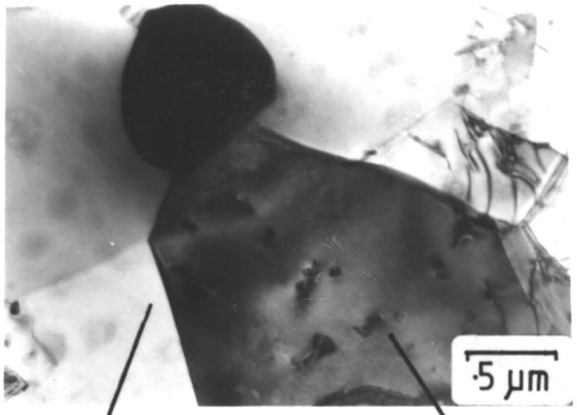


Fig.139 Dynamically recrystallized grain at a second phase particle

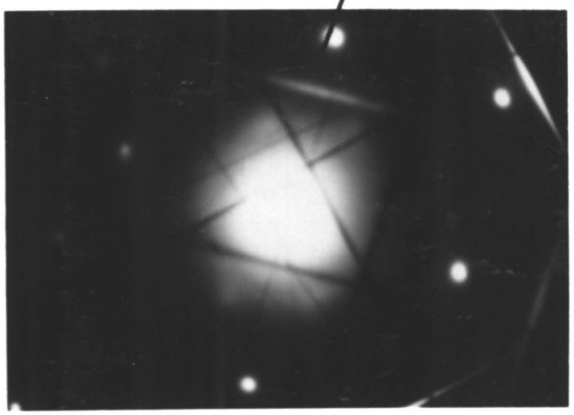


Fig. 140

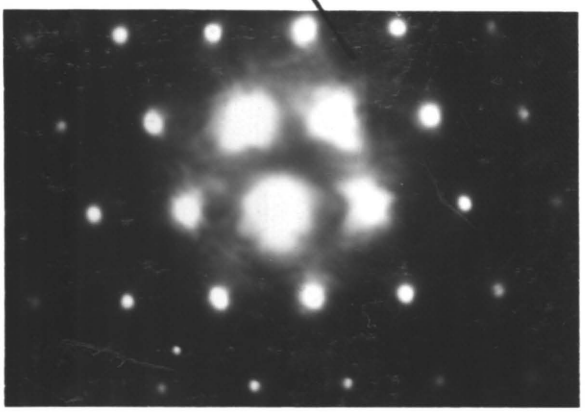


Fig. 141

Selected area diffraction patterns from locations above

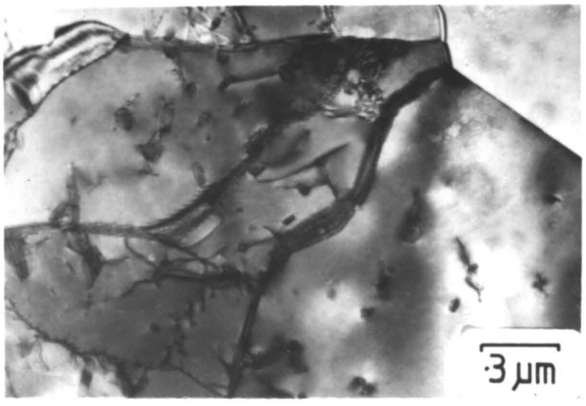


Fig. 142 Dislocation activity within the recrystallized grain in Fig. 139

also show a higher internal dislocation density upon moving forward through the deformation zone which is consistent with the observations for the super-pure material. Typical structures may be seen in Figs. 143 and 144. The latter is taken at location A and shows the increased effect of the deformation upon the precipitate morphology. The lining up in the potential extrusion direction is highly pronounced and sub-grain boundaries appear to fall in a more uniform direction and manner. Investigation of these samples did not reveal any recrystallized grains similar to those found previously. This was due to the samples not including such regions as Fig. 145 shows there still appears to be equi-axed grains at the elongated original grain boundaries.

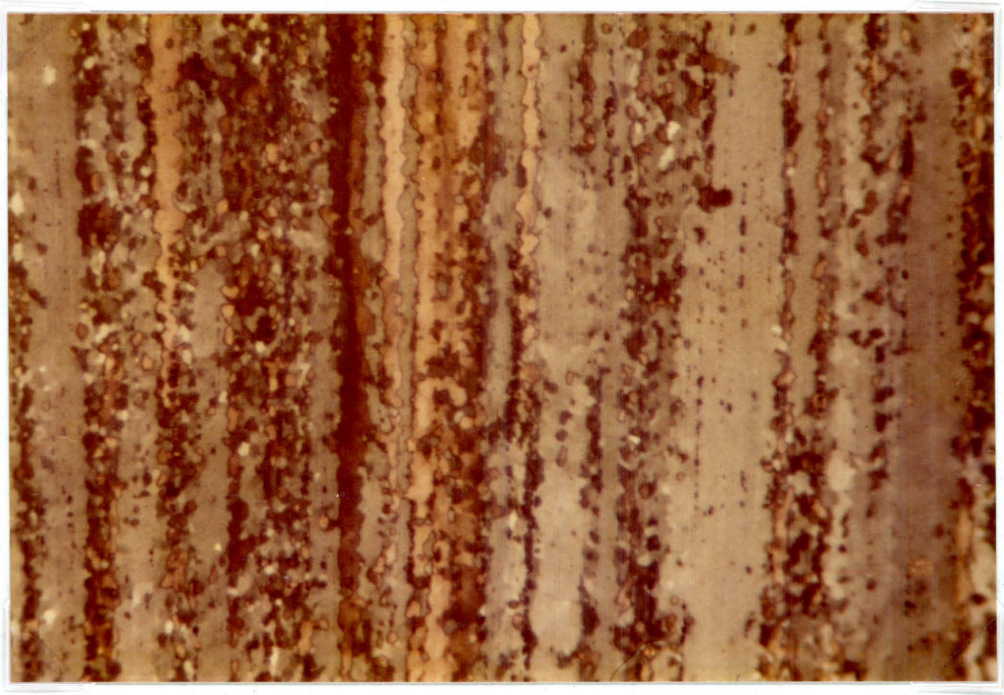


Fig. 145. Equi-axed grains at original grain boundaries.

Specimens extracted from the steady state location showed sub-grains at virtually all positions. Towards the rear, at location D, sub-grains were observed mainly at high angle grain boundaries where their size was small as seen in Fig. 146. Farther forward at location C the sub-grain structure was general but misorientations, estimated from trans-boundary contrast, appeared low. Even at these regions the second phase particles are beginning to line up as the flow develops. (Fig. 147)

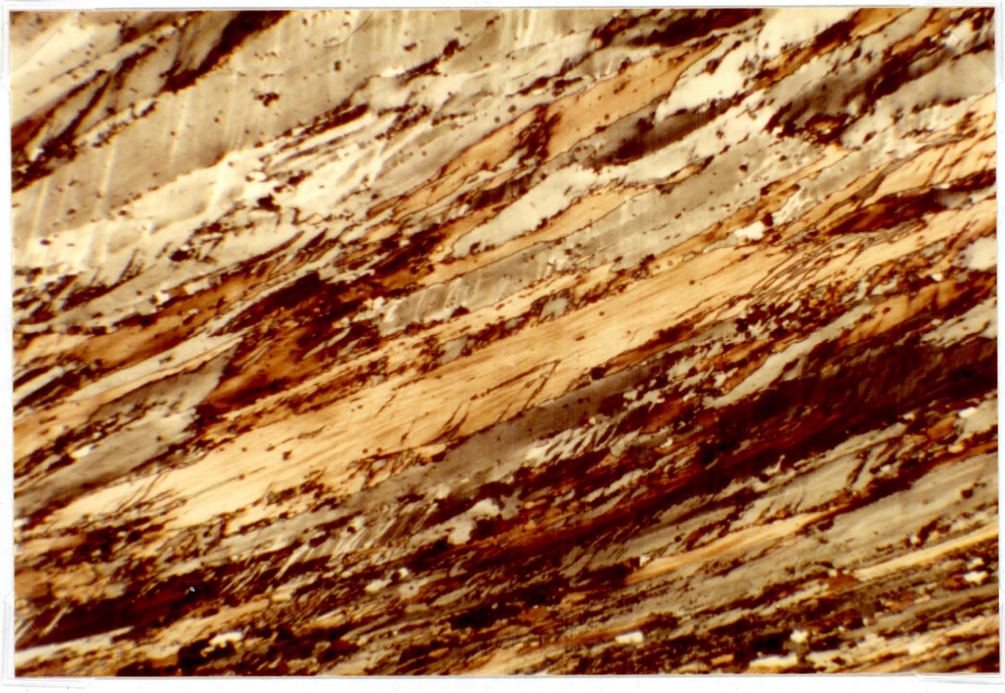


Fig. 148. Degradation of structure at location C.

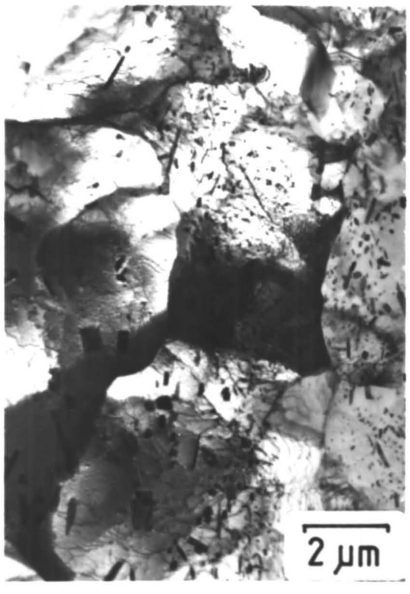
This feature may be seen in Fig. 148 which shows an optical micrograph corresponding to location C. The increasing structural break down may be observed upon the material moving farther to the left or nearer the base (i.e. towards the die orifice). Even at this advanced state of deformation, deformation bands can be seen traversing the elongated grains.

Farther forward an equi-axed sub-grain structure was revealed, Fig. 149, in which the internal dislocation density is quite high indicating the increased degree of strain. At location A, sub-grain

Fig. 143. Fig. 144.
Sub-grains in the deformation zone from location 6

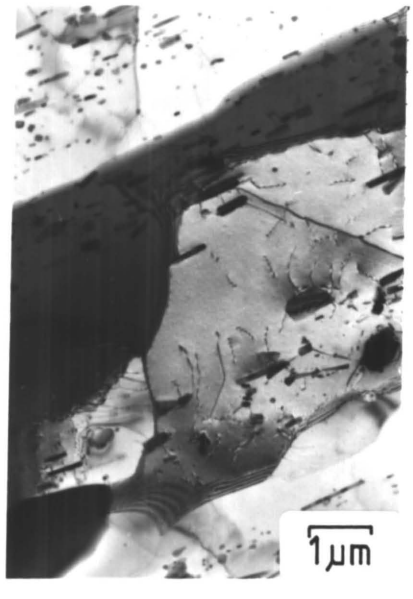
Fig. 146. Sub-grains at a high angle grain boundary from location D

Fig. 147. Sub-grains and lining up of precipitates


2 µm


2 µm


2 µm


1µm

banding was observed, Fig. 150. Although a degree of sub-grain alignment had been observed in earlier specimens, this was the first genuine case to be found in the commercial alloy. In this case the conclusions drawn for their appearance in the simpler material are not really applicable since the stress state at the die mouth is unlikely to be so inhomogeneous at this more advanced stage. In addition, the smaller grain size should reduce the likelihood of its occurrence. Thus in this case the cause may be due to the reasons presented by Rhines,[227] who suggested they form when deformation of a pair of grains is possible in only one direction. Elsewhere sub-grains were observed, Fig. 151, in many cases the boundaries pinned by second phase particles.

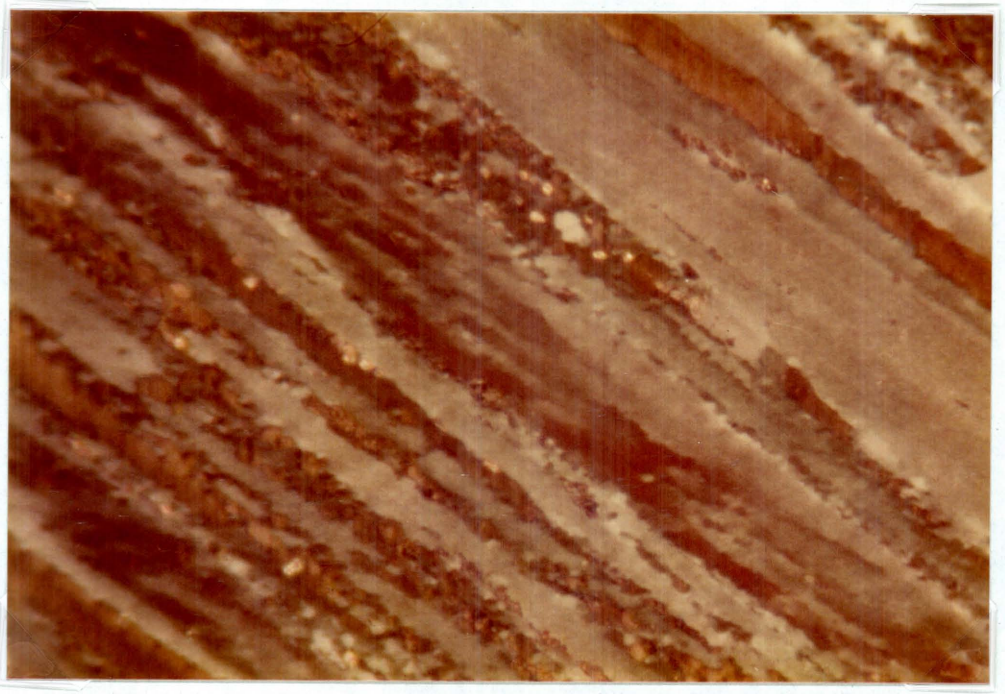


Fig. 152. Small equi-axed grains at original grain boundary

The optical micrograph of the die mouth region, Fig. 152, shows that once again there is the appearance of small equi-axed grains at original grain boundaries indicating the possible emergence of dynamically recrystallized grains within transmission electron microscope samples. Fig. 153 shows a low magnification

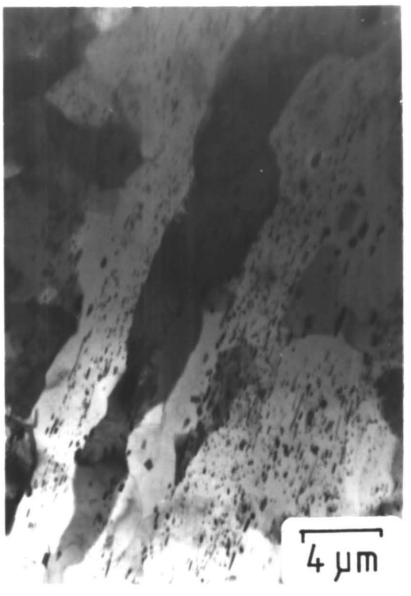
Fig. 149. Equi-axed sub-grains at location 7-B

Fig. 150. Sub-grain banding in the die mouth region

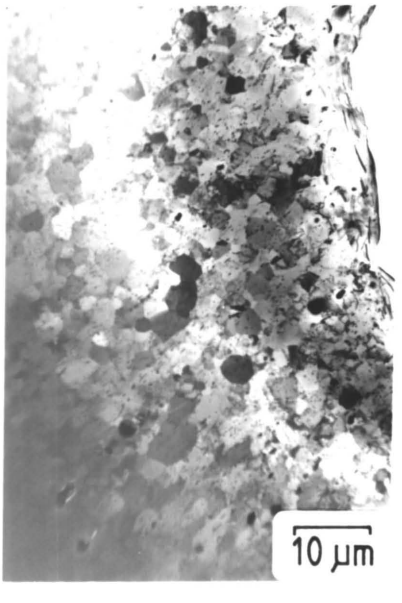
Fig. 151. Sub-grains in the die mouth region

Fig. 153. Sub-structure within the deformation zone


1 µm


4 µm


2 µm


10 µm

electron micrograph of position A in which the distribution of sub-grains can be seen. Although the general picture is one of low contrast grains, certain ones appear which have a considerably increase contrast indicating a larger misorientation. A higher magnification photograph of the three such grains in the centre of Fig. 153 may be seen in Fig. 154. As the figure shows, there is some considerable dislocation activity within these three and from the diffraction patterns shown (a, b, c, d and e) the misorientations relative to each other and relative to the surroundings exceed 25° and in most cases exceed 45°. Thus these are not sub-grains, but rather recrystallized grains, the dislocation activity showing them to have been formed dynamically. Further examples may be found in Figs. 155-158. Fig. 155 shows another highly contrasted grain with the boundary indicated having a misorientation of 30°. The enlarged view in Fig. 156 of this grain shows a dislocation wall with misorientation less than 1°. Similar features can be seen in Fig. 157 where the boundary indicated has a misorientation of 20° and the enlarged view of this grain in Fig. 158 where the dislocation wall has a misorientation of 0.9^{o}. Further examples were found within this region indicating that dynamic recrystallization is occurring simultaneously with the dynamic recovery.

4.4.2.3. Extrudate Structure

The operation of the two high temperature restoration processes discussed above has a marked effect upon the resulting product structure. In the super-pure case a simple duplex structure was observed containing an annular ring of statically recrystallized material and a fibrous inner core. In this case a statically recrystallized peripheral zone is also produced but the inner regions show fibrous elongated original grains with equi-axed dynamically recrystallized grains at their boundaries. This feature is easily recognisable in Fig. 159.

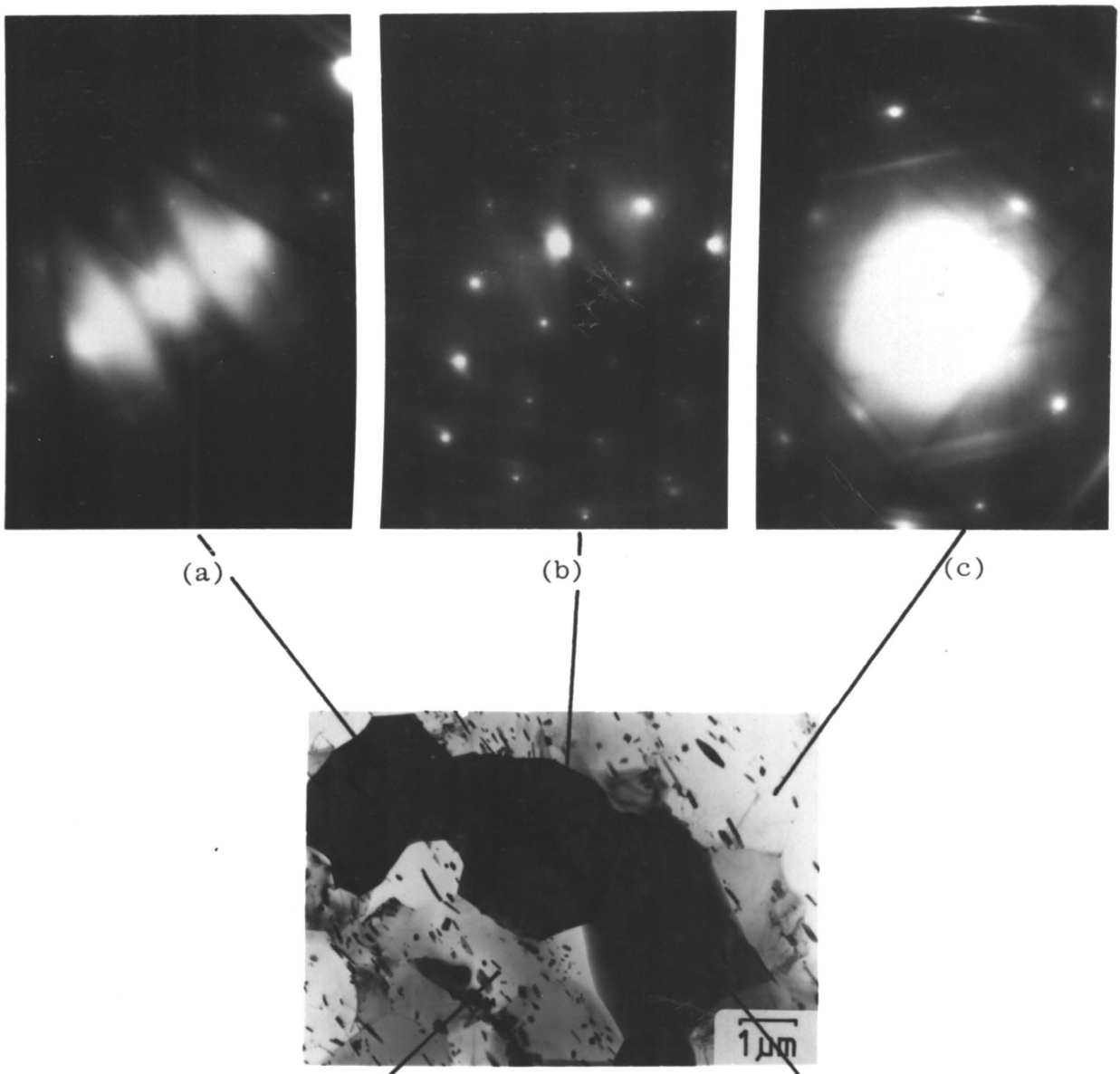


Fig. 154 Dynamically recrystallized grains from location 7-A, observed as dark grains in Fig. 153.

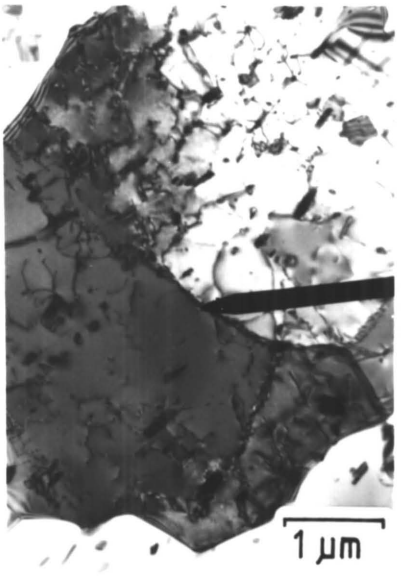
Fig. 155. Darker dynamically recrystallized grain.

Fig. 156. Internal dislocation structure of recrystallized grain

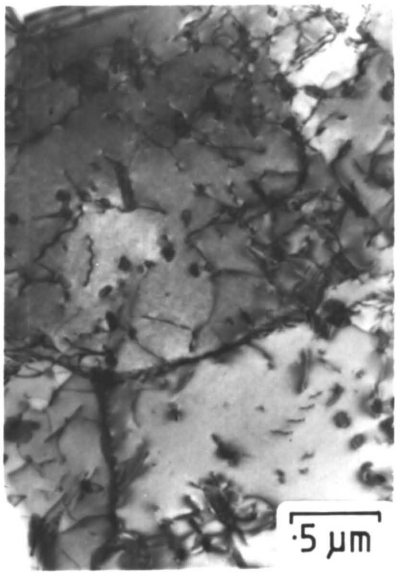
Fig. 157. Darker dynamically recrystallized grain

Fig. 158. Internal dislocation structure of recrystallized grain


1 µm


1 µm


1 µm


·5 µm

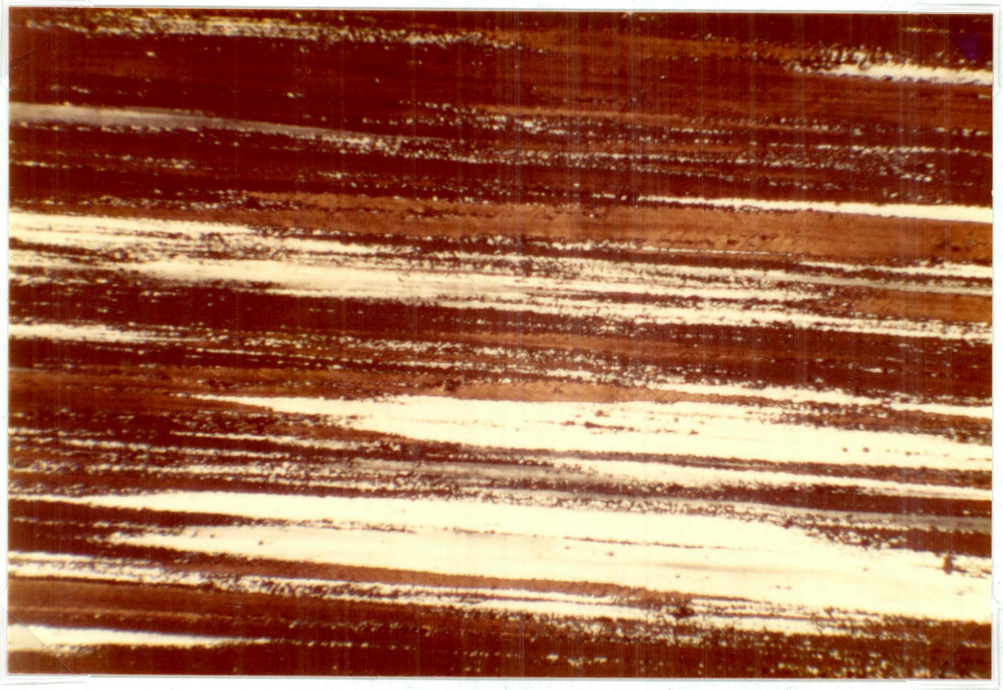


Fig. 159. Commercial alloy extrudate structure

4.4.2.4. Development of Dislocation Structure in Commercial 5456(D222)

As in the previous case, dislocation generation commences and spreads from the die entry as the pressure increases. Dislocation activity is greatest in those regions in which strain and strain gradients are greatest. In addition, high dislocation densities may accumulate at second phase particles that are non-deformable introducing additional sites for sub-grain formation. The development is therefore very similar to that for the super-pure material prior to the peak pressure being attained.

Subsequent to this stage being achieved, the critical strain for dynamic recrystallization is attained in selected regions. These are necessarily those near to the die mouth where the strain is greatest and at suitably sized second phase particles where, as reported by Humphries,[145] large lattice rotations may be apparent.

The fine sub-grain structure developed prior to the onset of dynamic recrystallization means that nucleation by grain boundary bulging is unlikely due to the short lengths of unpinned boundary. Nucleation is probably by preferential misorientation increase in certain favourable sub-grains similar to that observed by McQueen and Bergerson.[229] Nucleation is thus more likely in regions close to

grain boundaries where the strain is greatest due to accommodation of plastic annisotropy, and adjacent to the second phase particles where the dislocation density is greater. It is, however, apparent that the critical strain for nucleation has not been attained in the bulk of the material since only isolated occurrences of the phenomenon may be found. Farther into the ram stroke the average strains have increased, as has the mean strain rate, and nucleation is more plentiful. It is the continued straining of the material during and subsequent to nucleation that causes their deformation and therefore their internal dislocation structure. In this higher strain rate process, the gradient of deformation from centre to boundary of a recrystallized grain is high, and so there is a considerable dislocation density just behind the advancing boundary. By diminishing the driving force in this way, the rate of migration is reduced relative to that found during the growth stage of static recrystallization. This accounts for the very small grain size observed in this case. In addition, the higher the value of the Z parameter pertaining, the smaller are the dynamically recrystallized grains because the associated increase in dislocation density gives rise to a higher density of nuclei.

However, the sporadic occurrence of such grains means that the bulk structure is one of equi-axed sub-grains indicating the dynamic recovery is operating in conjunction with dynamic recrystallization. It would seem apparent that at these strains and strain rates the former recovery mechanism is inadequate in annihilating sufficient dislocations for the necessary reduction in stored energy. Thus dynamic recrystallization is initiated in support.

4.4.2.5. Sub-grain size

In this case the measured sub-grain sizes showed a large spread ranging from 0.035 μm up to 6 μm. This is caused by the presence of the second phase particles which serve to restrict boundary movement and sub-grain growth. The results are shown in Table 4.25. In general terms, the sub-grains were smaller for the commercial alloy than for the super-pure material. Sub-grains are locally smaller at second phase particles and high angle grain boundaries although the latter observation could be reversed at some locations. Also noted are the sizes of some dynamically recrystallized grains which shows them to be very close to the sub-grain dimensions.

Although no definite result may be gathered from Table 4.25., it can be stated that in general terms, sub-grain size reduces upon passing forward into the deformation zone and also as the distance into the ram stroke is increased. This is consistent with the observations made concerning the super-pure material.

4.4.2.6. Misorientations in 5456 (D222)

Sub-grain misorientations measured, showed their values to lie in the same range as those in the previous investigation. The maximum values were of the order of a few degrees, most lying about 2°.

Table 4.26. shows the misorientations calculated for the dynamically recrystallized grains and, where possible, the value for dislocation walls within. These values are of an order of magnitude greater than those for the sub-grains while the interior misorientations are slightly lower. Clearly these misorientations will result in an increased barrier to dislocation movement in the product under loading compared with an equivalent sub-grain structure, producing an enhanced strength value.

4.4.2.7. Comparison of restoration Processes for Super-pure and Commercial Al-5% Mg

Considering that the prevailing conditions under which deformation took place were identical for both materials, the resultant structural developments are radically different. For the super-pure case, the overwhelming softening by dynamic recovery agrees well with the traditional ideas relating to aluminium alloys, considered to have high stacking fault energies and thus permitting uninhibited dislocation mobility. In the case of the commercial alloy, the appearance of dynamically recrystallized grains infers that dislocation motion is impeded and the necessary reductions in internal energy caused by their anninilation are prevented.

If the reported reductions in stacking fault energy associated with magnesium additions to aluminium are correct, then some other features must be involved to explain the inconsistencies.

The major contribution to the difference arises from the vastly differing initial grain sizes in the two materials. Sah et al.[176]

working with commercial purity nickel in torsion showed how grain size affected dynamic recrystallization initiation. They found that decreasing the grain size resulted in a marked increase in recrystallization rate and also produced a decrease in the critical strain for its initiation. They attributed this to the greater number of potential sites for nucleation when the grain size is small encouraging nucleation at lower strains.

In addition, the presence of the dispersed second phase in the commercial alloy must serve to adjust the restoration processes. McQueen and Jonas[150] report that their presence tends to stabilize the substructure and prevent or restrain grain boundary migration. Such inhibition or retardation of dynamic recrystallization would therefore serve to contradict the evidence found to date. Although their conclusions may in fact be correct, it must also be recognised that the particles serve to restrain dislocation mobility and therefore recovery processes. Humphries [145] has also reported how second phase particles may increase dislocation densities and so an overall picture would be one of the restriction upon dislocation activity exceeding that upon grain boundary migration. In addition, we have established that nucleation by grain boundary migration is unlikely and so its mobility is immaterial and in addition the minimal growth stage, subsequent to nucleation, needs very limited boundary movement.

It would appear therefore, that the reduced grain size primarily and the presence of the second phase particles serve to permit the reduction undertaken to exceed the critical strain for nucleation of dynamic recrystallization in the commercial alloy. Under either higher temperature or increased deformation the superpure material would also be expected to show similar features.

4.5.1. Structure of the Extrude

In the following sections both the surface and internal structure of the extrudates will be discussed. The range of extrusion conditions employed resulted in wide ranging product structures being produced.

4.5.1.1. Surface Condition of the Extrude

Depending upon the combinations of process variables employed, four surface conditions were produceable, examples of which are shown in Figs. 160-163.

Under normal extrusion conditions of moderate temperature, in the range 300°C-400°C, and moderate ram speed, up to 8 mms/sec, a sound product was generated with a good surface finish, as seen in Fig. 160. The surface showed a matt finish of light grey appearance.

Under higher temperature conditions lines were observed on the product running longitudinally along its length as seen in Fig.161. These are caused by small pieces of aluminium or large precipitates adhering to the die, a phenomenon known as pick up. One theory is that the die deflects under the high pressure and only the entrance to the die is in contact with the extrude. Thus in the gap behind this contact some aluminium tends to collect. The presence of these lines emphasises the need for die cleaning; although even with a new die, scoring could appear midway through a run.

Under conditions of higher temperature, faster speed or increased reduction, transverse cracks appeared upon the surface at the rear end of the product. An example of this may be found in Fig. 162. This is generally accepted to be the result of temperature rises during the cycle causing surface temperatures to exceed or approach the solidus for the material resulting in melting. This of course necessitates the removal of the rear end of the product and is both time-consuming and wasteful.

The final structure is an extreme of that observed above in which melting occurs along the entire length. The condition was only observed when high temperatures and ram speeds were employed. The high rate of heat generation causes melting to be observed after a short length of product is produced and the situation then becomes progressively worse as the temperature continues to rise. The depth of cracking increases along the extrude length resulting in the extreme case in complete disintegration of the product. An example of this may be seen in Fig. 163. The resulting product is of no commercial value and so the situation should be avoided at all costs.

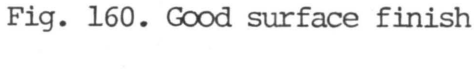


Fig. 160. Good surface finish

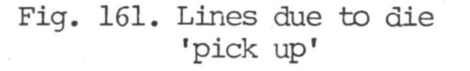


Fig. 161. Lines due to die 'pick up'

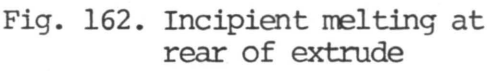


Fig. 162. Incipient melting at rear of extrude

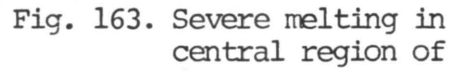
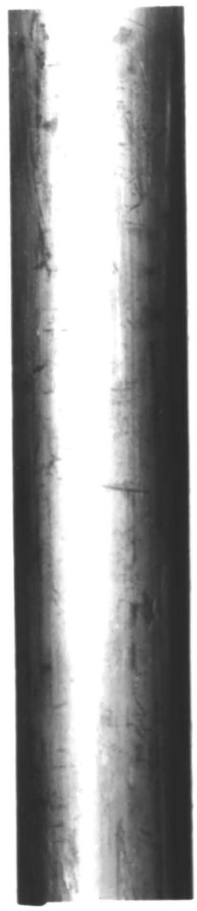
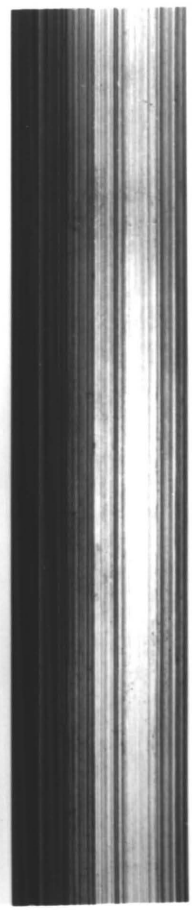


Fig. 163. Severe melting in central region of extrude









4.5.1.2. Initial Material Structure

The structure of the materials prior to extrusion may be observed in Figs. 164-167.

Fig. 164 shows the structure of the alloy D222 (5456). The homogenisation treatment applied to this material was significantly reduced as the cast cored structure and inter-dendritic segregation is minimal. Fig. 165 shows the structure for alloy 5052. The reduced heat treatment time employed means the interdendritic segregation is more significant in this case.

Figs. 166 and 167 shows the structures for alloys 5083 and 5456, which appear to be very similar. Results from microprobe microsegregation studies showed the dendritic centres to be denuded of magnesium while the remainder showed an even concentration. In opposition, the manganese, which forms a series of peritectics with aluminium, is found in concentrations directly opposed to the magnesium, i.e. its concentration is greatest at the dendrite core. Similar trends were found with chromium. Inter-dendritic segregations may also be observed, more especially in Fig. 167, probably containing Mg_2Si, $(FeMn)Al_6$ and $(CrFe)Al_7$.

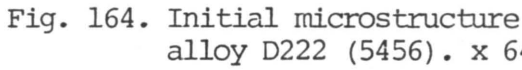


Fig. 164. Initial microstructure of alloy D222 (5456). x 64

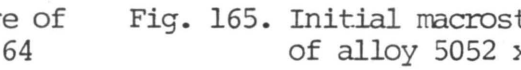


Fig. 165. Initial macrostructure of alloy 5052 x 64

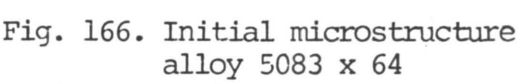


Fig. 166. Initial microstructure of alloy 5083 x 64

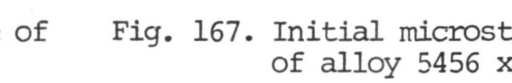
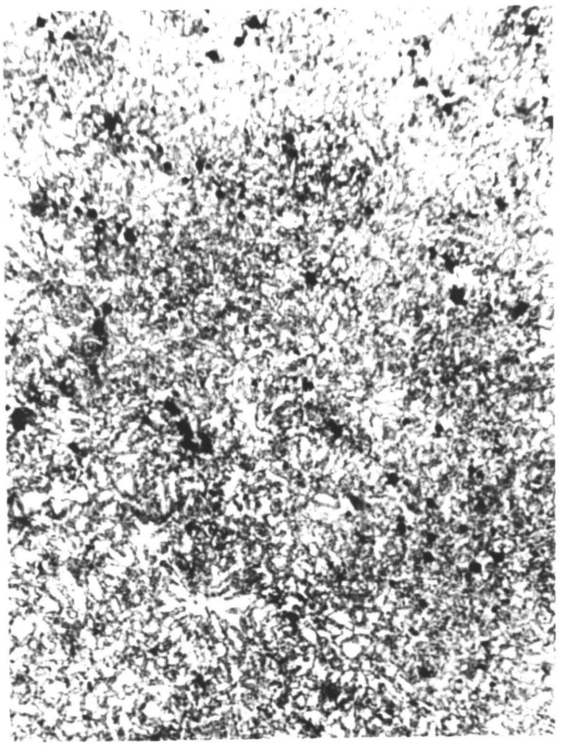
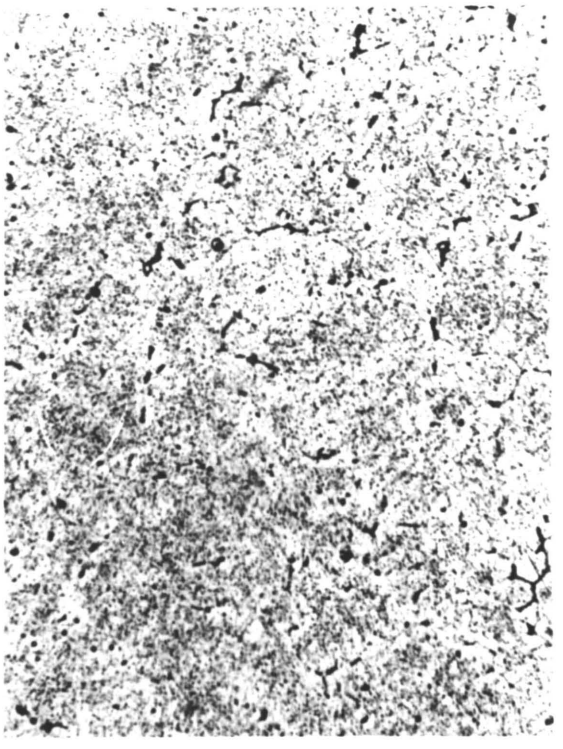
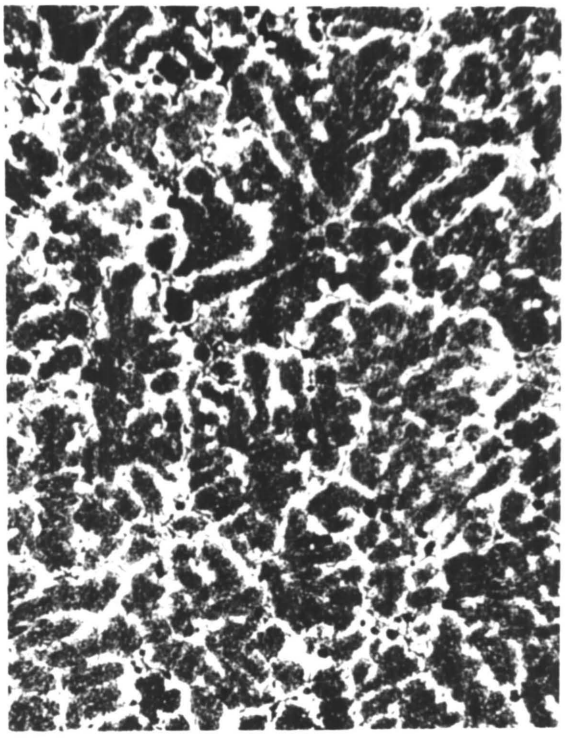
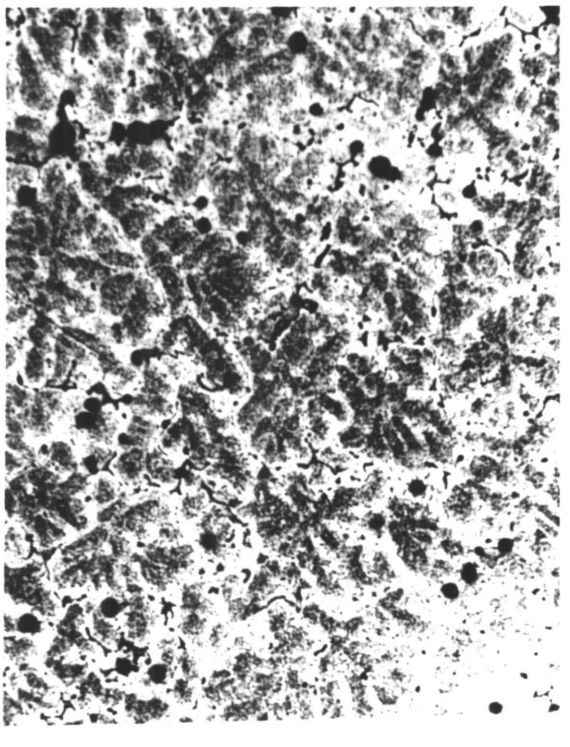


Fig. 167. Initial microstructure of alloy 5456 x 64.









4.5.1.3. The Variation of Microstructure across and along the Extrude

We now turn our attention to the structures found in the extruded product. The inhomogeneity of the deformation requires that the structures developed reflect this and we find variation both across the product width and along its length.

The difference in structure generated across the extrude diameter is a result of the inhomogeneous deformation within the billet. As was seen in section 4.4.2.1., intense bands of shear are developed within the quasi-static deformation zone which eventually appear as the material fed to the outer regions of the product. This increased degree of deformation necessitates an increased dislocation density and resultant internal energy increase. There is, therefore, an increased driving force for static restoration processes to be initiated in these regions. In the more central regions of the product this excess stored energy is not evident and recovery processes alone will be sufficient to cause a reduction. Thus under many conditions, a duplex structure is produced featuring a recrystallized outer rim surrounding an inner core of fibrous 'cold worked' grains. Typical structures may be seen in Figs. 168-171.

Figs. 168 and 169 apply to a low temperature extrusion, 322°C, carried out at a reduction of 10:1 and a ram speed of 5 mms/sec. The former figure shows the outer structure while the latter shows that pertaining to the central regions. In the peripheral region of the extrude, small relatively equi-axed recrystallized grains may be observed as well as a background of elongated fibrous grains. In this case the nucleation rate is high due to the incomplete dynamic restoration processes leaving a high stored energy content. Thus the grains appear at original grain boundaries where these energies are greatest. The low temperatures involved restrict the growth stage resulting in a small, high density of recrystallized grains. In the central regions where the degree of deformation has been smaller, the recrystallized grains are apparent since dynamic softening processes are capable of reducing the internal energy to an acceptable degree. The structure is composed of elongated fibrous grains which will be shown to contain an equi-axed sub-grain structure.

R = 10:1
T = 322°C
Ram speed = 5.4 mms/sec

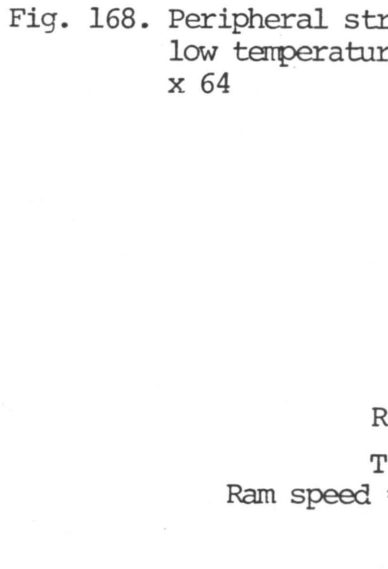


Fig. 168. Peripheral structure of low temperature extrude x 64

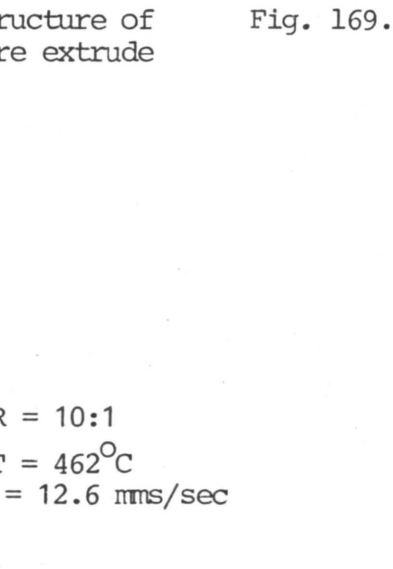


Fig. 169. Internal structure of low temperature extrude x 128

R = 10:1
T = 462°C
Ram speed = 12.6 mms/sec

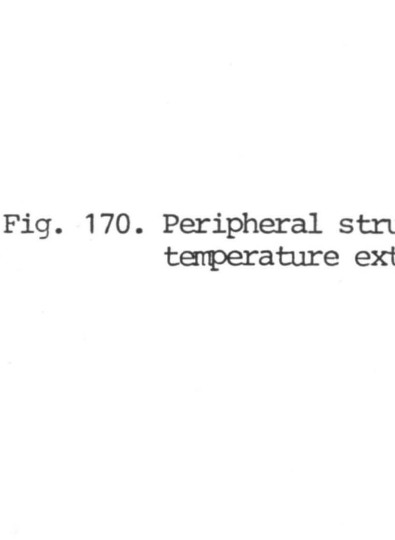


Fig. 170. Peripheral structure of high temperature extrude x 64

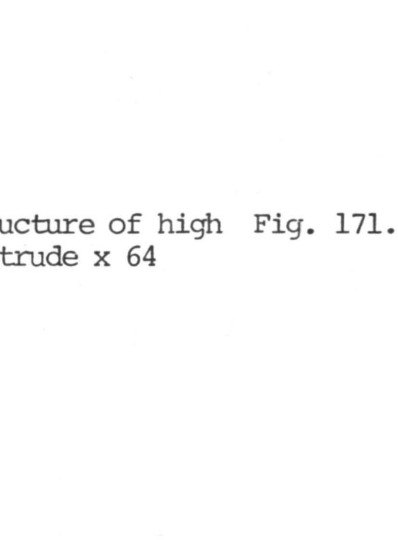
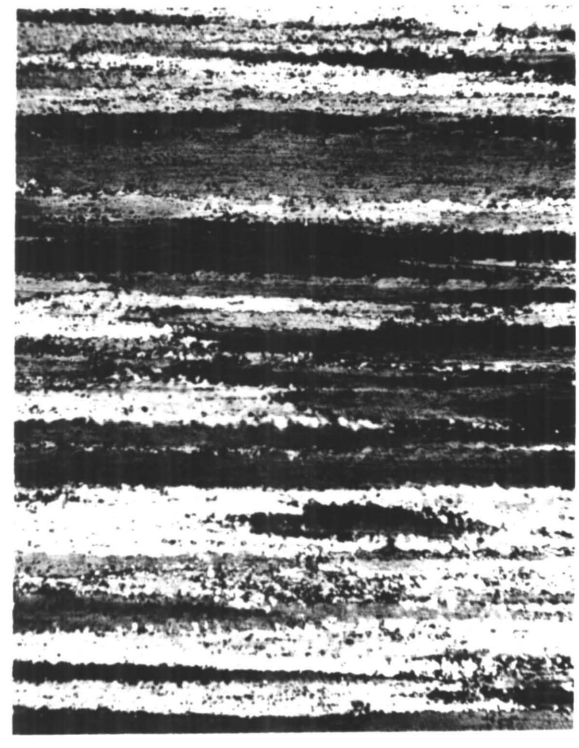


Fig. 171. Internal structure of high temperature extrude x 64









Figs. 170 and 171 show the structures produced for an increased temperature extrusion, 462°C, under similar conditions of ram speed and reduction. In this case the structures are considerably different. In Fig. 170 the peripheral structure may be observed in which an outer annulus of large statically recrystallized grains is apparent. The depth of penetration is significantly reduced and the majority of structure contains no such grains. In this case the higher temperature employed causes a more effective reduction in stored energy by the dynamic processes and thereby reduces the opportunity for nucleation. In addition, the higher thermal activation enhances the growth stage and as a result large recrystallized grains are produced. Their elongated aspect is due to the distribution of second phase particles which have lined up parallel to the product axis thus making the ease of boundary movement greater in the longitudinal direction as opposed to the transverse. In the remainder of this figure and the whole of Fig. 171, representing the inner structure, the results show a background of fibrous elongated grains plus a great deal of small equi-axed grains resulting from the dynamic recrystallization process initiated by the high temperature employed.

In both cases the trend is similar, an outer annular ring of recrystallized material surrounding an inner structure resulting from the dynamic restoration processes. The effect of a change in initial temperature has been discussed. Increasing the extrusion ratio serves to increase the strain and therefore the driving force for nucleation. The result is that the proportion of product containing recrystallized material is increased, but the grain size is reduced. Increasing the ram speed, and hence the strain rate, results in a decreased incubation time due, once again, to the increased internal energy, and an enhanced rate of subsequent recrystallization. As in the case of strain, a reduced grain size is observed for constant temperature conditions.

The effect of increased alloying additions is to reduce the recrystallization rate. This is due to the increased drag caused by the impurity atoms upon the moving grain boundary. Thus in the case of 5052, as will be seen in subsequent sections, and D75, as was observed in section 4.4.1.3., static recrystallization may encompass the bulk, if not all of the structure for most temperatures.

The growth of the statically recrystallized peripheral grains may be observed in Figs. 172-175. All of these figures relate to extrusion number 171 in which a reduction of 10:1 was employed at an initial temperature of 462°C and ram speed of 4 mms/sec. Figs. 172 and 173 illustrate the structure at the die mouth, the former at the periphery and the latter at the centre. In the outer regions a fine grained or sub-grained structure may be observed with one single statically recrystallized grain apparent. These grains are either sub-grains of high misorientation or, because of the high temperature, a mixture of sub-grains and dynamically recrystallized grains. The latter would appear more likely. To the right of the picture the beginning of the fibrous structure may be observed. The lack of recrystallized grains indicates that the 'incubation period' is applicable at this stage. Fig. 173 shows the central region in which the fibrous grains may be observed running vertically up the photograph. As well as the strings of second phase particles lined up in the extrusion direction and coincident with the grain boundaries, two other features may be observed. Scalloped grain boundaries can be seen which are indicative of an internal sub-grain structure within and the presence of small equi-axed grains resultant from the dynamic recrystallization process.

Figs. 174 and 175 depict the structure at a distance of less than 3 cms down the extrude from the previous two. In terms of time this describes a change of less than one second during the extrusion cycle. The structure at the periphery, Fig. 174, has changed significantly and shows a completely statically re-crystallized material on the left prior to the elongated fibrous grains on the right. These grains have grown from the small equi-axed ones found in Fig. 172 in a time of less than 1 second. Their morphology is such that the precipitate distribution has permitted enhanced growth in the longitudinal direction. Cotner and Tegart found that recrystallization subsequent to deformation in torsion, in an Al-5% Mg alloy took 7 secs at 500°C, a strain of 0.458 and surface shear strain rate of 3.93 sec^{-1}. Under the conditions imposed here of increased strain rate and strain, the time increment of 1 second is therefore not unrealistic. In the interior of the product, Fig. 175, the structure has not altered significantly. The elongated original grains may still be observed while grain

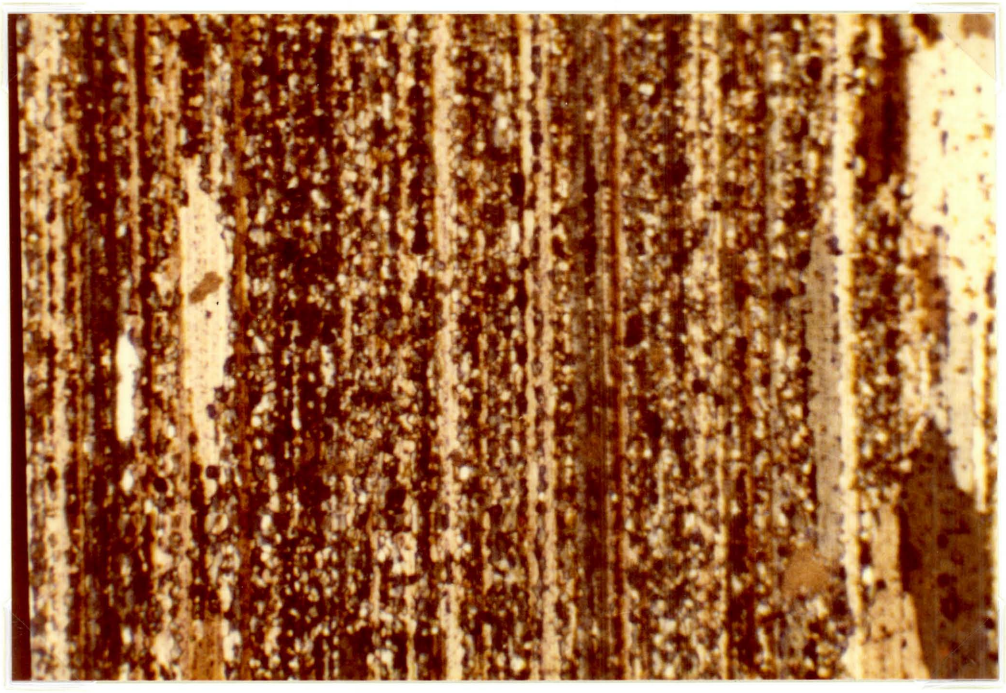


Fig. 172. Peripheral Structure at die mouth x 64

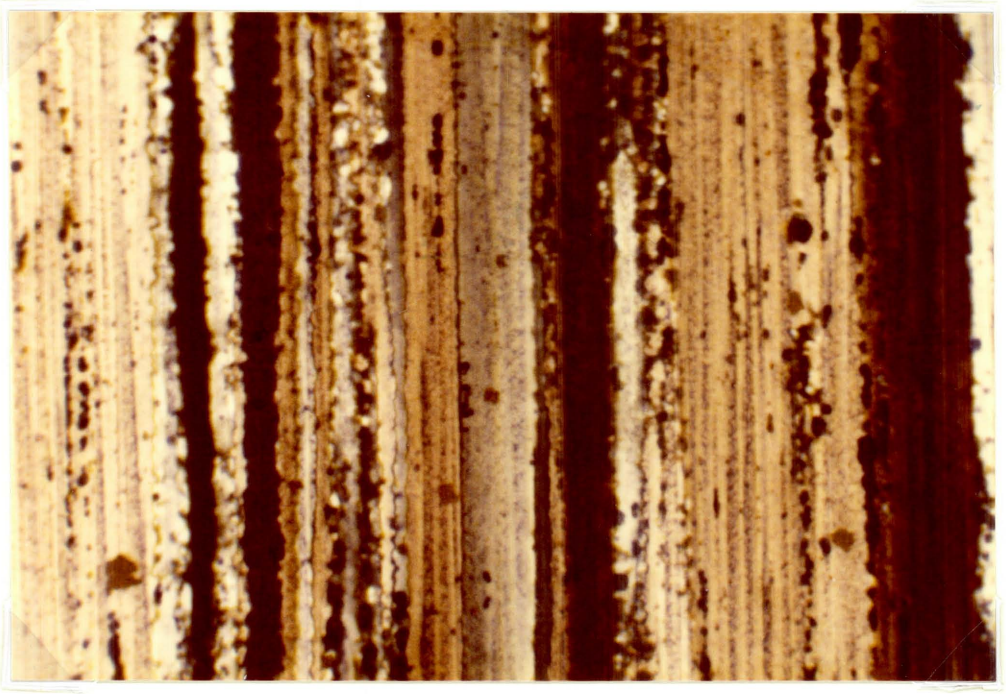


Fig. 173. Core structure at die mouth x 64

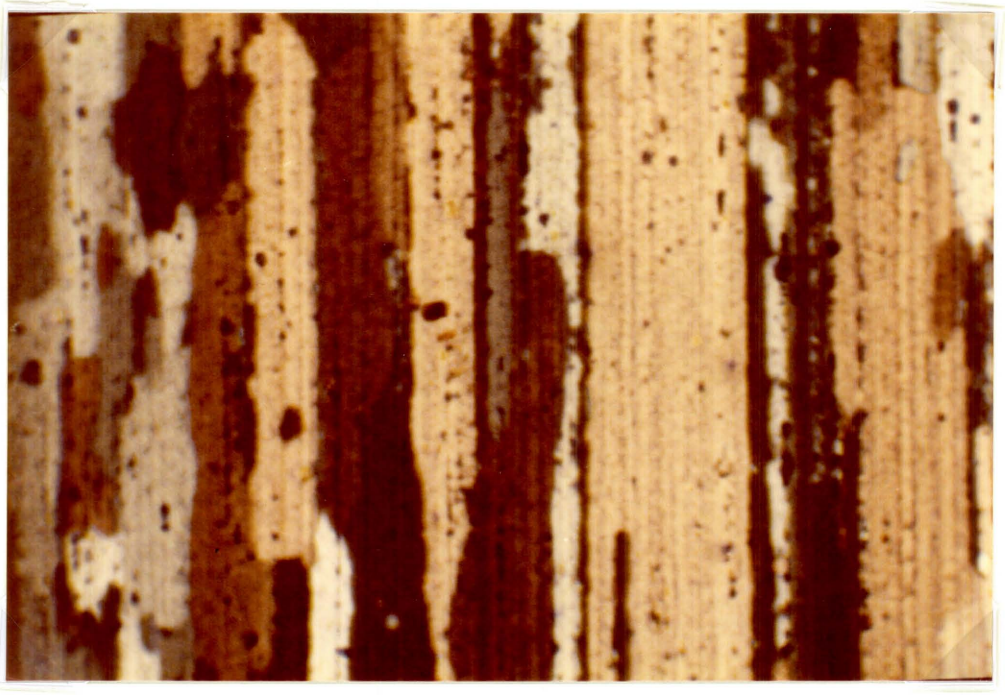


Fig. 174. Peripheral structure away from die x 64

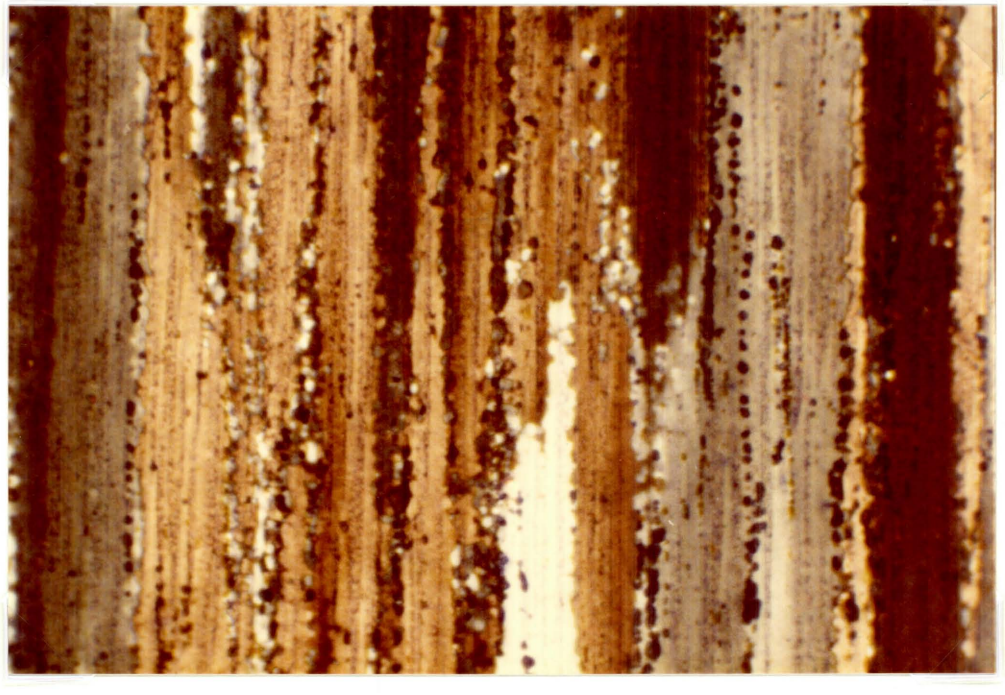


Fig. 175. Core structure away from die x 60

boundary scalloping and equi-axed dynamically recrystallized grains are both evident.

Changes along the length of extrude are primarily due to temperature variations. Over the initial few inches of product there is a structural change associated with the quasi-static deformation zone development. This was observed in Fig. 97. Over the remaining length the changes are more discrete being due to the temperature rise or fall associated with deformation. In the majority of cases the heat generated by the process was sufficient to overcome the heat lost to the surroundings and a nett temperature rise was observed. Thus the proportion of recrystallized grains increased along the product due to the higher temperatures pertaining. This will also be reflected in the properties of the material. In terms of hardness, the results for extrusion 121 may be seen in Table 4.27.

Location	Centre Hv	Mid-Radius Hv	Edge Hv
Front End	86	86	87
Middle	87	86	83
Rear	80	75	74

TABLE 4.27: Hardness variation with location on product.

As these figures show, a reduction in property is found at the rear of the product, notably at the edge and mid-radius as the statically recrystallized grain size increases and its depth into the product becomes greater.

4.5.1.4. Variation of Structure with Temperature and Strain Rate

The variation of structure with these parameters may conveniently be studied by considering extrusion runs 141 and 113-121. These encompass the largest variation in the Z parameter for any reduction ratio employed. Figs. 176-180 illustrate the typical structures found across the range. Fig. 176 corresponds to the low temperature run and shows an elongated, fibrous structure interspersed with statically recrystallized grains. These have arisen because of the incomplete recovery processes during deformation failing to reduce the stored energy levels. Fig. 177 illustrates the structure at a

R = 30:1
T = 244°C
Ram speed = 10 mm/sec

Fig. 176. Microstructure of run 141 x 25

R = 30:1
T = 395°C
Ram speed = 5.6 mms/sec

Fig. 177. Microstructure of run 117 x 25

R = 30:1
T = 443°C
Ram speed = 4.2 mms/sec

Fig. 178. Microstructure of run 119 x 200

R = 30:1
T = 443°C
Ram speed = 12.5 mms/sec

Fig. 179. Microstructure of run 120 x 25

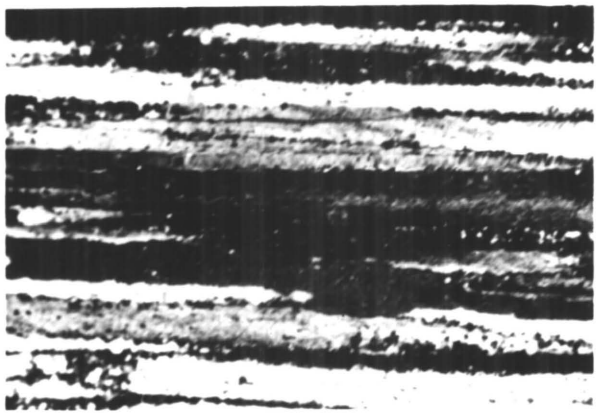
R = 30:1
T = 480°C
Ram speed = 4.0 mms/sec

Fig. 180. Microstructure of run 121 x 200

All for alloy D222 (5456)











higher temperature and slower ram speed and shows a fibrous structure again but containing larger statically recrystallized grains. These have developed due to the increased temperature and slower strain rate pertaining. Fig. 178, for the extrusion at 450°C shows a different picture. In this case the background is still one of a fibrous grain structure but in addition evidence of statically formed grains is removed and replaced by equi-axed dynamically formed ones. Thus the critical temperature for this process, under the applied conditions of reduction and ram speed, is between 400°C and 450°C. The dynamically recrystallized grains are associated with the original grain boundaries where the driving force for their formation is greatest. Fig. 179 shows the result for run 120 in which too great an initial temperature rise and ram speed were employed. The consequence is the onset of checking or incipient melting which produces that cracking shown. These cracks tend to run perpendicular to the surface initially before bending towards the rear. The bending and end of the cracks coincide with a structural change from a fine equi-axed recrystallized structure to a slightly larger and more elongated one, i.e. the reduction in transverse grain boundaries has inhibited the crack propagation. In the more central regions the grain size is considerably smaller than found earlier, indicating that dynamic recrystallization has become more pronounced. Virtually no fibrous grains were visible confirming that dynamic recovery has been superceded, certainly to some degree. Run number 121 was carried out at the same temperature as 120 but at a reduced ram speed, from 12.5 to 4 mms/sec. In this case no surface cracking was detected showing the relative importance of the ram speed in this respect. Internally a similar structure was observed with dynamically recrystallized grains being identified in all regions, Fig. 180.

Increasing the deformation temperature, therefore, initially decreases the nucleation of statically recrystallized grains while increasing their size prior to the onset of dynamic recrystallization which then increases directly with temperature.

Both materials 5456 and 5083 showed similar trends, examples for the latter being shown in Figs. 181 and 182. The results are shown for run 189 and typical structures are produced of statically recrystallized peripheral grains surrounding an inner fibrous core

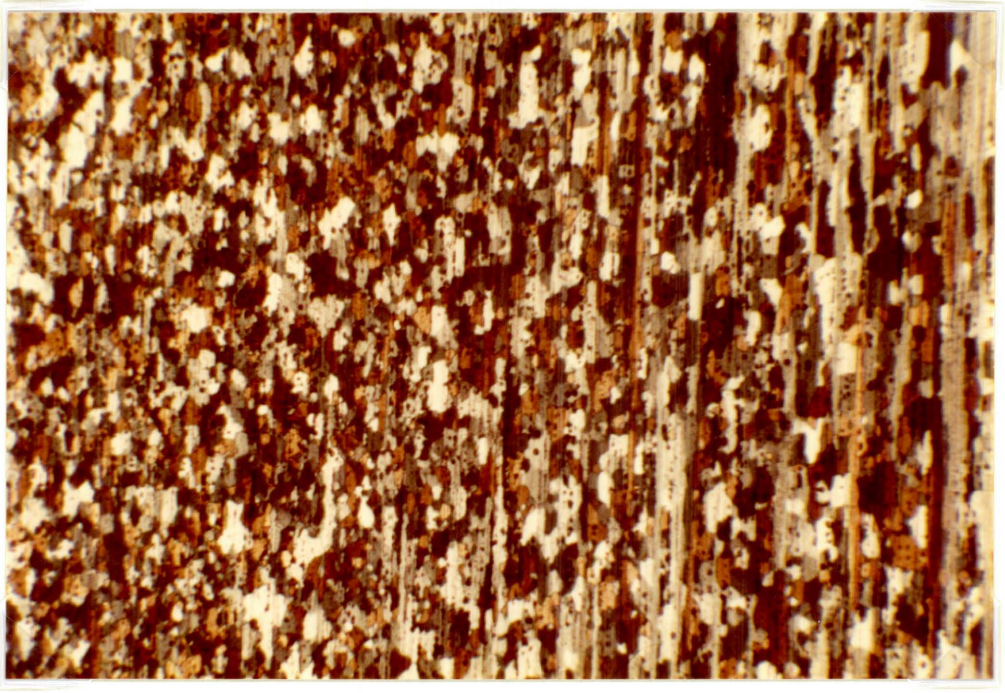


Fig. 181. Microstructure of 5083 x 64

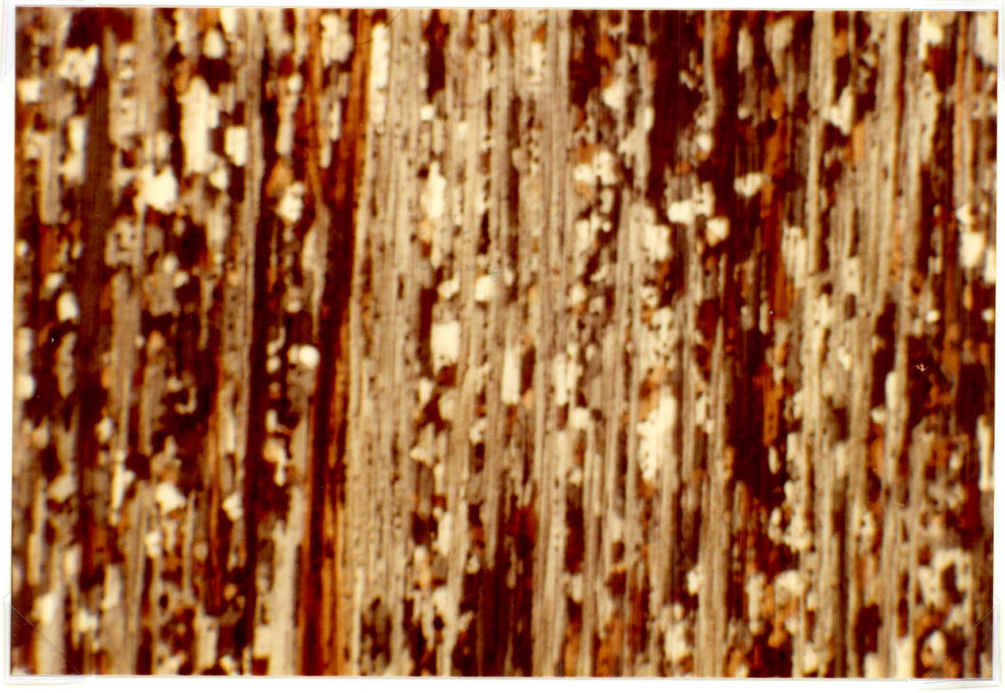


Fig. 182. Microstructure of 5083 x 64

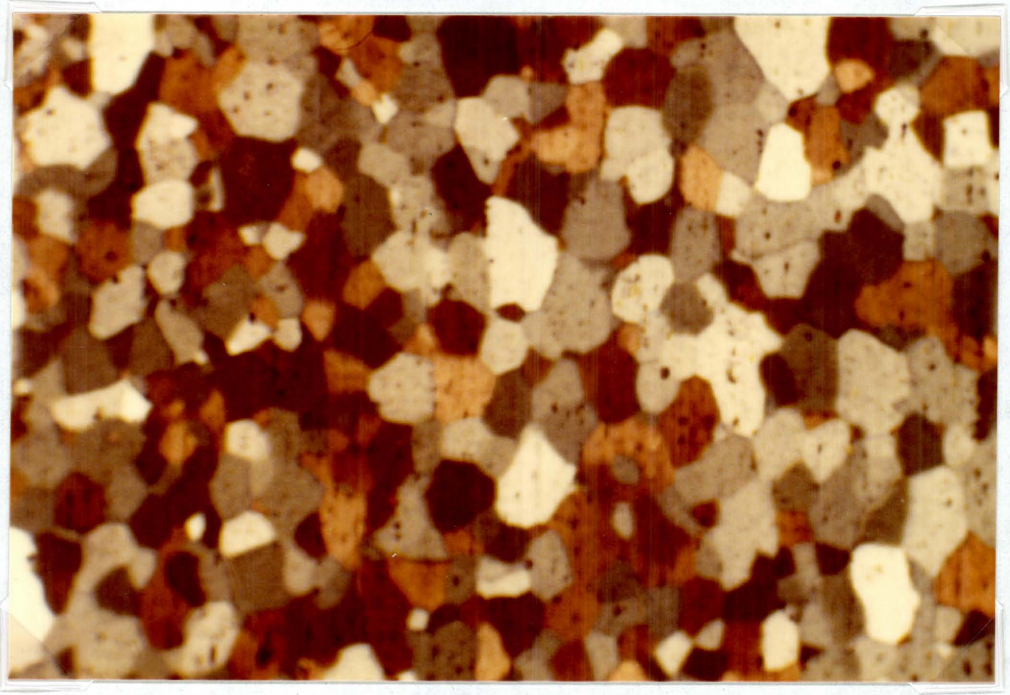


Fig. 183. Typical microstructure of alloy 5052.

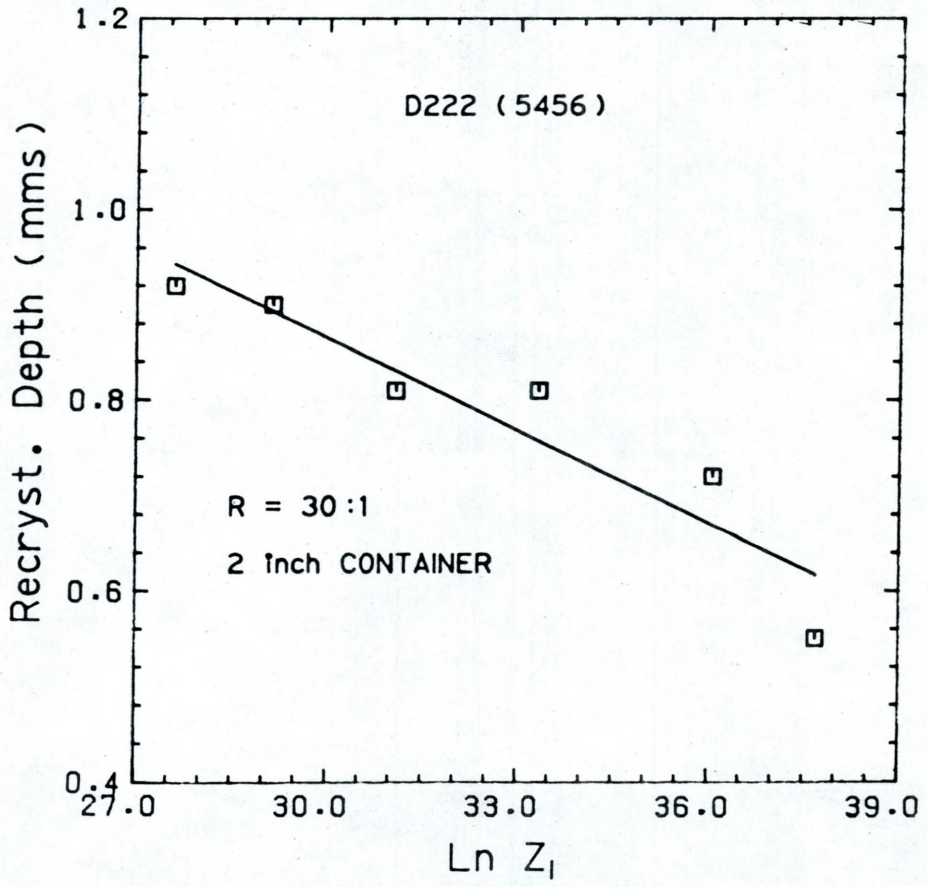


Fig. 184. Recrystalliaxed annullus depth vs. LnZ_i

containing some equi-axed recrystallized grains. With alloy 5052, the reduced volume of second phase and lower magnesium content causes the progress of static recrystallization to be unhindered and completely equi-axed recrystallized structures were produced as shown in Fig. 183.

The action of the progressive increase in temperature upon the recrystallized annular ring may be seen in Fig. 184. In this case the depth of continuous recrystallized grains is plotted against the Z parameter calculated for initial temperature conditions. This is not a measure of the number or percentage of recrystallized grains and takes no account of their size since this latter feature has been discussed previously. The result shows that the peripheral layer increases in depth as the temperature is raised or the strain rate reduced, observations which are consistent with the discussion in the previous section.

4.5.1.5. Variation of Substructure with the Process Variables

The development of the product structure has been discussed with relevance to the microstructure and the establishment of the quasi-static deformation zone in previous sections. These showed how the variations, notably in temperature, of the process parameters could cause vastly different microstructures to be produced. In this section, the substructures of the products discussed in section 4.5.1.4. will be investigated.

Figs. 185-187 show the substructure for the low temperature run number 141. The first shows a longitudinal section showing a band of sub-grains surrounded by regions of dislocation free material. The sub-grains are orientated parallel with the extrusion direction and represent an original grain containing the substructure surrounded by statically recrystallized grains. Second phase particles may be observed also elongated in the extrusion direction. Fig. 186 re-emphasises this structure with a band of sub-grains running across the centre, being surrounded by large sub-grain free regions. In Fig. 187 a longitudinal section is presented which shows the more equi-axed appearance of the sub-grains when viewed in this plane. It can also be noticed in many cases how the intersection of sub-grain boundaries coincides with second phase particles emphasising their potency in pinning. The structures are in agreement with the

optical microscopy of Fig. 176 and establish that dynamic recovery is the operative restoration process at this temperature. Increasing the temperature causes a minor change in general aspects of the structure. Regions may be found in which sub-grain formation is virtually negligible, Fig. 188, while in general sub-grains were found in more prevalence toward the product centre. During the deformation process, large precipitates are broken up and strung out parallel to the extrusion direction as seen in Fig. 189.

Increasing the temperature from this value of 300°C up to 400°C results in similar structures being produced (Figs. 190-193). While the presence of second phase particles serves to pin the sub-grain walls and thereby modify the structure, the only significant change is the increased dimensions of the sub-grains, improvement of their perfection and reduction in the boundary widths. This is a consequence of the enhanced thermal activation permitting easier cross-slip and climb and therefore a more complete recovery. Regions of recrystallized material could still be found in all specimens although their frequency in the more central positions was diminished at the higher temperatures.

In specimen 119, corresponding to an extrusion temperature of 450°C additional features become apparent in the structure. Areas originally believed to be sub-grains because of their similar size and shape were found to be associated with boundaries of high misorientation. This may have been anticipated from the increased contrast in these regions. Such a situation is illustrated in Fig. 194 in which the boundary marked has a misorientation of 17° indicating it to be of a greater magnitude than is normally associated with a sub-grain boundary. Deeper investigation of the dark grain in Fig. 194 shows it to contain a dislocation structure, Fig. 195, and to be the result of the dynamic recrystallization process described in section 4.5.4. The grain size of approximately 2.5 μm compares favourably with that estimated from optical microscopy for the equi-axed grains found at original grain boundaries. Thus more evidence is found for the hypothesis that these are the result of the dynamic recrystallization process. In the bulk of the specimen sub-grains were observed,

R = 30:1
T = 244°C
Ram speed = 10 mms/sec

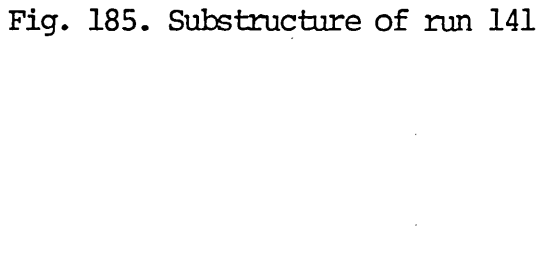


Fig. 185. Substructure of run 141

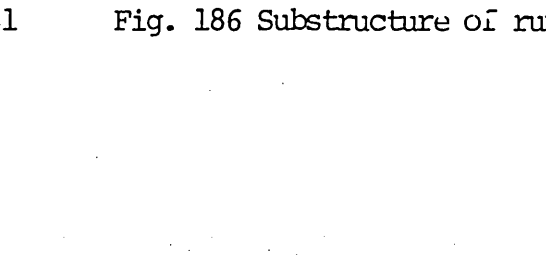


Fig. 186 Substructure of run 141

R = 30:1
T = 297°C
Ram speed = 12.6 mms/sec

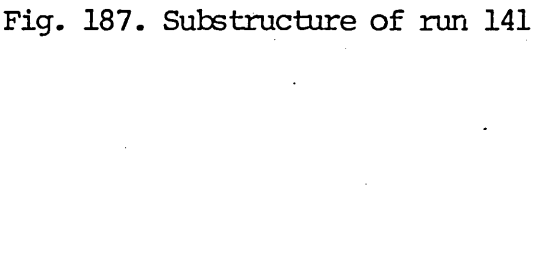


Fig. 187. Substructure of run 141

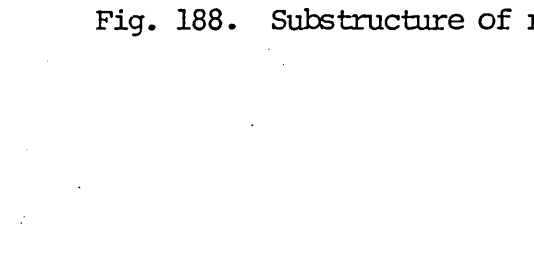


Fig. 188. Substructure of run 113

R = 30:1
T = 395°C
Ram speed = 5.6 mms/sec

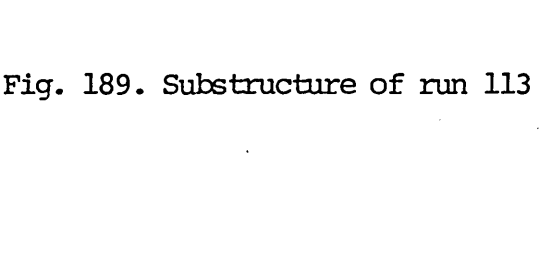


Fig. 189. Substructure of run 113

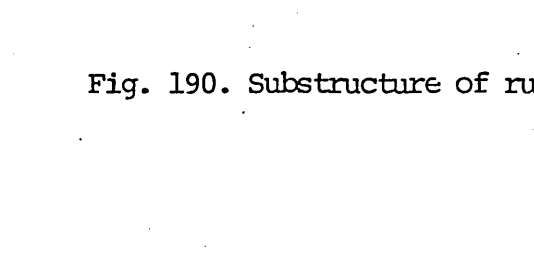
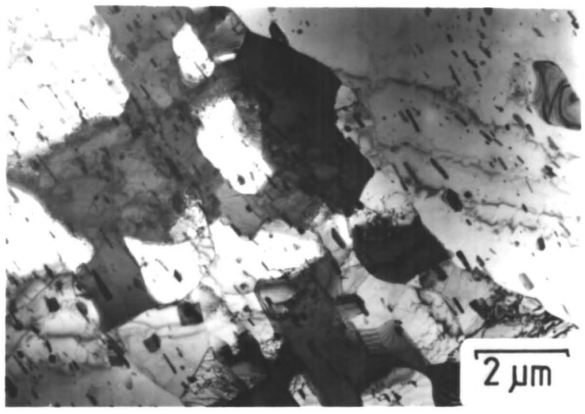
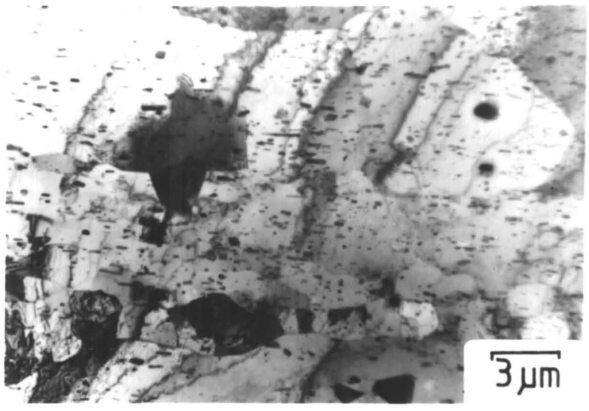
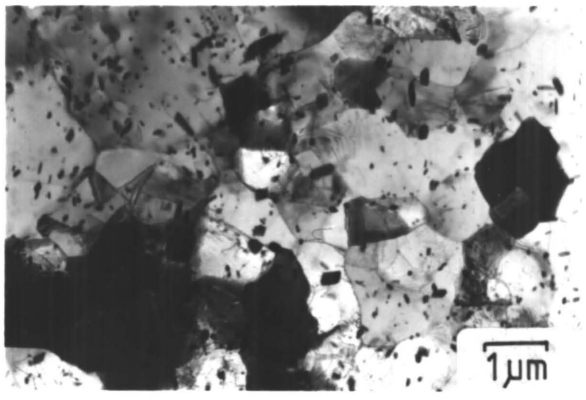
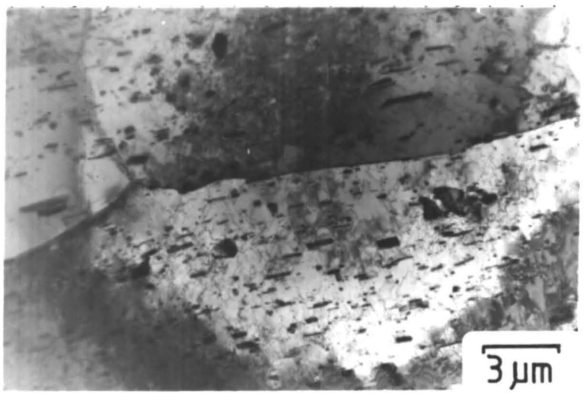


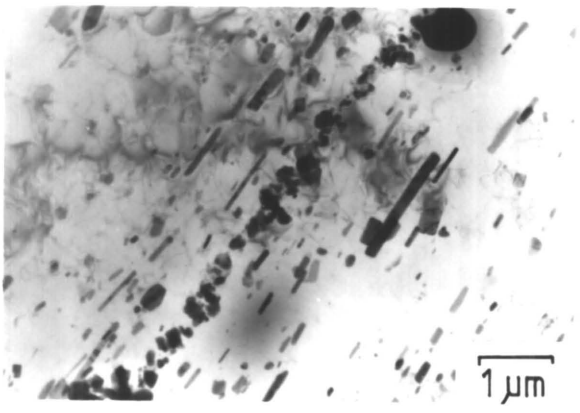
Fig. 190. Substructure of run 117

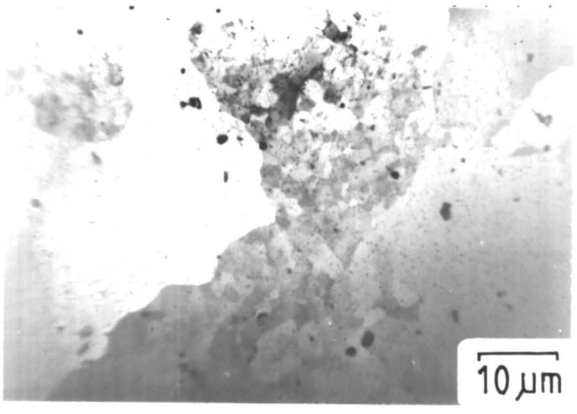

2 µm


3 µm


1 µm


3 µm


1 µm


10 µm

R = 30:1
T = 394°C
Ram speed = 4.0 mms/sec

Fig. 191 Substructure for run 117

Fig. 192. Substructure for run 118

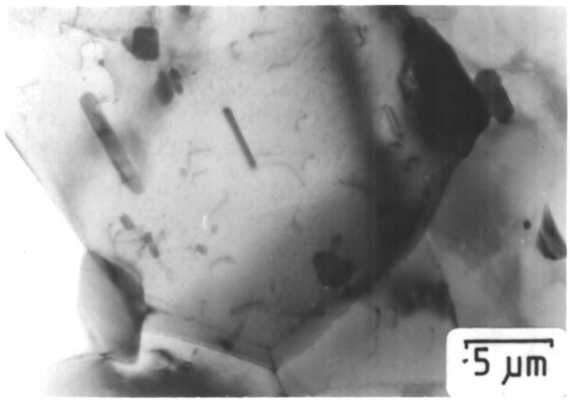
R = 30:1
T = 443°C
Ram speed = 4.2 mms/sec

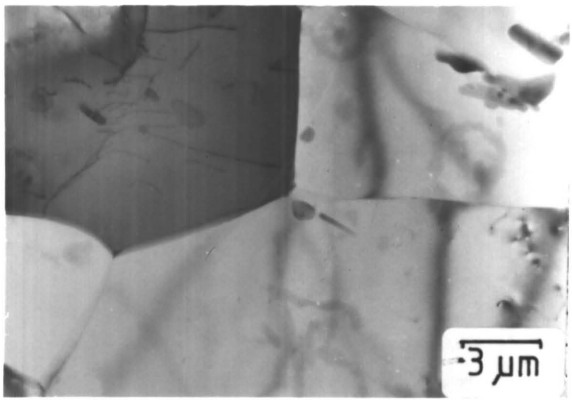
Fig. 193. Substructure for run 118

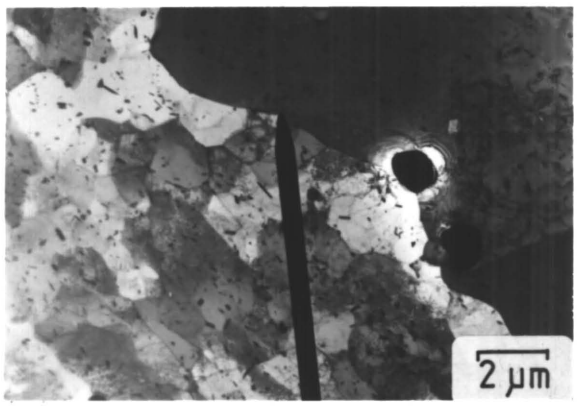
Fig. 194. Substructure for run 119

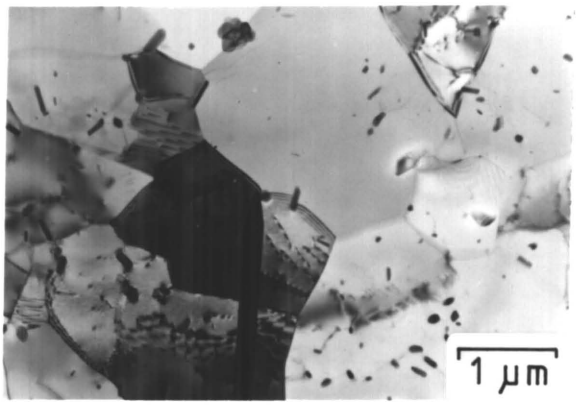
Fig. 195. Substructure for run 119

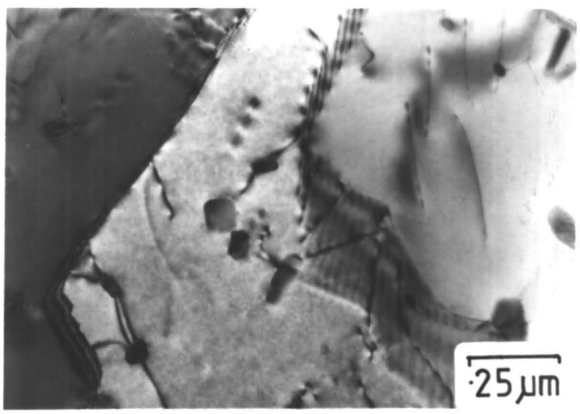
Fig. 196. Substructure for run 119


·5 µm


·3 µm


2 µm


1 µm


·25 µm

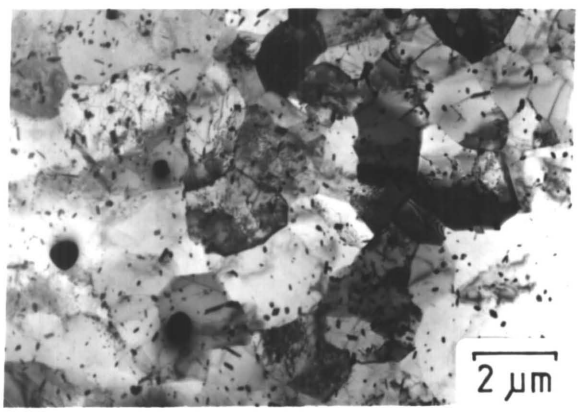

2 µm

Fig. 196, being equi-axed in nature and containing a very low internal dislocation density.

The other materials notably the 5083 and 5456 showed similar features. 5052 tended to recrystallize under most of the limited number of extrusions performed. This resulted in a structure as shown in Fig. 197 containing large statically recrystallized grains with small amounts of second phase coincident with the triple points. The reduced proportion of magnesium and distribution of second phase material causes the movement of high angle grain boundaries to be virtually unimpeded compared to the other alloys. The recrystallization process can therefore proceed with ease over large areas of the product.

Both 5083 and 5456 acted very much as the alloy D222 described previously. The small difference in magnesium contents creates no noticeable variations and the structure for alloy 5083 at a reduction of 30:1 and temperature of 400°C is seen in Fig. 198. This is comparable with Figs. 190-193 and shows essentially the same features. An elongated original grain is seen, containing quite equi-axed sub-grains, running diagonally across the photograph. On each side there appears areas of sub-grain free material indicative of re-crystallization.

The effects of changing the reduction ratio are considerably less than those of temperature variation. Fig. 199 illustrates the substructure for run 38, a reduction of 80:1 at 500°C. The sub-grains are large and well defined and internal dislocation activity is minimal. There is little doubt that dynamically recrystallized grains could be found in the structure probably in those regions where the contrast across boundaries is high. Fig. 200 shows the structure for run 60 carried out at a similar temperature but reduced reduction of 10:1. The structure is very similar. The sub-grains are well defined and large in size, consistent with the high thermal activation. The structure shows a low internal dislocation density in the region where the amount of second phase particles is lower reflecting the increased ease of dislocation motion in these areas. In the region of increased particles the internal density is higher showing the recovery processes to be incomplete and the strain gradients to be higher. It is in these regions that dynamic re-crystallization is most likely to be nucleated and observed.

Fig. 197. Substructure for alloy 5052

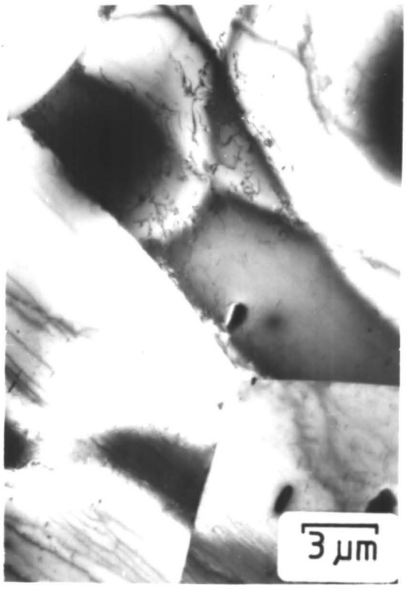
Fig. 198. Substructure for alloy 5083

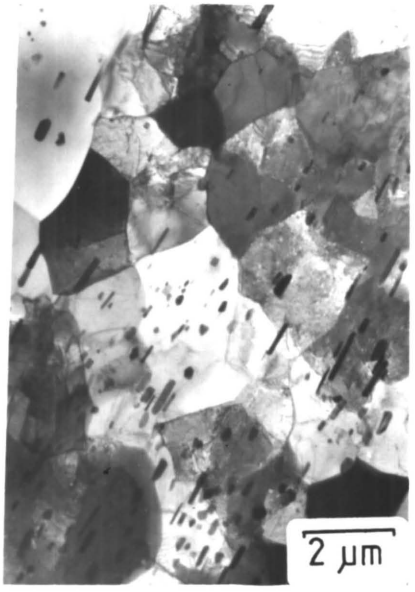
Fig. 199. Substructure for alloy D222 (5456)

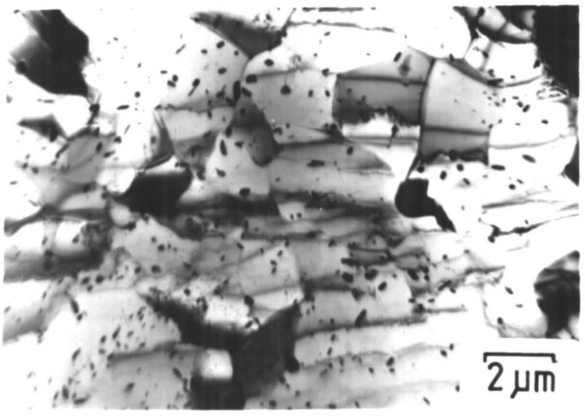
R = 10:1

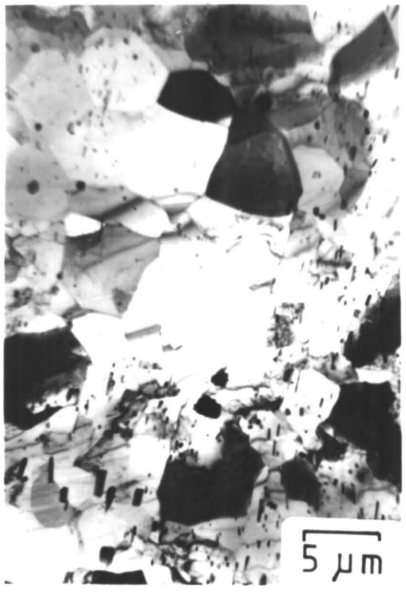
Fig. 200. High temperature substructure alloy D222 (5456)

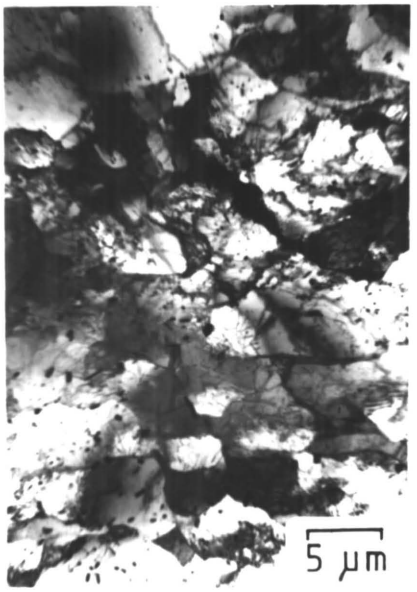
Fig. 201. Low temperature substructure alloy D222 (5456)


3 µm


2 µm


2 µm


5 µm


5 µm

Finally Fig. 201 shows the structure for a similar extrusion ratio but reduced deformation temperature to 322°C. In this case the structure shows a considerable alteration. The sub-grain walls are extremely ragged and wide and the sub-grain size is small. Internal dislocation density is high and the effect of particles in pinning walls is very apparent. These features are all indicative of incomplete recovery processes caused by the diminished thermal activation.

In conclusion then, it appears that a sub-grain structure is developed under all conditions to some degree. At low temperatures the structure is ragged and sub-grains contain high dislocation densities while at more elevated temperatures the recovery processes are more complete, sub-grain boundaries are more compact and well defined while internal dislocation density is negligible. In virtually all cases, regions of statically recrystallized material could be found notably towards the periphery of the product. At some temperature between 400°C and 450°C, dynamic recrystallization is initiated as an additional high temperature restoration process resulting in the appearance of small recrystallized grains containing a dislocation structure. These grains are of the same dimensions as the sub-grains but have a considerably enhanced misorientation associated with their boundaries.

4.6. Room Temperature Properties resulting from the High Temperature Deformation

Property evaluation was carried out by means of standard tensile, impact and both hardness and microhardness tests. The results may be found tabulated in Tables 4.28. - 32.

As was discussed in the previous section, various micro-structures were produced in the extrudates depending upon the conditions employed. These will consequentially affect the product properties and it is these relationships that will be discussed in the subsequent sections.

In order for the substructures to have an effect, they must be retained after deformation, which requires a suitable rate of cooling. This rate, in turn, must be sufficient to prevent the occurrence of both classical static and metadynamic recrystallization.

ROOM TEMPERATURE TESTS						
CROSSHEAD SPEED= 0.05 CMS/MIN				CROSSHEAD SPEED= 0.50 CMS/MIN		
RUN CODE	U.T.S. MN/M^2	.2 PROOF STRESS MN/M^2	ELONGATION	U.T.S. MN/M^2	.2 PROOF STRESS MN/M^2	ELONGATION
D222026	339.0	148.0	41.4			
D222040	332.4	138.0	40.4			
D222042	347.0	157.9	36.5			
D222043	336.1	151.1	40.5			
D222050	354.6	178.4	31.5	347.9	178.9	34.7
D222051	354.6	130.8	41.5	318.9	128.3	40.6
D222052	333.1	135.7	45.2	330.0	134.0	34.4
D222053	357.7	174.5	28.7	323.9	148.0	34.7
D222055	379.3	185.0	27.2	359.4	185.6	31.4
D222057	370.1	194.3	23.5	365.1	191.8	29.3
D222058	367.0	178.9	29.2			
D222059	385.6	212.8	21.7	382.4	189.9	25.7
D222060	376.2	200.5	20.2			
D222061	391.7	215.9	22.0	382.0	203.5	25.3
D222062	362.0	190.0	31.1	348.5	178.9	34.0
D222063	373.1	196.1	23.4			
D222066	404.1	231.3	21.3	389.2	228.2	23.9
D222068				378.1	203.5	22.8
D222073	400.9	219.0	20.1	386.7	215.9	26.3
D222074	391.7	210.9	24.0	337.4	169.6	32.9
D222075	395.1	222.6	19.2	391.6	215.9	22.5
D222076	376.8	197.4	25.8	376.8	215.9	25.8
D222077	371.3	191.2	28.4	326.9	172.7	35.6
D222079	388.6	203.5	25.9	373.1	209.0	28.7
D222080	379.3	197.4	29.0	370.1	185.0	30.1
D222084	376.3	203.5	22.8			
D222086	404.0	222.0	21.9	385.0	209.7	26.3
D222113	357.7	169.1	35.0	341.7	163.4	32.9
D222114	373.2	166.5	34.1	360.2	166.5	31.7
D222115	376.3	166.5	34.6	359.0	163.5	33.5
D222116	375.5	166.5	33.8	360.8	166.5	32.3
D222117	378.1	185.0	31.7	358.4	178.9	29.3
D222118	365.8	169.6	32.3	351.6	166.5	27.5
D222119	389.8	191.2	28.1	375.6	181.9	29.3
D222121	373.2	172.7	32.3	357.7	166.5	31.7
D222141	373.2	169.6	35.9	357.7	169.6	32.9
5456173				349.1	160.4	29.9
5052174	191.8	86.4	39.5	190.0	67.8	37.1
5083175	351.7	166.5	25.1	339.2	154.2	26.3
5052180	196.8	67.8	38.3	191.8	95.6	30.5
5083181	344.2	142.5	30.5	323.2	135.7	30.5
5456182	355.9	154.2	34.1	341.1	135.7	32.3
5083186	348.5	154.2	28.1	333.1	149.9	28.1
5052187	185.0	83.3	38.0	186.9	70.3	36.5
5456188	360.8	159.1	33.0	346.0	164.1	28.0
5083189	347.8	151.7	30.0	333.7	153.6	27.5
5052190	191.8	67.8	37.7	187.5	74.0	38.3
5456191	362.7	166.5	33.5	345.4	166.5	31.7
5052192	191.8	68.5	38.9	187.5	67.8	38.3
5083193	345.3	148.0	31.7	329.4	147.4	28.4
5456194	358.4	166.5	30.5	346.0	167.8	29.9
5052195	194.3	73.4	38.9	188.7	67.8	37.7
5083196	348.5	160.4	32.3	333.1	156.1	29.9
5456197	363.9	169.6	32.3	347.3	170.2	30.5

Table 4.28. Room Temperature Tensile Test Results

200 C TESTS						
CROSSHEAD SPEED= 0.05 CMS/MIN				CROSSHEAD SPEED= 0.50 CMS/MIN		
RUN CODE	U.T.S. MN/M^2	.2 PROOF STRESS MN/M^2	ELONGATION	U.T.S. MN/M^2	.2 PROOF STRESS MN/M^2	ELONGATION
D222026	194.3	136.9	53.1			
D222040	183.8	154.6	53.1	200.5	135.7	52.8
D222042	185.6	154.2	51.4	206.6	143.1	50.3
D222043	190.0	141.9	54.2	207.3	138.7	65.3
D222050	200.5	163.4	53.5			
D222051	160.4	126.4	60.8	188.1	125.2	52.1
D222052	172.7	122.1	75.5	199.2	138.8	56.9
D222053	199.2	158.5	47.3	246.7	185.1	50.3
D222055	217.9	178.9	44.9	238.7	173.3	53.3
D222057	228.2	186.9	57.5	254.1	185.6	45.8
D222059				250.4	191.8	47.9
D222060	226.4	186.9	54.9	259.0	203.5	55.6
D222061	234.4	204.8	41.0	252.4	190.0	50.0
D222062	166.0	154.0	72.9	210.9	164.7	54.2
D222063	234.4	204.8	41.0			
D222066	206.6	185.6	50.0	264.6	199.8	39.5
D222068	202.3	182.6	40.1	257.8	192.4	43.7
D222073	221.4	188.7	46.7	251.6	192.4	37.1
D222074	215.9	194.9	60.5	215.9	170.2	47.9
D222075	208.5	188.7	52.1	241.8	186.3	40.1
D222076	194.3	170.2	53.9	196.8	141.9	48.9
D222077	199.2	172.2	53.9	196.8	141.9	46.7
D222079	215.2	191.0	52.1	265.8	191.2	50.9
D222084	206.1	169.6	52.1			
D222086	272.0	217.1	46.7	251.6	191.8	41.9

Table 4.29. 200°C Tensile Test Results

TENSILE TEST RESULTS					
RUN CODE	CROSSHEAD SPEED	TEMP	U.T.S.	.2 PROOF STRESS	ELONGATION
	CMS/MIN	C	MN/M^2	MN/M^2	
D222080	0.1	21	370.1	185.0	30.1
D222080	0.2	21	365.1	187.3	29.3
D222115	0.5	60	357.8	163.5	32.3
D222115	0.5	113	345.4	160.3	41.3
D222115	0.5	150	313.9	160.3	47.9
D222115	0.5	225	201.1	148.0	76.1
D222115	0.1	21	371.3	169.6	34.7
D222115	1.0	21	354.6	169.6	33.5
D222115	2.0	21	348.5	169.6	33.4
D222115	5.0	21	345.4	169.6	33.8
D222115	10.0	25	339.3	166.5	35.9

Table 4.30. Tensile Test Results for various test conditions

	HARDNESS HV					MICRO-HARDNESS HV		
RUN CODE	CENTRE	MID-RADIUS	EDGE	SUB-GRAIN SIZE	IMPACT ENERGY J	CENTRE	MID-RADIUS	EDGE
D222015	87	86	84					
D222016	85	87	86					
D222017	86	84	81					
D222021	88	86	87					
D222022	84	84	84					
D222026	88	87	84					
D222027	85	84	83					
D222028	84	83	58					
D222030	85	86	84					
D222031	84	85	82					
D222032	88	88	86	1.3				
D222034	88	91	92					
D222036	88	86	80	1.3				
D222038	90	69	87					
D222040	83	85	84	1.4	67.5			
D222042	87	88	89					
D222043	82	82	82					
D222050	90	89	86	1.2				
D222051	79	79	79					
D222052	87	89	82					
D222053	91	87	82		54.8			
D222058	86	66	82					
D222059	91	88	83		77.8			
D222060	91	87	81	1.6				
D222061	88	88	78	1.2	71.7			
D222062	97	93	84	1.7	79.6			
D222063	91	89	83			94	74	74
D222064	93	95	99					
D222065					70.8			
D222066	96	92	92			108	110	94
D222072	94	91	90					
D222073	93	90	84		79.2			
D222074	93	92	86					
D222075					74.4			
D222076	95	94	83	1.1	78.2			
D222077	92	91	90		67.1			
D222079	92	88	85		76.2			
D222080	92	90	87					
D222084	90	90	87		83.1			
D222086	90	85	84	1.4	79.3			
D222089				1.3				
D222095	81	82	71					
D222096	83	84	76					
D222097	83	82	74					
D222102	81	82	71	1.4				
D222107	84	84	84					
D222108	92	87	87					
D222109	88	89	86	1.3				
D222110	90	85	88					

Table 4.31. Hardness and Impact Energy Results

	HARDNESS HV					MICRO-HARDNESS HV		
RUN CODE	CENTRE	MID-RADIUS	EDGE	SUB-GRAIN SIZE	IMPACT ENERGY J	CENTRE	MID-RADIUS	EDGE
D222113	78	74	71	1.0	60.1	100	100	97
D222114	84	86	85		63.7	110	100	88
D222115	84	82	78		63.7	85	86	7C
D222116	92	92	89	1.2	62.0	97	84	76
D222117	90	89	82	1.5	71.3	87	82	89
D222118	85	85	81	1.4	67.3	84	81	85
D222119					69.6			
D222120	86	86	83	1.4		110	93	96
D222121	88	86	83	1.6	73.2	100	94	81
D222125	83	84	84					
D222127	86	83	84					
D222131	80	77	78	1.5				
D222137	85	82	83					
D222138				1.1				
D222141	86	85	86	0.8	59.3	112	97	93
D222144	81	87	84					
5083159	76	77	76					
5456173	90	87	87		49.4			
5052174	48	51	51		86.6			
5083175	77	79	77		58.9			
5052180	49		51					
5083181	78		77					
5456182	84		84					
5052183	53		51					
5083184	78		79					
5456185	82		86					
5083186	82	84	82		55.9			
5052187	49	49	49		78.7			
5456188	86	85	85		46.2			
5083189					57.2			
5052190	49	50	49		78.7			
5456191	84	84	82		46.2			
5052192	51	50	51		78.0			
5083193	78	76	75		57.2			
5456194	84	84	83		43.6			
5052195	50	49	49		79.3			
5083196	81	83	79		55.9			
5456197	85	83	84		43.6			
D222200	78		83	1.5				
D222202	91		79	1.5				
D222203	95		86	1.5				
D222205	69		73	1.3				
D222206	98		97					
D222207	85		76	1.1				
D222208	66		62					

Table 4.31. Continued.

350 C SOAK 1.5 HOURS (WATER QUENCH)				500 C SOAK 1.5 HOURS (WATER QUENCH)			
AGE AT 120 C		AGE AT ROOM TEMP		AGE AT 120 C		AGE AT ROOM TEMP	
TIME MINS	HV	TIME MINS	HV	TIME MINS	HV	TIME MINS	HV
	C 88		C 88		C 87		C 87
0	M 88	0	M 88	0	M 85	0	M 87
	E 88		E 88		E 88		E 87
	C 88		C 87		C 88		C 86
60	M 89	60	M 88	60	M 88	60	M 86
	E 87		E 87		E 85		E 85
	C 87		C 89		C 85		C 85
440	M 88	440	M 89	440	M 88	440	M 87
	E 87		E 87		E 88		E 87
	C 88		C 86		C 88		C 85
7200	M 87	7200	M 86	7200	M 88	7200	M 85
	E 86		E 87		E 87		E 85
	C 87		C 86		C 88		C 86
21600	M 87	21600	M 86	21600	M 88	21600	M 86
	E 87		E 87		E 88		E 86
	C 86		C 87		C 88		C 87
44640	M 86	44640	M 87	44640	M 86	44640	M 87
	E 86		E 87		E 87		E 86

C=CENTRE M=MID-RADIUS E=EDGE

Table 4.32. Ageing results for alloy D222 (5456)

In the latter case, the rate will necessarily need to be higher since this mode of softening requires no incubation period as the dynamically recrystallized grains act as nuclei. The previous section revealed that the applied rate of quenching stabilised the sub-grain structure at most positions in the product while static recrystallization was initiated at the periphery and at some original grain boundaries, notably at lower processing temperatures. No evidence was presented for the appearance of metadynamic recrystallization although the dislocation structures may have annealed out of the dynamically recrystallized grains. Thus, no growth will result in the production of a fine grain sized material in these regions at high deformation temperatures.

Many workers[150,156,194,195] have observed that, in the presence of a hot worked substructure, the room temperature flow stress is related to the sub-grain diameter through a Hall-Petch type equation of the form:-

$$\sigma_{RT} = \sigma_o + Kd^{-m}$$

where σ_{RT} is the room temperature flow stress, σ_o is the friction stress, K a constant related to sub-grain boundary strength (i.e. stress concentration required to generate dislocations from the boundary), and d the sub-grain diameter. If this is true, then the room temperature properties will be related to the internal structure notably in the case of dynamic recovery as the operative high temperature restoration process. At higher temperatures, when the alternative process of dynamic recrystallization is initiated, the dependency may be changed because of the existence of the equi-axed recrystallized grains in the product.

4.6.1. Tensile Tests

4.6.1.1. Nature of the Stress-Strain Curves

Tensile tests were carried out upon selected extrudates at both room temperature and 200°C. Crosshead speeds of 0.05 and 0.5 cms/min were employed.

At room temperature and for all crosshead speeds a trace of the type shown in Fig. 202 was revealed. This is specifically for

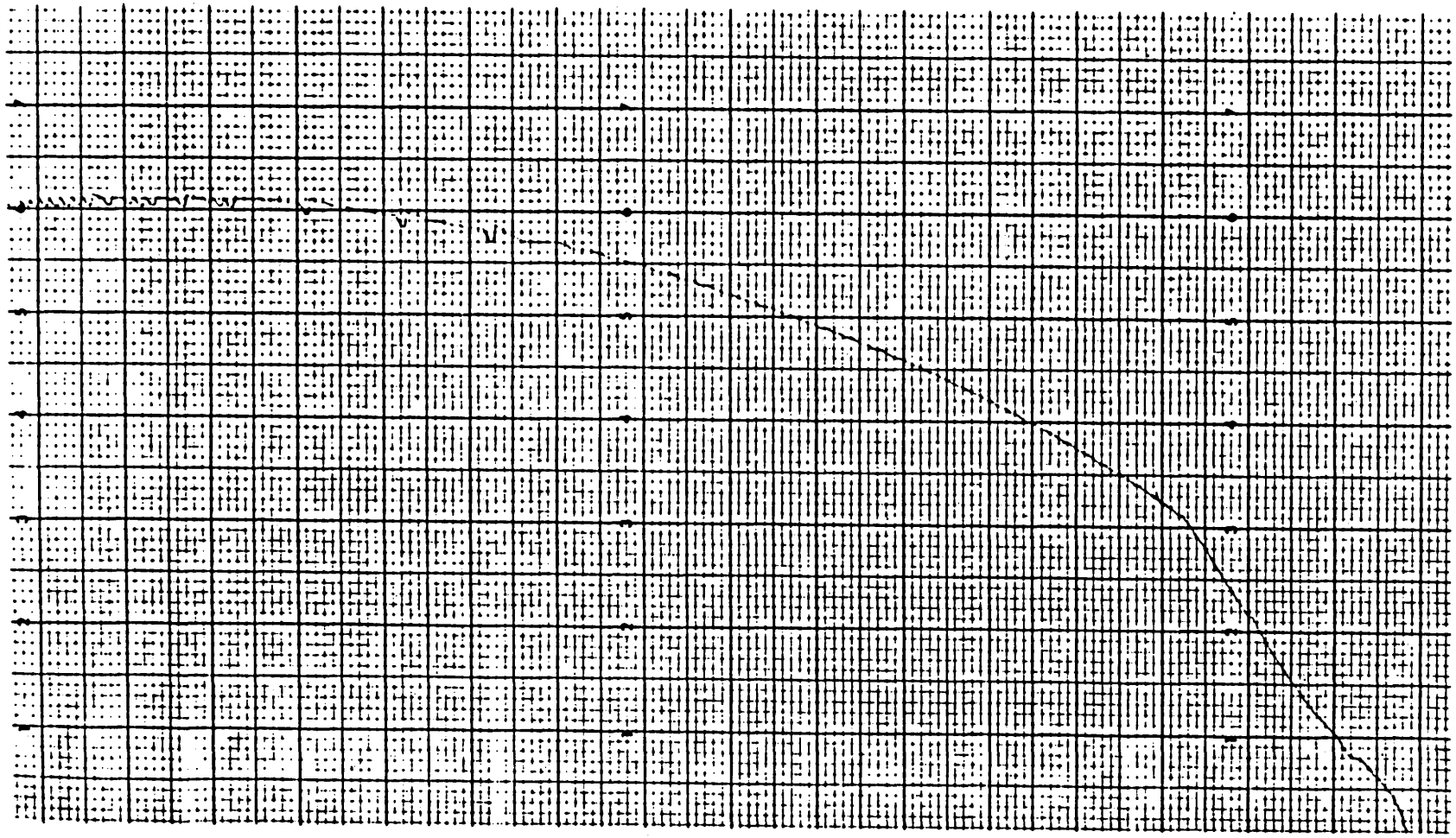


Fig. 202. Room Temperature stress-strain curve

run 63 tested at room temperature and crosshead speed of 0.05 cms/min. The chart was being run at a speed of 5 cms/min. The figure shows an initial approximately linear increase up to the yield point after which an extended plastic region exists with the load steadily increasing to a maximum value at which necking occurs. The load then steadily decreases to fracture or, as in this case, fracture occurred immediately after the maximum load was achieved. The appearance of instability in the curve at some strain subsequent to yielding has been recognised by many workers[230-235] investigating aluminium-magnesium alloy. The phenomenon is known as serrated yielding or the Portevin-Le-Chatelier effect and is manifested by the appearance of jerks in the plastic region of the stress-strain curve. Cottrell[236] suggested a mechanism whereby moving dislocations are repeatedly locked by solute atoms. Upon a sufficient stress being applied, the dislocations break away and the load drops. The solute, magnesium atoms, then diffuse to catch up the dislocations and re-pin them; the process is then a repetition. The large size of the magnesium atoms would seem to suggest that this mechanism is unlikely because of the slow rates of diffusion involved. However, the increased density of vacancies resulting from the deformation will permit an enhanced rate of diffusion and make the mechanism feasible. The strain between yielding and the first appearance of instability is associated with the generation of these vacancies. At higher testing temperatures the feature was removed. Thomas[231] has reported that an increase in temperature serves to increase both the strain and stress at which the serrations appear. Increasing the strain rate, via a crosshead speed increase, causes the serrations to appear at lower strains and stresses. Phillips et al.[230] studied the deformation behaviour of aluminium-magnesium sheet during stretching and correlated the onset of serrated yielding with the appearance of surface markings on the specimen. Thus the phenomenon has industrial implications since surface finish will be of prime importance in sheet applications.

4.6.1.2. Tensile Test Results

The results from the tensile tests may be found in Tables 4.28-4.30. The effect of varying test conditions upon the tensile properties may be found in Figs. 203 and 204. As the former shows,

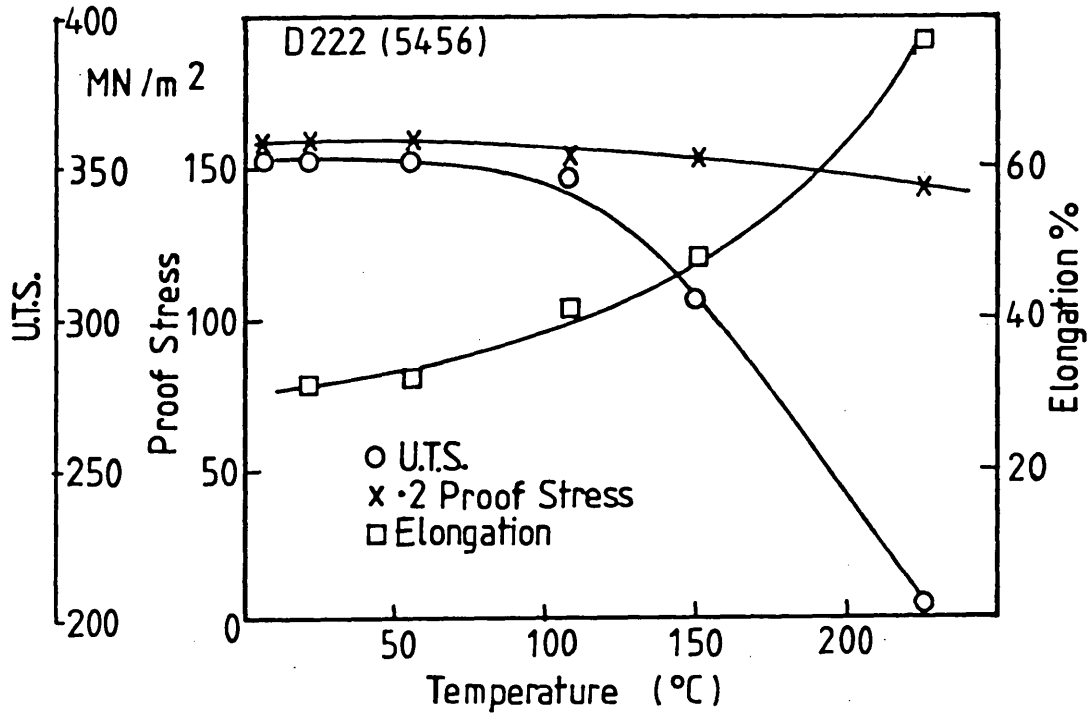


Fig. 203. Variation of tensile properties with test temperature, Crosshead speed 0.5 cms/min, for alloy D222 (5456)

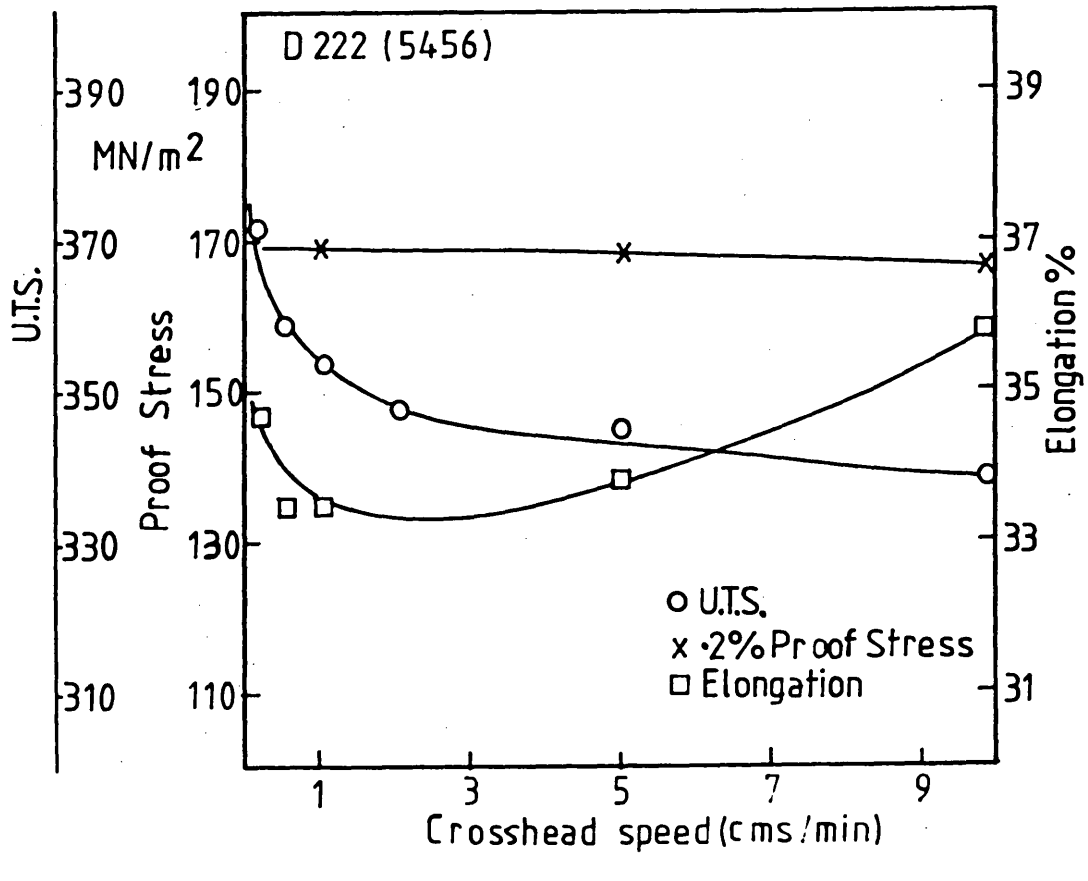


Fig. 204. Variation of tensile properties with crosshead speed during the test. Room Temperature tests, for alloy D222 (5456)

increasing the test temperature considerably decreases the material U.T.S. while the change in proof stress is much less obvious. At the same time the elongation shows a significant increase. The decrease in flow stress is associated with its two components; one an athermal component due to the stress needed to enable dislocations to overcome long range obstacles such as precipitates and other dislocations on parallel slip planes and the other a thermally activated component associated with the stress needed to overcome short range obstacles such as solute atoms and lattice friction effects. Thus the increased test temperature reduces the latter notably with respect to solute atoms. Varying the test crosshead speed, and therefore the initial strain rate, resulted in an initial rapid fall in the U.T.S. followed by a more gentle decrease which may be attributed to specimen heating from the deformation. The elongation shows an increase over the range which may also be attributed to the increased specimen temperature. These observations, although justified in respect of temperature changes, are opposite to those which would have been expected since the increasing strain rate was anticipated to increase the U.T.S. and decrease elongation because of its effect upon dislocation dynamics.

The effect of variation in process parameter upon the room temperature properties is not a simple one in any of the cases investigated. Figs. 205-207 illustrate the results while Figs. 208-210 show them for a test temperature of 200°C. In each case the Z parameter is utilised to incorporate temperature and ram speed effects while extrusion ratios are plotted separately. For the lower extrusion ratios, 5 and 10:1, an increase in extrusion temperature, decrease in Z, is associated with an increase in proof stress and U.T.S. prior to a fall at the highest temperatures. For a structure containing sub-grains alone we would have expected a gentle fall with increasing temperature due to enhanced perfection of the recovery process and enlargement of the substructure. The rise in properties observed here is associated with the onset of dynamic recrystallization during deformation producing small equi-axed recrystallized grains of high misorientation in the product. Thus the ease of slip propagation between these is reduced by the misorientation increase and together with the refined grain size results in an increased strength. Over this temperature range the

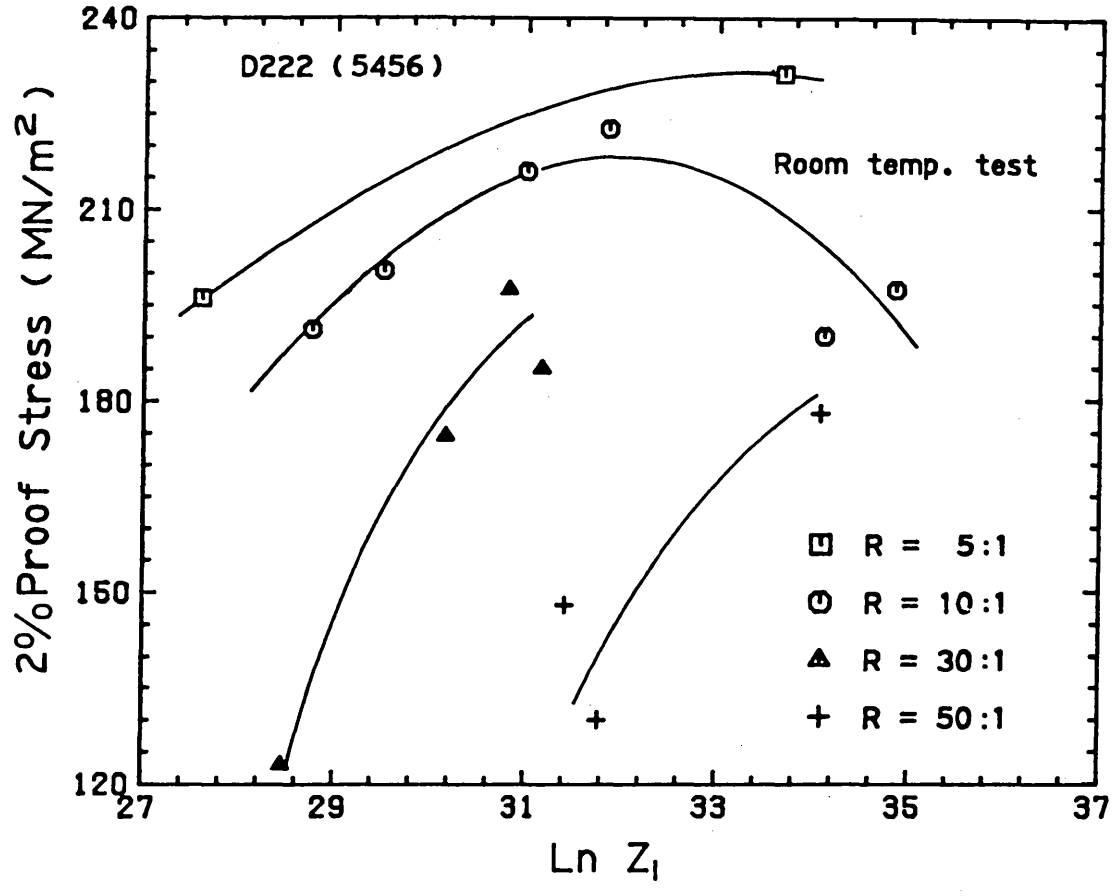


Fig. 205. Variation of tensile properties with LnZ_i, room temperature test for alloy D222 (5456)

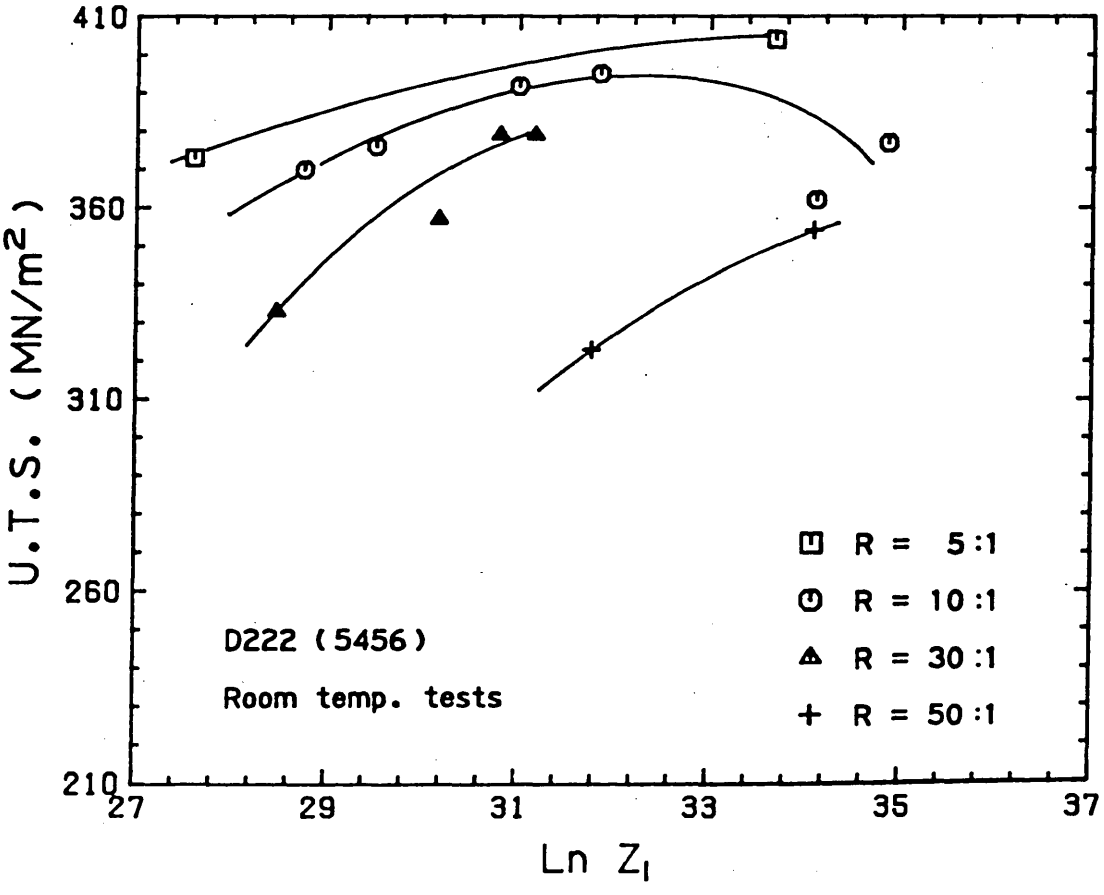


Fig. 206. Variation of tensile properties with LnZ_i, room temperature test. for allo D222 5456

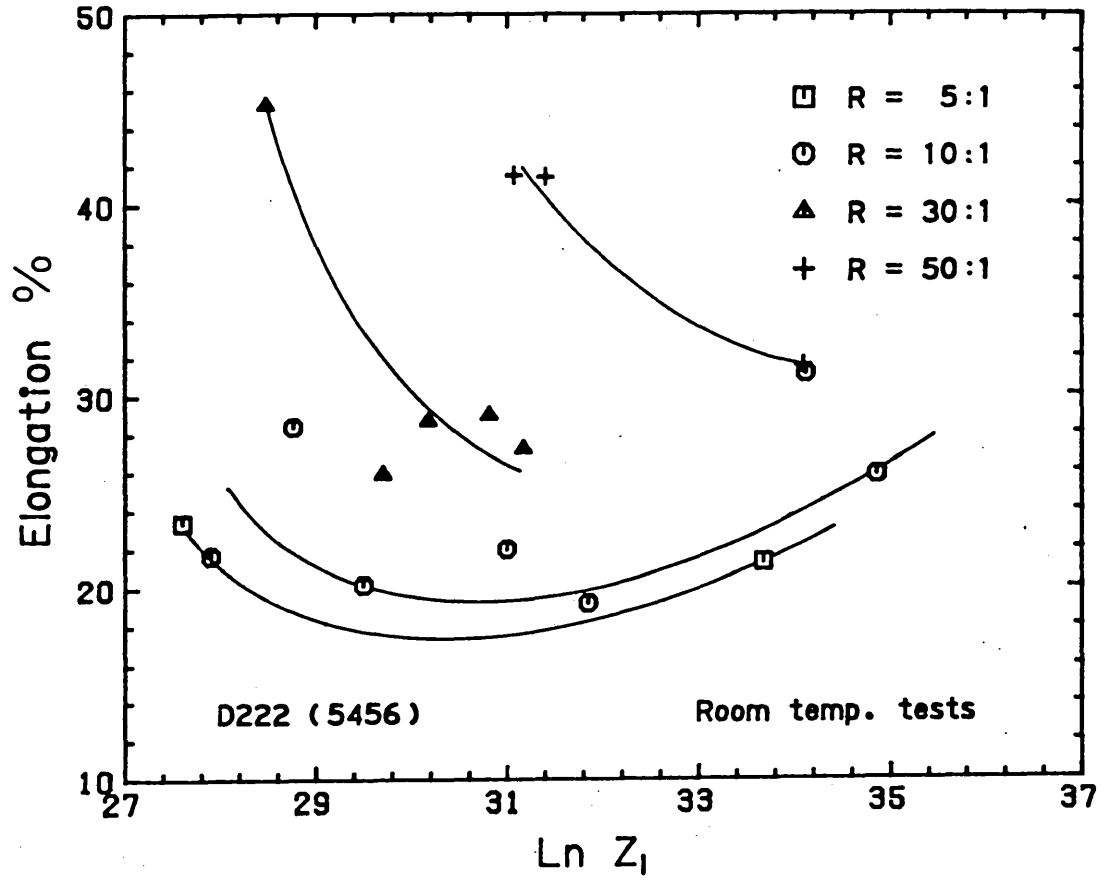


Fig. 207. Varation of Elongation with LnZ_i

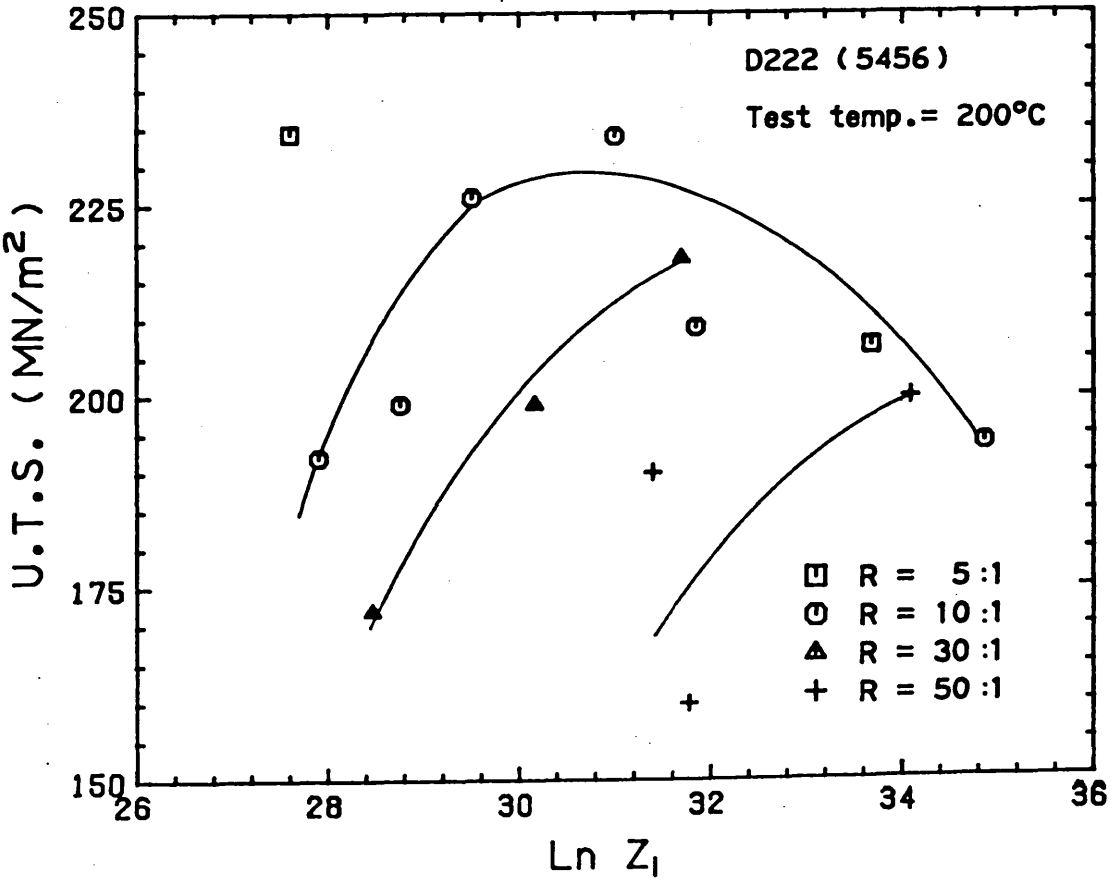


Fig . 208. Variation of U.T.S. with LnZ_i

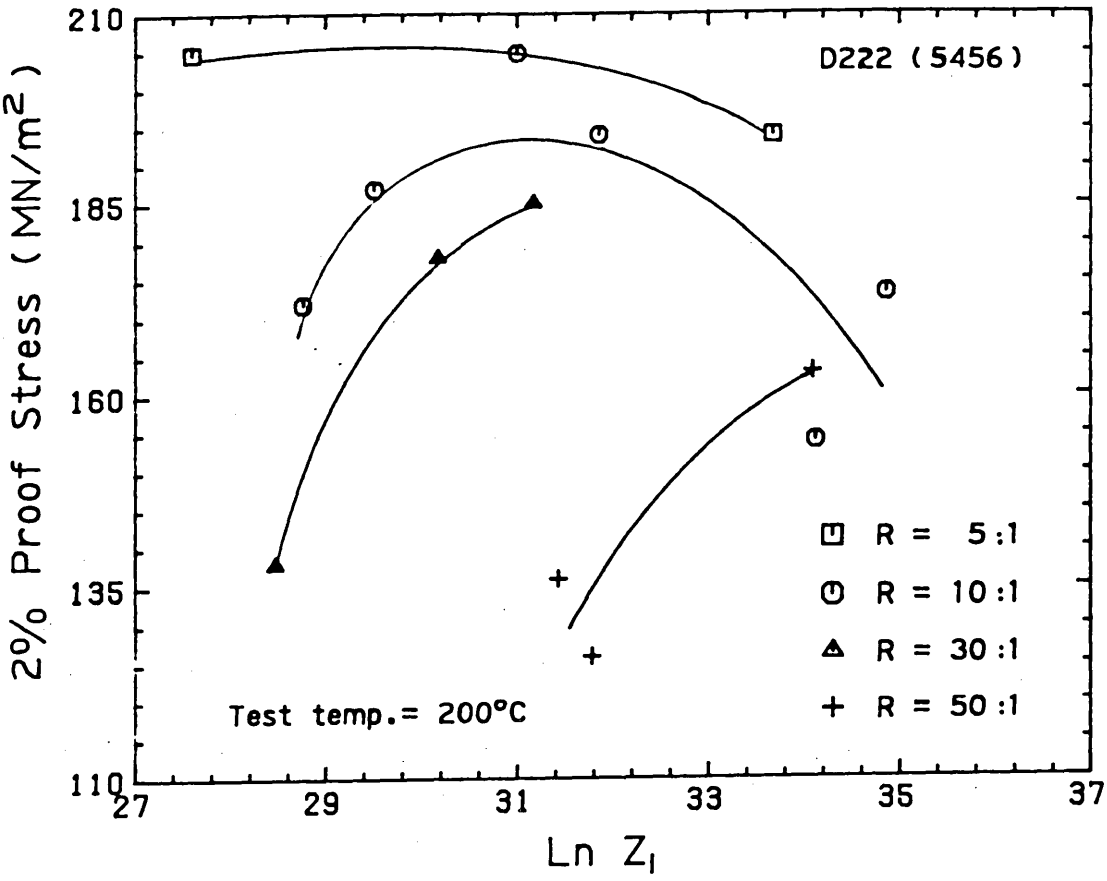


Fig. 209. Variation of Proof Stress with LnZ_i

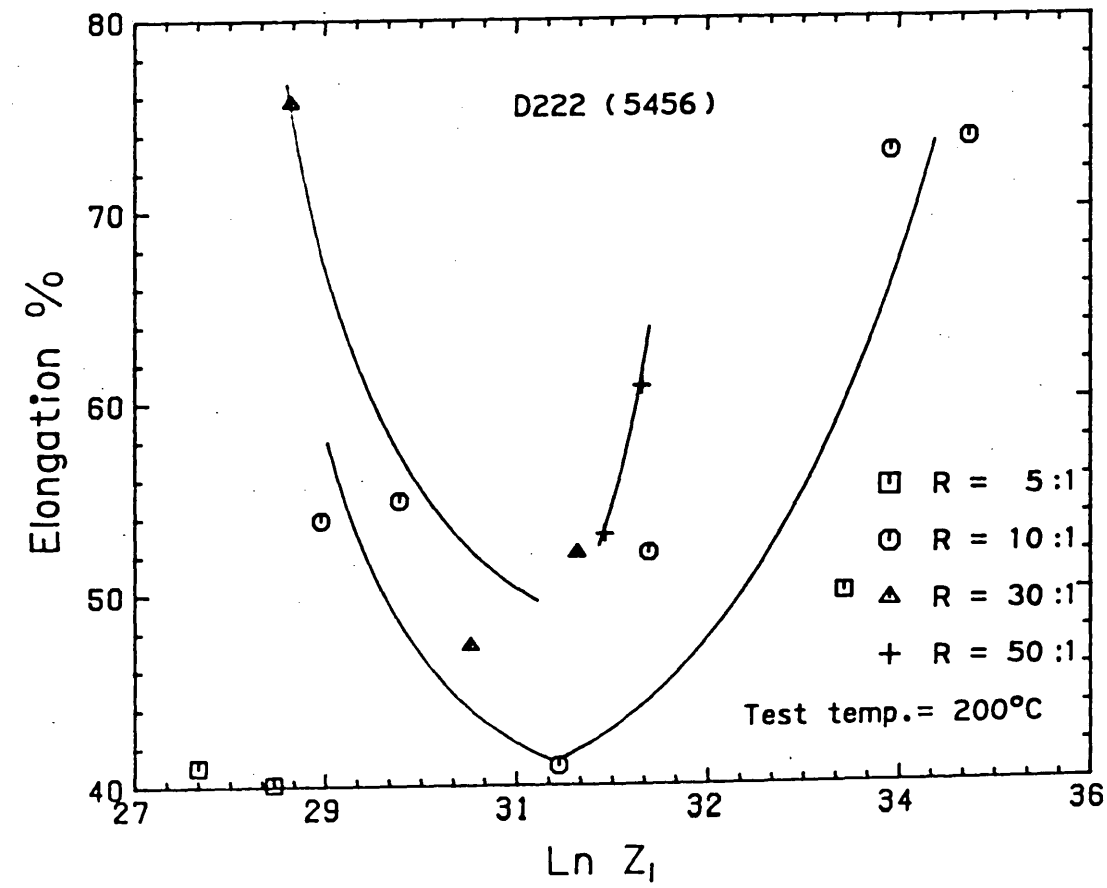


Fig. 210. Variation of Elongation with LnZ_i

ductility shows a minimum at the point of maximum strength. At higher reductions only a decrease in strength and increase in ductility is observed because of extrusion being impossible at lower temperatures. The changes are associated with the increased probability of static recrystallization at the higher temperatures and the reduced section dimensions causing the peripheral statically recrystallized annullus to increasingly approach the gauge of the specimen. Similar features are observed in testing at other temperatures and crosshead speeds. The values compare well with reported values[237] for U.T.S., 0.2% Proof Stress and elongation of 300 MN/m^2, 150 MN/m^2 and 25% respectively.

Figs. 211 and 212 show similar results for extrusions carried out at reductions of 30:1 in the smaller diameter container where a greater spread in Z values may be obtained. For Z values between 34 and 40 both ultimate and proof strengths show little variation although ductility shows a slight increase at higher Z values. At the lower values, around 28, the strength shows an increase, while the ductility a fall, as dynamic recrystallization becomes an operative restoration process. At still higher temperatures the opposite effects are found as static recrystallization effects become enhanced. The test temperature of 200°C results show similar trends, the increased slope of the ductility at higher Z's probably being due to some static recovery of the poorly recovered initial material.

Figs. 213 and 214 show the variation of U.T.S., 0.2% Proof Stress and elongation with the Z parameter for alloys of various magnesium content. In general there is a slight increase in strength with decrease in Z for the alloys 5083 and 5456 while the lower magnesium alloy shows very little change. The increased strength resulting from the greater magnesium additions in 5083 and 5456 is plainly obvious from Fig. 213. This feature is consistent with the increased number of solute atoms creating greater and more effective interaction with the mobile dislocations. In all cases ductility increases with an associated increase in the Z parameter which is consistent with a change in restoration process at higher temperatures. The ductility of 5052 is some 50% greater than the remaining two alloys (Fig. 214).

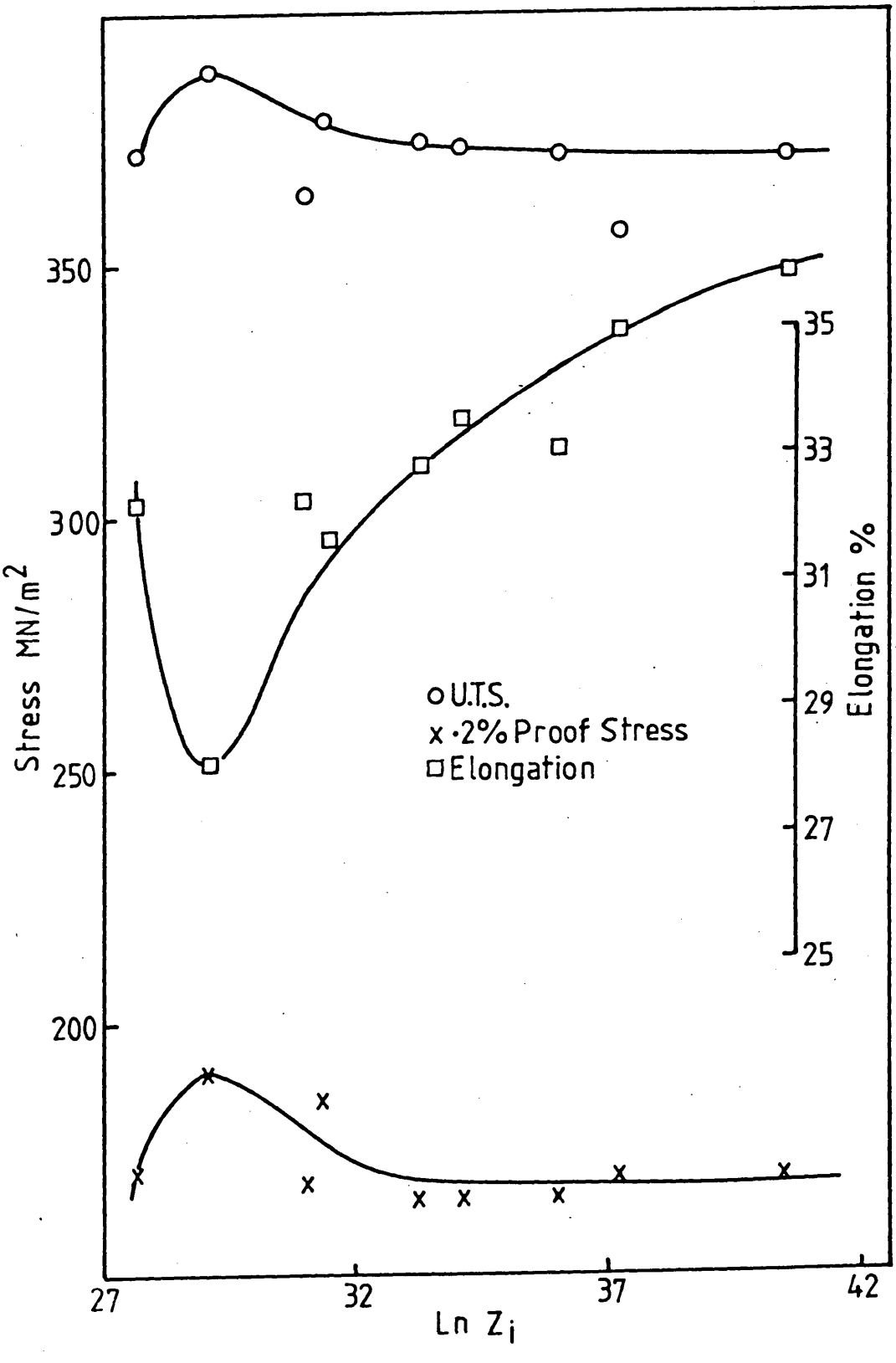


Fig. 211. Tensile property variation with LnZ_i for a reduction of 30:1, room temperature tests for alloy D222 (5456) for a crosshead speed of 0.05 cms/min.

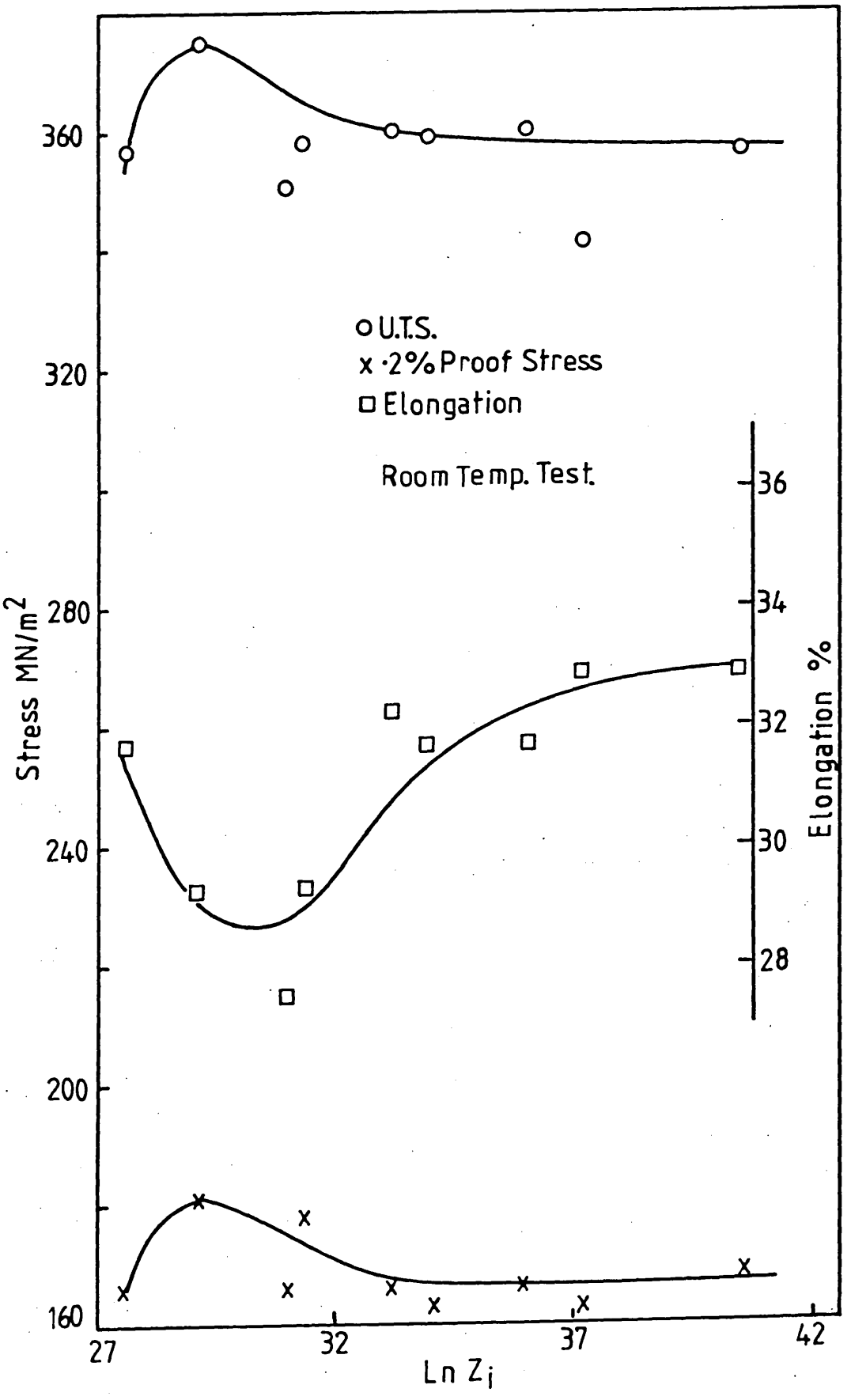


Fig. 212. Tensile property variation with $\ln Z_i$ for a reduction of 30:1, room temperature tests, for alloy D222 (5456) for a crosshead speed of 0.5 cms/min.

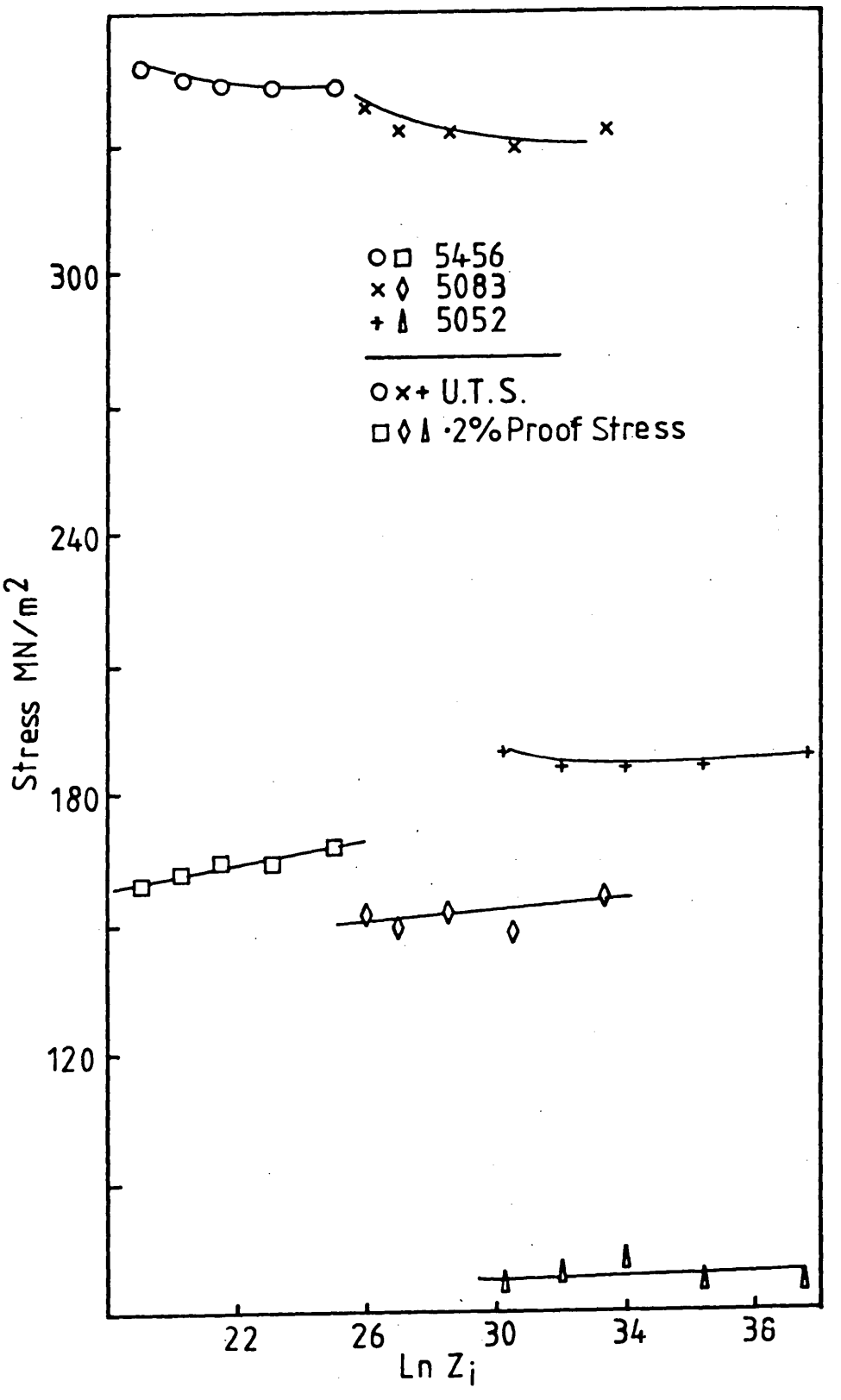


Fig. 213. Tensile property variation with $\ln Z_i$ for a reduction of 30:1, room temperature tests, alloys 5052, 5083 and 5456.

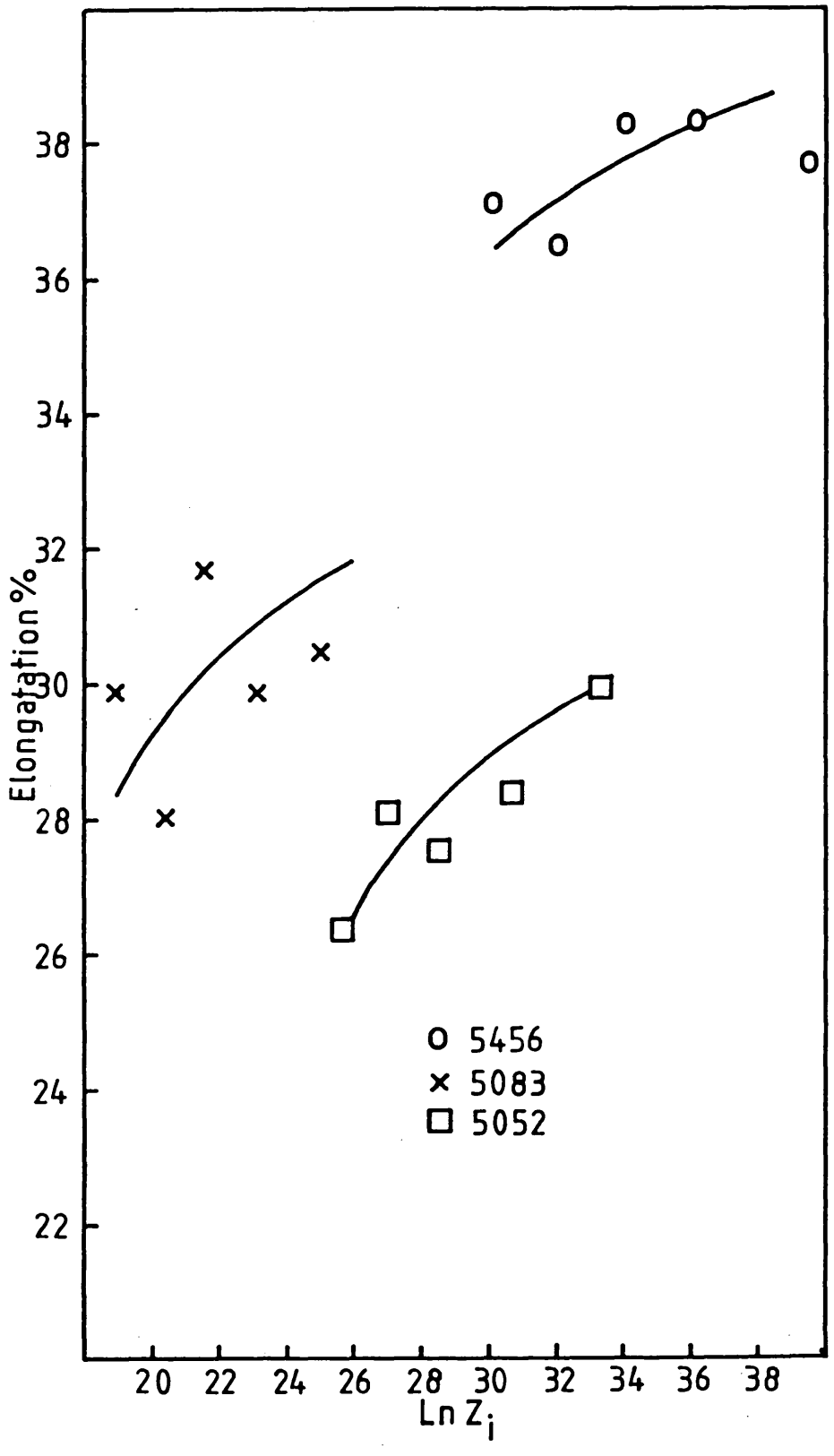


Fig. 214. Elongation variation with LnZ_i
Room Temperature tests, crosshead speed = 0.05 cms/min.

The results indicate the complex nature of property variation, from tensile tests, with the various process parameters in the aluminium-magnesium system. It is impossible to establish a single relationship between these property measurements and the Z parameter for a single or all extrusion ratios which means their inclusion in limit diagrams, following the method of Sheppard,[85] is impossible.

4.6.1.3. Hardness Measurements

The results of hardness tests carried out at the centre, mid-radius and edge of the extrudes may be seen in Table 4.31.

Variation of measured hardness with the Z parameter for two reduction ratios may be found in Figs. 215 and 216. Notably in the central regions a decrease in hardness was found with decreasing Z value showing the sub-grain size to be increasing with the higher thermal activation. After passing through a minimum value, the onset of dynamic recrystallization during the deformation process changes the structure and an increase in hardness is observed. These results are consistent with those found in tensile testing and illustrate the dramatic changes accompanying the introduction of an alternative high temperature restoration process. In both the tensile test and hardness tests, the minimum property is established at a Z_i value of approximately 31.0, which for the strain rates used corresponds to a temperature of around 400°C. It was at this temperature at which the dynamic recrystallization process was predicted to be initiated from the torsion and structural analyses.

The figures also show the variation in hardness across the extrude where the recrystallized outer grains show a much reduced value from the fibrous inner grains at low temperatures and equi-axed dynamically recrystallized grains at higher temperatures.

For various alloy contents, the greatest hardness was associated with the highest magnesium bearing alloy, (Fig. 217), the least being associated with 5052. Once again the same trend is observed with 5083 and 5456 for variation with the Z parameter while 5052 tended to be completely recrystallized throughout the processing range and reflected this with an invariant hardness result. Microhardness tests were performed on some material and the

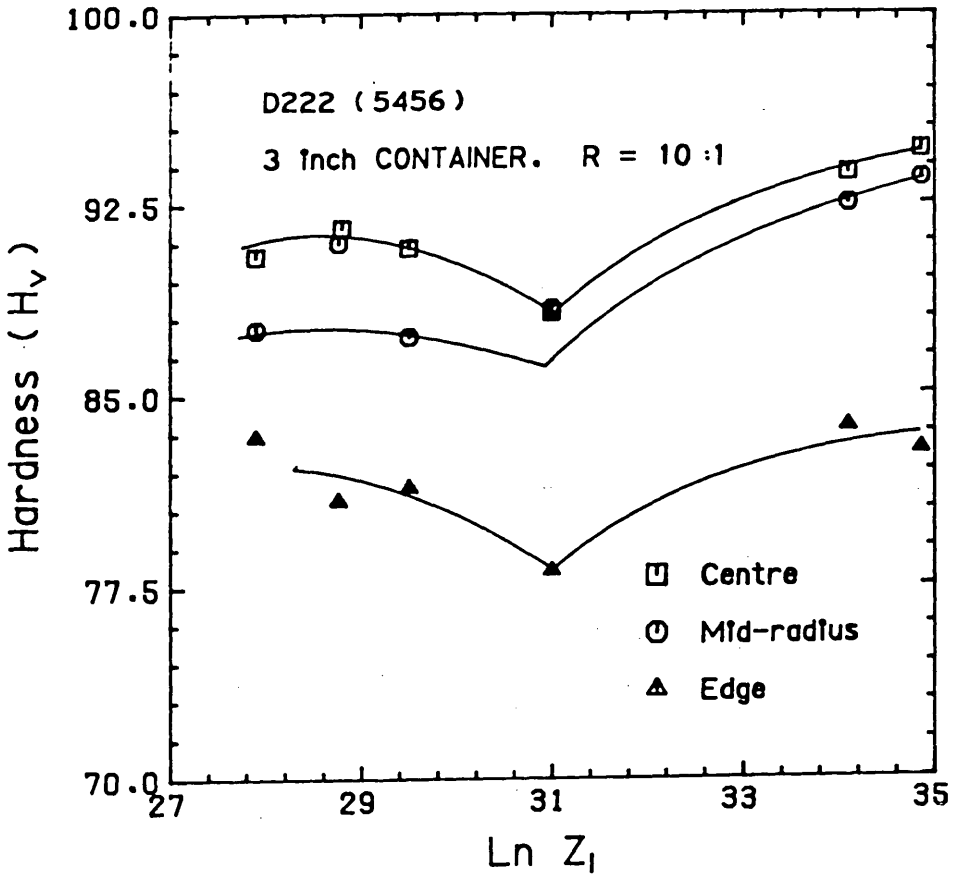


Fig. 215. Hardness vs. LnZ_i for a reduction of 10:1, alloy D222 (5456)

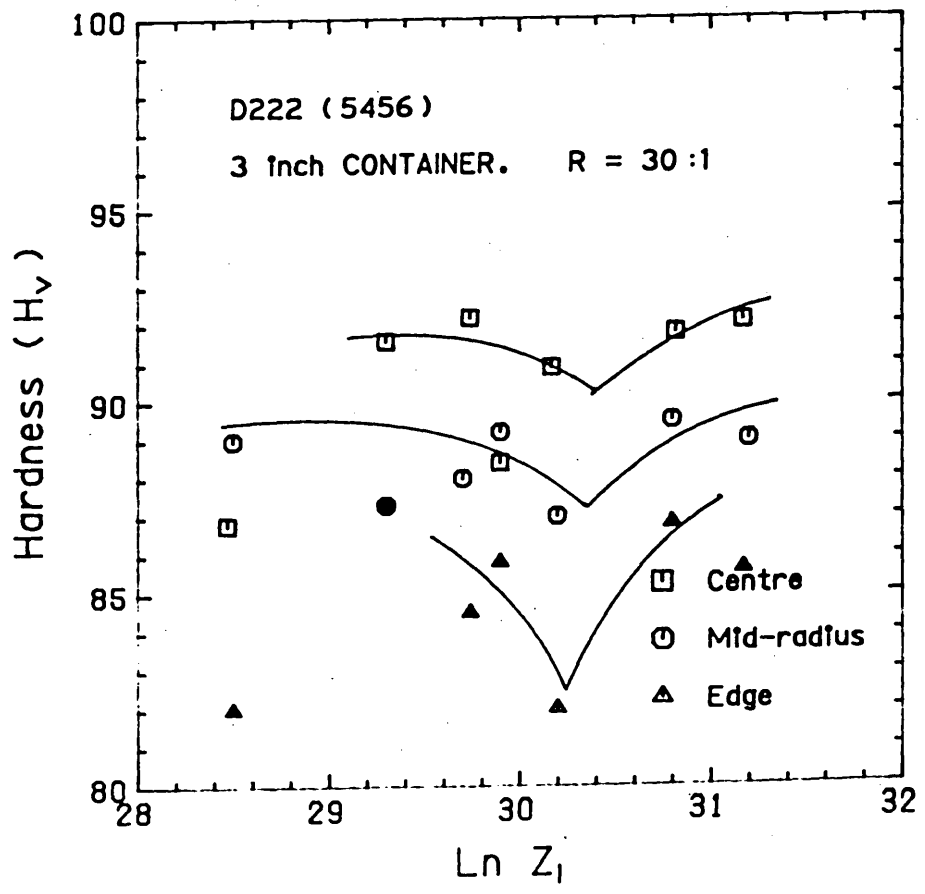


Fig. 216. Hardness vs. LnZ_i for a reduction of 30:1, alloy D222 (5456)

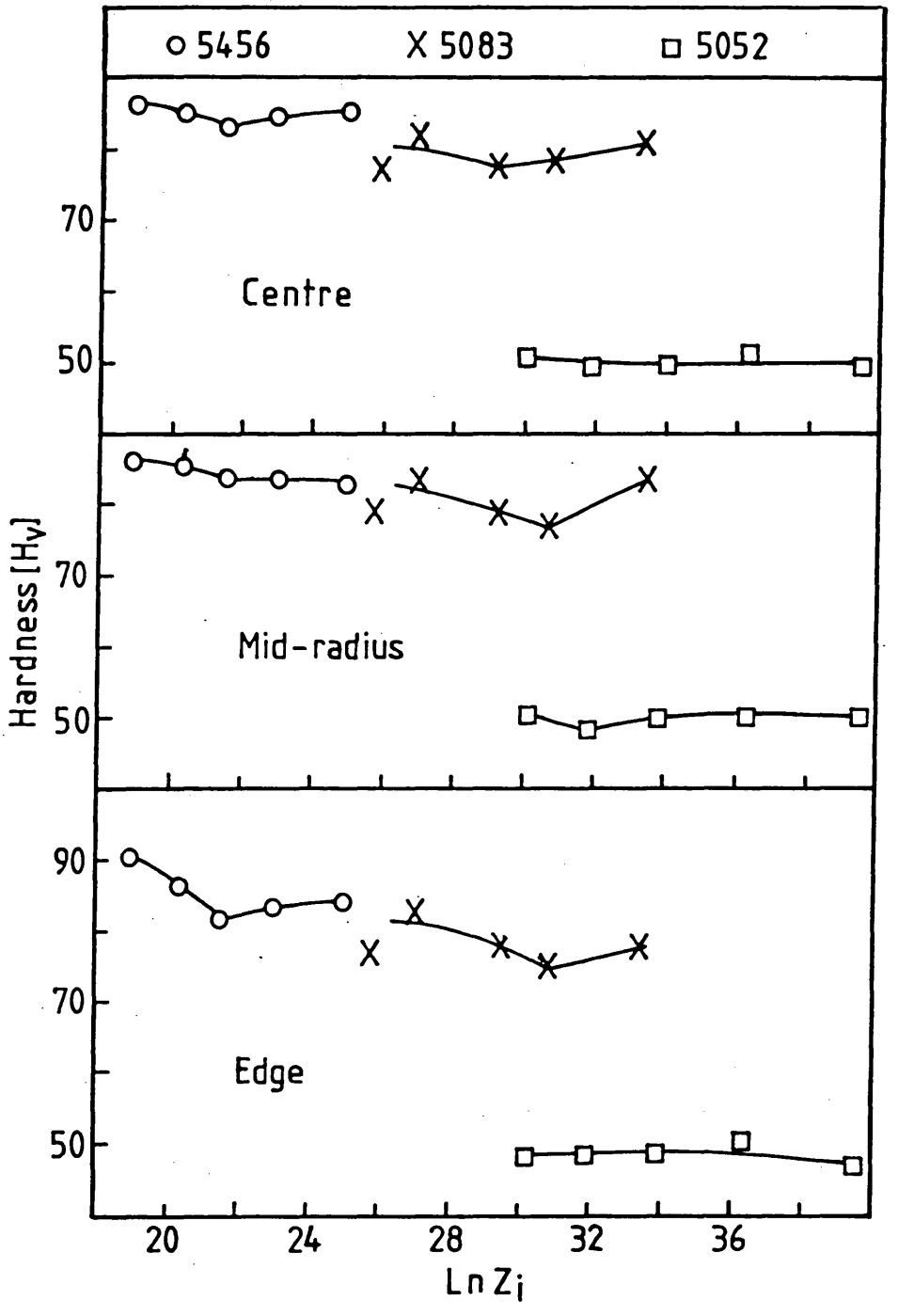


Fig. 217. Hardness vs. LnZ_i for a reduction of 30:1 for alloys 5052, 5083 and 5456.

results are shown in Table 4.30. As Fig. 218 shows, a similar trend is observed for variation with the Z parameter.

Once again the same trends are observed with these tests as with the tensile tests and the complex variation prevents any relationship being established between hardness and the process variables. Their inclusion in limit diagrams is, therefore, also prevented.

4.6.1.4. Fracture Toughness

Fracture toughness results, Table 4.31, were once again difficult to correlate to the process variables. Results for a reduction of 30:1 are shown in Fig. 219 for variation with the Z parameter. The fracture toughness is measured by the energy absorbed during impact and can be seen to show an increase with reducing Z value. This feature is probably due to the grain refinement resulting from the dynamic recrystallization process. Virtually no variation is observed with 5052 where the structure consists primarily of static recrystallized grains, and the effect is lost. The decrease in absorbed energy with increasing alloy content is due to the reduced ductility and associated ease of plastic deformation. The difference between 5456 and D222, apart from the lateral shift caused by differing activation energies, must be due to the initial conditions of the materials. The commercially homogenized material shows an average value which corresponds well with the published value[237] of 46J.

4.6.1.5. Heat Treatment of 5456

As was pointed out in section 1.2, the alloys containing less than 7% magnesium are never heat treated for property enhancement via ageing. To check the validity of this a series of tests were carried out upon material from extrusion run 116 in which the material was soaked at 350°C and 500°C, water quenched and then aged at both room temperature and 120°C.

The results are presented in Table 4.32 from which it may be ascertained that no property improvement is achieved and a reduction may be found in some cases. This is due to static recovery processes taking place at the elevated temperatures and producing a more stable sub-grain structure with an associated slight reduction in hardness.

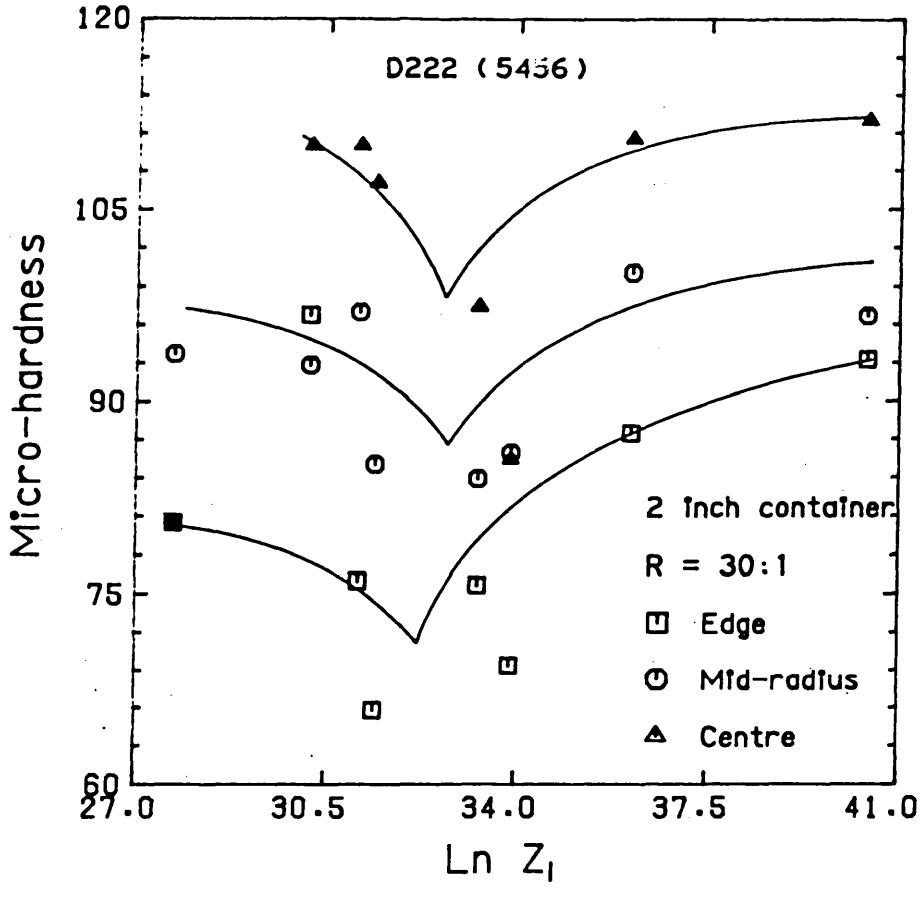


Fig. 218. Microhardness vs. LnZ_i for a reduction of 30:1 for alloy D222 (5456).

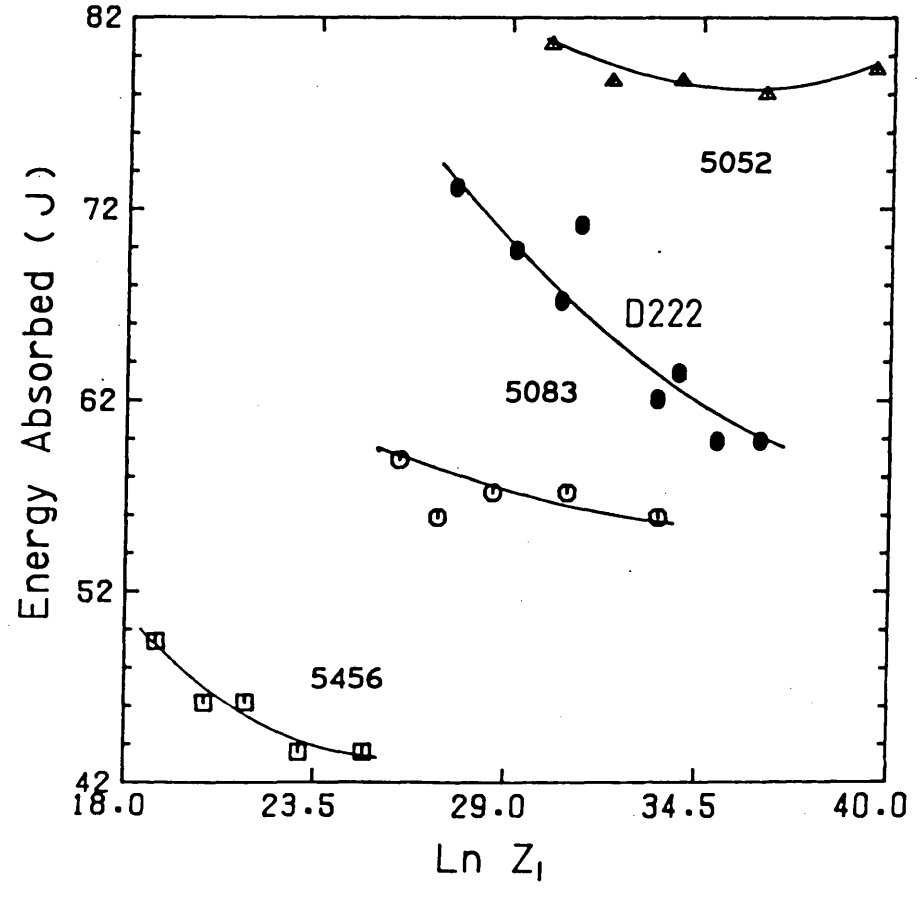


Fig. 219. Variation of Impact Energy with LnZ_i for all alloys.

4.6.1.6. Sub-grain Size Relationship to Process Variable

As was pointed out in section 4.6., many workers[150,156,194,195] have found a relationship between flow stress and sub-grain size. Although it has been shown that the room temperature properties are not solely dependent upon the sub-grain structure in this system, it is true that under all extrusion conditions sub-grains were observed and so it may be possible to correlate sub-grain size to the Z parameter in a manner similar to McQueen.[156] The results for this plot of d^{-1} vs LnZ may be seen in Fig. 220 where the intercept and slope are found to be -.41 and 0.037 respectively. The result shows a good correlation to the relationship $d^{-1} = a + b\text{Ln}Z$ and illustrates the effect of variations in both temperature and strain rate upon the sub-grain dimensions. At higher temperatures, low Z, the thermal activation is greater, dislocation mobility is enhanced and the resultant sub-grain size is large. The same applies for a reduction in strain rate.

The dependence of room temperature strength upon sub-grain size is not so obvious in this system. Strength measured by Hardness, is plotted against the reciprocal sub-grain diameter in Fig. 221. As in Fig. 220, the data includes results from work upon sectioned specimens having been deformed in torsion, more discussion of which will follow. In Fig. 221, the scatter appears to be quite large. However, inclusion of microhardness results at high Z values, in which case statically recrystallized regions may be avoided, shows a linear type of relationship to exist for sub-grain diameters below 1.3 μm. Thus, at low temperatures the room temperature strength is dependent upon the sub-grain structure, while for higher temperatures, lower values of d^{-1}, the dependency is removed as dynamic recrystallization is initiated.

4.7. Limit Diagrams

Using the relationships generated in sections 4.3.1.8 and 4.3.1.9 we may now turn to production of limit diagrams for the alloy D222. The ideas of Sheppard[85] for incorporating property values into these diagrams has been shown to be inappropriate for this alloy system in the preceding sections. The relationship between sub-grain size and the Z parameter, shown in Fig. 220,

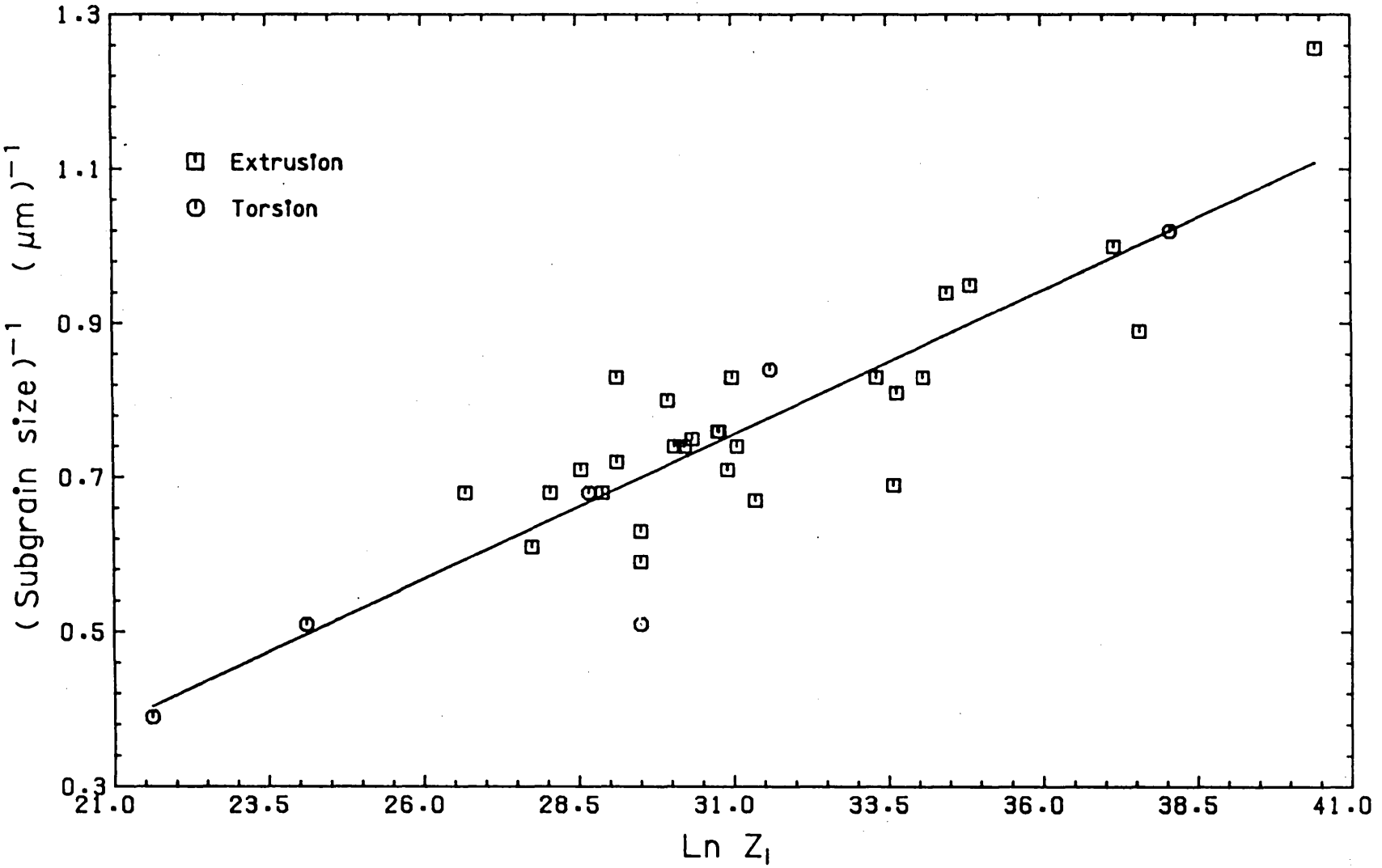


Fig. 220. (Subgrain diameter)$^{-1}$ vs. LnZ_i for alloy D222 (5456)

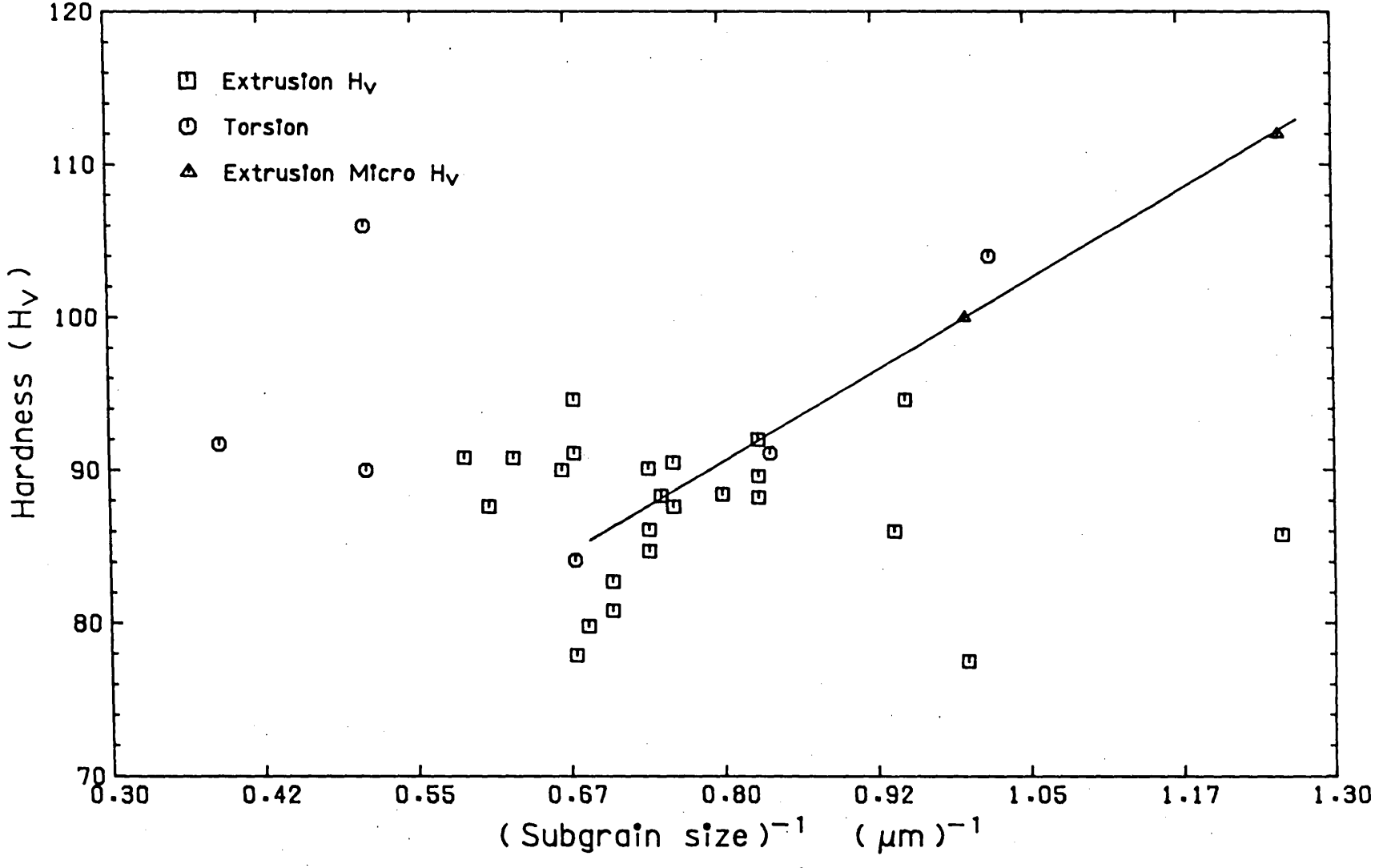


Fig. 221. Hardness vs. (sub-grain diameter)$^{-1}$ for alloy D222 (5456)

would enable lines of constant sub-grain size to be plotted on the diagrams, but since the material properties are not universally dependent upon this parameter there would appear to be little point.

4.7.1. The Pressure Line

Following the analysis described in section 4.3.1.8, it was illustrated how a relationship between pressure and flow stress could be developed incorporating the extrusion ratio and the Z parameter. By using this relationship to predict an extrusion pressure for given extrusion conditions, an indication of whether the process will take place may be gained by comparing this pressure with the maximum available. Thus if the predicted pressure exceeds that available, the billet will 'stick' in the container.

In a manner similar to Hirst and Ursell,[83] these limiting conditions for pressure may be plotted in a diagramatic fashion as shown in Fig. 222 and 223. The pressure lines, to the left, show that as the initial temperature of the billet is increased, the associated flow stress decreases and a higher extrusion ratio becomes possible. The pressure line shows a steady increase with increasing temperature for this reason. The lines shown in these figures are plotted for constant ram speeds and an increased value results in a depressed value of extrusion ratio for a given temperature. This is due to the increased ram speed causing an increase in strain rate and raising the flow stress of the material.

4.7.2. The Incipient Melting Line

The onset of bad or unacceptable surface finish was also incorporated into Hirst and Ursell's[83] original concept by plotting an incipient melting line. The derivation of a method for evaluating this was shown in section 4.3.1.9. and the result of its application may be seen in Figs. 217 and 218. Thus at a reduced initial temperature, higher extrusion ratios may be utilised before surface defects appear for a given ram speed. Increasing this parameter causes a dramatic decrease in the reduction ratio possible due to the increased temperature rise within the material during deformation.

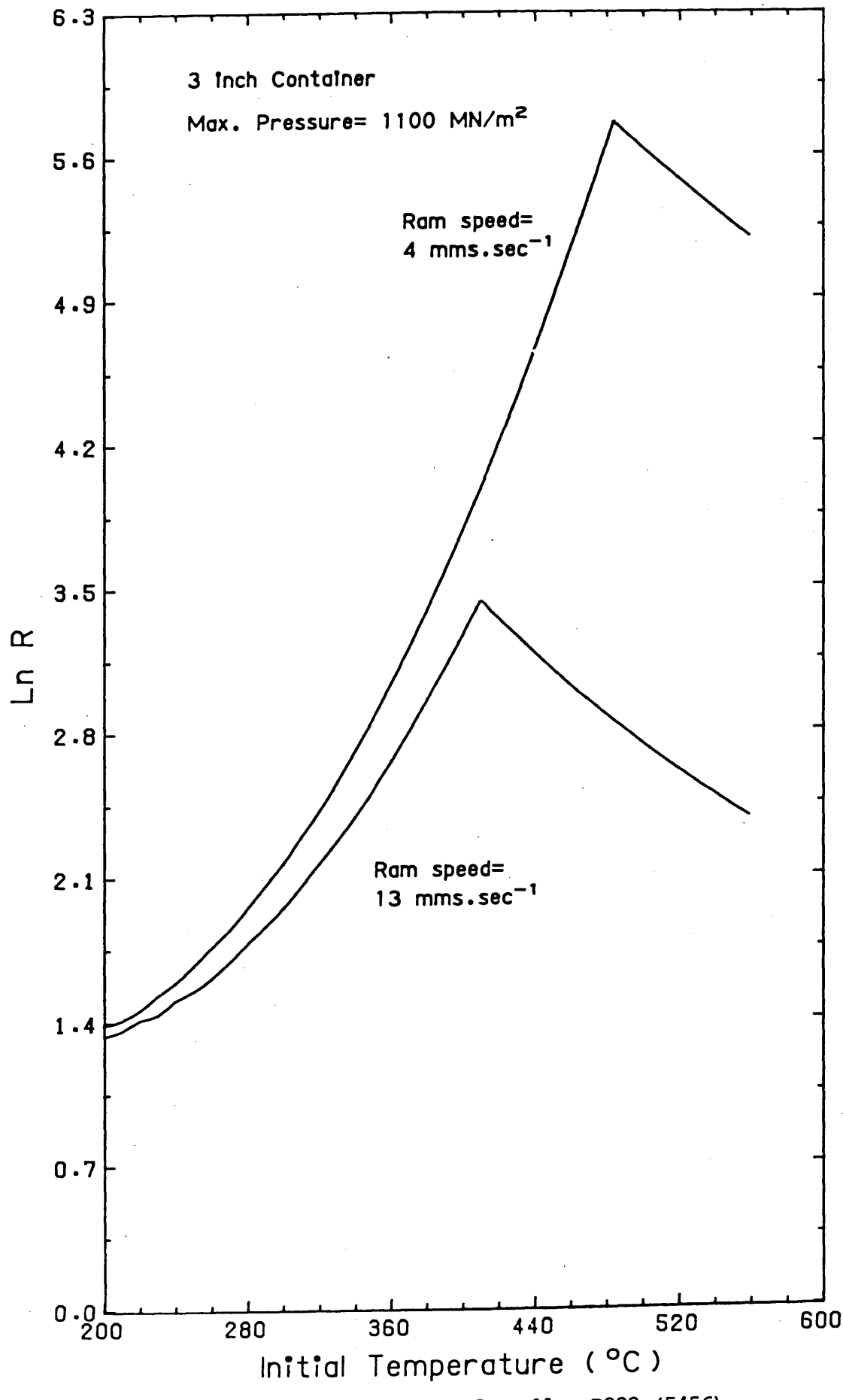


Fig. 222. Experimental limit diagram for alloy D222 (5456)

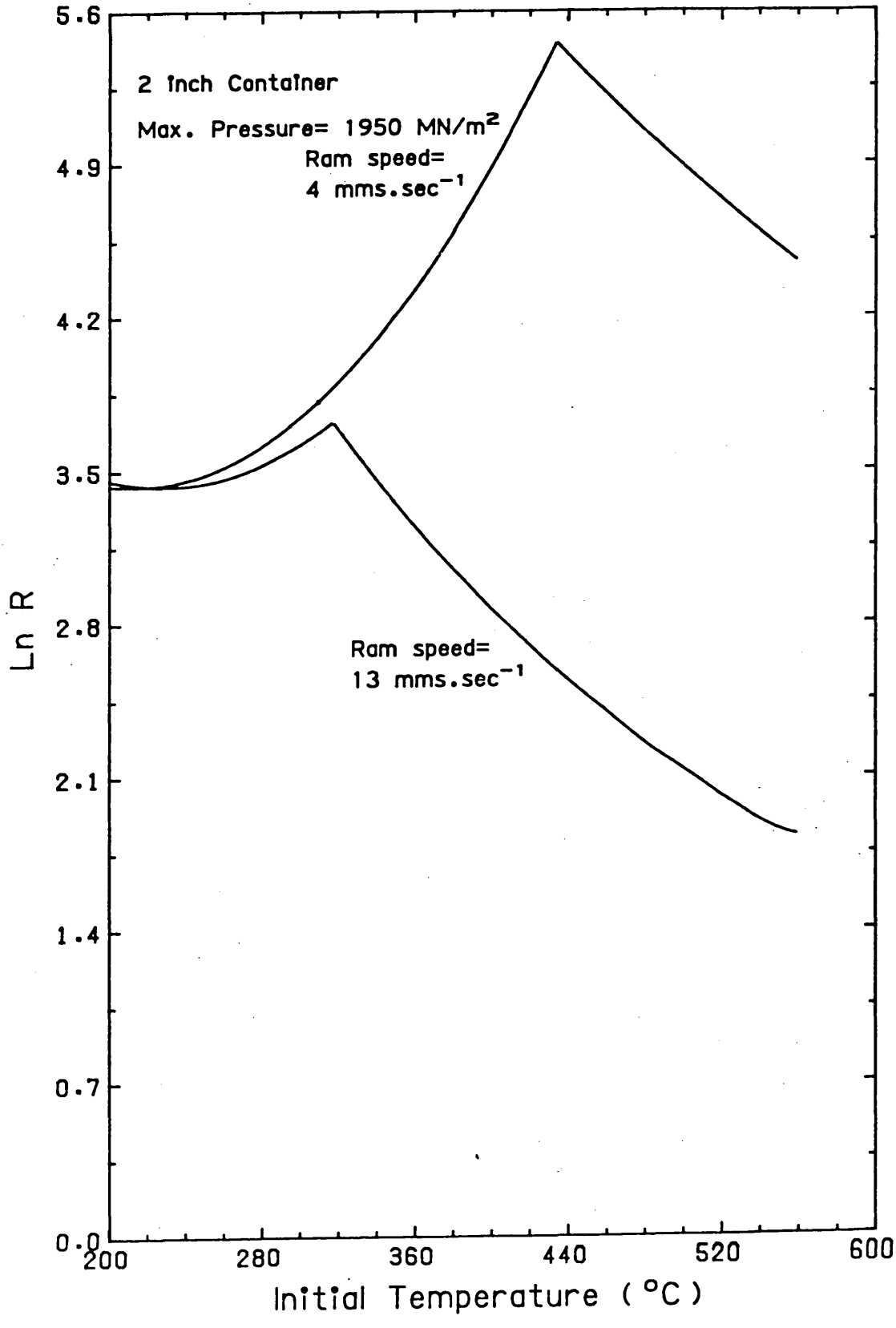


Fig. 223. Experimental limit diagram for alloy D222 (5456)

Comparing Fig. 222 with 223, for the 3 and 2 inch diameter containers respectively, shows that the increased pressure available in the latter case permits increased extrusion ratios to be utilised for given temperature and ram speed conditions. In this case, however, the melting line appears at lower ratios due to the enhanced strain rate for the smaller container causing a greater heat generation.

The basic limit diagram has therefore been compiled, but inclusion of structural features has been shown to be impractical due to the complex variation of structure and properties with the process variables.

4.8. Validity of Torsion as a Model for Extrusion

Using the hot torsion testing technique, the constants in the hot working equation were evaluated and used in the calculations carried out with the extrusion data. Thus, the mode of deformation is assumed to be similar in both processes or else the inter-change of results would not be justified. It is the further investigation of this thesis that this section concentrates upon.

As was discussed in section 2.4.1., the strain and strain rate in torsion vary from zero at the centre of the specimen to a maximum value at the edge. Therefore, as in the case of extrusion, we may expect structural changes across the section as the strain rate varies and heat generated varies.

Specimens taken from a low temperature torsion specimen may be seen in Figs. 224 and 225. Both figures, taken from the central and outer regions respectively, show predominantly statically recrystallized microstructures. The low thermal activation retards the dynamic recovery processes leaving a high residual stored energy term which creates the driving force for the process. The microstructure resulting from a high temperature test shows a considerably different structure (Figs. 226 and 227). In the central regions an equi-axed structure is observed where the deformation has been much less intense. In the outer regions, Fig. 227, the plastic flow has left a lining up of the second phase particles causing a modification of the recrystallized structure.

$T = 320^{\circ}C$

Surface strain rate = $8.46\ sec^{-1}$

Fig. 224. Low temperature torsion test specimen-centre x40

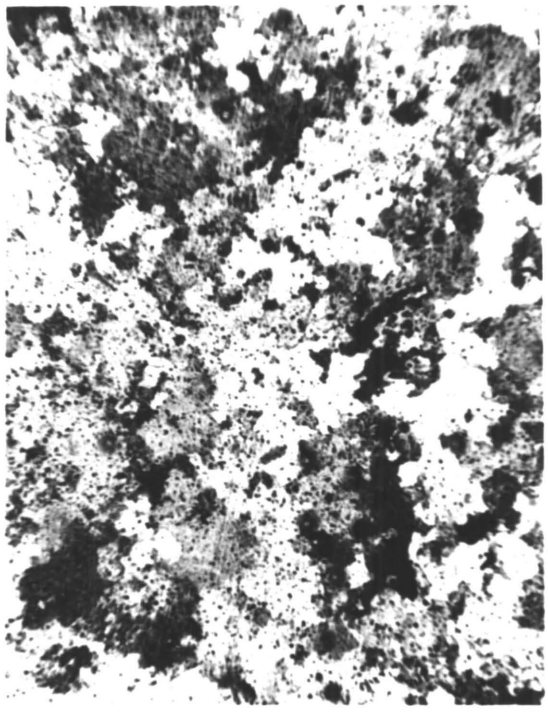
Fig. 225. Low temperature torsion test specimen-edge x 40

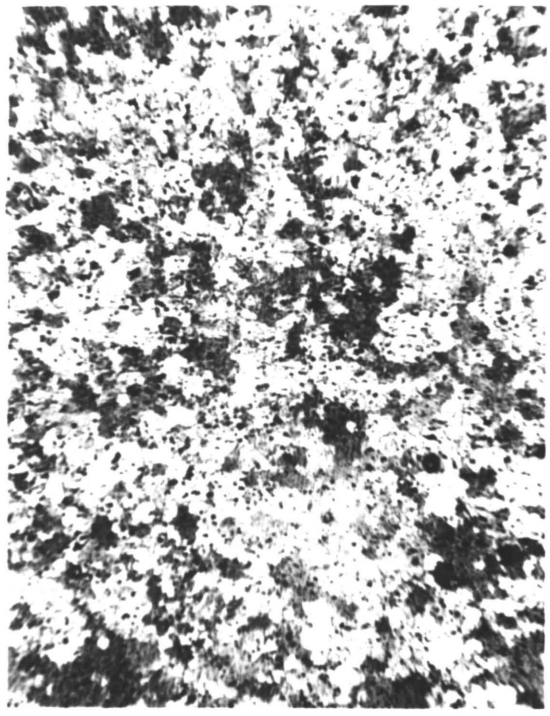
$T = 501^{\circ}C$

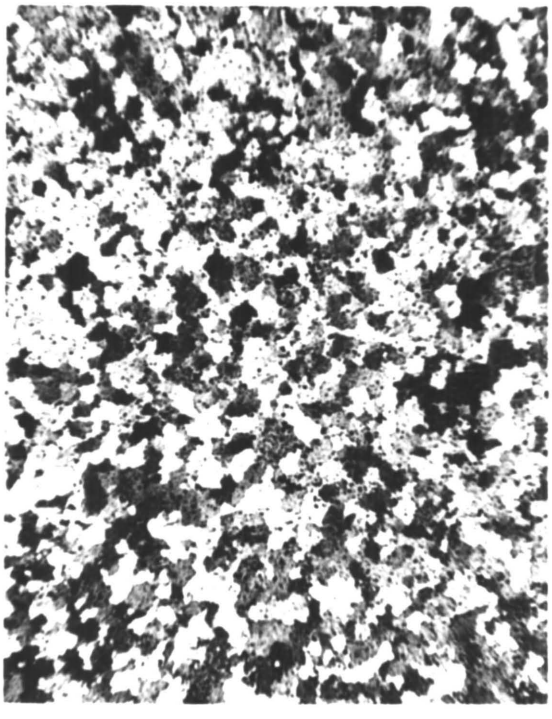
Surface strain rate = $0.033\ sec^{-1}$

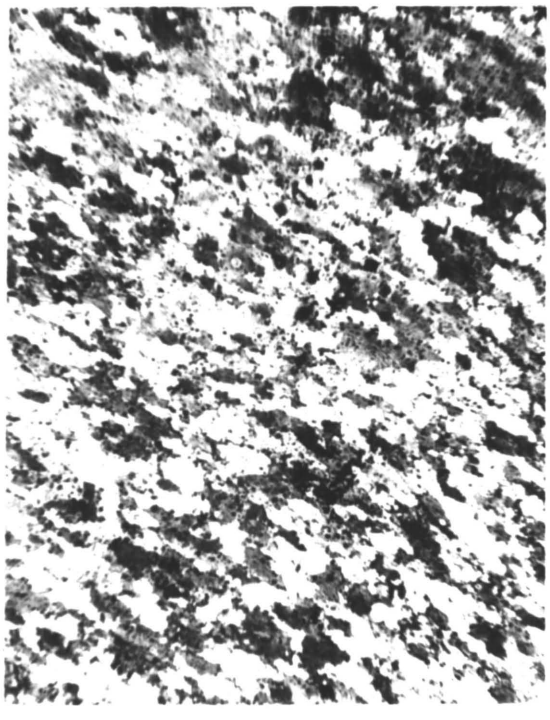
Fig. 226. High temperature torsion test specimen-centre x 40

Fig. 227. High temperature torsion test specimen-edge x 40









Electron microscopical examination reveals very similar substructures for both torsion and extrusion specimens deformed under comparable conditions. Figs. 228 and 229 show the structures for low temperature deformation corresponding to Z values of approximately 34. The low thermal activation results in a ragged sub-grain structure in both cases with a high internal dislocation density and small diameter. The elongated nature of these sub-grains is caused by the rearrangement of the precipitate distribution during the deformation. At higher temperatures, Figs. 230 and 231, corresponding to Z values of 28, the higher thermal activation results in a more perfectly formed sub-grain structure. The sub-grains are more equi-axed in nature since the pinning effect of the second phase particles is reduced. Regions of sub-grain free material may also be observed corresponding to statically recrystallized areas. At still higher temperatures, Z values of 26, the sub-grains have increased in dimensions but an increased internal dislocation density is found indicating that a driving force is present for the dynamic recrystallization process at these temperatures, Figs. 232 and 233.

The structures produced by both modes of deformation are therefore very close and would indicate that similar high temperature restoration processes are in operation.

The sub-grain diameter measurements for torsion specimens were included in Fig. 220 and were shown to agree very well with those found after extrusion. In the same way, Fig. 221 contained data from investigation of torsion samples and showed how hardness followed the same trend as with extrusion samples of property dependence upon sub-grain structure above a certain Z value and below this some other mechanism taking over.

Thus, the evidence presented here would tend to indicate that both extrusion and torsion are governed by similar high temperature restoration mechanisms and justifies the modelling of extrusion with the hot torsion deformation process.

$T = 320^{\circ}C$
$\dot{\varepsilon} = 8.46\ sec^{-1}$

Fig. 228.

$R = 10:1$
$T = 345^{\circ}C$
$\dot{\varepsilon} = 6.82\ sec^{-1}$

Fig. 229.

$T = 370^{\circ}C$
$\dot{\varepsilon} = 0.033\ sec^{-1}$

Fig. 230.

$R = 10:1$
$T = 384^{\circ}C$
$\dot{\varepsilon} = 4.15\ sec^{-1}$

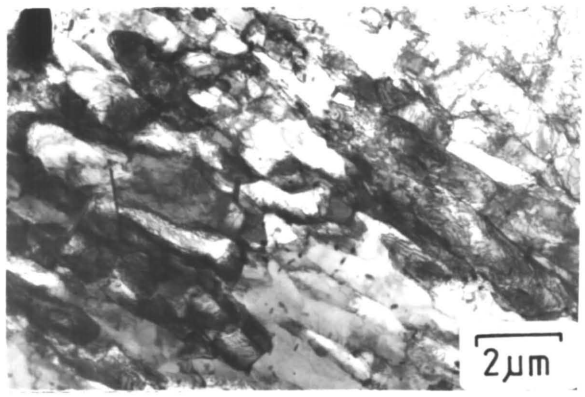
Fig. 231.

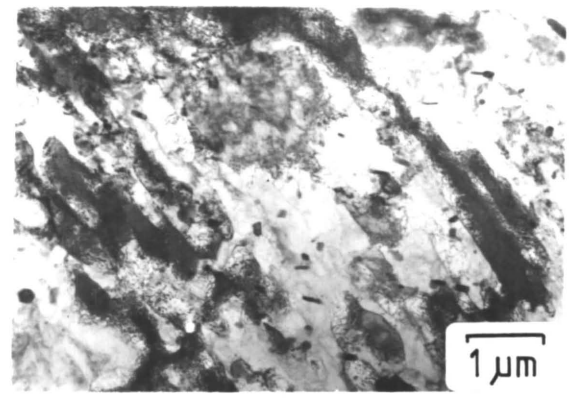
$T = 431^{\circ}C$
$\dot{\varepsilon} = 0.033^{\circ}C$

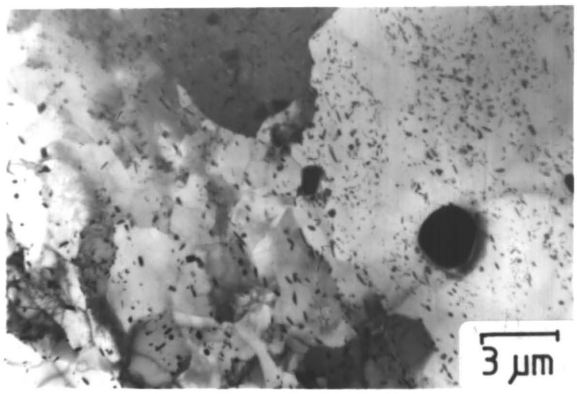
Fig. 232.

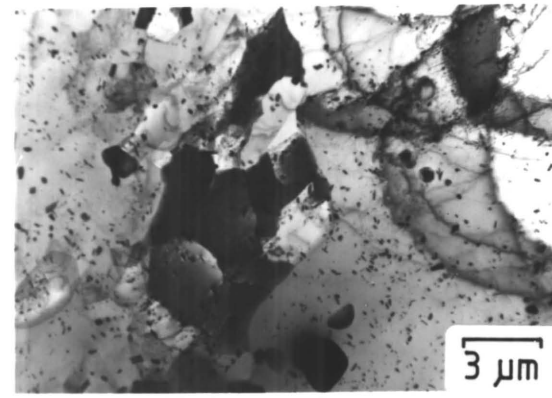
$R = 30:1$
$T = 437^{\circ}C$
$\dot{\varepsilon} = 7.1^{\circ}C$

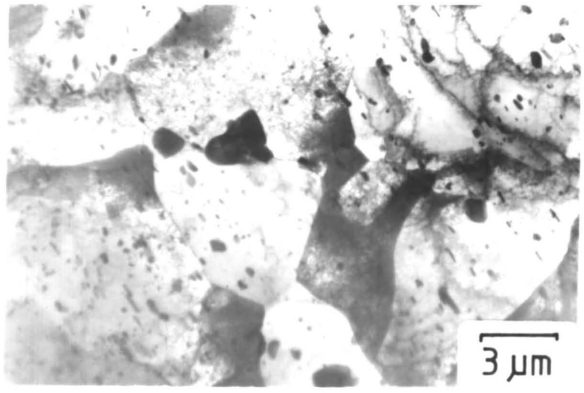
Fig. 233.

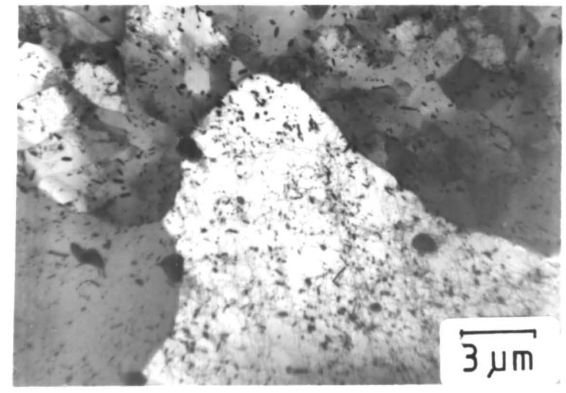

2 µm


1 µm


3 µm


3 µm


3 µm


3 µm

4.9. Effect of Billet Homogenization

In an attempt to attain a fuller understanding of the effects of a homogenization treatment, extrusion runs 209 and 210 were carried out to compare their microstructure with those shown for the homogenized material in Figs. 168-171. The results may be seen in Figs. 234-237. For the lower temperature case, Figs. 234 and 235, comparable results were found. At the periphery statically recrystallized grains were observed although their size was more heterogeneous. The small outer grains may be explained in terms of the water quench restricting grain growth while inside from these, the larger grains are the result of the less severe rate of cooling permitting growth. Near the centre again, the grain size is once again small prior to the appearance of a mixed structure of recrystallized and fibrous elongated grains. Thus the only significant difference between this and the homogenized case, Figs. 168 and 169, is the appearance of the small recrystallized grain size prior to the fibrous structure appearing. This may be due to some heterogeneous second phase distribution in the original billet or due to the reduced driving force for grain growth in this region caused by the non-homogeneous nature of the flow within the quasi-static deformation zone, i.e. the stored energy is reduced toward the product centre causing a diminished driving force.

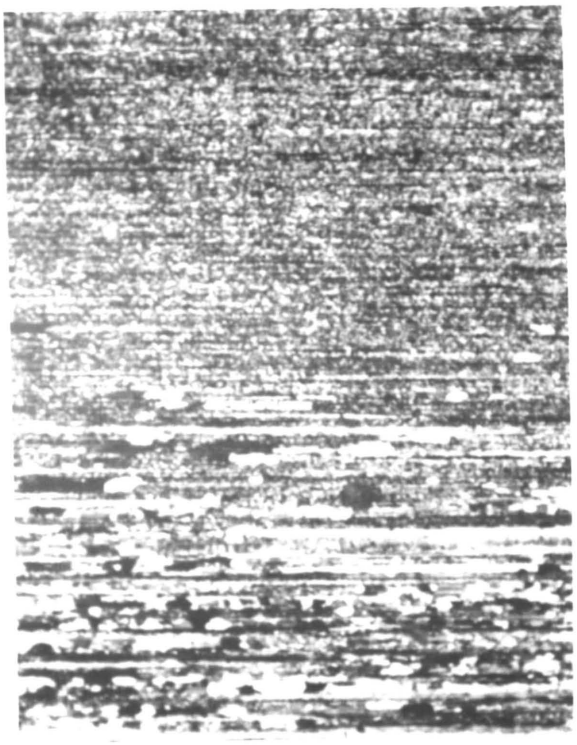
At the higher temperature, Figs. 236 and 237, the inner structure is very similar to that found for the homogenized billet in Fig. 171. The fibrous nature of the original grains may be seen with an associated high density of equi-axed grains resulting from the dynamic recrystallization process, operative at these temperatures. There would appear to be an increased amount of these in this case and is probably due to the reduced original grain size, in this case, lowering the critical strain for nucleation of the dynamic recrystallization process. In the peripheral regions there is a noticeable lack of large statically recrystallized grains. The structure appears to be one of continuous, small equi-axed grains that are produced by the dynamic recrystallization process. Thus, this restoration process is so effective that the residual internal energy is insufficient to promote grain growth even by

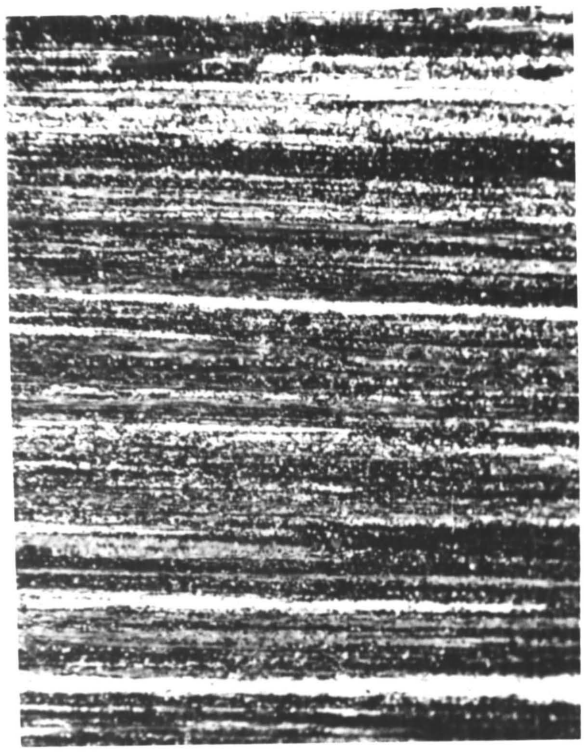
Fig. 234. Edge x 32 Fig. 235 Centre x 64

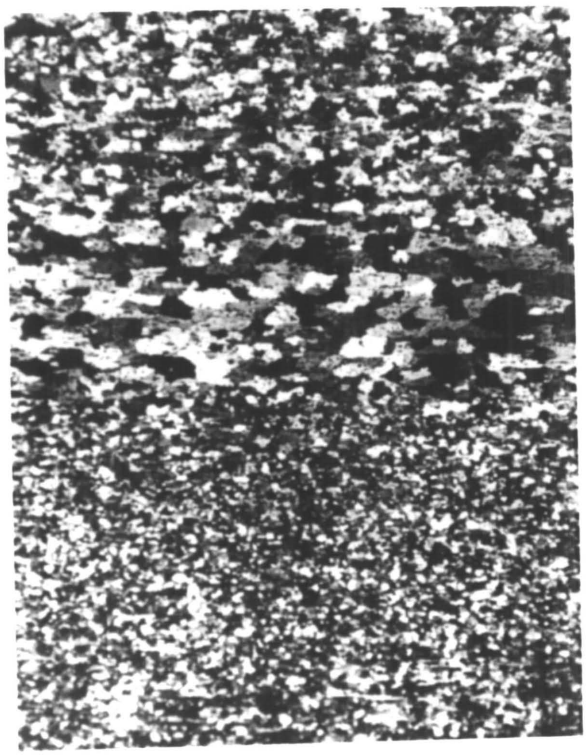
Low temperature unhomogenized D222 (5456)

Fig. 236. Edge x 32 Fig. 237 Centre x 64

High temperature unhomogenized D222 (5456)









metadynamic recrystallization when no incubation period is required. The enhanced appearance of the high temperature restoration mode in this region is a consequence of the reduced original grain size, lowering the strain for its nucleation. In addition, the increased shear associated with this material during deformation will serve to increase the driving force.

It would appear therefore, that the homogenization treatment serves to produce a slight increase in original grain size which retards the onset of dynamic recrystallization. Internally the structure appears much the same as with the homogenized material but at higher temperatures the peripheral large grains are not developed while at lower deformation temperatures the statically recrystallized grains appear, but are heterogeneous in size.

CHAPTER 5

CONCLUSIONS

1. Graphs of maximum torque vs Ln twist rate at constant temperature produced from torsion data for all alloys are linear. The materials also obey equations of the form:-

$$\text{Flow stress} = \text{constant } \dot{\varepsilon}^{m}$$

The strain rate exponent, m, increases with temperature.

2. The torsion data yields activation energies consistent with that for self diffusion in aluminium for the fully heat treated alloys. Commercial heat treatment leaves a magnesium gradient within the material and the activation energy decreases to that consistent with magnesium diffusion in aluminium.

3. The values of A, α and n in the hot working equation compare well with data from other workers notably in creep studies. The value of n of approximately 3 is consistent with viscous glide being the rate controlling process during deformation.

4. A trial hot working equation containing temperature variation for the four parameters of A, α, n and ΔHshows reasonable agreement with experimental results.

5. Results from minimized axi-symmetric upper bound solutions for direct and extrnsion show that a non linear relationship exists between P/σ and LnR. Pressure prediction for extrusion is in error by up to 16% at 500°C and up to 10% at 350°C for the best solutions. The increased error is a consequence of incorrect deformation zone modelling, non inclusion of a container/billet shear zone and lack of knowledge concerning temperature distributions in the material.

6. Derivation of deformation zone angle changes with extrusion ratio from the analysis above enables a modified form of Felthams strain rate to be proposed.

7. Strain rates from the upper bound analysis are in good agreement with those derived using the modified Felthams equation.

8. Load-Displacement loci for direct extrusion show initial peaks for all materials excepting 5052. This peak height increases with a strain rate increase, temperature reduction, extrusion ratio increase or increase in alloy content of the material. This indicates that the phenomenon is associated with a dynamic process involving dislocation generation and annihilation.

9. Maximum extrusion pressure is increased by a decrease in initial billet temperature, greater extrusion ratio and increased strain rate providing heat generation is not excessive in the latter case. Increasing the magnesium content of the material also causes an increase due to the enhanced resistance to deformation it causes.

10. Plotting experimental results for the relationship $^{P}/\sigma = a+b\text{LnR}$ shows a large spread and plotting $^{P}/\sigma$ vs LnZ shows a linear relationship to exist for each extrusion ratio. Partial extrusion of gridded billets at high and low temperatures indicated that a dramatic change in deformation zone geometry resulted and explained the inclusion of the Z term. Relationships of the form:-

$$^{P}/\sigma = a + b\ \text{LnR} - c\text{LnZ}$$

are derived for each container size which accurately relate the parameters.

11. The surface condition of the extrudes is very dependent upon strain rate and temperature. Equalities are derived which predict the onset of unacceptable surface finish relating the Z parameter and temperature.

12. Investigation of the structural development during extrusion of a super-pure aluminium 5% magnesium alloy reveals that dynamic recovery is the operative high temperature restoration process. This results in a duplex product structure of peripheral statically recrystallized grains and a fibrous, sub-grain containing core.

13. A similar investigation on the commercial equivalent of this alloy reveals dynamic recrystallization to be an auxilary process to that of dynamic recovery. This modifies the core structure to contain small equi-axed recrystallized grains in the regions of high shear, i.e. at original grain boundaries. The onset of this restoration process is associated with the reduced original grain size lowering the critical strain for its nucleation.

14. As a consequence of the dynamic recrystallization process, the product structure is considerably modified at high temperatures. At low temperatures the inner regions show a sub-grain structure with static recrystallized grains produced by the poor reduction in stored energy of the dynamic recovery process. Increased temperature perfects this process, reduces the occurrence of the recrystallized grains and enlarges the sub-grain size. Above a deformation temperature of around 400°C, small equi-axed recrystallized grains, containing a dislocation substructure are produced, their quantity increasing with temperature.

In all cases a peripheral ring of statically recrystallized grains is produced, their depth of penetration decreasing as the deformation temperature rises along with an associated increase in size by enhanced growth stage. All alloys show these features except 5052 which shows an almost completely statically re-crystallized grain structure throughout.

15. In tension, the higher magnesium bearing alloys show the most superior strength but poorest ductility. In contrast to a material displaying dynamic recovery alone, increasing the processing temperature increases the strength of the product and reduces ductility as dynamic recrystallization is initiated. At the highest temperatures strength is reduced as grain growth is enhanced.

16. At room temperature, the stress-strain curves exhibit serrated yielding in all materials.

17. Hardness testing shows a similar trend to that found in tensile testing.

18. The complex variation with processing variables precludes their inclusion in limit diagrams. These are produced showing limitting values from pressure and surface finish conditions alone.

19. The deformation mechanisms are shown to be the same in both extrusion and torsion.

20. The result of prior heat treatment upon the billet is shown to produce the statically recrystallized annular ring and slightly reduce the occurrence of dynamic recrystallization at higher temperatures in the central regions.

Recommendations for Further Work

This work has been centred upon three commercial aluminium-magnesium alloys namely 5052, 5083 and 5456 containing 2.5, 4.5 and 5.0% magnesium respectively. In a limited period of time such as three years it is impossible to investigate all the topics in a completely satisfactory manner. However, certain areas of specific interest appear which offer the basis for future valuable work, these include:-

(1) The application of a modified hot working equation including temperature dependence for the 'constants' A, α, n and ΔH has been shown to be applicable. Further work in this field may serve to improve this relationship, although the good fit found from non temperature dependence makes this a purely academic exercise.

(2) Results from load bounding techniques shows their application to practical extrusion results to be somewhat lacking and a further improvement is necessary. This may arise from improved deformation field modelling or from application of a finite element technique.

(3) The importance of temperature throughout this work cannot be over-stressed. Thus, a more accurate method of modelling and predicting temperature throughout both the deformation zone and outgoing product is highly desirable. This offers the most important field for future research and will probably be based upon a finite element solution.

(4) The conclusion that dynamic recrystallization is an operative restoration process in the higher magnesium bearing alloys opens the door for considerable research. Further work on these alloys may serve to produce a fuller understanding of the mechanisms involved while diversion to include higher magnesium containing alloys may also prove rewarding. At the same time other alloys in which magnesium is present in significant quantities may also be investigated.

Appendix A

Single Triangle Axi-symmetric Upper Bound Computer Programme - AXY1T

This programme solves the single triangle axi-symmetric upper bound situation for direct rod extrusion. Optimization is via a constrained minimization technique using a standard computer library routine named E04HAF.[200,201] This optimum result is obtained by variance of the two angles α and ϕ (defined in section 2.2.1.).

The programme is suitable for running on Telex.

Input:-

- Ram speed (mms/sec)
- Initial billet temperature (^{O}C)
- Billet diameter (mms)
- Billet length (mms)
- Extrusion ratio
- Initial guesses for α and ϕ (0° < angle < 90°)
- Friction factor m (0 < m < 1)

Internal Constants and values:-

Hot Working Equation Constants: $A = 1.614 \times 10^{10}$ (sec^{-1})

$\alpha = 0.0191$ (m^2/MN)

$n = 3.2$

$\Delta H = 161177$ J/mole

Gas Constant, $G = 8.314$ J/mole^{O}K

Output:-

- Values of input data
- Extrusion Pressure (MN/m^2)
- Angles α and ϕ (degrees)
- Number of iterations
- Volume, distance, time and mathematical mean strain rates
- Deformation zone volume

```
00100 PROGRAM AXYIT(INPUT,OUTPUT,TAPE5=INPUT,TAPE6=OUTPUT,TAPE8)
00200C
00300 COMMON/RATE/ AREA(5),TOTALT(5),TOTLENG(5),TOTL(5),ROWRATE(5),TMSTRN(5)
00400C
00500C  VERSION 1**********17:8:78**********
00600C
00700C
00800C THIS PROGRAM GIVES A MINIMISED UPPER BOUND SOLUTION FOR AXISYMMETRIC
00900C EXTRUSION USING A SINGLE TRIANGLE DEFORMATION FIELD. THIS SINGLE TRIANGL
01000C IS DIVIDED INTO A GRID OF 50 ELEMENTS DEFINED BY TEN UNITS DOWN THE
01100C D.M.Z. INTERFACE AND FIVE UNITS DOWN THE RADIUS. THE TEN UNITS ARE
01200C FORMULATED SUCH THAT THE INTERNAL ANGLE OF THE TRIANGLE IS SPLIT INTO
01300C TEN EQUAL ANGLES AND THE FIVE ARE FORMULATED SUCH THAT THE RADIUS IS
01400C SPLIT INTO FIVE EQUAL LENGTHS.
01500C THE GEOMETRY IS DEFINED SUCH THAT: ALPHA = D.M.Z. ANGLE: PHI= ANGLE
01600C BETWEEN VERTICAL AND THE FINAL VELOCITY DISCONTINUITY: RB = BILLET
01700C RADIUS: RE = EXTRUDE RADIUS: V1 = RAM APPROACH VELOCITY.
01800C
01900C
02000 COMMON/1/ R1,Y,Z,DELTAR,ALAMDAT,ALAMDAC,RR,RRC
02100 COMMON/2/ DELTT(10,5),RATE(10,5),ALENG(10,5),VOLUME(10,5),RB,RE,V1,V3,PI
02200 COMMON/3/ SNALPHA,SNBETA,SNGAM,CSGPA,CSALPHA,CSBETA,SNDTB2,CSDTB2,
02300+Q,QQ,CONSTAN,SNBMD,CSAMP,SNP,CSP,SNTHETA,CSTHETA,CSGAM
02400 COMMON/ANGLE/ ALPHA,GAMMA,PHI,THETA,DTHETA,BETA
02500 COMMON/ENER/ E2,E24,E23,E12,E12T,E23T,E24T,E2T
02600 LOGICAL LINE,LOGW
02700 DIMENSION IXTYP(2),IGTYP(5),LINE(5),LOGW(15),W(65),X(2)
02800 COMMON/HAF/ MET,IPRIN,IT
02900 COMMON/STN/ VOLRATE(10,5),TEMP4,STRAIN2(5),STRN(10,5),ST(10),STRAIN(5)
03000 COMMON/FLOWS/ EN,A,ALFA,DELTAH,SQRT3,TEMP1,G,EM,BILLENG
03100 EXTERNAL GRID,DGRID,DDGRID,MON,MONE
03200 DATA N,INF,IST,MAXI,IFAIL/2,0,1,500,0/
03300 DATA RAX,AAX/1.0E-3,1.0E-3/
03400C
03500C ***********************************************************
03600C
03700C  THE CALCULATION EVALUATES THE VALUE OF THE EXTRUSION PRESSURE
03800C  USING INITIAL BILLET TEMPERATURE AND STRAIN RATE IN THE SINH(ALFA
03900C  SIGMA) RELATIONSHIP TO EVALUATE THE FLOW STRESS.
04000C
04100C**************************************************************
04200C
04300 5555 PRINT*,' ENTER THE VALUE OF THE RAM SPEED IN MMS/SECOND.  INITIAL'
04400 PRINT*,' BILLET TEMPERATURE,BILLET DIAMETER AND LENGTH IN MMS.'
04500 READ(5,*) V1,TEMP1,BDIAM,BLENG
04600C
04700 V1=V1/1000.
04800 PI=3.14159
04900 BILLENG=BLENG/1000.
05000 RB=(BDIAM/1000.)*0.5
05100C
05200 PRINT*,'ENTER THE VALUES OF EXTRUSION RATIO AND GUESS OF ALPHA AND PHI'
05300 READ(5,*) ER,X(1),X(2)
05400 PRINT*,'ENTER THE VALUE OF THE FRICTION COEF..(0<M<1)'
05500 READ(5,*) EM
05600 EST=1.0
05700 EN=3.2
05800 A=0.16141E+11
05900 ALFA=0.02E-6
06000 DELTAH=161177.4
06100 SQRT3=SQRT(3.)
06200 G=8.314
06300C
06400C CONSTANTS Q,QQ AND CONSTAN ARE USED WHEN CONSIDERING
06500C POWDER EXTRUSION..THEY RELATE FLOW STRESS TO STRAIN AND STRAIN RATE
06600C
06700 Q=0.0
06800 QQ=0.0
06900 CONSTAN=1.0
07000C
07100 RE=RB/SQRT(ER)
07200 V3=V1*RB*RB/(RE*RE)
07300C
07400C**************************************************************
07500C   SET UP THE MINIMISATION CONSTANTS.
07600C
07700C**************************************************************
07800C
07900 M=4
08000 MET=0
08100C
08200C
08300 IPRIN=1
08400C
08500C
08600 IT=0
08700C
08800C
08900 IXTYP(1)=90
09000 IXTYP(2)=90
09100 IGTYP(1)=2
09200 IGTYP(2)=2
09300 IGTYP(3)=2
09400 IGTYP(M)=1
09500C
09600 LINE(1)=.TRUE.
09700 LINE(2)=.TRUE.
09800 LINE(3)=.TRUE.
09900 LINE(M)=.FALSE.
10000C
10100 M2N=M*2*N
10200 IW=5*N*4*M*M*N*2*N*N
10300C
10400C**************************************************************
10500C
10600C SUBROUTINE E04HAF IS THE LIBRARY MINIMISING ROUTINE
10700C
10800 CALL E04HAF(N,M,X,EST,RAX,AAX,IST,INF,MET,LOGW,M2N,W,IW,IXTYP,IGTYP,
10900+LINE,GRID,DGRID,DDGRID,MON,MONE,IPRIN,MAXI,IFAIL)
11000C
11100C**************************************************************
11200 V1=V1*1000.
```

```
11300C
11400C*****************************************************************
11500C
11600C
11700C   ADD CYLINDER WALL FRICTION EFFECTS
11800C
11900C
12000C
12100C
12200C        WRITE OUT THE ANSWERS.
12300C
12400 WRITE(6,981)
12500 WRITE(6,961)IFAIL
12600 WRITE(6,902)EST. (X(I),I=1,N)
12700 WRITE(6,966) ER,VI,TEMPI,BDIAM
12800 WRITE(6,901) IPRIN,MAXI
12900 TOTALV=0.0
13000 TOTALSV=0.0
13100 TOTALR=0.0
13200 AVSTRAT=0.0
13300 AVTMRTE=0.0
13400 DO 8001 MM=1,5
13500 TOTALT(MM)=0.0
13600 TOTLENG(MM)=0.0
13700 TOTL(MM)=0.0
13800 DO 8002 L=1,10
13900C
14000C CALCULATE THE AVERAGE STRAIN RATES.
14100C
14200C          SUM ELEMENT VOLUMES
14300 TOTALV=TOTALV+VOLUME(L,MM)
14400C          SUM ELEMENT (VOLUME*STRAIN RATE)
14500 TOTALSV=TOTALSV+VOLRATE(L,MM)
14600C          SUM ELEMENT STRAIN RATES
14700 TOTALR=TOTALR+RATE(L,MM)
14800C          SUM TIMES TO CROSS ROWS OF ELEMENTS
14900 TOTALT(MM)=TOTALT(MM)+DELTT(L,MM)
15000C          SUM (LENGTH*STRAIN RATE) FOR EACH ROW OF ELEMENTS
15100 TOTLENG(MM)=(ALENG(L,MM)*RATE(L,MM))+TOTLENG(MM)
15200C          SUM THE INDIVIDUAL ELEMENT LENGTHS PER ROW
15300 TOTL(MM)=TOTL(MM)+ALENG(L,MM)
15400C
15500 8002 CONTINUE
15600C          DIVIDE STRAIN IN ROW 10 BY TIME TO CROSS 10 ELEMENTS
15700  TMSTRN(MM)=STRAIN2(MM)/TOTALT(MM)
15800C
15900C          DIVIDE THE(ELEMENT LENG*RATE)/LENGTH PRE ROW
16000 ROWRATE(MM)=TOTLENG(MM)/TOTL(MM)
16100C          TOTAL RATE = AV ROWRATE * PROJECTED AREA
16200 AVSTRAT=(ROWRATE(MM)*AREA(MM))+AVSTRAT
16300C          TOTAL RATE/TIME = RATE/ROW*PROJECTED AREA
16400 AVTMRTE=(TMSTRN(MM)*AREA(MM))+AVTMRTE
16500C
16600 8001 CONTINUE
16700C
16800C          AVERAGE STRAIN RATE(LENGTH)
16900 AVSTRAT=AVSTRAT/(PI*RB*RB)
17000C          AVERAGE STRAIN RATE(MATHEMATICAL)
17100 TOTALRT=TOTALR/50.0
17200C          AVERAGE STRAIN RATE(VOLUME)
17300 SRT=TOTALSV/TOTALV
17400C          AVERAGE STRAIN RATE(TIME)
17500 AVTMRTE=AVTMRTE/(PI*RB*RB)
17600C
17700 WRITE(6,8003)TOTALRT,SRT,AVSTRAT,AVTMRTE,TOTALV
17800 8003 FORMAT(*MATHEMATICAL MEAN STRAIN RATE  *,F8.4,*S-1*,/,
17900+*VOLUME AVERAGE STRAIN RATE   *,F8.4,*S-1*,/,
18000+*DISTANCE AVERAGE STRAIN RATE   *,F8.4,*S-1*,/,
18100+*TIME AVERAGE STRAIN RATE   *,F8.4,*S-1*/
18200+*DEFORMATION ZONE VOLUME =*,E12.5)
18300 STOP
18400 981 FORMAT(75(1HX),/)
18500 901 FORMAT(/,17X,I5,* ITERATIONS *,I5,* PENALTY EVALUATIONS*,/75(1HX))
18600 902 FORMAT(20X,*PRESSURE IS *,E12.5,4X,*AT */17X,*ALPHA = *,F10.6,7X
18700+* PHI = *,F10.6)
18800 961 FORMAT(32X,*IFAIL =*,I2,/)
18900 966 FORMAT(4X,*EXTRUSION RATIO IS *,F6.2,* :   AT A RAM SPEED OF *,
19000+F10.4,*MMS/SEC.*,/,*INITIAL BILLET TEMPERATURE =*,F6.2,* DEG.C*
19100+*  BILLET DIAM =*,F6.3,* MMS*)
19200C
19300C
19400C
19500 END
19600C
19700C*****************************************************************
19800C
19900 SUBROUTINE MONE(N,M,URMIN,XMIN,GMIN,UMIN,IORD)
20000C
20100C
20200C THIS ROUTINE GIVES A MONITOR OF THE DUAL AND EXTRAPOLATED SOLUTIONS
20300C AT THE END OF EACH CYCLE.
20400C
20500 DIMENSION URMIN(5),XMIN(2),GMIN(5),UMIN(5)
20600C
20700 COMMON/HAF/ MET,IPRIN,IT
20800C
20900 WRITE(6,1007)
21000 WRITE(6,1006) (I,URMIN(I),I=1,M)
21100 WRITE(6,1000) IORD
21200 WRITE(6,1001)
21300 WRITE(6,1002) (I,XMIN(I),I=1,N)
21400 WRITE(6,1003)
21500 WRITE(6,1004) (I,GMIN(I),I=1,M)
21600 WRITE(6,1005)
21700 WRITE(6,1006) (I,UMIN(I),I=1,M)
21800C
21900C
22000 1000 FORMAT(/,*EXTRAPOLATION SOLUTION ORDER= *,I5)
22100 1001 FORMAT(/,*SOLUTION VECTOR*)
22200 1002 FORMAT(10(4(1X,1HX,I3,E12.5)/))
22300 1003 FORMAT(*CONSTRAINTS AND OBJECTIVE FNS*)
22400 1004 FORMAT(10(4(2X,3HCON,I3,E12.5)/))
```

```
22500 1005 FORMAT(*DUAL SOLUTION OF EXTRAPOLATED SOLUTIONS*)
22600 1006 FORMAT(10(4(1X,4HDUAL,I3,E12.5)/))
22700 1007 FORMAT(//*DUAL SOLUTION AT END POINT OF CYCLE*)
22800C
22900C
23000 RETURN
23100 END
23200C
23300C*****************************************************************
23400C
23500 SUBROUTINE MON(N,M,XR,PRXR,PG,PUPONK,R,ITCH,NEWCYC,NP,NG,NH,NRP)
23600C
23700C
23800C THIS ROUTINE MONITORS THE CHANGE OF ANGLES ALPHA AND PHI AND THE
23900C RESULTING CHANGE IN THE PRESSURE.
24000C
24100 LOGICAL NEWCYC
24200 COMMON/HAF/ MET,IPRIN,IT
24300 DIMENSION XR(2),PG(2),PUPONK(5)
24400C
24500 IT=IT+IPRIN
24600 IF(.NOT.NEWCYC) GO TO 101
24700 IT=0
24800C
24900 WRITE(6,1000) R
25000C
25100 WRITE(6,1001) IT,PRXR
25200C
25300C
25400 IF(ITCH.LE.0) WRITE(6,1006)
25500 IF(ITCH.EQ.3.OR.ITCH.EQ.-3) WRITE(6,1007)
25600 IF(ITCH.EQ.2.OR.ITCH.EQ.-2) WRITE(6,1008)
25700C
25800C
25900 WRITE(6,1009)
26000 WRITE(6,1010) (J,XR(J),J=1,N)
26100C
26200 IF(MET.LT.1) GO TO 106
26300C
26400 WRITE(6,1002)
26500 WRITE(6,1003) (I,PG(I),I=1,N)
26600C
26700 106 WRITE(6,1011)
26800 WRITE(6,1012) (I,PUPONK(I),I=1,M)
26900C
27000C
27100 1000 FORMAT(/*BEGINING OF CYCLE FOR R= *,E15.6)
27200 1001 FORMAT(/*ITERATION NO *,I3,*  PENALTY FUNCTION VALUE *,E15.6)
27300 1002 FORMAT(*PENALTY GRADIENT*)
27400 1003 FORMAT(10(4(3X,1HG,I3,E12.5)/))
27500 1006 FORMAT(/*LINE SEARCH TROUBLES*)
27600 1007 FORMAT(* H NOT PAC*)
27700 1008 FORMAT(* H INDEF*)
27800 1009 FORMAT(/*SOLUTION VECTOR*)
27900 1010 FORMAT(10(4(3X,1HX,I3,E12.5)/))
28000 1011 FORMAT(*CONSTRAINTS AND OBJECTIVE FNS*)
28100 1012 FORMAT(10(4(2X,3HCON,I3,E12.5)/))
28200C
28300C
28400 RETURN
28500 END
28600C
28700C*****************************************************************
28800C
28900C
29000 SUBROUTINE GRID(N,X,I,PUPONK)
29100C
29200C
29300C THIS IS THE MAIN CALCULATION ROUTINE CALLED BY THE MINIMISATION
29400C ROUTINE AND ITSELF CALLING THE REMAINING ROUTINES TO CALCILATE THE
29500C PRESSURE.
29600C
29700C
29800 COMMON/1/ R1,Y,Z,DELTAR,ALAMDAT,ALAMDAC,RR,RRC
29900 COMMON/2/ DELTT(10,5),RATE(10,5),ALENG(10,5),VOLUME(10,5),RB,RE,V1,V3,PI
30000 COMMON/RATE/ AREA(5),TOTALT(5),TOTLENG(5),TOTL(5),ROWRATE(5),TMSTRN(5)
30100 COMMON/3/ SNALPHA,SNBETA,SNGAM,CSGPA,CSALPHA,CSBETA,SNDTB2,CSDTB2,
30200*Q,QQ,CONSTAN,SNBMD,CSAMP,SNP,CSP,SNTHETA,CSTHETA,CSGAM
30300 COMMON/ANGLE/ ALPHA,GAMMA,PHI,THETA,DTHETA,BETA
30400 COMMON/ENER/ E2,E24,E23,E12,E12T,E23T,E24T,E2T
30500 COMMON/STN/ VOLRATE(10,5),TEMP4,STRAIN2(5),STRN(10,5),ST(10),STRAIN(5)
30600 COMMON/FLOWS/ EN,A,ALFA,DELTAH,SQRT3,TEMP1,G,EM,BILLENG
30700C
30800 DIMENSION X(2)
30900CWRITE(6,1) X(1),X(2)
31000 1 FORMAT(*NEW CYCLE OF CALCULATION. ALPHA = *,F6.3,*PHI= *,F6.3)
31100C              SET UP ANGLES IN RADIANS
31200 ALPHA=X(1)/57.2958
31300 PHI=X(2)/57.2958
31400C
31500C            TEST ANGLES TO BE WITHIN LIMITS.
31600C
31700 IF(I.EQ.1) GO TO 889
31800 IF(I.EQ.2) GO TO 999
31900C
32000C*****************************************************************
32100C
32200C            DEFINE LENGTHS AND REMAINING ANGLES.
32300C
32400C
32500 TGAMMA=ABS((((RB-RE)/TAN(ALPHA))-(RE*TAN(PHI)))/RB)
32600 GAMMA=ATAN(TGAMMA)
32700 IF(I.EQ.3) GO TO 699
32800 A1=RE*TAN(PHI)
32900 A2=(RB-RE)/TAN(ALPHA)
33000C           SET INITIAL TOTALS TO ZERO.
33100 E24T=0
33200 E12T=0
33300 E23T=0
33400 E2T=0
33500C            SET UP PROBLEM.
33600C
```

```
33700 JJ=10
33800 K=5
33900C
34000 IF(A1.GT.A2) GO TO 799
34100 DTHETA=(GAMMA+PHI)/10.
34200 THETA=((PI/2.)-GAMMA)-(DTHETA/2.)
34300 GO TO 599
34400 799 DTHETA=(PHI-GAMMA)/10.
34500 THETA=((PI/2.)+GAMMA)-(DTHETA/2.)
34600 599 Z=1
34700C
34800C THE FOLLOWING DO-LOOPS DO THE CALCULATIONS DOWN EACH SET OF ELEMENTS
34900C AND AROUND THE ELEMENTS RADIALLY.
35000C
35100 DO 100 L=1,JJ,1
35200C
35300 THETA=THETA+DTHETA
35400 Y=1
35500C
35600 DO 200 MM=1,K,1
35700C
35800 BETA=THETA-ALPHA
35900 SNALPHA=SIN(ALPHA)
36000 SNBETA=SIN(THETA-ALPHA)
36100 SNGAM=SIN(GAMMA)
36200 CSGAM=COS(GAMMA)
36300C
36400C
36500 IF(A1.GT.A2) GO TO 4001
36600C
36700C
36800 CSGPA=COS(GAMMA+ALPHA)
36900C
37000C
37100 GO TO 4002
37200 4001 CSGPA=COS(ALPHA-GAMMA)
37300 4002 CSALPHA=COS(ALPHA)
37400C
37500C
37600 CSBETA=COS(THETA-ALPHA)
37700 SNDTB2=SIN(DTHETA/2.)
37800 CSDTB2=COS(DTHETA/2.)
37900 SNBMD=SIN(BETA-(DTHETA/2.))
38000 CSAMP=COS(ALPHA-PHI)
38100 SNP=SIN(PHI)
38200 CSP=COS(PHI)
38300 SNTHETA=SIN(THETA)
38400 CSTHETA=COS(THETA)
38500C
38600C
38700 RI=RB/CSGAM
38800C
38900C
39000C
39100 CALL CENTRE (MM,L)
39200 IF(L.EQ.1) CALL E12CALC(MM,L)
39300 IF(MM.EQ.1) CALL E24CALC(MM,L)
39400 IF(MM.EQ.5) CALL TRIANGL(MM,L)
39500 IF(MM.EQ.5) GO TO 300
39600 CALL ENERGYC(MM,L)
39700 300 IF(L.EQ.10) CALL E23 CALC(MM,L)
39800C
39900C
40000C
40100C
40200 E2T=E2T+E2
40300C
40400C
40500 Y=Y+2.
40600C
40700C
40800 200 CONTINUE
40900C
41000 Z=Z+2.
41100C
41200 100 CONTINUE
41300C
41400 CALL FRICT(EFRICT)
41500C
41600C
41700C THE SEPERATE ENERGIES ARE SUMMED
41800C
41900 P=E12T+E23T+E24T+E2T+EFRICT
42000C
42100C
42200C THE TOTAL ENERGY IS THEN EQUATED TO THE PRESSURE.AREA.RAM VELOCITY.
42300C
42400 PUPONK=P/(PI*RB*RB*V1)
42500C
42600C
42700C
42800C THE FOLLOWING ARE THE CONSTRAINTS USED IN THE MINIMISATION. THEY ALL
42900C PASS THROUGH AS THE REQUIRED RESULT. I.E. IN PUPONK. THE CONSTRAINTS
43000C EMPLOYED ARE THAT: NEITHER ALPHA OR BETA CAN EXCEED 90 DEGREES.
43100C THAT ANGLE ALPHA MUST ALWAYS BE GREATER THAN ANGLE GAMMA.
43200C
43300C
43400 GO TO 1099
43500 889 PUPONK=(PI/2.)-ALPHA
43600 GO TO 1099
43700 999 PUPONK=(PI/2.)-PHI
43800 GO TO 1099
43900 699 PUPONK=ALPHA-GAMMA
44000 1099 RETURN
44100C
44200C
44300 END
44400C
44500C
44600 SUBROUTINE CENTREC(MM,L)
44700C
44800C
```

```
44900C ROUTINE TO CALCULATE THE BASIC GEOMETRICAL TERMS REQUIRED BY EACH
45000C ELEMENT. RR IS THE RADIUS FROM THE CENTRE TO THE EDGE OF THE ELEMENT
45100C RRC IS THE DISTANCE FROM THE CENTRE TO THE CENTRE OF GRAVITY.
45200C DELTAR IS THE ELEMENT HEIGHT. ALAMDAT IS THE TOP EDGE DIAMETER.
45300C ALAMDAC IS THE CENTRE OF GRAVITY DIAMETER.
45400C
45500C
45600 COMMON/1/ R1.Y.Z.DELTAR.ALAMDAT.ALAMDAC.RR.RRC
45700 COMMON/2/ DELTT(10.5).RATE(10.5).ALENG(10.5).VOLUME(10.5).RB.RE.V1.V3.PI
45800 COMMON/RATE/ AREA(5).TOTALT(5).TOTLENG(5).TOTL(5).ROWRATE(5).TMSTRN(5)
45900 COMMON /3/SNALPHA.SNBETA.SNGAM.CSGPA.CSALPHA.CSBETA.SNDTB2.CSDTB2.
46000+Q.QQ.CONSTAN.SNBMD.CSAMP.SNP.CSP.SNTHETA.CSTHETA.CSGAM
46100 COMMON /ANGLE/ALPHA.GAMMA.PHI.THETA.DTHETA.BETA
46200 COMMON/STN/ VOLRATE(10.5).TEMP4.STRAIN2(5).STRN(10.5).ST(10).STRAIN(5)
46300 COMMON/FLOWS/ EN.A.ALFA.DELTAH.SQRT3.TEMP1.G.EM.BILLENG
46400C
46500C
46600 RR=(R1*SIN(BETA-(Z*(DTHETA/2.))))/SNBETA
46700C
46800 DELTAR=RR/5.
46900 RRC=RR-Y*(DELTAR/2.)
47000C
47100 ALAMDAT=(2.*(RRC+(DELTAR/2.))*SNDTB2)/SNBMD
47200 ALAMDAC=(2.*RRC*SNDTB2)/SNBMD
47300C
47400 RETURN
47500 END
47600C
47700C
47800 SUBROUTINE E12 CALC(MM.L)
47900C
48000C
48100C ROUTINE TO CALCULATE THE ENERGY REQUIRED IN CROSSING THE DISCONTINUITY
48200C V12.
48300C
48400 COMMON/1/ R1.Y.Z.DELTAR.ALAMDAT.ALAMDAC.RR.RRC
48500 COMMON/2/ DELTT(10.5).RATE(10.5).ALENG(10.5).VOLUME(10.5).RB.RE.V1.V3.PI
48600 COMMON/RATE/ AREA(5).TOTALT(5).TOTLENG(5).TOTL(5).ROWRATE(5).TMSTRN(5)
48700 COMMON/3/ SNALPHA.SNBETA.SNGAM.CSGPA.CSALPHA.CSBETA.SNDTB2.CSDTB2.
48800+Q.QQ.CONSTAN.SNBMD.CSAMP.SNP.CSP.SNTHETA.CSTHETA.CSGAM
48900 COMMON/ENER/E2.E24.E23.E12.E12T.E23T.E24T.E2T
49000 COMMON/ANGLE/ALPHA.GAMMA.PHI.THETA.DTHETA.BETA
49100 COMMON/STN/ VOLRATE(10.5).TEMP4.STRAIN2(5).STRN(10.5).ST(10).STRAIN(5)
49200 COMMON/FLOWS/ EN.A.ALFA.DELTAH.SQRT3.TEMP1.G.EM.BILLENG
49300C
49400C
49500CPRINT*.V1.SNALPHA.CSGPA
49600 V12=(V1*SNALPHA)/CSGPA
49700  DV12=0.
49800 ELEMENL=(RB/CSGAM)/5.
49900 ELEMENR=(RB/CSGAM)*((10.-Y)/10.)
50000 AREA12=ELEMENL*ELEMENR*2.*PI*CSGAM
50100 AREA(MM)=AREA12
50200C
50300 CALL SRATE(V12.DV12.AK12.ELEMENR.STRATE)
50400 CALL FSTRESS(STRATE.STRESS)
50500 CALL STRAN12(MM.L.V12.BK12)
50600CBK12=1.0
50700C
50800 E12=V12*AREA12*(STRESS/SQRT3)
50900C
51000C
51100C THE ENERGY FOR THE PRESENTELEMENT IS THEN ADDED TO THAT FOR PREVIOUS
51200C SIMILLAR ELEMENTS.
51300C
51400 E12T=E12T+E12
51500C
51600C
51700 RETURN
51800 END
51900C
52000C
52100 SUBROUTINE E24 CALC(MM.L)
52200C
52300C
52400C ROUTINE CALCULATES THE ENERGY REQUIRED TO ACCELERATE THE MATERIAL
52500C DOWN THE D.M.Z BOUNDARY.
52600C
52700 COMMON/1/ R1.Y.Z.DELTAR.ALAMDAT.ALAMDAC.RR.RRC
52800 COMMON/2/ DELTT(10.5).RATE(10.5).ALENG(10.5).VOLUME(10.5).RB.RE.V1.V3.PI
52900 COMMON/RATE/ AREA(5).TOTALT(5).TOTLENG(5).TOTL(5).ROWRATE(5).TMSTRN(5)
53000 COMMON/3/ SNALPHA.SNBETA.SNGAM.CSGPA.CSALPHA.CSBETA.SNDTB2.CSDTB2.
53100C
53200+Q.QQ.CONSTAN.SNBMD.CSAMP.SNP.CSP.SNTHETA.CSTHETA.CSGAM
53300 COMMON/ENER/E2.E24.E23.E12.E12T.E23T.E24T.E2T
53400 COMMON/ANGLE/ALPHA.GAMMA.PHI.THETA.DTHETA.BETA
53500 COMMON/STN/ VOLRATE(10.5).TEMP4.STRAIN2(5).STRN(10.5).ST(10).STRAIN(5)
53600 COMMON/FLOWS/ EN.A.ALFA.DELTAH.SQRT3.TEMP1.G.EM.BILLENG
53700C
53800C
53900 V24=(V1*CSGAM*CSGAM*SNBETA)/(SNTHETA*CSGPA*CSGPA)
54000 DV24=((V1*CSGAM*CSGAM)/(CSGPA*CSGPA))*((SNTHETA*COS(ALPHA-
54100+THETA)-SNBETA*CSTHETA)/(SNTHETA*SNTHETA))
54200 AREA24=ALAMDAT*2.*PI*RR*COS(GAMMA-(Z*DTHETA/2.))
54300C
54400 CALL SRATE(V24.DV24.AK24.RR.STRATE2)
54500 CALL FSTRESS(STRATE2.STRESS)
54600C PRINT*,'POS 2', MM.L.RR.DELTAR.V24.STRATE2.BK24
54700 CALL STRAN24(MM.L.ALAMDAT.V24.STRATE2.BK24)
54800CBK24=1.0
54900C PRINT*,'POS 1', MM.L.RR.DELTAR.V24.STRATE2.BK24
55000C
55100C
55200 E24=V24*AREA24*(STRESS/SQRT3)
55300C
55400C
55500 E24T=E24T+E24
55600 RETURN
55700 END
55800C
55900C
56000 SUBROUTINE E23 CALC(MM.L)
```

```
56100C
56200C
56300C ROUTINE CALCULATES THE ENERGY INVOLVED IN CROSSING THE BOUNDARY 23.
56400C
56500 COMMON/1/ R1,Y,Z,DELTAR,ALAMDAT,ALAMDAC,RR,RRC
56600 COMMON/2/ DELTT(10,5),RATE(10,5),ALENG(10,5),VOLUME(10,5),RB,RE,V1,V3,PI
56700 COMMON/RATE/ AREA(5),TOTALT(5),TOTLENG(5),TOTL(5),ROWRATE(5),TMSTRN(5)
56800 COMMON/3/ SNALPHA,SNBETA,SNGAM,CSGPA,CSALPHA,CSBETA,SNDTB2,CSDTB2,
56900+0.00,CONSTAN,SNBMD,CSAMP,SNP,CSP,SNTHETA,CSTHETA,CSGAM
57000 COMMON/ENER/ E2,E24,E23,E12,E12T,E23T,E24T,E2T
57100 COMMON/STN/ VOLRATE(10,5),TEMP4,STRAIN2(5),STRN(10,5),ST(10),STRAIN(5)
57200 COMMON/FLOWS/ EN,A,ALFA,DELTAH,SQRT3,TEMP1,G,EM,BILLENG
57300C
57400 V23=(V3*SNALPHA)/CSAMP
57500 DV23=0.
57600 ELEMENL=(RE/CSP)/5.
57700 ELEMENR=(RE/CSP)*((10.-Y)/10.)
57800C
57900 AREA23=ELEMENL*ELEMENR*2.*PI*CSP
58000C
58100 CALL SRATE(V23,DV23,AK23,ELEMENR,STRATE)
58200 CALL FSTRESS(STRATE,STRESS)
58300 CALL STRAN23(MM,L,BK23)
58400CBK23=1.0
58500C
58600 E23=AREA23*V23*(STRESS/SQRT3)
58700C
58800 E23T=E23T+E23
58900 RETURN
59000 END
59100C
59200C
59300 SUBROUTINE ENERGY(MM,L)
59400C
59500C
59600C ROUTINE CALCULATES THE ENERGY DISSIPATED WITHIN EACH RECTANGULAR
59700C ELEMENT.
59800C
59900 COMMON/1/ R1,Y,Z,DELTAR,ALAMDAT,ALAMDAC,RR,RRC
60000 COMMON/2/ DELTT(10,5),RATE(10,5),ALENG(10,5),VOLUME(10,5),RB,RE,V1,V3,PI
60100 COMMON/RATE/ AREA(5),TOTALT(5),TOTLENG(5),TOTL(5),ROWRATE(5),TMSTRN(5)
60200 COMMON/3/ SNALPHA,SNBETA,SNGAM,CSGPA,CSALPHA,CSBETA,SNDTB2,CSDTB2,
60300+0.00,CONSTAN,SNBMD,CSAMP,SNP,CSP,SNTHETA,CSTHETA,CSGAM
60400 COMMON/ENER/E2,E24,E23,E12,E12T,E23T,E24T,E2T
60500 COMMON/ANGLE/ALPHA,GAMMA,PHI,THETA,DTHETA,BETA
60600 COMMON/STN/ VOLRATE(10,5),TEMP4,STRAIN2(5),STRN(10,5),ST(10),STRAIN(5)
60700 COMMON/FLOWS/ EN,A,ALFA,DELTAH,SQRT3,TEMP1,G,EM,BILLENG
60800C
60900C
61000C THIS ROUTINE USES A METHOD INVOLVING STRAIN RATE WHICH IS CALCULATED
61100C USING THE METHOD EMPLOYED BY ADIE AND ALEXANDER IN ADIES PH.D THESIS.
61200C
61300C
61400 ELEMENV=ALAMDAC*DELTAR*2.*PI*RRC*SNTHETA
61500 VELOC=(V1*CSGAM*CSGAM*SNBETA)/(SNTHETA*CSGPA*CSGPA)
61600C
61700 DVELOC=((V1*CSGAM*CSGAM)/(CSGPA*CSGPA))*((SNTHETA*COS(ALPHA-THETA)
61800+-SNBETA*CSTHETA)/(SNTHETA*SNTHETA))
61900C
62000 ETHET=((VELOC*CSBETA*2.)+(SNBETA*DVELOC))/RRC
62100 EPHI=(VELOC/RRC)*(CSBETA+(1./TAN(THETA)))*SNBETA)
62200C
62300 ERTHET=((-VELOC*SNBETA*2.)+(CSBETA*DVELOC))/RRC
62400 EBARDOT=SQRT((2./3.)*((ETHET*ETHET)+(EPHI*EPHI)+(0.5*(ERTHET*ERTHET))))
62500C
62600 CALL SRATE(VELOC,DVELOC,AK2,RRC,STRATE3)
62700 CALL FSTRESS(STRATE3,STRESS)
62800 CALL CNTSTRN(MM,L,ALAMDAC,VELOC,
62900+STRATE3,BK2)
63000CPRINT*,'MM,L AND STRAIN RATE IN ELEMENTS.',MM,L,STRATE3
63100CBK2=1.0
63200 E2=EBARDOT*ELEMENV*STRESS
63300 RATE(L,MM)=STRATE3
63400 VOLRATE(L,MM)=STRATE3*ELEMENV
63500 VOLUME(L,MM)=ELEMENV
63600CWRITE(6,8001) ELEMENV,VOLRATE
63700 8001 FORMAT('ELEMENTS     =',F10.5,3X,F10.5)
63800 ALENG(L,MM)=ALAMDAC
63900C
64000 RETURN
64100 END
64200C
64300C
64400 SUBROUTINE TRIANGL(MM,L)
64500C
64600C
64700C ROUTINE CALCULATES THE ENERGY DISSIPATED WITHIN THE 5 TRIANGULAR
64800C ELEMENTS AT THE CENTRE OF THE MESH.
64900C
65000C
65100 COMMON/1/ R1,Y,Z,DELTAR,ALAMDAT,ALAMDAC,RR,RRC
65200 COMMON/2/ DELTT(10,5),RATE(10,5),ALENG(10,5),VOLUME(10,5),RB,RE,V1,V3,PI
65300 COMMON/RATE/ AREA(5),TOTALT(5),TOTLENG(5),TOTL(5),ROWRATE(5),TMSTRN(5)
65400 COMMON/3/ SNALPHA,SNBETA,SNGAM,CSGPA,CSALPHA,CSBETA,SNDTB2,CSDTB2,
65500+0.00,CONSTAN,SNBMD,CSAMP,SNP,CSP,SNTHETA,CSTHETA,CSGAM
65600 COMMON/ANGLE/ ALPHA,GAMMA,PHI,THETA,DTHETA,BETA
65700 COMMON/ENER/ E2,E24,E23,E12,E12T,E23T,E24T,E2T
65800 COMMON/STN/ VOLRATE(10,5),TEMP4,STRAIN2(5),STRN(10,5),ST(10),STRAIN(5)
65900 COMMON/FLOWS/ EN,A,ALFA,DELTAH,SQRT3,TEMP1,G,EM,BILLENG
66000C
66100C
66200 XR1=((ALAMDAT/2.)*SNBETA)/SNDTB2
66300 TRIRAD=(2./3.)*(RR/5.)
66400 TRIC=(2.*TRIRAD*SNDTB2)/SNBMD
66500 TRIAREA=0.5*ALAMDAT*XR1*SIN(BETA-(DTHETA/2.))
66600 TRIVOL=TRIAREA*2.*PI*TRIRAD*COS(GAMMA-(Z*(DTHETA/2.)))
66700 VT=(V1*CSGAM*CSGAM*SNBETA)/(SNTHETA*CSGPA*CSGPA)
66800 DVT=((V1*CSGAM*CSGAM)/(CSGPA*CSGPA))*((SNTHETA*COS(ALPHA-
66900+THETA)-SNBETA*CSTHETA)/(SNTHETA*SNTHETA))
67000C
67100 CALL SRATE(VT,DVT,AKT,TRIRAD,STRATE4)
67200 CALL FSTRESS(STRATE4,STRESS)
```

```
67300 CALL CNTSTRN(MM.L.TRIC.VT.
67400+STRATE4.BKT)
67500CPRINT*. MM.L AND STRAIN RATE IN TRIANGLES'.MM.L.STRATE4
67600CBKT=1.0
67700 E2=TRIVOL*STRATE4*STRESS
67800 RATE(L.MM)=STRATE4
67900 VOLRATE(L.MM)=TRIVOL*STRATE4
68000 VOLUME(L.MM)=TRIVOL
68100CWRITE(6.8002) TRIVOL.VOLRATE
68200 8002 FORMAT(*TRIANGLES    *.F10.5.3X.F10.5)
68300 ALENG(L.MM)=2.0*TRIRAD*SNDTB2/SNBMD
68400C
6850) RETURN
6860) END
6870C
68800C
68900 SUBROUTINE DGRID(N.X.I.G)
69000C
69100C
69200C ROUTINE INCLUDED SINCE A DECLARATION IS REQUIRED BY THE LIBRARY ROUTINE.
69300C IT HAS NO USE IN THE CALCULATION.
69400C
69500 DIMENSION G(4).X(2)
69600 RETURN
69700 END
69800C
69900C
70000 SUBROUTINE DDGRID(N.X.I.DG)
70100C
70200C
70300C ROUTINE INCLUDED FOR THE SAME REASON AS DGRID
70400C
70500 DIMENSION DG(4.4).X(2)
70600 RETURN
70700 END
70800C
70900C
71000 SUBROUTINE SRATE(V.DV.AK.RADIUS.STRATE)
71100C
71200C
71300C THIS ROUTINE CALCULATES THE VALUE OF THE STRAIN RATE FOR EACH ELEMENT
71400C AND RAISES IT TO THE POWER Q DETERMINED ON ENTRY BY THE USER.
71500C
71600 COMMON/3/ SNALPHA.SNBETA.SNGAM.CSGPA.CSALPHA.CSBETA.SNDTB2.
71700+CSDTB2.Q.QQ.CONSTAN.SNBMD.CSAMP.SNP.CSP.SNTHETA.CSTHETA.CSGAM
71800 COMMON/ANGLE/ ALPHA.GAMMA.PHI.THETA.DTHETA.BETA
71900C
72000C
72100 STRAINT=(V*CSBETA*2.+(SNBETA*DV))/RADIUS
72200 STRAINP=(V/RADIUS)*(CSBETA+(1./TAN(THETA))*SNBETA)
72300 STRAINR=((-V*SNBETA*2.)+(CSBETA*DV))/RADIUS
72400 STRATE=SQRT((2./3.)*((STRAINT*STRAINT)+(STRAINP*STRAINP)
72500++(0.5*(STRAINR*STRAINR))))
72600C
72700CPRINT*.'STRAIN RATE  '.STRATE
72800CAK=CONSTAN*(STRATE**Q)
72900 AK=1.0
73000C
73100 RETURN
73200 END
73300C
73400C
73500 SUBROUTINE STRAN12(MM.L.V12.BK12)
73600C
73700C
73800C THIS ROUTINE CALCULATES THE STRAIN AT A DISCONTINUITY 12 AND RAISES
73900C TO THE POWER QQ AS DETERMINED BY THE USER.
74000C
74100 COMMON/2/ DELTT(10.5).RATE(10.5).ALENG(10.5).VOLUME(10.5).RB.RE.V1.V3.PI
74200 COMMON/RATE/ AREA(5).TOTALT(5). OTLENG(5).TOTL(5).ROWRATE(5).TMSTRN(5)
74300 COMMON/3/ SNALPHA.SNBETA.SNGAM.CSGPA.CSALPHA.CSBETA.SNDTB2.CSDTB2.
74400+Q.QQ.CONSTAN.SNBMD.CSAMP.SNP.CSP.SNTHETA.CSTHETA.CSGAM
74500 COMMON/STN/ VOLRATE(10.5).TEMP4.STRAIN2(5).STRN(10.5).ST(10).STRAIN(5)
74600C
74700C
74800 STRAIN(MM)=V12/(SQRT(3.)*V1*SNTHETA)
74900 IF(STRAIN(MM).LT.2.3) GO TO 1
75000CWRITE(6.11) L.MM.STRAIN(MM)
75100 11 FORMAT(*BOUNDARY 12. L= *.I2.* MM= *.I2.*STRAIN= *.E12.5)
75200 CALL FIRSTST(BK12)
75300 TEMP1=BK12
75400 RETURN
75500 1 EXPO1=(STRAIN(MM)**(QQ+1.))
75600C
75700 BK12=(EXPO1/STRAIN(MM))/(SQRT(3.)*(QQ+1.))
75800 TEMP1=BK12
75900 GO TO 3002
76000 3001 BK12=TEMP1
76100C
76200 3002 RETURN
76300 END
76400C
76500C
76600 SUBROUTINE CNTSTRN(MM.L.ALENGTH.VEL.STRATE.BK2)
76700C
76800C
76900C THIS ROUTINE CALCULATES THE STRAIN FO EACH ELEMENT EXCLUDING THE
77000C BOUNDARY.
77100C
77200  COMMON/2/ DELTT(10.5).RATE(10.5).ALENG(10.5).VOLUME(10.5).RB.RE.V1.V3.PI
77300 COMMON/RATE/ AREA(5).TOTALT(5).TOTLENG(5).TOTL(5).ROWRATE(5).TMSTRN(5)
77400 COMMON/3/ SNALPHA.SNBETA.SNGAM.CSGPA.CSALPHA.CSBETA.SNDTB2.CSDTB2.
77500+Q.QQ.CONSTAN.SNBMD.CSAMP.SNP.CSP.SNTHETA.CSTHETA.CSGAM
77600 COMMON/ANGLE/ ALPAH.GAMMA.PHI.THETA.DTHETA.BETA
77700 COMMON/STN/ VOLRATE(10.5).TEMP4.STRAIN2(5).STRN(10.5).ST(10).STRAIN(5)
77800C
77900C
78000 DT=ALENGTH/VEL
78100 DELTT(L.MM)=DT
78200 IF(L.GT.1) GO TO 777
78300 STRN(L.MM)=(STRATE*DT)+STRAIN(MM)
78400 IF(STRN(L.MM).LT.2.3) GO TO 1
```

```
78500CWRITE(6,11) L,MM,STRN(L,MM)
78600 11 FORMAT(=ENERGY DIS. IN 1ST ROW. L=,I2,=MM= ,I2,=STRAIN- =,E12.5)
78700 CALL FIRSTST(BK2)
78800 TEMP2=BK2
78900 RETURN
79000 1 P1=STRAIN(MM)*(QQ+1.)
79100 P2=STRN(L,MM)*(QQ+1.)
79200 BK2=((P2-P1)/(STRN(L,MM)-STRAIN(MM)))/(SQRT(3.)*(QQ+1.))
79300 TEMP2=BK2
79400 GO TO 778
79500 777 STRN(L,MM)=(STRATE*DT)+STRN(L-1,MM)
79600 IF(STRN(L,MM).GE.2.3) GO TO 4001
79700 POWER2=(STRN(L,MM)*(QQ+1.))
79800 POWER1=(STRN(L-1,MM)*(QQ+1.))
79900C
80000 BK2=((POWER2-POWER1)/(STRN(L,MM)-STRN(L-1,MM)))/(SQRT(3.)*(QQ+1.))
80100 TEMP2=BK2
80200 GO TO 778
80300 4001 BK2=TEMP2
80400CWRITE(6,2) L,MM,STRN(L,MM)
80500 2 FORMAT(=ENERGY DIS IN ELEMENTS. L= ,I2,=MM= ,I2,=STRAIN= ,E12.5)
80600C
80700 778 RETURN
80800 END
80900C
81000C
81100 SUBROUTINE STRAN23(MM,L,BK23)
81200C
81300C
81400C ROUTINE CALCULATES THE STRAIN AT THE BOUNDARY 23.
81500C
81600 COMMON/2/ DELTT(10,5),RATE(10,5),ALENG(10,5),VOLUME(10,5),RB,RE,V1,V3,PI
81700 COMMON/RATE/ AREA(5),TOTALT(5),TOTLENG(5),TOTL(5),ROWRATE(5),TM3TRN(5)
81800 COMMON/3/ SNALPHA,SNBETA,SNGAM,CSGPA,CSALPHA,CSBETA,SNDTB2,CSDTB2,
81900+Q,QQ,CONSTAN,SNBMD,CSAMP,SNP,CSP,SNTHETA,CSTHETA,CSGAM
82000 COMMON/STN/ VOLRATE(10,5),TEMP4,STRAIN2(5),STRN(10,5),ST(10),STRAIN(5)
82100C
82200C
82300 V203=V3*CSP/CSAMP
82400 V23=V3*SNALPHA/CSAMP
82500 STRAIN2(MM)=V23/(SQRT(3.)*V203*SNTHETA)+STRN(L,MM)
82600 IF(STRAIN2(MM).LT.2.3) GO TO 1
82700CWRITE(6,11) L,MM,STRAIN2(MM)
82800 11 FORMAT(=BOUNDARY 23. L= ,I2,=MM= ,I2,=STRAIN = ,E12.5)
82900 CALL FIRSTST(BK23)
83000 TEMP3=BK23
83100 RETURN
83200 1 EXPON1=(STRN(L,MM)*(QQ+1.))
83300 EXPON2=(STRAIN2(MM)*(QQ+1.))
83400C
83500 BK23=(EXPON2-EXPON1)/(STRAIN2(MM)-STRN(L,MM)))/(SQRT(3.)*(QQ+1.))
83600 TEMP3=BK23
83700 GO TO 5002
83800 5001 BK23=TEMP3
83900C
84000 5002 RETURN
84100 END
84200C
84300C
84400 SUBROUTINE STRAN24(MM,L,ALAMDAT,VELO,STR,BK24)
84500C
84600C
84700C
84800C THIS ROUTINE CALCULATES THE STRAIN AT THE BOUNDARY 24
84900C
85000 COMMON/3/ SNALPHA,SNBETA,SNGAM,CSGPA,CSALPHA,CSBETA,SNDTB2,CSDTB2,
85100+Q,QQ,CONSTAN,SNBMD,CSAMP,SNP,CSP,SNTHETA,CSTHETA,CSGAM
85200 COMMON/ANGLE/ ALPHA,GAMMA,PHI,THETA,DTHETA,BETA
85300 COMMON/STN/ VOLRATE(10,5),TEMP4,STRAIN2(5),STRN(10,5),ST(10),STRAIN(5)
85400C
85500C
85600 DT=ALAMDAT/VELO
85700 IF(L.GT.1) GO TO 7799
85800 ST(L)=(STR*DT)+STRAIN(MM)
85900CPRINT*,'LINE 73200CSTL AND STRAINMM.',ST(L),STRAIN(MM)
86000 IF(ST(L).LE.2.3) GO TO 1
86100CWRITE(6,11) L,MM,ST(L)
86200 11 FORMAT(=BOUNDARY 24. L= ,I2,=MM= ,I2,= STRAIN= ,E12.5)
86300 CALL FIRSTST(BK24)
86400 TEMP4=BK24
86500CPRINT*,'AT LINE 71153',TEMP4
86600 RETURN
86700 1 P3=ST(L)*(QQ+1.)
86800 P4=STRAIN(MM)*(QQ+1.)
86900CPRINT*,'P3 AND P4', P3,P4
87000 BK24=((P3-P4)/(ST(L)-STRAIN(MM)))/(SQRT(3.)*(QQ+1.))
87100 TEMP4=BK24
87200CPRINT*,'AT LINE 71211', TEMP4
87300CCPRINT*,BK24
87400 GO TO 7798
87500 7799 ST(L)=(STR*DT)+ST(L-1)
87600 IF(ST(L).GE.2.3) GO TO 6001
87700 POW2=(ST(L)*(QQ+1.))
87800 POW1=(ST(L-1)*(QQ+1.))
87900CPRINT*,'POW2 AND POW1',POW2,POW1
88000 BK24=((POW2-POW1)/(ST(L)-ST(L-1)))/(SQRT(3.)*(QQ+1.))
88100 TEMP4=BK24
88200 GO TO 7798
88300 6001 BK24=TEMP4
88400CWRITE(6,2) L,MM,ST(L)
88500 2 FORMAT(=BOUNDARY 24. L= ,I2,=MM= ,I2,= STRAIN = ,E12.5)
88600 7798 RETURN
88700 END
88800 SUBROUTINE FIRSTST(BK)
88900 COMMON/3/ SNALPHA,SNBETA,SNGAM,CSGPA,CSALPHA,CSBETA,SNDTB2,CSDTB2,
89000+Q,QQ,CONSTAN,SNBMD,CSAMP,SNP,CSP,SNTHETA,CSTHETA,CSGAM
89100 BK=((2.3*(QQ+1.))/(2.3))/(SQRT(3.)*(QQ+1.))
89200CPRINT*,'IN FIRSTST' ,BK
89300 RETURN
89400 END
89500C
89600C
```

```
89700 SUBROUTINE FSTRESS(STRATE,STRESS)
89800C
89900C CALCULATES THE FLOW STRESS FOR INDIVIDUAL ELEMENTS FROM A
90000C KNOWLEDGE OF INDIVIDUAL STRAIN RATES AND THE INPUT TEMPERATURE.
90100C
90200C COMMON/FLOWS/ EN,A,ALFA,DELTAH,SQRT3,TEMP1,G,EM,BILLENG
90300 TABS=TEMP1+273.0
90400 ZED=STRATE*EXP(DELTAH/(G*TABS))
90500 ZUPONA=ZED/A
90600 UPONN=1./EN
90700 UPON2N=2./EN
90800 STRESS=(1./ALFA)*ALOG((ZUPONA**UPONN)+SQRT((ZUPONA**UPON2N)+1.))
90900 RETURN
91000 END
91100C
91200C
91300 SUBROUTINE FRICT(EFRICT)
91400C
91500C CALCULATES THE ADDITIONAL ENERGY DISSIPATED DUE TO RELATIVE
91600C MOVEMENT OF BILLET AND CONTAINER WALL.
91700C
91800 COMMON/2/ DELTT(10,5),RATE(10,5),ALENG(10,5),VOLUME(10,5),RB,RE,V1,V3,PI
91900 COMMON/ENER/ E2,E24,E23,E12,E12T,E23T,E24T,E2T
92000 COMMON/ANGLE/ ALPHA,GAMMA,PHI,THETA,DTHETA,BETA
92100 COMMON/FLOWS/ EN,A,ALFA,DELTAH,SQRT3,TEMP1,G,EM,BILLENG
92200C
92300C
92400 DEFLENG=(RB-RE)*COS(ALPHA)
92500 CYLLENG=BILLENG-DEFLENG
92600 DB2=(2.0*RB)*(2.0*RB)
92700 DB3=DB2*(2.0*RB)
92800 DE3=(2.0*RE)**3
92900 ERATIO=(RB*RB)/(RE*RE)
93000 ALOGRAT=0.5*1.32*ALOG(ERATIO)
93100 TANALF=TAN(ALPHA)
93200 FELTHAM=6.0*DB2*V1*TANALF*ALOGRAT/(DB3-DE3)
93300 CALL FSTRESS(FELTHAM,STRESS)
93400 EFRICT=2.0*PI*RB*V1*CYLLENG*EM*STRESS/SQRT3
93500 RETURN
93600 END
```

Appendix B

Double Triangle Axi-symmetric Upper Bound Computer Programme - AXY2T

This programme solves the double triangle axi-symmetric upper bound problem for direct rod extrusion. A similar optimization technique is used as in Appendix A but incorporating variance of four angles, α, β, δ and ε (defined in section 2.2.2).

The programme is unsuitable for Telex operation and should be submitted as a J4 category job for overnight running.

Input:-

No requests for data input is made.

Internal Constants and Values:-

Extrusion Ratio (80:1)

Billet Radius 37.5 mms

Ram Speed 1 mm/sec

Guesses for initial angles: $\alpha = 40^{\circ}$

$\beta = 25^{\circ}$

$\delta' = 70^{\circ}$

$\varepsilon' = 80^{\circ}$

Output:-

Values of input data

Angles α, β, δ, ε.

Value of (Extrusion Pressure/σ)

```
00100 PROGRAM AXY2T(INPUT,OUTPUT,TAPE5=INPUT,TAPE6=OUTPUT)
00200C PROGRAMME TO EVALUATE THE SOLUTION FOR A DOUBLE TRIANGLE UPPER
00300C SOLUTION FOR DIRECT ROD EXTRUSION. THE METHOD IS THAT OF HALLING
00400C AND MITCHELL. OUTPUT IS IN THE FORM..(PRESSURE/STRESS).
00500C FOUR ANGLES ARE USED TO DESCRIBE THE DEFORMATION ZONE.
00600C
00700C*****************************************************************
00800 COMMON/1/ PE,RB,RE,V3,V1,ER,PI,ALPHA,BETA,DELTA,EPSYLON,ALAMBDA,GAMMA,
00900+S,T,U,KKK
01000 COMMON/2/ AA,B,C,D,E,A,G
01100 COMMON/3/ SA,SB,SC,SD,SE,SG,SL,SP,CA,CB,CC,CE,CL,SED,SDG,SAMG,SEMG,SGB
01200 COMMON/4/ E12,E23,E45,E46,E24,E2,E4,V46F,V45,V46H,V12,V23,V24D
01300 COMMON/5/ ERATIO(100),ALP(100),BET(100),DELT(100),EPSYL
01400+(100),ALOADS(100)
01500 COMMON/6/ X(4)
01600C
01700C
01800 PRINT*,'ENTER THE VALUE OF EXTRUSION RATIO.'
01900 ER=80.0
02000C
02100C
02200C
02300 RB=0.0375
02400 V3=0.001
02500C
02600C     INITIAL GUESSES OF THE FOUR ANGLES.
02700C
02800 X(1)=40.0
02900 X(2)=25.0
03000 X(3)=70.0
03100 X(4)=80.1
03200 PI=3.1415
03300C
03400C
03500C
03600C
03700 RE=RB/SQRT(ER)
03800 V1=V3*RB*RB/(RE*RE)
03900C
04000 CALL LIBRI
04100C
04200C
04300C
04400C
04500 STOP
04600 END
04700C
04800C
04900 SUBROUTINE CONVERT
05000C
05100C ROUTINE CHANGES THE UNITS TO MKS AND ANGLES TO RADIANS.
05200C
05300 COMMON/1/ PE,RB,RE,V3,V1,ER,PI,ALPHA,BETA,DELTA,EPSYLON,ALAMBDA,GAMMA,
05400+S,T,U,KKK
05500 COMMON/6/ X(4)
05600 RB=RB/1000.
05700 V3=V3/1000.
05800 RE=RE/1000.
05900 V1=V1/1000.
06000 ALPHA=ALPHA/57.2958
06100 BETA=BETA/57.2958
06200 DELTA=DELTA/57.2958
06300 EPSYLON=EPSYLON/57.2958
06400 RETURN
06500 END
06600C
06700C
06800 SUBROUTINE LIBRI
06900C
07000 SETS UP THE PROBLEM FOR MINIMIZATION.
07100 COMMON/1/ PE,RB,RE,V3,V1,ER,PI,ALPHA,BETA,DELTA,EPSYLON,ALAMBDA,GAMMA,
07200+S,T,U,KKK
07300 COMMON/2/ AA,B,C,D,E,A,G
07400 COMMON/3/ SA,SB,SC,SD,SE,SG,SL,SP,CA,CB,CC,CE,CL,SED,SDG,SAMG,SEMG,SGB
07500 COMMON/4/ E12,E23,E45,E46,E24,E2,E4,V46F,V45,V46H,V12,V23,V24D
07600 COMMON/5/ ERATIO(100),ALP(100),BET(100),DELT(100),EPSYL(100),ALOADS
07700+(100)
07800 COMMON/6/ X(4)
07900 LOGICAL LINE,LOGW
08000 DIMENSION IXTYP(4),IGTYP(3),LINE(3),LOGW(11),W(76)
08100 COMMON/HAF/ MET,IPRIN,IT
08200 COMMON/7/ M
08300 EXTERNAL CALC,DFUNC,DDFUNC,MON,MONE
08400 DATA N,INF,IST,MAXI,IFAIL/4,0,1,500,0/
08500 DATA EST,RAX,AAX/8.0,1.0E-3,1.0E-3/
08600 M=2
08700 MET=1
08800 IPRIN=0
08900 IT=0
09000C
09100C  MAX. VALUES OF THE ANGLES=90 DEG.
09200C
09300 IXTYP(1)=90
09400 IXTYP(2)=90
09500 IXTYP(3)=90
09600 IXTYP(4)=90
09700 IGTYP(1)=3
09800 IGTYP(2)=1
09900 LINE(1)=.FALSE.
10000 LINE(M)=.FALSE.
10100 M2N=M+2*N
10200 IW=5*N+4*M+M*N+2*N*N
10300 14 FORMAT(*POSITION 1*./4E12.5
10400C
10500C   LIBRARY MINIMIZATION ROUTINE.
10600C
10700 CALL E04HAF(N,M,X,EST,RAX,AAX,IST,INF,MET,LOGW,M2N,W,IW,IXTYP,
10800+IGTYP,LINE,CALC,DFUNC,DDFUNC,MON,MONE,IPRIN,MAXI,IFAIL)
10900 WRITE(6,961) IFAIL,ER
11000 WRITE(6,969) RE,A,E12,E23,E45,E46,E24,E2,E4
11100 WRITE(6,902) EST,(X(I),I=1,N)
11200 WRITE(6,901) IPRIN,MAXI
```

```
11300 STOP
11400 901 FORMAT(15,*ITERATIONS*,15,*PENALTY EVALUATIONS*////)
11500 902 FORMAT(*FINAL RESULT IS*,E20.8,*AT*/(10(6E15.6/)))
11600 961 FORMAT(/*IFAIL =*,I3,*       EXTRUSION RATIO IS  =  *,F8.3)
11700 969 FORMAT(*EXTRUSION RADIUS= *,E12.5,*A = *,E12.5,/* E12 = *,E12.5,
11800+* E23 = *,E12.5,* E45 = *,E12.5,/* E46 = *,E12.5,* E24 = *,E12.5,/
11900+* E2 = *,E12.5,* E4 = *,E12.5//)
12000C
12100 END
12200 SUBROUTINE MONE(N,M,URMIN,XMIN,GMIN,UMIN,IORD)
12300C
12400C PROGRESS MONITOR.
12500C
12600 DIMENSION URMIN(3),XMIN(4),GMIN(3),UMIN(3)
12700 COMMON/HAF/ MET,IPRIN,IT
12800 WRITE(6,1007)
12900 WRITE(6,1006) (I,URMIN(I),I=1,M)
13000 WRITE(6,1000) IORD
13100 WRITE(6,1001)
13200 WRITE(6,1002) (I,XMIN(I),I=1,N)
13300 WRITE(6,1003)
13400 WRITE(6,1004) (I,GMIN(I),I=1,M)
13500 WRITE(6,1005)
13600 WRITE(6,1006) (I,UMIN(I),I=1,M)
13700 1000 FORMAT(/,*EXTRAPOLATION SOLUTION ORDER= *,I5)
13800 1001 FORMAT(/,*SOLUTION VECTOR*)
13900 1002 FORMAT(10(4(3X,1HX,I3,E12.5)/))
14000 1003 FORMAT(*CONSTRAINTS AND OBJECTIVES FNS*)
14100 1004 FORMAT(10(4(4X,3HCON,I3,E12.5)/))
14200 1005 FORMAT(*DUAL SOLUTION OF EXTRAPOLATED SOLUTIONS*)
14300 1006 FORMAT(10(4(3X,4HDUAL,I3,E12.5)/))
14400 1007 FORMAT(///*DUAL SOLUTION AT END POINT OF CYCLE*)
14500 RETURN
14600 END
14700 SUBROUTINE MONI(N,M,XR,PRXR,PG,ALOAD,R,ITCH,NEWCYC,NP,NG,NH,NRP)
14800C
14900C  PROGRESS MONITOR.
15000C
15100 LOGICAL NEWCYC
15200 DIMENSION XR(4),PG(4),ALOAD(3)
15300 COMMON/1/ PE,RB,RE,V3,V1,ER,PI,ALPHA,BETA,DELTA,EPSYLON,
15400+ALAMDA,GAMMA,S,T,U,KKK
15500 COMMON/2/ AA,B,C,D,E,A,G
15600 COMMON/4/ E12,E23,E45,E46,E24,E2,E4,V46F,V45,V46H,V12,V23,V24D
15700 COMMON/HAF/ MET,IPRIN,IT
15800 IT=IT+IPRIN
15900 IF(.NOT.NEWCYC) GO TO 100
16000 IT=0
16100 WRITE(6,1000) R
16200 100 WRITE(6,1001) IT,PRXR
16300 IF(ITCH.LE.0) WRITE(6,1006)
16400 IF(ITCH.EQ.3.OR.ITCH.EQ.-3) WRITE(6,1007)
16500 IF(ITCH.EQ.2.OR.ITCH.EQ.-2) WRITE(6,1008)
16600 WRITE(6,1009)
16700 WRITE(6,1010) (J,XR(J),J=1,N)
16800 IF(MET.LT.1)GO TO 106
16900 WRITE(6,1002)
17000 WRITE(6,1003) (I,PG(I),I=1,N)
17100 106 WRITE(6,1011)
17200 WRITE(6,1012) (I,ALOAD(I),I=1,M)
17300 1000 FORMAT(/*BEGINING OF CYCLE FOR R= *,E15.6)
17400 1001 FORMAT(/*ITERATION NO *,I3,*   PENALTY FUNCTION VALUE=*,E15.6)
17500 1002 FORMAT(*PENALTY GRADIENT*)
17600 1003 FORMAT(10(4(3X,1HG,I3,E12.5)/))
17700 1006 FORMAT(/*LINE SEARCH TROUBLES*)
17800 1007 FORMAT(1H ,9HH NOT PAC)
17900 1008FORMAT(1H ,7HH INDEF)
18000 1009 FORMAT (/*SOLUTION VECTOR*)
18100 1010 FORMAT(10(4(3X,1HX,I3,E12.5)/))
18200 1011 FORMAT(*CONSTRAINTS AND OBJECTIVE FNS*)
18300 1012 FORMAT(10(4(4X,3HCON,I3,E12.5)/))
18400 WRITE(6,1013) RE,A,ER,PE
18500 WRITE(6,1014) E12,E23,E45,E46,E24,E2,E4
18600 1013 FORMAT(6X,*RE= *,E12.5,3X,*A= *,E12.5,*  ER= *,E12.5,* PE=*,E12.5)
18700 1014 FORMAT(*  E12= *,E12.5,*  E23= *,E12.5,*  E45= *,E12.5,
18800+*  E46= *,E12.5,/,*  E24= *,E12.5,*  E2= *,E12.5,*  E4= *,E12.5)
18900C PRINT*,V12,V23,V24D,V45,V46F,V46H
19000 RETURN
19100 END
19200C
19300 SUBROUTINE GEOM(ANGLE,PI)
19400C
19500C   ANGLES KEPT BELOW 90 DEG.
19600C
19700 IF(ANGLE)30,20,10
19800 10 IF(ANGLE.LT.PI/2.)RETURN
19900 ANGLE=ANGLE-PI/2.
20000 GO TO 10
20100 20 PRINT*,' THERE IS AN ERROR. ALPHA,BETA,DELTA,EPSYLON = 0 DEGREES
20200 30 IF(ANGLE.GT.0.)RETURN
20300 ANGLE=ANGLE+PI/2.
20400 GO TO 30
20500 END
20600C
20700C
20800 SUBROUTINE CALC(N,X,I,ALOAD)
20900C
21000C  MAIN CALCULATION.
21100C
21200 COMMON/1/ PE,RB,RE,V3,V1,ER,PI,ALPHA,BETA,DELTA,EPSYLON,ALAMBDA,GAMMA,
21300+S,T,U,KKK
21400 COMMON/2/ AA,B,C,D,E,A,G
21500 COMMON/3/ SA,SB,SC,SD,SE,SG,SL,SP,CA,CB,CC,CE,CL,SED,SDG,SAMG,
21600+SEMG,SGB
21700 COMMON/4/ E12,E23,E45,E46,E24,E2,E4,V46F,V45,V46H,V12,V23,V24D
21800 COMMON/7/ M
21900 DIMENSION X(4)
22000 15 FORMAT(*POSITION 2=*,/4E12.5)
22100 ALPHA=X(1)/57.2958
22200 BETA=X(2)/57.2958
22300 DELTA=X(3)/57.2958
22400 EPSYLON=X(4)/57.2958
```

```
22500 999 FORMAT(2X,E12.5,3X,E12.5,3X,E12.5,3X,E12.5)
22600 AA=1./TAN(ALPHA)
22700 B=1./TAN(BETA)
22800 C=1./TAN(DELTA)
22900 E=1./TAN(EPSYLON)
23000 A=((RB*(C+E))-(RE*(C+AA)))/(B+E)
23100 D=(RE*AA)+(A*B)
23200C
23300 GAMMA=ATAN(ABS((RE-A)/D))
23400 G=1./TAN(GAMMA)
23500 PE=ATAN(RE/(D+(A*E)))
23600 ALAMBDA=ATAN((RB-RE)/(D+(RB-A)*B))
23700 SL=SIN(ALAMBDA)
23800 CL=COS(ALAMBDA)
23900 IF(I.EQ.1) GO TO 400
24000 IF(A.GT.RE) GO TO 8000
24100 CALL VELOCIT
24200 GO TO 9000
24300 8000 CALL VELO
24400 9000 CALL ENERGYC
24500 16 FORMAT(=ENERGY VALUES=,3E12.5,/4E12.5)
24600 EK=E12+E23+E45+E46+E24+E2+E4
24700C
24800 ALOAD=EK/(PI*V3*RB*RB)
24900 17 FORMAT(=ALOAD=,E12.5)
25000 GO TO 600
25100 400 ALOAD=((RB-RE)*C)+((RB-A)*E)-(RE*AA)-(A*B)
25200 600 RETURN
25300 END
25400 SUBROUTINE VELO
25500C
25600C CALCULATES THE VELOCITY DISCONTINUITIES FOR A<RE.
25700C
25800 COMMON/1/ PE,RB,RE,V3,V1,ER,PI,ALPHA,BETA,DELTA,EPSYLON,ALAMBDA,GAMMA,
25900+S,T,U,KKK
26000 COMMON/2/ AA,B,C,D,E,A,G
26100 COMMON/3/ SA,SB,SC,SD,SE,SG,SL,SP,CA,CB,CC,CE,CL,SED,SDG,SAMG,SEMG,SGB
26200 COMMON/4/ E12,E23,E45,E46,E24,E2,E4,V46F,V45,V46H,V12,V23,V24D
26300 SE=SIN(EPSYLON)
26400  SA=SIN(ALPHA)
26500 SB=SIN(BETA)
26600 CA=COS(ALPHA)
26700 CB=COS(BETA)
26800 CC=COS(DELTA)
26900 CE=COS(EPSYLON)
27000 SG=SIN(GAMMA)
27100 CG=COS(GAMMA)
27200 SDG=SIN(DELTA+GAMMA)
27300 SAMG=SIN(ALPHA-GAMMA)
27400 SEMG=SIN(EPSYLON-GAMMA)
27500 SGB=SIN(GAMMA+BETA)
27600 SED=SIN(EPSYLON+DELTA)
27700 SC=SIN(DELTA)
27800 V46F=V3*SE/SED
27900 V45=V3*SC/SED
28000 V46H=V46F*RB/RE
28100 V12=V1*SL/SIN(ALPHA+ALAMBDA)
28200 SBMG=SIN(BETA-GAMMA)
28300 V23=V45*SIN(GAMMA+EPSYLON)/SBMG
28400 V24D=V45*SIN(BETA+EPSYLON)/SBMG
28500 RETURN
28600 END
28700 SUBROUTINE VELOCIT
28800C
28900C CALCULATES THE VELOCITY DISCONTINUITIES FOR A> E.
29000C
29100 COMMON/1/ PE,RB,RE,V3,V1,ER,PI,ALPHA,BETA,DELTA,EPSYLON,ALAMBDA,GAMMA,
29200+S,T,U,KKK
29300 COMMON/2/ AA,B,C,D,E,A,G
29400 COMMON/3/ SA,SB,SC,SD,SE,SG,SL,SP,CA,CB,CC,CE,CL,SED,SDG,SAMG,SEMG,SGB
29500 COMMON/4/ E12,E23,E45,E46,E24,E2,E4,V46F,V45,V46H,V12,V23,V24D
29600C
29700C
29800 SA=SIN(ALPHA)
29900 SB=SIN(BETA)
30000 SC=SIN(DELTA)
30100 SE=SIN(EPSYLON)
30200 CA=COS(ALPHA)
30300 CB=COS(BETA)
30400 CC=COS(DELTA)
30500 CE=COS(EPSYLON)
30600 SG=SIN(GAMMA)
30700 CG=COS(GAMMA)
30800 SED=SIN(EPSYLON+DELTA)
30900 SDG=SIN(DELTA+GAMMA)
31000 SAMG=SIN(ALPHA-GAMMA)
31100 SEMG=SIN(EPSYLON-GAMMA)
31200 SGB=SIN(GAMMA+BETA)
31300C
31400 V45=V3*SC/SED
31500 V46F=V45*SE/SC
31600 V23=V45*SEMG/SGB
31700 V12=V1*SIN(ALAMBDA)/SIN(ALAMBDA+ALPHA)
31800 V24D=V23*SIN(BETA+EPSYLON)/SEMG
31900 V46H=(V1*SA*SIN(ALAMBDA+GAMMA)/SIN(ALAMBDA+ALPHA))/SDG
32000C
32100 RETURN
32200 END
32300C
32400C
32500 SUBROUTINE ENERGYC
32600C
32700C  CALCULATE THE ENERGY DISSIPATIONS.
32800C
32900 COMMON/1/ PE,RB,RE,V3,V1,ER,PI,ALPHA,BETA,DELTA,EPSYLON,ALAMBDA,GAMMA,
33000+S,T,U,KKK
33100 COMMON/2/ AA,B,C,D,E,A,G
33200 COMMON/3/ SA,SB,SC,SD,SE,SG,SL,SP,CA,CB,CC,CE,CL,SED,SDG,SAMG,SEMG,
33300+SGB
33400 COMMON/4/ E12,E23,E45,E46,E24,E2,E4,V46F,V45,V46H,V12,V23,V24D
33500 DIMENSION F1(200),F2(200),F3(200),F4(200),F5(200),F6(200),F7(200)
33600CPRINT*,PI,A,V23,SB
```

```
33700 SP=SIN(PE)
33800 CP=1./TAN(PE)
33900 NSTEP=50
34000 E12=PI*RE*RE*V12/SA
34100C
34200 E23=PI*A*A*V23/SB
34300 E45=PI*V45*((RB*RB)-(A*A))/SE
34400 XMAX=EPSYLON
34500 XMIN=PE
34600 XSTP=(XMAX-XMIN)/50.
34700 X=XMIN-XSTP
34800 DO 22 I=1,NSTEP+1
34900 X=X+XSTP
35000 CSX=1./SIN(X)
35100 CTX=1./TAN(X)
35200 22 F4(I)=(C+E)*(CSX*CSX)/((CTX+C)*(CTX+C))
35300 CALL SIMPV(F4,NSTEP,XSTP,SINT)
35400 E46=2.*PI*V46F*RB*RB*SINT/SC
35500 IF(A.GT.RE) GO TO 6000
35600 EXMAX=EPSYLON
35700 EXMIN=PE
35800 EXSTP=(EXMAX-EXMIN)/50.
35900 EX=EXMIN-EXSTP
36000 DO 21 I=1,NSTEP+1
36100 EX=EX+EXSTP
36200 SEX=SIN(EX)
36300 CEX=COS(EX)
36400 COTEX=1./TAN(EX)
36500 COSECEX=1./SIN(EX)
36600 21 F3(I)=(C+COTEX)*(COSECEX*COSECEX)/((G-COTEX)*(G-COTEX)*(G-COTEX))
36700 CALL SIMPV(F3,NSTEP,EXSTP,SINT)
36800 E24=(2.*PI*V24D*(A*A)*(G-E)*(G-E)*SINT)/(SG*(C+E))
36900C
37000 SOIGMAX=(PI-BETA)
37100 SOIGMIN=ALPHA
37200 SOIGSTP=(SOIGMAX-SOIGMIN)/50.
37300 SOIG=SOIGMIN-SOIGSTP
37400 DO 20 I=1,NSTEP+1
37500 SOIG=SOIG+SOIGSTP
37600 SS=SIN(SOIG)
37700 CS=COS(SOIG)
37800 CTS=1./TAN(SOIG)
37900 CSSOIG=1./SS
38000C
38100 COSONE=COS(PI-DELTA-GAMMA)
38200 SINONE=SIN(PI-DELTA-GAMMA)
38300 VEL=(V46F*V46F)+(V24D*V24D)-(2.*V46F*V24D*COSONE)
38400 AINVEL=((C/(C+E))+(CTS*(G-E)+G*(E+B))/(G+B))*SQRT(VEL)
38500 DIFFVEL=(-CSSOIG*CSSOIG*(G-E)/(G+B))*SQRT(VEL)
38600 EDOTHET=SINONE*DIFFVEL
38700 EDOTPHI=AINVEL*(COSONE+CTS*SINONE)
38800 EDORTHE=COSONE*DIFFVEL
38900 EITHET=SQRT((EDOTHET*EDOTHET)+(EDOTPHI*EDOTPHI)+(0.5*EDORTHE
39000+*EDORTHE))
39100 AR=RE*(G-AA)*CSSOIG/(G-CTS)
39200 20 F1(I)=AR*AR*EITHET*SS
39300 CALL SIMPV(F1,NSTEP,SOIGSTP,SINT)
39400 E2=PI*SINT*SQRT(3.)
39500C
39600 ANUMAX=EPSYLON
39700 ANUMIN=PE
39800 ANUSTP=(ANUMAX-ANUMIN)/50.
39900 ANU=ANUMIN-ANUSTP
40000C
40100 DO 30 I=1,NSTEP+1
40200 ANU=ANU+ANUSTP
40300C
40400 SN=SIN(ANU)
40500 CN=COS(ANU)
40600 CSN=1./SN
40700 CTN=1./TAN(ANU)
40800 SDA=SIN(DELTA-ANU)
40900 CDA=COS(DELTA-ANU)
41000 VEL=V46F*(C+CTN)/(C+E)
41100 DVEL=-V46F*CSN*CSN/(C+E)
41200 ETHET=SDA*DVEL
41300 EPHI=VEL*(CDA+(CTN*SDA))
41400 ERTHET=CDA*DVEL
41500 EITHET=SQRT((ETHET*ETHET)+(EPHI*EPHI)+(0.5*ERTHET*ERTHET))
41600 E4A=RB*(C+E)*CSN/(C+CTN)
41700 E4B=A*(G-E)*CSN/(G-CTN)
41800 30 F2(I)=((E4A*E4A)-(E4B*E4B))*EITHET*SN
41900 CALL SIMPV(F2,NSTEP,ANUSTP,SINT)
42000 E4=PI*SINT*SQRT(3.)
42100 GO TO 7000
42200 6000 EXMAX=EPSYLON
42300 EXMIN=PE
42400 EXSTP=(EXMAX-EXMIN)/50.
42500 EX=EXMIN-EXSTP
42600 DO 24 I=1,NSTEP+1
42700 EX=EX+EXSTP
42800 SEX=SIN(EX)
42900 CEX=COS(EX)
43000 COTEX=1./TAN(EX)
43100 COSECEX=1./SEX
43200 24 F5(I)=COSECEX*COSECEX*(C+COTEX)/((G+COTEX)*(G+COTEX))
43300 CALL SIMPV(F5,NSTEP,EXSTP,SINT)
43400 E24=2.*PI*(A*A)*(SINT)*(G+E)/(SG*(C+E))
43500 SOIGMAX=(PI-BETA)
43600 SOIGMIN=ALPHA
43700 SOIGSTP=(SOIGMAX-SOIGMIN)/50.
43800 SOIG=SOIGMIN-SOIGSTP
43900 DO 25 I=1,NSTEP+1
44000 SOIG=SOIG+SOIGSTP
44100 SS=SIN(SOIG)
44200 CS=COS(SOIG)
44300 CTS=1./TAN(SOIG)
44400 CSSOIG=1./SS
44500 COSONE=COS(PI-DELTA+GAMMA)
44600 SINONE=SIN(PI-DELTA+GAMMA)
44700 VEL=(V46F*V46F)+(V24D*V24D)-(2.*V46F*V24D*COSONE)
44800 AINVEL=((C/(C+E))+(CTS*(G+E)+G*(E+B))/(G-B))*SQRT(VEL)
```

```
44900 DIFFVEL=(1-CSSQIG*CSSQIG*((G+E)/(G-B)))*SQRT(VEL)
45000 EDOTHET=SINONE*DIFFVEL
45100 EDOTPHI=AINVEL*(COSONE+CTS*SINONE)
45200 EDORTHE=COSONE*DIFFVEL
45300 EITHET=SQRT((EDOTHET*EDOTHET)+(EDOTPHI*EDOTPHI)+(0.5*EDORTHE
45400+*EDORTHE))
45500 AR=RE*(G+AA)*CSSQIG/(G+CTS)
45600 25 F6(I)=AR*AR*EITHET*SS
45700 CALL SIMPV(F6,NSTEP,SQIGSTP,SINT)
45800 E2=PI*SINT*SQRT(3.)
45900 ANUMAX=EPSYLON
46000 ANUMIN=PE
46100 ANUSTP=(ANUMAX-ANUMIN)/50.
46200 ANU=ANUMIN-ANUSTP
46300 DO 26 I=1,NSTEP+1
46400 ANU=ANU+ANUSTP
46500 SN=SIN(ANU)
46600 CN=COS(ANU)
46700 CSN=1./SN
46800 CTN=1./TAN(ANU)
46900 SDA=SIN(DELTA-ANU)
47000 CDA=COS(DELTA-ANU)
47100 VEL=V46F*(C CTN)/(C+E)
47200 OVEL=-V46F*CSN*CSN/(C+E)
47300 E HET=SDA*OVEL
47400 EPHI=VEL*(CDA+(CTN*SDA))
47500 ERTHET=CDA*OVEL
47600 EITHET=SQRT((ETHET*ETHET)+(EPHI*EPHI)+(0.5*ERTHET*ERTHET))
47700 E4A=RB*(C+E)*CSN/(C+CTN)
47800 E4B=A*(G+E)*CSN/(G+CTN)
47900 26 F7(I)=((E4A*E4A)-(E4B*E4B))*EITHET*SN
48000 CALL SIMPV(F7,NSTEP,ANUSTP,SINT)
48100 E4=PI*SINT*SQRT(3.)
48200 7000 RETURN
48300 END
48400C
48500C
48600 SUBROUTINE RECONVT(ALOAD)
48700C
48800C  CONVERTS ANGLES BACK TO DEGREES.
48900C
49000 COMMON/1/ PE,RB,RE,V3,V1,ER,PI,ALPHA,BETA,DELTA,EPSYLON,ALAMBDA,GAMMA,
49100+S,T,U,KKK
49200 COMMON/2/ AA,B,C,D,E,A,G
49300 COMMON/5/ ERATIO(100),ALP(100),BET(100),DELT(100),EPSYL(100),ALOADS(100)
49400C
49500 ALP(KKK)=ALPHA*57.2958
49600 BET(KKK)=BETA*57.2958
49700 DELT(KKK)=DELTA*57.2958
49800 EPSYL(KKK)=EPSYLON*57.2958
49900 ERATIO(KKK)=ER
50000 ALOADS(KKK)=ALOAD
50100C
50200 RETURN
50300 END
50400C
50500C
50600 SUBROUTINE SIMPV(F,NSTEP,H,SINT)
50700C
50800C  PERFORMS SIMPSONIS RULE INTEGRATION.
50900C
51000 DIMENSION F(200),X(4)
51100C
51200 IF(MOD(NSTEP,2).EQ.0)GO TO 1
51300 WRITE(6,61)NSTEP
51400 61 FORMAT(*EXECUTION TERMINATEDIN SIMPV BY ODD NTEP= *,I6)
51500 STOP 3
51600 1 SINT=0
51700 DO 2 J=2,NSTEP,2
51800 2 SINT=SINT+F(J-1)+4.*F(J)+F(J+1)
51900 SINT=SINT*H/3.
52000C
52100 RETURN
52200 END
52300C
52400C
52500 SUBROUTINE RITOUT
52600C
52700C  WRITES OUT THE ANSWER.
52800C
52900 COMMON/1/ PE,RB,RE,V3,V1,ER,PI,ALPHA,BETA,DELTA,EPSYLON,ALAMBDA,
53000+GAMMA,S,T,U,KKK
53100 COMMON/5/ ERATIO(100),ALP(100),BET(100),DELT(100),EPSYL(100),ALOADS
53200+(100)
53300 INTEGER S,T,U
53400 V3=V3*1000.
53500 PRINT 40,RB,V3
53600 40 FORMAT(*BILLET RADIUS= *,F4.1,*MMS. RAM VELOCITY= *,F4.1,
53700+*MM/SEC*//*EXTRUSION RATIO*,8X,*ALPHA*,8X,*BETA*,8X,
53800+*DELTA*,8X,*EPSYLON*,8X,*P/K= *)
53900 WRITE(6,50)(ERATIO(I),ALP(I),BET(I),DELT(I),EPSYL(I),ALOADS(I),
54000+I=S,T,U)
54100 50 FORMAT(4X,F7.3,6X,F7.3,6X,F7.3,6X,F7.3,6X,F7.3,6X,F7.3,6X,F7.3)
54200C
54300 RETURN
54400 END
54500C
54600 FOLLOWING ROUTINES MUST BE SPECIFIED FOR THE MINIMIZATION
54700C ROUTINE TO OPERATE, BUT DO NOT BECOME INVOLVED IN THE CALC.
54800C
54900 SUBROUTINE DFUNC(N,X,I,G)
55000 DIMENSION G(4),X(4)
55100 RETURN
55200 END
55300 SUBROUTINE DDFUNC(N,X,I,DG)
55400 DIMENSION DG(4,4),X(4)
55500 RETURN
55600 END
```

Appendix C

Computer Programme for calculating Equivalent Stress and Strain values from Torsion Data.
The programme uses the analysis of Fields and Backhoffen.[204] (section 2.4.1.1.).

Input:

Torque data must be available on local file 'tape 5' in the form:- Run Code, temperature, twist rate, number of data points, value of torque at each 0.1 revolution for the specified number of points. (^{o}C, rev/min, N)

Internal Values

Specimen radius = 5mms
Specimen gauge length = 10 mms

External References

The programme requires the curve fitting routine 'LSFIT' to be available.[205]

Output

Local file 'Tape 6' contains equivalent stress and strain values in ascending strain rate, in groups of equal temperature.

```
00100 PROGRAM TORANAL (INPUT,OUTPUT,TAPE5,TAPE6,TAPE7)
00200 DIMENSION TOR(14,150),ALT(14,150),ALM(14,150),
00300*ENI(14,150),ALE(14),F(14),EM(150),GAMMA(150),EDOT(14)
00400*,DX(150),DY(150),IBCD(8),INAM(14)
00500 COMMON /COEFF /COEFFS (210)
00600 DATA IBCD/8H10H          /
01200C  PROGRAM CALCULATES SHEAR STRESS/ SHEAR STRAIN FROM
01300C  RAW TORQUE TWIST DATA, FOLLOWING THE METHOD
01400C  OF FIELDS AND BACKHOFFEN.
01500C
01600C********************
01700C  CUBIC FIT FOR N
01800C*****************
01900C  I IS USED TO DEFINE ANGLE THETA..RADIANS/UNIT LENGTH
02000C  K DEFINES THE STRAIN RATE
02100C
02200C  SET UP INITIAL CONSTANTS
02300C
02400 PI = 3.141592654
02500 R = 0.005
02600 EL = 0.01
02700 ITEMP = 250
02800 GAMMA (1) = 0.0
02900 CONST = 2.0*PI*R*R*R
03000 SQRT3 = SQRT(3.0)
03100C
03200 10 K = 1
03300    IBCD(1) = 10H3RD ORDER
03400    NMIN = 900
03500    READ (5,500)NAME
03600 20 READ (1,END.=40,5,510)NAME,TEMP,EDOT(K),NPTS,(TOR(K,I),I=1,NPTS)
03700C
03800C  SELECT RUNS OF DESIRED CONSTANT TEMPERATURE
03900C
04000    IF (ITEMP .NE. IFIX(TEMP)) GO TO 20
04300    NMIN = MIN0(NMIN,NPTS)
04400C
04500    WRITE (6,620) NAME
04600    PRINT 620,NAME
04700C  CALCULATE THETA,GAMMA,LN(THETA),LN(TORQUE)
04800C
04900          MIN = NMIN - 1
05000    DO 30 II=1,MIN
05100          III = II + 1
05200          THET = PI*FLOAT(III)/(EL*5.0)
05300          GAMMA(III) = THET*R
05400          ALT(K,III) = ALOG(THET)
05500       30 ALM(K,III) = ALOG(TOR(K,III))
05600          KMAX = K
05700          K = K + 1
05800          GO TO 20
05900C
06000C  CALCULATE 'N' AS A FUNCTION OF TORQUE AND THETA
06100C  USING A THIRD ORDER POLYNMIAL TO FIT THE CURVE, AND
06200C  HENCE GET THE GRADIENT AT EVERY POINT.
06300C
06400 40 DO 75 K=1,KMAX
06500    DO 50 I=1,MIN
06600          DY(I) = ALM(K,I)
06700       50 DX(I) = ALT(K,I)
06800          CALL LSFIT(DX,DY,MIN,0,0,3,7,IBCD  )
06900C  EXTRACT COEFFICIENTS OF FITTED CURVE
07000    DO 60 II=1,4
07100       60 F(II) = COEFFS(6*II)
07200    DO 70 I=1,MIN
07300          II = I+1
07400          ENI = F(2)+2.*F(3)*ALT(K,I)
07500          ENJ = ENI + 3.0*F(4)*ALT(K,I)*ALT(K,I)
07600C      70 EN(K,II) = ENJ + 4.0*F(5)*(ALT(K,I)**3)
07700       70 EN(K,II) = ENJ
07800       75 ALE(K) = ALOG(EDOT(K))
07900C
08000C  CALCULATE 'M' FROM A LINEAR FIT OF LOG TORQUE VS LOG TWIST RATE
08100C
08200 IBCD(1) = 10HLINEAR FIT
08300       DO 90 I=1,MIN
08400       DO 80 K=1,KMAX
08500          80 DY(K) = ALM(K,I)
08600          CALL LSFIT(ALE,DY,KMAX,0,0,1,7,IBCD )
08700          GAMMA(I) = GAMMA(I)/SQRT3
08800       90 EM(I+1) = COEFFS(3)
08900C
09000C  FINALLY CONVERT TORQUE TO SHEAR STRESS AND WRITE OUT RESULTS
09100C
09200 WRITE (6,610) ITEMP
09300          DO 100 K=1,KMAX
09400          DO 110 I=2,NMIN
09500                T1 = TOR(K,I)/CONST
09600            110 TOR(K,I) = T1*(3.0+EM(I)+EN(K,I))*SQRT3
09700                TOR(K,1) = 0.0
09800     100 WRITE (6,600) NMIN,(GAMMA(I),TOR(K,I),I=1,NMIN)
09900          IF (ITEMP .EQ.500) GO TO 120
10000          ITEMP = ITEMP + 60
10050 IF(ITEMP.EQ.490) ITEMP=ITEMP+10
10100          REWIND 5
10200          GO TO 10
10300 120 PRINT*,'OUTPUT ON TAPE 6 CONTAINS ETA,SIGMA,DATA IN ASCENDING'
10400*,/,'STAIN RATE, IN GROUPS BY TEMPERATURE, 3RD ORDER FIT '
10500     STOP
10600 500 FORMAT (A10)
10700 510 FORMAT (A5,1X,F5.1,1X,F5.2,I3/9(1X,F6.3))
10800 600 FORMAT (13,5(E12.5))
10900 610 FORMAT (13,' DEG C.  EQUIVALENT STRAIN-EQUIVALENT STRESS (N/M**2)')
11000 620 FORMAT (A5)
11100     END
```

Appendix D

Computer Programme to derive the constants in the hot working equation from either torque of flow stress data (sections 4.1.3.1 and 4.1.3.2.). The solution is obtained by variance of the values of A, α, n and ΔH via the constrained minimization technique - EO4HAF.[200,201]

Input:-

Data Type
Title to be printed above results
Initial guesses for A, α, n, ΔH.

Local file 'Tape 5' contains test data as:-

Outer radius, inner radius, gauge length (m)
Number of data sets
either - Torque, twist rate, temperature (N, rev/min, ^{o}C)
or Stress, strain rate, temperature (MN/m^2, sec^{-1}, ^{o}C)

Internal Constants and Values

$1.0 \times 10^{3} < A < 1.0 \times 10^{11}$ (sec^{-1})
$0.001 < \alpha < 1.0$ (m^2/MN)
$10 < n < 1.0$
$90000 < \Delta H < 400000$ (J/mole)

Output

Title
Constrained bounds for A, α, n, ΔH
Computed values for A, α, n, ΔH
Experimental torque, (stress), computed torque (stress), difference.

```
00100 PROGRAM TORMODL (INPUT,OUTPUT,TAPE6,TAPE5,TAPE7=INPUT)
00200C
00300C            VERSION 1.5       12 DEC 1977
00400C
00500 COMMON /DATA/ G,PI,SQRT3
00600 COMMON /LIMITS/ AMIN(4),MAX(4)
00700 COMMON/FACTOR/ FAC(4)
00800C
00900C CALCULATION OF VALUES OF CONSTANTS DELTA(M),N,ALPHA,AND A
01000C  FROM GIVEN INPUT VALUES OF EXPERIMENTAL TORQUE,TWIST RATE, AND TEMP
01100C  OR FROM STRESS,STRAIN RATE AND TEMP.
01200C
01300 PI = 3.14159
01400 G = 8.3143
01500 SQRT3 = SQRT(3.0)
01600C    SET LIMITS.  (1)=A  (2)=ALPHA  (3)=N   (4)=DELTA H
01700C              ALPHA IS IN M**2/MN UNITS  ALL ELSE IN MKS
01800C     ALL VARIABLES SCALED BY THE FACTORS SHOWN BELOW
01900   FAC(1) = 1.0E+06
02000   FAC(2) = 1.
02100   FAC(3)   1.
02200   FAC(4) = 10000.
02300 1 AMIN(1) = 1.0E-04
02400 AMIN(2) = .001
02500 AMIN(3) = 1.0
02600 AMIN(4) = 9.0
02700 MAX(1) = 100000
02800 MAX(2) = 1
02900 MAX(3) = 10
03000 MAX(4) = 40
03100 CALL DATA IN
03200 CALL CALCS
03300 CALL CONTROL
03400 CALL RESULTS
03500 CALL REDO (IK)
03600 IF (IK .EQ. 1) GO TO 1
03700 STOP
03800 END
03900C*************************************************************************
04000 SUBROUTINE DATA IN
04100 COMMON/1/ITYPE,MM,RMAX,RMIN,SL
04200 COMMON/2/GDOT(60),TEMP(60),T(60),TE(60)
04300 COMMON/3/X(4)
04400 COMMON /INFO/ NAME(80)
04500 PRINT*,'ENTER DATA TYPE---(1)TORQUE,TWIST,TEMP.'
04600 PRINT*,'                 (2)FLOW STRESS,STRAIN RATE,TEMP.'
04700 READ 101,ITYPE
04800 101 FORMAT(I1)
04900 403 FORMAT(*ENTER VALUES OF MAXIMUM AND MINIMUM SPECIMEN RADIUS AND*
05000+*SPECIMEN LENGTH,ALL IN METRES*)
05100 READ(5,*)RMAX,RMIN,SL
05200 404 FORMAT(*ENTER NUMBER OF POINTS,FOLLOWED BY THAT NUMBER OF*
05300+*VALUES OF TORQUE,TWIST RATE AND TEST TEMPERATURE,DEG C*)
05400 READ(5,*)MM,(TE(I),GDOT(I),TEMP(I),I=1,MM)
05500 PRINT*,'ENTER A HEADING TO BE PRINTED ABOVE THE OUTPUT LISTING'
05600 READ 100,NAME
05700 100 FORMAT(80A1)
05800 RETURN
05900 END
06000C*************************************************************************
06100 SUBROUTINE CONTROL
06200 LOGICAL LINE,LOGW
06300 DIMENSION IX(4),IC(5),LINE(5),LOGW(60),W(120)
06400 COMMON/1/ITYPE,MM,RMAX,RMIN,SL
06500 COMMON/2/GDOT(60),TEMP(60),T(60),TE(60)
06600 COMMON/3/X(4)
06700 COMMON/4/SUM
06800 COMMON/5/DIF(60)
06900 COMMON /LIMITS/ AMIN(4),MAX(4)
07000 COMMON /FACTOR/ FAC(4)
07100 EXTERNAL FUNCT,DFUNC,DDFUNC,MON,MONE,FLOWFUN
07200 DATA INF,IST/0,2/
07300C
07400 MAXI = 7000
07500 IFAIL = 1
07600C   ESTIMATED VALUE OF OBJECTIVE FUNCTION AT MINIMUM
07700   EST = 100
07800 5 PRINT 970,EST
07900   READ (*,END.=12,ERR.=5,7,*) EST
08000   GO TO 10
08100 12 EST = 100
08200 10 RAX = EST*1.0E-12
08300    AAX = EST/1000.
08400C
08500 CALL MODIF
08600C
08700C  M = NO. OF PROB FUNCTS.  N = NO. OF INDEPENDENT VARIABLES
08800 M = 5
08900 N = 4
09000 MET = INF + 1
09100 IPRIN = 5
09200 PRINT 980 ,IPRIN
09300 IT = 0
09400 M2N=M+2*N
09500 IW=5*N+4*M+M*N+2*N*N
09600C  LIMIT VARIABLES TO GE 0 LE FIGURES BELOW
09700 IX(4) = MAX(4)
09800 IX(3) = MAX(3)
09900 IX(2) = MAX(2)
10000 IX(1) = MAX(1)
10100C  NATURE OF PROB FUNCTS.  1=OBJ FUNCT.   2=NON NEGATIVE
10200 IC(5)=1
10300 IC(4)=2
10400 IC(3)=2
10500 IC(2)=2
10600 IC(1)=2
10700C NATURE OF PROB FUNCTS   .TRUE. = LINEAR FUNCTION
10800 LINE(5)=.FALSE.
10900 LINE(4)=.TRUE.
11000 LINE(3)=.TRUE.
11100 LINE(2)=.TRUE.
11200 LINE(1)=.TRUE.
```

```
11300C
11400C    ESTIMATE OF VALUES OF VARIABLES AT START
11500 15 X(1) = 1.5E+09
11600    X(2) = 0.04
11700    X(3) = 4.0
11800    X(4) = 156000.0
11900    PRINT 950,X
12000    READ (.END.=22,.ERR.=15,7,*) X
12100    GO TO 20
12200 22 X(1) = 1.5E+09
12300   X(2) = .04
12400   X(3) = 4.0
12500   X(4) = 156000.0
12600 20 X(1) = X(1)/FAC(1)
12700    X(4) = X(4)/FAC(4)
12800 25 DO 30 I=1,4
12900          IF(X(I).GT.AMIN(I).AND.X(I).LT.FLOAT(MAX(I))) GO TO 30
13000          PRINT 990,I
13100          READ (7,*) X(I)
13200           X(I) = X(I)/FAC(I)
13300          GO TO 25
13400       30 CONTINUE
13500C
13600 IF(ITYPE.EQ.1) GO TO 8001
13700 IF(ITYPE.EQ.2) CALL E04HAF(N,M,X,EST,RAX,AAX,IST,INF,MET,LOGW,M2N,W,IW
13800+,IX,IC,LINE,FLOWFUN,OFUNC,DDFUNC,MON,MONE,IPRIN,MAXI,IFAIL)
13900 GO TO 8002
14000 8001 CALL E04HAF(N,M,X,EST,RAX,AAX,IST,INF,MET,LOGW,M2N,W,IW,IX,IC,LINE,
14100+FUNCT,OFUNC,DDFUNC,MON,MONE,IPRIN,MAXI,IFAIL)
14200 8002 SUM=EST
14300 IF(IFAIL .NE. 0) GO TO 900
14400 PRINT 965
14500 RETURN
14600 700 FORMAT (A1)
14700 900 PRINT 961,IFAIL
14800 950 FORMAT (* ESTIMATES OF A, ALPHA, N, DELTA H  AT THE START ARE*/
14900+             E12.5,1X,F5.2,1X,F5.2,1X,F8.1/
15000+             * ENTER NEW VALUES IF REQUIRED, OR ELSE (CR)*)
15100 961 FORMAT(*IFAIL=*,I2,'( 0=SUCCESSFUL . CONSULT BULLETIN FOR ERROR )')
15200 965 FORMAT(//*SUCCESSFUL MINIMISATION.  MINIMUM FOUND*/
15300+* THE RESULTS ARE ON LOCAL FILE ITAPE6I IN PRINTSF FORMAT*)
15400 970 FORMAT (* ESTIMATE OF THE SOLUTION MINIMUM IS *,E12.5/
15500+             * ENTER ANOTHER VALUE IF REQUIRED, OR ELSE (CR)*)
15600 980 FORMAT (* OUTPUT WILL BE GIVEN EVERY *,I2,* ITERATIONS*)
15700 990 FORMAT (* PRESENT ESTIMATE OF VARIABLE *,I1,* IS OUTSIDE THE*/
15800+             * SET LIMITS.....ENTER A NEW VALUE FOR THE ESTIMATE*)
15900 RETURN
16000 END
16100C*************************************************************
16200 SUBROUTINE MON(N,M,X,PRXP,PG,SUM,R,ITCH,NEWCYL,NP,NG,NH,NRP)
16300 LOGICAL NEWCYL
16400 DIMENSION X(4),PG(4),SUM(5)
16500C
16600 IF (ITCH .NE. 1) PRINT*,'ITCH HAS VALUE',ITCH,'CHECK BULLETIN'
16700 PRINT 92,SUM
16800 92 FORMAT(*SUM=*,5(E12.5))
16900 PRINT 99,X
17000 99 FORMAT(*A,ALPHA,N,DH=*,4(E15.5))
17100 RETURN
17200 END
17300C*************************************************************
17400 SUBROUTINE SIMPV(F,NSTEP,H,SINT)
17500C
17600C ROUTINE FOR APPPLYING SIMPSONTS RULE FOR INTEGRATION.
17700C
17800 DIMENSION F(200),X(4)
17900 IF(MOD(NSTEP,2).EQ.0)GO TO 1
18000 WRITE(6,61)NSTEP
18100 61 FORMAT(*EXECUTION TERMINATED IN SIMPV BY ODD NSTEP=*,I6)
18200 STOP
18300 1 SIN = 0.0
18400 DO 2 J=2,NSTEP,2
18500 2 SIN=SIN+F(J-1)+4.*F(J)+F(J+1)
18600 SINT=SIN*H/3.
18700 RETURN
18800 END
18900C*************************************************************
19000 SUBROUTINE CALCS
19100C                  EVALUATES VARIOUS CONSTANTS FOR SUB FUNCT
19200 COMMON /1/ ITYPE,MM,RMAX,RMIN,SL
19300 COMMON /2/ GDOT(60),TEMP(60),T(60),TE(60)
19400 COMMON /DATA/ G,PI,SQRT3
19500 COMMON /CALC/ NSTEP,NSTEP1,CONST(60),PI2,ASQRT3,R(60),RR(60),RSTEP
19600C
19700 NSTEP = 20
19800 NSTEP1 = NSTEP + 1
19900 RSTEP = (RMAX-RMIN)/FLOAT(NSTEP)
20000 PI2 = 2.0*PI
20100 DO 10 K=1,MM
20200       TEMP(K) = (TEMP(K) + 273.1)*G
20300    10 CONST(K) = PI2 *GDOT(K)/(SQRT3*SL)
20400 ASQRT3 = 1.0E-06*SQRT3
20500 R(1) = RMIN
20600 RR(1) = RMIN * RMIN
20700 DO 20 I=2,NSTEP1
20800       R(I) = R(I-1) + RSTEP
20900    20 RR(I) = R(I) * R(I)
21000 RETURN
21100 END
21200C*************************************************************
21300 SUBROUTINE FUNCT(N,X,I,SUM)
21400 DIMENSION X(4),F(200)
21500 COMMON/1/ITYPE,MM,RMAX,RMIN,SL
21600 COMMON/2/GDOT(60),TEMP(60),T(60),TE(60)
21700 COMMON/5/DIF(60)
21800 COMMON /DATA/ G,PI,SQRT3
21900 COMMON /CALC/ NSTEP,NSTEP1,CONST(60),PI2,ASQRT3,R(60),RR(60),RSTEP
22000 COMMON /LIMITS/ AMIN(4),MAX(4)
22100 COMMON /FACTOR/ FAC(4)
22200 IF (I.LT.5) GO TO 80
22300 SUM = 0.0
22400 POWER = 1.0/X(3)
```

```
      POWER2 = 2.0*POWER
      DO 10 K=1,MM
            EXPOW = EXP(X(4)*FAC(4)/TEMP(K))
            DO 20 J=1,NSTEP1
                  ZED = R(J) * CONST(K) * EXPOW
C           ZED = GOOT(K) * EXPOW
                  VAL1 = ZED/(X(1)*FAC(1))
                  VAL2 = VAL1**POWER+SQRT(1.0+(VAL1**POWER2))
               20 F(J) = RR(J) * ALOG(VAL2)
            CALL SIMPVIF,NSTEP,RSTEP,SINT)
            T(K) = PI2*SINT/(X(2) *RSQRT3)
C           T(K) = ALOG(VAL2)/X(2)
            DIF(K) = TE(K) - T(K)
         10 SUM = SUM + DIF(K) * DIF(K)
      RETURN
C
      80 SUM = X(1) - AMIN(1)
      RETURN
      END
C*****************************************************************
      SUBROUTINE RESULTS
      COMMON/1/ITYPE,MM,RMAX,RMIN,SL
      COMMON/2/GOOT(60),TEMP(60),T(60),TE(60)
      COMMON/3/X(4)
      COMMON/4/SUM
      COMMON/5/DIF(60)
      COMMON /LIMITS/ AMIN(4),MAX(4)
      COMMON /INFO/ NAME(80)
      COMMON /FACTOR/ FAC(4)
      DIMENSION AMAX(4)
      DO 10 I=1,4
            AMIN(I) = AMIN(I)*FAC(I)
            AMAX(I) = FAC(I) * FLOAT(MAX(I))
         10 X(I) = X(I)*FAC(I)
      WRITE(6,590)NAME
            590 FORMAT (/80A1)
      WRITE(6,600)
            600 FORMAT(//*MINIMISATION LIMITS ARE*/10X,*  MAX          MIN*)
      WRITE(6,610)AMAX(1),AMIN(1)
            610 FORMAT(*  A  =*,2(E12.5,2X))
      WRITE(6,615)AMAX(2),AMIN(2)
            615 FORMAT(*ALPHA*,6X,F5.3,7X,F5.3)
      WRITE(6,620)AMAX(3),AMIN(3)
            620 FORMAT(*  N  =*,5X,F5.2,7X,F5.2)
      WRITE(6,630)AMAX(4),AMIN(4)
            630 FORMAT(*D.H  =*,3X,F8.1,4X,F8.1)
      WRITE(6,1001)
      WRITE(6,1002)
      WRITE(6,1003)(X(I),I = 1,2)
      WRITE(6,1007)
      WRITE(6,1008)(X(I),I = 3,4)
      WRITE(6,1004)
      WRITE(6,1005)
 1001 FORMAT(//*VALUES OF CONSTANTS CALCULATED BY MINIMIZATION*/)
 1002 FORMAT(*     A (PER SEC)      ALPHA (M**2/MN)*)
 1003 FORMAT(E15.5,5X,F5.3)
 1007 FORMAT(*          N           DELTA(H) (J/MOLE)*)
 1008 FORMAT(8X,F4.2,8X,F8.1)
 1004 FORMAT(/'VALUES OF STRESS IN MN/M**2'/)
 1004 FORMAT(/*VALUES OF THEORETICAL AND EXPERIMENTAL TORQUE (N.M)*/)
 1005 FORMAT(*   EXPERIMENTAL     THEORETICAL     DIFFERENCE*)
      DO 100 I = 1,MM
      WRITE(6,1006)TE(I),T(I),DIF(I)
 1006 FORMAT(4X,F7.3,10X,F7.3,7X,F8.5)
  100 CONTINUE
      RETURN
      END
C*****************************************************************
C       UNUSED SUBROUTINES WHICH MUST BE PROVIDED FOR E04HAF
      SUBROUTINE MONE(N,M,DUEL,XMIN,FMIN,DMIN,IORD)
      DIMENSION DUEL(5),XMIN(5),FMIN(5),DMIN(5)
      RETURN
      END
      SUBROUTINE DFUNC(N,X,I,G)
      DIMENSION G(5),X(4)
      RETURN
      END
      SUBROUTINE DDFUNC(N,X,I,DG)
      DIMENSION DG(4,4),X(4)
      RETURN
      END
C*****************************************************************
      SUBROUTINE MODIF
C
C ROUTINE ENABLES THE MAX. AND MIN. VARIABLE LIMITS TO
C BE ALTERED.
C
      DIMENSION NUM(4),AMAX(4)
      DATA NUM(1),NUM(2),NUM(3),NUM(4)/0,0,0,0/
      COMMON /LIMITS/ AMIN(4),MAX(4)
      COMMON /FACTOR/ FAC(4)
C
      10 DO 20 I=1,4
            AMIN(I) = AMIN(I)*FAC(I)
         20 AMAX(I) = FAC(I)*FLOAT(MAX(I))
C
      PRINT 100,AMIN,AMAX
  100 FORMAT(24X,*A       ALPHA*,10X,*N*,9X,*DELTA H*/
     +*  MINIMUM VALUES :*,4E12.5/* MAXIMUM VALUES :*,
     +4E12.5)
      PRINT*,'DO YOU WANT TO CHANGE ANY OF THEM'
      READ 200,NSWER
  200 FORMAT (A1)
      IF (NSWER .NE. 'Y') GO TO 500
      PRINT*,'ENTER NUMBER 9 FOR THE VARIABLES THAT REQUIRE CHANGING. OR 0 FOR'
     +,' NO CHANGE.IN THE ORDER 1=A  2=ALPHA  3=N  4=DELTA H...IN FREE FORMAT'
      READ*,NUM
  500 DO 300 I=1,4
      IF (NUM(I) .EQ. 0) GO TO 450
      PRINT 400,I
      400 FORMAT(*ENTER NEW MIN AND MAX VALUES FOR VARIABLE *,I1)
      READ*,AMIN(I),AMAX(I)
```

```
33700         450 AMIN(I) = AMIN(I) /FAC(I)
33800         MAX(I) = IFIX(1.000001*AMAX(I)/FAC(I))
33900         NUM(I) = 0
34000     300 CONTINUE
34100     IF(MAX(2) .LT. 1) MAX(2) = 1
34200         IF(MAX(I).LE.0) MAX(I) = 1
34300     IF (NSWER .NE. IHY) GO TO 600
34400     PRINT*, NEW LIMITS ACCEPTED. VALUES ARE NOW'
34500     GO TO 10
34600 600 RETURN
34700     END
34800C*************************************************
34900 SUBROUTINE REDO (IK)
35000 IK = 0
35100 PRINT*,'DO YOU WANT TO RERUN THE PROGRAM WITH NEW LIMITS OR DATA'
35200 READ (7,700) NSWER
35300 IF (NSWER .NE. IHY) RETURN
35400 IK = 1
35500 PRINT*,'DO YOU WANT TO HAVE NEW INPUT DATA'
35600 READ (7,700) NSWER
35700 IF (NSWER .EQ. IHY) GO TO 10
35800 REWIND 5
35900 RETURN
36000 10 PRINT*,'ENTER DATAFILE NAME'
36100 READ (7,710) NAME
36200 CALL RETURN (SMTAPES)
36300 CALL GET(SMTAPES,NAME)
36400 REWIND 5
36500 RETURN
36600 700 FORMAT (A1)
36700 710 FORMAT (A7)
36800 END
36900CCCCCCCCCCCCCCCCCCCCCCCCCCCCCCCCCCCCCCCCCCCCCCCCCCCCCCCCCCCCCCCCCCCCCCCCCCCCCCCCCCCCCCCCCCCCCCCCCCCCCCCC
37000C
37100 SUBROUTINE FLOWFUN(N,X,I,SUM)
37200C
37300C ROUTINE USED WHEN STRESS,STRAIN RATE AND TEMPERATURE
37400C ARE TO BE MINIMIZED.
37500C
37600 DIMENSION X(4)
37700 COMMON/1/ ITYPE,MM,RMAX,RMIN,SL
37800 COMMON/2/ GDOT(60),TEMP(60),T(60),TE(60)
37900 COMMON/5/ DIF(60)
38000 COMMON/DATA/ G,PI,SQRT3
38100 COMMON/LIMITS/AMIN(4),MAX(4)
38200 COMMON/FACTOR/ FAC(4)
38300C
38400 IF(I.LT.5) GO TO 7001
38500 SUM = 0.0
38600 POWER=1.0/X(3)
38700 POWER2=2.0*POWER
38800 DO 7002 K=1,MM
38900 EXPON=EXP(X(4)*FAC(4)/TEMP(K))
39000 ZED=GDOT(K)*EXPON
39100 VAL1=ZED/(X(1)*FAC(1))
39200 VAL2=(VAL1**POWER)+SQRT((1.0+(VAL1**POWER2)))
39300 T(K)=(1.0/X(2))*ALOG(VAL2)
39400 DIF(K)=TE(K)-T(K)
39500.7002 SUM=SUM+(DIF(K)*DIF(K))
39600 RETURN
39700 7001 SUM=X(I)-AMIN(I)
39800 RETURN
39900 END
```

Appendix E

Computer programme to derive the constants in the hot working equation by the alternative manipulation of the torsion data, (section 4.1.3.3.). Solution is obtained by internal variation of A, α, n and ΔH and application of a least squares regression.

Input:-

Local file 'Tape 7' containing: outer radius, inner radius, gauge length (m) number of data sets
Torque, twist rate, temperature (N, rev/min, ^{o}C)

or:- manual input of data above.

Alloy identification number (numeric - 10 characters)

Internal Constants and Values:-

$100000 < \Delta H < 200000$ (J/mole)

$1 < n < 9$

$5 < LnA < 35$

Initial guesses:-

LnA = 20.0

n = 4.0

ΔH = 145000 J/mole

Output:

Values of constants, A, α, n, ΔH.
Specimen geometry
point number, twist rate (rev/sec), Temperature ^{o}C),
experimental torque (N.mm)
calculated torque (N.mm), difference.

```
00100 PROGRAM FSTORQ(INPUT,OUTPUT,TAPE5=INPUT,TAPE6=OUTPUT,TAPE7,TAPE9)
00200C      PROGRAM FSTORQ.FOR
00300C
00400C PROGRAM TO ANALYZE FLOW STRESS DATA OBTAINED IN A TORSION TEST
00500C
00600 DIMENSION NPPN(3),IFORM(16),MINVIO(3),MAXVIO(3),PRMIN(3),PRMAX(3)
00700 DIMENSION TORQ(150),THETA(150),TMP(150),C(3,3),CINV(3,3),D(3)
00800 DIMENSION X(150,3),U(150,3),V(150),XBAR(3),XSD(3),PAR(3),IDP(3)
00900 DIMENSION R(2),GT(150),RL(2),BETA(3),RHO(3),PHAT(3),RCUB(2),PNU(3)
01000 DATA IDP/'DEL H','N','LN A'/,CON/1.2092/
01100C
01200 PRINT*,'REMEMBER TO HAVE TAPE7 AS DATA FILE.'
01300 2 PRINT*,'DO YOU HAVE DATA ON TAPE7?'
01400 READ(5,1) NSWER
01500 1 FORMAT(A1)
01600 IF(NSWER.EQ.1HY) GO TO 3
01700 IF(NSWER.NE.1HN) GO TO 2
01800 PRINT*,'ENTER MAX AND MIN RADIUS,GAUGE LENGTH AND NO OF POINTS(>5)'
01900 READ(5,*) R(2),R(1),EL,NPTS
02000 PRINT*,'ENTER POINTS***TORQUE(NM),TWIST RATE(REV/SEC)AND TEMP(DEG.C)'
02100 READ(5,*)(TORQ(I),THETA(I),TMP(I),I=1,NPTS)
02200 PRINT*, ENTER AN ALLOY IDENTIFICATION (LESS THAN 10 CHARAC)'
02300 READ(5,*) IFILNAM
02400 GO TO 4
02500 3 PRINT*,'ENTER AN ALLOY IDENTIFICATION NUMBER'
02600 READ(5,*) IFILNAM
02700C
02800C READ IN THE DATA ON TAPE7: MAX RAD.MIN RAD. GAUGE LENGTH.NPTS.
02900C MAX TORQUE.REV PER SEC.TEMP(DEG.C)
03000C
03100 READ(7,*) R(2),R(1),EL,NPTS
03200 READ(7,*) (TORQ(I),THETA(I),TMP(I),I=1,NPTS)
03300C
03400 4 R(2)=R(2)*1000.0
03500 R(1)=R(1)*1000.0
03600 EL=EL*1000.0
03700C CONVERT TORQUE TO NEWTON-MILLIMETERS (INPUT AS NEWTON-METERS)
03800C
03900 DO 130 I=1,NPTS
04000 TORQ(I)=1000.0*TORQ(I)
04100C
04200C CONVERTS TWIST RATE TO RADIANS PER SECOND (INPUT AS REV PER MIN)
04300C
04400 THETA(I)=60.0*0.104720*THETA(I)
04500 130 CONTINUE
04600 WRITE(6,150) NPTS
04700 150 FORMAT(14,' DATA POINTS READ')
04800C
04900C
05000C CONVERT DATA TO REGRESSION FORM AND STANDARDIZE
05100C
05200C 1. CALCULATION OF MEANS FOR Y=TORQ. X1=LN(THETA). X2=1/(TMP+273)
05300C
05400 170 YBAR=0.0
05500 SSTRQ=0.0
05600 DO 180 I=1,3
05700 XBAR(I)=0.0
05800 XSD(I)=0.0
05900 180 CONTINUE
06000 DO 190 I=1,NPTS
06100 YBAR=YBAR+TORQ(I)
06200 XT=ALOG(THETA(I))
06300 X(I,1)=XT
06400 XBAR(1)=XBAR(1)+XT
06500 XT=1.0/(TMP(I)+273.0)
06600 X(I,2)=XT
06700 XBAR(2)=XBAR(2)+XT
06800 190 CONTINUE
06900 ENPTS=FLOAT(NPTS)
07000 ENPSQ=ENPTS*ENPTS
07100 YBAR=YBAR/ENPTS
07200 DO 200 I=1,2
07300 XBAR(I)=XBAR(I)/ENPTS
07400 200 CONTINUE
07500C
07600C 2. CALCULATION OF STANDARD DEVIATIONS FOR X1 AND X2
07700C
07800 DO 220 J=1,2
07900 SUM=0.0
08000 XB=XBAR(J)
08100 DO 210 I=1,NPTS
08200 XT=X(I,J)-XB
08300 U(I,J)=XT
08400 SUM=SUM+XT*XT
08500 210 CONTINUE
08600 XSD(J)=SQRT(SUM/ENPTS)
08700 220 CONTINUE
08800 DO 240 I=1,3
08900 DO 230 J=1,3
09000 C(I,J)=0.0
09100 230 CONTINUE
09200 C(I,I)=ENPTS
09300 D(I)=0.0
09400 240 CONTINUE
09500C
09600C 3. CALCULATION OF TOTAL SUM OF SQUARES ABOUT MEAN FOR Y
09700C 4. STANDARDIZATION OF X1 AND X2 INTO U1 AND U2
09800C 5. CALCULATION OF CROSS-PRODUCT SUMS NOT CHANGING IN ITERATION
09900C     (D1, D2, C(1,2))
10000C
10100 DO 250 I=1,NPTS
10200 YT=TORQ(I)-YBAR
10300 V(I)=YT
10400 SSTRQ=SSTRQ+YT*YT
10500 XT=U(I,1)/XSD(1)
10600 U(I,1)=XT
10700 D(1)=D(1)+XT*YT
10800 UT=U(I,2)/XSD(2)
10900 U(I,2)=UT
11000 D(2)=D(2)+UT*YT
11100 C(1,2)=C(1,2)+UT*XT
11200 250 CONTINUE
```

```
11300C
11400C PARAMETER RANGES AND VIOLATION INDICATORS
11500C
11600 PRMIN(1)=100000.0
11700 PRMIN(2)=1.0
11800 PRMIN(3)=5.0
11900 PRMAX(1)=200000.0
12000 PRMAX(2)=9.0
12100 PRMAX(3)=35.0
12200 DO 260 I=1,3
12300 MAXVIO(I)=-5
12400 MINVIO(I)=-5
12500 260 CONTINUE
12600C
12700C INITIALIZATION OF THE ITERATION
12800C
12900 K=0
13000C
13100C INITIAL PARAMETER VALUES FOR DELTA M = PAR(1), N = PAR(2), AND
13200C LN A = PAR(3)
13300C
13400 300 PAR(1)=145000
13500 PAR(2)=4.0
13600 PAR(3)=20.0
13700C
13800C LAMBDA, THE ITERATION STEP SIZE, MUST SATISFY 0 < LAMBDA <=1
13900C THE DEFAULT VALUE FOR LAMBDA IS 0.5
14000C
14100 ELMBDA=0.5
14200 390 FLMBDA=1.0-ELMBDA
14300C
14400C DELTA, THE CONVERGENCE CRITERION, MUST BE POSITIVE.  ITS DEFAULT
14500C VALUE IS 0.001
14600C
14700 DELTA=0.001
14800C
14900 490 ITMAX=25
15000 NSIMP=10
15100 WRITE(6,492) IOP
15200 492 FORMAT(=  K    ALPHA=,4X,A5,5X,A1,2X,A4)
15300C
15400C CALCULATE THE X3 VECTOR AND STANDARDIZE
15500C
15600 493 G=8.31
15700 ELSR3=1.732051*EL
15800 ELSR3L=ALOG(ELSR3)
15900 DELR3=0.0
16000 DELR3L=0.0
16100 SIGN=-1.0
16200 DO 495 I=1,2
16300 RT=R(I)
16400 XT=RT*RT*RT
16500 RCUB(I)=XT
16600 IF (RT.LE.0.0) GO TO 494
16700 XT=SIGN*XT
16800 DELR3=DELR3+XT
16900 DELR3L=DELR3L+XT*ALOG(RT)
17000 494 SIGN=1.0
17100 495 CONTINUE
17200 DO 500 I=1,NPTS
17300 GT(I)=G*(TMP(I)+273.0)
17400 500 CONTINUE
17500 510 POW=2.0/PAR(2)
17600 ENINV=1.0/PAR(2)
17700 EXPO=1.5*PAR(2)-0.5
17800 XBAR(3)=0.0
17900 XSD(3)=0.0
18000 D(3)=0.0
18100 C(1,3)=0.0
18200 C(2,3)=0.0
18300 DO 530 I=1,NPTS
18400 ARG=(PAR(1)/GT(I))-PAR(3)-ELSR3L
18500 CFN=THETA(I)=EXP(ARG)
18600 CFN=CFN**ENINV
18700 CSQD=CFN*CFN
18800 GAMMA=0.0
18900 SIGN=-1.0
19000 DO 520 J=1,2
19100 RT=R(J)
19200 IF (RT.LE.0.0) GO TO 519
19300 RT=RT**POW
19400 WT=SQRT(1.0+1.0/(CSQD*RT))
19500 GAMMA=GAMMA+SIGN*RCUB(J)*ALOG(1.0+WT)
19600 519 SIGN=1.0
19700 RL(J)=RT
19800 520 CONTINUE
19900 A14=SMPSN4(RL,CSQD,EXPO,NSIMP)
20000 XT=GAMMA-0.5*CFN*A14
20100 X(I,3)=XT
20200 XBAR(3)=XBAR(3)+XT
20300 530 CONTINUE
20400 XBAR(3)=XBAR(3)/ENPTS
20500 DO 540 I=1,NPTS
20600 UT=X(I,3)-XBAR(3)
20700 U(I,3)=UT
20800 XSD(3)=XSD(3)+UT*UT
20900 540 CONTINUE
21000 XSD(3)=SQRT(XSD(3)/ENPTS)
21100 DO 560 I=1,NPTS
21200 UT=U(I,3)/XSD(3)
21300 U(I,3)=UT
21400 D(3)=D(3)+UT*V(I)
21500 DO 550 J=1,2
21600 C(J,3)=C(J,3)+UT*U(I,J)
21700 550 CONTINUE
21800 560 CONTINUE
21900C
22000C DETERMINANT OF THE C-MATRIX
22100C
22200 DETC=ENPTS*(ENPTSQ-C(1,2)*C(1,2)-C(1,3)*C(1,3)-C(2,3)*C(2,3)) +2.
22300+0*C(1,2)*C(1,3)*C(2,3)
22400C
```

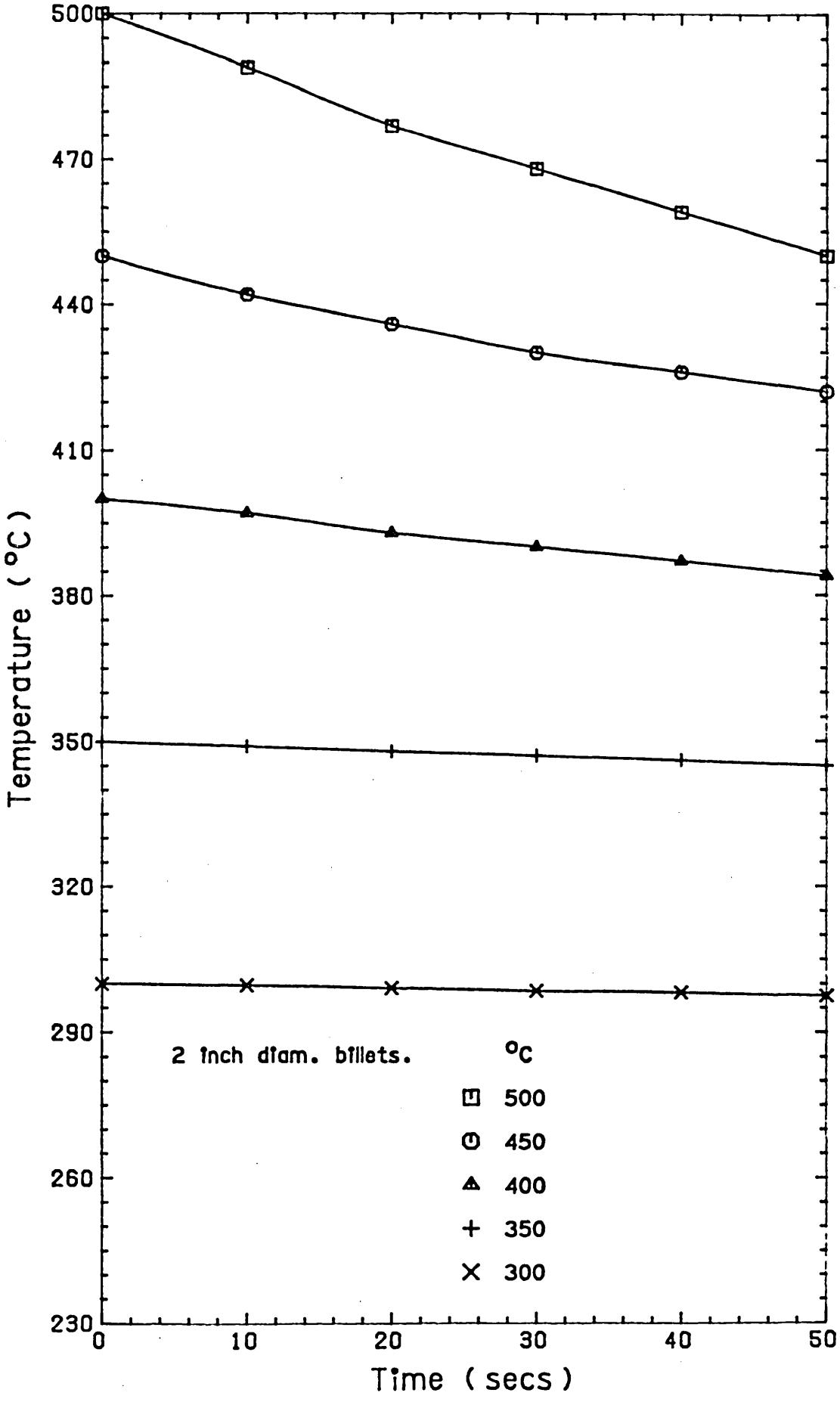
```
22500C INVERSE OF C. NOT SCALED BY DETC
22600C
22700 CINV(1.1)=ENPSQ-C(2.3)*C(2.3)
22800 CINV(2.2)=ENPSQ-C(1.3)*C(1.3)
22900 CINV(3.3)=ENPSQ-C(1.2)*C(1.2)
23000 CINV(1.2)=C(1.3)*C(2.3)-ENPTS*C(1.2)
23100 CINV(1.3)=C(1.2)*C(2.3)-ENPTS*C(1.3)
23200 CINV(2.3)=C(1.2)*C(1.3)-ENPTS*C(2.3)
23300 DO 580 I=1.2
23400 DO 570 J=I+1.3
23500 CINV(J.I)=CINV(I.J)
23600 570 CONTINUE
23700 BETA(I)=0.0
23800 580 CONTINUE
23900 BETA(3)=0.0
24000 DO 600 I=1.3
24100 DT=D(I)
24200C
24300C ESTIMATE THE REGRESSION PARAMETERS IN V=U*B
24400C
24500 DO 590 J=1.3
24600 BETA(J)=BETA(J)+DT*CINV(J.I)
24700 590 CONTINUE
24800 600 CONTINUE
24900C
25000C CONVERT BETAS TO RHOS AND THEN TO ESTIMATES OF ORIGINAL PARAMETERS
25100C
25200 RHOZ=YBAR
25300 DO 610 I=1.3
25400 XT=BETA(I)/DETC
25500 BETA(I)=XT
25600 XT=XT/XSD(I)
25700 RHO(I)=XT
25800 RHOZ=RHOZ-XT*XBAR(I)
25900 610 CONTINUE
26000 ENHAT=RHO(3)*DELR3/RHO(I)
26100 PHAT(2)=ENHAT
26200 PHAT(I)=G*RHO(2)/RHO(I)
26300 PHAT(3)=((RHO(3)*DELR3L/ENHAT)-RHOZ)/RHO(I)-ELSR3L
26400 ALFHAT=CON/RHO(3)
26500C
26600C OUTPUT CURRENT AND PREDICTED PARAMETER VALUES
26700C
26800 WRITE(6.620) K.PAR.ALFHAT.PHAT
26900 620 FORMAT(I3.8X.F9.0.F6.2.F6.1/3X.F8.4.F9.0.F6.2.F6.1)
27000C
27100C CHECK FOR CONVERGENCE. RELATIVE CHANGE FOR EACH PARAMETER
27200C MUST BE LESS THAN OR EQUAL TO DELTA
27300C
27400 DO 630 I=1.3
27500 XT=PAR(I)
27600 IF (ABS(XT-PHAT(I)).GT.(DELTA*XT)) GO TO 640
27700 630 CONTINUE
27800 GO TO 790
27900C
28000C HAS MAXIMUM ITERATIONS BEEN REACHED
28100C
28200 640 IF (K.LT.ITMAX) GO TO 680
28300 645 WRITE(6.650) ITMAX
28400 650 FORMAT(* MAXIMUM NUMBER OF ITERATIONS (*.I2.*) HAS BEEN REACHED WITHO
28500+UT CONVERGENCE*/* DO YOU WANT TO CONTINUE (Y OR N)  *)
28600 READ(5.660) I
28700 660 FORMAT(A1)
28800 IF (I.EQ.1HY) GO TO 670
28900 IF (I.EQ.1HN) GO TO 880
29000 GO TO 645
29100C
29200C ITERATION TO BE CONTINUED FOR UP TO 25 MORE LOOPS
29300C
29400 670 ITMAX=ITMAX+25
29500 WRITE(6.492) IDP
29600C
29700C DEFINE ESTIMATES FOR NEXT ITERATION AND CHECK FOR BOUNDARY VIOLATIONS
29800C
29900 680 K=K+1
30000 690 DO 700 I=1.3
30100 PNU(I)=ELMBDA*PAR(I)+ELMBDA*PHAT(I)
30200 700 CONTINUE
30300 DO 710 I=1.3
30400 XT=PNU(I)
30500 IF (XT.LT.PRMIN(I)) GO TO 730
30600 IF (XT.GT.PRMAX(I)) GO TO 760
30700 710 CONTINUE
30800 DO 720 I=1.3
30900 PAR(I)=PNU(I)
31000 720 CONTINUE
31100 GO TO 510
31200C
31300C TERMINATE ON SUCCESSIVE VIOLATIONS.  OTHERWISE RECALCULATE ESTIMATES
31400C
31500 730 IF (MINVIO(I).GE.(K-2)) GO TO 770
31600 MINVIO(I)=K-1
31700 XT=PAR(I)
31800 SCA=(XT-PRMIN(I))/(XT-PHAT(I))
31900 740 DO 750 J=1.3
32000 XT=PAR(J)
32100 PHAT(J)=XT+SCA*(PHAT(J)-XT)
32200 750 CONTINUE
32300 GO TO 690
32400 760 IF (MAXVIO(I).GE.(K-2)) GO TO 770
32500 MAXVIO(I)=K-1
32600 XT=PAR(I)
32700 SCA=(PRMAX(I)-XT)/(PHAT(I)-XT)
32800 GO TO 740
32900 770 WRITE(6.780) IDP(I)
33000 780 FORMAT(* BOUNDARY VIOLATIONS ON SUCCESSIVE ITERATIONS FOR *.A5)
33100 GO TO 880
33200C
33300C SOLUTION HAS BEEN FOUND.  OUTPUT RESULTS
33400C CALCULATE RESIDUAL SUM OF SQUARES AND R-SQUARED
33500C
33600 790 WRITE(9.781)
```

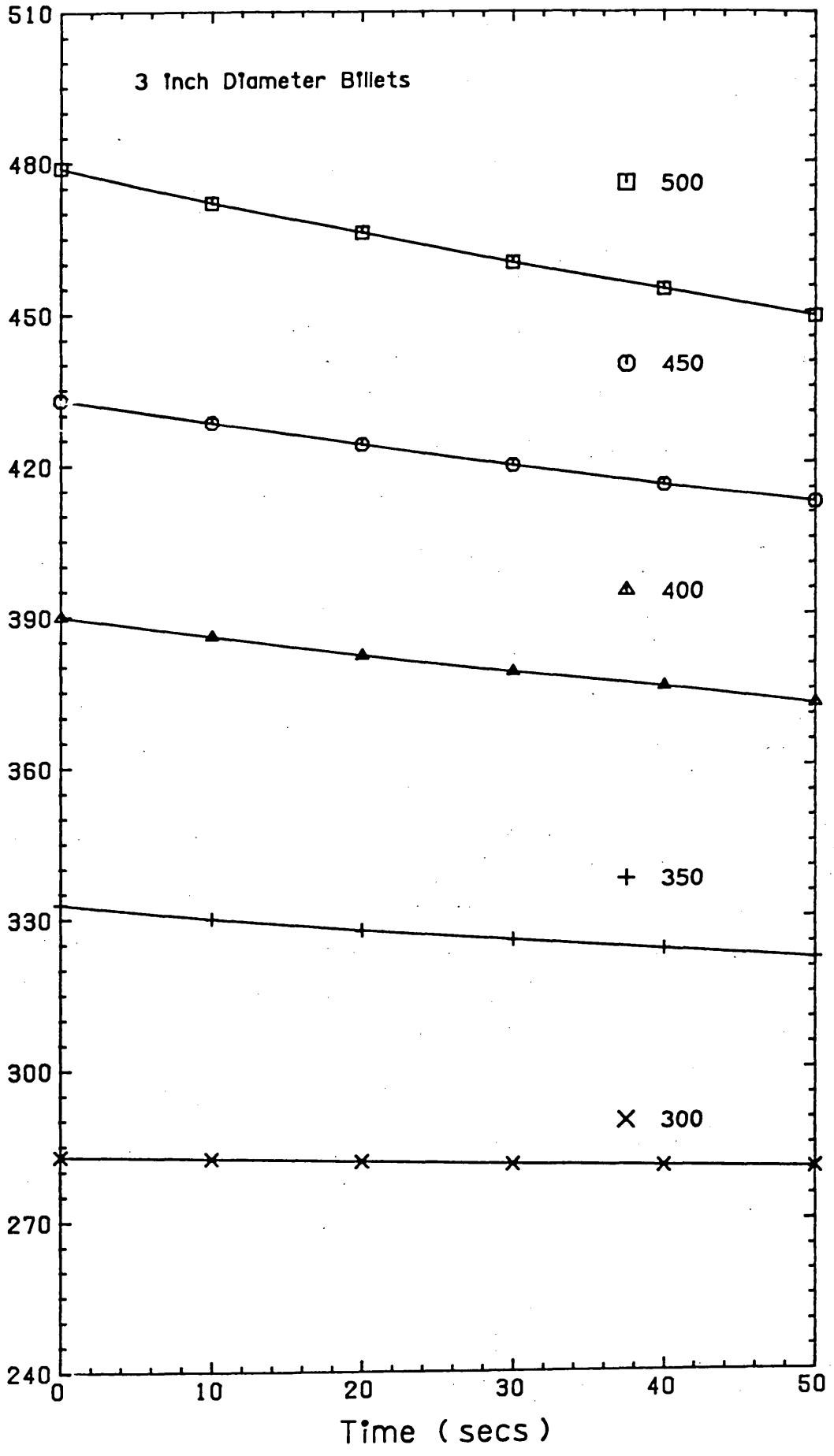
```
781 FORMAT(*FORTRAN HIGH SPEED MINIMISATION.(MGT-1.3.79-VERS1.1)*)
 WRITE(6,800) ALFHAT,PAR
800 FORMAT(* CONVERGENCE HAS BEEN ATTAINED TO THE SOLUTION*/6X,    *ALP
+HA =*,F8.5/6X,*DELTA H =*,F8.0/6X,*N =*,F5.2/6X,*LN A =*,F6.2)
IF (NOINT.GE.1) R(1)=S1
WRITE(9,810) IFILNAM,R,EL,ALFHAT,PAR
810 FORMAT(* FLOW STRESS DATA ANALYSIS FOR THE TORSION TEST*/ * TA
+BLE OF RESIDUALS FOR *,I5/* THE SPECIMEN DIMENSIONS ARE*/6X,*INNER RA
+DIUS =*,F6.2/6X,*OUTER RADIUS =*,F6.2/       6X,*LENGTH =*,F6.2/*
+ THE PARAMETER VALUES ARE*/      6X,*ALPHA =*,F8.5/6X,*DELTA
+H =*,F8.0/6X,*N =*,F5.2/6X,*LN A =*   F6.2)
WRITE(9,820)
820 FORMAT(*  POINT    TWIST  TEMPER  OBSRVD  ESTIM.   RESI- */
+    * NUMBER     RATE  -ATURE  TORQUE  TORQUE    DUAL */              *
+        (RPS)     (C)  (N-MM)*/                                  * ------
+----  ------  ------  ------   ----- *)
SUM=0.0
DO 850 I=1,NPTS
YT=YBAR
DO 830 J=1,3
YT=YT+BETA(J)*U(I,J)
830 CONTINUE
XT=TORQ(I)
RESID=XT-YT
SUM=SUM+RESID*RESID
WRITE(9,840) I,THETA(I),TMP(I),XT,YT,RESID
840 FORMAT(I7,F9.3,F8.0,3F8.0)
850 CONTINUE
WRITE(9,860)
860 FORMAT(*APPROXIMATE VALUES*)
WRITE(6,870) SUM
870 FORMAT(* RESIDUAL SUM OF SQUARES = *,F10.0)
WRITE(9,870) SUM
RSQD=1.0-(SUM/SSTRQ)
WRITE(9,875) RSQD
875 FORMAT(* R-SQUARED =*,F7.4)
WRITE(6,875) RSQD
PRINT*,'RESULTS ARE ON TAPE9 IN PRINTSF FORMAT.'
C
880 STOP
END
FUNCTION SMPSN4(RP,CSQD,EXPO,NPTS)
C SIMPSON'S RULE INTEGRATION OF F(Z)=(Z**EXPO)/SQRT(1.0+CSQD*Z)
DIMENSION RP(2)
F(Z)=(Z**EXPO)/SQRT(1.0+CSQD*Z)
RANGE=RP(2)-RP(1)
SUM=F(RP(1))+F(RP(2))
SUMODD=0.0
SUMEVN=0.0
EN=FLOAT(NPTS)
LAST=NPTS/2
DO 10 I=1,LAST
EI=FLOAT(2*I-1)
X=RP(1)+(EI*RANGE)/EN
SUMODD=SUMODD+F(X)
10 CONTINUE
IF (LAST.LE.1) GO TO 30
LAST=LAST-1
DO 20 I=1,LAST
EI=FLOAT(2*I)
X=RP(1)+(EI*RANGE)/EN
SUMEVN=SUMEVN+F(X)
20 CONTINUE
30 SMPSN4=RANGE*(SUM+4.0*SUMODD+2.0*SUMEVN)/(3.0*EN)
RETURN
END
```

Appendix F

Billet Cooling Curves

The following curves were established by the method outlined in section 3.2.2. and were used to calculate the actual temperature at the commencement of extrusion. Where lines were unavailable for the temperature required, interpolation was carried out.
0.075 m (3 inch) diameter billets were heated by induction heater
0.057 (2 inch) diameter billets by air circulating furnace.


500
470
440
410
380
350
320
290
260
230
Temperature (°C)
0
10
20
30
40
50
Time (secs)
2 inch diam. billets.
°C
500
450
400
350
300


3 Inch Diameter Billets
500
450
400
350
300
510
480
450
420
390
360
330
300
270
240
0
10
20
30
40
50
Time (secs)

Appendix G

Extrusion Results

The results from the 228 extrusions carried out are presented on the following pages. The tables contain:-

Run Code

Extrusion Ratio

Initial Temperature (Temperature, the billet was heated to)

Actual Temperature (Temperature of billet after transfer to the container)

Peak Temperature (Calculated Temperature corresponding to peak load calculated using method described in section 2.5.1.)

Final Temperature (Calculated temperature corresponding to minimum load calculated using the method described in section 2.5.2.)

Billet length

Billet diameter

Ram Speed

Feltham's Strain Rate (Calculated using method described in section 2.3)

Ln (Feltham's Strain Rate)

Maximum Pressure

Minimum Pressure

Pressure increment at peak, Δp (defined in Fig. 78)

Initial Z (calculated using Feltham's strain rate and actual temperature)

Peak Z (calculated using peak temperature)

Final Z (calculated using final temperature)

Initial Flow Stress (calculated from constituitive equation using Feltham's strain rate and actual temperature)

Peak Flow Stress (calculated using peak temperature)

Final Flow Stress (calculated using final temperature)

Extrude quality Remarks concerning product:-

Sticker Extrusion impossible

Billet remains in container

O.K.	Acceptable surface finish
I.M.	Incipient melting
Line	Die lines on product
Frict Test	Short billet used for friction work
Partial	Partial Extrusion for microstructural work
Grid	Gridded billet
Unhom.	Non preheat treated billet

RUN CODES	EXT RATIO	INITIAL TEMP	ACTUAL TEMP	PEAK TEMP	FINAL TEMP	BILLET LENG	BILLET DIAM	RAM SPEED	FELTHAM ST.RATE	LOG FELT	MAXIMUM PRESS	MINIMUM PRESS	PEAK DELTAP
		DEG.C	DEG.C	DEG.C	DEG.C	MMS	MMS	MMS/S	-1 SEC		2 MN/M	2 MN/M	MN
D222001	5.0	200.0	185.0	0	0	100.0	75.0	200.0	121.88	4.80	1127.70	0	0
D222002	5.0	300.0	280.0	0	0	100.0	75.0	106.0	64.60	4.17	800.66	0	0
D222003	5.0	350.0	325.0	0	0	100.0	75.0	400.0	243.77	5.50	552.57	0	0
D222004	5.0	400.0	387.0	0	0	100.0	75.0	233.0	141.99	4.96	541.29	0	0
D222005	5.0	450.0	427.0	0	0	100.0	75.0	410.0	249.86	5.52	507.46	0	0
D222006	5.0	400.0	385.0	0	0	100.0	75.0	440.0	268.14	5.59	507.46	0	0
D222007	5.0	500.0	470.0	0	0	100.0	75.0	620.0	377.84	5.93	338.31	0	0
D222008	5.0	250.0	225.0	0	0	100.0	75.0	200.0	121.88	4.80	1127.70	0	0
D222009	5.0	250.0	235.0	0	415.2	100.0	75.0	280.0	170.64	5.14	755.56	607.83	0
D222010	5.0	450.0	417.0	0	0	100.0	75.0	580.0	353.46	5.87	473.63	0	0
D222011	5.0	300.0	280.0	0	502.9	100.0	75.0	422.0	257.17	5.55	845.77	764.80	0
D222012	5.0	350.0	325.0	0	470.6	100.0	75.0	490.0	298.61	5.70	608.96	507.46	0
D222013	30.0	300.0	280.0	0	0	100.0	75.0	150.0	213.00	5.36	947.26	0	0
D222014	30.0	350.0	324.0	0	0	100.0	75.0	150.0	213.00	5.36	913.43	0	0
D222015	30.0	400.0	384.0	0	543.2	100.0	75.0	150.0	213.00	5.36	811.94	623.39	0
D222016	30.0	450.0	420.0	0	581.7	100.0	75.0	222.0	315.23	5.75	699.17	631.51	0
D222017	30.0	500.0	462.0	0	0	100.0	75.0	280.0	397.59	5.99	597.68	0	0
D222018	40.0	200.0	185.0	0	0	100.0	75.0	200.0	320.30	5.77	917.94	0	0
D222019	40.0	250.0	235.0	0	0	100.0	75.0	200.0	320.30	5.77	951.77	0	0
D222020	40.0	300.0	280.0	0	0	100.0	75.0	200.0	320.30	5.77	958.54	0	0
D222021	40.0	400.0	385.0	0	560.8	100.0	75.0	164.0	262.64	5.57	902.16	684.06	0
D222022	40.0	450.0	420.0	0	566.3	100.0	75.0	197.0	315.49	5.75	755.56	584.37	0
D222023	50.0	350.0	321.0	0	0	100.0	75.0	200.0	350.90	5.86	1014.93	0	0
D222024	50.0	400.0	385.0	0	0	100.0	75.0	200.0	350.90	5.86	1037.48	0	0
D222025	50.0	400.0	385.0	0	0	100.0	75.0	4.0	7.02	1.95	915.69	0	0
D222026	50.0	450.0	410.0	426.5	531.5	100.0	75.0	12.0	21.05	3.05	1021.69	726.24	.39
D222027	50.0	500.0	453.0	467.1	541.6	100.0	75.0	12.0	21.05	3.05	870.56	647.30	.58
D222028	50.0	540.0	495.0	508.8	565.2	100.0	75.0	12.0	21.05	3.05	852.54	636.02	.63
D222029	60.0	400.0	385.0	0	0	100.0	75.0	8.0	15.11	2.72	1014.93	0	0
D222030	60.0	450.0	420.0	436.3	521.5	100.0	75.0	8.0	15.11	2.72	1010.41	726.24	.30

RUN CODES	EXT RATIO	INITIAL TEMP	ACTUAL TEMP	PEAK TEMP	FINAL TEMP	BILLET LENG	BILLET DIAM	RAM SPEED	FELTHAM ST.RATE -1	LOG FELT	MAXIMUM PRESS 2	MINIMUM PRESS 2	PEAK DELTAP
		DEG.C	DEG.C	DEG.C	DEG.C	MMS	MMS	MMS/S	SEC		MN/M	MN/M	MN
D222031	60.0	500.0	460.0	472.3	538.0	100.0	75.0	8.0	15.11	2.72	872.84	692.40	.33
D222032	70.0	450.0	419.0	0	0	100.0	75.0	8.0	16.06	2.78	992.37	0	0
D222033	70.0	500.0	463.0	490.3	589.1	100.0	75.0	44.7	89.75	4.50	969.82	647.30	.69
D222034	70.0	500.0	463.0	475.7	523.7	100.0	75.0	5.6	11.24	2.42	906.67	699.17	.25
D222035	70.0	450.0	420.0	0	0	100.0	75.0	5.6	11.24	2.42	1014.93	0	0
D222036	70.0	450.0	421.0	438.2	508.7	100.0	75.0	5.6	11.24	2.42	1062.29	737.51	.18
D222037	80.0	450.0	421.0	0	0	100.0	75.0	4.3	9.10	2.21	1014.93	0	0
D222038	80.0	500.0	463.0	0	0	100.0	75.0	4.3	9.10	2.21	958.54	0	0
D222039	80.0	450.0	417.0	0	0	100.0	75.0	4.3	9.10	2.21	969.82	0	0
D222040	80.0	500.0	463.0	0	513.2	100.0	75.0	4.3	9.10	2.21	965.31	717.21	0
D222041	60.0	300.0	300.0	0	0	100.0	57.0	10.0	24.84	3.21	1835.24	0	0
D222042	60.0	350.0	350.0	378.5	520.3	100.0	57.0	10.0	24.84	3.21	1249.52	874.67	.50
D222043	60.0	400.0	400.0	420.9	534.1	100.0	57.0	10.0	24.84	3.21	1132.38	804.38	.46
D222044	76.0	350.0	350.0	386.3	522.2	100.0	57.0	11.0	30.02	3.40	1292.48	874.67	.46
D222045	76.0	400.0	400.0	421.8	550.2	100.0	57.0	11.0	30.02	3.40	1179.24	866.86	.54
D222046	76.0	450.0	450.0	466.9	574.9	100.0	57.0	11.0	30.02	3.40	1046.48	843.43	.46
D222047	81.0	350.0	350.0	379.8	519.4	100.0	57.0	12.0	33.59	3.51	1304.19	851.24	.50
D222048	81.0	400.0	400.0	421.0	546.4	100.0	57.0	12.0	33.59	3.51	1140.19	835.62	.43
D222049	81.0	450.0	450.0	468.8	569.9	100.0	57.0	12.0	33.59	3.51	1163.62	804.38	.25
D222050	50.0	350.0	350.0	373.5	525.0	100.0	57.0	8.5	19.62	2.98	1272.95	917.62	.46
D222051	50.0	400.0	400.0	0	532.0	100.0	57.0	8.5	19.62	2.98	1124.57	820.00	.67
D222052	30.0	500.0	466.0	476.4	520.2	100.0	75.0	6.6	9.37	2.24	739.77	608.96	.13
D222053	30.0	450.0	421.0	435.9	498.5	100.0	75.0	6.6	9.37	2.24	924.71	627.00	.20
D222054	30.0	400.0	384.0	0	0	100.0	75.0	6.6	9.37	2.24	1039.73	0	0
D222055	30.0	425.0	397.0	413.5	485.9	100.0	75.0	6.6	9.37	2.24	1021.69	631.51	.28
D222056	40.0	500.0	464.0	473.0	529.1	100.0	75.0	7.0	11.21	2.42	789.39	654.06	.18
D222057	40.0	450.0	419.0	432.4	523.6	100.0	75.0	8.0	12.81	2.55	954.03	726.24	.21
D222058	40.0	425.0	400.0	414.8	516.2	100.0	75.0	8.0	12.81	2.55	1055.52	744.28	.12
D222059	10.0	500.0	462.0	467.6	503.9	100.0	75.0	5.4	4.67	1.54	577.38	541.29	0
D222060	10.0	450.0	420.0	431.9	484.9	100.0	75.0	5.4	4.67	1.54	737.51	559.34	.26

RUN CODES	EXT RATIO	INITIAL TEMP	ACTUAL TEMP	PEAK TEMP	FINAL TEMP	BILLET LENG	BILLET DIAM	RAM SPEED	FELTHAM ST.RATE $^{-1}$	LOG FELT	MAXIMUM PRESS ^{2}	MINIMUM PRESS ^{2}	PEAK DELTAP
		DEG.C	DEG.C	DEG.C	DEG.C	MMS	MMS	MMS/S	SEC		MN/M	MN/M	MN
D222061	10.0	400.0	385.0	399.4	474.4	100.0	75.0	5.4	4.67	1.54	893.13	599.93	.21
D222062	10.0	350.0	322.0	338.6	446.8	100.0	75.0	5.4	4.67	1.54	1026.20	631.51	.29
D222063	5.0	500.0	461.0	467.6	478.0	100.0	75.0	5.4	3.29	1.19	469.12	394.69	0
D222064	5.0	450.0	420.0	426.0	471.8	100.0	75.0	5.2	3.17	1.15	622.49	473.63	0
D222065	5.0	400.0	385.0	397.1	447.5	100.0	75.0	5.2	3.17	1.15	746.53	451.08	.27
D331066	5.0	350.0	323.0	336.8	423.6	100.0	75.0	5.2	3.17	1.15	852.54	496.19	.34
D331067	5.0	300.0	280.0	293.5	440.4	100.0	75.0	5.2	3.17	1.15	963.05	676.62	.18
D222068	5.0	500.0	465.0	472.6	517.7	100.0	75.0	12.6	7.68	2.04	543.55	428.52	.20
D222069	5.0	450.0	419.0	429.8	484.2	100.0	75.0	12.6	7.68	2.04	665.34	419.50	.20
D331070	5.0	400.0	385.0	397.9	485.5	100.0	75.0	12.6	7.68	2.04	796.15	518.74	.28
D331071	5.0	350.0	323.0	339.3	437.9	100.0	75.0	12.7	7.74	2.05	886.37	496.19	.34
D331072	5.0	300.0	280.0	296.7	434.6	100.0	75.0	13.2	8.04	2.08	1030.71	599.93	.39
D331073	9.0	500.0	462.0	471.3	526.7	100.0	75.0	12.6	10.34	2.34	658.57	496.19	.25
D331074	9.0	450.0	420.0	431.9	503.9	100.0	75.0	12.6	10.34	2.34	737.51	518.74	.28
D331075	10.0	400.0	385.0	399.4	489.3	100.0	75.0	12.6	10.89	2.39	890.88	559.34	.28
D331076	10.0	350.0	324.0	340.5	460.3	100.0	75.0	12.6	10.89	2.39	1042.67	608.96	.35
D331077	10.0	500.0	462.0	472.6	525.8	100.0	75.0	12.6	10.89	2.39	658.57	496.19	.31
D331078	10.0	300.0	280.0	0	0	100.0	75.0	12.6	10.89	2.39	1041.99	0	0
D331079	30.0	475.0	449.0	464.0	547.7	100.0	75.0	12.6	17.89	2.88	930.35	663.08	.36
D331080	30.0	450.0	421.0	441.1	539.6	100.0	75.0	12.6	17.89	2.88	1087.10	708.19	.44
D331081	50.0	500.0	459.0	473.9	517.4	100.0	75.0	4.5	7.90	2.07	924.71	721.72	.18
D331082	50.0	450.0	411.0	0	0	100.0	75.0	4.5	7.90	2.07	1093.86	0	0
D331083	50.0	475.0	438.0	456.7	510.3	100.0	75.0	4.5	7.90	2.07	1014.93	739.77	.20
D331084	40.0	500.0	459.0	474.5	507.0	100.0	75.0	4.6	7.37	2.00	841.26	654.06	.20
D331085	40.0	450.0	417.0	436.3	534.3	100.0	75.0	8.7	13.93	2.63	1048.76	766.83	.21
D331086	40.0	450.0	417.0	433.6	497.8	100.0	75.0	4.5	7.21	1.98	996.88	721.72	0
D331087	40.0	500.0	462.0	477.6	532.0	100.0	75.0	8.6	13.77	2.62	848.03	631.51	.30
D331088	70.0	300.0	300.0	0	0	76.0	75.0	4.8	9.64	2.27	999.14	0	0
D331089	70.0	350.0	350.0	388.4	500.5	76.0	57.0	4.8	12.68	2.54	1659.52	984.00	.34
D331090	70.0	400.0	400.0	435.1	515.4	76.0	57.0	4.8	12.68	2.54	1444.76	937.14	.32

RUN CODES	EXT RATIO	INITIAL TEMP	ACTUAL TEMP	PEAK TEMP	FINAL TEMP	BILLET LENG	BILLET DIAM	RAM SPEED	FELTHAM ST.RATE -1	LOG FELT	MAXIMUM PRESS 2	MINIMUM PRESS 2	PEAK DELTAP
		DEG.C	DEG.C	DEG.C	DEG.C	MMS	MMS	MMS/S	SEC		MN/M	MN/M	MN
D331091	70.0	450.0	442.0	467.0	533.6	76.0	57.0	4.8	12.68	2.54	1351.05	929.33	.31
D331092	70.0	500.0	500.0	518.1	553.7	76.0	57.0	4.8	12.68	2.54	1120.67	890.29	.17
D331093	60.0	350.0	344.0	383.8	504.5	76.0	57.0	4.8	11.93	2.48	1640.00	1015.24	.31
D331094	60.0	450.0	442.0	474.0	531.0	76.0	57.0	4.8	11.93	2.48	1401.81	913.71	.28
D331095	60.0	350.0	345.0	384.6	451.2	76.0	57.0	2.0	4.97	1.60	1632.19	921.52	.20
D331096	60.0	400.0	394.0	421.4	467.6	76.0	57.0	1.9	4.72	1.55	1483.81	944.95	.16
D331097	60.0	450.0	445.0	468.1	478.9	76.0	57.0	1.9	4.72	1.55	1249.52	913.71	.10
D331098	60.0	400.0	400.0	431.1	448.2	50.0	57.0	1.9	4.72	1.55	1362.76	968.38	.18
D331099	60.0	350.0	350.0	400.4	441.7	50.0	57.0	1.9	4.72	1.55	1495.52	1046.48	.20
D331100	60.0	350.0	350.0	394.4	531.1	76.0	57.0	8.4	20.87	3.04	1600.95	1015.24	.34
D331101	70.0	350.0	350.0	0	0	76.0	57.0	1.3	3.43	1.23	1722.00	0	0
D331102	70.0	400.0	383.0	417.0	438.6	76.0	57.0	1.3	3.43	1.23	1522.86	909.81	.12
D331103	60.0	350.0	350.0	398.5	511.1	60.0	57.0	5.8	14.41	2.67	1507.24	1073.81	.36
D331104	60.0	350.0	350.0	405.8	441.8	55.0	57.0	1.9	4.72	1.55	1663.43	991.81	.34
D331105	70.0	475.0	476.0	449.9	534.4	100.0	75.0	5.0	10.04	2.31	987.86	857.05	0
D331106	60.0	475.0	438.0	448.5	540.5	100.0	75.0	7.2	13.60	2.61	999.14	789.39	.11
D331107	60.0	425.0	401.0	0	0	100.0	75.0	8.0	15.11	2.72	1051.01	0	0
D331108	30.0	475.0	437.0	449.0	522.0	100.0	75.0	5.4	7.67	2.04	978.84	739.77	.18
D331109	30.0	475.0	438.0	453.9	536.5	100.0	75.0	10.4	14.77	2.69	983.35	676.62	.29
D331110	40.0	475.0	436.0	452.4	524.5	100.0	75.0	6.6	10.57	2.36	1012.67	721.72	0
D331111	50.0	475.0	438.0	456.7	556.8	100.0	75.0	10.2	17.90	2.88	1044.25	789.39	1.80
D331112	5.0	300.0	300.0	0	0	100.0	75.0	6.0	3.66	1.30	965.31	0	0
D331113	30.0	300.0	297.0	344.1	499.3	76.0	57.0	12.6	23.54	3.16	1616.57	921.52	.46
D331114	30.0	300.0	297.0	343.2	465.9	76.0	57.0	4.2	7.85	2.06	1585.33	917.62	.43
D331115	30.0	350.0	348.0	389.4	521.2	76.0	57.0	8.0	14.95	2.70	1444.76	952.76	.42
D331116	30.0	350.0	346.0	386.9	481.0	76.0	57.0	4.0	7.47	2.01	1425.24	890.29	.31
D331117	30.0	400.0	395.0	430.5	515.5	76.0	57.0	5.6	10.46	2.35	1280.76	874.67	.26
D331118	30.0	400.0	394.0	429.0	489.4	76.0	57.0	4.0	7.47	2.01	1261.24	820.00	.25
D331119	30.0	450.0	443.0	463.3	506.5	76.0	57.0	4.2	7.85	2.06	1097.24	780.95	.19
D331120	30.0	450.0	443.0	469.4	565.3	76.0	57.0	12.5	23.35	3.15	1140.19	812.19	.30

RUN CODES	EXT RATIO	INITIAL TEMP	ACTUAL TEMP	PEAK TEMP	FINAL TEMP	BILLET LENG	BILLET DIAM	RAM SPEED	FELTHAM ST.RATE -1	LOG FELT	MAXIMUM PRESS 2	MINIMUM PRESS 2	PEAK DELTAP
		DEG.C	DEG.C	DEG.C	DEG.C	MMS	MMS	MMS/S	SEC		MN/M	MN/M	MN
D331121	30.0	500.0	480.0	497.8	510.4	76.0	57.0	4.0	7.47	2.01	960.57	726.29	.12
D331122	50.0	500.0	481.0	501.2	580.6	76.0	57.0	8.0	18.47	2.92	1093.33	905.90	.23
D331123	60.0	500.0	480.0	500.9	535.6	76.0	57.0	4.0	9.94	2.30	1128.48	898.10	.12
D331124	40.0	500.0	479.0	496.6	538.4	76.0	57.0	4.0	8.43	2.13	1085.52	898.10	.17
D331125	40.0	450.0	443.0	466.1	522.6	76.0	57.0	4.0	8.43	2.13	1249.52	898.10	.22
D331126	40.0	450.0	443.0	466.4	585.3	76.0	57.0	12.6	26.55	3.28	1265.14	913.71	.33
D331127	50.0	450.0	444.0	467.2	531.4	76.0	57.0	4.5	10.39	2.34	1253.43	917.62	.21
D331128	50.0	400.0	399.0	438.0	494.6	76.0	57.0	4.0	9.23	2.22	1405.71	859.05	.29
D331129	40.0	400.0	395.0	434.3	505.7	76.0	57.0	4.0	8.43	2.13	1417.43	921.52	.26
D331130	40.0	400.0	395.0	435.4	569.3	76.0	57.0	12.6	26.55	3.28	1456.48	976.19	.34
D331131	40.0	350.0	343.0	388.1	485.6	76.0	57.0	4.0	8.43	2.13	1522.86	937.14	.34
D331132	40.0	350.0	343.0	391.5	537.3	76.0	57.0	12.6	26.55	3.28	1640.00	976.19	.44
D331133	60.0	350.0	343.0	390.3	498.2	76.0	57.0	4.2	10.43	2.35	1624.38	1015.24	.37
D331134	50.0	350.0	343.0	387.4	490.0	76.0	57.0	4.2	9.70	2.27	1600.95	960.57	.35
D331135	50.0	300.0	295.0	0	0	76.0	57.0	4.0	9.23	2.22	1698.57	0	0
D331136	50.0	300.0	296.0	349.4	526.2	76.0	57.0	10.6	24.47	3.20	1804.00	1093.33	.44
D331137	40.0	300.0	293.0	341.8	519.2	76.0	57.0	11.0	23.18	3.14	1761.05	1054.29	.52
D331138	40.0	300.0	294.0	346.4	527.2	76.0	57.0	14.0	29.50	3.38	1800.09	1054.29	.69
D331139	60.0	300.0	295.0	0	0	76.0	57.0	4.2	10.43	2.35	1800.09	0	0
D331140	30.0	250.0	245.0	0	0	76.0	57.0	4.2	7.85	2.06	1874.29	0	0
D331141	30.0	250.0	244.0	277.8	481.7	76.0	57.0	10.0	18.68	2.93	1827.43	1015.24	0
D331142	100.0	500.0	475.0	499.3	547.1	76.0	57.0	4.0	12.16	2.50	1365.90	999.62	.18
D331143	80.0	450.0	438.0	470.9	528.6	76.0	57.0	4.0	11.14	2.41	1421.33	976.19	.23
D331144	100.0	450.0	443.0	476.3	531.8	76.0	57.0	4.0	12.16	2.50	1440.86	991.81	.29
D331145	10.0	500.0	457.0	468.7	0	75.0	75.0	4.0	3.46	1.24	622.49	0	0
D331146	10.0	400.0	384.0	404.5	0	75.0	75.0	4.0	3.46	1.24	832.24	0	0
D331147	10.0	400.0	384.0	408.0	0	50.0	75.0	4.0	3.46	1.24	757.81	0	0
D331148	10.0	350.0	322.0	339.1	0	80.0	75.0	4.0	3.46	1.24	974.33	0	0
D331149	10.0	500.0	459.0	470.1	0	50.0	75.0	4.0	3.46	1.24	527.76	0	0
5456150	10.0	480.0	440.0	452.6	488.9	100.0	75.0	4.0	3.46	1.24	719.47	586.40	.29

RUN CODES	EXT RATIO	INITIAL TEMP	ACTUAL TEMP	PEAK TEMP	FINAL TEMP	BILLET LENG	BILLET DIAM	RAM SPEED	FELTHAM ST.RATE -1	LOG FELT	MAXIMUM PRESS 2	MINIMUM PRESS 2	PEAK DELTAP
		DEG.C	DEG.C	DEG.C	DEG.C	MMS	MMS	MMS/S	SEC		MN/M	MN/M	MN
5456151	10.0	450.0	419.0	436.3	485.8	100.0	75.0	4.0	3.46	1.24	820.96	622.49	.31
5456152	10.0	420.0	401.0	420.6	460.4	100.0	75.0	4.0	3.46	1.24	890.88	541.29	.33
5456153	10.0	400.0	385.0	404.5	469.0	100.0	75.0	4.0	3.46	1.24	926.97	622.49	.20
5456154	10.0	360.0	330.0	0	0	100.0	75.0	4.0	3.46	1.24	983.35	0	0
5083155	10.0	480.0	440.0	452.2	488.9	100.0	75.0	4.0	3.46	1.24	692.40	586.40	.15
5083156	10.0	450.0	417.0	430.6	477.5	100.0	75.0	4.0	3.46	1.24	773.60	586.40	0
5083157	10.0	420.0	389.0	403.7	454.4	100.0	75.0	4.0	3.46	1.24	836.75	541.29	.31
5083158	10.0	400.0	384.0	403.2	465.7	100.0	75.0	4.0	3.46	1.24	911.18	608.96	.33
5083159	10.0	380.0	365.0	381.5	451.7	100.0	75.0	4.0	3.46	1.24	940.50	586.40	0
5052160	10.0	480.0	441.0	447.2	471.0	100.0	75.0	4.0	3.46	1.24	500.70	496.19	0
5052161	10.0	450.0	420.0	427.6	456.0	100.0	75.0	4.0	3.46	1.24	543.55	473.63	0
5052162	10.0	420.0	404.0	412.5	457.3	100.0	75.0	4.0	3.46	1.24	602.19	518.74	0
5052163	10.0	400.0	384.0	397.5	447.4	100.0	75.0	4.0	3.46	1.24	640.53	518.74	0
5052164	10.0	360.0	329.0	344.5	433.9	100.0	75.0	4.0	3.46	1.24	737.51	586.40	0
5083165	10.0	500.0	460.0	473.5	0	100.0	75.0	4.0	3.46	1.24	638.28	0	0
5083166	10.0	380.0	364.0	383.5	0	100.0	75.0	4.0	3.46	1.24	924.71	0	.17
5456167	10.0	500.0	460.0	474.1	0	100.0	75.0	4.0	3.46	1.24	669.85	0	0
5456168	10.0	380.0	365.0	378.4	0	100.0	75.0	4.0	3.46	1.24	956.29	0	0
5052169	10.0	500.0	461.0	466.6	0	100.0	75.0	4.0	3.46	1.24	498.44	0	0
5052170	10.0	350.0	322.0	337.6	0	100.0	75.0	4.0	3.46	1.24	742.02	0	0
D331171	10.0	500.0	462.0	475.6	0	100.0	75.0	4.0	3.46	1.24	645.04	0	0
D331172	10.0	335.0	335.0	348.1	0	100.0	75.0	4.0	3.46	1.24	1064.54	0	0
5456173	30.0	492.0	487.0	516.2	529.9	75.0	57.0	4.0	7.47	2.01	960.57	820.00	.19
5052174	30.0	493.0	477.0	492.1	508.6	75.0	57.0	4.0	7.47	2.01	714.57	726.29	0
5083175	30.0	495.0	472.0	497.4	532.4	75.0	57.0	4.8	8.97	2.19	902.00	812.19	0
D331176	5.0	495.0	480.0	498.7	499.9	75.0	57.0	4.8	3.85	1.35	663.81	534.95	0
5052177	5.0	494.0	479.0	493.4	0	75.0	57.0	4.8	3.85	1.35	511.52	0	0
5083178	5.0	494.0	480.0	499.1	0	75.0	57.0	4.8	3.85	1.35	628.67	0	0
5456179	5.0	494.0	480.0	497.2	0	75.0	57.0	4.8	3.85	1.35	613.05	0	0
5052180	60.0	495.0	478.0	494.7	529.8	75.0	57.0	4.8	11.93	2.48	792.67	812.19	0

RUN CODES	EXT RATIO	INITIAL TEMP	ACTUAL TEMP	PEAK TEMP	FINAL TEMP	BILLET LENG	BILLET DIAM	RAM SPEED	FELTHAM ST.RATE s^{-1}	LOG FELT	MAXIMUM PRESS MN/m^2	MINIMUM PEAK PRESS MN/m^2	DELTAP MN
		DEG.C	DEG.C	DEG.C	DEG.C	MMS	MMS	MMS/S	SEC		MN/M	MN/M	MN
5083181	60.0	494.0	478.0	509.1	545.3	75.0	57.0	4.8	11.93	2.48	1105.05	898.10	.14
5456182	60.0	496.0	480.0	506.8	549.8	75.0	57.0	4.8	11.93	2.48	1101.14	917.62	.10
5052183	70.0	496.0	481.0	501.0	538.5	75.0	57.0	4.8	12.68	2.54	855.14	859.05	0
5083184	70.0	496.0	481.0	507.9	549.0	75.0	57.0	4.8	12.68	2.54	1105.05	917.62	.10
5456185	70.0	496.0	481.0	516.0	538.5	75.0	57.0	4.8	12.68	2.54	1148.00	859.05	.21
5083186	30.0	450.0	438.0	474.2	517.8	75.0	57.0	4.8	8.97	2.19	1105.05	820.00	.20
5052187	30.0	447.0	437.0	458.1	495.6	75.0	57.0	4.8	8.97	2.19	749.71	702.86	0
5456188	30.0	446.0	436.0	471.7	514.0	75.0	57.0	4.8	8.97	2.19	1089.43	804.38	.28
5083189	30.0	400.0	395.0	428.5	496.1	75.0	57.0	4.8	8.97	2.19	1190.95	812.19	0
5052190	30.0	397.0	392.0	416.3	481.6	75.0	57.0	4.8	8.97	2.19	862.95	741.90	0
5456191	30.0	398.0	392.0	438.1	494.7	75.0	57.0	4.8	8.97	2.19	1230.00	812.19	.39
5052192	30.0	350.0	345.0	373.8	459.4	75.0	57.0	4.8	8.97	2.19	944.95	741.90	0
5083193	30.0	350.0	345.0	393.6	481.3	75.0	57.0	4.8	8.97	2.19	1296.38	859.05	.34
5654194	30.0	347.0	342.0	393.2	469.7	75.0	57.0	4.8	8.97	2.19	1366.67	804.38	.29
5052195	30.0	300.0	293.0	325.3	448.0	75.0	57.0	4.8	8.97	2.19	1062.10	812.19	0
5083196	30.0	300.0	293.0	350.8	461.1	75.0	57.0	4.8	8.97	2.19	1452.57	882.48	.38
5456197	30.0	298.0	292.0	351.2	446.1	75.0	57.0	4.8	8.97	2.19	1487.71	804.38	.53
D331198	30.0	450.0	420.0	457.1	0	50.0	75.0	5.0	7.10	1.96	811.94	0	0
D331199	30.0	470.0	440.0	471.0	0	50.0	75.0	5.0	7.10	1.96	802.92	0	0
D331200	30.0	540.0	500.0	513.7	527.8	100.0	75.0	4.8	6.82	1.92	708.19	631.51	0
D331201	30.0	500.0	460.0	478.5	0	48.0	75.0	4.8	6.82	1.92	721.72	0	0
D331202	30.0	500.0	460.0	478.6	507.1	100.0	75.0	4.8	6.82	1.92	814.20	631.51	.10
D331203	30.0	470.0	437.0	463.6	508.7	100.0	75.0	5.0	7.10	1.96	947.26	690.15	0
D331204	30.0	450.0	420.0	447.0	501.5	100.0	75.0	5.0	7.10	1.96	960.80	699.17	.25
D331205	10.0	400.0	384.0	408.9	471.9	100.0	75.0	4.8	4.15	1.42	884.11	608.96	.25
D331206	10.0	370.0	345.0	372.7	457.3	100.0	75.0	5.0	4.32	1.46	985.61	631.51	0
D331207	10.0	340.0	311.0	352.2	439.1	100.0	75.0	5.0	4.32	1.46	976.58	631.51	0
D331208	5.0	340.0	315.0	328.0	437.0	100.0	75.0	6.0	3.66	1.30	924.71	563.85	0
D331209	10.0	500.0	457.0	475.7	497.9	100.0	75.0	5.0	4.32	1.46	665.34	541.29	.21
D331210	10.0	350.0	321.0	352.0	438.7	100.0	75.0	5.0	4.32	1.46	978.84	604.44	0

RUN CODES	EXT RATIO	INITIAL TEMP	ACTUAL TEMP	PEAK TEMP	FINAL TEMP	BILLET LENG	BILLET DIAM	RAM SPEED	FELTHAM ST.RATE -1	LOG FELT	MAXIMUM PRESS 2	MINIMUM PRESS 2	PEAK DELTAP
		DEG.C	DEG.C	DEG.C	DEG.C	MMS	MMS	MMS/S	SEC		MN/M	MN/M	MN
D331211	30.0	540.0	500.0	520.5	566.0	100.0	75.0	10.5	14.91	2.70	728.49	631.51	.33
D331212	40.0	480.0	440.0	461.4	520.0	100.0	75.0	7.0	11.21	2.42	935.99	676.62	.35
D331213	40.0	480.0	440.0	481.2	490.2	50.0	75.0	7.0	11.21	2.42	782.62	766.83	.10
D331214	50.0	540.0	500.0	513.9	534.7	100.0	75.0	4.0	7.02	1.95	793.90	739.77	.17
D331215	50.0	540.0	500.0	525.1	0	40.0	75.0	4.4	7.72	2.04	816.45	0	0
D331216	60.0	540.0	500.0	518.0	553.5	100.0	75.0	8.0	15.11	2.72	789.39	654.06	.33
D331217	60.0	480.0	440.0	465.0	527.6	100.0	75.0	8.0	15.11	2.72	1014.93	699.17	.47
D331218	20.0	450.0	420.0	438.4	472.5	100.0	75.0	3.2	3.81	1.34	807.43	631.51	.11
D331219	20.0	450.0	420.0	437.5	492.6	100.0	75.0	5.2	6.19	1.82	829.98	631.51	.33
D331220	20.0	450.0	420.0	438.9	537.7	100.0	75.0	13.0	15.49	2.74	895.39	685.64	.29
D331221	20.0	450.0	420.0	425.7	0	100.0	75.0	152.0	181.06	5.20	714.96	0	0
D331222	20.0	450.0	420.0	425.2	0	100.0	75.0	168.0	200.12	5.30	739.77	0	0
D331223	10.0	310.0	310.0	0	0	100.0	75.0	5.0	4.32	1.46	1127.70	0	0
D331224	10.0	310.0	10.0	0	0	100.0	75.0	5.0	4.32	1.46	1127.70	0	0
D331225	5.0	350.0	340.0	365.7	444.8	76.0	57.0	3.8	3.05	1.11	925.43	624.76	0
D331226	5.0	400.0	385.0	408.9	0	76.0	57.0	3.8	3.05	1.11	862.95	0	0
D331227	5.0	450.0	435.0	455.6	0	76.0	57.0	3.8	3.05	1.11	741.90	0	0
D331228	5.0	500.0	490.0	507.3	0	76.0	57.0	3.8	3.05	1.11	624.76	0	0

RUN CODES	INITIAL Z	LOG Z I	PEAK Z	LOG Z P	FINAL Z	LOG Z F	INITIAL FLOW STRESS 2 MN/M	PEAK FLOW STRESS 2 MN/M	FINAL FLOW STRESS 2 MN/M	EXTRUDE QUALITY
D222001	.29427E+21	47.13	0	0	0	0	422.85	0	0	STICKER
D222002	.10840E+18	39.22	0	0	0	0	293.49	0	0	O.K.
D222003	.29249E+17	37.91	0	0	0	0	272.06	0	0	I.M.
D222004	.81063E+15	34.33	0	0	0	0	213.40	0	0	I.M.
D222005	.26626E+15	33.22	0	0	0	0	195.20	0	0	I.M.
D222006	.16738E+16	35.05	0	0	0	0	225.26	0	0	I.M.
D222007	.81065E+14	32.03	0	0	0	0	175.78	0	0	I.M. (BAD)
D222008	.98225E+19	43.73	0	0	0	0	367.22	0	0	STICKER
D222009	.63907E+19	43.30	0	0	.13202E+15	32.51	360.19	0	183.74	LINES REAR
D222010	.56268E+15	33.96	0	0	0	0	207.43	0	0	I.M.+ LINE
D222011	.43157E+18	40.61	0	0	.84296E+13	29.76	316.09	0	138.94	I.M.+ LINE
D222012	.35830E+17	38.12	0	0	.36037E+14	31.22	275.38	0	162.56	I.M.+ LINE
D222013	.35743E+18	40.42	0	0	0	0	313.01	0	0	STICKER
D222014	.26983E+17	37.83	0	0	0	0	270.74	0	0	STICKER
D222015	.13905E+16	34.87	0	0	.26626E+13	28.61	222.23	0	120.36	O.K.
D222016	.44436E+15	33.73	0	0	.14025E+13	27.97	203.57	0	110.12	I.M.
D222017	.11332E+15	32.36	0	0	0	0	181.25	0	0	I.M. (BAD)
D222018	.77332E+21	48.10	0	0	0	0	438.66	0	0	STICKER
D222019	.11996E+20	43.93	0	0	0	0	370.49	0	0	STICKER
D222020	.53749E+18	40.83	0	0	0	0	319.69	0	0	STICKER
D222021	.16394E+16	35.03	0	0	.19330E+13	28.29	224.92	0	115.23	O.K.
D222022	.44472E+15	33.73	0	0	.21836E+13	28.41	203.59	0	117.18	V B I.M.
D222023	.52376E+17	38.50	0	0	0	0	281.59	0	0	STICKER
D222024	.21903E+16	35.32	0	0	0	0	229.66	0	0	STICKER
D222025	.43807E+14	31.41	0	0	0	0	165.74	0	0	NO RECORD
D222026	.44700E+14	31.43	.22873E+14	30.76	.41348E+12	26.75	166.07	155.15	91.00	O.K.
D222027	.83215E+13	29.75	.50087E+13	29.24	.34260E+12	26.56	138.73	130.52	88.12	I.M.(BACK)
D222028	.19320E+13	28.29	.12382E+13	27.84	.18308E+12	25.93	115.22	108.15	78.68	I.M.
D222029	.94291E+14	32.18	0	0	0	0	178.25	0	0	STICKER
D222030	.21293E+14	30.69	.11183E+14	30.05	.42425E+12	26.77	153.99	143.52	91.39	FAINT I M

RUN CODES	INITIAL Z	LOG Z I	PEAK Z	LOG Z P	FINAL Z	LOG Z F	INITIAL FLOW STRESS 2 MN/M	PEAK FLOW STRESS 2 MN/M	FINAL FLOW STRESS 2 MN/M	EXTRUDE QUALITY
D222031	.46266E+13	29.16	.29937E+13	28.73	.28256E+12	26.37	129.24	122.24	85.19	I.M.
D222032	.23577E+14	30.79	0	0	0	0	155.65	0	0	STICKER
D222033	.24680E+14	30.84	.96338E+13	29.90	.36523E+12	26.62	156.39	141.11	89.09	NO RECORD
D222034	.30919E+13	28.76	.19749E+13	28.31	.33929E+12	26.55	122.76	115.57	87.97	I.M.
D222035	.15850E+14	30.39	0	0	0	0	149.19	0	0	STICKER
D222036	.15224E+14	30.35	.77561E+13	29.68	.48852E+12	26.91	148.53	137.59	93.57	I.M.
D222037	.12323E+14	30.14	0	0	0	0	145.10	0	0	STICKER
D222038	.25029E+13	28.55	0	0	0	0	119.36	0	0	STICKER
D222039	.14490E+14	30.30	0	0	0	0	147.73	0	0	STICKER
D222040	.25029E+13	28.55	0	0	.39085E+12	26.69	119.36	0	90.13	O.K.
D222041	.12265E+17	37.05	0	0	0	0	257.84	0	0	STICKER
D222042	.81172E+15	34.33	.20774E+15	32.97	.57707E+12	27.08	213.42	191.15	96.15	O.K.
D222043	.80423E+14	32.02	.33791E+14	31.15	.43437E+12	26.80	175.65	161.51	91.76	O.K.
D222044	.98089E+15	34.52	.17661E+15	32.80	.65619E+12	27.21	216.52	188.49	98.16	I.M.FAINT
D222045	.97185E+14	32.21	.39439E+14	31.31	.31716E+12	26.48	178.74	164.03	86.94	I.M.WHOLE
D222046	.13257E+14	30.22	.71823E+13	29.60	.17673E+12	25.90	146.29	136.35	78.16	I.M.WHOLE
D222047	.10973E+16	34.63	.26529E+15	33.21	.80185E+12	27.41	218.35	195.14	101.29	I.M.WHOLE
D222048	.10872E+15	32.32	.45416E+14	31.45	.39926E+12	26.71	180.57	166.33	90.46	I.M.WHOLE
D222049	.14830E+14	30.33	.75150E+13	29.65	.22891E+12	26.16	148.11	137.08	82.01	I.M.WHOLE
D222050	.64110E+15	34.09	.20706E+15	32.96	.39052E+12	26.69	209.57	191.09	90.12	O.K.
D222051	.63519E+14	31.78	0	0	.36631E+12	26.63	171.80	0	89.14	O.K.
D222052	.23157E+13	28.47	.16093E+13	28.11	.32028E+12	26.49	118.12	112.31	87.09	O.K.
D222053	.12689E+14	30.17	.70417E+13	29.58	.58038E+12	27.09	145.57	136.03	96.24	O.K.
D222054	.61183E+14	31.74	0	0	0	0	171.19	0	0	STICKER
D222055	.34513E+14	31.17	.17208E+14	30.48	.83833E+12	27.45	161.85	150.52	101.99	O.K.
D222056	.29744E+13	28.72	.21646E+13	28.40	.28359E+12	26.37	122.13	117.04	85.24	I.M.WHOLE
D222057	.18805E+14	30.57	.11041E+14	30.03	.33498E+12	26.54	151.97	143.32	87.77	OK IM FRNT
D222058	.41472E+14	31.36	.22282E+14	30.73	.40240E+12	26.72	164.85	154.73	90.58	O.K.
D222059	.13301E+13	27.92	.10904E+13	27.72	.27624E+12	26.34	109.28	106.14	84.84	O.K.
D222060	.65783E+13	29.51	.40991E+13	29.04	.47190E+12	26.88	134.93	127.29	93.04	O.K.

RUN CODES	INITIAL Z	LOG Z I	PEAK Z	LOG Z P	FINAL Z	LOG Z F	INITIAL FLOW STRESS 2 MN/M	PEAK FLOW STRESS 2 MN/M	FINAL FLOW STRESS 2 MN/M	EXTRUDE QUALITY
D222061	.29130E+14	31.00	.15477E+14	30.37	.61063E+12	27.14	159.09	148.80	97.03	O.K.
D222062	.65939E+15	34.12	.27253E+15	33.24	.13964E+13	27.96	210.03	195.58	110.05	O.K.
D222063	.97225E+12	27.60	.76854E+12	27.37	.50048E+12	26.94	104.33	100.63	93.95	O.K.
D222064	.44670E+13	29.13	.35114E+13	28.89	.52352E+12	26.98	128.68	124.80	94.64	O.K.
D222065	.19781E+14	30.62	.11637E+14	30.09	.11865E+13	27.80	152.79	144.17	107.47	O.K.
D331066	.42394E+15	33.68	.20328E+15	32.95	.24886E+13	28.54	202.80	190.79	119.27	O.K.
D331067	.53179E+16	36.21	.23015E+16	35.37	.10347E+13	27.67	244.17	230.47	105.31	O.K.
D222068	.19660E+13	28.31	.15021E+13	28.04	.28551E+12	26.36	115.50	111.21	85.34	O.K.
D222069	.11270E+14	30.05	.73413E+13	29.62	.79325E+12	27.40	143.65	136.70	101.13	O.K.
D331070	.47930E+14	31.50	.27239E+14	30.94	.66716E+12	27.23	167.21	158.00	98.42	O.K.
D331071	.10354E+16	34.57	.43444E+15	33.71	.33316E+13	28.83	217.40	203.21	123.96	O.K.
D331072	.13499E+17	37.14	.48428E+16	36.12	.33225E+13	28.83	259.41	242.64	123.91	O.K.
D331073	.29483E+13	28.71	.21238E+13	28.38	.28161E+12	26.36	121.99	116.74	85.14	O.K.
D331074	.14581E+14	30.31	.90859E+13	29.84	.52865E+12	26.99	147.83	140.16	94.79	O.K.
D331075	.67970E+14	31.85	.36169E+14	31.22	.82406E+12	27.44	172.90	162.62	101.72	O.K.
D331076	.13795E+16	34.86	.57645E+15	33.99	.19302E+13	28.29	222.10	207.83	115.21	O.K.
D331077	.31035E+13	28.76	.21298E+13	28.39	.30510E+12	26.44	122.82	116.78	86.35	O.K.
D331078	.18273E+17	37.44	0	0	0	0	264.36	0	0	STICKER
D331079	.81991E+13	29.74	.47410E+13	29.19	.23793E+12	26.20	138.49	129.64	82.59	I.M.(REAR)
D331080	.24224E+14	30.82	.11055E+14	30.03	.28103E+12	26.36	156.09	143.34	85.10	I.M.(REAR)
D331081	.25071E+13	28.55	.14759E+13	28.02	.28993E+12	26.39	119.39	110.93	85.58	I.M.WHOLE
D331082	.16081E+14	30.41	0	0	0	0	149.42	0	0	STICKER
D331083	.54814E+13	29.33	.27233E+13	28.63	.34425E+12	26.56	131.98	120.72	88.19	I.M.WHOLE
D331084	.23393E+13	28.48	.13500E+13	27.93	.38671E+12	26.68	118.28	109.52	89.97	INIT MELT
D331085	.22180E+14	30.73	.10309E+14	29.96	.25555E+12	26.27	154.65	142.20	83.67	MLT AFT 4F
D331086	.11472E+14	30.07	.59208E+13	29.41	.45137E+12	26.84	143.94	133.23	92.35	O.K.
D331087	.39254E+13	29.00	.22656E+13	28.45	.31434E+12	26.47	126.59	117.77	86.80	BAD I M
D331088	.47576E+16	36.10	0	0	0	0	242.35	0	0	STICKER
D331089	.41431E+15	33.66	.68155E+14	31.85	.57308E+12	27.07	202.43	172.95	96.05	I.M.
D331090	.41049E+14	31.35	.98577E+13	29.92	.40872E+12	26.74	164.68	141.48	90.82	I.M.

RUN CODES	INITIAL Z	LOG Z I	PEAK Z	LOG Z P	FINAL Z	LOG Z F	INITIAL FLOW STRESS 2 MN/M	PEAK FLOW STRESS 2 MN/M	FINAL FLOW STRESS 2 MN/M	EXTRUDE QUALITY
D331091	.75586E+13	29.65	.30261E+13	28.74	.25762E+12	26.27	137.18	122.41	83.79	I.M.
D331092	.98836E+12	27.62	.55626E+12	27.04	.16390E+12	25.82	104.58	95.58	77.05	I.M.
D331093	.52731E+15	33.90	.78545E+14	31.99	.45989E+12	26.85	206.37	175.26	92.64	V FAINT IM
D331094	.76699E+13	29.67	.22233E+13	28.43	.26173E+12	26.29	137.41	117.47	84.03	I.M.
D331095	.20882E+15	32.97	.31558E+14	31.08	.13665E+13	27.94	191.23	160.39	109.71	O.K.
D331096	.19800E+14	30.62	.62796E+13	29.47	.82765E+12	27.44	152.81	134.18	101.79	O.K.
D331097	.25123E+13	28.55	.10826E+13	27.71	.65507E+12	27.21	119.42	106.02	98.13	O.K.
D331098	.15280E+14	30.36	.42775E+13	29.08	.18263E+13	28.23	148.59	127.98	114.33	SHORT O.K.
D331099	.15423E+15	32.67	.14994E+14	30.34	.19439E+13	28.30	186.28	148.29	115.32	SHORT O.K.
D331100	.68184E+15	34.16	.86002E+14	32.09	.34210E+12	26.56	210.57	176.74	88.09	I.M.FAINT
D331101	.11221E+15	32.35	0	0	0	0	181.09	0	0	STICKER
D331102	.26864E+14	30.92	.54763E+13	29.33	.18222E+13	28.23	157.77	131.96	114.29	O.K.
D331103	.47080E+15	33.79	.49654E+14	31.54	.45316E+12	26.84	204.52	167.78	92.41	O.K. SHORT
D331104	.15423E+15	32.67	.11953E+14	30.11	.19331E+13	28.29	186.28	144.60	115.23	O.K. SHORT
D331105	.75272E+13	29.65	.44522E+13	29.12	.19484E+12	26.00	137.11	128.62	79.61	I.M.AT BK
D331106	.94387E+13	29.88	.63398E+13	29.48	.21850E+12	26.11	140.77	134.33	81.32	O.K.
D331107	.46851E+14	31.48	0	0	0	0	166.83	0	0	STICKER
D331108	.55320E+13	29.34	.35091E+13	28.89	.22400E+12	26.13	132.13	124.79	81.69	O.K.
D331109	.10253E+14	29.96	.56486E+13	29.36	.26981E+12	26.32	142.12	132.46	84.49	I.M.FAINT
D331110	.79249E+13	29.70	.42762E+13	29.08	.28309E+12	26.37	137.94	127.97	85.22	I.M.
D331111	.12425E+14	30.15	.61750E+13	29.45	.17356E+12	25.88	145.23	133.90	77.89	V.BAD I.M.
D331112	.18050E+16	35.13	0	0	0	0	226.49	0	0	O.K.
D331113	.13886E+17	37.17	.10366E+16	34.57	.92403E+12	27.55	259.87	217.42	103.52	O.K. CK RR
D331114	.46288E+16	36.07	.36194E+15	33.52	.10166E+13	27.65	241.90	200.22	105.03	O.K.
D331115	.53982E+15	33.92	.76684E+14	31.97	.33525E+12	26.54	206.76	174.87	87.79	O.K.CK BK.
D331116	.29855E+15	33.33	.42951E+14	31.39	.66458E+12	27.22	197.07	165.42	98.36	O.K.
D331117	.42018E+14	31.37	.97050E+13	29.90	.33079E+12	26.52	165.06	141.22	87.58	O.K.
D331118	.31348E+14	31.08	.73646E+13	29.63	.58178E+12	27.09	160.29	136.75	96.28	O.K.
D331119	.45035E+13	29.14	.21356E+13	28.39	.39633E+12	26.71	128.81	116.82	90.35	O.K.
D331120	.13403E+14	30.23	.51257E+13	29.27	.17867E+12	25.91	146.46	130.90	78.32	I.M.(BAD)

RUN CODES	INITIAL Z	LOG Z I	PEAK Z	LOG Z P	FINAL Z	LOG Z F	INITIAL FLOW STRESS 2 MN/M	PEAK FLOW STRESS 2 MN/M	FINAL FLOW STRESS 2 MN/M	EXTRUDE QUALITY
D331121	.11339E+13	27.76	.62647E+12	27.16	.37510E+12	26.65	106.75	97.43	89.50	O.K.
D331122	.27080E+13	28.63	.13837E+13	27.96	.10087E+12	25.34	120.63	109.91	70.01	I.M.(BAD)
D331123	.15078E+13	28.04	.75308E+12	27.35	.21398E+12	26.09	111.27	100.31	81.00	O.K.
D331124	.13234E+13	27.91	.73477E+12	27.32	.16511E+12	25.83	109.20	99.93	77.16	O.K.
D331125	.48373E+13	29.21	.20749E+13	28.36	.24638E+12	26.23	129.96	116.36	83.12	O.K.
D331126	.15237E+14	30.35	.64694E+13	29.50	.11372E+12	25.46	148.55	134.66	71.73	SLIGHT I.M
D331127	.57410E+13	29.38	.24620E+13	28.53	.22815E+12	26.15	132.73	119.10	81.96	O.K.
D331128	.31200E+14	31.07	.64132E+13	29.49	.60774E+12	27.13	160.21	134.52	96.96	O.K.
D331129	.33849E+14	31.15	.67448E+13	29.54	.37156E+12	26.64	161.54	135.33	89.36	O.K.
D331130	.10663E+15	32.30	.20374E+14	30.65	.15680E+12	25.78	180.25	153.27	76.40	SLIGHT I.M
D331131	.39220E+15	33.60	.45913E+14	31.46	.62709E+12	27.16	201.53	166.50	97.45	O.K.
D331132	.12354E+16	34.75	.12411E+15	32.45	.35069E+12	26.58	220.29	182.73	88.47	SLIGHT I.M
D331133	.48554E+15	33.82	.51452E+14	31.57	.49786E+12	26.93	205.02	168.36	93.86	O.K.
D331134	.45115E+15	33.74	.54362E+14	31.63	.61703E+12	27.15	203.82	169.26	97.20	O.K.
D331135	.61398E+16	36.35	0	0	0	0	246.52	0	0	STICKER
D331136	.15323E+17	37.27	.82489E+15	34.35	.39452E+12	26.70	261.48	213.69	90.28	I.M.FAINT
D331137	.17387E+17	37.39	.11441E+16	34.67	.46304E+12	26.86	263.55	219.04	92.74	O.K.
D331138	.20832E+17	37.58	.11534E+16	34.68	.45880E+12	26.85	266.51	219.17	92.60	CHECK REAR
D331139	.69382E+16	36.48	0	0	0	0	248.52	0	0	STICKER
D331140	.14068E+18	39.49	0	0	0	0	297.75	0	0	STICKER
D331141	.36011E+18	40.43	.36084E+17	38.12	.11206E+13	27.74	313.13	275.49	106.57	O.K.
D331142	.21914E+13	28.42	.96848E+12	27.60	.17848E+12	25.91	117.24	104.26	78.31	CHECK REAR
D331143	.77347E+13	29.68	.23197E+13	28.47	.26289E+12	26.30	137.55	118.15	84.10	O.K.
D331144	.69787E+13	29.57	.20947E+13	28.37	.26264E+12	26.29	135.88	116.52	84.08	CHECK REAR
D331145	.11803E+13	27.80	.77735E+12	27.38	0	0	107.39	100.81	0	FRICT TEST
D331146	.22568E+14	30.75	.92537E+13	29.86	0	0	154.93	140.45	0	FRICT TEST
D331147	.22568E+14	30.75	.79899E+13	29.71	0	0	154.93	138.07	0	FRICT TEST
D331148	.48844E+15	33.82	.19640E+15	32.91	0	0	205.12	190.23	0	FRICT TEST
D331149	.10977E+13	27.72	.73841E+12	27.33	0	0	106.24	100.00	0	FRICT TEST
5456150	.23147E+09	19.26	.16911E+09	18.95	.64630E+08	17.98	120.72	112.45	88.73	O.K.

RUN CODES	INITIAL Z	LOG Z I	PEAK Z	LOG Z P	FINAL Z	LOG Z F	INITIAL FLOW STRESS 2 MN/M	PEAK FLOW STRESS 2 MN/M	FINAL FLOW STRESS 2 MN/M	EXTRUDE QUALITY
5456151	.39992E+09	19.81	.25424E+09	19.35	.66133E+08	18.01	135.63	123.24	89.26	O.K.
5456152	.65662E+09	20.30	.38354E+09	19.76	.12001E+09	18.60	149.57	134.47	103.69	O.K.
5456153	.10438E+10	20.77	.59436E+09	20.20	.92295E+08	18.34	162.89	146.74	97.20	O.K.
5456154	.61956E+10	22.55	0	0	0	0	215.62	0	0	STICKER
5083155	.19437E+12	25.99	.12833E+12	25.58	.33694E+11	24.24	108.97	101.52	79.08	O.K.
5083156	.44357E+12	26.82	.27065E+12	26.32	.45798E+11	24.55	124.29	115.04	84.00	O.K.
5083157	.13086E+13	27.90	.73334E+12	27.32	.93557E+11	25.26	145.14	133.89	95.99	O.K.
5083158	.16029E+13	28.10	.74736E+12	27.34	.61366E+11	24.84	149.12	134.25	88.82	O.K.
5083159	.35673E+13	28.90	.17746E+13	28.20	.94562E+11	25.27	164.98	151.12	96.18	O.K.
5052160	.23284E+14	30.78	.18088E+14	30.53	.62362E+13	29.46	82.00	79.24	67.70	O.K.
5052161	.56991E+14	31.67	.40898E+14	31.34	.10829E+14	30.01	91.84	88.19	73.66	O.K.
5052162	.11700E+15	32.39	.79640E+14	32.01	.95606E+13	29.89	99.78	95.53	72.31	O.K.
5052163	.30202E+15	33.34	.15823E+15	32.70	.13514E+14	30.23	110.28	103.12	76.06	O.K.
5052164	.56721E+16	36.27	.23480E+16	35.39	.19303E+14	30.59	142.83	133.03	79.95	O.K.
5083165	.98928E+11	25.32	.64097E+11	24.88	0	0	96.96	89.55	0	PARTIAL
5083166	.37257E+13	28.95	.16365E+13	28.12	0	0	165.85	149.53	0	PARTIAL
5456167	.14157E+09	18.77	.10165E+09	18.44	0	0	107.87	99.56	0	PARTIAL
5456168	.19251E+10	21.38	.12706E+10	20.96	0	0	180.79	168.61	0	PARTIAL
5052169	.10412E+14	29.97	.83746E+13	29.76	0	0	73.23	70.88	0	PARTIAL
5052170	.85653E+16	36.69	.34547E+16	35.78	0	0	147.41	137.32	0	PARTIAL
D331171	.98525E+12	27.62	.61021E+12	27.14	0	0	104.53	97.02	0	GRID
D331172	.24336E+15	33.13	.12428E+15	32.45	0	0	193.73	182.75	0	GRID
5456173	.16420E+09	18.92	.87758E+08	18.29	.60569E+08	17.92	111.68	95.97	87.23	O.K.
5052174	.12194E+14	30.13	.70096E+13	29.58	.34642E+13	28.87	74.95	68.96	61.44	O.K.
5083175	.17415E+12	25.88	.79860E+11	25.10	.24569E+11	23.92	106.98	93.27	74.20	O.K.
D331176	.58396E+12	27.09	.31336E+12	26.47	.27988E+12	26.36	96.34	86.76	85.04	O.K.
5052177	.58275E+13	29.39	.34433E+13	28.87	0	0	66.97	61.37	0	O.K.
5083178	.58110E+11	24.79	.32501E+11	24.20	0	0	87.91	78.52	0	O.K.
5456179	.98954E+08	18.41	.67555E+08	18.03	0	0	98.90	89.76	0	O.K.
5052180	.18743E+14	30.56	.10171E+14	29.95	.25371E+13	28.56	79.63	72.98	58.16	O.K.

RUN CODES	INITIAL Z	LOG Z I	PEAK Z	LOG Z P	FINAL Z	LOG Z F	INITIAL FLOW STRESS 2 MN/M	PEAK FLOW STRESS 2 MN/M	FINAL FLOW STRESS 2 MN/M	EXTRUDE QUALITY
5083181	.19164E+12	25.98	.75363E+11	25.05	.22807E+11	23.85	108.71	92.28	73.07	O.K.
5456182	.30660E+09	19.54	.17049E+09	18.95	.62352E+08	17.95	128.31	112.66	87.90	O.K.
5052183	.17824E+14	30.51	.86425E+13	29.79	.20018E+13	28.33	79.08	71.22	55.70	O.K.
5083184	.18560E+12	25.95	.82825E+11	25.14	.21989E+11	23.81	108.13	93.89	72.53	O.K.
5456185	.31873E+09	19.58	.14981E+09	18.82	.84132E+08	18.25	129.37	109.32	94.96	I.M.
5083186	.54063E+12	27.02	.16223E+12	25.81	.34432E+11	24.26	128.04	105.70	79.43	O.K.
5052187	.71345E+14	31.90	.30305E+14	31.04	.58952E+13	29.41	94.32	84.89	67.10	O.K.
5456188	.66476E+09	20.31	.27871E+09	19.45	.92363E+08	18.34	149.92	125.72	97.21	O.K.
5083189	.26720E+13	28.61	.75733E+12	27.35	.59547E+11	24.81	159.22	134.51	88.32	O.K.
5052190	.53253E+15	33.91	.17444E+15	32.79	.85649E+13	29.78	116.57	104.20	71.12	O.K.
5456191	.22049E+10	21.51	.63019E+09	20.26	.13015E+09	18.68	184.80	148.40	105.73	O.K.
5052192	.22655E+14	30.75	.63593E+13	29.48	.17328E+12	25.88	202.28	176.57	106.89	O.K.
5083193	.59409E+16	36.32	.49387E+15	33.83	.71992E+13	29.60	143.34	115.73	69.24	O.K.
5654194	.10606E+11	23.08	.21284E+10	21.48	.21139E+09	19.17	231.81	183.76	118.31	O.K.
5052195	.13662E+18	39.46	.18232E+17	37.44	.22903E+14	30.76	178.17	155.80	81.82	O.K.
5083196	.31233E+15	33.38	.17341E+14	30.48	.13629E+12	25.64	255.92	196.85	102.59	O.K.
5456197	.67369E+11	24.93	.77853E+10	22.78	.34025E+09	19.65	287.89	222.49	131.16	O.K.
D331198	.10008E+14	29.93	.24168E+13	28.51	0	0	141.72	118.80	0	FRICT
D331199	.45663E+13	29.15	.14692E+13	28.02	0	0	129.03	110.86	0	FRICT
D331200	.53122E+12	27.00	.34340E+12	26.56	.20254E+12	26.03	94.87	88.15	80.18	O.K.
D331201	.20876E+13	28.37	.10890E+13	27.72	0	0	116.46	106.12	0	O.K.
D331202	.20876E+13	28.37	.10851E+13	27.71	.35767E+12	26.60	116.46	106.06	88.77	O.K.
D331203	.51222E+13	29.26	.19092E+13	28.28	.32649E+12	26.51	130.88	115.03	87.38	O.K.
D331204	.10008E+14	29.93	.35049E+13	28.89	.39406E+12	26.70	141.72	124.77	90.26	O.K.
D331205	.27081E+14	30.93	.92391E+13	29.85	.59382E+12	27.11	157.90	140.43	96.60	O.K.
D331206	.18159E+15	32.83	.47272E+14	31.49	.93601E+12	27.56	188.95	166.98	103.73	O.K.
D331207	.11278E+16	34.66	.12670E+15	32.47	.16850E+13	28.15	218.80	183.07	113.04	O.K.
D331208	.76146E+15	34.27	.37328E+15	33.55	.15813E+13	28.09	212.38	200.72	112.03	O.K.
D331209	.14754E+13	28.02	.76004E+12	27.36	.31094E+12	26.46	110.93	100.45	86.64	UNHOM. O.K
D331210	.64497E+15	34.10	.12810E+15	32.48	.17829E+13	28.21	209.67	183.25	113.94	UNHOM. O.K

RUN CODES	INITIAL Z	LOG Z I	PEAK Z	LOG Z P	FINAL Z	LOG Z F	INITIAL FLOW STRESS 2 MN/M	PEAK FLOW STRESS 2 MN/M	FINAL FLOW STRESS 2 MN/M	EXTRUDE QUALITY
D331211	.11620E+13	27.78	.60836E+12	27.13	.13229E+12	25.61	107.14	96.98	73.91	I.M.
D331212	.72099E+13	29.61	.32676E+13	28.82	.35369E+12	26.59	136.41	123.64	88.60	I.M.
D331213	.72099E+13	29.61	.16301E+13	28.12	.10016E+13	27.63	136.41	112.51	104.79	FRICTION
D331214	.54697E+12	27.03	.35070E+12	26.58	.16619E+12	25.84	95.32	88.47	77.25	O.K.
D331215	.60167E+12	27.12	.27341E+12	26.33	0	0	96.80	84.69	0	FRICTION
D331216	.11773E+13	27.79	.66477E+12	27.22	.19639E+12	26.00	107.35	98.36	79.73	I.M.
D331217	.97152E+13	29.90	.38730E+13	28.99	.37033E+12	26.64	141.24	126.38	89.31	I.M.FAINT
D331218	.53733E+13	29.31	.26023E+13	28.59	.61198E+12	27.14	131.66	119.99	97.07	O.K.
D331219	.87316E+13	29.80	.43844E+13	29.11	.47188E+12	26.88	139.51	128.38	93.04	O.K.
D331220	.21829E+14	30.71	.10397E+14	29.97	.25692E+12	26.27	154.39	142.34	83.75	O.K.
D331221	.25523E+15	33.17	.20354E+15	32.95	0	0	194.51	190.81	0	I.M.
D331222	.28210E+15	33.27	.22906E+15	33.07	0	0	196.15	192.74	0	I.M.
D331223	.11939E+16	34.72	0	0	0	0	219.73	0	0	STICKER
D331224	.11939E+16	34.72	0	0	0	0	219.73	0	0	STICKER
D331225	.16539E+15	32.74	.46397E+14	31.47	.10611E+13	27.69	187.42	166.68	105.71	O.K.
D331226	.19020E+14	30.58	.67623E+13	29.54	0	0	152.15	135.37	0	O.K.
D331227	.23746E+13	28.50	.10957E+13	27.72	0	0	118.52	106.21	0	O.K.
D331228	.32990E+12	26.52	.18764E+12	25.96	0	0	87.54	79.05	0	O.K.

Appendix H
Errors

In the present investigation, during each series of tests, certain runs were duplicated to discover the reproducibility of the results. Listed below are the percentage reproducibility errors for the parameters of prime importance.

% Reproducibility Error	Parameter
8%	Extrusion Load
4%	Extrusion Ram Speed
3%	Tensile strength (room temperature)
5%	Tensile strength (200°C)
8%	Elongation (room temperature)
10%	Elongation (200°C)
4%	Energy absorbed (Impact Tests)

The accuracy of the integral profile techniques to predict final extrusion temperatures is rather uncertain. Sheppard and Raybould, who developed the technique, carried out some aluminium extrusions using thermocouples to monitor the die surface and dead-metal-zone temperatures. For reductions of 30 and 50:1 and ram speeds up to 100 mms/sec they found the difference between experimental and predicted temperatures was usually less than 10°C. These results were obtained for a billet temperature equal to the container temperature, but with the modifications included to overcome this, the difference should not exceed 20°C which represents a 5% error for a 400°C extrusion.

NOMENCLATURE

A	Area Constant in flow stress equation Distance in axisymmetric velocity field
A_B	Cross sectional area of ram
A_1, A_2, A_3	Constants in the hot working theory
D_E	Diameter of extrude
D_B	Diameter of billet
$\dot{E}$	Rate of energy dissipation
ΔH	Activation energy
J_1, J_2, J_3	Integrals in torsion data analysis
K	Shear flow stress
K_{ij}	Shear flow stress at discontinuity ij
l	Torsion specimen gauge length
L_p	Peak extrusion load
m	Multiplying factor for friction inclusion Strain exponent
n	Strain rate exponent Constant in the hot working theory
n_2	Constant in the hot working theory
Δp	Peak pressure increment
P	Extrusion pressure
R	Extrusion ratio
R_B	Billet radius
R_E	Extrude radius
r	Radius
r_1, r_2	Torsion specimen inner and outer radii
$r(\theta)$	Radial distance from O_2
S	Area of velocity discontinuity
T	Temperature
T_m	Melting temperature

ΔT	Temperature rise
t	Time
U_{ij}	Velocity perpendicular to discontinuity ij
v	Ram speed
V	Volume
Z	Zener-Holloman Parameter
Z_i	Z calculated using initial temperature
Z_p	Z calculated using peak temperature
Z_f	Z calculated using final temperature
α	Angle in axisymmetric velocity field Constant in hot working theory
β	Angle in axisymmetric velocity field
γ	Angle in axisymmetric velocity field
$\dot{\gamma}$	Shear strain rate
δ	Angle in axisymmetric velocity field
ε	Angle in axisymmetric velocity field
$\dot{\varepsilon}$	Natural strain rate
$\bar{\dot{\varepsilon}}$	Mean strain rate
η	Angle in axisymmetric velocity field
ξ	Angle in axisymmetric velocity field
ϕ	Angle in axisymmetric velocity field
ρ	Density
θ	Angle in axisymmetric velocity field Torsional twist
λ	Angle in axisymmetric velocity field
σ	Flow stress
τ	Shear stress
ω	Deformation zone semi-angle

REFERENCES

1 C.E. PEARSON AND R.N. PARKINS. THE EXTRUSION OF METALS. 1961. CHAPMAN AND HALL LTD., LONDON.
2 R. HILL. 'THE MATHEMATICAL THEORY OF PLASTICITY'. 1950. OXFORD UNIV. PRESS.
3 W. JOHNSON AND H. KUDO. THE MECHANICS OF METAL EXTRUSION. 1962. MANCHESTER UNIVERSITY PRESS.
4 L.E. FARMER AND P.L.B. OXLEY. J.MECH.PHYS.SOLIDS. 1971. 19. 369.
5 P.L.B. OXLEY. PROC.CONF.MECH.PROPS.OF MATERIALS AT HIGH RATES OF STRAIN. INST.OF PHYS. 1973.
6 J.F.W. BISHOP. QUART.J.MECH.APPL.MATH. 1956. 9. 236.
7 R.I. TANNER AND W. JOHNSON. INT.J.MECH.SCI. 1960. 1. 28.
8 M.T. WATKINS.K. ASHCROFT AND J. MCKENZIE. MECH.ENG.RES.LAB.(PLASTICITY DIV). REP. 1954. (102). 1956. (111).
9 K. ASHCROFT AND G.S. LAWSON. J.I.M. 1960-61. 89. 369.
10 A.R.E. SINGER AND S.H.K. AL-SAMMARAI. IBID. 1960. 89. 225.
11 A.R.E. SINGER AND J.W. COAKHAM. IBID. 1960. 89. 177.
12 R. AKERET. IBID. 1967. 95. 204.
13 T. SHEPPARD AND D. RAYBOULD. IBID. 1973. 101. 33 AND 73.
14 F.W. SHARMAN. METALS.TECH. 1977. 4. 91.
15 P.M. REYNOLDS. J.I.M. 1966. 94. 379.
16 A.F. CASTLE AND T. SHEPPARD. METALS.TECH. 1976. 3. 454.
17 G.D. LAHOTI AND T. ALTAN. 21ST SAGAMORE ARMY MAT.RES.CONF.PROC.
18 C.P. HINESLEY AND H. CONRAD. MAT.SCI AND ENG. 1973. 12. 47.
19 C. GAGNON AND J.J. JONAS. TRANS.MET.SOC A.I.M.E. 1969. 245. 2581.
20 D. RAYBOULD AND T. SHEPPARD. J.I.M. 1973. 101. 65.
21 M. FARAG AND C.M. SELLARS. IBID., 1973. 101. 137.
22 W.A. WONG AND J.J. JONAS. TRANS.MET.SOC.A.I.M.E. 1968. 242. 2271.
23 A.F. CASTLE AND T. SHEPPARD. IBID. 1976. 3. 465.
24 W. JOHNSON AND A.G. MAMALIS. 17TH M.T.D.R. MACMILLAN AND CO.LONDON 1976. 539.
25 W.R.D. WILSON. INT.MECH.J.SCI. 1971. 13. 17.
26 W. ZIEGLER AND K. SIEGART. Z.METALLK. 1973. 64. 224.
27 K. ASHCROFT AND D. LAWSON. J.I.M. 1960. 89. 369.
28 M. FARAG AND C.M. SELLARS. J.I.M. 1973. 101. 137.
29 B. AVITZUR. METALFORMING:PROCESS AND ANALYSIS. 1968. MCGRAW-HILL.N-Y.
30 C.R. SHAKESPEARE AND D.A. OLIVER. POWDER MET.1964. 7. 203.
31 H. HIROMASI AND K. MAYASHI. LIGHT METAL AGE. 1975. 33. 10.
32 J.H. ALEXANDER AND B. LENGYEL. PROC.INST.MECH.E. 1965-66.
33 D. GREEN. J.I.M. 1972. 100. 295.
34 D.J. MARSH. PROC.15TH INT.M.T.D.R. 1974. MACMILLAN AND CO. LONDON.
35 C. SMITH. J.I.M. 1949-50. 76. 435.
36 R. CHADWICK. MET.REV., 1959. 4. 15.
37 E.P. WOOD. PH.D THESIS. UNIVERSITY OF LONDON. 1978.
38 C.P. HINESLEY AND H. CONRAD. MAT.SCI.ENG. 1973. 12. 47.
39 S. IKEDA ET AL. J.JAPAN INST.OF LIGHT METALS. 1975. 25. 344.
40 D. ACHEBBACH. ALUMINIUM. 1971. 47. 203.
41 M. VAN LANKER. METALLURGY OF AL ALLOYS. CHAPMAN AND HALL LTD. LONDON.
42 H.K. HARDY. METALLURGIA. 1944. 30. 240.
43 A. PLUMTREE AND G. DEEP. METALS TECH. 1977. 4. 1.
44 J.F.W. BISHOP. MET.REV. 1957. 2. 361.
45 K.R. VAN HORN. ALUMINIUM A.S.M. METALS PARK. OHIO. CHAPMAN AND HALL. LONDON.
46 D. HARDY AND R.N. PARKINS. J.I.M. 1956-57. 85. 449.
47 E.C.W. PERRYMAN AND G.B. BROOK. J.I.M. 1951. 79. 19.
48 L.F. MONDOLFO. ALUMINIUM ALLOYS: STRUCT. AND PROP., 1976. BUTTERWORTHS.
49 J. BEIZER. IRON AGE. 1974. 214. 27.
50 W.F. KEHLER. SCHWEITZ. ALUM. RUNDSCH. 1975. 25. 348.
51 K. MASUBUCHI. 'MATERIALS FOR OCEAN ENGINEERING'. M.I.T. SEA GRANT PROJECT GHI
52 H. HERMS. SCHIFFEN HAFEN. 1975. 27. 659.
53 R.R. IRVING. IRON AGE. 1976. 218. 35.
54 P.C. VARLEY. 'THE TECHNOLOGY OF ALUMINIUM AND ITS ALLOYS.' NEWNES AND BUTTERWORTH. LONDON.
55 M. TANI AND H. TANAKA. PAPER 2.6. 'ALUMINIUM VEHICLES FOR RAIL GUIDED TRANSPORT'. DUSSELDORF. 1974
56 R.M. HART. MET. PROGR., 1974. 105. 41
57 H. WINTERMARK. SCAND. J. METALL., 1975. 4. 121
58 J. STAEHELM. SCHWEIZER ALUM. RUNDSCH. 1973. 23. 304
59 J.M. ALEXANDER. J.I.M., 1961-62. 90. 361
60 K.E. HUGHES. METALLURGIST. 1973. 5. 572
61 R. HILL. J.I.S.I., 1948. 158. 177

62 W. JOHNSON. J. MECH. PHYS. SOLIDS. 1955. 3. 218
63 L.C. DODEJA AND W. JOHNSON. IBID. 1957. 5. 267 AND 281.
64 R. SOWERBY. W. JOHNSON AND S.K. SAMANTA. IBID. 1968. 10. 231.
65 W. JOHNSON. PROC. INST. MECH. ENG.. 1959. 173. 61.
66 E.G. THOMSON ET AL.. PLASTIC DEFORMATION IN METAL PROCESSING.. 1965.
MCMILLAN AND CO.. 122
67 J. ALEXANDER. PROC. INST. MECH. ENG.. 1959. 176. 85 AND 91
68 W. JOHNSON AND H. KUDO. INT. J. MECH. SCI.. 1960. 1. 175.
69 H. KUDO. IBID. 1960. 2. 102.
70 S. KOBAYASHI. TRANS. A.S.M.E.. 1964. 868. 122 AND 326.
71 S. KOBAYASHI AND E. THOMSEN. INT. J. MECH. SCI.. 1965. 7. 127.
72 J. HALLING AND L. MITCHELL. INT. J. PROD. RES.. 1965. 4. 141.
73 J. HALLING AND L. MITCHELL. INT. J. MECH. SCI.. 1965. 7. 227.
74 J.F. ADIE AND J. ALEXANDER. IBID. 1967. 9. 349.
75 J.F. ADIE. PH.D THESIS. UNIVERSITY OF LONDON. 1966.
76 O. ZIENKIEWICZ AND P. GODBOLE. INT. J. NUM. METHOD END.. 1974. 8. 3.
77 O. ZIENKIEWICZ. P. JAIN AND E. OVIATE. INT. J. SOLID STRUCT.. 1978. 14. 15.
78 W. JOHNSON. J. MECH. PHYS. SOLIDS. 1954. 4. 269.
79 W. JOHNSON. J.I.M.. 1956-57. 85. 403.
80 J. ALEXANDER. IBID. 1961-62. 90. 193.
81 N. PURCHASE AND S. TUPPER. J. MECH. PHYS. SOLIDS. 1953. 1. 277.
82 P. WILCOX AND P. WHITTON. J.I.M.. 1961-62. 90. 193.
83 S. HIRST AND D. URSELL. METAL TREATMENT. 1958. 25. 409.
84 W. JOHNSON. B.I.R.S.A. REPORT NO MW/E/55/54. 1955.
85 T. SHEPPARD. PROC 2ND. INT. AL. EXTRUSION TECH. SEMINAR. 1977. ATLANTA.1.331
86 P. FELTHAM. METAL TREATMENT. 1956. 23. 440.
87 P. WILCOX AND P. WHITTON. J.I.M.. 1958-59. 87. 289.
88 A.F. CASTLE. PH.D THESIS. UNIVERSITY OF LONDON. 1974.
89 T. CHANDRA AND J. JONAS. MET. TRANS.. 1970. 1. 2079.
90 T. CHANDRA AND J. JONAS. IBID. 1971. 2. 877.
91 J. JONAS AND T. CHANDRA. 'METAL FORMING:INTERRELATION BETWEEN THEORY AND
PRACTISE. PLENUM PRESS. N.Y.
92 J. BISHOP. QUART.. J. MECH. APPL. MATH. AND MECH.. 1956. 9. 236.
93 M. WATKINS. K. ASHCROFT AND J. MCKENZIE. N.E.L (PLASTICITY DIV.) REPORT NO.
102(1954) AND 111(1956).
94 K. ASHCROFT AND G. LAWSON. IBID. REPORT NO. 149(1958).
95 A. SINGER AND J. COAKHAM. METALLURGIA. 1959. 60. 239.
96 K. HUGHES AND C.M. SELLARS. J.I.S.I.. 1972. 210. 661.
97 T. ALTAN AND S. KOBAYASHI. TRANS. A.I.M.E.. CONF. ON PROGRESS IN ENG..
1967. P67.
98 G.A. WOOLVET AND J. ALEXANDER. J.I.M.. 1964. 92. 430.
99 O. KLAHN. A. MUKHERJEE AND J. DORN. 2ND. CONF.'THE STRENGTH OF METALS AND
ALLOYS.' PACIFIC GROVE. CALIFORNIA.1970.
100 J. JONAS. C.M. SELLARS AND W.MCG. TEGART. MET. REV.. 1969. 14. 1.
101 H. MCQUEEN AND J. JONAS. 'PLASTIC DEFORMATION OF METALS'. ACADEMIC PRESS.N.Y..
102 C. ROSSARD AND P. BLAIN. REV. MET.. 1958. 55. 573.
103 J. BAILEY AND A. SINGER. J.I.M.. 1963-64. 92. 404.
104 J. BAILEY. INT. J. MECH. SCI.. 1972. 14. 375.
105 R. ARNOLD AND B. PARKER. J.I.M.. 1959-60. 88. 255.
106 J. ALDER AND V. PHILLIPS. IBID. 1954-55. 83. 80
107 M. MOTOMURA AND T. NISHIMURA. REP. CAST RES. LAB. WASEDA UNIV.. 1976. NO.27.
108 H. MCQUEEN.'MATERIALS TECHNOLOGY. THE AMERICAN APPROACH.' A.S.M.E. 1968. 379
109 C. SELLARS AND W.MCG. TEGART. INT. MET. REV.. 1972. 17. 1.
110 A. NICHILSON. IRON AND STEEL. 1964. 37. 290 AND 363.
111 H. MCQUEEN AND J. JONAS. 4TH. CONF.'STRENGTH OF METALS AND ALLOYS.' NANCY.
FRANCE. 1976.
112 P. MOORE. 'DEFORMATION UNDER HOT WORKING CONDITIONS.' IRON AND STEEL INST..
1968. P103.
113 S. SAMANTA. INT. J. MECH. SCI.. 1968. 10. 614.
114 J. HOCKETT. TRANS.MET.SOC.A.I.M.E.. 1967. 239. 969.
115 C. REDFERN AND C.M. SELLARS. 'DEFORMATION UNDER HOT WORKING CONDITIONS'.
I.S.I.. 1968. P29.
116 M. FARAG AND C.M. SELLARS. IBID.. P60.
117 Y. OHTAKARA ET AL.. TRANS.I.S.I.J.. 1972. 12. 36 AND 207.
118 F.A. HODIERNE. J.I.M.. 1969. 97. 73.
119 D. HARDWICK AND W.MCG.TEGART. MEM. SCI. REV. MET.. 1961. 58. 869.
120 J. BAILEY. S. HAAS AND M. SHAH. INT. J. MECH. SCI.. 1972. 14. 735.
121 J. ROBINS ET AL.. J. OF METALS. 1967. 2. 271.
122 F. GARAFALO. TRANS.MET.SOC.A.I.M.E.. 1963. 227. 351.
123 C.M. SELLARS AND W.MCG. TEGART. MEM. SCI. REV. MET.. 1966. 63. 731.
124 C. ZENER AND J. HOLLOMAN. J. APPL. PHYS.. 1944. 15. 22.
125 J. MORRIS AND B. ROOPCHAND. MAT. SCI. AND ENG.. 1975. 17. 77.
126 P.R. SWANN. 'ELECTRON MICROSCOPY AND THE STRENGTH OF METALS.' INTER SCI..
1963. N.Y..

127 J. JONAS AND M. LUTON. 'ADVANCES IN DEFORMATION PROCESSING'. 21ST. SAGAMORE ARMY MAT. RES. CONF.. PLENUM PRESS. N.Y AND LONDON.
128 G. SCHARF AND D. ACHENBACH. Z. METALLK.. 1960. 60. 904.
129 J. JONAS. H. MCQUEEN AND W. WONG. 'DEFORMATION UNDER HOT WORKING CONDITIONS'. I.S.I.. 1968. P49.
130 J. COTNER AND W.MCG. TEGART. J.I.M.. 1969. 97. 73.
131 D. HARDWICK AND W.MCG. TEGART. IBID.. 1961. 90. 17.
132 H. MCQUEEN AND J. HOCKETT. MET. TRANS.. 1970. 1. 2997.
133 R. REYNOLDS AND W.MCG. TEGART. J.I.S.I.. 1962. 200. 1004.
134 J. JONAS. 4TH. INT. CONF.. 'THE STRENGTH OF METALS'.NANCY.FRANCE. 1976. P1324
135 J. HOCKETT AND H. MCQUEEN. 2ND. CONF.'THE STRENGTH OF METALS AND ALLOYS'. CALIFORNIA. 1970. PAPER 15A. 3. P991.
136 J. BYRNE. 'RECOVERY.RECRYSTALLIZATION AND GRAIN GROWTH'. COLLIER MACMILLAN. 1956. N.Y..
137 R. GRIMES. CONF. ON'RECRYSTALLIZATION IN THE CONTROL OF MICROSTRUCTURE'. 1973. I.S.I-I.O.M..
138 C. CORTI. G. FITZPATRICK AND P. COTTERILL. IBID..
139 R. DOHERTY. IBID..
140 R. DOHERTY. METAL SCI.. 1974. 8. 132.
141 B. SUBRAMANYA. SHEET METAL IND.. 1969. 46. 895.
142 J. BLADE. METAL SCI.. 1979. 13. 206.
143 J.E. BAILEY. REF.126. P535.
144 H. HU. REF.126. P564.
145 F.J. HUMPHERIES. ACTA MET.. 1977. 11. 1323.
146 F.J. HUMPHERIES. METAL SCI.. 1979. 13. 131.
147 R. KASPAR AND J. PLUHAR. METAL SCI.. 1975. 9. 104.
148 C. ROSSARD AND P. BLAIN. MEM. SCI. REV. MET.. 1960. 57. 173.
149 M. LUTON AND J. JONAS. PROC. 2ND. CONF.' STRENGTH OF METALS AND ALLOYS'. A.S.M.. METALS PARK OHIO. 1970. P1100.
150 H. MCQUEEN AND J. JONAS. 'PLASTIC DEFORMATION OF MATERIALS'. ACADEMIC PRESS. NEW YORK. P 393.
151 O. SHERBY. R. KLUNDT AND A. MILLER. MET. TRANS. A. 1977. 8. 843.
152 R. SANDSTROM. ACTA MET.. 1977. 25. 897.
153 E. PERRYMAN. IBID.. 1954. 26. 1954.
154 J. LI. J. AUST. I. M.. 1963. 8. 207.
155 W. WONG. H. MCQUEEN AND J. JONAS. J.I.M.. 1967. 95. 129.
156 H. MCQUEEN. MET. TRANS. A. 1977. 8. 807.
157 H. STUWE. 'DEFORMATION UNDER HOT WORKING CONDITIONS'. 1968. I.S.I..
158 H. ORMEROD AND W.MCG. TEGART. J.I.M.. 1960-61. 89. 94.
159 D. MCLEAN. 'MECHANICAL PROPERTIES OF METALS.' 1962.
160 R. SANDSTROM. ACTA MET.. 1977. 25. 905.
161 H. HU. TRANS. MET. SOC. A.I.M.E.. 1965. 230. 570.
162 D. SASTRY. M. LUTON AND J. JONAS. PHIL. MAG.. 1974. 30. 1187.
163 R. DEWIT AND R. HOWARD. ACTA MET.. 1962. 10. 655.
164 A. HOWIE. MET. REV. 1961. 6. 467.
165 H. TENSI. P. DROPMAN. AND H. BORCHERS. Z. METALLK.. 1970. 61. 518.
166 A. HOWIE AND P.R. SWANN. PHIL. MAG.. 1961. 6. 1215.
167 W. TRUSKOWSKI. A. PAWLOWSKI AND J. DUTKIEWICZ. BULL. ACAD. POL. SCI. SER. SCI. TECH.. 1971. 19. 55.
168 E.G. VAN BUERON. NORTH HOLLAND PUBLISHING CO.. AMSTERDAM. FROM R. BERNER. Z. NATURF.. 1960. 15A. 689.
169 G.F. ROLLING. L.E. HAYS AND W. WIEDERSICH. ACTA MET. 1962. 10. 185.
170 J. LI AND B. CHALMERS. IBID.. 1963. 11. 243.
171 M.C. INMAN AND A.R. KHAN. PHIL. MAG.. 1961. 6. 937.
172 M. LUTON AND C.M. SELLARS. ACTA MET.. 1969. 17. 1033.
173 W. HIRST. PROC. AUST. INST. MIN. MET.. 1940. 120. 777.
174 H. MCQUEEN AND S. BERGERSON. METAL SCI. J.. 1972. 6. 25.
175 G. GLOVER AND C.M. SELLARS. MET. TRANS. A.. 1973. 4. 765.
176 J. SHAH. G. RICHARDSON AND C.M. SELLARS. 'RECRYSTALLIZATION IN THE CONTROL OF MICROSTRUCTURE'. 1973. ISI-IOM.
177 J. SHAH. G. RICHARDSON AND C.M. SELLARS. J. AUST. INST. MET. 1969. 15. 292.
178 C. SELLARS AND J. WHITEMAN. METAL SCI.. 1979. 13. 187.
179 R. PETHEN AND R. HONEYCOMBE. REF.176.
180 V. SEDLACEK. REF. 176.
181 H.P. STUWE. REF. 176.
182 G. GOTTSTEIN. D. ZABARDJADI AND H. MECKING. REF.176.
183 K. GARDNER AND R. GRIMES. METAL SCI.. 1979. 13. 216.
184 W. BLUM. Z. METALLK.. 1977. 68. 480.
185 C. BARRET AND W. NIX. ACTA MET.. 1965. 13. 1247.
186 J. WEERTMAN. J. APPL. PHYS.. 1955. 26. 1213.
187 J. WEERTMAN. IBID.. 1957. 28. 362.
188 F. GARAFALO AND J. HOLLOMAN. TRANS. A.S.M.. 1944. 33. 163.
189 D. MCLEAN. REP. PROG. PHYS.. 1966. 29. 1.
190 D. MCLEAN. MET. REV.. 1962. 7. 481.

191 H. STUWE AND B. ORTNER, METAL SCI., 1974, 8, 161.
192 W. ROBERTS AND B. AHLBLOM, ACTA. MET., 1978, 26, 81.
192 D. KOSIK, D. ABSON AND J. JONAS, J.I.S.I., 1971, 209.624.
194 A. THOMPSON, MET. TRANS. A, 1977, 8, 833.
195 R. MCELROY AND Z. SZKOPIAK, INT. MET. REV., 1972, 17, 175.
196 A. BRYANT, Z. METALLK., 1971, 62, 701.
197 T. WILLIAMS, M.SC. THESIS, 1954, CARDIFF UNIVERSITY.
198 B. MEADOWS AND M. CUTLER, J.I.M. 1969, 97, 321.
199 T. SHEPPARD AND A.F. CASTLE, PROC. 16TH M.T.D.R..CONF. MANCHESTER, 1975.
200 NAG. LIBRARY CONSTRAINED MINIMIZATION ROUTINE-E04HAF.
201 F.A. LOOTSMA,'A SURVEY OF METHODS FOR SOLVING CONSTRAINED MINIMIZATION PROBLEMS VIA UNCONSTRAINED MINIMIZATION. NUMERICAL FOR NON-LINEAR OPTIMIZATION', ACADEMIC PRESS. LONDON, 1972.
202 G.D. RICHARDSON AND M.P. STUWE, I.S.I., SPECIAL REPORT 108, 1968, P131.
203 A. NADAI,'THEORY OF FLOW STRESS AND FRACTURE OF SOLIDS', MCGRAW-HILL, N.Y. 1950, P 349.
204 D.S. FIELDS AND W.A. BACKHOFEN, PROC. A.S.T.M., 1957, 57, 1259.
205 D.S. WRIGHT, PH.D. THESIS, UNIVERSITY OF LONDON, 1978.
206 G.W. ROWE,' AN INTRODUCTION TO THE PRINCIPLES OF METALWORKING', E. ARNOLD. LONDON, 1965.
207 T. SHEPPARD, PRIVATE COMMUNICATION.
208 G.D. LAHOTI AND T. ALTAN, TRANS. A.S.M.E..(J. ENG. MAT. AND TECH.). 1975, APRIL.113.
209 J.G. TWEEDALE, M.SC. THESIS, UNIVERSITY OF LONDON, 1974.
210 T. SHEPPARD AND D. RAYBOULD, J.I.M., 1973, 101, 45.
211 H. OIKAWA, J. KARIYA AND S. KARASHIMA, METAL SCI., 1974, 8, 106.
212 K.L. MURTY, F.A MOHAMED AND J.E. DORN, ACTA MET., 1972, 20, 1009.
213 R. MORIUCHI AND M. OTSAKA, TRANS. JAP.I.M., 1972, 13, 82.
214 K. KUCHAROVA, I. SAXELAND J. CADEK, ACTA MET, 1974, 22, 465.
215 J.G. MORRIS, PROC. 4TH INTER AMERICAN CONF. ON MAT. TEST., 1975, P385.
216 N.R. BORSCH, L.A. SHEPARD AND J.E. DORN, TRANS. A.S.M. 1960, 52, 494.
217 H. OIKAWA, N. MATSUNO AND S. KARASHIMA, METAL SCI., 1975, 9, 209.
218 T. SHEPPARD, PRIVATE COMMUNICATION.
219 H.B. MCSHANE, PH.D. THESIS, UNIVERSITY OF LONDON, 1978.
220 D. RAYBOULD, PH.D. THESIS, UNIVERSITY OF LONDON.
221 Z. ZIMMERMAN AND B. AVITZUR, J. ENG. IND., 1970, 92, 119.
222 S. SOHRABOPOUR, A.H. SHABAIK AND E.G. THOMSEN, IBID., 1970, 92, 461.
223 P.B. HIRSCH,'THE PHYSICS OF METALS', VOL.2, CAMBRIDGE UNIV. PRESS, 1975.
224 B. AVITZUR,' METAL FORMING: PROCESS AND ANALYSIS', 1968, MCGRAW-HILL, N.Y.
225 H.J. MCQUEEN, W.A. WONG AND J. JONAS, CAN. J. PHYS., 1967, 45, 1225.
226 T. SHEPPARD AND A.F. CASTLE, METALS TECH, 1976, 2, 433.
227 F.N. RHINES,' THE INHOMOGENEITY OF PLASTIC DEFORMATION', CH.10, A.S.M..1973.
228 I.L. DILAMORE, P.L. MORRIS, C.J.E. SMITH AND W.B. HUTCHINSON. PROC. R. SOC., 1972, 329, 405.
229 H.J. MCQUEEN AND S. BERGERSON, METAL SCI. J., 1972, 6, 25.
230 V.A. PHILLIPS AND A.J. SWAN, J.I.M., 1952-53, 81, 625.
231 A.T. THOMAS, ACTA MET., 1966, 14, 1363.
232 B.J. BRINDLEY AND P.J. WORTHINGTON, IBID., 1969, 17, 1357.
233 K. MATSUURA, T. NISHIYAMA AND S. KODA, TRANS. JAP. INST. MET., 1969, 10, 429
234 J. MUKHERJEE, T. MAY AND C. DIANTONIO, MET. TRANS., 1970, 1, 3233.
235 J. DECERF AND J.C. BAUWENS, Z. METALLK., 1974, 65, 215.
236 A.H. COTTRELL, PHIL. MAG., 1958, 44, 829.
237 C.J. SMITHELS, METALS REF. BOOK, 2ND. ED., BUTTERWORTHS, LONDON.

Development of recovered dislocation substructures during plastic flow

T. Sheppard, M. G. Tutcher, and H. M. Flower

A study has been made of the macroscopic and microstructural changes which occur during the hot extrusion of a single phase Al–5%Mg alloy. The load/displacement curve exhibits a typical peak in load after a small ram displacement. Light microscopy has shown that a quasi-static deformation zone is not fully established until a short time after this peak, and no significant deformation occurs in the rear of the billet until this state is achieved. Electron microscopy has shown that the attainment of steady state extrusion is associated with dynamic recovery leading to the formation of an equiaxed subgrain structure in the deformation zone. The extremely heterogeneous nature of the deformation on a macroscopic and microscopic scale (including the formation of deformation bands of high local lattice rotation) determines the positions at which the dynamic recovery occurs at any stage in the development of steady state extrusion.

Manuscript received 20 January 1978; in final form 23 October 1978. T. Sheppard, PhD, DIC, MIM, CEng, MIMechE, M. G. Tutcher, BSc, ARSM, and H. M. Flower, PhD, DIC, MIM, are in the Department of Metallurgy and Materials Science, Imperial College of Science and Technology, London.

During all mechanical processing operations it is necessary to establish a deformation zone which is quasi-static. The material must thus be transformed from a state of as-cast dislocation density to one consistent with the thermally activated events obtaining during deformation. The establishment of this steady state density produces a non-linear external energy vs. time relationship which varies with the process. Of the major processing routes rolling is limited by friction conditions at roll entry but extrusion is very much governed by the pressure necessary to initiate the process. The present paper considers the development of the quasi-static deformation zone during the extrusion process.

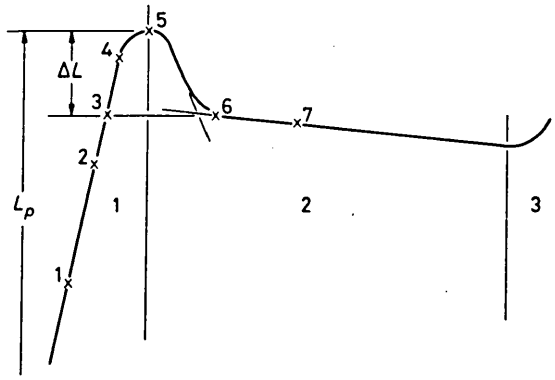
In direct extrusion the pressure displacement (or time) locus may conveniently be divided into three distinct stages as shown in Fig. 1. During the first stage the billet is upset to fill the container, there is limited ram travel, and temperature changes will affect dislocation mobility and instantaneous values of flow stress. Since mathematical models are not available to describe non-equilibrium flow the strain rate is indeterminate. The second stage is referred to as steady state flow although for most complex alloys there is a rapid decrease in pressure between Stages 1 and 2, usually accompanied in the industrial operation by an increase in ram velocity associated with the bulk modulus of the hydraulic fluid. During Stage 3 the pressure rises rapidly as the dummy block interferes with the deformation zone and for this reason a discard is left in the container and must be ejected and, in the case of aluminium alloys, recycled.

The controlling feature which determines whether extrusion proceeds or whether the billet sticks in the container is the maximum pressure which occurs at the boundary between Stages 1 and 2. This pressure is referred to as the breakthrough pressure and clearly must lie within the capacity of the press. Hence the magnitude of this pressure imposes limitations upon the extrusion ratio, the initial billet temperature, the ram velocity, and the billet length/diameter geometry. Each of these parameters affects the magnitude of the extrusion pressure. If it were possible to reduce the breakthrough pressure, then larger reductions, longer billets, lower temperatures, and higher ram speeds might be possible. Thus any contribution which explains the mechanism of peak pressure formation could be of direct benefit to the commercial extruder. The 'peak' or 'breakthrough' pressure is defined by intersecting tangents as shown in Fig. 1.

Wilson[1] recognized the existence of this peak and using mathematical techniques suggested that it was caused by a transition from sticking to full-film lubrication. Since full-film lubrication is unlikely in the industrial situation such a transition could not occur. Furthermore, Ziegler[2] has presented evidence that the peak exists in indirect extrusion where friction effects are virtually zero if a flat-faced die is used. Ashcroft and Lawson[3] associated the phenomenon with the temperature differential which exists between billet and die, while Farag and Sellars[4] presented evidence supporting its connection with the die entrant angles. It has also been proposed[5] that this additional pressure represents the energy required to set up the dead-metal zone but since the peak has been observed[1,2,4] under conditions in which such a zone does not exist this explanation appears to be invalid. Thus it appears that mathematical explanations which ignore structural changes occurring in the material are unlikely to be useful.

Castle and Sheppard[6] indicated that it was much more likely that the additional pressure was associated with the energy required to establish the quasi-static deformation zone. They proposed that the formation of the zone required an excess of dislocation sources leading to a greater than equilibrium dislocation density. This excess of dislocation production necessary to establish the steady state process would also imply a non-equilibrium flow stress resulting in the requirements of excess pressure. The present paper presents a more detailed investigation of this thesis.

Microstructural investigations[7–9] of aluminium alloys have shown that dynamic recovery is the major softening process. The dislocation substructure produced is a direct result of stress- and temperature-induced mobility due to



1 Load/displacement curve showing peak geometry and sample locations.

plastic deformation. This rapid increase in dislocation density produces a corresponding increase in the elastic strain energy (stored energy) which is released when dislocations meet and annihilate or rearrange themselves into lower energy configurations. It is this rearrangement which typically produces regular low-angle boundaries forming subgrains. The mechanism of boundary formation is by cross-slip and climb which, being thermally activated, is aided by high homologous temperatures. The distribution and mobility of dislocations is also affected by stacking fault energy, crystal structure, strain rate, grain boundaries, and precipitates. Dislocation movement is relatively easy in the aluminium alloys because of their high stacking fault energy which suppresses the formation of dissociated dislocations and extended nodes which would inhibit cross-slip and climb. Magnesium is not expected to modify the stacking fault energy of aluminium significantly, and therefore the cross-slip and climb characteristics of the alloy would be expected to be similar to aluminium itself. Magnesium exhibits limited solid solubility in aluminium, but in the alloy studied the solubility limit is not exceeded under the experimental conditions employed. The only particles present which could affect the development of the dislocation substructure are the small number of intermetallic phases containing the other elements present.

The development of substructure during deformation has been studied extensively and many theories have been proposed to account for the observed work-hardening characteristics. The most detailed models for work-hardening apply to cold deformation processes in which climb is not involved. However, the build-up in dislocation density to a level where either dynamic recovery or recrystallization takes place in hot work, presumably involves similar work-hardening mechanisms to those taking place at lower temperatures. These mechanisms have been reviewed critically by Hirsch[10] and therefore will not be discussed here.

EXPERIMENTAL PROCEDURE

The experimental work was carried out on a direct operating 5 MN Enefco press operated at a ram speed of 14 mm s^{-1}. The details of recording techniques and operation have been documented elsewhere.[6] Billets were supplied by Alcan International Ltd. After homogenizing the as-cast billets at 500°C for 24 h they were machined to 75 mm in diameter and 75 mm long. The alloy composition is shown in Table I. The billets were heated to 450°C in a Banyard Metalheat induction furnace, and were then transferred automatically to the container, maintained at 300°C, and extruded at an extrusion ratio of 40 : 1.

Table I Composition of billets, wt-%

Mg	Mn	Si	Ti	Cr	Fe	Al
4·9	0·001	0·003	0·001	0·001	0·001	Remainder

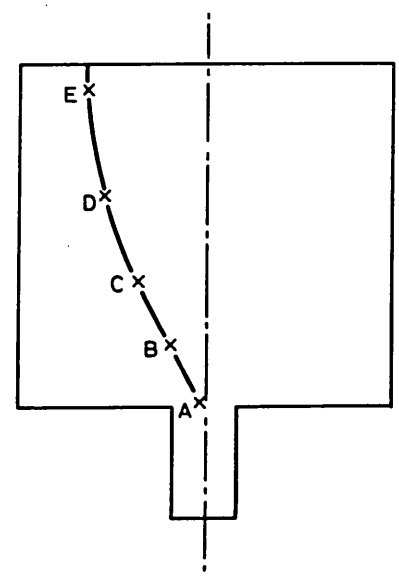
In order to investigate the development of structure, the extrusion cycle was stopped at preselected positions as shown in Fig. 1. The billets were rapidly removed and cooled. It has been shown previously that no significant microstructural changes occur during this procedure. Seven partially extruded billets were produced which were then sectioned to produce optical and electron microscopy specimens.

Specimens for electron microscopy were prepared by a standard window technique using a 30% solution of nitric acid in methanol at a potential of 15 V and a bath temperature of −20 to −30°C. The specimens were taken from the billets according to a flowline found from observation and substantiated by a combination of upper bound[11] and spherical velocity field.[5] The locations from which specimens were cut are shown in Fig. 2. Specimens from the 28 locations were then examined in an effort to determine the development of the dislocation structure during the extrusion process.

RESULTS AND DISCUSSION

Macrostructural results

Owing to the lack of an efficient recrystallization inhibitor during casting, the grains can be seen to be relatively large, especially towards the periphery of the billet. There is no significant volume fraction of precipitate. Figure 3(*a*) depicts the billet during the upsetting stage. The macrostructure does not vary from that of the original billet with the exception of the region adjacent to the die entry where some deformation may be detected. There is no evidence of deformation elsewhere in the billet although container/billet shear is suggested by the grain structure at the periphery. Figure 3(*b*), illustrating the structure at a later stage in the upsetting process, does not exhibit radical



2 Positions of electron microscopy specimens.

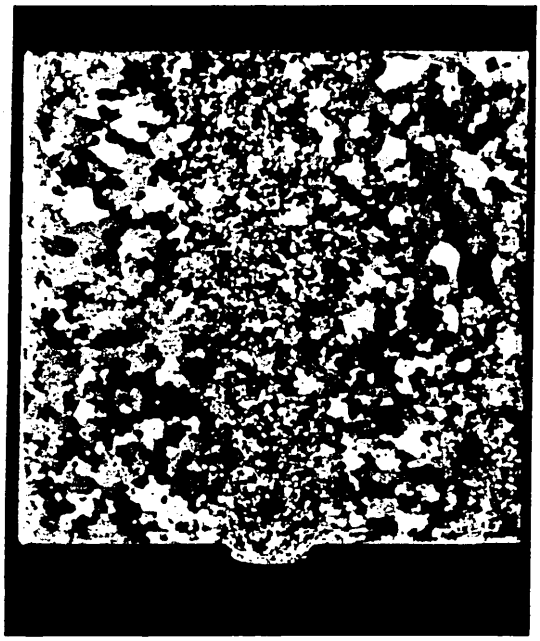
changes, but an extension of the main deformation zone has occurred and the grains in this die entry region have become elongated. It is interesting to note that a small quantity of material has been forced through the orifice and that the extreme front end reveals quite clearly the original undeformed structure. Even at this stage, however, there is a variation in structure from front to rear of the extruded pip. Figure 3(*c*) shows the situation after a further increase in pressure but with little ram travel and shows the deformation zone extending back into the billet. There is still little change in bulk structure and no identifiable dead-metal zone but cylinder wall shear appears to have extended over the complete billet surface. Figure 3(*d*), corresponding to Location 4 in Fig. 1, shows an almost identical macrostructure but the fibrous nature of the extruded structure suggests an increase in total deformation. The structure in Fig. 3(*e*) is located approximately at the point of peak pressure and shows very pronounced changes in morphology. The extrudate exhibits the typical fibrous or 'cold worked' structure and it should be noted that at this stage a considerable length of material has been extruded. Clearly the 'breakthrough' pressure does not correspond to the commencement of extrusion. The deformation zone has again extended backwards into the billet and dead-metal zones are becoming apparent. Considerable cylinder wall shear is apparent and the billet peripheral layers are quite heavily deformed. The latter feature is less predominant in the surfaces adjacent to the die plane, supporting the observation that the dead-metal zone will be established in this area. In fact the deformation zone extends well back into the billet and grains can quite easily be identified which have been elongated within the central deformation zone. Figure 3(*f*) shows the structure when the pressure has fallen by an amount ΔL after the peak pressure and considerable ram travel has occurred. The central deformation zone has now developed fully and intense shear is occurring at this location; cylinder wall shear also appears to be more intense but it should be recalled that it is a deformation history which is being observed since quasi-static conditions do not obtain at this location. It should also be noted that although the dead-metal zones can be identified clearly it is the lessening of surface shear and gradation of grain deformation which allows this observation; there is definite evidence that the quasi-static deformation zone is about to be established. Figure 3(g) illustrates the macrostructure in the steady state region. The quasi-static deformation zone is fully developed and the dead-metal zone can very easily be identified. Regions of significant shear can be seen extending from die entry and along the central axis and from die entry to the periphery of the billet bounded by the dead-metal zone and the container/billet interface. The large initial grain size allows the recognition of grains passing through three regions of intense deformation. The identification of two regions of lesser deformation on either side of the central zone and sandwiched by it and the 'peripheral' zone suggests a buffer zone which serves primarily to supply material to the regions of high deformation in the billet. Material flowing from the peripheral region of the billet can be seen to occupy about 35% of the extrudate cross-section while material from the axial deformation zone occupies about 55%. This implies that the two zones of lesser deformation are feeding only about 10% in total of the material section shown in Fig. 3(g). Clearly, if these zones were not primarily feeding the intense shear zones, vortices would form within the deformation zone. This can, of course, occur when the dummy block destroys the mass balance of the various deformation zones.

In summary, it appears that significant macrostructural changes occur only after the peak pressure. During upsetting the deformation zone extends backward from the die mouth and along the cylinder wall and dead metal zone. At the peak pressure, deformation is well developed but steady state macroconditions develop between the instant of peak pressure and a time corresponding to a decrease of ΔL from this point. The steady state region is characterized by much greater intensity of shear at the axis and periphery of the billet.

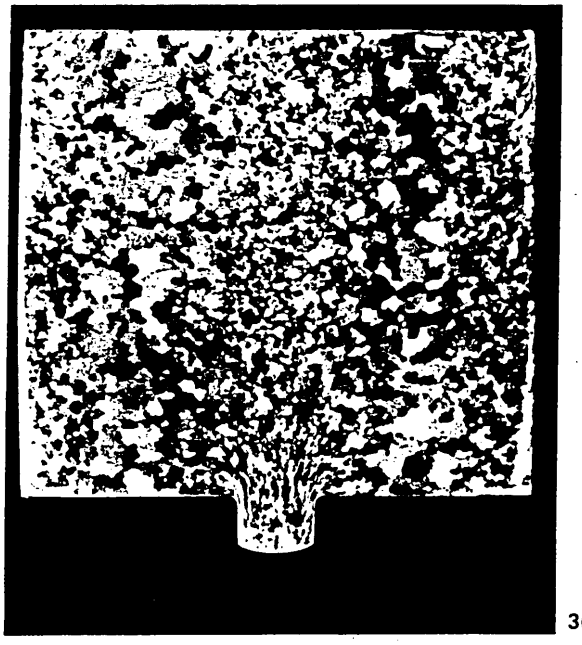
Substructural investigations

The dislocation structure within the billet arrested at Position 1 in Fig. 1 was heterogeneous. Specimens extracted from the rear of the billet (Positions C, D, and E) had similar structures having a uniform dislocation density. In isolated areas, however, walls of dislocations were beginning to form. Similar walls were observed in the other rear positions indicating that the upsetting operation causes deformation throughout the billet. There did not appear to be any special deformation associated with possible ram/billet interaction. Further forward, in Position B, dislocation wall formation was more pronounced and outcrops of subgrains were observed at high-angle boundaries. In general subgrains were not observed consistently at any position in this billet, which is consistent with the thesis that strains imposed on the material during the upsetting process are absorbed by shear at the grain boundaries. This will involve the production of dislocations to produce the strain and additional dislocation generation for storage within grains to maintain the strain gradients imposed by grain boundary shear. Thus the dislocation density is necessarily increased and a driving force for subgrain formation created; Fig. 4 illustrates this feature. Although most grains were devoid of subgrains the specimen extracted from the die mouth (Position A) showed a subgrain banding phenomenon. Bands of subgrains were observed bisecting the grains and being elongated quite severely in the potential extrusion direction (at this stage extrusion has not commenced). Misorientations were higher between these bands than between the subgrains along them which can be seen in Fig. 5 by noting the small contrast between the individual subgrains and the large difference in contrast between these and the remainder of the grain. This was confirmed by measurement of misorientations from selected-area diffraction patterns. The banding would seem to be the result of strains exerted upon abnormally large grains as they pass the velocity discontinuity associated with entry to the die mouth. These grains are preferentially elongated and the resulting localized regions of high strain require that areas of higher dislocation density also exist. Hence in this area there is sufficient dislocation mobility and density to effect the formation of subgrains. This observation may be even more significant in the industrial context where we would expect greater heterogeneity in the 'homogenized' billet by larger grain sizes, more diverse dendritic morphology, and the presence of dissociated soluble constituents.

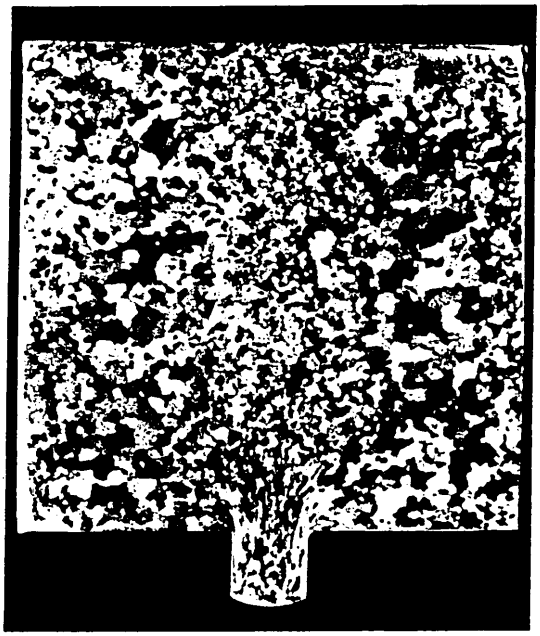
Specimens extracted at Times 2 and 3 during the process exhibited similar structures. Banding was once more observed in the die entry region; in this case producing more equiaxed subgrains as shown in Fig. 6. It should also be noted that in these subgrains there is considerable internal dislocation density and, in general, the walls are more clearly defined than those observed earlier in the extrusion cycle. The selected-area diffraction patterns (Fig. 6) show that the misorientation between the bands consists of a lattice rotation of 33° which reverses in sign across alternate bands. This was generally the case for all



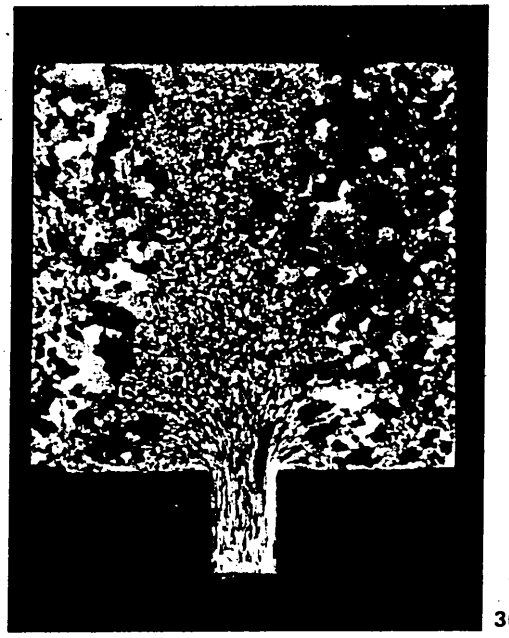
3(a)



3(b)



3(c)

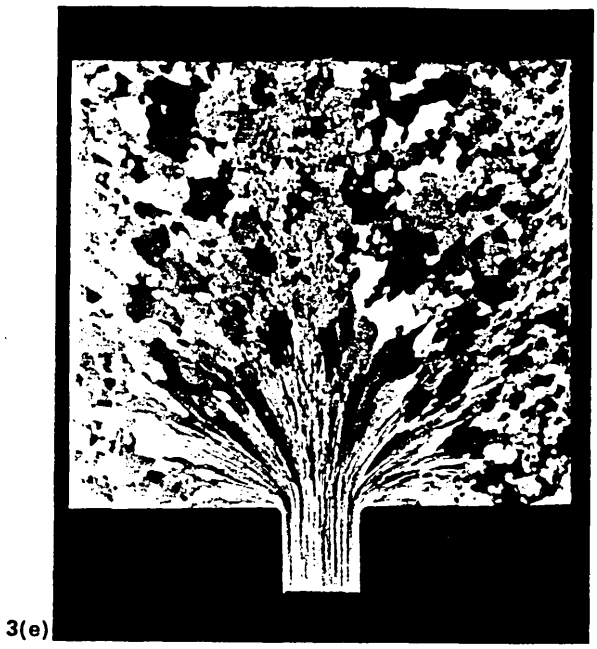


3(d)

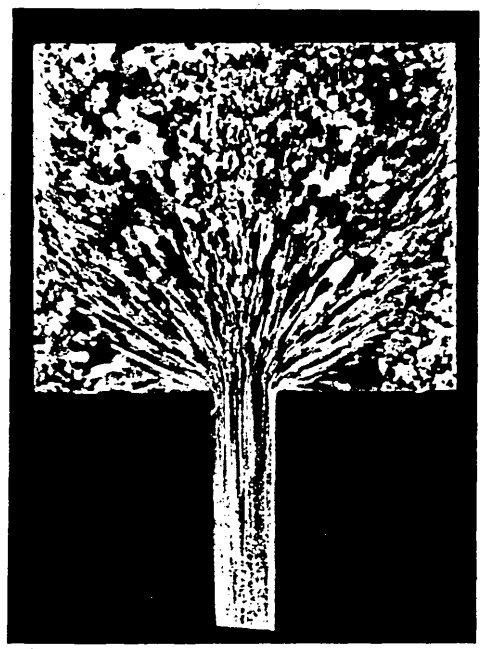
such bands investigated. At locations towards the rear of the billet dislocation wall build-up is more pronounced and isolated outcrops of small subgrains emanating from high-angle boundaries can be identified. Dislocation wall formation was also observed to be aided by precipitates; these sites clearly act as locking points and extended walls can be observed which have their extremities at precipitates. Humphreys[18] has shown recently that very large lattice rotations may occur at second-phase particles and this will require high dislocation densities. The probability that subgrain wall formation will develop is thus enhanced at these sites. This could also be an important feature in the industrial alloy (AA5456) in which a greater volume fraction of precipitate will be present. The dislocation density within subgrains indicates incomplete recovery, and within completely unrecovered regions the dislocation density is much greater than earlier in the ram stroke.

Specimens taken from the billet corresponding to the point of peak pressure (Location 5) show an equiaxed subgrain structure in Positions A, B, and C. These subgrains are slightly elongated in the die mouth (Fig. 7) and are heterogeneous in size, being smaller at high-angle boundaries. It is interesting to note that the dislocation density within subgrains is lower in Specimens B and C (i.e. proceeding backwards into the deformation zone) which is consistent with lower strains and lower strain gradients in these regions than those which occur around the theoretical exit-velocity discontinuity. Nevertheless it is clear that at this stage the deformation zone is not quasi-static and the dead-metal zone has not been fully developed since areas can be identified within the deformation zone in which subgrain formation is incomplete and the macrographs indicate that the dead-metal zone is not well defined.

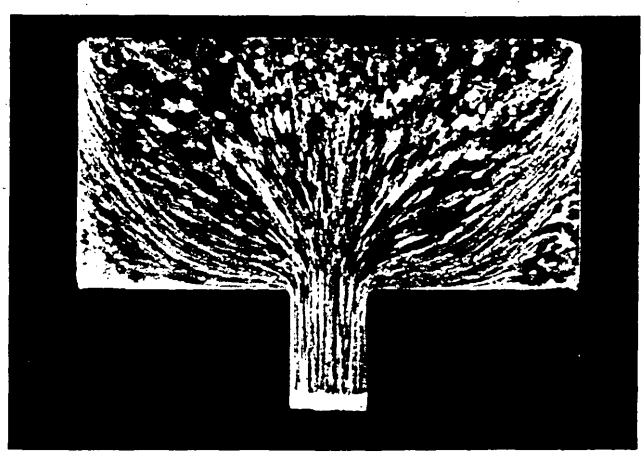
When the ram has advanced to Location 6, an equiaxed



3(e)



3(f)



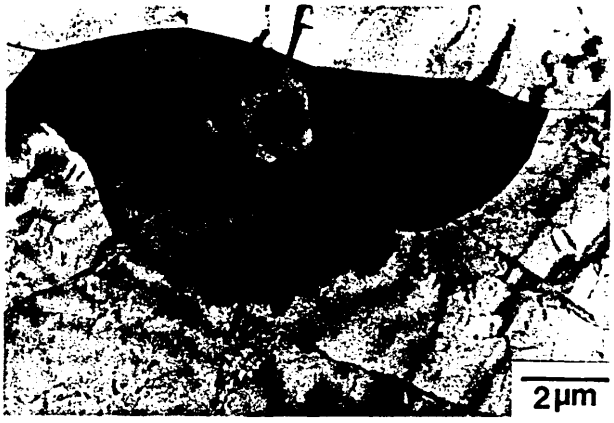
3(g)

(a) Location 1, (b) Location 2, (c) Location 3, (d) Location 4, (e) Location 5, (f) Location 6, (g) Location 7.

3 Development of macrostructure during hot direct extrusion with specimens corresponding to locations shown in Fig. 1.

subgrain structure can be observed in Positions A, B, C, and D. Some banding can still be detected at Position A (Fig. 8) but, in general, subgrains are equiaxed, locally smaller at high-angle grain boundaries and having a high internal dislocation density (Fig. 9). The specimen from the back of the billet contains only small outcrops of subgrains located at high-angle grain boundaries and intergranular dislocation walls. These subgrains and dislocation wall formations are most probably remnants from compression during the upsetting stage. Although this deformation is not detectable in the macrosections it is clear that compressive flow must occur throughout the billet during the initial ram contact. Proof that large strain gradients are associated with high-angle grain boundaries is shown in Fig. 10. This depicts a section of high-angle grain boundary involving a bend through 90°. Subgrains which are formed heterogeneously at high-angle grain boundaries can be seen to be much better defined along the boundary aligned parallel to the billet axis (and the vertical axis of the micrograph and at the grain extremity than along the segment at right angles to it. The latter is a region of much smaller strain gradient. Tilting experiments showed that this is a genuine effect and not due simply to a particular set of imaging conditions being employed.

Samples inspected from the steady-state position (Location 7) revealed equiaxed subgrain structures. In Locations A and B the subgrains were of uniform size but Location C included smaller subgrains at high-angle boundaries. Presumably this phenomenon is associated with a less acute breakdown of original structure than has occurred at later stages in the deformation zone, i.e. Locations A and B. Original high-angle grain boundaries were impossible to find in the deformation zone exit region because of the intense deformation history of the material in

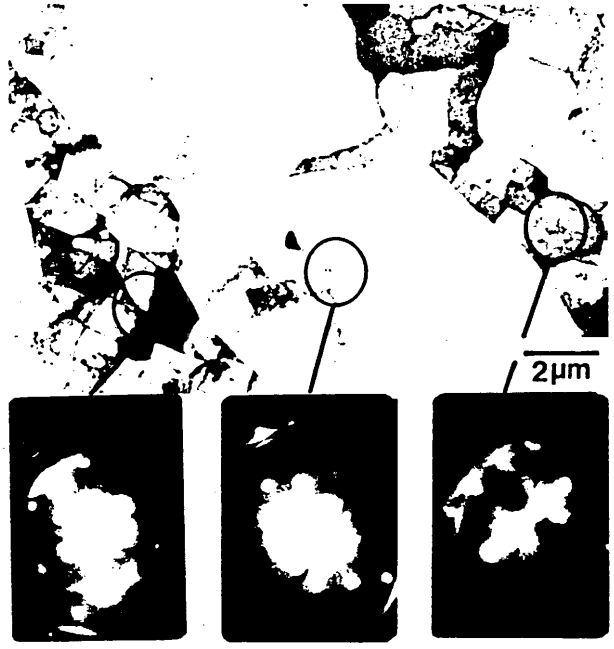


4 Subgrain formation at high-angle grain boundary (which runs from left to right across top of micrograph) during initial upsetting of billet. Sample taken from Position C in billet where general subgrain formation is not observed at this stage of deformation.

that location. Typical structures are illustrated in Fig. 11. The dislocation density within subgrains is higher at the deformation zone exit than at Position C which is consistent with the very rapid increase in strain rate (and hence strain) which occurs in that region.[12]

Extrudate structure

The extruded structure exhibited a fibrous type core consisting of equiaxed subgrains surrounded by an annulus of recrystallized grains containing no substructure. The recrystallized grain boundaries could be seen to be pinned at some locations by precipitates at triple points. This duplex structure is produced because much higher strains are imposed upon the material fed to the surface layers and these provide a driving force for recrystallization which is not present in the central regions of the extrudate. Nucleation probably originates at subgrain boundaries and must involve rapid subgrain coalescence and subgrain boundary migration. In the commercial alloy this process would be aided by additional sites available at second-phase particles but in this superpurity-base system there is a very low volume fraction of precipitates.



6 Deformation bands containing subgrains formed in large grain. Sample taken from Position A in billet at Location 2 on load/displacement curve. Selected-area diffraction patterns from the three areas indicated all have zone axis very close to ⟨112⟩ but central band is rotated by 33° about this axis with respect to its neighbours.

Subgrain misorientation

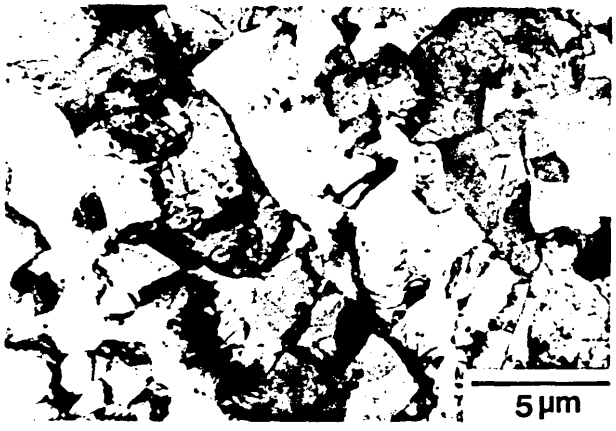
Misorientation between subgrains was established by analysis of selected-area diffraction patterns and associated Kikuchi lines using standard techniques. The subgrain misorientation depends not only upon the extent of deformation at the selected site and the position of that site but also upon the presence of heterogeneities such as grain boundaries, shear bands, and second-phase particles. Misorientations measured are shown in Table II which also provides information on the type of site at which the observation was made. For detailed analysis a substantially greater number of measurements would clearly be required.



5 Bands of elongated subgrains formed in material at die mouth (Position A) during initial upsetting of billet (Location 1 in load/extension curve).



7 Elongated subgrains containing very high dislocation density observed at die mouth at peak pressure. Dynamic recovery is incomplete.



8 Equiaxed subgrains within deformation bands in sample taken from the same position as that in Fig. 7 but at Location 6 in the load/displacement curve when steady state deformation is attained.

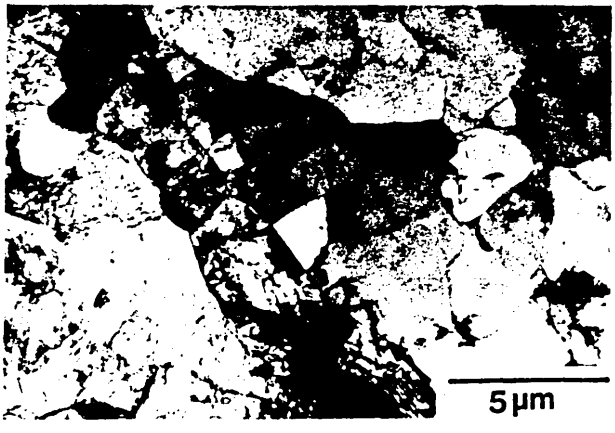


10 Specimen taken from the back of the billet at Location 6 in the load/displacement curve. Deformation in this zone is still limited although steady state deformation has essentially been attained.

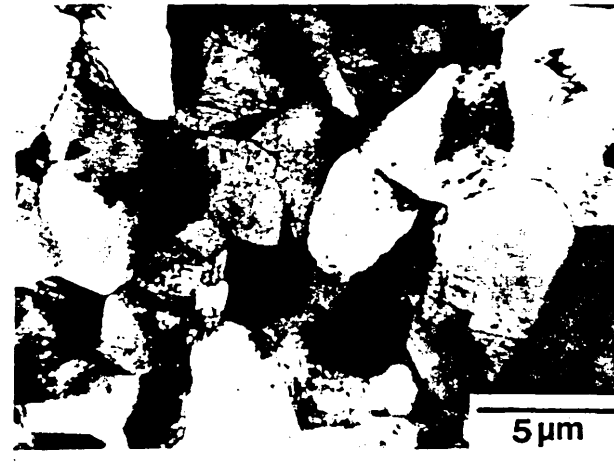
However, there is an increase in misorientation with increased deformation at any given position in a billet and misorientation also increases from entry to exit of the deformation zone. The maximum misorientation observed was about 4° which is much greater than that observed by Raybould and Sheppard[13] but supports their view that the idea of some constant misorientation is erroneous.

Subgrain size

Subgrain sizes were measured by an intercept method and the values listed are the mean of at least five readings incorporating about 100 subgrains. Table III notes those cases where subgrains were found only at grain boundaries. Since average strain rates must increase greatly throughout the ram stroke and in addition must be very low at the rear of the billet (due to compression only) these observations are consistent with the concept that the subgrain size is dependent upon the temperature-compensated strain rate Z. However, there is no noticeable change in subgrain size when moving from Position C to Position A in any of the billets. This is somewhat surprising since we would expect[12] the strain rate to vary by a factor of about two during this period. This will also produce a temperature rise and in general $\ln Z$ would be expected to decrease, perhaps by an order of magnitude, between Locations C and A. Some difference in subgrain size should therefore be detected. It is clear that the equation of state relating Z to subgrain size must therefore be violated in this region, and this perhaps explains why so many workers have obtained excellent substructural correlations using initial extrusion conditions[14] or models based upon bulk temperature rise and average strain rates.[15] It is clear that the substructure cannot change as rapidly as any equation of state would dictate and it is not sufficient to propose a model which does not include time as a variable. Moreover, there must therefore be a critical rate of change of Z or $\ln Z$ beyond which the equation of state cannot be observed. If, for example, at entry to the deformation zone the material contains larger subgrains with low density walls (as has been observed) and at exit contains smaller subgrains with



9 Sample containing high-angle grain boundary (arrowed) taken from the same location and position in the load/displacement curve as Fig. 8. Comparison of the two micrographs shows that once steady state deformation is achieved the microstructure becomes much more uniform.



11 Typical subgrain and dislocation structure observed during steady state extrusion. Sample taken from Position B in billet at Location 7 in load/displacement curve.

Table II Subgrain misorientations

Specimen code	Misorientation, degrees	Remarks
6A	3·7	Across subgrain band
	2·0	Along subgrain band
6D	0·6	General
5B	0·7	General
	0·8	General
	0·9	General
3E	1·4	General
2A	3·25	Across subgrain band
	4·0	Across subgrain band
	1.6	Across subgrain band
	1·4	Across subgrain band
2B	1·7	Near high-angle grain boundary
	2·2	Away from high-angle grain boundary
2C	0·5	General
	0·3	General
1B	0·1	General
	0·25	General
1E	0·25	General

high density walls and some internal dislocation density then rearrangement is necessary as an element passes through the deformation zone. The final subgrains were in general equiaxed and the number of subgrains at exit is unlikely to be a number which would integrally fit the subgrain size pertaining at entry to the deformation zone. Therefore, at each step during continuous deformation considerable adjustment must be required. This clearly implies that any equation of state must be sensitive to the rate of change of strain and must include at least a limiting time factor.

Development of dislocation structure related to peak pressure

The general reduction of pressure during the extrusion process has always been attributed to the reduction in friction as the billet length decreases. The pressure curves observed for this alloy indicate that the reduction in pressure is so non-linear that this explanation cannot be justified. Castle and Sheppard[6] showed that the peak increased as extrusion rates increased and was reduced by increasing initial temperature. The relationship between peak pressure and temperature was shown to be of an Arrhenius type with an activation energy of about 160 kJ mol^{-1} which is close to the activation energy for bulk self-diffusion in aluminium. The results indicate strongly that the peak is controlled by thermally activated events involving the production, interaction, and annihilation of dislocations.

The work reported here indicates that dislocation generation and motion commences and spreads from the die entry as the pressure is applied. Dislocation density increases rapidly as a consequence of the interaction of mobile dislocations with each other and with dislocations stored within grains. These latter dislocations are a necessary consequence of the strain gradients which exist both on a macroscopic scale (e.g. between the deformation zone and regions of undeformed material) and on a microscopic scale i.e. across grain boundaries at which multiple slip is required from the start of deformation in order for the grains to remain conterminous. Dislocation density increases most rapidly in these regions in which strain and strain gradients are highest. Grain boundaries, at which dislocations are generated, are necessarily such sites. Eventually the stored dislocation density achieves a magnitude such that recovery by cross-slip and climb occurs resulting in the formation of subgrains. This mechanism is consistent with the observation that subgrains are first observed at grain boundaries and at high strain regions near the die entry. As extrusion proceeds the deformation extends backwards to form the deformation zone and isolated subgrain outcrops are observed progressively further back in the billet. In the later stages of extrusion when steady state conditions obtain the generation and annihilation of dislocations are in balance so that recovery and subgrain formation ensure zero work-hardening effects. At this stage subgrains are equiaxed and constant in size and misorientation. It should be recalled that in the earlier stages of deformation subgrain walls are ragged and elongated in the extrusion direction and the cells contain a high internal dislocation density.

At peak pressure the steady state deformation zone is not fully established but this condition is achieved by the time the pressure has diminished by an amount equal to the additional increment required. Considering the necessary fact that changes in substructure require finite time intervals it is clear that the pressure peak is required to effect the establishment of the quasi-static deformation zone. A side-effect is quite obviously that a quasi-static dead-metal zone is also formed. Hence it is not surprising that the pressure peak is associated with an activation energy similar to that for bulk self-diffusion and for creep since the climb of dislocations is the controlling process in each case.

Table III Subgrain sizes

Specimen code	Subgrain size, μm	Remarks
7A	2·40	General
7B	2·54	General
7C	2·36	General
6A	2·08	General
6B	2·60	General
6C	2·98	General
6D	1·37	Across subgrain band
6D	2·60	Along subgrain band
6E	11·50	Not typical
5A	2·6	General
5B	2·24	General
5C	2·3	General
3A	2·9	General
3B	2·69	General
3E	1·53	At high-angle grain boundary
2A	1·41	Across subgrain band
1A	0·85	Across subgrain band
1A	3·6	Within subgrain band
1D	2·77	At high-angle grain boundary

Subgrain banding

Banding of subgrains was observed in specimens taken before the peak pressure in regions where deformation was greatest. Misoreintation was greater across the bands than along them while subgrain size was greater along it than across it. Studies of diffraction patterns show very large rotations across the bands. Starting within one band with a set diffraction pattern, this changed on moving into the next band but then returned to the original pattern in the following band and so on. In Fig. 6, for example, a rotation of 33° about a ⟨112⟩ direction was observed between bands. Similar banding has been observed previously by a number of workers. For example, Rhines[16] has shown qualitatively similar bands in aluminium deformed in creep and suggested that they form when deformation of a pair of grains is possible in only one direction. To accommodate the shape change, one grain must deform by the alternating slting of bands running across the crystal. Such a situation can readily be envisaged in the early stages of extrusion of a large-grained material. Dillamore *et al.*[17] also considered the possibility that local differences in stress state produce varying strains within a crystal causing a relative rotation between segments of the grain. This would be true in the case of extrusion because of the inhomogeneous stress states in the die mouth region during upsetting. The situation is further worsened by the large original grain size and variation in grain size in the billets which tend to permit greater strain gradients. The banding observed in this work is almost certainly due to the necessity to accommodate strain sizes of widely varying magnitude in the die entry region. The large misorientation between the bands is similar to misorientations encountered across high-angle grain boundaries; thus, dislocation activity is enhanced in these regions, leading to the early formation of subgrains and propagation of the subgrain structure into the grain interiors.

CONCLUSIONS

1. The quasi-static deformation zone is not fully established until a short time after the peak pressure is attained which implies that an additional increment of pressure is required to establish this zone.

2. Conclusion 1 suggests that the peak pressure is associated with the ease of dislocation mobility and should therefore be alloy dependent, varying with volume fraction precipitate size, second-phase particles, etc.

3. There is no deformation of any consequence at the rear of the billet until steady state is achieved.

4. The softening process in this alloy system is dynamic recovery producing a stable equiaxed subgrain structure of approximately constant size and misorientation.

5. Subgrain banding occurs in the die entry region during upsetting and is a result of inhomogeneous deformation. This is probably aided by large grain sizes and heterogeneous grain size distribution.

ACKNOWLEDGEMENTS

The authors gratefully acknowledge the help and co-operation of Alcan International Ltd who supplied the material used in this work.

REFERENCES

1. W. R. D. WILSON: *Int. J. Mech. Sci.*, 1971, **13**, 17.
2. W. ZIEGLER and K. SIEGERT: *Z. Metallkd.*, 1973, **64**, 224.
3. K. ASHCROFT and D. LAWSON: *J. Inst. Met.*, 1960, **89**, 369.
4. M. FARAG and C. M. SELLARS: *ibid.*, 1973, **101**, 137.
5. B. AVITZUR: 'Metalforming: process and analysis', **1968**: New York (McGraw-Hill).
6. A. F. CASTLE and T. SHEPPARD: *Met. Technol.*, 1976, **3**, 465.
7. W. WONG, H. McQUEEN, and J. JONAS: *J. Inst. Met.*, 1967, **95**, 129.
8. J. JONAS, C. M. SELLARS, and W. McTEGART: *Metall. Rev.*, 1969, **130**, 7.
9. H. McQUEEN and J. HOCKETT: *Metall. Trans.*, 1970, **1**, 2997.
10. P. B. HIRSCH: 'The Physics of Metals', Vol. 2. **1975**: Cambridge (University Press).
11. D. RAYBOULD: PhD thesis, University of London, 1971.
12. T. SHEPPARD, H. B. McSHANE, and M. G. TUTCHER: *Powder Metall.*, 1978, **21**, 47.
13. D. RAYBOULD and T. SHEPPARD: *J. Inst. Met.*, 1973, **101**, 45.
14. H. J. McQUEEN, W. A. WONG, and J. J. JONAS: *Can. J. Phys.*, 1967, **45**, 12225.
15. T. SHEPPARD and A. F. CASTLE: *Met. Technol.*, 1976, **2**, 433.
16. F. N. RHINES: 'The inhomogeneity of plastic deformation', chapter 10. **1973**: Metals Park, Ohio (ASM).
17. I. L. DILLAMORE, P. L. MORRIS, C. J. E. SMITH, and W. B. HUTCHINSON: *Proc. R. Soc.*, 1972, **A329**, 405.
18. F. J. HUMPHREYS: *Acta Metall.*, 1977, **25**, 1323.

© THE METALS SOCIETY 1979